

به نام خدا



مرکز دانلود رایگان مهندسی متالورژی و مواد

www.Iran-mavad.com



Advances in the Bonded Composite Repair of Metallic Aircraft Structure

VOLUME 1



Edited by

Alan Baker

Francis Rose

Rhys Jones

www.iran-mavad.com

مرجع دانشجویان و مهندسين مواد

ELSEVIER

ADVANCES IN THE BONDED COMPOSITE REPAIR OF METALLIC AIRCRAFT STRUCTURE

Volume 1

Elsevier Science Internet Homepage - <http://www.elsevier.com>

Consult the Elsevier homepage for full catalogue information on all books, journals and electronic products and services.

Elsevier Titles of Related Interest

VALERY V. VASILEV & EVGENY V. MOROZOV

Mechanics and Analysis of Composite Materials

ISBN: 0 08 042702 2

JANG-KYO KIM & YIU WING MAI

Engineered Interfaces in Fiber Reinforced Composites

ISBN: 0 08 042695 6

J.G. WILLIAMS & A. PAVAN

Fracture of Polymers, Composites and Adhesives

ISBN: 0 08 043710 9

D.R. MOORE, A. PAVAN & J.G. WILLIAMS

Fracture Mechanics Testing Methods for Polymers Adhesives and Composites

ISBN: 0 08 043689 7

Related Journals:

Composite Structures - www.elsevier.com/locate/compstruct

Composites Part A: Applied Science and Manufacturing - www.elsevier.com/locate/compositesa

Composites Part B: Engineering - www.elsevier.com/locate/compositesb

Composites Science and Technology - www.elsevier.com/locate/compscitech

Major Reference Work:

Comprehensive Composite Materials - www.elsevier.com/locate/isbn/0080429939

To contact the Publisher

Elsevier Science welcomes enquiries concerning publishing proposals: books, journal special issues, conference proceedings, etc. All formats and media can be considered. Should you have a publishing proposal you wish to discuss, please contact, without obligation, the publisher responsible for Elsevier's Composites and Ceramics programme:

Emma Hurst
Assistant Publishing Editor
Elsevier Science Ltd
The Boulevard, Langford Lane
Kidlington, Oxford
OX5 1GB, UK

Phone: + 44 1865 843629
Fax: + 44 1865 843931
E.mail: e.hurst@elsevier.com

General enquiries, including placing orders, should be directed to Elsevier's Regional Sales Offices – please access the Elsevier homepage for full contact details (homepage details at the top of this page).

Book Butler logo to search for more Elsevier books, visit the Books Butler at <http://www.elsevier.com/homepage/booksbutler/>

ADVANCES IN THE BONDED COMPOSITE REPAIR OF METALLIC AIRCRAFT STRUCTURE

Volume 1

Editors

A.A. Baker

*Defence Science and Technology Organisation,
Air Vehicles Division,
Victoria, Australia*

L.R.F. Rose

*Department of Defence,
Defence Science and Technology Organisation,
Air Vehicles Division,
Victoria, Australia*

R. Jones

*Mechanical Engineering Department,
Monash University, Victoria, Australia*



2002

ELSEVIER

Amsterdam – Boston – London – New York – Oxford – Paris
San Diego – San Francisco – Singapore – Sydney – Tokyo

www.iran-mavad.com

مرجع دانشجویان و مهندسين مواد

ELSEVIER SCIENCE Ltd
The Boulevard, Langford Lane
Kidlington, Oxford OX5 1GB, UK

© 2002 Elsevier Science Ltd. All rights reserved.

This work is protected under copyright by Elsevier Science, and the following terms and conditions apply to its use:

Photocopying

Single photocopies of single chapters may be made for personal use as allowed by national copyright laws. Permission of the Publisher and payment of a fee is required for all other photocopying, including multiple or systematic copying, copying for advertising or promotional purposes, resale, and all forms of document delivery. Special rates are available for educational institutions that wish to make photocopies for non-profit educational classroom use.

Permissions may be sought directly from Elsevier Science via their home page (<http://www.elsevier.com>), by selecting 'Customer support' and the 'Permissions'. Alternatively you can send an e-mail to: permissions@elsevier.co.uk, or fax to: (+44) 1865 853333.

In the USA, users may clear permissions and make payments through the Copyright Clearance Center, Inc., 222 Rosewood Drive, Danvers, MA 01923, U.S.A.; phone (+1) 978 750 8400, fax: (+1) 978 750 4744, and in the UK through the Copyright Licensing Agency Rapid Clearance Service (CLARCS), 90 Tottenham Court Road, London W1P 0LP; phone (+44) 207 631 5555; fax: (+44) 207 631 5500. Other countries may have a local reprographic rights agency for payments.

Derivative Works

Tables of contents may be reproduced for internal circulation, but permission of Elsevier Science is required for external resale or distribution of such material.

Permission of the Publisher is required for all other derivative works, including compilations and translations.

Electronic Storage or Usage

Permission of the Publisher is required to store or use electronically any material contained in this work, including any chapter or part of a chapter.

Except as outlined above, no part of this work may be reproduced, stored in a retrieval system or transmitted in any form or by any means, electronic, mechanical, photocopying, recording or otherwise, without written permission of the Publisher.

Address permission requests to: Elsevier Science Global Rights Department, at the mail, fax and email addresses note above.

Notice

No responsibility is assumed by the Publisher for any injury and/or damage to persons or property as a matter of products liability, negligence or otherwise, or from any use or operation of any methods, products, instructions or ideas contained in the material herein. Because of rapid advances in the medical sciences, in particular, independent verification of diagnosis and drug dosages should be made.

First Edition 2002

Library of Congress Cataloging in Publication Data

A catalog of record from the Library of Congress has been applied for.

British Library Cataloguing in Publication Data

A catalogue record from the British Library has been applied for.

ISBN: 0-08-042699-9

♾ The paper used for this publication meets the requirements of ANSI/NISO Z39.48-1992 (Permanence of Paper). Printed in The Netherlands.

BIOGRAPHIES

Dr. Alan Baker

Dr. Alan Baker is Research Leader Aerospace Composite Structures, in Airframes and Engines Division, Defence Science and Technology (DSTO), Aeronautical and Maritime Research Laboratory and Technical Adviser to the Cooperative Research Centre—Advanced Composite Structures, Melbourne Australia. He is a Fellow of the Australian Academy of Technological Sciences and Engineering and an Adjunct Professor in Department of Aerospace Engineering, Royal Melbourne Institute of Technology. Dr. Baker is a member of the International Editorial Boards of the Journals Composites Part A Applied Science and Manufacturing, Applied Composites and International Journal of Adhesion and Adhesives.

He is recognised for pioneering research work on metal-matrix fibre composites while at the Rolls Royce Advanced Research Laboratory. More recently, he is recognised for pioneering work on bonded composite repair of metallic aircraft components for which he has received several awards, including the 1990 Ministers Award for Achievement in Defence Science.

Dr. Francis Rose

Dr. Francis Rose is the Research Leader for Fracture Mechanics in Airframes and Engines Division, Defence Science and Technology (DSTO), Aeronautical and Maritime Research Laboratory. He has made important research contributions in fracture mechanics, non-destructive evaluation and applied mathematics. In particular, his comprehensive design study of bonded repairs and related crack-bridging models, and his contributions to the theory of transformation toughening in partially stabilised zirconia, have received international acclaim. His analysis of laser-generated ultrasound has become a standard reference in the emerging field of laser ultrasonics, and he has made seminal contributions to the theory of eddy-current detection of cracks, and early detection of multiple cracking.

He is the Regional Editor for the *International Journal of Fracture* and a member of the editorial board of *Mechanics of Materials*. He was made a Fellow of the Institute of Mathematics and its Applications, UK, in 1987, and a Fellow of the Institution of Engineers, Australia, in 1994. He is currently President of the Australian Fracture Group, and has been involved in organising several local and international conferences in the areas of fracture mechanics and engineering mathematics. He currently serves on the Engineering Selection Panel of the Australian Research Council and of several other committees and advisory bodies.

Professor Rhys Jones

Professor Rhys Jones joined Monash University in early 1993 and is currently Professor of Mechanical Engineering, and Head of the Defence Science and Technology Organisation Centre of Expertise on Structural Mechanics. Professor Jones' is best known for his in the fields of finite element analysis, composite repairs and structural integrity assessment. Professor Jones is the Founding Professor of both the BHP-Monash Railway Technology Institute and the BHP-Monash Maintenance Technology Institute. He is heavily involved with both Australian and overseas industry. In this context he ran the mechanical aspects of the Australian Governments Royal Commission into the failure at the ESSO plant in Victoria, and the Tubemakers-BHP investigation into the failure of the McArthur River gas pipe line in the Northern Territory.

He is the recipient of numerous awards including the 1982 (Australian) Engineering Excellence Award, for composite repairs to Mirage III, the Institution of Engineers Australia George Julius Medal, for contributions to failure analysis, a TTCP Award, for contributions to Australian, US, UK, Canada and NZ Defence Science in the field of composite structures, and a Rolls-Royce-Qantas Special Commendation, for his work on F-111 aircraft. Since 1999 Professor Jones has been Co-Chair of the International Conference (Series) on Composite Structures.

Acknowledgement

The editors are very pleased to acknowledge their appreciation of the great assistance provided by Drs Stephen Galea and Chun Wang of the Defence Science and Technology Organisation, Aeronautical and Maritime Research Laboratory, who made important contributions, in the collation and editing of this book.

FOREWORD

The introduction of the technology for bonded composite repairs of metallic airframe structures could not have come at a more opportune time. Today, many countries are facing the challenge of aging aircraft in their inventories. These airframes are degrading due to damage from fatigue cracking and corrosion. Repair with dependable techniques to restore their structural integrity is mandatory. The concept of using bonded composite materials as a means to maintain aging metallic aircraft was instituted in Australia approximately thirty years ago. Since that time it has been successfully applied in many situations requiring repair. These applications have not been limited to Australia. Canada, the United Kingdom, and the United States have also benefited from the use of this technology. The application for the solution of the problem of cracking in the fuel drain holes in wing of the C-141 is credited with maintaining the viability of this fleet.

The concept for composite repair of metallic aircraft is simple. The bonded repair reduces stresses in the cracked region and keeps the crack from opening and therefore from growing. This is easy to demonstrate in a laboratory environment. It is another thing to do this in the operational environment where many factors exist that could adversely affect the repair reliability. The researchers at the Aeronautical and Maritime Research Laboratory in Australia realized there were many obstacles to overcome to achieve the desired reliability of the process. They also realized that failures of the repair on operational aircraft would mean loss of confidence and consequently enthusiasm for the process. They proceeded slowly. Their deliberate approach paid off in that they developed a process that could be transitioned to aircraft use by engineers and technicians. The essential ingredient for application of this technology is discipline. When the applicator of this process maintains the discipline required for the process and stays within the bounds of appropriate applications, then the repair will be successful.

This book, edited by Drs A.A. Baker, L.R.F. Rose and R. Jones, includes the essential aspects of the technology for composite repairs. The editors have chosen some of the most knowledgeable researchers in the field of bonded repairs to discuss the issues with the many aspects of this technology. Included are discussions on materials and processes, design of repairs, certification, and application considerations. These discussions are sufficiently in-depth to acquaint the reader with an adequate understanding of the essential ingredients of the procedure. The application case histories are especially useful in showing the breadth of the possible uses of the technology.

It is easy to be excited about the future of composite repairs to metallic airframes. It has all the ingredients for success. Today's applications have shown that it is reliable, there is typically a significant return on the investment, and it can be transitioned to potential users. Additional research will open up possible new applications.

This book is intended to provide the reader with a good understanding of the basic elements of this important technology. It fulfills that purpose.

John W. Lincoln
Technical Adviser for Aircraft Structural Integrity
United States Air Force

DEDICATION

The Editors would like to dedicate these volumes to Dr J.W Lincoln who passed away a few months after he wrote this foreword. Jack's outstanding contributions to the many fields related to the structural airworthiness of aircraft are legend and need not be repeated here. He was very supportive of the work on bonded repair technology, as indicated in the foreword, and, indeed, was the Chairman of an international group addressing certification issues. This report is referenced in Chapter 1.

It is rare to find in science and engineering, such a giant in the field who was so modest, approachable and friendly. Jack was regarded both as a supportive father figure and the expert to be convinced on all airworthiness issues, particularly as related to the USAF.

DEFAULT NOMENCLATURE

Boron/epoxy	<i>b/ep</i>	graphite/epoxy	<i>gr/ep</i>
Shear modulus (also used for strain energy release rate)	<i>G</i>	Young's modulus	<i>E</i>
Characteristic crack length	λ	Poissons ratio	ν
Stress intensity	<i>K</i>	Crack length	<i>a</i>
Cycles	<i>N</i>	Disbond length	<i>b</i>
Paris Coefficient	<i>A</i>	Paris Exponent	<i>n</i>
Shear stress	τ	Stress	σ
Shear strain	γ	Strain	<i>e</i>
Thickness	<i>t</i>	Displacement	<i>u or \delta</i>
Length	<i>L</i>	Thickness	<i>t</i>
Width	<i>W</i>	Applied load	<i>P</i>
Elastic shear strain exponent	β	Force per unit width	<i>F</i>
Inclusion factor	ϕ	Stiffness ratio	<i>S</i>
Stress Ratio	<i>R</i>	Thermal expansion coefficient	<i>\alpha</i>
Angle	θ	Temperature range	ΔT

SUBSCRIPTS/SUPERSCRIPTS

Panel	<i>P</i>	Plastic condition	<i>p</i>
Elastic condition	<i>e</i>	Maximum value	<i>max</i>
Ultimate value	<i>u</i>	Minimum value	<i>min</i>
Adhesive	<i>A</i>	Outer adherend	<i>o</i>
Temperature	<i>T</i>	Inner adherend	<i>i</i>
Value at infinity	∞	Allowable value	*
Critical value	<i>c</i>		
Reinforcement	<i>R</i>		

CONTENTS

Biographies	v
Foreword	vii
Dedication	ix

Volume 1

Chapter 1. Introduction and Overview	1
A.A. Baker	
1.1. Aim of book	1
1.2. Classification of aircraft structures for inspection and repair	2
1.2.1. Design and certification of airframe structures	2
1.2.2. Problems with ageing metallic airframe components	3
1.3. Repair requirements	5
1.3.1. Repair levels	6
1.4. Repair procedures	6
1.5. The case for adhesively bonded repairs	7
1.6. Composite versus metallic patches	9
1.7. Scope of applications	10
1.8. Some experimental comparisons of bonding versus bolting	11
1.9. R&D requirements	14
1.10. Conclusion	17
References	17
Chapter 2. Materials Selection and Engineering	19
R. Chester	
2.1. Introduction	19
2.1.1. Factors affecting adhesion	20
2.2. Materials for patches and reinforcements	21
2.2.1. Metallic materials	21
2.2.2. Non-metallic materials	24
2.2.3. Patch material selection	26
2.3. Adhesive systems	28
2.3.1. Adhesive types	28
2.3.2. Adhesive properties	29
2.3.3. Adhesive selection	30
2.4. Primers and coupling agents	32
2.5. Adhesive and composite test procedures	34
2.6. Materials engineering considerations	35
2.6.1. Residual stresses	35
2.6.2. Cure pressure and voids	36
2.6.3. Spew fillet	38
2.6.4. Composites offer the possibility of embedded strain sensors to form "SMART" repairs	39
References	39

Chapter 3. Surface Treatment and Repair Bonding	41
D. Arnott, A. Rider and J. Mazza	
3.1. Introduction	41
3.1.1. Surface energy and wetting	41
3.1.2. Bondline pressurisation and adhesive cure	42
3.1.3. Adhesive bond performance	43
3.1.4. Standards and environments for adhesive bonding	44
3.2. Mechanical tests	45
3.2.1. Loading and failure modes	45
3.2.2. Qualification of bonding procedures and performance	46
3.3. Standard tests	47
3.3.1. Wedge durability test	47
3.3.2. Fracture mechanics and the cleavage specimen	48
3.4. Fundamentals of durable bonding	48
3.4.1. Surface roughness and bond durability	49
3.4.2. Surface hydration and bond durability	50
3.4.3. Surface contamination and bond durability	51
3.4.4. Bond durability model	53
3.5. Requirements of surface preparation	56
3.5.1. Degreasing	57
3.5.2. Abrasion, grit-blasting or etching	58
3.5.3. Creation of a high energy surface oxide	60
3.5.4. Coupling agent	61
3.5.5. Adhesive primer	63
3.5.6. Drying	63
3.6. Adhesive application	64
3.6.1. Factors controlling bondline thickness	65
3.6.2. Void formation and minimisation	65
3.7. Surface treatment quality control	66
3.7.1. Waterbreak Test	66
3.7.2. Surface work function methods	67
3.7.3. Fourier transform infrared spectroscopy	67
3.7.4. Optical reflectivity	68
3.7.5. Process control coupons (traveller or witness specimens)	68
3.7.6. Practitioner education, skill and standards	68
3.8. Surface preparations for aluminium adherends	69
3.8.1. Factory processes	69
3.8.2. On-aircraft acid anodisation and acid etch processes	72
3.9. Surface preparations for titanium adherends	74
3.9.1. Factory processes	74
3.9.2. On-aircraft processes	76
3.10. Surface preparations for steel adherends	77
3.10.1. Factory processes	77
3.10.2. On-aircraft processes	78
3.11. Surface preparations for thermosetting-matrix composites	78
3.11.1. Precured patches	80
3.12. Recent surface preparation research	80
3.12.1. Sol-Gel technology for adhesive bonding	80
3.12.2. Hot solution treatment for adhesive bonding	81
References	82

Chapter 4. Adhesives Characterisation and Data Base	87
P. Chalkley and A.A. Baker	
4.1. Introduction	87
4.2. Common ASTM and MIL tests	88
4.2.1. Stress-strain allowables	89
4.3. Fatigue loading	94
4.4. Fracture-mechanics allowables	94
4.4.1. Static loading	95
4.4.2. Mode I	95
4.4.3. Mode II and mixed mode	96
4.4.4. Fatigue loading	96
4.5. FM73 database	98
4.5.1. In situ shear stress-strain allowables	98
4.5.2. Yield criterion	99
4.5.3. The glass transition temperature	99
4.5.4. Fickian diffusion coefficients for moisture absorption	100
4.5.5. Mode I fracture toughness	100
References	101
 Chapter 5. Fatigue Testing of Generic Bonded Joints	 103
P.D. Chalkley, C.H. Wang and A.A. Baker	
5.1. Introduction	103
5.1.1. Damage-tolerance regions in a bonded repair	103
5.1.2. The generic design and certification process	104
5.2. The DOFS	104
5.2.1. Stress state in the DOFS	106
5.2.2. Experimental method	108
5.2.3. Experimental results	109
5.3. The skin doubler specimen	114
5.3.1. Stress state in the skin doubler specimen	115
5.3.2. Experimental method and results	120
5.3.3. Fracture mechanics approach	123
5.4. Discussion	124
References	125
 Chapter 6. Evaluating Environmental Effects on Bonded Repair Systems	 127
Using Fracture Mechanics	
L.M. Butkus, R.V. Valentin and W.S. Johnson	
6.1. Introduction	127
6.2. Materials and specimens	128
6.2.1. Bonded material system and fabrication	128
6.3. Experimental procedures	129
6.3.1. Pre-test environmental conditioning	129
6.3.2. Testing procedures	129
6.4. Analysis	131
6.5. Results and discussion	132
6.5.1. Fracture toughness	131
6.5.2. Fatigue behavior	134
6.6. Summary and conclusions	135
References	135

Chapter 7. Analytical Methods for Designing Composite Repairs	137
L.R.F. Rose and C.H. Wang	
7.1. Introduction	137
7.2. Formulation and notation	139
7.3. Load transfer of bonded reinforcement	141
7.4. Symmetric repairs	144
7.4.1. Stage I: Inclusion analogy	144
7.4.2. Stage II: Stress intensity factor	147
7.4.3. Plastic adhesive	149
7.4.4. Finite crack size	150
7.4.5. Finite element validation	154
7.5. Shear mode	155
7.6. One-sided repairs	157
7.6.1. Geometrically linear analysis	157
7.6.2. Crack bridging model	162
7.6.3. Geometrically non-linear analysis	163
7.7. Residual thermal stress due to adhesive curing	167
7.7.1. Temperature distribution	168
7.7.2. Residual stress due localised heating	170
7.7.3. Residual stresses after cooling from cure	171
7.7.4. Thermal stress due to uniform temperature change	173
7.7.5. Validation	173
References	174
 Chapter 8. Recent Expansions in the Capabilities of Rose's Closed-form Analyses for Bonded Crack-patching	 177
L.J. Hart-Smith	
8.1. Introduction	177
8.1.1. Rose's use of the inclusion model to establish stress fields	178
8.1.2. Rose's solution for stress-intensity factor K at the crack tips	180
8.2. Universal efficiency charts for isotropic patches	183
8.3. Equivalence between octagonal and elliptical patch shapes	184
8.4. Effects of patch tapering on the adhesive stresses	186
8.5. Universal charts for the effects of corrosion	189
8.6. Design of patches to compensate for corrosion damage	191
8.7. Analysis of patches over cracks in stiffened panels	192
8.8. Designing to avoid crack initiation	194
8.9. Universal efficiency charts for orthotropic patches	196
8.10. Effects of residual thermal stresses on bonded repairs	197
8.11. Effects of adhesive non-linearity and disbonds on crack-tip stress-intensity factors	200
8.11. Out-of-plane bending effects with one-sided patches	202
8.12. Remaining challenges involving closed-form analyses	204
8.13. Concluding remarks	204
References	205
 Chapter 9. Numerical Analysis and Design	 207
R. Jones	
9.1. Analysis and design	207
9.2. The 2D finite element formulation	208
9.2.1. Element stiffness matrix	210

9.2.2.	Repair of cracks in aircraft wing skin	212
9.3.	Initial design guidelines	215
9.4.	Comparison with experimental results for non rib stiffened panels	227
9.5.	Repair of thick sections	229
9.5.1.	Experimental results	231
9.6.	Repair of cracked holes in primary structures	233
9.7.	Repair of cracked lugs	236
9.7.1.	Numerical analysis	238
9.7.2.	Experimental test	240
9.7.3.	Discussion	241
9.8.	Repairs to interacting surface flaws	242
9.9.	Material nonlinearities	243
9.9.1.	Governing differential equations for bonded joints/repairs	245
9.10.	Effect of variable adhesive thickness	251
9.10.1.	The effect of variable adhesive thickness and material non-linearity	256
9.11.	Repairs to cracked holes under bi-axial loading	258
9.12.	Findings relevant to thick section repair	262
9.12.1.	Comparison of commercial finite element programs for the 3D analysis of repairs	264
	References	266
Chapter 10.	Shape Optimisation for Bonded Repairs	269
	M. Heller and R. Kaye	
10.1.	Introduction	269
10.1.1.	Context for finite element based shape optimisation	270
10.1.2.	Finite element modelling considerations	271
10.1.3.	Outline of chapter	271
10.2.	Analytical formulation for improved stepping in patch taper region	272
10.2.1.	General configuration for symmetric stepped patches	272
10.2.2.	Analysis for single step case	273
10.2.3.	Analysis for patch with multiple steps	274
10.2.4.	Estimate for optimal first step length	275
10.2.5.	Minimum bound for peak shear strain due to patch length	276
10.2.6.	Minimum bound for peak shear strain due to stiffness of first step	277
10.2.7.	Numerical examples	277
10.2.8.	Discussion	280
10.3.	FE analysis for adhesive stress and plate stress concentration	281
10.3.1.	Configuration and finite element analysis method	281
10.3.2.	Results for no-fillet case	283
10.3.3.	Results for fillet case	283
10.3.4.	Discussion of results	283
10.4.	Gradientless FE method for optimal through-thickness shaping	285
10.4.1.	Optimal adherend taper profile at the end of a bonded joint	286
10.5.	Sensitivity FE method for optimal joint through-thickness shaping	288
10.5.1.	Initial geometry, materials and loading arrangement	289
10.5.2.	Optimisation method	289
10.5.3.	Analysis for symmetric crack repair with aluminium patch	292
10.5.4.	Analysis for non-symmetric crack repair with boron/epoxy patch	294
10.6.	Optimal through-thickness shaping for F/A-18 bulkhead reinforcement	297
10.6.1.	Initial geometry, materials and loading arrangement	297
10.6.2.	Parameters for reinforcement optimisation analyses	298
10.6.3.	Stress results for optimal reinforcement designs	300

10.6.4.	Discussion	300
10.7.	Optimisation for F/A-18 aileron hinge reinforcement	300
10.7.1.	Initial geometry, materials and loading arrangement	303
10.7.2.	Shape optimisation before reinforcement	303
10.7.3.	Iterative reinforcement design	305
10.7.4.	Discussion	308
10.8.	In-plane shaping effects	308
10.8.1.	Geometry, loading and modelling considerations	308
10.8.2.	Determination of K_t from FEA output	309
10.8.3.	Uniaxial loading and patches with aspect ratios of 2:1	310
10.8.4.	Uniaxial loading and other patch aspect ratios	310
10.8.5.	Analogy with hole-in-a-plate problem.	311
10.8.6.	Stress reduction at the centre of the patch for uniaxially loaded plate	312
10.8.7.	Summary of results and discussion	312
10.9.	Conclusions	313
	References	314
Chapter 11.	Thermal Stress Analysis	317
	R.J. Callinan	
11.1.	Introduction	317
11.2.	Analytical expression for initial stresses in a circular plate due to heating	318
11.2.1.	Comparison of F.E. and analytic results	324
11.2.2.	Orthotropic solution	328
11.2.3.	Thermal stresses in a one-dimensional strip	330
11.2.4.	Peel stresses	332
11.2.5.	Coefficients of thermal expansion of a laminate	333
11.3.	Finite element thermal stress analysis	335
11.3.1.	Two-dimensional strip joints	337
11.3.2.	Three-dimensional strip joints	339
11.4.	Application of analysis to large repairs of aircraft wings	341
11.4.1.	F.E. analysis	343
11.4.2.	Edge restraint factor	346
11.5.	Conclusions	349
11.6.	Acknowledgment	350
	References	350
	Appendix	351
Chapter 12.	Fatigue Crack Growth Analysis of Repaired Structures	353
	C.H. Wang	
12.1.	Introduction	353
12.2.	Crack-closure analysis of repaired cracks	354
12.2.1.	Small-scale yielding	354
12.2.2.	Large-scale yielding solution for a stationary crack	357
12.2.3.	Plasticity induced crack closure under large-scale yielding solutions	361
12.3.	Overload effect and validation using finite element method	361
12.4.	Thermal residual stresses and comparison with experimental results	365
12.4.1.	Thermal residual stresses	365
12.4.2.	Experimental results under spectrum loading	367
12.5.	Conclusions	372
	References	373

Chapter 13. Boron/epoxy Patching Efficiency Studies	375
A.A. Baker	
13.1. Introduction	375
13.2. Stress intensity analysis of patched cracks	376
13.2.1. Model for estimating stress intensity	376
13.2.2. Use of model to estimate crack growth	378
13.2.3. Extension of the model for growth of disbond damage	379
13.3. Experimental approach	379
13.4. Fatigue studies	381
13.4.1. Disbond damage in the patch system	381
13.4.2. Influence of stress range	383
13.4.3. Influence of patch thickness	384
13.4.4. Influence of R ratio	384
13.4.5. Influence of temperature	386
13.4.6. Influence of panel thickness variation	387
13.4.7. Residual strength of patched panels	389
13.5. An approach to b/ep patch design	392
13.5.1. Cyclic loading	392
13.5.2. Spectrum loading	394
13.5.3. Check on residual strength	396
References	396
Chapter 14. Glare Patching Efficiency Studies	399
R. Fredell and C. Guijt	
14.1. Introduction	399
14.1.1. Overview and background of fibre metal laminates	399
14.2. Parametric studies of various patch materials	400
14.3. Experimental results	408
14.4. Discussion	410
14.5. Summary and conclusions	412
References	413
Chapter 15. Graphite/epoxy Patching Efficiency Studies	415
P. Poole	
15.1. Introduction	415
15.2. Repair of thin skin components	416
15.3. Repair of thick sections	418
15.4. Graphite/epoxy versus boron/epoxy	424
15.5. Effect of bondline defects	427
15.6. Effect of impact damage	433
15.7. Effect of service temperature	435
15.8. Effect of exposure to hot-wet environments	436
15.9. Repair of battle damage	438
15.10. Future work	440
15.11. Acknowledgements	440
References	441
Chapter 16. Repair of Multi-site Damage	443
R. Jones and L. Molent	
16.1. Introduction	443
16.2. Specimen and loading	444

16.2.1.	Boeing lap joints	444
16.2.2.	Airbus lap joints	449
16.3.	Repairs	450
16.3.1.	Repair philosophy	451
16.3.2.	Repair details	452
16.4.	Stress analyses	453
16.4.1.	Thermo-elastic analysis	453
16.4.2.	Finite element analyses	456
16.5.	Specimen fatigue test results	459
16.5.1.	Unreinforced baseline fuselage lap joint specimens	459
16.5.2.	Reinforced baseline fuselage lap joint specimens	464
16.5.3.	Environmental evaluation of repairs	464
16.5.4.	Hot/wet	465
16.5.5.	NaCl aqueous	466
16.6.	Damage tolerant evaluation of specimens	468
16.6.1.	Adhesive disbonds	468
16.6.2.	Impact damage	469
16.6.3.	Tension testing	472
16.7.	Full scale repair demonstrators	474
16.7.1.	Airbus A330/A340 fatigue test article	474
16.7.2.	Boeing 727, 747 and 767 in-flight demonstrators	477
16.7.3.	Doubler inspections	479
16.7.4.	Demonstrator summary	480
16.8.	Conclusions	480
	References	482
Chapter 17.	Damage Tolerance Assessment of Bonded Composite Doubler Repairs for Commercial Aircraft Applications	485
	D. Roach	
17.1.	Introduction	485
17.1.1.	Damage tolerance and fracture control plan	486
17.1.2.	Damage tolerance establishes fracture control plan	488
17.2.	Composite doubler damage tolerance tests	491
17.3.	Conformity inspection and FAA oversight	492
17.4.	Test results	500
17.4.1.	Fatigue tests	500
17.4.2.	Strain field measurements	506
17.5.	Conclusions	514
	References	515
Chapter 18.	Validation of Stress Intensity Estimations in Patched Panels	517
	B. Aktepe and A.A. Baker	
18.1.	Introduction	517
18.2.	The K -gauge	518
18.2.1.	K -gauge equations	518
18.3.	Theory of K_I measurement using strain gauges	519
18.3.1.	Westergaard equations	519
18.3.2.	Rose's inclusion model for stress intensity	521
18.3.3.	Wang's crack-bridging model	521
18.4.	Experimental procedure	522
18.5.	Strain surveys	524
18.5.1.	Unpatched specimen	524

18.5.2. Patched specimen	525
18.6. Crack length	526
18.7. Time-dependent behaviour	527
18.8. Conclusions	529
18.9. Nomenclature	529
References	530

Volume 2

Chapter 19. Bonded Repair of Acoustic Fatigue Cracking	531
R.J. Callinan and S.C. Galea	
19.1. Introduction	531
19.2. Cracking history	533
19.2.1. Inlet nacelle	533
19.2.2. Aft fuselage cracking	536
19.3. Sound pressure levels	536
19.3.1. Inlet nacelle	536
19.3.2. Aft fuselage	536
19.3.3. Power spectral density	537
19.4. Random response analysis	537
19.5. Stress intensity factors	538
19.6. FEA of cracked nacelle inlet	539
19.6.1. Crack growth study	540
19.6.2. Summary of repair failure investigation	546
19.7. Highly damped repairs for cracked panels	546
19.7.1. Design of highly damped patch	547
19.7.2. Damping of highly damped patch	547
19.7.3. Analysis of repaired cracked plate	551
19.7.4. Results and discussion	551
19.8. Aft fuselage finite element model	557
19.8.1. Modes and frequencies	558
19.8.2. Acoustic fatigue crack growth data	559
19.8.3. Residual thermal stresses	560
19.8.4. Damping data	561
19.8.5. Adhesive data	561
19.9. Thermal environment for F/A-18	562
19.10. Analytical results	563
19.11. Experimental work	566
19.12. Conclusions for aft fuselage repair	568
References	568
Chapter 20. Smart Patch Systems	571
S.C. Galea	
20.1. Introduction	571
20.2. Smart patch approach	573
20.3. Damage detection studies	578
20.3.1. Load transfer (strain) technique	578
20.3.2. Residual strain technique	588
20.3.3. Electro-mechanical impedance, transfer function and stress wave technique	593
20.3.4. Adhesive bond degradation sensors – active sensing technique	597
20.4. Laboratory smart patch conceptional demonstrators	599

20.5.	In-flight demonstrator	604
20.5.1.	Finite element analysis – damage sensing technique	604
20.5.2.	Health monitoring systems	607
20.6.	Conclusions	611
	References	612
Chapter 21.	Adhesively Bonded Repairs: Meeting the Safety Requirements Implied within Existing Aviation Industry Certification Regulations	615
	D. Bond	
21.1.	Introduction	615
21.2.	Certification of an adhesively bonded repair	617
21.2.1.	The need to certify a repair	617
21.2.2.	Adhesively bonded repairs	617
21.2.3.	Regulatory deficiencies	618
21.3.	Repair design information	619
21.3.1.	Existing requirements	619
21.3.2.	Additional guidance	621
21.4.	Analysis and development testing	621
21.4.1.	Design allowables	621
21.4.2.	Static analysis	626
21.4.3.	Fatigue and damage tolerance analysis	630
21.4.4.	Development testing	635
21.5.	Full scale testing	637
21.5.1.	Existing requirements	637
21.6.	In-service management and inspection	637
21.6.1.	Existing requirements	637
21.6.2.	Additional guidance	637
21.7.	Future approaches to bonded repair certification	638
21.8.	Conclusions	638
	References	639
Chapter 22.	Certification Issues for Critical Repairs	643
	A.A. Baker	
22.1.	Current limitations of crack patching	643
22.2.	Justifying credit for patching efficiency – fatigue concerns	644
22.2.1.	Influence of fatigue on patching efficiency	645
22.2.2.	Obtaining patch system fatigue allowables	646
22.2.3.	Validation of patching analysis	648
22.3.	Justifying credit for patching efficiency – environmental durability concerns	648
22.3.1.	Assurance of patch system environmental durability	650
22.3.2.	Australian experience on service durability	653
22.4.	Justifying credit for patching efficiency – the Smart Patch approach	654
22.5.	Discussion	655
22.6.	Conclusions	656
	References	656
Chapter 23.	Nondestructive Evaluation and Quality Control for Bonded Composite Repair of Metallic Aircraft Structures	659
	D.P. Roach and C.M. Scala	
23.1.	Introduction	659
23.1.1.	NDI needs and damage tolerance	660

23.1.2.	NDI assessments	663
23.2.	Inspection for delaminations, disbonds and adhesion failure	664
23.2.1.	Pulse-echo ultrasonics	665
23.2.2.	Through-transmission ultrasonics	679
23.2.3.	Guided waves	680
23.2.4.	Resonance test inspection method	683
23.2.5.	Thermography	685
23.2.6.	Other techniques	689
23.3.	Inspections for cracks in parent material beneath composite doublers	694
23.3.1.	Eddy-current inspections	694
23.3.2.	X-radiographic inspections	701
23.3.3.	Challenges in crack monitoring	703
23.4.	Quality control issues in service	714
23.4.1.	Quality assurance	714
23.4.2.	Use of realistic calibration standards	715
23.5.	Conclusions	719
23.6.	Acknowledgements	723
	References	724
Chapter 24.	Practical Application Technology for Adhesive Bonded Repairs	727
	M. Davis	
24.1.	Introduction	727
24.1.1.	Management of repair technology	730
24.2.	Repair application technology	730
24.2.1.	Materials selection	731
24.2.2.	Surface preparation	732
24.2.3.	Heating procedures for on-aircraft repairs	742
24.2.4.	Repair pressurisation	748
24.3.	Occupational health and safety (OHS)	750
24.3.1.	Solvents	751
24.3.2.	Grit	752
24.3.3.	Fibres	752
24.3.4.	Risks to aircraft	752
24.4.	Quality management	752
24.5.	Facilities	754
24.6.	Training and certification	755
24.7.	Deficient repair concepts	755
24.8.	Conclusion	757
	References	757
Chapter 25.	Rapid Application Technology: Aircraft Battle Damage Repairs	761
	R. Bartholomeusz, P. Pearce and R. Vodicka	
25.1.	Introduction	761
25.2.	Aircraft battle damage repair	762
25.2.1.	Battle damage	762
25.2.2.	ABDR criteria	763
25.2.3.	Types of ABDR	764
25.3.	Comparison of metallic mechanically fastened repairs to bonded composite repairs for ABDR	765
25.3.1.	Adaptation of bonded composite repairs for battle damage	766
25.3.2.	The composite laminating resin and adhesive	766
25.3.3.	Fibre	767

25.3.4.	Simplified design methods for ABDR	767
25.3.5.	Surface treatment	768
25.3.6.	Forming the bonded composite patch	768
25.3.7.	Mechanically fastened, metallic repair	769
25.3.8.	Fatigue and static testing of specimens	769
25.3.9.	Comparison of test results	769
25.4.	Development of a bonded composite ABDR system	771
25.4.1.	Resin development	772
25.4.2.	Repair durability, strength and surface treatment	773
25.4.3.	Mechanical properties	774
25.5.	Application of the DSTO/ABDR system	776
25.5.1.	Resin measurement, mixing and dispensing	776
25.5.2.	Pre-bonding surface treatment procedures	777
25.5.3.	Repair consolidation and application	777
25.5.4.	Heating procedures	777
25.5.5.	Vacuum moulding tool	778
25.6.	Conclusions	779
	References	779
Chapter 26.	Standardized Training and Certification for Bonded Repair Specialists	783
	Marty A. Smith	
26.1.	Introduction	783
26.1.1.	Benefits of improved training and process control – an example	783
26.2.	The task at hand – a uniform approach	784
26.2.1.	Advantages of standardization	784
26.2.2.	Building a database of reliable repairs – “We’re all in this together”	785
26.3.	Current approaches to training and certification	785
26.4.	Formalized trade structure	786
26.4.1.	The purpose of a trade structure	786
26.4.2.	A four-tiered trade structure – the ARTI model	786
26.5.	The ARTI model for training of bonded repair specialists	787
26.6.	Certification of bonded repair specialists	791
26.6.1.	The Boeing wedge test (BWT) – an accepted standard	791
26.6.2.	Administration of certification tests	793
26.7.	Conclusion	795
	References	795
Chapter 27.	Case History: F-111 Lower Wing Skin Repair Substantiation	797
	K.F. Walker and L.R.F. Rose	
27.1.	Introduction	797
27.2.	Crack location and residual strength	798
27.3.	Repair substantiation requirements	800
27.3.1.	Design load cases	800
27.3.2.	Fatigue loading	801
27.4.	Validation strategy	801
27.5.	Design validation (finite element analysis)	802
27.5.1.	Uncracked, unpatched wing model	802
27.6.	Cracked, patched model including thermal effects	803
27.7.	Repair substantiation (representative specimen testing)	805
27.7.1.	Representative bonded joints	805

27.7.2. Panel specimens	807
27.8. Box specimens	809
27.9. Repair history	809
27.10. Conclusion	811
References	811
 Chapter 28. Case History: Composite Doubler Installation on an L-1011 Commercial Aircraft D. Roach	 813
28.1. Introduction	813
28.2. Fuselage door surround structure tests	814
28.2.1. Full-scale structural testing philosophy	814
28.2.2. L-1011 fuselage structure	815
28.2.3. Repair of fuselage test article with a composite doubler	815
28.2.4. Biaxial test facility description	817
28.3. Fuselage door surround structure test results	819
28.3.1. Structural tests before composite doubler installation	819
28.3.2. Structural tests after composite doubler installation	820
28.3.4. Validation of finite element model analytical results	825
28.3.5. Nondestructive inspection	826
28.4. Component level tests: door corner specimen	826
28.4.1. Door corner test overview	826
28.4.2. Subsize door corner test results	828
28.5. L-1011 composite doubler installation	832
28.5.1. Composite doubler repair of L-1011 aircraft passenger door	832
28.5.2. Non-destructive inspection of door surround structure and composite doubler	836
28.5.3. Inspection intervals for L-1011 aircraft	839
28.5.4. Quality assurance measures	839
28.6. FAA and industry approvals	840
28.7. Conclusions	841
References	842
 Chapter 29. Case History: F-111 Wing Pivot Fitting Reinforcement R. Chester	 845
29.1. Introduction	845
29.2. Reinforcement design	846
29.3. Selection and evaluation of materials	849
29.4. Selection and evaluation of the reinforcement	850
29.4.1. Mechanical test evaluation	851
29.4.2. Cure characterisation and formability studies	851
29.4.3. Selection and evaluation of candidate adhesives	852
29.4.4. Selection and evaluation of surface treatment procedures	853
29.4.5. Modifications to doubler system	853
29.4.6. Residual stress minimisation	853
29.5. Doubler application technology	854
29.5.1. Temperature	854
29.5.2. Pressure	854
29.6. Doubler fitment	855
29.7. Fitment to fleet aircraft	856
29.8. Conclusions	857
References	858

Chapter 30. Case History: Bonded Composite Reinforcement of the F/A-18 Y470.5 Centre Fuselage Bulkhead	859
R.A. Bartholomeusz and A. Searl	
30.1. Introduction	859
30.1.1. Background	860
30.2. FE analysis of bulkhead and reinforcement	860
30.2.1. Results of the bulkhead FE analysis	862
30.2.2. Measurement of adhesive through-thickness stresses	862
30.3. FE design of representative specimen (curved beam specimen)	864
30.4. Experimental test program	864
30.4.1. Static testing of curved beam specimen	864
30.4.2. Durability testing of the curved beam specimen	865
30.4.3. Residual strength after fatigue	866
30.5. Trial installation of reinforcement to full-scale fatigue test article	866
30.6. Discussion	867
30.6.1. Pre ECP reinforcement	867
30.6.2. Post ECP reinforcement	868
30.7. Conclusions	869
30.8. Acknowledgments	869
References	869
Chapter 31. C-5A Fuselage Crown Cracking	871
C. Guijt and S. Verhoeven	
31.1. Introduction	871
31.2. Damage tolerance analysis	872
31.3. Repair options	874
31.4. Design of the bonded repair	875
31.5. FEM model of the patched crack	879
31.6. Conclusions	883
References	884
Chapter 32. Case History: F-16 Fuel Vent-hole Repairs	885
C. Guijt and J. Mazza	
32.1. Introduction	885
32.2. Damage tolerance analysis	885
32.3. Repair options	887
32.3.1. Mechanically fastened aluminum patch	888
32.4. Design of the bonded repair	889
32.4.1. Operating temperatures	890
32.4.2. Maximum operating temperature	890
32.4.3. Cumulative temperatures	891
32.5. Testing	892
32.5.1. Fatigue analysis of the aluminum doubler	892
32.6. Bonded repairs	892
32.6.1. Repair installation procedures	894
32.7. Conclusions	895
References	895
Chapter 33. Reinforcement of the F/A-18 Inboard Aileron Hinge	897
R. Chester	
33.1. Introduction	897

33.2.	Load cases	898
33.3.	Design and stress analysis	899
33.4.	Static testing and repair validation	903
33.5.	Certification and implementation to aircraft	905
33.6.	Conclusions	906
	References	906
Chapter 34.	UK Applications	907
	P. Poole	
34.1.	Introduction	907
34.2.	Design studies	908
34.3.	Repairs to RAF aircraft	909
	34.3.1. Secondary structure repairs	909
	34.3.2. Primary structure repairs	911
	34.3.3. Birdstrike protection	912
34.4.	Repairs to EH101 development airframe full scale fatigue test specimen	913
34.5.	Acknowledgements	918
	References	918
Chapter 35.	Case History: Repair Applications On DC-10/MD-11 Aircraft	919
	D. Roach	
35.1.	Introduction	919
35.2.	Repair development and validation tasks to support on-aircraft installation	921
	35.2.1. Repair design	921
35.3.	Repair analysis	921
35.4.	Repair design validation	926
35.5.	Nondestructive inspection	933
35.6.	Current status of DC-10/MD-11 commercial aircraft repairs	934
Chapter 36.	Case History: CF-116 Upper Wing Skin Fatigue Enhancement Boron Doubler	937
	D. Raizenne	
36.1.	Introduction	937
36.2.	Background	937
	36.2.1. Compression induced fatigue cracking	939
36.3.	Repair considerations	940
36.4.	Bonded composite doublers	941
36.5.	Doubler design and analysis	941
36.6.	Doubler manufacturing and installation procedures	946
	36.6.1. Doubler qualification testing	947
36.7.	Doubler fractographic analysis	949
36.8.	Fleet experience	951
36.9.	Discussion	954
36.10.	Conclusions	954
36.11.	Composite repair lessons learned	955
36.12.	Acknowledgements	956
	References	956
	Appendix A	957
	Material properties	957

Chapter 37. In-service Durability of Bonded Composite Repairs – Commercial Demonstrator Programs	959
R.A. Bartholomeusz and R.C. Geddes	
37.1. Introduction	959
37.2. Demonstrator doublers	960
37.2.1. QANTAS demonstrator program	960
37.2.2. Ansett keel beam reinforcement	962
37.3. In-service environment and repair location	962
37.3.1. Temperature	962
37.3.2. Foreign object damage.	963
37.3.3. Airflow and erosion	964
37.3.4. Aircraft fuels, hydraulics and lubricants	964
37.3.5. Miscellaneous	964
37.4. Bond durability and surface treatment	964
37.5. Case study results	965
37.5.1. QANTAS program	965
37.5.2. Ansett keel beam demonstrator reinforcement	968
37.6. Discussion and lessons learnt	970
37.6.1. Erosion protection by the use of shields	971
37.6.2. Repair location and design	971
37.6.3. Applicability of demonstrator programs	971
37.7. Conclusions	972
References	972
 Chapter 38. Case History: Bonded Composite Repair of A CH-47 Cargo Hook Beam	 973
B.J. Harkless, A.P. Kerr and M.A. Shupick	
38.1. Introduction	973
38.2. Defect description	973
38.3. Justification of approach	974
38.3.1. Loads analysis	975
38.3.2. Design loads	975
38.3.3. Static strength analysis	975
38.3.4. Fatigue analysis	977
38.3.5. Proof testing	977
38.4. Patch system and environmental protection	978
38.5. Repair procedure	978
38.6. Continuing airworthiness/inspection	979
References	979
 Chapter 39. Case History: Application of Bonded Repair Technology to Large Areas	 983
B. Harkless and A. Kerr	
39.1. Background	983
39.2. Examples of applicability to large areas	984
39.2.1. Full length rotor blade doublers	984
39.2.2. Large scale wing reinforcement	984
39.2.3. Large scale fuselage reinforcement	894
39.3. Current state of the technology	985
39.3.1. Critical features of the bonding process	985
39.3.2. Grit blast/silane process steps	986

39.4.	Process areas requiring adaptation	987
39.4.1.	Solvent scrubbing step	987
39.4.2.	Grit blast step	988
39.4.3.	Heating methods	988
39.5.	Large area repairs in a production environment	989
39.6.	Conclusions	994
	References	995
Chapter 40.	Case History: Composite Patch Reinforcement of T-38 Lower Wing Skin	997
	M.M. Ratwani, J. Helbling, B. Heimerdinger and N.M. Ratwani	
40.1.	Introduction	997
40.2.	Validation testing	999
40.2.1.	Test specimen description	999
40.2.2.	Composite reinforcement fabrication and bonding	1000
40.2.3.	Strain gage installation	1000
40.2.4.	Test spectrum and equipment	1001
40.3.	Test results	1001
40.3.1.	Strain gage results	1001
40.3.2.	Crack growth results	1003
40.4.	Comparison between test results and analytical predictions	1005
40.5.	Application of composite reinforcement to a full scale wing test	1007
40.6.	Conclusions	1007
	References	1008
Chapter 41.	Case Histories: Advanced Composite Repairs of USAF C-141 and C-130 Aircraft	1009
	W.H. Schweinberg and J.W. Fiebig	
41.1.	Background	1009
41.2.	Repair design	1012
41.3.	Installation development	1016
41.4.	Industrialization and repair	1014
41.5.	Success and failures	1017
41.6.	Other applications	1020
41.7.	Cost savings	1024
41.8.	Additional research	1025
41.9.	Lessons learned	1029
41.10.	Summary	1032
	References	1032
Chapter 42.	Case History: Bonded Composite Reinforcement of Ship Structures	1035
	I. Grabovac	
42.1.	Introduction	1035
42.2.	Materials development and characterisation	1038
42.3.	Installation of composite reinforcement	1042
42.4.	Reinforcement efficiency assessment	1044
42.5.	Service performance	1046
42.6.	Technology improvement	1047
42.7.	The current status – year 2000	1048
42.8.	Conclusion	1048

42.9. Acknowledgement	1049
References	1049
Index	1051

Chapter 1

INTRODUCTION AND OVERVIEW

A.A. BAKER

Defence Science and Technology Organisation, Air Vehicles Division, Fishermans Bend, Victoria 3207, Australia

1.1. Aim of book

In 1988 the book “Bonded Repair of Aircraft Structures” [1] was published. This book described the status of the technology, in the late 1980s, on bonded composite repair of conventional metallic, adhesively bonded metallic and fibre-composite airframe components. Because over the last fourteen years the technology has progressed considerably and become widely exploited, a decision was made to produce this follow-up book “Advances in Bonded Composite Repairs of Metallic Airframe Structure”.

This aim of this book is to provide a comprehensive coverage of the current research and technology highlighting advances in capabilities, and case histories of recent applications. It is intended to be useful both to researchers in the field and to practicing aerospace engineers.

Contributions to the book are largely drawn from the Defence Science and Technology Organisation, Australia, where this technology was pioneered in the early 1970s. Significant contributions are also provided by the USA Air Force (USAF), Sandia Laboratories of the USA, Defence Evaluation and Research Agency UK and the National Aeronautical Laboratory of Canada, reflecting the worldwide interest in this technology. As may be expected with ongoing R&D, these contributions often differ in technical approach and conclusions.

The purpose of this chapter is to set the scene for this book. To this end, a brief background is provided on structural problems in ageing aircraft and on the requirements for repairs. A case is then made for use of adhesively bonded composite (fibre-reinforced plastic or metal-laminate) reinforcements for repairs as compared to standard mechanical procedures, based on mechanically fastened

metallic patches. The requirements for future research and development are then discussed, based, in part, on a recent USAF study on ageing aircraft [2].

Before introducing repair issues, some brief background is provided in the next section on the key issues and terminology associated with the design and maintenance of airframe structures.

1.2. Classification of aircraft structures for inspection and repair

For the purpose of engineering management (including repairs) aircraft structures are generally classified as follows:

- **Primary structure:** a structure that is critical to the safety of the aircraft;
- **Secondary structure:** a structure that, if it were to fail, would affect the operation of the aircraft but not lead to its loss;
- **Tertiary structure:** a structure in which failure would not significantly affect operation of the aircraft.

Inspection, damage assessment, and repair requirements differ significantly between these classified structures. Even within a single component, the allowable damage type and size (and consequently acceptable repair actions) may vary according to the criticality of the damaged region. The component is generally zoned by the original equipment manufacturer (OEM) in the structural repair manual (SRM) to indicate these regions. Mainly, the SRM addresses repairs to non-primary structure or non-critical repairs to primary structure. Repairs outside the scope of the SRM, particularly repair of critical damage in primary structure, require engineering design and approval by the OEM (or its delegate).

1.2.1. Design and certification of airframe structures

Certification of airframe structure generally requires that the structure (by test and/or analysis) demonstrates the following capabilities:

- **Static strength:**
 - Design limit load (DLL) no failure or unacceptable deformations;
 - Design ultimate load (DUL) no failure, although permanent deformation is acceptable; $DUL = DLL \times 1.5$ (generally).
 - **Fatigue strength:**
 - Safe life approach – No cracking should occur in the life of the airframe that could lead to failure. This approach was used in design of most of the older fighter aircraft, and is still used for US Navy fighter aircraft, such as the F-18 and helicopters.
- Or
- Fail safe approach – The structure is damage tolerant in that cracking may occur but will not reduce strength below acceptable level before being detected. This requirement is generally met by multi-load-path design where should one load path fail the remaining load paths can continue to provide the required

level of residual strength until the damage is detected. This approach is generally used in the structure of large transport (and civil) aircraft.

Or

- Slow crack growth approach – The structure is damage tolerant in that cracking may occur but cracks will grow slowly and will not cause failure for the full life of the structure or before detection by planned inspection (safety by inspection). This approach can be applied to single-load-path structure, where failure would be catastrophic. Damage tolerant design for single-load-path structure is based on the assumed presence of flaws at critical locations. This is the design approach adopted for USAF fighter aircraft, such as F-16.

- **Damage tolerance general requirement:**

- The strength will not fall below an acceptable level (typically $1.2 \times \text{DLL}$) due to representative damage to the structure, e.g. caused by fatigue cracking, or corrosion or accidental mechanical contact before being detected. Critical damage must be of a size that can be detected with a high degree of probability.

- **Durability, economic requirement:**

- For the life of the airframe, damage requiring costly repairs will not occur for example, due to fatigue or corrosion.

Essentially, certification of a repair requires demonstration [3,4] that the repaired structure is as flight-worthy as the original structure, possibly allowing for life already consumed. According to the latest civil regulations, FAR 25.571, this demonstration must include damage-tolerant behaviour of the repaired structure, even if the original structure was designed on a safe-life basis.

1.2.2. Problems with ageing metallic airframe components

To minimise weight, metallic airframes are predominantly made of high-strength aluminium alloys. Steel and titanium alloys are also used but only where higher strength or temperature capabilities are required and the weight penalty can be accepted.

All metallic structures are prone to degradation by cracking and corrosion in service, particularly when design, manufacture or environmental protection is inadequate to meet actual serviced usage. In military aircraft fatigue cracking may be more of a problem than originally envisaged because of exposure to more severe usage (higher loading) than originally anticipated. Corrosion is a problem with older aircraft because of the use of susceptible alloys and inadequate corrosion-protective processes.

Because of limited budgets and escalating replacement costs, many military aircraft are being maintained in service well past their planned life. Thus these degradation problems are becoming a major operational and economic issue. For example, Australia is planning to maintain the F-111 in service until the year 2020, when it will be over 50 years old. Several aircraft in the USAF fleet, for example C-141 and B-52, are currently over 30 years old, most with no plans for replacement within the next 10–20 years.

Corrosion imposes a very high maintenance cost burden [2] for ageing airframes since many man-hours can go into its detection, treatment and eradication. Consequently corrosion, although generally not as critical structurally as fatigue cracking, may determine the economic life of the airframe.

Unfortunately, management of corrosion by the setting of inspection intervals is not always effective since the location of corrosion and its rate of growth are hard to predict. Management problems can be reduced when a history of occurrence for a particular airframe is obtained. Hidden corrosion in joints and faying surfaces is particularly difficult to detect and very costly to treat.

Damage caused by corrosion includes uniform section loss, pitting, exfoliation (grain boundary attack) and cracking. Other than stress-corrosion cracking, considered later, exfoliation and pitting are the most damaging to structural capability since they can result in extensive local loss of section and can initiate fatigue cracking. The implication of corrosion damage on structural integrity [5] is usually difficult to assess. In the absence of this capability, there is a tendency to remove excessive amounts of metal including much sound material. The current approach [6] is to quantify the corrosion damage (pitting) as an equivalent initial flaw, then use conventional fracture mechanics to predict its growth.

Cracks can arise from repeated loading (fatigue) or stress-corrosion. Stress-corrosion cracks arise in susceptible alloys (particularly thick 7000 series T6 forgings and machined, integrally stiffened plate) in the short-transverse grain direction from the combination of stress and adverse environment. The stresses can be internal arising during forming or externally caused, for example by forced fit or excessive use of oversized fasteners. Stresses caused by corrosion product trapped between layers can also result in stress-corrosion cracking. Fortunately, stress-corrosion cracks often lie parallel to the grain direction and thus the loading direction so may not constitute a major threat to structural integrity unless they initiate transverse fatigue cracks.

Fatigue cracks arise from highly localised cyclic plastic deformation caused by fluctuating service loads. These cracks pose the greatest threat to structural integrity since they grow perpendicularly to the applied load direction and eventually severing the load path.

Low-cycle fatigue cracks, caused by manoeuvre and gust loads, generally initiate from local regions of high surface stresses. These high stresses occur due to faulty design, materials defects (including voids and inclusions) or poor manufacturing procedures, including notches and scratches.

Fatigue crack growth from known "hot spots", such as highly loaded fastener holes, can be managed by basing inspection intervals of these regions on conservative estimates of the rate of crack growth. The USAF damage-tolerance approach based on slow crack growth is to assume the presence of a crack typically just at the limits of easy detectability in each critical region.

This inspection approach, called safety by inspection, may not be feasible in some of the older aircraft. In these aircraft the tendency was to choose high strength alloys to maximise the safe life, which have long (nominal) crack initiation

lives at the expense of poor fracture toughness and therefore small critical crack size and relatively high rates of crack growth.

The presence of an aggressive environment can also markedly increase the rate of crack growth, making inspection intervals very difficult to estimate, or too short to be economic. In this case management on a safe-life basis is the only option, possibly following a rework of the area to remove small cracks and reduce stress concentrations.

Planning of the inspection intervals and locations is much more difficult when cracks can initiate at random points in the structure, e.g. from pitting corrosion or large inclusions. This is particularly a problem in structures with enhanced fatigue resistance, for example with “fatigue-resistant holes” – produced by cold expansion or by using interference-fit fasteners.

Widespread damage, viz, extensive minor cracking in multi-load-path structure, is a significant concern with ageing aircraft [2]. This is because of loss of the ability of the structure to maintain the required level of residual strength (above DLL) in case of failure of one of the loading paths. Multiple-site damage, viz, extensive local minor cracking in a single-load-path structure (or in an element of multi-load-path structure), is a related problem that can result in an abnormally fast crack growth as the cracks link up to form a large crack, again compromising residual strength.

High-cycle fatigue is caused by high-frequency aerodynamic or acoustic excitation of the structure. It differs from low-cycle fatigue in that the high numbers of cycles imposed on the structure can result in crack initiation and growth, even in unflawed structure. Crack growth is generally very rapid on a service time basis, making management by standard damage tolerance [7] approaches infeasible.

1.3. Repair requirements

When significant structural degradation is detected, a decision must be made on the need for a repair. Essentially [8] one of the following decisions is required:

1. No-repair action is required.
2. Cosmetic or sealing repair is required to correct minor damage.
3. Structural repair is required (if feasible), because strength has been reduced below the design limits or has the potential to be reduced in subsequent service.
4. Repair is not economical and the component must be replaced.

Generally, the repair scheme employed for structural restoration should be the simplest and least intrusive to the structure that can restore structural capability to the required level. The repair must be able to be implemented in the repair environment, without compromising other functions of the component or structure, such as clearance on moving parts, aerodynamic smoothness and balance (control surfaces).

Important additional requirements are that implementation of the repair should:

- Require minimal down-time of the aircraft
- Use readily available and easily storable materials

- Remove as little sound material as possible
- Minimise degradation or damage to the surrounding region
- Require only simple procedures or tooling.

1.3.1. Repair levels

A major consideration in the choice of repairs is the level at which the repair can be implemented. Repair activities on military aircraft are performed at one of the following levels:

- Field level: Undertaken directly on the aircraft in a situation where skilled personnel and/or adequate facilities are unavailable. Such activities will generally be limited to fairly minor repairs to non-primary structure or non-critical repairs to primary structure. However, aircraft battle-damage repairs (ABDR) to primary structure may be undertaken very rapidly to make the aircraft operational or to ferry it back to base. Since battle damage repairs will subsequently be replaced with permanent repairs, they must cause minimum damage to the airframe. ABDR can strongly influence aircraft availability and so can prove to be a decisive factor in times of conflict.
- Depot level: Undertaken in a situation where skilled personnel and facilities are available (up to factory capability in some cases). However, if the component is too large or difficult to remove from the aircraft, repairs are implemented directly on the aircraft.

1.4. Repair procedures

Repairs can be broadly divided into non-patch procedures for minor damage and patch (or reinforcement) procedures to restore structural capability.

Patch repairs restore the load path weakened or removed by damage or cracking, ideally without significantly changing the original load distribution. Reinforcements or doublers are used to replace lost strength or stiffness (for example after removal of corrosion damage), correct design errors, or to improve performance. The patch repair approach recommended in the OEM's SRM is generally based on the use of bolted or riveted metal plates, generally of a similar alloy to the parent material – often one gauge thicker.

Non-patch repair of corrosion types such as pitting or exfoliation in aircraft aluminium alloy structure generally involves the removal of visible damage by grinding usually followed by an extra confidence cut to ensure that all the corrosion is removed. The region is then treated, primed and painted. In the case of severe corrosion, panel thickness may be reduced below the allowable thickness (according to the SRM) and must be reinforced to make it airworthy.

Simple non-patch repair of cracking involves stop drilling the crack tip. This is only a temporary and relatively ineffective measure, since it is difficult to find the tip of the crack. Even if the tip is found, cracking resumes very shortly after stop drilling because of the high stress concentration associated with the shank of the crack.

A much superior approach is to stop drill and then expand the stop-drilled hole, usually with a special sleeve to develop favourable compressive stresses that reduce or prevent crack opening. While this approach is often highly effective in stopping crack growth it is not damage tolerant, because when the crack does eventually grow through the compressive zone, growth is unrestrained and will be rapid.

1.5. The case for adhesively bonded repairs

Repairs based on mechanically fastened metallic patches are currently the recommended SRM approach, however, compared to adhesively bonded patches they are less efficient and more problem prone for the reasons described in this section. To illustrate the reinforcing efficiency of mechanical fastening versus bonding, a simple comparison is made by modelling the repairs as equivalent overlap joints as shown in Figures 1.1 and 1.2. These diagrams depict joints representing patch repairs to a cracked parent structure where the crack is represented by the gap in the lower joint member.

In mechanical joints, referring to Figure 1.1, loads are transferred between the joint elements primarily by compression on the internal faces of the fastener holes, resulting in high local stress concentrations. A smaller component of load is transmitted by shear on the outer faces of the elements through friction, depending on the stress level on the joint surface produced by clamp-up as the fastener is applied. The mechanical joint is generally fairly compliant or flexible for several reasons, including:

- (a) The requirement for a finite edge distance (generally $2-3 \times$ (hole diameter) for fasteners results in a long fastener-free zone spanning the gap (simulating the crack).
- (b) Large hole tolerances, as may be expected in a repair, allow movement and rotation of fasteners [9].
- (c) The high stresses at the fasteners and fastener holes result in significant local displacements.
- (d) The frictional shear component can relax under cyclic loading or due to the lubricating effect of water-displacing compounds and other aircraft fluids.

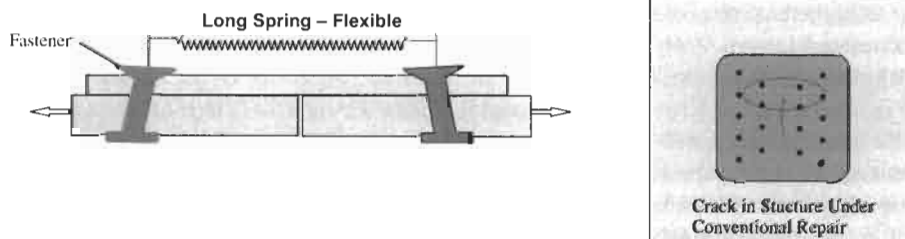


Fig. 1.1. Schematic of a joint representing a region of the patch spanning the crack. This joint may be relatively flexible because of the high local stresses, the large span needed to provide a reasonable edge distance for the fasteners and the tendency of the fasteners to rotate or move to take up any tolerances.

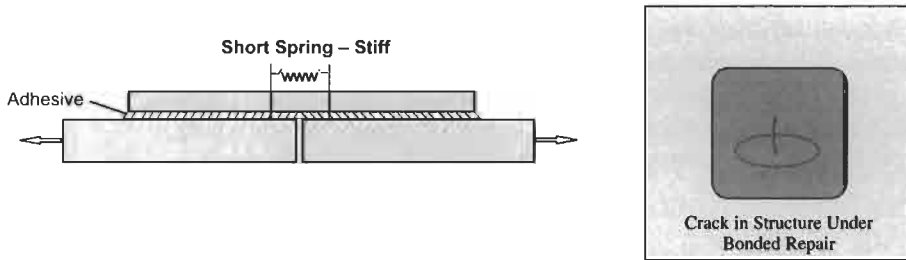


Fig. 1.2. Schematic of a bonded joint representing a section through the repaired region. This is relatively stiff because loading is distributed over the whole surface of the joint, the span over the gap is very short and there is no tolerance take-up to allow movement.

The low stiffness and therefore patching efficiency of the mechanically fastened joint is illustrated by the long spring in Figure 1.1.

As a result of the relatively low reinforcing efficiency in mechanical repairs, components with cracks generally cannot be satisfactorily reinforced. Thus, the cracked region must be removed prior to application of the repair and the resulting hole filled with an insert before covering with the reinforcing patch. In relatively thick-skinned components crack removal is a costly, time-consuming requirement and may be impractical in many repair situations. Furthermore, *in situ* drilling of new fastener holes can cause internal damage (e.g. to hydraulic lines, electrical wires or optical fibres) as well as introducing swarf into the structure.

Mechanical repairs are generally designed simply to restore static strength. Swift [10] shows that these repairs, if not well designed, can significantly reduce fatigue life. The main concern is the danger of initiation of a crack from a fastener hole (usually in the first row where stresses are highest). The crack may initiate at quite low stresses because of high stress concentrations (usually at the first row of fasteners) or because of poor quality hole drilling or riveting – common problems under field conditions. There is also the danger of cracks initiating from hidden corrosion which can develop under a poorly sealed mechanical repair. Additionally, there is concern with the difficulty of detecting the crack by standard non-destructive inspection (NDI) procedures, until it emerges from under the repair – when growth may be very rapid because of low reinforcing efficiency. Thus, mechanical repairs are inherently not damage tolerant.

By contrast, loads in bonded joints are transferred by shear over the surface area of the elements. Because of the large area for load transfer, which extends right up to the gap (crack), the bonded joint is intrinsically much stiffer than the mechanical joint. This is despite the low stiffness of the adhesive compared to the metal fasteners. The transfer length determines the rate of load transfer from the cracked region into the composite adherends, which is a function of the joint geometry and mechanical properties. A low transfer length equates to high joint stiffness. The transfer length increases as a (square-root) function of the adhesive thickness and shear compliance and is strongly dependent on its shear yield strength.

Relative stiffness for the bonded joint is further increased compared to the mechanical joint (unless it has interference-fit fasteners) since there are no slacks to be taken up.

Thus, as illustrated by the short spring in Figure 1.1, bonded joints provide a very stiff and therefore very efficient reinforcement. This minimises the gap opening and therefore the stress intensity in the case of a patched crack. It then becomes feasible to successfully patch live cracks.

Finally, in a well-designed joint, one with optimally tapered ends, there are only minor local regions of high deformation in the adhesive at the ends of the joint and thus no major stress concentrations in the joint elements where the patch terminates.

1.6. Composite versus metallic patches

The advantages of high performance fibre composite graphite/epoxy (gr/ep) and boron/epoxy (b/ep) materials for patches when compared with metallic alloys include:

- High directional stiffness, which allows use of thin patches (important for external repairs) and allows reinforcement to be applied only in desired directions;
- High failure strain and durability under cyclic loading, which minimises danger of patch failure at even quite high elastic strain levels in the parent metal structure;
- Low density, an important advantage where changes in the balance of a control surface must be minimised; and
- Excellent formability that allows low-cost manufacture of patches with complex contours.

Another important advantage of composites is that the pre-bonding surface treatment of composite patches (with thermosetting matrices) for adhesive bonding is less demanding than for metals. This is because mechanical abrasion to produce a high-energy uncontaminated surface is all that is required. Alternatively, the composite patch can be cocured on the metallic component with the adhesive, which obviates the need for any surface treatment of the patch and simplifies the patch fabrication procedure. The choice of material type for bonded patches or reinforcements is considered in more detail in Chapter 2.

In most repair applications use of unidirectional patches (all 0° plies) is optimal since this provides the highest reinforcement efficiency in the loading direction, and minimises undesirable stiffening in other directions. However, in some applications with high biaxial stress components, or where there is concern that the crack may change orientation, it may be desirable to provide transverse and/or shear reinforcement. This can be achieved by using a laminate with the appropriate number of $\pm 45^\circ$ and 90° plies.

The main disadvantage of using gr/ep or b/ep results from a mismatch in thermal expansion coefficient between the composite and the metal [1], and Chapter 2.

Residual stresses are tensile in the metal and compressive in the composite. These stresses are particularly severe when elevated-temperature-curing adhesives are used to bond the patch and when operating temperatures are very low, typically -10 to -50°C . The tensile residual stress could be expected, for example, to increase the growth rate of the patched crack by increasing the stress ratio R , reducing patching efficiency. Further, thermal cycling of the patched region causes cyclic stresses that could result in crack growth, independent of external stressing.

The desire to avoid the residual stress problem is the major reason why Fredel as described in Chapter 14 and [11] developed the use of GLARE patches for repairs to thin-skin fuselage structure. GLARE is a glass-fibre/epoxy-reinforced aluminium alloy laminate, the epoxy matrix also acts as an adhesive which bonds the aluminium alloy layers. GLARE has a similar expansion coefficient to aluminium alloys and excellent fatigue crack growth resistance compared to normal aluminium alloy materials; the glass fibres bridge any fatigue crack which may develop in the metal layers.

GLARE is less suited for repair of thick structures since it has a lower modulus than aluminium alloys and has limited formability (similar to that of sheet aluminium alloy), compared with fibre composites. ARALL (Aramid Reinforced Aluminium Laminate) is a similar concept using higher modulus aramid fibres instead of glass. Although ARALL has a higher stiffness, it has somewhat inferior fatigue properties to those of GLARE.

Despite the residual stress concerns, the composites b/ep and gr/ep offer excellent properties for patches or reinforcements. However, b/ep is generally considered to be the superior because of its:

- Superior combination of strength and stiffness which provides the highest efficiency reinforcement;
- Higher coefficient of thermal expansion, which reduces the severity of the residual stress problem;
- Low electrical conductivity, which:
 - avoids the danger associated with gr/ep of inducing galvanic corrosion of the metal, and
 - allows optimal use of eddy-current NDI to detect and monitor cracks under the patch.

However, gr/ep is chosen if patches with low radii of curvature (less than 30 mm) are required or if b/ep cost (which is very much higher than gr/ep) or availability is a concern.

1.7. Scope of applications

Bonded composite repairs can be regarded as a versatile cost-effective method of repairing, strengthening or upgrading inadequate metallic structures. The reinforcements or patches are ideally implemented *in situ*, avoiding the need for costly disassembly of built-up structures.

Potential applications can be summarised as follows:

- (a) **Reduce stress intensity:**
 - in regions with fatigue cracks
 - in regions with stress-corrosion cracks
 - to increase damage tolerance (provide slow crack-growth characteristics) in safe-life structure or structure with multi-site damage
- (b) **Restore strength and stiffness:**
 - after removal of corrosion damage to below allowable SRM limits
 - after removal of flaws
 - after re-shaping to minimise stress concentrations
 - after heat damage
 - after failure of a load path in multi-load-path structure
- (c) **Stiffen under-designed regions:**
 - to reduce strain at stress concentrations
 - to reduce secondary bending
 - to reduce vibration and prevent acoustic damage.

1.8. Some experimental comparisons of bonding versus bolting

Experiments to compare the effective stiffness of bonded or bolted joints were made using the double overlap joint specimen illustrated schematically in Figure 1.3. The double overlap joint represents a slice through a two-sided repair over the cracked region. The ability of the joint to restrict “crack” opening was measured using a clip gauge, as shown. In each joint the nominal stiffness of the outer adherends are similar on the basis of modulus \times thickness. This work was conducted as part of an early study on joints representing repairs [12].

The results, Figure 1.4, show the much superior stiffness of a joint (a) bonded with the 120 °C curing epoxy-nitrile structural film adhesive over the bolted joint (c), confirming the much higher reinforcing efficiency of bonded over traditional mechanically fastened repairs.

Joint (b), bonded with the relatively soft modified epoxy-paste adhesive, had intermediate stiffness, which is what would be expected of the joint bonded with the 120 °C curing epoxy-nitrile adhesive at temperatures above 70 °C or so.

Note also the marked viscoelastic behaviour of the joint bonded with this adhesive as indicated by the open hysteresis loops and the time-dependent recovery. Even joint (a) exhibits small viscoelastic effects as indicated by the reduction in hysteresis and increase in stiffness with increasing rates of loading.

To highlight the advantages of the use of bonded composite repairs for crack repair (known as “Crack Patching”), fatigue tests were performed on patched edge-notched panels, shown inset in Figure 1.5. The total thickness of the aluminium patches, both sides, was equal to the panel for metal patches and 1/3 of this for the b/ep.

It is seen from Figure 1.6 that the mechanically attached metallic patch provides rather poor reinforcing efficiency since there is only a very slight reduction in crack growth rate; it is also seen from the figure that the crack once it emerges from under

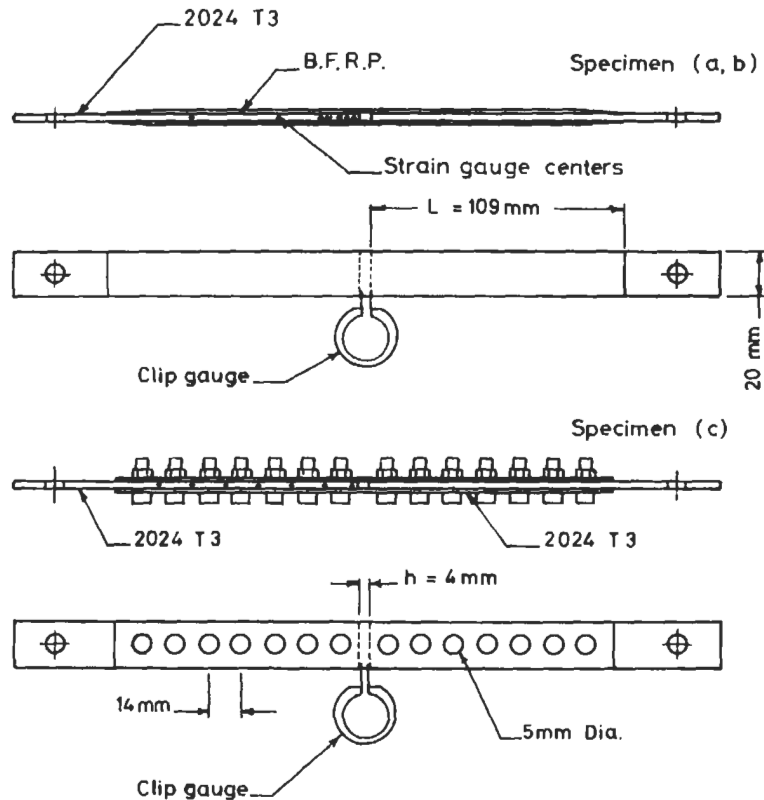


Fig. 1.3. Double-overlap joints with 2024 T3 inner member showing the position of clip gauge and strain gauges. Specimen (a) boron/epoxy patch bonded with an epoxy-nitrile structural film adhesive (AF126) and (b) bonded with a relatively soft modified epoxy paste adhesive (EC2216). Specimen (c) has an outer member 2024 T3 of nominally similar stiffness to the boron/epoxy mechanically fastened with M5 high-strength steel bolts, torque 11 N-m.

the patch grows very rapidly. The metallic patch can appear to be effective in some cases if the crack arrests temporarily at a fastener hole. In contrast, the adhesively bonded b/ep patch is shown to greatly reduce the growth rate, even when the crack emerges from under the patch. The growth rate of the emerging crack with the b/ep patch is similar to that expected for a crack of the emerged length, indicating that the patch is still operating very effectively in restraining crack opening.

Based on these observations and the previous discussion, the advantages of bonded composite repairs for fatigue crack are summarised in Figure 1.6.

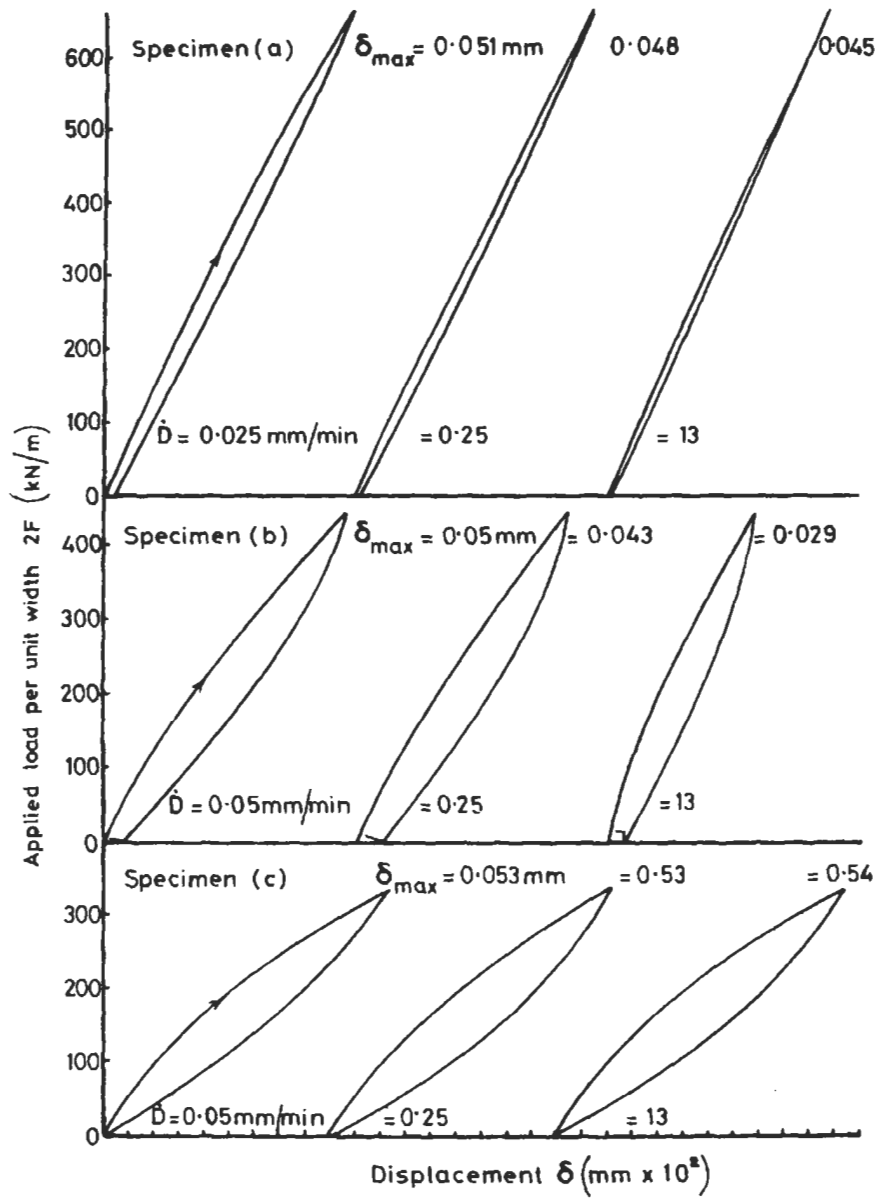


Fig. 1.4. Stress-displacement plots from the clip-gauge measurements for the (a), (b) and (c) specimens from Fig. 1.3. Note the relatively low stiffness of the mechanical joint and to a lesser extent specimen (b) compared with specimen (a). Also note the time-dependent behaviour of specimen (b).

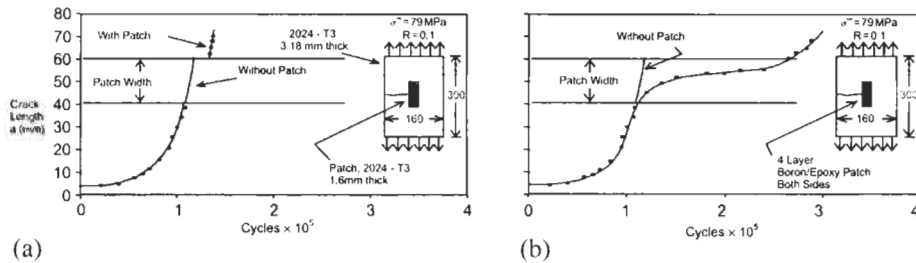


Fig. 1.5. Comparison of crack growth performance of patching efficiency between a) a mechanically fastened mechanical repair and b) an adhesively bonded composite repair.

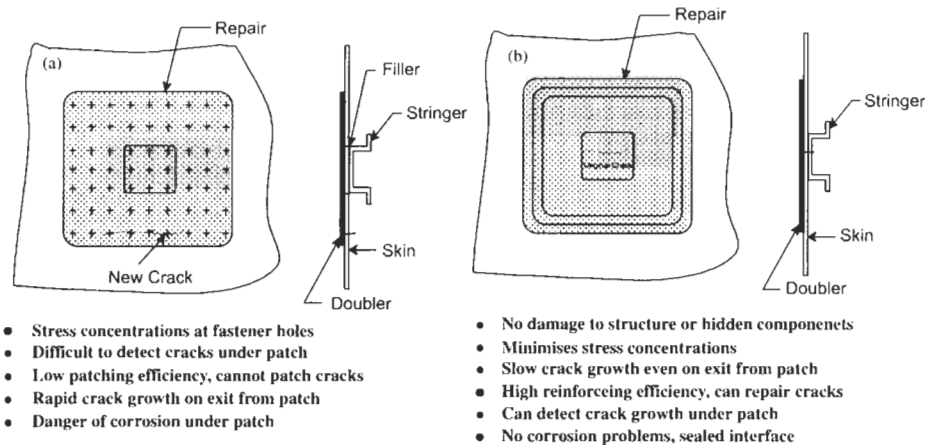


Fig. 1.6. (a) Some disadvantages of standard mechanically fastened repairs and (b) advantages of bonded composite repairs.

1.9. R&D requirements

At the time of writing of the first book [1] bonded composite repair technology had advanced to the stage that repairs and reinforcements could be applied with some confidence to non-flight critical components. Since then technological capabilities have improved and long-term experience has been accumulated such that the scope and range of applications can be extended with some confidence.

The challenges (as viewed in Australia) are to push the boundaries for application of bonded composite repairs to increasingly demanding situations; for example, to repair critical damage in primary structure. A recent example [13] is the development of a repair of a crack in the lower wing skin of Australian F-111 aircraft. This crack had reduced the residual strength of the wing below DLL. Such a repair would probably not be accepted by UK or US military airworthiness authorities; indeed a very lengthy and costly program was required to have it accepted in Australia, which may not be cost effective in many applications.

Currently most airworthiness authorities will only accept bonded repairs to critical structure on the basis that a margin on DLL is retained in case of complete

failure of the repair. Essentially this implies that no credit is permitted for the patch in improving residual strength and slowing crack growth [4,14]. However, it is possible this limitation will be overcome by the "Smart Patch" approach. R&D on this topic is described in Chapter 20. The smart patch is a patch (or reinforcement) capable of monitoring and reporting its own structural integrity and, if required, that of the damaged structure.

Recently, three major reviews were undertaken to define the general R&D needs for further development of bonded composite repair technology. These reviews were by the Committee on Aging of US Airforce Aircraft in 1997, the technical cooperation program (TTCP) Aeronautical Vehicles Action Group on Certification on Bonded Structure in 1999 and an Australian Defence Science and Technology (DSTO) in 1998.

The USAF review [2] formed part of a major study on aging USAF aircraft, undertaken by a select US committee. In this review, the capability of bonded composite repairs to prolong the life of ageing aircraft was recognised. They state that:

"The primary emphasis is on the maturation of bonded composite repairs, especially for metallic structures. The committee believes that the focus on optimisation of materials and processes, repair criteria and analysis tools for bonded composite repair of metallic structure is appropriate".

TTCP is a program for collaboration in (non-nuclear) defence science involving UK, US, Canada, New Zealand and Australia. The Air Vehicles Sub Group in TTCP established an Action Group (AER 13) to review issues related to the certification of bonded structures for military aircraft structures [15].

In the Terms of Reference for the study it was stated that "one of the primary applications of bonded structures is the application of composite patching of metallic structures. The benefits from this application are the cost savings over other types of repairs and the aircraft availability improvement through reducing need for procurement of long lead items. Even wider use of this application would achieve these benefits, while maintaining flight safety, through the development of suitable certification procedures".

The third study was an in-house strategic review conducted in 1998 in the author's organisation DSTO with input from the Royal Australian Air Force. The aim was to establish the needs, topics and aims for future work on bonded composite repairs.

In addition to these reviews, the author in references [4,14] address certification R&D issues for bonded composite repairs to primary aircraft structure.

Table 1.1 lists recommendations from these reviews. Those related to certification issues are listed under the major headings of (a) Acquisition of Design Data, (b) Validation of Procedures, (c) Assessment of Bond Environmental Durability. Those related to improved technology are listed under the major headings of (d) Improved Design Capability and (e) Improved Materials and Processing and (f) Improved NDI. To fit more clearly under these headings some of the recommendations have been edited, without significantly changing the aim or meaning.

Table 1.1

R&D requirements from various studies on bonded repairs.

<i>A. Acquire design data</i>	
Acquisition of data on static and fatigue stresses patch/reinforcement system properties	Methods to acquire design stresses and usage spectra by analysis or by direct measurement [DSTO] Develop damage criteria that correctly predict observed patch system static and fatigue failure modes [TTCP] Obtain materials allowables and knockdown factors for the relevant failure modes, including degradation caused by moisture and other service environments [TTCP]
Parent structure properties	Determine influence of patch application procedure, including residual stresses on parent allowables [DSTO]
<i>B. Validate design procedures</i>	
Design models	Validation of analysis techniques to evaluate continuing damage growth beneath repairs [USAF, TTCP] Validation of models for single-sided repairs and complex geometries [TTCP] Check ability of models to allow for variables, including R ratio, holds, temperature-residual stress, spectrum loading and environment [TTCP, DSTO]
<i>C. Assess bond environmental durability</i>	
Quality assurance	Correlate accelerated tests such as the Boeing Wedge Test with actual service performance [TTCP, DSTO] Develop methods for risk assessment of bonded repairs [TTCP, DSTO]
Self-assessment	Develop smart patch approach to patch system self-health assessment [TTCP, DSTO]
<i>D. Improve design capability</i>	
Increased scope	Develop design procedures able to minimise stress concentrations in parent structure and patch system [DSTO] Develop analytical methods for complex and curved structures [USAF] Develop design guidelines for dynamically loaded structures [USAF] Develop design methodology for corrosion damage [DSTO] Develop models which include effects of thermal mismatch, bending and disbonding [TTCP]
Design aids	Simplified approaches to be programmed into notebook PCs [TTCP] Develop Expert system to aid assessment of repair, the need for repair and design analysis of repairs [USAF]
Optimisation	Optimisation procedures for patch geometry to minimise stresses in adhesive bond layer and parent structure [TTCP]

Table 1.1
Continued

<i>E. Improve materials and processes</i>	
Screening	Develop rapid screening tests for new adhesives, composites and processes suitable for repair applications [DSTO]
Bonding	Develop/evaluate improved pre-bonding surface treatments if required [TTCP]
Patch systems	Establish processing window for existing and new systems [TTCP] Develop composites with tougher surface layer matrices to improve fatigue resistance [DSTO]
<i>F. Improve NDI</i>	
Pre-bond NDI	Develop pre-bond NDI capability [TTCP, DSTO]
Post-bond NDI	Determine adhesive bond quality, degradation, accept/reject standards [USAF] Capability for detecting cracks under patches in complex geometries [DSTO]

1.10. Conclusion

While simple in concept and often in application, bonded composite repair technology can be challenging from both the scientific and engineering viewpoint, particularly for the repair of primary structures. This is because it involves interdisciplinary inputs from several fields, including aerodynamic loading, stress analysis, fibre composites, structural adhesive bonding, linear-elastic fracture mechanics and fatigue. The technologies of non-destructive inspection and, more recently smart materials, must also to be included. Operational issues are equally critical, including airworthiness certification, application technology (including health and safety issues) and training.

It is hoped that the material provided in this book will provide at least partial answers to many of the R&D issues and promote the required degree of interactions between experts in the various fields mentioned.

References

1. Baker, A.A. and Jones, R. (1988). Bonded Repair of Aircraft Structures. Martinus Nijhoff.
2. *Aging of U.S. Airforce Aircraft*. Publication NMAB-488-2 National Academy Press, Washington D.C. 1997.
3. Baker, A.A. (1994). Bonded Composite Repair of Metallic Aircraft Components, Paper 1 in AGARD-CP-550 Composite Repair of Military Aircraft Structures.
4. Baker, A.A. (1997). On the certification of bonded composite repairs to primary aircraft structures. *Proc. 11th Int. Conf. on Comp. Mat. (ICCM-11)*, Gold Coast, Australia, volume 1, pp. 1-24.
5. Simpson, D.L. and Brooks, C.L. (1999). Tailoring the structural integrity process to meet the challenges of aging aircraft. *Int. J. of Fatigue*, 21, S1-S14.

6. Clark, G. (1999). Corrosion and the management of structural integrity. In *Structural Integrity for the Next Millennium* (J.L. Rudd, ed.) EMAS, Warley.
7. Nicholas, T. (1997). Critical issues in high cycle fatigue. *Int. J. of Fatigue*, **21**, S221–231.
8. Baker, A.A. (1997). Joining and repair of aircraft composite structures. Chapter 14 in *Composite Engineering Handbook* (P.K. Mallick, ed.) Marcel Dekker, Inc.
9. Hart-Smith, L.J. (1989). The Design of Efficient Bolted and Riveted Fibrous Composite Structures. Douglas Paper 8335, July.
10. Swift, T. (1990). Repairs to damage tolerant aircraft. *Proc. Int. Symp. on Structural Integrity of Aging Airplanes*, FAA-AIR-01.
11. Fredell, R.S., van Barnveld, W. and Vlot, A. (1994). Analysis of composite crack patching of fuselage structures: High patch modulus isn't the whole story. *SAMPE Int. Symp.* 39, April.
12. Baker, A.A., Roberts, J.D. and Rose, L.R.F. (1981). Use of joint parameters in estimating the K reduction due to crack patching. *Proc. of an Int. Workshop on Defence Applications for Advanced Repair Technology for Metal and Composite Structure*, Naval Research Labs., Washington.
13. Baker, A.A., Rose, L.R.F., Walker, K.F., et al. (1999). Repair substantiation for a bonded composite repair to an F-111 lower wing skin. *Applied Composites*, **6**, 251–256.
14. Baker, A.A. (1999). Issues in the certification of bonded composite patch repairs for cracked metallic aircraft structures. *Proc. Int. Conf. on Aircraft Fatigue*, Seattle.
15. Certification of Bonded Structures Action Group 13 Report of the Technical Co-Operation Program, Feb. 2001.

Chapter 2

MATERIALS SELECTION AND ENGINEERING

R. CHESTER

Air Vehicles Division, Defence Science and Technology Organisation, Fishermans Bend, Victoria 3207, Australia

2.1. Introduction

The three critical steps in implementing a bonded repair are design, choice of materials and application. In this chapter the various considerations associated with the selection of materials will be discussed along with some of the various materials engineering issues associated with repair application [1].

A well-designed repair can only be effective if it is strongly bonded to the parent adherend and therefore the issues of adhesive bond strength and bond durability are absolutely crucial for a fully successful repair. These issues will be introduced in this chapter and explored in more detail in Chapter 3. The material selected for the patch will almost always be either metallic or composite and within these classes are many different materials with different advantages and disadvantages associated with their use. These issues will be considered together with those of adhesive selection where two of the important factors are the operating temperature and nature of the applied loads.

The use of chemicals to modify the adherend surface prior to bonding is an essential step in the repair process and needs careful consideration as the inappropriate use of some of these chemicals can cause further damage to the structure, as in the case of acids for example. The selection of chemicals which reduce the likelihood of such damage while retaining high levels of effectiveness will be discussed. Various mechanical tests will be described which may be required for either quality assurance reasons or for generation of design allowables for the patch materials or adhesives. It is common to find that data suitable for design is not available from the material manufacturer (especially for adhesives), and the only alternative is to perform the appropriate tests to generate the data.

Finally, the application of an adhesively bonded repair to a structure creates a number of materials engineering design issues which may be important depending on the repair circumstances. An example is the development of residual stresses when an elevated temperature adhesive is used to bond a repair patch to a substrate with a different coefficient of thermal expansion. Issues such as these will be raised and discussed in the final section.

2.1.1. Factors affecting adhesion

Although there are many theories of adhesion, it is generally considered that strong adhesion can only take place when the adhesive is in sufficiently intimate contact with the adherends to enable the development of chemical or physical bonds. These surface attachments are the mechanism by which the load is transferred into the repair and is uniformly distributed across the interface. To achieve the required level of intimate contact, the adhesive needs to behave as a liquid in order to wet the adherend surface. When a strong bond is achieved, it is important to maintain that level of strength over time and such strength retention in the operating environment is termed durability in this book. Adhesive bond durability is not solely a function of the adhesive type but also depends critically on the other components of the joint such as the adherends, and any interfacial layers between the adherends and the adhesive.

Wetting of the adherend by the adhesive is an essential part of the bonding process. Adhesives used for Bonded Repairs are either in the form of pastes or films and these two categories will be discussed further in Section 2.3.1. Regardless of the initial form of the adhesive, it is important that at some stage of the cure cycle, the viscosity of the adhesive should be sufficiently low so as to enable the adhesive to flow and wet the adherend. Adhesives cured at room temperature are often already in the form of a liquid or paste, however, higher temperature curing adhesives may initially be in the form of a film or sheet which softens significantly as the temperature is increased. Any factor which inhibits the ability of the adhesive to flow and wet the adherend will potentially reduce the adhesion strength.

Three important factors which can influence the flow characteristics of an adhesive are temperature, contaminants and adhesive age. If the correct temperature during the cure is not reached at the correct time, the adhesive may not reach the right level of viscosity. For example if the cure temperature increases slightly and is then held for some time, the adhesive may not have dropped sufficiently in viscosity but may be beginning to cure and develop cross links. If the temperature is then raised again, the crosslinking will have increased the viscosity of the adhesive and proper flow will not take place. At the end of the cure cycle, the adhesive may be fully cured (crosslinked) but as proper wetting did not take place the adhesion strength may be low. Contaminants such as absorbed water may change the chemical characteristics of the adhesive and inhibit the proper level of flow. Adhesive that has passed its storage date may also be incapable of achieving the correct level of viscosity. This is because the adhesive will have been slowly crosslinking during storage and then during the cure cycle, the crosslinks prevent proper flow in the same

way as the improper cure cycle described above. Tests described in Section 2.5 can be used to determine if the adhesive is in an acceptable state for use.

Although wetting is a necessary condition for the development of strong bonds, it is not a sufficient condition. An adhesive can wet an adherend surface but still have low adhesive strength because of the presence of contamination or weak surface layers on the adherend. On aluminium surfaces for example, the adhesive can form a strong bond to old, thick (hydrated) oxide layers on the surface which themselves have relatively low cohesive strength. Under the action of structural loads the joint can subsequently fail through these weak layers. Other forms of organic contamination on the surface can have much the same effect. A clean contaminant-free surface is therefore an essential requirement for the development of a strong adhesive bond. Producing such a surface is known as surface preparation.

While attention to these factors will permit the development of good initial bond strength, they will not provide any guarantee of good bond durability. The durability of an adhesive bond is dependent on the adherend materials, the adhesive and the interfacial layers between the adhesive and adherends. The presence of water is by far the most serious cause of bond degradation, and metallic adherend surfaces are commonly affected. Water can degrade the bond strength to a metallic surface by causing the surface to either oxidise (steel) or hydrate (aluminium). In both cases the new interfacial layer formed has poor cohesive strength and the adhesive no longer adheres to the metallic adherend. An essential requirement then for the production of durable adhesive bonds to metallic surfaces, is the production of a bonding layer on the adherend which is resistant to degradation mechanisms by moisture such as oxidation or hydration. Producing such a layer is known as surface treatment.

Composite or polymeric surfaces are not susceptible to these degradation mechanisms and therefore the preparation of composite patches for bonding generally only requires the use of surface preparation methods (Chapter 3). For metallic adherends, however, it is essential to use both surface preparation and surface treatment methods

2.2. Materials for patches and reinforcements

The two main categories of materials for patches or reinforcements are metals and composites. More recently, laminated metallic materials such as ARALL and GLARE have been developed and are being used successfully for Bonded Repairs. These new materials will be discussed together with the conventional metallic materials. The main points are summarised in Table 2.1.

2.2.1. Metallic materials

The usual objective of a Bonded Repair is to restore the damaged structure back to its original condition in terms of strength and stiffness. For this reason, perhaps

Table 2.1

Summary of the advantages and disadvantages of metallic and composite materials for bonded repairs.

Material type	Advantages	Disadvantages
Metallic	<ul style="list-style-type: none"> • Long shelf life • Properties well known • Isotropic properties • High coefficient of thermal expansion 	<ul style="list-style-type: none"> • Requires careful surface treatment • Susceptible to corrosion and fatigue • Inspections of underlying structure can be difficult • Difficult to form to curved surfaces
Composite	<ul style="list-style-type: none"> • Lightweight • Corrosion and fatigue resistant • High specific stiffness • Easy to form strong durable bond (if thermoset) • Comparatively easy to inspect substructure • Excellent formability to curved surfaces 	<ul style="list-style-type: none"> • Low coefficient of thermal expansion • Comparatively short shelf life (in uncured state)

the most obvious choice of repair material is that which the structure is already made from. For aircraft this is commonly an aluminium alloy from either the 2000 or 7000 series. The other common materials are steel and titanium. These three materials can usually be successfully treated to produce durable bonds and therefore can be considered as potential repair materials. Magnesium on the other hand is difficult to bond to, and while some Bonded Repairs have been carried out to magnesium components, it would not generally be considered as a repair material.

The use of the original materials for design of the repair may help to simplify the design process, however, there are also very good reasons to consider the use of an alternate material; composites make exceptionally good repair materials due to their resistance to fatigue stresses and corrosion as well as many other advantages which are discussed later.

Metallic repair materials are often readily available and of course, compared with uncured composites have an infinite shelf life. Compared with composites, metals have isotropic properties that may be important if there is concern about unusual stress states. A metallic repair may be better able to withstand multi-axial loads and perhaps high levels of through-thickness stresses. On the other hand, many repairs are required on relatively flat structure where the loads causing cracking are in one direction and here the use of unidirectional composites can produce a much more efficient repair. For the same level of repair efficiency, a metallic repair in this situation would be thicker and heavier and this may be a problem where balance or aerodynamic smoothness is required. Metals have a higher coefficient of thermal expansion than composites and this can be an advantage where elevated temperature curing adhesives are used. This topic is discussed further in Section 2.6.

If the problem causing the need for the repair was fatigue or corrosion, it may be more appropriate to use a composite for the repair as these materials are effectively immune to these problems (composite repair layups generally have fibre dominated properties which are immune to fatigue whereas layups with matrix dominated properties may be susceptible to fatigue). The repair material chosen can also be important where subsequent inspections are required and in many cases the use of boron/epoxy composites is advantageous as eddy current methods can be used to readily detect the crack underneath the repair. This is usually more difficult if a metallic or graphite fibre patch is used due to the fact that these materials are electrically conducting. Metallic materials will require the use of stringent surface preparation and surface treatment processes to obtain a durable bond, however, if a corrosion inhibiting primer is used, these processes could be conducted elsewhere and the patch stored prior to use. Composite repairs using thermosetting matrices such as epoxies are comparatively easier to prepare for bonding, although the processes required are still important [2]. Thermoplastic composites are in general harder to bond to than the more commonly used thermoset composites. Finally metals lend themselves best to relatively flat repair locations due to the difficulty in accurately forming a metallic sheet to a curved profile. This is one of the strengths of composites where the desired shape can be formed into the repair during cure.

Further considerations for the selection of a metallic material may include corrosion and patch thickness. To avoid galvanic corrosion problems between dissimilar metals, a sensible choice would be to use the original material for the repair material as well. Where this is not possible, a check should be made to ensure that different repair materials would not be susceptible to corrosion. For example, repairs to a graphite/epoxy component will often be performed with a graphite/epoxy material as well. Use of an aluminium material in this situation would be unusual as the aluminium will readily corrode if in galvanic contact with the graphite fibres. The adhesive should serve as an electrically insulating layer, however, the more usual alternative to a graphite patch in this situation would be titanium which will not corrode should the insulation break down.

In situations where the thickness of the repair is critical (on an aerodynamic surface for example) consideration may be given to either steel or titanium to repair aluminium. The greater stiffness of these materials should permit the design of a thinner patch than would be possible with aluminium. Again consideration should be given to possible galvanic coupling and potential corrosion problems in this situation and it is possible that the choice of a composite may be preferable.

Laminated metallic materials have been developed in the Netherlands which consist of layers of composite sandwiched between thin aluminium alloy sheets [3]. Where the composite used is kevlar (or aramid) the laminate is referred to as ARALL (aramid reinforced aluminium laminate) and if the composite used is glass fibre, the laminate is referred to as GLARE (Chapter 14). The fundamental idea behind the development of these materials is to combine the traditional advantages of both metals and composites. The composite component confers increased fatigue strength and damage tolerance to the structure, while the aluminium allows the use

of conventional metallic forming, fastening and manufacturing processes for reduced cost.

GLARE has been proposed as a possible material for use in bonded repairs and in particular has been used as a material for the repair of damage to the fuselages of transport aircraft. The principal advantage of GLARE in this situation is the high coefficient of thermal expansion. Work by Fredell *et al.* [4] and Chapter 14, has shown that for repairs to thin fuselage skins which will mostly see pressurisation loads at cruising altitudes (-55°C), the higher coefficient of thermal expansion of GLARE provides structural advantages compared with composite alternatives (see Section 2.6 for further discussion). On the other hand the low specific stiffness of GLARE results in a much thicker patch than for a high modulus composite material, and this needs to be carefully considered in the design to ensure that bending effects due to neutral axis offset are not excessive and that high stresses at the ends of the patch are alleviated by tapering for example.

Finally, it may be possible to use nickel as a repair material in some specific circumstances for example where geometry is complex. The repair of a crack in the corner of a bulkhead pocket is a good example. Nickel can be electroformed to replicate the surface of a mould with very high precision, and therefore it should be possible to produce an electroformed nickel patch which will fit precisely into the pocket. As mentioned above, the isotropic nature of the nickel would be an advantage in this situation, although care needs to be made to ensure that the electroforming process does not produce planes of weakness within the electroform. Work is underway to evaluate this method as a repair option for a damaged army gun support structure [5]. In situations such as this where a certain degree of rough handling can be expected, the hard, damage resistant surface of the nickel provides another important advantage over a fibre composite repair.

2.2.2. Non-metallic materials

The two main non-metallic materials used are boron/epoxy and graphite/epoxy composites. Glass fibre composites are not used due to their low stiffness and kevlar composites while strong and stiff in tension have relatively poor compression performance.

Boron fibres were first reported in 1959 and were the original high modulus fibre before the development of graphite fibres in the 1960s. Boron composites were used to produce aircraft components such as the skins of the horizontal stabilisers on the F-14 and the horizontal and vertical stabilisers and rudders on the F-15. The use of boron composites in large-scale aircraft manufacturing has largely stopped now due to the development of more cost-effective graphite fibres. The production process for boron fibres is time consuming and does not lend itself to mass production in the same way as modern methods for producing graphite fibres. For this reason the price of boron fibres has not dropped as significantly as that of graphite fibres which are now at around 1/10th the cost. Boron fibres are manufactured individually by chemically vapour depositing boron onto a heated tungsten wire substrate from boron trichloride gas in a reactor. The fibres are

available from Textron Speciality Materials in 100 and 140 micron diameters and commercial pre-pregs are available with either 120°C or 175°C curing epoxies. The fibre diameter is significantly larger than normal graphite fibres due to the presence of the tungsten core. Attempts have been made in the past to use a carbon filament precursor to reduce the production costs, however, these boron-carbon filaments have generally not had the high level of strength that can be produced with the tungsten filament precursor.

Boron fibre is an extremely hard material with a Knoop value of 3200 which is harder than tungsten carbide and titanium nitride (1800–1880) and second only to diamond (7000). Cured boron composites can be cut, drilled and machined with diamond tipped tools and the pre-pregs are readily cut with conventional steel knives. In practice the knives cannot actually cut the hard fibres, however, gentle pressure fractures the fibres with one or two passes. “Snap-off” knife blades are commonly used as the cutting edge is rapidly worn by the hard fibres. Although it is possible to cut complex shapes with the use of templates, laser cutting has been shown to be the most efficient way to cut a large amount of non-rectangular boron plies. Circular patches, for example, are readily cut using a laser cutter with the pre-preg supported on a backing material such as Masonite.

The combination of very high compressive stiffness, large fibre diameter and high hardness means that boron fibres can readily penetrate skin and care must be exercised in handling boron pre-preg to reduce the chance of splinter-type injuries. If a fibre does enter the skin, it should be removed very carefully with fine tweezers. Trying to squeeze the fibre out must be avoided as the fibre may fracture into smaller segments.

The stiffness and diameter of boron fibres also restricts their use in small radius corners. The 100 micron diameter fibre can be formed into a radius of 30 mm, but this is about the limit than can be comfortably achieved. The smaller diameter of graphite fibres makes it the choice for smaller radii situations. In most other aspects, boron pre-pregs handle and process in a similar fashion to the more common graphite pre-preg materials.

As a repair material, boron/epoxy composites have a number of advantages [1,6] including;

- an intermediate coefficient of thermal expansion which helps to minimise the level of thermally induced residual stress which results from an elevated temperature cure. This contrasts with graphite fibres mentioned below.
- relatively simple NDI is possible using eddy currents through the repair patch to detect the extent of the defect. This is possible due to the non-conducting nature of the fibres.
- no galvanic corrosion problems when bonded to common airframe materials.
- a good combination of high compressive and tensile strength and stiffness (the compressive strength of a unidirectional B/EP composite is 2930 MPa compared with 1020 MPa for HMS GR/EP)

Graphite fibres are now available in a very wide range of properties and forms and improvements in manufacturing processes has seen the cost of the fibres reduce over the past 25 years. Although the fibres are not as hard as boron, the cured

composites are very abrasive and diamond tipped tools are normally used for cutting or machining. The fine graphite laden dust from such operations is believed to be a health hazard and so measures to control this hazard must be taken. This electrically conducting dust can also cause problems with electrical equipment if it is not removed and filtered from the room air. Graphite pre-pregs are commonly available as 120°C and 175°C curing systems and lower temperature cure resins are also available now for use in repair situations.

Graphite fibre is an unusual material in that it has a slightly negative coefficient of thermal expansion, which means that the fibres contract slightly in the axial direction when heated. This results in relatively high levels of thermally induced residual stress if the cured composite is bonded to the structure with an elevated temperature curing adhesive. As well, the fibres are electrically conducting and will cause galvanic corrosion of aluminium if the two are in electrical contact. Due to the electrical conductivity it is more difficult to use eddy-current NDI methods with these materials to check the position of a crack under the patch for example.

Graphite composites are significantly cheaper than boron composites and are available from a very wide range of suppliers. They offer a wide range of properties for design and with epoxy resin matrices are readily processed and can be cured to complex shapes to suit the damaged structure. If a repair is required to a tight corner with a small radius, graphite fibres would be preferred to boron as mentioned above.

Repairs to aircraft are usually weight critical and so the specific properties of the various repair materials are therefore of interest. Table 2.2 compares the mechanical and thermal properties of some candidate patch or reinforcing materials. This comparison includes boron/epoxy (b/ep) and graphite/epoxy (gr/ep), the metal/composite laminates GLARE and ARALL and typical high-strength aluminium and titanium alloys – which also represent the metals to be repaired.

2.2.3. Patch material selection

Many of the criteria for selection of a successful repair material have been discussed in the above two sections. The reader is referred to Sections 2.1 and 2.2 for a complete discussion of the issues and in this section a summary of the main points is given referring to the four main repair materials and some of the main design issues that are commonly faced.

- Patching efficiency: High tensile stiffness is required to minimise the crack opening displacement after repair and therefore keep the stress intensity and crack growth down. The fibre composite materials are naturally more efficient than either the conventional or laminated metallic materials (refer Table 2.2 for specific stiffness i.e. modulus divided by density).
- Operating temperature: For sustained high temperature operation over 150°C, a titanium patch may prove to be the best solution. Conventional aluminium alloys and the laminated metals would need to be carefully investigated as there are a range of upper temperature limits depending on the alloy and heat treatment involved. In general, most aluminium alloys could withstand extended

Table 2.2

Relevant materials mechanical and physical properties for component and patch materials.

Material	Modulus GPa	Shear modulus GPa	Critical strain $\times 10^{-3}$	Fatigue Strain $\times 10^{-3}$	Density (g/cm ³)	Thermal expansion coefficient °C $\times 10^{-6}$
Aluminium alloy 7075 T6	72	27	6.5	3.3	2.8	23
Aluminium alloy 2025 T3	72	27	4.5	3.3	2.8	23
Titanium alloy 6 Al/4V	110	41	8.8	6.8	4.5	9
Boron/epoxy b/ep (unidirectional)	208 max 20 min	7	7.3	7.0	2.0	4.5 min 23 max
Graphite/epoxy gr/ ep (unidirectional)	148 max 12 min	5	13	12.0	1.6	- 0.3 min 28 max
Aluminium laminate GLARE 2	65	na	5.2	3.3	2.5	~ 15
Aluminium laminate ARALL 3	68	na	8.9	3.3	2.3	~ 16
Electroformed Nickel	207	76	1.7-3.4	na	~ 9	~ 13

Notes: (a) Maximum modulus and minimum expansion coefficient are in the fibre direction, other values are for the transverse direction, (b) shear modulus values for the composite are for through-thickness deformation, (c) critical strain refers to failing strain for the composites and yield strain for the metals, (d) fatigue strain refers to approximate strain for crack initiation at 10^6 cycles, $R \sim 0$.

periods at 120°C, which is slightly higher than the normal operating temperature of 105°C for a 175°C curing composite pre-preg. Higher temperature curing resins are available for composites, although the availability is not as high and depending on the system involved, processability may be reduced.

- Residual stress: If a repair (cured at elevated temperature) is likely to see extended service at low temperatures (for example a fuselage repair to a transport aircraft – [4]), the best choice may be either a conventional or laminated metallic material where the coefficient of thermal expansion is more nearly matched to the structure. In this situation, graphite/epoxy repairs and to a lesser extent boron/epoxy repairs will result in higher levels of thermally induced residual stress [7].
- Cost: Although not usually a major driver, conventional metallic materials would offer the lowest material costs, followed by the laminated metals, graphite composites and the boron fibre composites are the most expensive. Analysis of repair costs need to be done carefully as often a composite repair may prove to be cheaper than a metallic repair despite greater material costs. This is largely due to the excellent formability of composites and the reduced time required to form the repair patch to the desired shape.
- Inspections: If full use is made of the benefits of bonded repair technology and the defect is left in the structure under the repair, it is likely that future non-

destructive inspections will be required to confirm that the defect has not grown significantly in size. Boron composites are well suited to such circumstances, as the routine use of eddy currents will detect the presence of fatigue cracks for example under the patch. The detection of defects with eddy currents under highly curved boron repairs is more difficult as is the detection of defects under any sort of graphite repair due to the conductivity of the fibres. Detection of defects under bonded metallic repairs can be difficult and may involve the use of X-rays or ultrasonics.

- **Weight:** If the repair is to be made to a weight critical component such as a flight control surface, materials with the highest specific properties are desirable. The composite materials will enable repairs with greatly reduced weight compared with the metallic materials. This same point is also of relevance where aerodynamic smoothness is important. Composite repairs will typically be one-third the thickness of an aluminium repair and so will provide significantly less drag.

2.3. Adhesive systems

Adhesive technology has undergone rapid growth over the past 50 years and adhesives are now widely used in markets such as automotive, aerospace, construction, packaging and consumer appliances. Most common adhesives can be usefully categorised as belonging to one or more of the following classes; structural, hot melt, water-based or pressure sensitive. Of these only the structural class is of interest in this book. Structural adhesives are defined as those adhesives capable of withstanding significant loads and capable of bonding together adherends also capable of carrying significant loads. For the purposes of this book, shear strengths of 10 MPa would be seen as the minimum requirement.

2.3.1. Adhesive types

Within the structural adhesive class are a number of adhesive types based on chemistry. The most important are epoxies, modified acrylics, polyurethanes, cyanoacrylates, anaerobics, phenolics and polyimides. Anaerobics cure in the absence of oxygen by free radical polymerisation and are widely used in threaded assemblies to prevent loosening of nuts. They can develop high shear strengths but generally have limited temperature capability and are not used for Bonded Repairs. Cyanoacrylates cure due to the presence of water molecules on the adherends which act as initiation sites for polymerisation. They have excellent shear strength but are comparatively brittle with poor peel strength, are not suitable for filling gaps and are degraded by moisture. Relatively high shrinkage stresses on cure also mitigate against their use in Bonded Repairs. Polyurethanes have good toughness and flexibility, but tend not to have the high shear strength and temperature capabilities that are required for bonded repairs. Phenolic adhesives were the original structural adhesives used in aircraft construction but tended to be very brittle until the

introduction of modified phenolics (the “Redux” adhesives) which had higher peel strength. Phenolic adhesives exhibit excellent bond durability and the modern nitrile modified phenolics are widely used in a range of demanding applications. In general, however, they require high cure temperatures and pressures which may be difficult to accommodate in a repair situation. The other main structural adhesives are those capable of very high temperature operation such as the polyimide (PI) or bismaleimide (BMI) adhesives. These could be considered in specialised repair applications, however, compared with epoxies or acrylics they tend to be difficult to cure.

The two adhesive types used most successfully for Bonded Repairs are the epoxies and modified acrylics. The properties of these adhesives are discussed in greater detail in the next section. Acrylics are normally produced in paste form, however, epoxies are commonly available in both paste and film versions. Film adhesives have the resin and curing agents pre-mixed at the factory and are then coated onto a thin carrier cloth or scrim in the form of a thin film. The advantages of this are that mistakes can't be made in mixing the correct ratio of hardener, the film makes it easy to achieve uniform thickness bondlines and film adhesives are much easier to apply and handle than pastes. Disadvantages are increased cost and the resin is effectively curing as soon as the hardener is mixed and therefore film adhesives must be refrigerated to provide a reasonable shelf life.

2.3.2. Adhesive properties

Epoxies come in a very wide range of formulations and types but are generally characterised by high levels of strength, good temperature capability, low shrinkage stresses on cure and the ability to form durable bonds. Epoxies are normally considered to be the most expensive of the common adhesive types (although are not as expensive as the high temperature polyimides). The ability to form durable bonds is highly dependent on the level of surface treatment that is applied to metallic adherends in contrast to the behaviour of acrylic adhesives. The temperature capability of the adhesive is dependent on the cure temperature and so for repairs to structure that sees high temperatures, an elevated temperature cure is required. Room temperature curing epoxies are commonly available in paste form (usually two components) and these adhesives can often provide moderate temperature capability with a post cure to above the operating temperature. Some pastes can also provide higher temperature capability, however, for service at 100 °C or higher, film adhesives are commonly used. Unmodified epoxies are inherently brittle materials like phenolics and so most commercial systems are modified with the addition of the toughening agent which is commonly an elastomer.

Modified acrylics or second generation acrylics were developed during the 1960s from the original acrylics which were too brittle to be of practical use in structural joints. The rubber toughened acrylics have good shear and peel strengths although the shear strengths are generally not as high as those of the epoxies. They usually cure rapidly at room temperature, in some cases within 1 to 2 min, and they have

the ability to readily bond a range of different adherend materials. The ability of these adhesives to develop good adhesion strengths with limited surface treatment is due to the acrylic monomer which is a free flowing liquid of low surface tension. Modern acrylics are able to produce strong, durable bonds to unprepared aluminium and steel surfaces; epoxy adhesives are unable to achieve this. Commercially available systems now do not require mixing of two components but instead can use an activator applied to one adherend and the adhesive to the other which simplifies the use compared with two-part epoxies. Disadvantages include an odour that some people find objectionable, limited temperature capability and limited pot life which can be a problem for larger repairs. Acrylics are widely used in industrial applications where the ability to rapidly bond poorly prepared steel sheet is an important advantage and is able to replace the use of spot welding or riveting.

2.3.3. Adhesive selection

The designer of a bonded repair has a very wide range of adhesives to choose from, although in practice the selection is usually made from those adhesives that are readily available to the company. The two most important selection criteria are temperature and load carrying capability. A conservative approach is to use an adhesive for the repair of equal temperature capability to the original structure. This is typically 120 °C cure for commercial (subsonic) aircraft and 175 °C cure for military (supersonic) aircraft. However, the use of a 175 °C curing adhesive during manufacture does not necessarily mean the structure will be exposed to such high temperatures. Often a 175 °C adhesive is used in manufacture to be compatible with the 175 °C curing pre-preg so that the part can be cured and bonded in one autoclave cycle. If the actual operating temperature of the component can be shown to be 60 °C for example, it is possible to produce a sound repair with a 120 °C curing adhesive.

It should be noted that the use of 175 °C curing adhesives for repair has in itself caused significant problems when the structure to be repaired contains honeycomb core and water is present within the core. At around 140 °C, the pressure generated inside the core by the air and water exceeds the flat-wise tension strength of the skin to core adhesive and the skin can be disbanded by the pressure. The risk of such damage occurring is greatly reduced at 120 °C and at least one adhesive manufacturer has developed a 120 °C version of the standard 175 °C adhesive system for use during repair to honeycomb structure.

Bond durability (particularly for epoxies) is generally related to cure temperature and it is common to find excellent bond durability for 175 °C systems, good durability at 120 °C but only fair to good durability for room temperature curing adhesives. The improvement in durability for the 175 °C cure, however, needs to be weighed up against the other problems which can develop such as blown skin to honeycomb core bonds and increased thermally-induced residual stresses.

The required load carrying capacity of the adhesive needs to be carefully considered. Some manufacturers of structural adhesives are now beginning to

provide design data in the form of shear stress/shear strain data. The more common lap shear strength is not suitable for use in a bonded repair and is generally only useful in comparing one adhesive to another. Details of the data that is required for design based on adhesive properties is given in Chapter 4, and if it is necessary to generate this data, appropriate test methods are described in Section 2.5 and Chapter 4. Two key parameters are the shear strength and plastic strain to failure. The adhesive needs to have sufficient shear strength so as not to yield excessively under the design loads, and care should be taken in designing with relatively brittle adhesives which cannot provide a soft, yielding type of failure under high loads.

Less well understood is the ability of the adhesive to withstand through-thickness stresses, i.e. those perpendicular to the plane of the joint. Conventional design wisdom with adhesive joints is to eliminate such stresses by the use of different design techniques. In many cases it is possible to eliminate or greatly reduce the magnitude of these stresses simply by the use of sensible design features such as tapering of the end of the repair. In some circumstances, however, it is not possible to reduce these stresses and some examples are given in Chapters 30 and 33. In repairs to structure involving a high degree of curvature, the question then becomes one of determining the capacity of the adhesive to withstand the through-thickness or peel stresses that are present. There is currently no generally agreed test method to generate design data for this situation, although a novel test specimen has been proposed which may be suitable for this purpose [8,9]. Any repair design where high levels of peel stress are likely to be present needs to be very carefully considered and would be expected to require extensive analysis and experimental validation for certification. The work described in [8] is aimed at increasing the understanding of the performance of adhesives under peel stresses, however, while this may lead to some easing of certification requirements, the sound engineering practice will continue to be to design peel stresses out of an adhesive joint where ever possible.

Other criteria which may be important in the selection of a repair adhesive could be availability and the ability to cure at low temperatures. Availability and the requirement for refrigerated storage could be important at some forward Air Force bases for example, where only a very limited range of adhesives may be available at short notice. When rapid repairs have to be made in primitive conditions, for example to battle damage, it may not be possible to provide refrigerated storage and therefore only two-part adhesives would be available. As described in Section 2.6, thermally-induced residual stresses are produced when the repair material has a different coefficient of thermal expansion to the substrate and an elevated temperature cure is necessary. The obvious way of reducing the level of such stresses is by reducing the cure temperature of the adhesive as much as possible. Some adhesives are able to cure at temperatures lower than their advertised cure temperature although this is not always the case [10]. Film adhesives are often sold as either 120 °C or 175 °C curing systems (partly for compatibility with other pre-pregs etc.), however, a careful examination of the thermodynamics of cure can indicate that the optimum cure temperature is different from these advertised temperatures. Considerable care must be taken if a decision is made to cure at

temperatures other than those advertised to ensure that other properties are not compromised.

The ability of the adhesive to remain durable in the operating environment is normally of critical importance and consideration may need to be given to the influence of solvents or chemicals which the adhesive may be exposed to. For example some repairs have been applied inside aircraft fuel tanks or in regions where the adhesive is exposed to hydraulic oil. Most epoxies and acrylics have very good resistance to solvents and chemicals and so these types of exposures have not been of major concern to date, but do need to be checked on an individual basis [11].

Where possible it is recommended that repairs are cured under positive (as compared to vacuum) pressure and further details are given in Chapter 25. When the use of vacuum bag pressure is the only alternative, consideration may need to be given to the void content in the cured adhesive bondline (Section 6.2). Some adhesives do not cure well under vacuum and heavily voided bondlines can result. There is some evidence to suggest that moderate amounts of voids do not adversely affect fatigue strength, however, in general significant void contents in structural adhesive bondlines are to be avoided.

2.4. Primers and coupling agents

A range of different chemicals may be required for effective surface preparation and a detailed scientific discussion of these is given in Chapter 3. This section will look at some of these chemicals from a materials engineering perspective and consider some of the common factors that may be need to be considered in the overall design of the repair.

From Section 2.1 it is clear that significant attention must be paid to the surface treatment of metallic adherends prior to bonding if a strong, durable adhesive bond is to be produced. There are two major types of treatments for aluminium alloys that for historical reasons have developed in Europe and North America. In Europe, the preferred treatment is the use of a chromic acid etch to produce a hydration resistant oxide, whereas in North America the use of phosphoric acid is preferred. Both treatments have been used successfully in aircraft manufacturing and are capable of producing highly durable bonds. Components are dipped into tanks of acids and other chemicals in the factory to produce the required oxide structure for bonding. The difficulty comes in transferring this technology to a repair situation. For example when acids are used on an assembled aircraft structure, care must be taken to completely remove the acids or corrosion may result. Boeing in particular have developed procedures whereby the same technology as used in manufacturing can be applied to some repairs. The phosphoric acid containment system (PACS) uses vacuum bags over the repair site to transport the acid across the surface. This contains the acids to minimise health and safety concerns and permits a final flush with water to remove the acid from the aircraft surface. The anodisation is carried out under the bag as well. This

procedure can produce bonds with durabilities close to the best factory treatment such as a full phosphoric acid anodisation (PAA). While this process can be highly effective, it requires specialised equipment, it is relatively complicated to perform and cannot be used in many repair situations.

A common requirement in repair situations is for a surface treatment method which is simple to use, preferably does not require use of anodisation (the electrical voltage of which can create a hazard inside wing tanks for example) and does not use chemicals that could cause harm to either the operator or aircraft. In some situations a repair must be applied to two different materials at the same time and so the ability to treat both metals at the same time can be an advantage. The use of silane coupling agents can meet all of these requirements. Silanes are well known as adhesion promoters and are bi-functional molecules containing polar silanol groups and organofunctional groups capable of reacting with the chosen adhesive. The silanol group forms a strong bond with the oxide surface that is hydrolytically stable, and the organofunctional group forms a strong bond with the adhesive. It is of course important to choose a silane that is compatible with the adhesive being used. Silanes are available for both epoxy and acrylic adhesives.

The use of silanes as a coupling agent is advantageous in a repair situation for several reasons. Silanes do not cause any damage to the surrounding structure if they are not completely removed following application. They are very simple to apply requiring only hydrolysis prior to use and can be applied simply with no special equipment required. They are relatively safe to use, although care must be taken to avoid ingestion and contact with the eyes. Silanes can effectively treat a range of different materials thereby greatly reducing the complexity of the repair application. Finally they are very effective as coupling agents and can produce adhesive bonds with durabilities close to that produced by the factory PAA treatments.

Further improvement in the bond durability can be achieved with the use of a corrosion inhibiting primer after the application of the silane or other surface treatment. Primers are normally dilute polymeric solutions which are usually sprayed onto the bonding surface and are able to easily wet the surface. If the surface has been roughened by abrasion, the primer is able to flow easily over the surface irregularities to provide a thin polymeric layer in intimate contact with and having strong bonds with the surface. The polymer is chosen to readily bond to the repair adhesive and is often the same type of polymer. Primers commonly require a period after spraying to enable volatiles to evaporate before the primer is cured at elevated temperature. A surface primed in this way can be stored for several months prior to bonding, requiring only a careful solvent wipe to remove surface contamination prior to bonding. The primer will often contain fine chromate particles which help to prevent the hydration of the adjacent metal oxide layer. The chromate particles are however toxic and care must be taken in the use of such primers. The thickness of chromated primer layers for use in an adhesively bonded joint is also important and care must be taken to follow the manufacturers' directions and not to build up too much thickness in the sprayed layer.

2.5. Adhesive and composite test procedures

There are a wide range of test procedures that are directly applicable to adhesives and composites and these range from quality assurance type tests to chemical and physical tests to measure adhesive properties to static and fatigue tests aimed at generating mechanical design data. Mechanical tests are covered in Chapter 4, where the use of the thick-adherend lap shear test is described to generate adhesive shear stress and shear strain data. Also in this section is a description of the skin doubler specimen for fatigue testing and the double cantilever beam specimen for Mode I fracture toughness.

An important test for quality assurance is the flow test that measures the ability of the adhesive to flow when heat and pressure are applied. This is particularly important for film adhesives where the catalyst and resin are pre-mixed in the factory and so the adhesive is effectively curing all the time. As described in Section 2.3.1, film adhesives require refrigeration to ensure the curing reaction is reduced to a level where the adhesive has a reasonable shelf life. When stored under the appropriate conditions, the shelf life of the adhesive should be as specified by the manufacturer. If there is any doubt as to whether the adhesive may have cured or "advanced" too far to be of use, a flow test can be performed. There are many forms of flow tests in existence and a typical example is that specified in [12]. In this test, discs of film adhesive are punched from the film and subjected to heat and pressure in a controlled manner. The adhesive flows and cures and the degree of flow is measured as a function of the increase in perimeter or area. Flow of an adhesive drops rapidly as the adhesive crosslinks and it is possible to set flow criteria beyond which the adhesive is deemed to be no longer useable. As described in Section 2.1.1, it is essential for the adhesive to flow during the cure to adequately wet the adherends and produce high bond strengths. The advantage of the flow test is that it is relatively simple to perform and does not require particularly sophisticated equipment. A similar result can be obtained from chemical tests such as Differential Scanning Calorimetry in which the amount of unreacted epoxide is measured. Tests such as these are perhaps more precise than a flow test, but require sophisticated equipment and skilled operators to perform the tests. Although simple mechanical tests such as lap shear strength have been used to determine whether an adhesive is still in life, this property is not very sensitive to overageing and so the much more sensitive flow measurement is to be preferred.

When film adhesive is used for a repair, there are often good reasons to deliberately advance or "B-stage" the adhesive prior to cure (see Section 2.6.2 for details). Where this is done it is very important to ensure that the adhesive is not B-staged to the extent that flow is compromised. A flow test can be used to confirm that sufficient flow remains in the adhesive after the B-staging process. Using this method, a B-staging time of 45 min at 80 °C has been proposed for use with fresh FM73 adhesive [13]. Note that the B-staging conditions will change as the adhesive stock ages. B-staging for 45 min at 80 °C will not be appropriate for FM73 adhesive which exhibits only marginal flow in the un B-staged condition. One way of managing film adhesives (for repair situations) is to always use the adhesive in

the same flow condition. When the adhesive stock is fresh, the adhesive may require considerable B-staging prior to use, but the amount of B-staging will reduce progressively as the stock ages, until the flow limit is reached. At this time the adhesive could be used without B-staging, but any further ageing of the stock would take it over the flow limit and would require that stock to be scrapped.

If a composite material is being used for the patch, a simple test to confirm that it is within life and is suitable for use is the interlaminar shear (ILS) test or short beam shear (SBS) test. One form of this test is described in ASTM D2344. As for the flow test, the test is relatively simple to perform and only requires a small amount of material and mechanical testing equipment. This test measures the interlaminar shear strength of a small sample of the material, and this strength is a resin dominated property. If the resin in the pre-preg is too advanced, the pre-preg will not flow adequately during cure and high shear strengths between the laminae of the composite will not be developed. In this test, the critical factor is the correct ratio of the support span to specimen thickness. For the 5521/4 B/Ep composite, an ILS value of 97 MPa or above, indicates the material is in good condition.

An advantage of the use of metallic materials for repair patches is their infinite shelf life. No testing is required before use, other than to confirm that the alloy and heat treatment are correct.

2.6. Materials engineering considerations

2.6.1. Residual stresses

An adhesively bonded repair may experience high levels of residual stress [1]. These stresses are thermally induced and generally arise from the different coefficients of thermal expansion of the repair substrate and repair material respectively. The influence of these stresses can be readily seen in a coupon specimen as shown in Figure 2.1. Note that in a real repair, the restraint from the

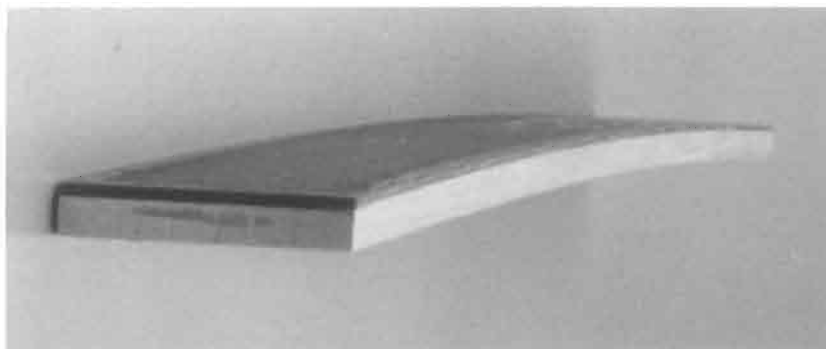


Fig. 2.1. Photograph of a 3 mm thick 2024 aluminium specimen with a 0.6 mm thick boron patch. The curvature results from the 121 °C cure temperature used to cure the FM73 adhesive.

substructure will minimise any actual bending, however, the residual stresses will still be present. Often, if an elevated-temperature curing adhesive is used, residual stresses will exist when the repair has cooled to ambient temperature. On the other hand if an ambient-temperature curing adhesive is used with different repair materials, residual stresses can be induced if the repair has to operate at temperatures significantly different from that at which the cure was achieved. The level of stress is highest when the difference between the coefficients of thermal expansion (α) are greatest. The use of a unidirectional gr/ep repair patch (which has an α of $-0.3^{\circ}\text{C}^{-1}$) will create a large residual stress when bonded to aluminium ($\alpha = 23.5^{\circ}\text{C}^{-1}$).

If the repair material is different to the substrate, the level of residual stress should be calculated during the design process. Procedures for analysing the residual stress level are given in Chapter 11. In extreme cases, the level of thermally induced residual stress can be large enough to fail the joint, although this is not usual. Residual stresses will influence the stress intensity at the defect site after repair and possibly the static and fatigue strength of the repair and therefore it is important that they be carefully considered during the repair design.

There are several ways in which the level of residual stress in an adhesive joint can be minimised. Clearly choosing the repair material to be the same as the substrate is the easiest, however, this may often not be the optimum choice. Usually the benefits of using a fibre reinforced composite as the repair material outweigh the disadvantage of increased residual stress levels. Secondly, it may be possible to reduce the temperature of cure so as to keep the residual stress levels as low as possible and the factors to consider in such a situation have been discussed in Section 2.3.3. Thirdly, if the extent of the structure to be heated is minimised, this will act to keep the residual stresses low. For example, when an aluminium skin of an aircraft is heated, the skin is not able to expand in an unconstrained manner. The structure surrounding the heated zone will be cooler, will not expand as much and will therefore act as a constraint to the expansion of the repair zone. For this reason, when it is important to minimise residual stresses, consideration can be given to heating the smallest possible repair zone so as to maximise the constraint. Analytical considerations for constrained expansion are discussed in Chapter 11. Of course care must be taken to ensure that the adhesive is uniformly heated and that the edges of the repair are not under cured (Chapter 24). Finally, it may be possible to apply a pre-load to the structure to off-set the expected thermal expansion. This has been done successfully during an important reinforcement to the F-111 Wing Pivot Fitting [10]. An upload was applied to the wing, prior to the repair, placing the upper wing skin in compression. Normally the metallic substrate is left in a state of tension following the elevated temperature cure. By releasing the compressive pre-load after the repair, the extent of the tensile residual stress was substantially reduced.

2.6.2. Cure pressure and voids

Voids within the adhesive bondline are generated during the cure from either entrapped air or from gases generated from the adhesive or adherends. The gas will

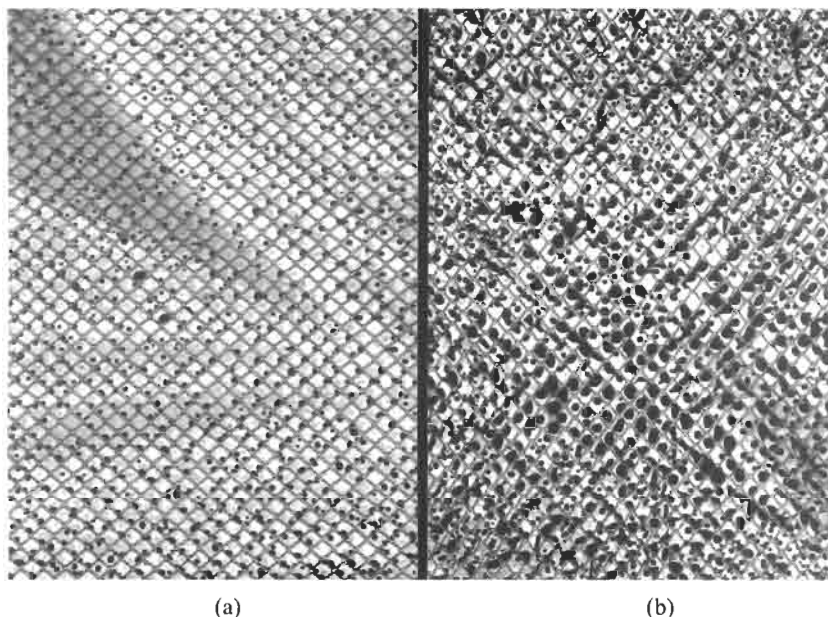


Fig. 2.2. Micrographs showing fractured adhesive surfaces containing voids. The void concentration seen in (b) resulted from the aluminium substrate being heavily grit blasted before application of the silane solution. The only different process applied to (a) was a drying period at 110 °C in an oven after the application of the silane.

typically form a bubble within the liquid adhesive and when the adhesive has cross-linked and solidified, the bubble remains as a void as shown in Figure 2.2. Gases that are commonly involved in this process are water vapour present on the adherends [13], water or other chemicals generated during the curing reaction, or solvents such as MEK or acetone present within the adhesive that are liberated during the cure. The gases themselves are not normally of any concern, however, the voids that are created by the gases can act as stress concentration sites within the adhesive. If the void concentration is sufficiently high, there could be a reduction in the mechanical properties of the joint. In extreme cases the void content can be more than 50% of the joint area, and at these levels significant reductions in strength can be expected. A preliminary study into the influence of voids on fatigue strength indicated that for FM300 adhesive, a void content of more than 30% was required before there was a noticeable drop in fatigue performance. A possible reason for this was that the scrim cloth inside the adhesive acts as a site for fatigue initiation and occupies approximately 30% of the joint area. It is not until the void content exceeds this level that there is a marked reduction in fatigue life.

Void contents less than 5% should be readily achievable in adhesive bondlines during repair procedures. Keeping void contents low is a matter of recognising the origins of the voids and ensuring that appropriate procedures are used. If the

voids arise from adsorbed water vapour on the adherends, the bonding surfaces should be dried prior to bonding [13]. Entrapped air can be minimised by correct procedures such as avoiding blending air into paste adhesives during mixing, and avoiding applying film adhesives to adherends at too high a temperature where they become too tacky. Voids generated from volatiles within the adhesive are perhaps the most common reason for voids in film adhesives and can be minimised in several ways. Before using the adhesive, it may be possible to “B-stage” the adhesive film by gently heating in an oven. This permits the volatiles to be released and partially cures the adhesive. This partial cross-linking prior to the full cure helps to prevent the expansion of voids. Care needs to be taken during a B-staging operation to ensure the adhesive is not advanced too far so that flow is restricted. Pressure applied to the joint during the cure helps to restrict the expansion of the volatile gases within the voids. In this regard the use of positive pressure is much preferred to the use of a vacuum bag, as the negative pressure within the bag can allow the expansion of the voids at some locations such as around the edges or where the bag is unable to transmit the atmospheric pressure. With either type of pressure application, it is difficult to generate the high pressure desired in the interior of the joint if the joint is too narrow [13]. Figure 2.2 illustrates the improvements in void contents that are possible by using improved processes and with a fully optimised bond procedure, negligible void contents should be readily achievable.

2.6.3. Spew fillet

For structurally loaded joints, it is well known [14] that the adhesive spew fillet that forms around the edge of the joint is beneficial. This spew is formed as some of the adhesive flows out from under the repair patch during the cure and the resulting fillet acts to soften the stress concentration at the edge of the repair patch. The presence of the fillet can reduce the magnitude of the shear stresses at the end of the joint by around 30%. It is thus very important that this adhesive fillet is not removed during the final clean up procedure.

The condition of the fillet can also be an important point to visually check after the repair has been completed. Some information about the quality of the adhesive bond can be gained by this visual inspection. The absence of a well formed, smooth fillet would indicate poor flow of the adhesive and this may have been due to inadequate pressurisation, out of life adhesive or perhaps the heat up rate being too slow. An extremely high void content in the fillet could be an indication of an excessively high volatile content within the adhesive or perhaps the use of poor pressurisation procedures involving a vacuum bag. A large amount of adhesive in the fillet may indicate that the bond has been subjected to excessive pressure and that the bondline around the edge of the joint may be starved of adhesive due to excessive flow. If the spew is not fully hardened, it would indicate that the cure is not complete and either the required time or temperature has not been reached.

2.6.4. Composites offer the possibility of embedded strain sensors to form “SMART” repairs

There are a number of materials engineering advantages when a composite material is used to form the repair patch rather than a metallic material. One of these is that the patch can be readily formed to match the complex curvatures that are often found on aircraft surfaces. Another is that by virtue of the way in which composite materials are produced, it is comparatively easy to include small sensors within the patch material. In the short term this is unlikely to be cost effective for routine repairs as the additional costs involved will be high, however, this is expected to change as the costs of sensors and associated instrumentation reduce. For critical repairs to primary structure, these extra costs are less important and repairs are being developed for such applications with inbuilt sensing mechanisms. These patches will have the ability to detect strain transfer into the patch and therefore will be able to determine if the patch is disbonding. When combined with the ability to transfer the data collected by remote means (infra red or high frequency communication for example), the “Smart” repair will be able to inform the maintenance crew if there is any important structural problem. This topic is covered in more detail in Chapter 20, where some examples are given of the way in which the technology can be used.

References

1. Baker, A.A. and Jones, R. (eds.) (1988). *Bonded Repair of Aircraft Structures*, Martinus Nijhoff Publishers, Dordrecht.
2. Hart-Smith, L.J., Brown, D. and Wong, S. (1993). Surface Preparations for ensuring that the Glue will stick in Bonded Composite Structures, 10th DoD/NASA/FAA Conference on Fibrous Composites in Structural Design, Hilton Head Is, SC.
3. Vlot, A., Vogelesang, L.B. and de Vries, T.J. (1999). Towards application of fibre metal laminates in large aircraft. *Aircraft Engineering and Aerospace Technology*, **71**(6), pp. 558–570.
4. Fredell, R., van Barneveld, W. and Vogelesang, L.B. (1994). Design and testing of bonded GLARE patches in the repair of fuselage fatigue cracks in large transport aircraft. *Proceedings of the 39th International SAMPE Symposium*, 11–14 April, pp. 624–638.
5. Solly, R.K., Chester, R.J. and Baker, A.A. Bonded Repair of a Damaged Army Field Gun, Using Electroformed Nickel Patches, in preparation.
6. Chester, R.J., Clark, G., Hinton, B.R.W., *et al.* (1993). Research into materials aspects of aircraft maintenance and life extension. *Aircraft Engineering*, Part 1, **65**(1) pp. 2–5, Part 2, **65**(2) pp. 2–5, Part 3, **65**(3), pp. 2–6.
7. Fredell, R., van Barneveld, W. and Vlot, A. (1994). Analysis of composite crack patching of fuselage structures: High patch elastic modulus isn't the whole story. *Proceedings of the 39th International SAMPE Symposium*, 11–14 April, pp. 610–623.
8. Bartholomeusz, R.A., Baker, A.A., Chester, R.J., *et al.* (1999). Bonded joints with through thickness adhesive stresses – reinforcing the F/A-18 Y470.5 Bulkhead. *Int. J. of Adhesion and Adhesives*, **19**, pp. 173–180.
9. Chester, R.J., Chalkley, P.D. and Walker, K.F. (1999). Adhesively bonded repairs to primary aircraft structure. *Int. J. of Adhesion and Adhesives*, **19**, pp. 1–8.
10. Baker, A.A., Chester, R.J., Davis, M.J., *et al.* (1993). Reinforcement of the F-111 wing pivot fitting with a boron/epoxy doubler system – materials engineering aspects. *Composites*, **24**, pp. 511–521.

11. Chalkley, P.D. and Geddes, R. (1999). Fatigue testing of bonded joints representative of the F-111 WPF Upper Plate Doublers. DSTO - TR - 0920, December.
12. Boeing System Support Standard BSS 7240 Adhesive Flow Test.
13. Chester, R.J. and Roberts, J.D. (1989). Void minimisation in adhesive joints. *Int. J. of Adhesion and Adhesives*, **9**, p. 129.
14. Adams, R.D. and Peppiatt, N.A. (1974). Stress analysis of adhesive-bonded lap joints. *J. Strain Analysis*, **9**, pp. 185–196.

Chapter 3

SURFACE TREATMENT AND REPAIR BONDING

D. ARNOTT, A. RIDER and J. MAZZA*

Defence Science and Technology Organisation, Air Vehicles Division, Australia

**Materials and Manufacturing Directorate, U.S. Air Force Research Laboratory (AFRL/MLSA), Australia*

3.1. Introduction

Adhesion can be seen as the force or energy of attraction between two materials or phases in contact with each other [1]. In order to achieve intimate contact, one phase called the adhesive must behave as a liquid at some stage and wet the second phase called the adherend. It may be necessary to apply heat or pressure for the adhesive to behave as a liquid. Once formed, the adhesive bond is expected to carry loads throughout the life of the joint. Although many substances can act as an adhesive, the discussion here is restricted to toughened epoxy adhesives used to bond metallic aircraft structure. Discussion of adherends will also be restricted to metals and composites.

This chapter focuses on prebonding surface treatments and bonding procedures leading to the development of durable void-free adhesive bonds for repair applications. It describes both fundamental aspects, including some current research work, and practical procedures. A basic understanding is required to avoid some of the many pitfalls that can lead to inadequate bonding. It is complimentary to Chapter 24 which deals also with practical bonding.

There is no doubt that the reproducible development of durable bonds is a key issue for bonded repair technology [2].

3.1.1. Surface energy and wetting

The complex interface between an adhesive and a metal adherend is best described as an interphase in which critical dimensions are measured in nanometres. Although there is controversy over the exact nature of the interactions between epoxy polymers and metal oxides on the adherend [3], it is generally believed that the predominant forces involve hydrogen bonds in which the hydroxyl

groups on the metal oxide interact with hydroxyl groups in the polymer [4]. However, it is very likely that a variety of chemical bonds and interaction forces are involved as well.

The interactions between an adhesive and an adherend are often described in thermodynamic terms with expressions derived for the case of a liquid drop adsorbed on a flat, homogeneous substrate in the presence of vapour [5]. The balance of forces between the liquid drop and the solid substrate in equilibrium with vapour (Figure 3.1) can be expressed in terms of the Young equation [6]:

$$\gamma_{sv} = \gamma_{sl} + \gamma_{lv} \cos \theta \quad , \quad (3.1)$$

where γ represents the relevant surface tensions at the three-phase contact point (i.e. solid-vapour (sv), solid-liquid (sl) and liquid-vapour (lv)) and θ is the equilibrium contact angle. Low values of θ suggest strong attractive interfacial forces between the liquid and the adherend or a tendency to wet the substrate and to establish intimate atomic contact with the solid. Contaminant present on the solid can lead to a weakening of the attractive forces with the liquid phase and hence to a change in the contact angle.

The issues of wetting are complex, particularly in response to chemical inhomogeneity [6], rough surfaces [1,7], capillary forces [8] and the dynamic spreading of viscous liquids [8]. Theoretical considerations indicate that external pressure to assist the capillary driving pressure and heat (or solvent) to lower the viscosity of the adhesive will aid wetting and penetration [9,10]. Adherend surface preparation plays a pivotal role in the formation of a strong and durable adhesive bond.

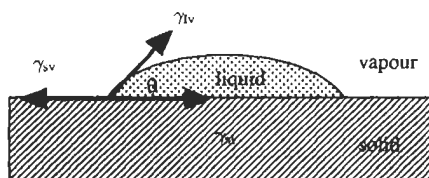


Fig. 3.1. Balance of surface tensions for a liquid drop on a solid surface.

3.1.2. Bondline pressurisation and adhesive cure

The structural film adhesives are cured thermally using controlled heating rates. During heating, the adherends are pressurised either mechanically or hydrostatically. As the temperature is ramped up, the viscosity of the adhesive initially decreases, then it increases as the polymer crosslinks [11]. In a pressurised sandwich of 2 metal plates separated by a film adhesive, the adhesive will flow during the low viscosity phase and the plate separation will decrease (Figure 3.2). A quadratic pressure profile is developed within the adhesive [11]. The local pressure in the adhesive at the centre of the sandwich is higher than the applied load on the plate

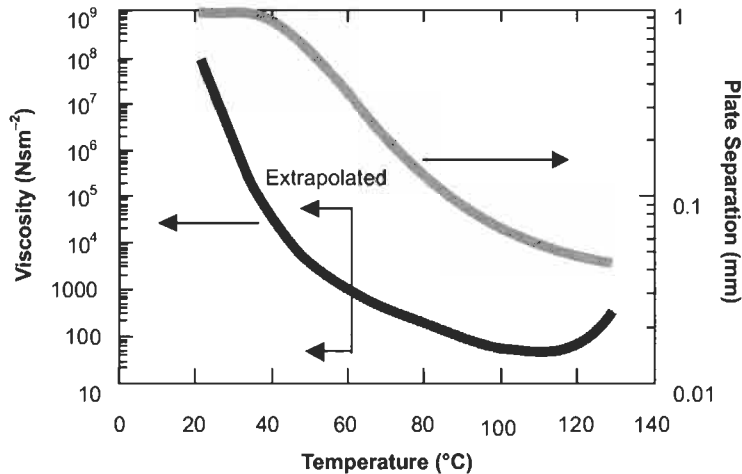


Fig. 3.2. Pressurised sandwich panel showing viscosity changes with temperature and consequent calculated plate separation for a typical thermoset epoxy film adhesive.

and can lead to deformation of thin adherend plates loaded by hydrostatic pressure. The thickness of the bondline at the plate edges can be less than at the centre for cures conducted using vacuum bag procedures. The pressure profile also applies a hydrostatic constraint to bubble development in the adhesive and it is not uncommon for voids to develop at the periphery of a repair when using a vacuum bag for bond pressurisation. It must be kept in mind that almost all structural film adhesives are designed for a positive pressure constraint on volatile gases to minimise bubble development.

3.1.3. Adhesive bond performance

A strong adhesive bond does not imply a long-lasting or durable bond. Water is the environment most commonly assessed in the literature, although other fluids such as fuel and hydraulic fluid may degrade a bond. This chapter will focus on the critical role of adherend surface treatment on the durability of a stressed adhesive bond exposed to a humid atmosphere [12].

Whilst much has been written on the subject of adhesive bonding, knowledge is still inadequate, and the engineering tools available for the through-life management of adhesively bonded structure are primitive. The books by Kinloch [13] and Minford [14] are, respectively, an excellent introduction to adhesion and adhesives and a compendium for adhesion with aluminium alloys. It is not the intent of the authors to reproduce a summary of these works here. The focus will be on surface treatments for repair bonding, giving consideration to the atomic nature of the bond interface and the relationship between microscopic behaviour and macroscopic mechanical properties. It cannot be over emphasised that a strong adhesive

bond does not imply a durable bond. The influence of adherend surface treatment on bond durability is therefore a key issue.

3.1.4. Standards and environments for adhesive bonding

The facilities, environment, conditions, skills and techniques available for adhesive bonding vary widely. However, it must be emphasised that the quality and long-term performance of an adhesive bond relies on attention to standards and the skill of the technician, together with controls over processes and procedures for all bonding situations.

3.1.4.1. Bond integrity and standards

Adhesively bonded components are manufactured, and bonded repairs are conducted, without the benefit of a comprehensive set of effective nondestructive process control tests or techniques to fully assess the through-life integrity of the bonded product. Nondestructively inspected (NDI) techniques may be able to detect physical defects leading to voids or airgaps in bondlines but they cannot detect weak bonds or bonds that may potentially weaken in service. The quality and integrity of the bonded component, thus, relies upon a fully qualified bonding procedure, together with the assurance that the process was carried out correctly. The Aloha Airlines Boeing 737 incident in April 1988, where the aircraft lost part of the cabin roof in an explosive decompression [15,16], illustrates the importance of bond durability and more importantly, the ease with which this issue was overlooked.

In the repair environment, experience has shown that some bonded repair designs and application procedures have little chance of success and can, in some cases, decrease the service lives of components [17]. A survey of defect reports conducted at one Royal Australian Air Force (RAAF) Unit [17–19] indicated that 53% of defects outside structural repair manual limits were related to adhesive bond failure. In addressing the standards applied to adhesively bonded repairs, the RAAF [20] have established a substantial improvement in the credibility of bonded repair technology.

3.1.4.2. Adhesive bonding environments

The performance of an adhesive bond is sensitive to the adherend surface treatment and the environmental conditions under which the bond is prepared. Facilities located adjacent to operational airbases or in industrial environments need to have concern for the effect of hydrocarbon contamination. Facilities in tropical locations need special consideration for the effect of heat and high humidity.

Factory manufacture uses specialised facilities and staff. The facilities will include vapour degreasing or alkaline cleaning, etching tanks, anodising tanks, jigs, autoclaves and appropriate environmental controls. Adhesives will be stored in freezers, and monitoring procedures will be in place. There is a well trained workforce with skills maintained through production volumes, and highly developed inspection procedures are available.

At the other extreme, field repairs are generally conducted with relatively unsophisticated facilities, minimal surface treatments, vacuum bag or reacted force pressurisation and little or no environmental control. Staff multiskilling and rotation influence the currency of experience and hence the quality and performance of adhesive bonds [21]. The requirement for environmental controls, the attention to bonding procedure detail and the need for staff training and supervision is of particular concern.

Depot-level repairs are conducted with facilities and staff skills that vary considerably. Some depots have almost factory-level facilities and high level of staff skill. Other depots are capable of only low-level bonded repairs and are little removed from a field repair capability.

Laboratory experiments are designed to establish knowledge and principles. It is easy to overlook important detail from factory or field experience since most laboratories are held to close environmental tolerances and do not resemble the workshop environment.

3.1.4.3. Constraints for on-aircraft repairs

On-aircraft repairs impose additional constraints on processes and procedures. The considerations include: accessibility of the area, limitations in the use of corrosive chemicals, adequacy of environmental controls and constraints on the tools for pressurisation and heating of the bond during cure. Safety, health and environmental issues are more demanding for on-aircraft bonding since it is harder to control, contain and clean-up hazardous chemicals. Constraints on the use of electrical power on fuelled aircraft, or those with inadequately purged fuel tanks, can restrict the range of treatment and bonding methods available. The surrounding aircraft structure imposes constraints on the choice of surface preparation, heating arrangements and pressurisation tools.

3.2. Mechanical tests

3.2.1. Loading and failure modes

The most common method used to assess the relative performance of an adherend surface pretreatment involves loading an adhesive joint asymmetrically in tension, as shown in Figure 3.3, described as mode I opening. The stresses leading to failure are localised in a region adjacent to the crack tip. The extent of this region depends on the stiffness of the adherends, the toughness of the adhesive and, importantly, the effectiveness of the adherend surface treatment.

The mechanical performance of a bond should be accompanied by an inspection of the fracture surface. Visual inspection assisted with optical microscopy will provide macroscopic information concerning the locus of fracture and the presence of voids or defects. The term cohesive failure describes fracture totally within the adhesive, leaving adhesive on both separated adherends. The term adhesive failure describes a fracture at one interface with the adherend, resulting in one face

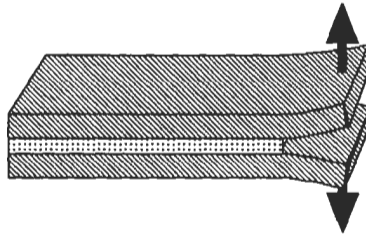


Fig. 3.3. Asymmetric tension or mode I opening of an adhesive joint.

having the visual appearance of the adherend material and the mating face with the appearance of the adhesive. Visual inspection alone does not convey the complete picture. Because an adhesive bond is formed as a result of atomic interactions, closer inspection of adhesional failures with surface composition analysis techniques can provide detailed insight into the material leading to the weakness at the fracture site.

3.2.2. Qualification of bonding procedures and performance

An adhesive bond represents a complex system of materials, treatments and processing steps. The issue of qualification of the adhesive system is complex since specific requirements depend on the application. The focus must be on mechanical performance and durability because the bonded joint is expected to transfer load for the service life. For structural joints, strength is typically evaluated using shear tests (for static properties and fatigue) and toughness with cleavage tests. For honeycomb structure, properties are typically evaluated with flatwise tension and peel tests. Tests are conducted at representative temperatures experienced throughout the service environment, including the operating extremes. Tests are also conducted using moisture-conditioned specimens to evaluate durability performance. Other conditioning may include exposure to salt fog, SO_2 , hydraulic fluids, fuels, de-icers and more. Subcomponent or component testing normally follows coupon testing.

The failure modes of test specimens are as important as the strength or toughness values obtained. Failure modes at interfaces between the treated metal surface and the adhesive or primer are generally not acceptable. The primary objective is for the mechanical properties of joint to be limited by the properties of the cured adhesive, not the surface treatment.

Qualification of the adherend surface treatment procedure is of particular importance. Many surface preparations can provide adequate initial bond strength, however, maintaining this strength for the life of a system in its operating environment is a more difficult challenge. Moisture durability is of primary concern. However, for certain titanium applications, long-term durability at elevated temperature is important.

3.3. Standard tests

3.3.1. Wedge durability test

The ASTM D 3762 wedge test is often called the Boeing wedge durability test. A crack is initiated in a bonded joint through insertion of a wedge into the bondline (Figure 3.3). The test specimen is then exposed to hot/wet conditioning and crack growth is monitored. The initial pre-exposure fracture is expected to be cohesive within the adhesive layer, and the equilibrium crack length is therefore expected to reflect the toughness of the adhesive system under dry conditions. An excessive initial crack length accompanied by interfacial failure, even before environmental exposure, reflects a poor surface treatment. The specimen failure mode is a critical piece of information. Cracks that remain within the adhesive are desirable since they indicate that the surface preparation is not the weak link in the bonded joint. Poor surface preparations readily lead to interfacial failures accompanied by substantial crack growth. The wedge test is properly employed to compare a surface preparation against a control, provided all aspects of specimen configuration and conditioning are held constant as the surface treatment is varied.

The wedge test is widely misused because ASTM D 3762 is not fully prescriptive. Difficulties in the comparison of published data occur because pass/fail criteria, conditioning environment, time of conditioning, and limits on adhesive systems are not fully specified. By way of illustration, the US Services mostly condition wedge specimens at 60 °C and 95% relative humidity (RH), whereas the Australian counterpart test in condensing humidity at 50 °C. As a second illustration, the high fracture energy characteristics of tough adhesives place higher demands on the performance of the surface treatment than do brittle adhesives. The testing of tough adhesives introduces the essential requirement to conduct a simple calculation to ensure that the adherends will not plastically deform in cases where fracture energy measurements are made [22]. However, bonded joints that strain significantly when exposed to hot/wet environment may provide a less rigorous test and, generally, the wedge test is not used to provide quantitative data.

The wedge test is a severe test, since the adhesive is at its breaking stress at the crack tip while directly exposed to the conditioning environment. For this reason, surface preparations that allow limited interfacial failures may be satisfactory. The RAAF Engineering Standard C5033 [20] uses crack growth criteria and allows some interfacial failure in relation to one particular tough adhesive based on service histories of RAAF aircraft. However as a general rule, without service experience to correlate with test results, the safe approach is to insist on a cohesive failure mode, where the adhesive, rather than the surface treatment, limits the mechanical properties of the adhesive bond.

There is ongoing pressure to establish a relationship between service life and the performance of an accelerated durability test. Although the wedge test has been correlated to adhesive bond service life for limited applications, similar durability performance for new treatments does not imply similar service lives [23]. With

current understanding and the complexity of the bonded joint, there is no reliable way to accelerate nature to obtain a quantitative correlation [24].

3.3.2. Fracture mechanics and the cleavage specimen

Fracture mechanics has been applied to the cleavage specimen in an attempt to quantify the test. The elastic energy release rate, G_1 , is the energy delivered from the stressed cantilevers to create a unit area of fresh fracture surface. For the double cantilever beam specimen [22,25–27]:

$$G_1 = \frac{3h^3 \cdot Ew^2}{16a^4} (\text{Jm}^{-2}) \quad , \quad (3.2)$$

where h and E are the thickness and modulus of the adherends respectively, w is the load point displacement and a is the effective crack length. Corrections can be made to the measured crack length to improve precision of the effective crack length [28,29]. A small fraction of G_1 is dissipated in breaking atomic bonds whilst the remainder is dissipated as thermal energy as a result of deformation processes in the stressed polymer. Equation (3.2) shows that for a plane double cantilever beam bonded specimen, G_1 decreases as the crack grows since the stress intensity at the crack tip decreases. It is thus common practice to assess a critical elastic energy release rate, G_{1c} , at some arbitrarily long time where the crack velocity is small.

It is now becoming more common practice to use longer and thicker adherends for durability tests [30], primarily to avoid plastic bending of the adherends. Longer adherends allow a choice of a longer initial crack length and hence the change in G_1 with crack length is less pronounced and much closer to G_{1c} . To avoid adherend bending, the adherend thickness must exceed a critical value, h_{crit} given by [22]:

$$h_{crit} = \frac{3 \cdot G_1 \cdot E}{\sigma_y^2} \quad , \quad (3.3)$$

where σ_y is the yield stress of the cantilevers.

3.4. Fundamentals of durable bonding

The employment of complex surface treatments to prepare high-energy surfaces (such as metals) prior to bonding is primarily conducted to ensure adequate service life of the joint when it is exposed to aqueous environments. Moisture will always eventually gain access to a bonded joint. The surface preparation must ensure that: (1) the adhesion forces between the substrate and the adhesive are stable in the presence of moisture and (2) the surface regions of the substrate will not weaken and form an in-situ weak boundary layer as can occur when an oxide layer hydrates. The choice of the surface treatment must follow a “systems” approach since consideration must be given to the nature of the substrate and its initial

condition, the type of adhesive to be used and the intended service environment [31].

Surface treatments modify both the physical and the chemical properties of the adherend. In general, the relative contribution of the physical roughness and the chemical character of the adherend to bond strength and durability is not known as it is quite difficult to design experiments to separate these effects. A review of experiments to highlight the relative effect of physical and chemical properties of the adherend on bond durability is described below.

3.4.1. Surface roughness and bond durability

The surface roughness profile has a dramatic effect on the fracture toughness of an adhesive bond when the bond is degraded by exposure to a humid environment [32–34]. Wedge durability tests conducted with aluminium adherends, surface prepared using an ultramilling method, showed that the elastic energy release rate at the slow crack velocities in a humid environment, G_{1sc} , depended strongly on the adherend surface profile angle (α) (Figure 3.4). The ultramilling method created either a flat adherend surface with a 0° profile angle, or sawtooth profile angles of either 30° or 60° and a peak to valley depth of $10\text{ }\mu\text{m}$. The surface relief on the 0° ultramilled terraces was less than 5 nm (Figure 3.5) indicating that mechanical

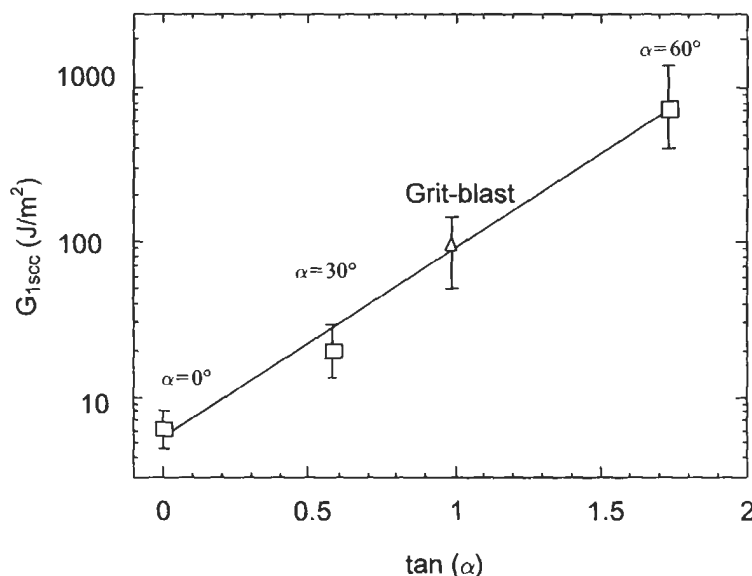


Fig. 3.4. Equilibrium elastic energy release rate for a degraded adhesive bond (G_{1sc}), determined using crack-length data measured from wedge tests conducted in 95% relative humidity at 50°C showing the effect of surface roughness profile angle (α). The adherends were 2024 clad aluminium alloy surface prepared with an ultramilling or grit-blast (GB) treatment. The ultramilled adherends had either ultraflat surfaces (0°) or sawtooth profiles with angles of $\alpha = 30^\circ$ or 60° and peak to valley depths of $10\text{ }\mu\text{m}$. The adhesive used was Cytec FM 73.

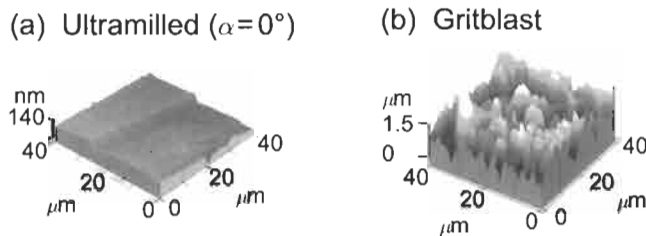


Fig. 3.5. Atomic force micrographs of (a) ultramilled (180°) and (b) grit-blasted surfaces. The micrographs show that the relief on the terraces of the ultramilled surface is less than 5 nm.

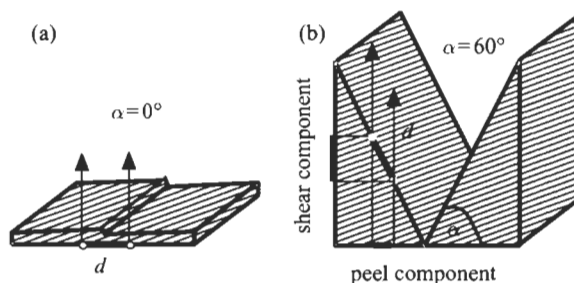


Fig. 3.6. The interfacial peel and shear components of interfacial loading for (a) 0° ultraflat surface and (b) 60° sawtooth surface.

interlocking between the adhesive and the adherend was not significantly contributing to the durability performance of the joint. The flat 0° ultramill surface provided a baseline for bond durability in the absence of mechanical effects. In this case, load transfer depends primarily on basic chemical interactions occurring at the interface between the adhesive and the flat aluminium adherend. These experiments suggested that surface roughness may introduce an interfacial shear component (Figure 3.6) at the adhesive to adherend interface, that contributes to improvements in fracture toughness in humid environments. Introducing surface roughness is a critical aspect of producing a durable adhesive bond.

3.4.2. Surface hydration and bond durability

Epoxy resins have a high polarity which provide strong hydrogen bonding attraction between epoxy molecules and metal oxides [35]. DeBruyn [4] showed that the nominal breaking stress of an aluminium epoxy single lap joint depended strongly on the hydroxyl content of the epoxy. This observation leads to the expectation that the interfacial strength of an adhesive bond would similarly depend on the hydroxyl content of the surface oxides on the adherend. Plasma oxidation experiments were conducted on ultramilled aluminium adherends [34] to systematically change the hydroxyl concentration of planar γ -alumina films from very low levels to concentrations expected for pseudoboehmite-type hydrated oxides. These experiments demonstrated that the initial strength and the durability

of the adhesive bond were both independent of the oxide hydroxyl concentration. This led to the conclusion that the hydroxyl content on the metal oxide was sufficient to form an adequate density of linkages between the adhesive and the metal oxide for the adhesive itself to be the fracture-limiting material in dry conditions. It was also concluded that changes in adhesive bond durability were controlled more by the surface microtopography and hydrophobic contaminant than by the hydration state of the oxide.

It is important that the surface oxide is cohesively strong i.e. the oxide should not fail or separate from the metal surface. It is well known that hydration and growth of the oxide in water can lead to weakness of the oxide structure and that these conditions should be avoided. In the plasma experiments, planar cohesive γ -alumina films were formed and the contributions of a weak oxide were avoided [34].

3.4.3. Surface contamination and bond durability

It is universally acknowledged that an unprepared surface covered with thick layers of hydrophobic contamination leads to a weak adhesive bond with very poor long-term durability. Reduction of the contaminant concentration will ultimately lead to adequate initial bond strength, limited by fracture in the adhesive, but the long-term durability may still be poor due to the overriding influence of environment-induced failure at the adhesive to adherend interface. The adhesive bond durability is very sensitive to the presence of hydrophobic contaminant on the adherend, but the dependence involves a complex combination of the nature, the concentration and the distribution of the contaminant.

Studies of bond durability with one epoxy film adhesive following deliberate contamination of prepared aluminium adherends showed sensitivity to the nature of the hydrocarbon contaminant [36]. The durability was remarkably tolerant to contamination with aviation kerosene and a homologous series of alkanes of lower chain length than C16. This suggested that the adhesive was capable of displacing sufficient area of some surface contaminants for the adhesive to make good bonding attachment with the adherend. It is expected that the durability response to the nature of the contaminant will be adhesive specific as it is well known that some adhesives are formulated for application to grossly soiled surfaces [37].

In some surface treatments, an aqueous organosilane coupling agent is applied to improve bond durability performance [36]. The ability of this organosilane coupling agent solution to wet an adherend surface is very sensitive to the presence of contaminant. Aviation fuel contamination before organosilane application leads to a marked reduction in adhesive bond durability, whereas, contamination after the organosilane is dried has minimal effect on durability (Figure 3.7) [38].

Hydrocarbon contaminants are not uniformly distributed over the surface. Angle resolved X-ray photoelectron spectroscopy (XPS) studies show that hydrocarbon is distributed as islands on the surface [38]. Some surface treatments will accentuate the island distribution of residual contaminant, whereas, others will lead to a more uniform distribution.

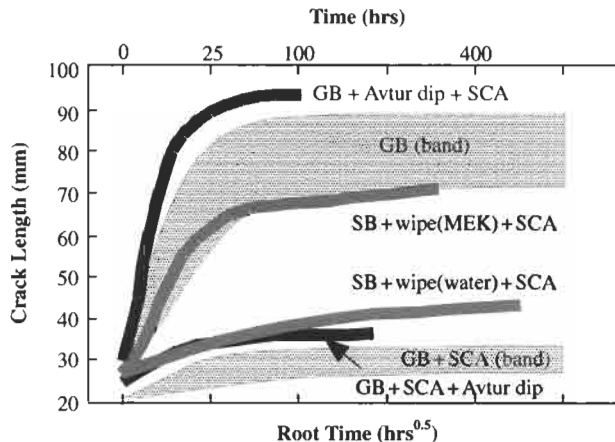


Fig. 3.7. Crack growth rate curves from wedge tests conducted in condensing humidity at 50 °C for clad 2024 aluminium adherends and FM 73 adhesive showing the effect of abrasive surface treatments and the introduction of aviation kerosene. Labels indicated on the plot correspond to the following:
 SB + wipe (MEK) + SCA = Scotch-Brite abrade then wipe with MEK soaked tissues then organosilane coupling agent application
 SB + wipe (water) + SCA = Scotch-Brite abrade then wipe with water soaked tissues then organosilane coupling agent application
 GB + SCA = grit-blast then organosilane coupling agent application
 GB + Avtur + SCA = grit-blast then contaminate with aviation kerosene then organosilane coupling agent application
 GB + SCA + Avtur = grit-blast then organosilane coupling agent then contaminate with aviation kerosene
 GB = grit-blast.

Abrasion and grit-blasting processes roughen the surface, but an estimated 5 to 10 atomic layers of residual contaminant remain on the surface, distributed nonuniformly [12,38]. By contrast, wiping the surface with a solvent-soaked cloth or tissue will spread solvent containing dissolved organic material uniformly across the surface. The solvent evaporates leaving the surface uniformly covered with hydrophobic contaminant. A contact angle experiment conducted on polished aluminium, as shown in Figure 3.8, illustrates the importance of considering the solvent, and the tool used to apply it, as a source of unwanted contamination [39].

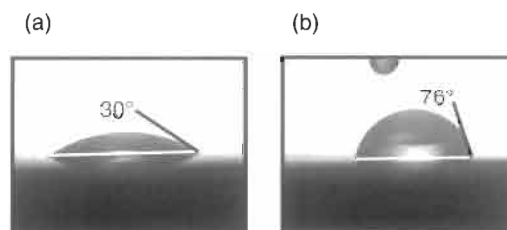


Fig. 3.8. Contact angle between a 5 μ l water droplet and a polished aluminium surface ultrasonically degreased in (a) high purity MEK and (b) MEK containing tissue residues.

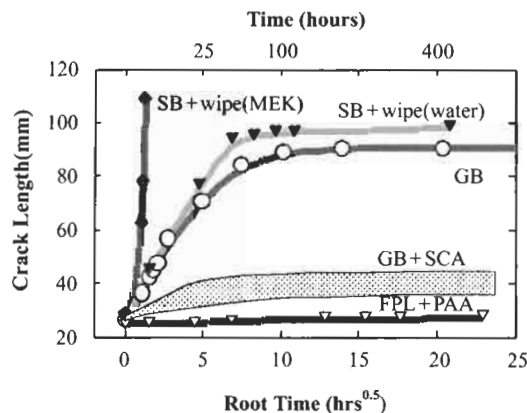


Fig. 3.9. Crack growth rate curves from wedge durability tests conducted in condensing humidity at 50 °C for clad 2024 aluminium adherends and FM 73 adhesive, showing the effect of abrasive surface treatments. The treatments are (a) Scotch-Brite abrade plus wipe with MEK soaked tissues (SB + wipe (MEK)), (b) Scotch-Brite abrade plus wipe with water soaked tissues (SB + wipe (water)), (c) Scotch-Brite abrade plus wipe with water soaked tissues + grit-blast (GB) (d) forest products laboratory etch followed by phosphoric acid anodisation (FPL + PAA representing a factory benchmark treatment) [40] and (e) the grit-blast then organosilane coupling agent application (GB + SCA).

The contamination deposited by the solvent can have a dramatic effect on bond durability, as illustrated in Figure 3.9. Here, clad 2024 aluminium alloy was surface prepared by abrasion with Scotch-Brite followed by debris removal, or grit-blast, then bonded with FM73 adhesive. The debris removal with aerospace wipes soaked in methyl ethyl ketone (MEK) leads to very poor durability, whereas, the debris removal with wipes soaked in water lead to durability approaching that of the grit-blast. Composition analysis of the failure surface (Figure 3.10) shows that the very poor durability of the solvent-wiped adherend is associated with weakness at the adhesive to metal oxide interface due to the contaminant. The water-wiped and grit-blasted surfaces failed within the oxide film.

3.4.4. Bond durability model

A stress based diffusion model (Figure 3.11) was developed to describe the rates of bond degradation and modes of fracture for a series of aluminium/epoxy wedge test specimens exposed to humid environments [34,41,42]. Large interfacial cavities were observed along the bondline of wedge test specimens exposed to humid environments [43]. Observations by other workers [44] and scanning electron microscopy (SEM) micrographs (Figure 3.12), indicate that microcavities exist at the interface in the crack tip region for stressed wedge test samples. Under stress, the size and distribution of these microcavities could be determined by variations in bond strength along the interface induced by the distribution of contaminant or by inhomogeneous stress distributions induced by surface roughness.

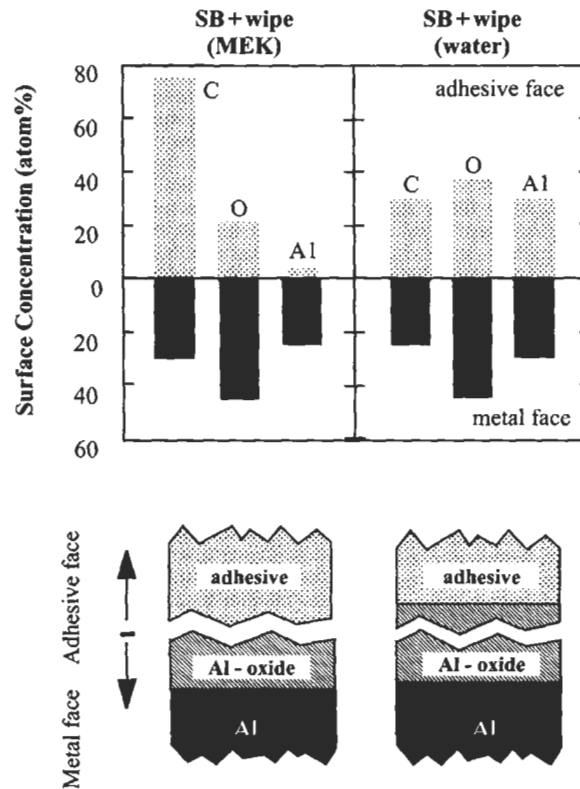


Fig. 3.10. Surface composition of both fracture faces measured with XPS for the treatments (a) Scotch-Brite abrade plus wipe with MEK soaked tissues (SB + wipe (MEK)) and (b) Scotch-Brite abrade plus wipe with water soaked tissues (SB + wipe (water)).

Firstly, all practical adherends will have several atomic layers of residual contaminant distributed nonuniformly on the surface [38]. During cure, adhesive bonds will form more efficiently in the uncontaminated surface regions. Increased concentrations of contaminant may lead to less effective bonding. This has the capacity to explain a variation in cavity size with changes in contaminant levels.

Secondly, inhomogeneous stress distributions induced by surface roughness have been used by several workers to describe adhesive joint fracture [45,46]. At a microscopic level, surface roughness may introduce a surface shear component to the existing surface peel component in a normally stressed bond and thereby would change the effectiveness of the interfacial transfer of load. This may potentially influence the size of microcavity formation.

Microcavities represent paths for moisture ingress. The size and distribution of microcavities will determine the ease of moisture access and the fractions of the adherend surface subjected to rapid bond degradation. At these localised sites of

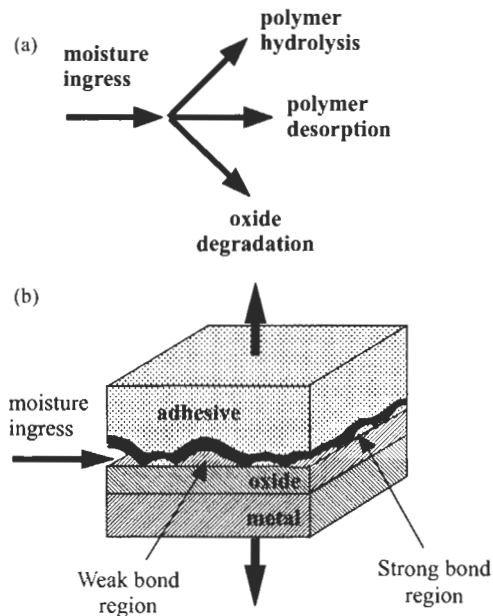


Fig. 3.11. Stress based diffusion model that describes moisture ingress to the adhesive metal interface and three degradation reactions. The magnitude of microcavities ahead of the crack tip would control the rate of moisture diffusion and the dominant degradation reaction path would determine the position of bond weakening and the dominant locus of failure.

moisture ingress, the adhesive bond can degrade by any one of three reaction paths as shown in Figure 3.11(a): polymer degradation, polymer desorption or oxide degradation. With time, the sites of adhesive bond degradation expand and coalesce, leading to a reduction in the fracture strength and crack propagation [32–34]. Moisture in contact with the metal oxide at the bond interface will lead to oxide growth and hydration. The presence of localised sites of oxide growth some hundreds of microns ahead of the crack tip is illustrated by the Scanning Auger Micrographs of the fracture surface of a forcibly opened wedge test specimen with ultramilled adherends (Figure 3.13). This supports the concept that bond degradation occurs in advance of the crack tip. Mechanical strength may be sustained by stress sharing networks in the polymer bridging load across the degraded regions of the interface.

The stress based diffusion model has the potential to be developed to describe a more comprehensive view of adhesive bond durability and its dependence upon interfacial stress, contaminant concentration, surface roughness, coupling agent performance and other relevant influences. An opportunity exists for modelling the micromechanics of the bondline and moisture diffusion behaviour. Microscale finite element modelling may aid progress in the development of a quantitative bond degradation model.

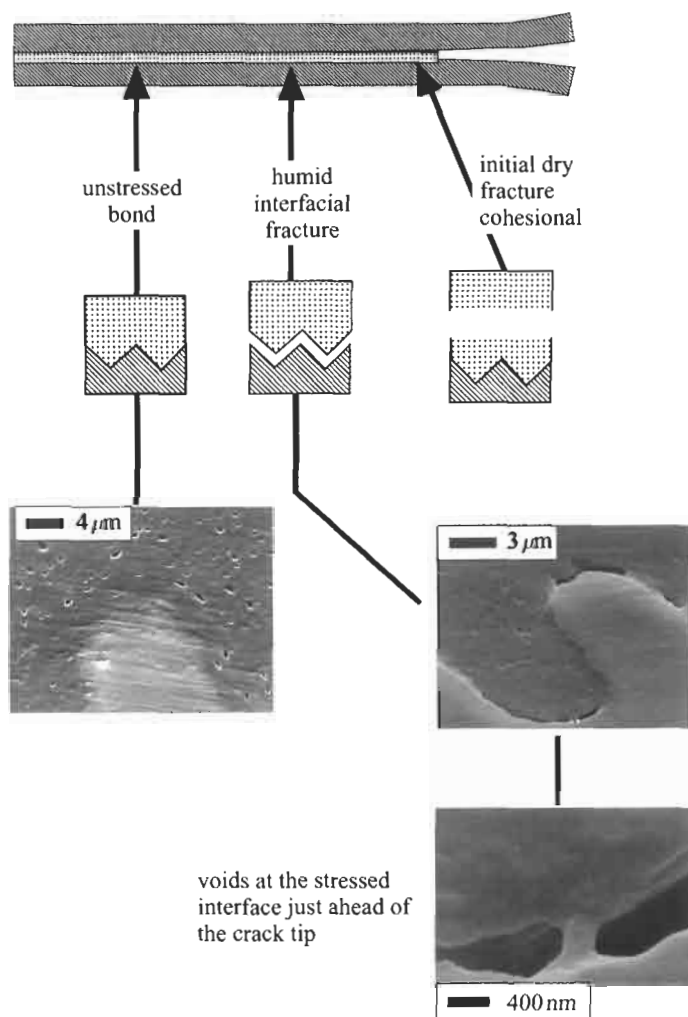


Fig. 3.12. SEM micrographs showing the presence of microcavities in the stressed regions just ahead of the crack tip of a wedge test specimen exposed to condensing humidity at 50 °C.

3.5. Requirements of surface preparation

Adherend preparation typically involves a series of steps, each with an important purpose. Whilst the surface preparation affects the initial bond strength, it is the influence of surface preparation on the long-term environmental durability of bonded structures that is of particular concern.

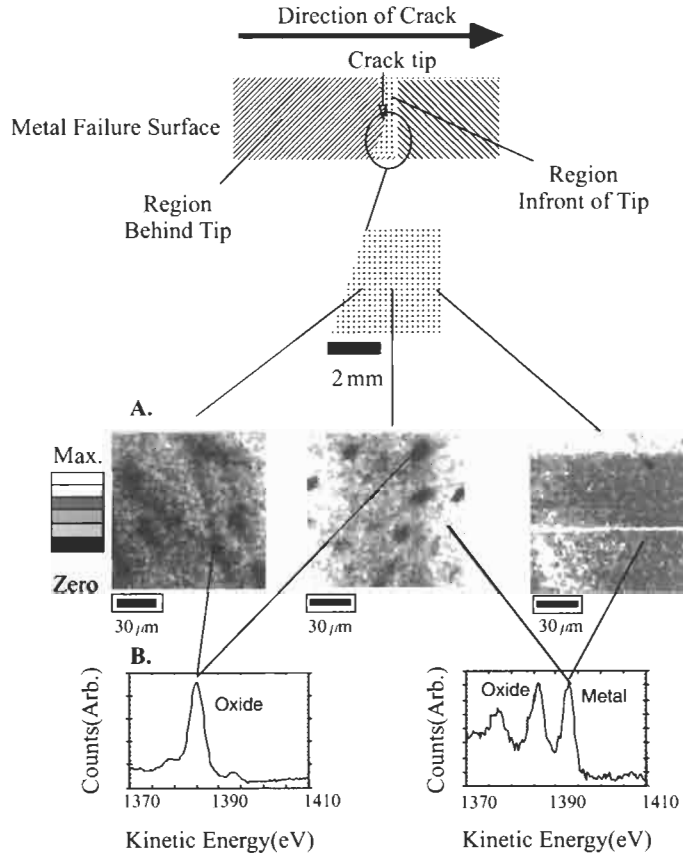


Fig. 3.13. Scanning auger microprobe (SAM) analysis of the crack tip region of a failed wedge sample pre-treated with a 180° ultramill. The SAM maps indicate the distribution of metallic aluminium at positions ahead of the crack tip and the spectra show the relative concentrations of aluminium oxide and aluminium metal at the locations indicated.

3.5.1. Degreasing

Degreasing is conducted to remove gross organic contamination. Greases and oils are usually present on alloys received from the manufacturer. After prolonged service, components are expected to have a wide variety of organic contaminants, with some so aged and firmly adsorbed that they are resistant to solvents. Degreasing is used to decrease the concentration these organic contaminants on the adherend surface prior to subsequent preparation steps.

Factory facilities often use vapour degreasing to reduce the concentration of organic contaminant on components to be bonded. A solvent such as trichloroethylene is evaporated in a closed space then allowed to condense and drip from the soiled components. Organic contaminants are slowly dissolved in the

liquid phase whilst it is in contact with the component and are transported to the solvent reservoir under gravity. In many cases, tank based cleaning using alkaline aqueous solutions has replaced vapour degreasing due to environmental and safety concerns. Degreasing is typically the only surface preparation used for aluminium honeycomb.

In the repair environment, degreasing is frequently conducted with solvent-soaked tissues or cloths. Common solvents used are MEK and acetone. Again, the solvent dissolves the organic contaminant on the soiled component, but it is important to ensure that sufficient solvent volume is swept over the component to ensure a solvation gradient. A unidirectional sweep to the edge of the region is important to ensure that the dissolved organic contaminant is adequately flushed from the zone undergoing the degreasing process. None-the-less, a volatile solvent will evaporate and can leave a thin film of organic contaminant uniformly spread over the adherend surface. Further, the solvent can dissolve polymers and residual greases from the tissue or cloth and deposit these on the adherend surface as the solvent evaporates (Figure 3.9) [39].

The waterbreak test is widely used to assess the presence of contaminant on an adherend surface. However, the waterbreak test must be treated with caution because contaminants such as water-displacing fluids yield low contact angles [39].

3.5.2. Abrasion, grit-blasting or etching

Abrasion, grit-blasting or etching is conducted to remove loosely adherent oxides, to prepare a contaminant-free active surface and to generate a rough surface topography. Abrasion physically removes metal by the action of hard particles bonded to a carrier cloth or pad. This creates a surface with furrows and leaves residual metal debris on the surface.

The practice of removing debris from an abraded aluminium alloy adherend using clean tissues must be approached with caution. Debris removal with tissues soaked in MEK led to poorer bond durability than removal using tissues soaked in water (Figure 3.9) [39]. The reason is that the MEK solvent can dissolve organic material from certain tissues and leaves the contaminant distributed across the surface as the solvent evaporates. This contaminant then interferes with the bond between the adhesive and the metal surface allowing moisture to diffuse into the stressed bondline at a faster rate than for a bondline where there is better attachment between the adhesive and the metal surface [36].

The grit-blast process uses fine abrasive particles carried in a high velocity stream of clean, dry air or nitrogen to impact the adherend surface. Plastic deformation of the metal surface is more dominant than metal removal and crater formation in the surface is evident [47] (Figure 3.14). Pre-existing debris is consolidated into the surface during impact deformation of the metal surface.

The grit-blast treatment improves the hydrophilic wetting of the surface (Figure 3.15) [36] and the durability of the bond (Figure 3.9) over that of the abraded surface. Some of the improvement in wetting can be attributed to a decrease in the concentration of hydrophobic contaminant and some to the roughening of the

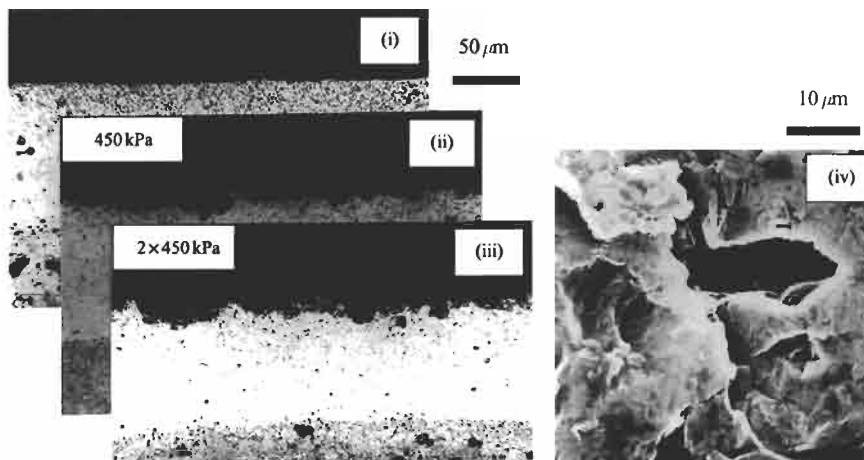


Fig. 3.14. Micrograph cross sections showing (i) no grit-blast, (ii) single impact grit-blast and (iii) double impact grit-blast. The micrograph of the double impact grit-blast shows the degree of overfolding and cavities formed on the surface (iv).

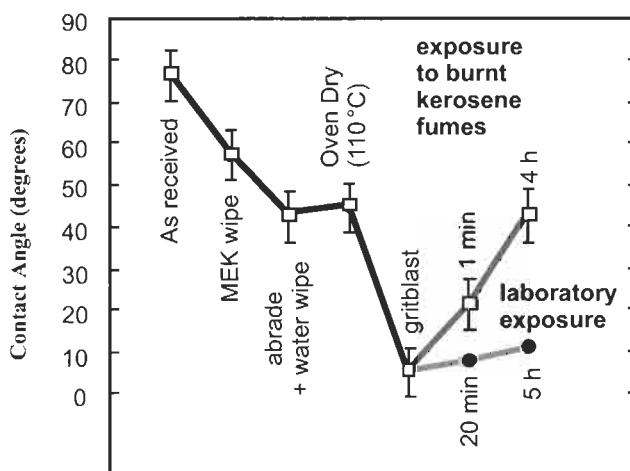


Fig. 3.15. The contact angle for clad 24 aluminium following degreasing (MEK wipe), abrasion with Scotch-Brite plus debris removal with water soaked tissues (SB + wipe (water)), dry at 110 °C, grit-blast (GB), recontamination with either exposure to burnt aviation kerosene or a laboratory environment.

surface. Measurements with XPS show that hydrocarbon concentrations are decreased by solvent degreasing and further reduced by abrasion [36]. Curve fitting of the C1s peak in XPS spectra of solvent degreased and grit-blasted surfaces shows the reduction of a species containing a C=O bond, which could be attributed to the removal of residual MEK solvent.

The severity of grit-blast must be controlled. Insufficient grit-blasting leads to ineffective preparation of a contaminant-free active surface. The threshold

grit-blast density for 50 micron alumina grit to achieve full surface coverage is 0.5 gcm^{-2} [48]. It is recommended that 1 gcm^{-2} should be used to ensure complete surface impact and contamination removal. Excessive grit-blasting does not improve the durability performance of the adhesive bond, although additional deformation of the surface has occurred. This additional surface deformation gives rise to subsurface cavities in the adherend which become sites for the entrapment of moisture and other volatile materials. During cure of the adhesive at elevated temperatures, these volatile materials form bubbles in the adhesive leading to voids in the cured bond [11,49,50]. Void formation will be discussed in Section 3.6.2

Chemical etching dissolves metal from the surface in a complex process involving dissolution and regrowth of the oxide film. Aluminium alloys immersed in chromic acid etches develop a relatively flaw-free oxide due to the absence of contaminants [51]. The chemical dynamics of the etching process leads to a microporous structure [52] on the metal surface which leads to similar bond durability performance to that of the grit-blast treatment [47].

3.5.3. Creation of a high energy surface oxide

Creation of a high energy surface oxide implies the optimisation of surface wetting. It may be an automatic result of abrasion, grit-blasting or etching processes. Alternatively, processes such as anodising may be employed to create hydrophilic surface oxides. The creation of a high energy surface oxide implies that steps to minimise the readsorption of hydrophobic contamination have been taken.

Surface oxides form rapidly on almost all metal and alloy surfaces. Abrasion and chemical surface treatments are conducted to reduce contaminant, to remove pre-existing loose oxides, to generate compact mechanically robust surface oxides and to produce an hydroxylated oxide surface on the metal which will bond to the hydroxylated moieties in the adhesive. Most surface treatments are optimised by trial and error with very little fundamental understanding of properties at the nanometre scale. The oxides formed on structural metals such as aluminium, steel and titanium will be sufficiently hydroxylated to form strong bonds [34]. However, the possibility of forming a weak oxide on the adherend must be considered. Extended etching of a nickel surface in a nitric acid solution produced an appropriately rough surface, but the smut and thickened oxide produced a weak bond interface [53]. The presence of residual contaminant or the possibility of reintroduction of contaminant is of concern.

Anodising is a process involving electrolytic treatment of metals in which a stable, porous oxide is intentionally grown on the surface of the metal [54,55]. This oxide is mechanically cohesive and tenaciously adheres to the metal surface. In a typical anodising bath, the metal alloy is connected as the anode in an electric circuit, is immersed in an oxidising electrolyte of usually low pH and a positive dc (direct current) potential is applied [56]. Whilst most anodising baths use acidic electrolytes and dc potentials, some use alkaline electrolytes and some use alternating current. The oxide is formed on the metal surface as a result of controlled chemical dissolution of the metal and electrochemical oxidation of the

surface [57]. The microtopography of the outer oxide is very sensitive to bath composition, anodising parameters, alloy composition and the surface finish on the metal. Since the best durability performance is generally obtained with a high degree of microroughness of the metal oxide surface, it is not surprising that attention to details of the bath and alloy is essential to obtain optimum surface oxide film properties. There is extensive literature on factory anodising [57].

In field repair applications, tank anodisation is often not practical. The electrolyte is either formed into a self-supporting gel or special approaches for the containment of circulating electrolyte over the treatment region are used. The use of anodisation for on-aircraft repairs needs to consider issues including the potential for unwanted corrosion, the potential for hydrogen embrittlement of fasteners, difficulties with the removal of the electrolyte, difficulties with the use of electrical equipment in the vicinity of flammable vapours and the potential for damaging the oxide film with the post-anodising processes.

3.5.4. Coupling agent

The purpose of the coupling agent is to enhance the effectiveness of the hydroxyl (OH) terminations on the metal oxide in linking with the adhesive. In the case of the organosilane coupling agents, the organic head group is chosen for crosslink compatibility with the adhesive polymers and the silanol groups formed during hydrolysis (Figure 3.16) either react chemically with the hydroxyl groups on the metal oxide surface to form oxirane bonds ($M-O-Si$) or form hydrogen bonds with these hydroxy groups ($M-OH \dots HO-Si$) [58]. The exact nature of the interaction remains speculative. The organosilane forms strong polysiloxane networks which play a significant role in interfacial durability enhancement [58].

Characteristics of a good coupling agent are the crosslinking with the adhesive and hydrolytic stability to water, which can hydrate the oxide film. Both are essential, but the crosslink connection into the adhesive and increased load sharing appears to be most important. Nitrilotris methylene phosphonic acid (NTMP) is an outstanding hydration inhibitor and was reported by Venables to improve bond durability [59]. However other research [42] suggests that the inability of NTMP molecules to crosslink through primary chemical interactions prevents a cohesively strong film forming and leads to ineffective performance as a durability improver.

Mazza *et al.* [60] conducted a detailed investigation of “the Australian Silane Surface Treatment” [61] by varying the process parameters. This work identifies the optimum organosilane concentration, silane hydrolysis time, application time, drying time and drying temperature. This data supports the defined processes in the Royal Australian Air Force Engineering Standard C5033 [20]. Whilst Mazza initially reported that the optimum temperature for drying organosilane coupling agent was 93 °C for 90 min, other work suggests that higher temperatures may be required for void minimisation [50]. Later work by Mazza *et al.* also supports the use of a higher drying temperature [62].

The presence of contaminant on the metal surface plays a significant role in the ability of the organosilane coupling agent to attach to the hydroxyl groups on the

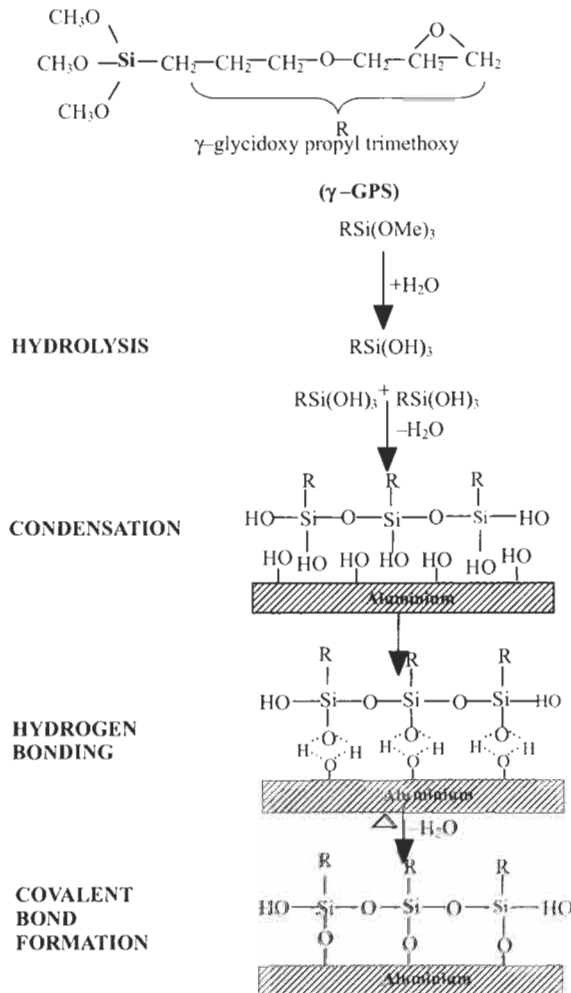


Fig. 3.16. Organosilane coupling agent γ -glycidoxypropyltrimethoxy silane showing the hydrolysis, condensation and surface reactions.

metal oxide. This is illustrated in Figure 3.7 where it is shown that the durability enhancement afforded by the organosilane coupling depends strongly on the surface treatment prior to the application of the coupling agent. Analysis of the failure surface with XPS indicates that as the durability improves, fracture shifts from the oxide film toward the interface between the coupling agent and the metal oxide [36]. The effectiveness of the coupling between the organosilane and the metal oxide has an influence on the ability of water to diffuse to the interface between the adhesive and the metal adherend together with the hydrolytic stability of the metal oxide. In practical terms, it is essential to ensure that the surface treatment has produced a hydrophilic surface and to ensure that contamination is avoided before

the application of the organosilane coupling agent [39]. Brushes or tissues used to apply organosilane can transfer organic contaminant to the prepared metal surface leading to deterioration in bond durability performance [39].

3.5.5. Adhesive primer

Most adhesive suppliers recommend a primer for metal bonding. Primers protect the adherend surface from contamination or chemical changes between surface preparation and the bonding process. Since they are low-viscosity fluids, primers can readily penetrate surface roughness and microporosity developed by the surface preparation and better wet the adherend surface. Primers also help protect the bonded adherend from moisture attack in order to improve long-term durability. For this reason, adhesive primers often contain corrosion inhibitors [63]. Popular adhesive primers are epoxy-phenolic based and contain chromate inhibitors. Whilst hexavalent chromium ions provide the best protection to the metal oxide surface, these materials are toxic to the environment, are known carcinogens and as a result there is pressure to find alternative inhibiting agents.

Application of a corrosion-inhibiting adhesive primer to enhance bond durability for on-aircraft repair is as desirable as it is for factory and depot processes. However, priming on aircraft is more difficult to control both from the application and the environmental hazard point of view. Wipe-on or brush application of the primer is frequently substituted for spray application used in off-aircraft bonding. It is important to recognise that improperly applied primer, especially if it is too thick, can lead to inadequate initial bond strengths.

Primer thickness may be measured by eddy current thickness gauges. Primers also may have pigments added as an aid to visual thickness control, particularly in the case of sprayed application. However, this optical method limits thickness control to fractions of a micron and the choice of the pigment can influence the visual sensitivity. The performance on thickness control is very dependent on operator skill and ability. The RAAF Engineering Standard C5033 [20] does not include a primer specification. This follows concern over the ability of technicians to adequately control primer thickness and cure properties in a repair environment. The elimination of primer usually results in some reduction in wedge test performance, but RAAF service experience has indicated good performance using only the grit-blast /silane treatment.

3.5.6. Drying

Drying the surface thoroughly following any treatment involving solvents or water is absolutely essential to minimise the evolution of volatile materials responsible for void formation during the cure phase of the adhesive. Measurements of water evolution from a grit-blasted aluminium alloy surface indicate that sufficient steam can be generated by a poorly dried surface to eject most of the adhesive from the bondline [11]. Some of the water on the adherend is physisorbed and some is bound in the hydrated surface oxide film (Figure 3.17). Curing an

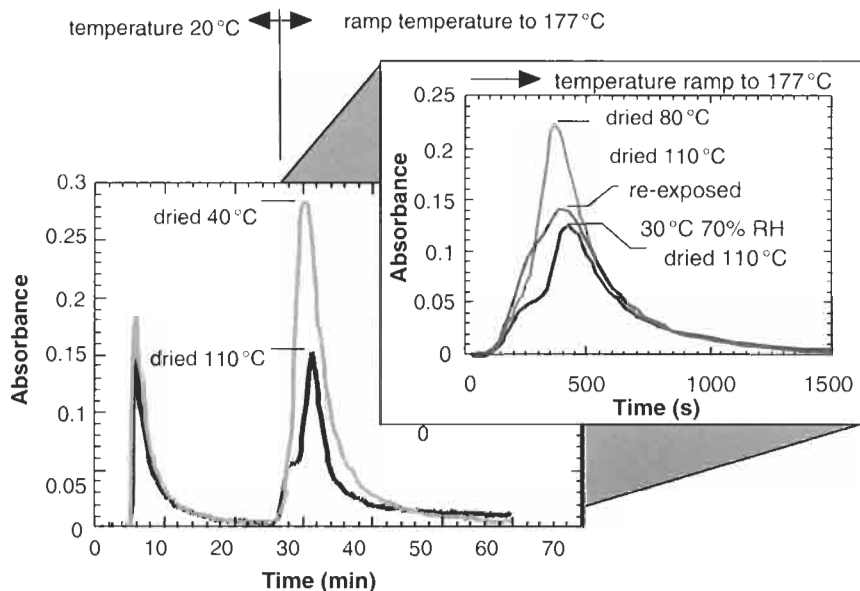


Fig. 3.17. FTIR water evolution profile for grit-blasted clad 2024 aluminium alloy illustrating the chemical affinity of the adsorbed water with the aluminium oxide surface and the effect of drying for 1 h at a range of temperatures.

adhesive bond at elevated temperature will release even the chemically bound water as steam [50]. Experiments have shown that drying at 110 °C for at least an hour is essential to minimise void formation in some epoxy adhesives where cure is conducted using vacuum bag pressurisation. Conducting the bonding process in low humidity to avoid readsorption of moisture is also essential (Figure 3.17).

3.6. Adhesive application

Adhesives (and primers) have a limited shelf life, and refrigerated storage in sealed containers is essential for most. Repacking of application lots of film adhesives in sealed polyethylene bags must be conducted in controlled atmospheric conditions to minimise moisture absorption. Quality assurance requires careful documentation of histories and conditions of storage. The quality of the bonding process relies on the flow of adhesive and the curing conditions. Process control of the temperature ramp rate and final temperature is essential. Aircraft structure has differential heat sinks leading to a requirement for zoned heating and looped control to avoid local over-temperature and under-temperature regions. Experience has shown that there is a general lack of care with ensuring that temperature-sensing devices are properly located and properly calibrated to ensure that the temperature sensed reflects the temperature in the curing adhesive.

Trivial mistakes such as leaving the peel plies or separator sheets on the adhesive are committed even by the most experienced technicians. Fortunately, the consequences are quite apparent. However, the use of peel plies and other materials containing a silicone release agent is a more insidious error of judgement. The RAAF has taken steps to ban these materials from all bonding operations.

3.6.1. Factors controlling bondline thickness

The mechanical properties of an adhesive joint are influenced by the thickness of the bondline [64,65]. Many film adhesives contain a supporting scrim, which exercises some control over bondline thickness. The scrim may also act as a strength-limiting defect, or can toughen the bond, or can provide a path for moisture ingress into the bond.

3.6.2. Void formation and minimisation

Periodically, high levels of void formation in the bond have been observed for repairs conducted at tropical airbases [66]. Calculations show that the water content of the bondline in which the adhesive and the adherend are both exposed to humid, tropical conditions can be sufficient to produce enough steam during an elevated temperature cure to eject most of the adhesive from the bondline (Figure 3.18) [11]. The resultant degradation in mechanical properties has airworthiness implications and, therefore, must be addressed.

The volatile gases present in the bond have three potential sources [49]:

Firstly, the adhesive supplied from the manufacturer may contain solvents with their concentration limits defined by a specification designed for positive pressure cure. There will be batch-to-batch variations in the concentration of these volatile materials [49].

Secondly, the adhesive can quickly absorb water [49] if exposed to hot, humid tropical conditions. The equilibrium concentration of moisture depends strongly on the relative humidity of the atmosphere.

Thirdly, moisture is readily adsorbed by the rough overfolded surface (Figure 3.14) of the abraded and grit-blasted aluminium alloy adherend, [49,67]. This moisture is both physisorbed and chemisorbed by the aluminium alloy surface (Figure 3.17).

Whilst each source of volatile gases on its own may be relatively innocuous, the combined effect of all three sources can lead to a level of voiding which will affect mechanical properties (Figure 3.18) [50].

Void minimisation strategies are generally centred on minimising the moisture content of the bondline or by constraining the volatile gases using hydrostatic pressure. The most effective strategies are to conduct bonding in a temperature controlled, dehumidified atmosphere and to use positive pressurisation of the bondline with an autoclave, press or pressurised bladder.

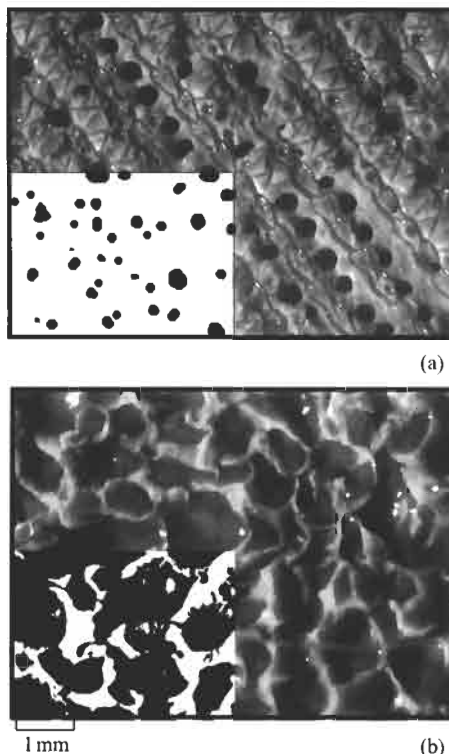


Fig. 3.18. Void formation in Cytac FM 300 epoxy film adhesive where both the adhesive and adherend were exposed to (a) temperate (50% RH at 20 °C) and (b) tropical (70% RH at 30 °C), conditions.

3.7. Surface treatment quality control

Tools to assist with quality control during the production of an adhesive bond and nondestructive evaluation of the bonded joint are very limited and not particularly reliable. The production of a strong and durable adhesive joint depends critically on the skill and the integrity of qualified personnel manufacturing the bonded joint. Strict adherence to a qualified procedure is essential. A benchmarking activity conducted for the RAAF [21] indicates that adherence to well-defined qualified procedures, underpinning standards, staff training, regular reviews of staff qualification and continuity of experience were of utmost importance to achieving acceptable bond durability performance in the repair environment.

3.7.1. Waterbreak Test

The aerospace industry routinely uses the tendency of clean water to “bead” or “break” as an indication of the presence of hydrophobic contaminant on an adherend during surface preparation. In practice, the waterbreak test relies on the

skill and experience of the technician and is not necessarily reliable. Surface roughness has a significant influence on the outcome. Some contaminants have hydrophilic characteristics and therefore lead to a waterbreak free indication. Examples of hydrophilic contaminants commonly encountered are water-displacing fluids used in aircraft maintenance.

3.7.2. Surface work function methods

The electron work function of a metal surface is very sensitive to its chemical state. A number of methods based on work function are in use to assess contaminated surfaces [68–70]. However, the work function methods have difficulty in discriminating between oxide growth, contaminant concentration and surface roughness.

The Fokker surface contamination tester is based on the Kelvin vibrating capacitor surface potential difference method [68]. The physical size of the measurement area, the sensitivity to interelectrode spacing and potential contamination of the gold reference electrode are limitations.

The optically stimulated electron emission (OSEE) method is also commercially available [71]. The method is based on the emission of photoelectrons with energies of less than 6.7 eV, stimulated by ultraviolet radiation from a mercury vapour source. The photocurrent is measured in air using an electrically biased plate located 1 to 6 mm from the sample surface [70]. Aluminium metal with a work function of 4.08 eV [72] will emit photoelectrons whereas aluminium oxide with a work function greater than 6.7 eV will not [70]. It was found [73] that the principal impediments to quality control in the base repair environment is the absence of a suitable simple reference calibration and the convoluted response to contaminant concentration, oxide growth and surface roughness.

3.7.3. Fourier transform infrared spectroscopy

Advances in fourier transform infrared (FTIR) spectroscopy have led to some promise as a technique to evaluate contaminants on a rough metal surface. However, the complexity of infrared spectroscopy leads to the requirement for a skilled analyst to interpret the data, and it may be some time for expert systems to be developed to the point where semiskilled technicians can routinely apply infrared spectroscopy to quality control in the field. Commercial instrument manufacturers [74] have developed infrared spectroscopic systems for noncontact evaluation of surfaces. It should, however, be clearly understood that the depth discrimination of infrared spectroscopy is typically in the hundreds of nanometres range and that special grazing incidence techniques are required to bring the sensitivity down to monolayer coverage levels.

3.7.4. Optical reflectivity

Inspection of the quality of a grit-blasted surface is performed visually and, for aluminium surfaces prepared with fine grit, optical reflectance characteristics are a good indicator of the severity of grit-blast impact [48,73].

Commercial reflectance colourimeters have been used to quantitatively assess the reflectivity of aluminium alloys and show an exponential dependence on the density of impact of fine 50 micron alumina particles [48,73]. A very simple hand-held instrument has been shown to adequately monitor grit-blast severity on aluminium alloys and is currently being used as a training and qualification tool by the RAAF.

The polarisation response of reflected polarised light is used as a quality control tool for phosphoric acid anodised surfaces. The method indicates defects in the thickness and maturity of the porous anodised film [75].

3.7.5. Process control coupons (traveller or witness specimens)

In the absence of a comprehensive array of quantitative quality control tools, it is common practice for process control coupons, also known as traveller or witness specimens, to be prepared in parallel to the production or repair task. Whilst these provide a form of quality assurance, there is no guarantee that the surface treatment or the bonding conditions were identical to those on the real component. The potential exists for the technician to apply undue care with the traveller specimen or to prepare the traveller specimen at a different time to the bonded component. The RAAF Engineering Standard C5033 [20] places emphasis on quality control through a strategy of qualification of processes, procedures and personnel.

3.7.6. Practitioner education, skill and standards

Quality control in the manufacture and repair of bonded components relies on a strategy of qualification of processes, procedures and personnel [17]. It is essential for the procedures to include a quality assurance trail to ensure that the task was performed in strict accordance with the qualified specification. It is to be noted that the regulatory framework used to manage the structural integrity of bonded components is currently not capable of identifying bonded components which are susceptible to time-dependent bond degradation [16]. There is much work to be done toward developing regulations addressing preproduction validation tests to eliminate practices which lead to bond degradation. The lack of reliable nondestructive evaluation tools has led to a reluctance by many engineers to accept the engineering risks involved in an adhesively-bonded joint, particularly for primary load-bearing structure [2].

3.8. Surface preparations for aluminium adherends

The overwhelming majority of failures in aluminium adhesive joints in aircraft have been initiated by moisture [76]. Thus, the employment of complex chemical treatments ensures adequate service life of the joint when it is exposed to aqueous environments. In general, the surface preparation of aluminium is designed to remove weak boundary layers (oxide scale and organic contaminants) and to form stable layers that adhere well to the base metal and are chemically and physically compatible with the adhesive or primer [54,77]. This is required of both factory and field surface preparation processes, including on-aircraft treatments. The extent of the surface treatment depends upon the demands of the application.

3.8.1. Factory processes

Considerable research has been conducted regarding preparation of aluminium for adhesive bonding, particularly for 2000 and 7000 series alloys since they are most used in aerospace applications. Most factory processes for aluminium surface preparation involve etching in acid solutions or electrochemical anodisation or both. These treatments are intended to produce a stable oxide layer that tenaciously adheres to the metal surface. The best durability performance is generally obtained with a high degree of microroughness on the surface. Durability is further increased when the adherend surface is also chemically compatible with the adhesive or primer [54].

3.8.1.1. Phosphoric acid anodise (PAA)

Phosphoric acid anodise (PAA) is currently the most widely used anodisation for aluminium prebond treatment [55]. This is largely due to the superior performance the treatment demonstrated during the United States Air Force's Primary Adhesively Bonded Structure Technology (PABST) program [78,79]. PAA is characterised by its simple chemistry, room-temperature requirements, low electrical needs, relatively good environmental acceptability and fairly wide tolerances for process parameters [80]. The PAA process produces an approximately 400 nm thick amorphous aluminium oxide characterised by a thin inner barrier layer, an outer porous layer, external whiskers and a phosphate rich surface [76]. In relation to alternative anodise processes, the PAA oxide will not hydrate or "seal", is much thinner and has the largest pore sizes [56].

Anodisation is carried out in 10% aqueous H_3PO_4 (by weight) at 10 V. The exact details of the procedure vary slightly between using organisations [31,81,82]. The best durability performance is obtained by employing an acid etch prior to anodising [83]. Both Forest Products Laboratory and P2 etch [83] have been employed in this way. In order to obtain repeatable durability results, key process variables, such as tank make-up and rinse water, must be controlled.

The microporous PAA oxide is fragile and must be primed or bonded as soon as practical. A low-viscosity primer can penetrate the pores, stabilise the oxide layer and protect the adherend surface from corrosion, given that the thin PAA oxide

provides little inherent corrosion protection. Although the use of a few rubber-containing 177 °C curing adhesive primers led to suboptimal bond strengths when used with PAA, most primers are compatible with PAA oxides [84–86]. PAA-primer systems yield good bond strengths and are generally considered to provide the best long-term durability performance for joints made with typical aerospace aluminium alloys and epoxy adhesives [31,55,87].

3.8.1.2. Chromic acid anodise (CAA)

Chromic acid anodise (CAA) is the other common, high-performance anodise for aluminum alloys. The overall oxide thickness is nearly four times that of PAA (approximately 1500 nm). This thicker, denser oxide is less fragile than the PAA oxide and provides greater corrosion protection to the base alloy. Although the CAA oxide provides less developed porosity than does the PAA oxide, primers have been shown to penetrate the pores.

Anodisation is conducted in 5% aqueous CrO_3 (by weight) at a temperature in the range of 32 °C to 42 °C with the potential gradually raised to 40–50 V. The oxide morphology can be altered by varying the process parameters [81]. Cleaning and deoxidizing steps are similar to those for PAA. The pretreatment acid etch step for the CAA process influences the porosity of the outer surface of the oxide [76]. The CAA treatment is optimal when preceded by a chromic-sulphuric acid etch [88].

Corrosion protection provided by CAA can be enhanced by sealing the oxide with hot water or dichromate solution [89], but sealing fills the pores and decreases adhesion. Although sealed CAA has performed well in some applications [90], the process is generally not recommended for adhesive bonding applications [31,88].

The unsealed oxide may be primed with a corrosion-inhibiting adhesive primer or an organosilane coupling agent. The CAA-primer systems yield good initial bond strengths and durability. Performance in moist environments is slightly inferior to PAA [31,55,91] when tested with toughened epoxy adhesives. In actual service with vinyl-phenolic adhesives, CAA-treated aluminium joints have an outstanding durability record. The CAA process has recently become less popular as environmental and safety concerns regarding hexavalent chromium are making it more expensive and difficult to use.

Recently, boric-sulfuric acid anodise (BSAA) has been developed to produce an oxide similar to the CAA oxide without the use of chromium. Although the treatment was intended originally for paint adhesion applications, a variant called sulphuric boric acid anodise (SBAA) was optimised for aluminium adhesive bonding [92].

3.8.1.3. Optimised Forest Products Laboratory (FPL) etch

The optimised forest products laboratory (FPL) etch produces a 40 nm thick amorphous Al_2O_3 film [93] with an outer network of shallow pores and whisker-like protrusions on top of a thin barrier layer. This microroughness is less pronounced than that of the PAA oxide.

The optimised FPL etch is 5% by weight $\text{Na}_2\text{Cr}_2\text{O}_7 \cdot 2\text{H}_2\text{O}$, 26.7% H_2SO_4 and 68.3% water with a small quantity of 2024 aluminium to seed the bath [81]. Etching is conducted for 10 min at a temperature of about 65 °C. Pretreatment steps include solvent degreasing and/or alkaline cleaning. As with the other chemical processes, rinse steps are important. The FPL etch variables must be carefully controlled. The etched aluminium surface is usually primed with a corrosion-inhibiting adhesive primer prior to adhesive bonding.

The FPL etch process is less expensive and time-consuming than the anodise procedures. It yields good initial bond strengths, but inferior moisture durability compared to the CAA or PAA anodises [55,31,91,93,94].

3.8.1.4. P2 etch

The P2 etch uses ferric sulphate in place of the toxic sodium dichromate as the oxidiser (15% by weight FeSO_4 , 37% H_2SO_4 and 48% water [81]) and produces an oxide with a similar morphology to those obtained using the various chromic-sulphuric etches [54]. The P2 etch produces similar initial bond strengths and durability to those of FPL etch. Its performance as an anodisation pretreatment is comparable to FPL etch [54,83,95].

Three factory aluminium surface preparations are compared on the basis of wedge test data, indicated in Figure 3.19, for Cytec BR 127-primed Al-7075-T6 alloy bonded with Loctite Hysol EA 9628 adhesive [83]. The failure modes are indicated on the plot, where “Adhesive” failure represents interfacial failure between the adhesive and the metal surfaces and “Cohesive” failure represents failure within the adhesive layer.

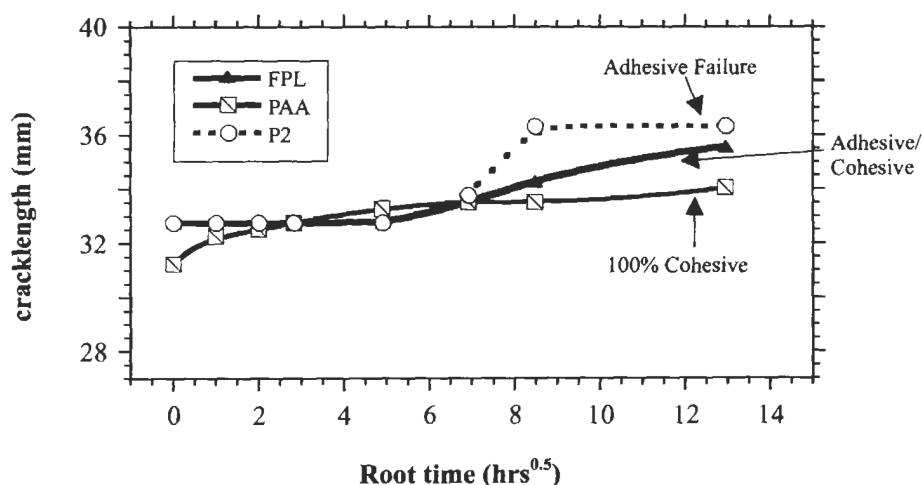


Fig. 3.19. Wedge test data comparing the relative durability performance of the PAA, FPL and P2 factory based surface pretreatment processes for BR 127-primed Al-7075-T6 alloy bonded to EA 9628 adhesive and tested at 50 °C/95% RH [83].

3.8.2. On-aircraft acid anodisation and acid etch processes

The limitations imposed by the on-aircraft environment lead to a demand for simple surface preparations. Solvent degreasing and manual abrasion alone lead to extremely poor long-term durability [31,87].

Adaptations of factory acid etch and anodisation processes have been made to enable their use on aircraft to obtain adequate bond performance. Care must be exercised with the use of acids since these can cause either corrosion in joints and around fasteners or embrittlement of high-strength steel fasteners [96].

Some aircraft structural repair manuals specify primer application with cheesecloth [87]. Inadequate control over primer thickness, often encountered during aircraft repairs, such as with wipe-on or brush applications, can lead to poor initial bond strength. The elimination of the primer can decrease the long-term bond durability. Decisions regarding priming and the entire surface preparation process must often be made on a case-by-case basis for on-aircraft repair.

3.8.2.1. On-aircraft phosphoric acid anodise

PAA has been adapted to on-aircraft use. Pretreatment steps involve the removal of organic coatings, solvent degreasing, manual abrasion and dry-wipe removal of abrasives and debris. Two anodising approaches have been developed:

The phosphoric acid non-tank anodise (PANTA) process uses phosphoric acid, thickened with fumed silica, in a gauze sandwich with a stainless steel mesh cathode [97]. Precautions to keep the gel moist and to avoid trapping hydrogen gas are essential during anodisation. After anodisation, the acid must be removed quickly and without damaging the fragile oxide surface. The surface is then dried prior to priming [87].

The phosphoric acid containment system (PACS) contains the phosphoric acid under a double vacuum bag [98,99]. For the PACS process, the steel cathode screen is placed on top of a nylon breather material. Vacuum is used to pull phosphoric acid through the bag, and anodising is conducted for 25 min with a continual flow of acid over the repair area. Rinsing is accomplished by drawing clean water through the vacuum bag. Final rinsing is conducted after removing the vacuum bag, breather and cathode screen. The surface is then dried and primed prior to bonding.

The advantages of the PACS process over PANTA include acid containment, the ability to more conveniently conduct overhead applications, the avoidance of electrolyte drying and the minimisation of trapped gas against the repair area. However, limited access to the repair area or leaking fasteners under the containment bag could prevent the use of PACS in some applications.

Morphology studies of PANTA and PACS oxides created under controlled laboratory conditions indicate they are similar to those obtained with the factory PAA process. Mechanical testing shows initial bond strength and durability comparable with the tank PAA process [87,97,99].

Both the PANTA and PACS preparations should be followed by application of a corrosion-inhibiting adhesive primer to protect the anodised surface.

3.8.2.2. Acid paste etching processes

The popular chromic-sulphuric acid etches have also been adapted for on-aircraft application using fumed silica, barium sulphate or other suitable material to thicken the acid. Ambient-temperature etching increases the application time. Typical pretreatment steps include a solvent degrease and manual deoxidisation by abrasion or grit-blasting. The paste etches can be difficult to apply or rinse. They generally provide good initial bond strengths but poorer durability than the factory etch processes.

Pasa-Jell 105 (Semco® Products Division of PRC-DeSoto International) is an inorganically thickened blend of acids, activators and inhibitors that is specified in many aircraft repair manuals. Durability results obtained using Pasa-Jell 105 are much better than the simple hand cleaning approaches but are inferior to those obtained using the factory optimised FPL etch and PAA processes as well as PANTA [87].

The P2 paste etch uses a thickened version of the factory P2 solution and delivers performance similar to that obtained with the chromic-sulphuric etches. Ideally, a corrosion-inhibiting adhesive primer is applied after rinsing and drying the repair surface.

3.8.2.3. Chromate conversion coatings

Certain conversion coating processes that are primarily intended to promote the adhesion of paint to aluminium have been used as prebond treatments. In general, conversion coatings should not be used where good adhesive bond durability [100] and cohesive failure modes [101] are desired. The best results employ a 2% hydrofluoric acid etch prior to conversion coating within 15 min of the etch [101]. Durability results show the process can be superior to Pasa-Jell 105 but inferior to factory processes and PANTA. Although the 2% hydrofluoric acid method has been included in aircraft repair manuals, it is really no longer a viable on-aircraft surface preparation due to the hazardous chemicals involved.

3.8.2.4. Silane surface preparation

The application of γ -glycidoxypyriltrimethoxy silane coupling agent following grit-blast produces very good durability results [60–62]. The silane coupling agent is applied from a dilute aqueous solution which deposits an ultrathin layer that dramatically improves the durability of adhesive bonds formed with a grit-blasted aluminium surface (Figure 3.7). The fundamental chemistry that explains the mechanism of the silane layer is explained in Section 3.5.4. Versions of the grit-blast/silane surface preparation, known as the “Australian Silane Surface Treatment”, are popular for aluminium treatment for repair bonding applications worldwide. The primary reason for the use of the silane treatment is the ability to achieve high-performance bond strength and durability without the use of acids that can be problematic for on-aircraft processing. Application of BR 127 chromate-containing primer after the silane surface treatment can offer improved durability in applications where harsher environmental conditions may be experienced.

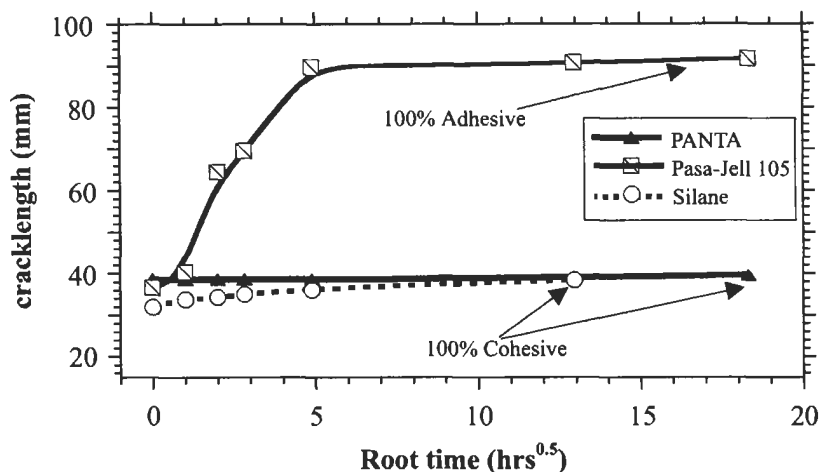


Fig. 3.20. Wedge test data comparing the relative durability performance of the PANTA, Pasa-Jell 105 [102] and Silane on-aircraft [62] surface treatment processes for BR 127-primed Al-7075-T6 alloy bonded with FM 73 adhesive and tested at 50 °C/95% RH.

The relative performance of PANTA, Pasa-Jell 105 and silane on-aircraft aluminium surface preparations are indicated by the wedge test data shown in Figure 3.20 for BR 127-primed Al-7075-T6 alloy bonded to FM73 adhesive [62,102]. The failure modes for each treatment are also indicated on the plot.

3.9. Surface preparations for titanium adherends

Titanium alloys are found in specialised aerospace applications due to their high strength-to-weight ratios, retention of mechanical properties at elevated temperatures (exceeding 400 °C), excellent fracture toughness and corrosion resistance [103]. The most widely-used aerospace titanium alloy, Ti-6Al-4V, will be the focus of this discussion.

As with aluminium, moisture is the environment of primary concern, limiting the long-term durability of the bonded joint. Long-term exposure to high temperatures is also a durability concern for titanium bonded joints.

3.9.1. Factory processes

Most factory processes for titanium surface preparation involve etching or electrochemical anodisation in acidic or alkaline baths. The best durability performance is obtained when the treatment creates microroughness, moderate to good durability is obtained with treatments generating macroroughness and poor durability performance is generally obtained with smooth titanium surfaces [103].

Plasma spray is one potential nonetching factory treatment, driven by the need to find a surface preparation for titanium that can withstand long-term exposure to

elevated temperatures. Good durability results have been obtained when Ti-6Al-4V powder was sprayed on the same alloy. A microscopically rough metallic film is deposited. Its morphology is more random than those obtained with the chemical treatments, having deep pores and many knob-like protrusions [104].

3.9.1.1. Chromic acid anodise (CAA)

The CAA process is a widely utilised and accepted process for prebond treatment of titanium, particularly Ti-6Al-4V. CAA leaves a durable, porous layer of amorphous TiO_2 that is microrough to increase surface area for physical and chemical bonding [103]. Both 5-volt and 10-volt CAA processes exist. These differ from the CAA procedures used for aluminium preparation since they contain hydrofluoric acid. A study conducted by the U.S. Navy in 1982 found the 5-volt CAA process to provide the best overall moisture durability as determined by the wedge test (ASTM D 3762) with conditioning at 60 °C and 100% (condensing) relative humidity. Four epoxy film adhesives, 121 °C-curing and 177 °C-curing, were used. For the study, various organisations provided treated titanium panels to the U.S. Navy for testing. The 10-volt process also provided very good durability [105]. Although there is regulatory pressure in many areas to eliminate the use of hexavalent chromium, the CAA process is still popular. Its use will likely decline when a high-performance alternative is identified.

3.9.1.2. Phosphate fluoride

Several phosphate fluoride procedures have been developed. Although phosphate fluoride treatments are still used for titanium prebond surface preparation, long-term durability is generally not good. These processes ranked at the bottom of the 1982 U.S. Navy study, with markedly poorer wedge test results than the other processes evaluated [105].

3.9.1.3. Pasa-Jell 107-M

Pasa-Jell 107-M is a proprietary (Semco® Products Division of PRC-DeSoto International) blend of mineral acids (nitric and chromic), activators and inhibitors that is specifically formulated for treatment of titanium. It is intended to clean and chemically activate the titanium surface to improve chemical bonding of the adhesive or primer. The process, including rinsing, is conducted at ambient temperature (less than 38 °C) [106]. Pretreatment steps include degreasing and mechanically abrading the titanium surface. Solvents or alkaline cleaners can be used for the former. Dry or wet abrasive blasting with aluminium oxide grit is recommended for the latter. In the 1982 U.S. Navy evaluation, the Pasa-Jell 107 process, preceded by a liquid hone step, provided very good wedge test durability, refer to Figure 3.21. This treatment ranked just behind the 10-volt CAA process [105]. The dry blasting step prior to Pasa-Jell 107 treatment produced poorer durability.

3.9.1.4. TURCO® 5578

TURCO® 5578 (TURCO® Products Division of Henkel Surface Technologies) is an alkaline etchant containing sodium hydroxide. The process, including rinsing,

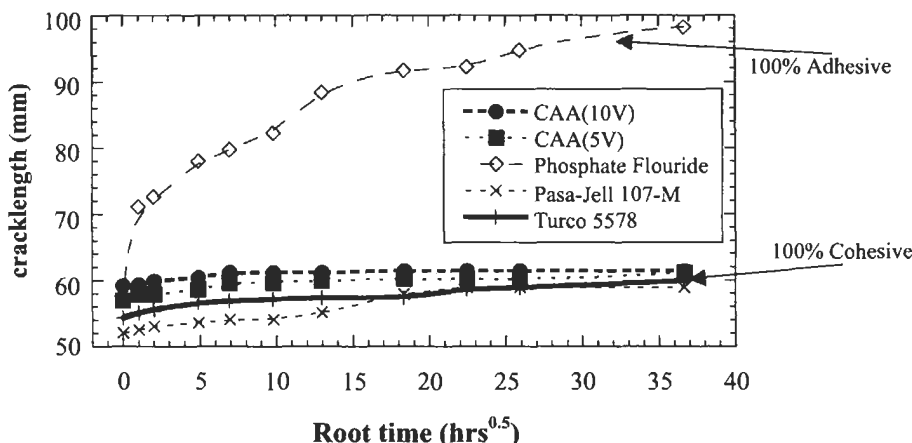


Fig. 3.21. Wedge test data comparing the relative durability performance of the CAA, Phosphate Fluoride, Pasa-Jell 107M and TURCO[®] 5578 factory-based surface treatment processes for Ti-6Al-4V alloy primed with BR 127, bonded with FM 300 K adhesive and tested at 60 °C/100% RH [105].

is conducted at elevated temperature (80–95 °C). TURCO[®] 5578 can be used to remove contaminants and evenly etch titanium surfaces. It does not contain chromates, phenol or hydrofluoric acid [107]. The TURCO[®] 5578 process does not etch titanium as quickly as the common acid etchants and it is slightly more difficult to maintain in the process tank, however, it does not cause the hydrogen embrittlement that can be a concern with acid etchants. Although the TURCO[®] 5578 process was not found to produce a great deal of microroughness on the treated titanium surface [103], the US Navy showed that it provided very good wedge test durability, similar to the two CAA processes [105].

Five factory titanium surface preparations are compared on the basis of wedge test data indicated in Figure 3.21 for BR 127-primed Ti-6Al-4V alloy bonded with FM 300 K adhesive [105]. The failure modes for each surface treatment are indicated in the plot.

3.9.2. On-aircraft processes

Due to restrictions imposed by the on-aircraft environment, there are fewer titanium treatment options. The key on-aircraft challenges are the inability to use an elevated-temperature process, the difficulty in containing and rinsing the highly acidic or alkaline etchants and controlling hazardous materials. Although on-aircraft CAA could be conducted in a manner similar to on-aircraft PAA for aluminium, this does not appear to be common. The viable options for on-aircraft repair include grit-blasting, Pasa-Jell 107 (a thickened version of the tank etchant) and grit-blast/silane identical to the process used for aluminium (Section 3.8.2.4).

3.9.2.1. Grit-blasting

Grit-blasting is often used as a stand-alone titanium prebond treatment [108]. In contrast to the case for aluminium, grit-blasting treatment of titanium is one of the best procedures for obtaining good initial joint strength. For this reason and the fact it is relatively easy and nonhazardous, grit-blasting is often used for on-aircraft titanium treatment. However, although adequate joint durability can often be obtained, long service life in moisture or other aggressive environments requires alternate approaches [31]. It is best to use grit-blasting as a pretreatment step for Pasa-Jell 107 or the silane process.

3.9.2.2. Pasa-Jell 107

The paste version of Pasa-Jell 107 (inorganically thickened Pasa-Jell 107-M) can be used to treat titanium on aircraft since it is an ambient-temperature process. Pretreatment via grit-blasting with aluminium oxide is required for best durability performance. Care must be taken to contain the acid and properly rinse the aircraft components after etching.

3.10. Surface preparations for steel adherends

Surface preparations for steels, particularly chemical treatments, are greatly influenced by the nature of the substrate and its initial condition. The large number of steels makes the objective of achieving a universal treatment difficult [108]. The approach of intentionally forming a coherent, adherent oxide with fine microroughness on the surface of steel is not an effective strategy for good adhesion [108].

In general, the important factors for steel surface preparation are cleanliness and descaling or rust and oxide removal, and passivation for stainless steels [109]. Care must be taken during the preparation process, since many steel alloys rapidly form surface oxides. For instance, drying cycles after treatment can be critical. Also, alcohol is often found in treatment solutions, and alcohol rinses may be used after water rinses. Primers are also desirable to help protect the bonded joint from moisture attack [110].

3.10.1. Factory processes

For surface preparation, three general approaches exist: mechanical abrasion, chemical etching and conversion coating.

3.10.1.1. Grit-blasting

The formation of a macro-rough surface using grit-blasting is a very common surface treatment for steels. Angular alumina grit is often used for this process. This approach can readily yield good, reproducible initial bond strengths [31] and adequate durability may be realised for many applications. However, to obtain the longest service life, additional treatment is usually required [31,108].

3.10.1.2. Acid etches

The morphologies produced on acid-etched steel surfaces are a function of the steel microstructures. Acid etchants can create surface roughness by attacking the grain boundaries of the metal. Some of these processes include the following: nitric-phosphoric acid, phosphoric acid-alcohol, chromic acid, nitric-hydrofluoric acid, sulphuric acid-sodium dichromate, sulphuric acid-sodium bisulphate, oxalic-sulphuric acid and hydrochloric acid-ferric chloride [108,110,111]. Many of the acid etches leave a deposit of carbon, known as smut, on the steel surface. Therefore, a desmutting step, typically using another acid, must also be conducted.

It has been suggested that chemical etches for steels, other than stainless, are not desirable. The many different etches investigated do not tend to outperform grit-blasting, even in durability testing. The ultimate performance for stainless steel bonded joints is obtained when the steel is chemically treated, although little is known about the mechanisms that lead to this improved performance [31]. Furthermore, there is no consensus regarding which treatment is best for a particular alloy.

3.10.1.3. Conversion coatings

Corrosion-resistant conversion coatings are available for steel and are used as treatments prior to painting. Several of these have also been evaluated for adhesive bonding applications. Wegman found the conventional phosphate coatings for steel did not provide adequate bond durability and were adversely affected by elevated-temperature adhesive cure cycles [111]. Improved results are obtained when the phosphating process is closely controlled [108,111].

3.10.2. On-aircraft processes

Preparation of steel is even more difficult for on-aircraft adhesive bonding. Most of the factory processes are impractical since they rely on strong acids, typically used at elevated temperatures. Grit-blasting is a viable option for on-aircraft repair of steel as it was for titanium. In order to improve environmental durability, a corrosion-inhibiting adhesive primer should be applied.

The silane surface preparation successfully employed for numerous aluminium repair applications can also be used to treat many steel substrates. The process is the same as that used on aluminium. It can also be used as a factory treatment for steel. The silane surface treatment has been applied successfully to prepare D6AC steel wing skin surfaces for bonded repair using boron/epoxy patches bonded with epoxy adhesive [112].

3.11. Surface preparations for thermosetting-matrix composites

Many types of composite materials exist and, as with metals, the nature of the adherend to be bonded determines the best surface preparation. The types of composites used in structural applications in the aerospace industry are typically fibre-reinforced thermosetting resins. The fibres contribute strength and stiffness to

the composite while the resin matrix transfers loads. This discussion concentrates on epoxy matrices reinforced with graphite or boron fibres and bonded with epoxy adhesives.

While most people realise adhesive bonding of metal structures requires strict adherence to proper processes, many pay little attention to the need for proper processing for adhesive bonding of composite adherends [113]. Obviously, surface preparation of composites is critical since, impact damage aside, the only in-service failures of bonded composite structures have been interfacial and most relate to durability problems. The durability issue primarily concerns marginal surface preparations that typically result in some surface contamination [31]. Weak initial bonds cannot be nondestructively tested, and in-service loading may lead to bond failure [113].

Two main techniques are used to prepare thermosetting matrix composites for bonding: (1) the peel-ply method and (2) solvent cleaning and abrasion, often conducted after a peel-ply surface has been exposed [114].

Solvent cleaning followed by mechanical abrasion is the primary means to remove contamination from a composite surface. For badly contaminated surfaces, a solvent-soak process using reagent-grade acetone has been recommended [115]. If the condition of the surface is poor, Scotch-Brite abrasion may be employed. Pumice has also been used as an abrasive. Deionised water should be used, especially for the final rinsing, to prevent surface contamination [115]. The standard waterbreak test can be used to verify cleanliness of the composite surface [113].

Grit-blasting should be conducted after abrasive scrubbing and/or solvent degreasing procedures. A light grit-blast with aluminium oxide results in optimal bond strengths with a minimum of variability [115]. Practice is essential, and limiting the blast pressure is critical to preventing surface damage. Very little material should be removed, and the blasted surface should have a dull or matt finish [115]. A pressure of 140 kPa has been recommended using No. 280 dry alumina grit [115].

Manual abrasion with 80–120 grit aluminium oxide paper can be employed as an inferior alternative to grit-blasting. If the composite surface ply is unidirectional, sanding should be in parallel with the fibres to minimise damage [114].

Removal of the grit and other debris can be achieved by a pressurised jet of clean, dry nitrogen or air, or wiping. Dry-wiping is preferred given the potential for solvent wiping to recontaminate the surface (refer to Section 3.4.3). Hart-Smith *et al.* [115] suggest a final cleaning operation with isopropyl alcohol since it is more miscible in water than the stronger solvents and can be removed by rinsing with deionised water, then waterbreak tested. The present authors recommend dry removal of blasting residue followed by a waterbreak test using deionised water.

Composite surfaces must be dry as well as cleaned prior to bonding. After the waterbreak test, the surface should be dried at 120 °C [113]. However, the real moisture problems result from environmental moisture absorbed by the matrix resin. Drying times depend on the laminate thickness. For example, laminates 6.3 mm thick require 24 h of drying at 135 °C to enable the moisture to migrate out. It is most important to dry laminates slowly and thoroughly prior to bonding at

elevated temperature. Special care should be taken if honeycomb or foam core is present since any moisture in the cells could convert to steam and destroy the component. Drying temperatures should be limited to 70 °C in these cases [115].

Following surface preparation and drying, composite substrates are sometimes primed prior to bonding to take advantage of flow and wetting properties of the primer [115]. However, priming does not necessarily improve bond performance.

3.11.1. Precured patches

Precured patch preparation typically involves peel ply removal prior to bonding. Debate continues as to the type of peel ply that should be used and whether additional treatment is needed after peel ply removal [31,113,116].

The peel ply can prevent gross contamination of the patch surface up to the time it is removed. In principle, the peel ply should tear a very thin layer of resin from the composite to create a fresh clean surface. However, peel plies, particularly nylon [116] and those using release agents, have the potential to transfer material to the composite surface. Peel plies containing silicone release agents must be avoided. Although polyester peel plies seem to be better than nylon, the best approach for patch preparation is a light grit-blasting step [116].

3.12. Recent surface preparation research

Few advances in metal prebond surface preparation technology were made during the 15 years following the aluminium treatment work conducted in the late 1970s as part of the United States Air Force PABST program. Acid etch and anodisation processes continued to form the basis for durable bonded joints. A notable exception were the silane surface preparations developed for on-aircraft repair bonding by the Defence Science and Technology Organisation (DSTO) in Australia. In the 1990s, the need to develop environmentally friendly processes and better methods for high-temperature titanium bonding spurred new interest in the area.

In 1993, the Materials and Manufacturing Directorate of the United States Air Force Research Laboratory (AFRL/ML) became active in metal surface preparation research and funded multiple efforts through 1997. The technologies investigated included excimer laser, plasma polymerisation, ion beam enhanced deposition (IBED), plasma spray and sol-gel [117]. The focus was on structural adhesive bonding of aluminium, titanium and stainless steel alloys using epoxy adhesives. The sol-gel work clearly showed the greatest potential for application due to its performance as well as scale-up potential. For this reason, AFRL focused its efforts on optimising sol-gel technologies.

3.12.1. Sol-Gel technology for adhesive bonding

The area of sol-gel chemistry represents a branch of polymer science that, beyond silicones, has only recently been exploited for aerospace applications [118]. The

term “sol-gel” is a contraction for solution-gelation and refers to a series of reactions where soluble precursors (typically metal alkoxides, substituted metal alkoxides or metal salts) undergo hydrolysis and condensation to form a sol and then crosslink to become a gel. This crosslinked structure can be deposited as a coating and consolidated by dehydration. Many different metal atoms can be used to produce films with a wide variety of properties. Organic functionalities can be attached to the hybrid metal-oxygen framework to create organometallic polymer systems with even more diversity.

Sol-gel technology has the potential to revolutionise metal adhesive bonding by providing an environmentally compliant, high-performance, simple and inexpensive approach for surface preparation [118]. One of the big advantages to sol-gel chemistry is its versatility and the ability to be tailored for specific applications. Solution chemistry can be controlled to vary deposited film density, porosity and microstructure. Ideally, adhesion is via direct chemical bonding at the coating/substrate interface as well as the coating/adhesive interface [119].

Several sol-gel chemistries are under development by a number of organisations [120,121]. AFRL has focused its efforts on technology that leads to a surface preparation similar to the existing silane processes while using a more reactive water-based silicon-zirconium chemistry [118,122,123]. This approach is intended to improve performance while eliminating the need for grit-blasting pretreatment and elevated temperature cures [124].

As with the silane preparations, sol-gel chemistry investigated by AFRL eliminates the dependency on strong acids and bases. Also, there are no power requirements as required for anodisation, and wastewater is greatly reduced over conventional wet chemistry approaches since rinsing is not required. There is no need for hexavalent chromium in the sol-gel process, and it may be possible to eliminate chromates from the priming step. Formulations that contain both the sol-gel and primer constituents in one solution that can be applied via spraying or brushing, after pretreatment consisting of degreasing and manual abrasion, are being developed and evaluated [125]. Simple on-aircraft repair versions intended for use in repair bonding of noncritical structure are being evaluated, without adhesive primer, and show promise with both film and paste epoxy adhesives [126].

Sol-gel methodologies are being evaluated for adhesive bonding applications for factory, rework and on-aircraft applications. In limited situations, the technology has already been implemented for several applications, primarily to treat titanium. Repair demonstrations conducted on several aircraft included the treatment of aluminium, titanium and steel.

3.12.2. Hot solution treatment for adhesive bonding

A process termed the “Hot Solution” treatment has been developed at DSTO also in response to the need for environmentally friendly surface treatments. The process involves immersion of aluminium alloys in boiling water followed by immersion in a 1% solution of epoxy silane. Wedge test experiments indicate that

the durability of this treatment may perform as well as phosphoric acid anodisation for some aluminium alloy and epoxy adhesive combinations [127].

Fundamental research has identified that optimum durability is achieved for immersion of the aluminium between 4 min and 1 h in the distilled water heated to between 80 °C and 100 °C. These conditions enable a platelet structure to grow in the outer film region, which, combined with the formation of hydrolytically stable adhesive bonds made to the epoxy silane, appears to be critical in the development of the excellent bond durability [127].

References

1. Huntsberger, J.R. (1981). Interfacial energies, contact angles and adhesion. In, *Treatise on Adhesion and Adhesives*, (R.L. Patrick, ed.), Marcel Dekker Inc., NY, 5, p. 1.
2. Baker, A.A. (1999). Bonded composite repair of primary aircraft structure, *Composite Structures* 47, pp. 431–443.
3. Kinloch, A.J. (1986). *Adhesion and Adhesives, Science and Technology*. Chapman & Hall, London & New York, pp. 56–57.
4. DeBruyne, N.A. (1956). *J. Appl. Chem.*, 6, July, p. 303.
5. Huntsberger, J.R. (1981). *J. Adhesion*, 12, pp. 3–12.
6. Hiemenz, P.C. (1986). *Principles of Colloid and Surface Chemistry*, revised and expanded, (2nd ed.), Marcel Dekker, Chapter 6.
7. Wenzel, R.N. (1936). *Ind. Eng. Chem.*, 28, p. 988.
8. Bascom, W.D. and Partick, R.L. (1974). *Adhesives Age*, 17(10), p. 25.
9. DeBruyne, N.A. (1956). Aero Research Tech Notes No 168, p. 1.
10. Packham, D.E. (1983). In *Adhesion Aspects of Polymeric Coatings* (K. Mittal, ed.) Plenum N.Y., p. 19.
11. Arnott, D.R., Wilson, A.R., Pearce, P.J., et al. (1997). Void development in aerospace film adhesives during vacuum bag cure. *Int. Aerospace Congress 97*, Sydney Australia, 24–27 February, p. 15.
12. Arnott, D.R., Wilson, A.R., Rider, A.N., et al. (1993). *Appl. Surf. Sci.*, 70/71, p. 109.
13. Kinloch, A.J. (1987). *Adhesion and Adhesives – Science and Technology*, Chapman and Hall.
14. Minford, J.D. (1993). *Handbook of Aluminium Bonding Technology and Data*, Marcel Dekker.
15. Macarthur Job Air Disaster Volume 2 Aerospace Publications PO Box 3105 Weston Creek ACT, (1996) Chapter 11.
16. Davis, M.J. (1997). Deficiencies in regulations for certification and continuing airworthiness of bonded structures. *Int. Aerospace Congress 97*, 24–27 February, Sydney, Australia, IEAust. p. 215.
17. Davis, M.J. (1996). *Pro. 41st Int. SAMPE Symp.* March, p. 936.
18. Davis, M.J. (1995). *Pro. Int. Symp. on Composite Repair of Aircraft Structure*, Vancouver, 9–11 August.
19. Hart-Smith, L.J. and Davis, M.J. (1996). *Pro. of 41st Int. SAMPE Symp. and Exhibition*, Anaheim, 25–28 March.
20. Royal Australian Air Force Engineering Standard CS033, Composite Materials and Adhesive Bonded Repairs, September 1995, RAAF Headquarters Logistics Command, Melbourne, Vic., Australia.
21. Pearce, P.J., Camilleri, A., Olsson-Jacques, C.L., et al. (1999). A Benchmarking Review of RAAF Structural Adhesive Bond Procedures, DSTO-Aeronautical and Maritime Research Laboratory Report DSTO-TR-0267. May.
22. Gurney, G. and Amling, R. (1969). *Adhesion Fundamentals and Practice*, McLaren, pp. 211–217.
23. Baker, A.A. (1988). In *Bonded Repair of Aircraft Structures*, (A.A. Baker, and R. Jones, eds.) Martinus Nijhoff, Dordrecht, p. 118.

24. Ashcroft, I.A., Digby, R. and Shaw, S.J. (1998). Accelerated Ageing and life prediction of Adhesively-bonded Joints, Abstracts Euradhesion 98/WCARP 1, Garmisch Partenkirchen Germany, 6–11 September, p. 285.
25. Hardwick, D.A., Ahearn, J.S. and Venables, J.D. (1984). *J. Mat. Sci.*, **19**, p. 223.
26. Cognard, J. (1986). *J. Adhesion*, **20**, p. 1.
27. Broek, D. (1986). Elementary Engineering Fracture Mechanics, Martinus Nijhoff, p. 128.
28. Stone, M.H. and Peet, T. (1980). Evaluation of the Wedge Test For Assessment of Durability of Adhesive Bonded Joints Royal Aircraft Establishment Tech. Memo, Mat 349, July.
29. Mostovoy, S., Crosley, P.B. and Ripling, E.J. (1967). *J. of Materials*, **2**(3), p. 661.
30. Grosko, J., Lockheed Aeronautical systems Co, Georgia Division (communication).
31. Kinloch, A.J. (1987). Adhesion and Adhesives Science and Technology, Chapman and Hall, London, pp. 123–151.
32. Rider, A.N. and Arnott, D.R. (2000). The influence of adherend topography on the fracture toughness of aluminium-epoxy adhesive joints in humid environments, (2001) *J. of Adhesion* **75**, pp. 203–228.
33. Rider, A.N. and Arnott, D.R. (1998). Influence of Adherend Topography on the Durability of Adhesive Bonds Structural Integrity and Fracture (Wang, Chun H., ed.) 21–22 Sept., Melbourne Australia (ISBN (Book) 0 646 36038 8), pp. 121–132.
34. Rider, A.N. (1998). Surface Properties Influencing the Fracture Toughness of Aluminium Epoxy Joints Ph.D. University of New South Wales, Australia.
35. Schmidt, R.G. and Bell, J.P. (1986). *Advances in Polymer Science*, **19**, p. 41.
36. Arnott, D.R., Rider, A.N., Olsson-Jacques, C.L., et al. (1998). Bond durability performance – The Australian Silane Surface Treatment, *21st Congress of ICAS*, 13–18 Sept, Melbourne, Australia.
37. Hong, S.G. and Boerio, F.J. (1990). *J. Adh.*, **32**, p. 67.
38. Olsson-Jacques, C.L., Wilson, A.R., Rider, A.N., et al. (1996). The Effect of Contaminant on the Durability of Bonds Formed with Epoxy Adhesive Bonds with Alclad Aluminium Alloy, *Surface and Interface Analysis*, **24**(9), pp. 569–577.
39. Arnott, D.R., Wilson, A.R., Rider, A.N., et al. (1997). Research underpinning the adherend surface preparation aspects of the RAAF engineering standard C5033, *Int. Aerospace Congress 97*, Sydney, Australia, 24–27 February, p. 41.
40. Venables, J.D. (1984). *J. Mater. Sci.* **19**, p. 2431.
41. Rider, A.N., Arnott, D.R., Wilson, A.R., et al. (1995). Materials Science Forum, pp. 189–190, 235–240.
42. Rider, A.N. and Arnott, D.R. (1996). Surface and Interface Analysis, **24**(9), p. 583.
43. Arnott, D.R. and Kindermann, M.R. (1995). *J. of Adhesion*, **48**, pp. 101–119.
44. Cognard, J. (1996). *J. Adhes.*, **57**, p. 31.
45. Evans, J.R. and Packham, D.E. (1979). *J. Adhesion*, **10**, p. 177.
46. Packham, D.E. (1986). *Int J. Adhesion & Adhesives*, **2**(4), p. 225.
47. Wilson, A.R., Farr, N.G., Arnott, D.R., et al. (1989). Relationship of Surface Preparation of Clad 2024 Aluminium Alloy to Morphology and Adhesive Bond Strength, *Australian Aeronautical Conf.*, Melbourne 9–11 Oct., pp. 221–225.
48. Lambrianidis, L.T., Arnott, D.R., Wilson, A.R., et al. (1995). The Effect and Evaluation of Grit-blast Severity on Adhesive Bond Durability for Aircraft Repairs. *2nd Pacific and Int. Conf. on Aerospace Science and Technology and 6th Australian Aeronautical Conf.*, 20–23 March, Melbourne, Australia, pp. 355–360.
49. Arnott, D.R., Pearce, P.J., Wilson, A.R., et al. (1995). The effect on mechanical properties of void formation during vacuum bag processing of epoxy film adhesives. *Proc. 2nd Pacific and Int. Conf. on Aerospace Science and Technology*, The Australian Institute of Engineers, Melbourne 21–23 March, pp. 811–816.
50. Pearce, P.J., Arnott, D.R., Camilleri, A., et al. (1998). *J. Adh. Sci Technol.* **12**(6), p. 567.
51. Arnott, D.R., Baxter, W.J. and Rouze, S.R. (1981). *J. Electrochem Soc.* (Solid State Science and Technology), **128**(4), pp. 843–847.
52. Venables, J.D. (1984). *J. Mat. Sci.* **19**, pp. 2431–2453.

53. Solly, R.K., Chester, R.J. and Baker, A.A. (2000). Bonded Repair with Nickel Electroforms, DSTO Technical Report, in preparation.
54. Clearfield, H.M., McNamara, D.K. and Davis, G.D. (1990). Engineered Materials Handbook, Vol. 3 Adhesives and Sealants, H.F. Brinson (technical chairman), ASM International, p. 259.
55. Landrock, A.H. (1985). Adhesives Technology Handbook, Noyes Publications, Park Ridge, NJ, p. 66.
56. Marceau, J.A. (1985). Adhesive Bonding of Aluminum Alloys, (E.W. Thrall and R.W. Shannon, eds.) Marcel Dekker, Inc., New York, **51**, p. 51.
57. Young, L. (1961). Anodic Oxide Films, Academic Press, pp. 1–3.
58. Schmidt, R.G. and Bell, J.P. (1986). Advances in Polymer Science, **15**, p. 33.
59. Davis, G.D., Ahearn, J.S., Matienzo, L.J., et al. (1985). *J. Mat. Sci.*, **20**, p. 975.
60. Kuhbander, R.J. and Mazza, J.P. (1993). *Proc. 38th Int. SAMPE Symp.*, May 10–13, p. 1225.
61. Baker, A.A. and Chester, R.J. (1992). *Int. J. Adhesion and Adhesives*, **12**, p. 73.
62. Mazza, J.J., Avram, J.B. and Kuhbander, R.J. Grit-blast/Silane (GBS) Aluminium Surface Preparation for Structural Adhesive Bonding, WL-TR-94-4111 (interim report under US Air Force Contracts F33615-89-C-5643 and F33615-95-D-5617).
63. Clearfield, H.M., McNamara, D.K. and Davis, G.D. (1990). Engineered Materials Handbook, Vol. 3 Adhesives and Sealants, H.F. Brinson (technical chairman), ASM International, p. 254.
64. Dukes, W.A. and Brient, R.W. (1969). *J. Adhesion* **1**, p. 48.
65. Wolfe, H.F., Rupert, C.L. and Schwartz, H.S. (1981). AFWAL-TR-81-3096 August.
66. Internal communication, Royal Australian Air Force, Amberley Air Force Base.
67. Wilson, A.R., Kindermann, M.R. and Arnott, D.R. (1995). Void development in an epoxy film adhesive during vacuum bag cure, *Proc. 2nd Pacific and Int. Conf. on Aerospace Science and Technology*, The Institution of Engineers, Australia, Melbourne, 20–23 March, pp. 625–630.
68. Bijlmer, P.F.A. (1979). Characterisation of the Surface Quality by Means of Surface potential Difference in Surface Contamination, Genesis Detection and Control, **2**, (K.L. Mittal, ed.) Plenum Press, p. 723.
69. Smith, T. (1975). *J. Appl. Phys.*, **46**, p. 1553.
70. Gause, R. (1987). *A non Contacting Scanning Photoelectron Emission Technique for Bonding Surface Cleanliness Inspection Fifth Annual NASA NDE Workshop*, Cocoa Beach, Florida, Dec. 1–3.
71. Photo Emission Technology, 766 Lakefield Rd. Suite h, Westlake Ca 91361.
72. CRC Handbook of Chemistry and Physics, 54th edn. (1973/74) (R.C. Weast, ed.) Chemical Rubber Co, p. E80.
73. Olsson-Jacques, C.L., Arnott, D.R., Lambrianidis, L.T., et al. (1997). Toward quality monitoring of adherend surfaces prior to adhesive bonding in aircraft repairs. *The Int. Aerospace Congress 1997 – 7th Australian Aeronautical Conf.*, 24–27 February, Sydney, Australia, pp. 511–520.
74. Foster Miller Inc 195 Bearhill Rd. Waltham MA 02451-1003 and cstevenson@foster-miller.com.
75. Minford, J.D. (1993). Handbook of Aluminium Bonding Technology and Data, Marcel Dekker, p. 58.
76. Clearfield, H.M., McNamara, D.K. and Davis, G.D. (1990). Engineered Materials Handbook, Vol. 3 Adhesives and Sealants, Brinson, H.F. (technical chairman), ASM International, p. 261.
77. Kinloch, A.J. (1987). Adhesion and Adhesives Science and Technology. Chapman and Hall, London, pp. 101–103.
78. Thrall, E.W. (1979). Failures in Adhesively Bonded Structures (Lecture No. 5). Douglas Paper 6703, Presented to AGARD-NATO Lecture Series 102: Bonded Joints and Preparation for Bonding, Oslo Norway and The Hague, Netherlands, April 2–3.
79. Shannon, R.W., et al. (1978). Primary Adhesively Bonded Structure Technology (PABST) General Material Property Data, AFFDL-TR-77-107 (report for US Air Force Contract F33615-75-C-3016), September.
80. Reinhart, T.J. (1988). Bonded Repair of Aircraft Structures, (A.A. Baker and R. Jones, eds.), Martinus Nijhoff Publishers, Dordrecht, The Netherlands, **23**.
81. Clearfield, H.M., McNamara, D.K. and Davis, G.D. (1990). Engineered Materials Handbook, Vol. 3 Adhesives and Sealants, Brinson, H.F. (technical chairman), ASM International, p. 260.

82. ASTM D 3933-93, Standard guide for preparation of aluminum surfaces for structural adhesives bonding (phosphoric acid anodising), 1997 Annual Book of ASTM Standards, **15.06**, American Society for Testing and Materials, West Conshohocken, PA, (1997), pp. 287-290.
83. Griffen, C. and Askins, D.R. (1988). Non-Chromate Surface Preparation of Aluminum, AFWAL-TR-88-4135 (interim report for US Air Force Contract No. F33615-84-C-5130), August.
84. Marceau, J.A. (1985). Adhesive Bonding of Aluminum Alloys, (E.W. Thrall and R.W. Shannon, eds.), Marcel Dekker, Inc., New York, p. 55.
85. Askins, D.R. and Byrge, D.R. (1986). Evaluation of 350 °F Curing Adhesive Systems on Phosphoric Acid Anodised Aluminum Substrates, AFWAL-TR-86-4039 (interim report for US Air Force Contract Nos. F33615-82-C-5039 and F33615-84-C-5130), August.
86. Peterson, E.E., Arnold, D.B. and Locke, M.C. (1981). Compatibility of 350 °F curing honeycomb adhesives with phosphoric acid anodising. *Proc. of 13th National SAMPE Technical Conf.*, pp. 177-188.
87. Kuperman, M.H. and Horton, R.E. (1985). Adhesive Bonding of Aluminum Alloys, (E.W. Thrall and R.W. Shannon, eds.), Marcel Dekker, Inc., New York, pp. 430-446.
88. Bijlmer, P.F. (1985). Adhesive Bonding of Aluminum Alloys, (E.W. Thrall and R.W. Shannon, eds.), Marcel Dekker, Inc., New York, pp. 28-32.
89. Rogers, N.L. (1985). Adhesive Bonding of Aluminum Alloys, (E.W. Thrall and R.W. Shannon, eds.), Marcel Dekker, Inc., New York, pp. 41-49.
90. Rogers, N.L., (1977). *J. of Applied Polymer Science: Applied Polymer Symp.*, **32**, pp. 37-50.
91. Thrall, E.W. Jr., (1979). Failures in Adhesively-bonded Structures, Douglas Aircraft Company Paper 6703, pp. 2-3.
92. Gaskin, G.B., *et al.* (1994). Investigation of sulfuric-boric acid anodizing as a replacement for chromic acid anodization: Phase I. *Proc. 26th Int. SAMPE Technical Conf.*, Atlanta GA, October, pp. 258-264.
93. Clearfield, H.M., McNamara, D.K. and Davis, G.D. (1990). Engineered Materials Handbook, Vol. 3 Adhesives and Sealants, Brinson, H.F. (technical chairman), ASM International, pp. 260-263.
94. Packham, D.E. (1992). Handbook of Adhesion, (D.E. Packham, ed.), Longman Scientific & Technical, UK, p. 201.
95. Adelson, K.M., Garnis, E.A. and Wegman, R.F. (1982). Evaluation of the Sulfuric Acid-Ferric Sulfate and Phosphoric Acid Anodise Treatments prior to Adhesive Bonding of Aluminum, ARSCD-TR-82013 (US Army Final Report), September.
96. Pinnell, W.B. (1999). Hydrogen Embrittlement of Metal Fasteners Due to PACS Exposure, AFRL-ML-WP-TR-2000-4153, (Report for Delivery Order 0004, Task 2 of US Air Force Contract F33615-95-D-5616), August.
97. Locke, M.C. and Scardino, W.M. Phosphoric Acid Non-Tank Anodise (PANTA) Process for Repair Bonding, *Proc. of*, pp. 218-241.
98. Pergan, I. (1999). *Int. J. Adhesion and Adhesives*, **19**, p. 199.
99. Saliba, S.S. (1993). Phosphoric acid containment system (PACS) evaluation for on-aircraft anodisation of aluminum surfaces. *Proc. of 38th Int. SAMPE Symp.*, **38**, pp. 1211-1224.
100. Podoba, E.A., McNamara, D., *et al.* (1981). *Appl. Surf. Sci.* **9**, pp. 359-376.
101. Kuperman, M.H. and Horton, R.E. (1985). Adhesive Bonding of Aluminum Alloys, (E.W. Thrall and R.W. Shannon, eds.), Marcel Dekker, Inc., New York, pp. 430-446.
102. Locke, M.C., Horton, R.E. and McCarty, J.E. (1978). Anodize Optimization and Adhesive Evaluations for Repair Applications, AFML-TR-78-104 (final report for US Air Force Contract F33615-73-C-5171), July.
103. Shaffer, D.K., Clearfield, H.M. and Ahearn, J.S. (1991). Treatise on Adhesion and Adhesives, **7**, (J.D. Minford, ed.), Marcel Dekker, Inc., New York, pp. 437-444.
104. Clearfield, H.M., *et al.* (1989). *J. Adhesion*, **29**, pp. 81-102.
105. Brown, S.R. and Pilla, G.J. (1982). Titanium Surface Treatments for Adhesive Bonding, NADC-82032-60 (phase report for US Navy Airtask No. WF61-542-001), March.
106. Semco Pasa-Jell 107 Technical Data Sheet, February 1996.

107. TURCO[®] 5578 Technical Data Bulletin, February 1999.
108. Clearfield, H.M., McNamara, D.K. and Davis, G.D. (1990). Engineered Materials Handbook, Vol. 3 Adhesives and Sealants, Brinson, H.F. (technical chairman), ASM International, pp. 264–273.
109. Snogren, R.C. (1974). Handbook of Surface Preparation, Palmerton Publishing Co., Inc., New York, p. 265.
110. Landrock, A.H. (1985). Adhesives Technology Handbook, Noyes Publications, Park Ridge, NJ, pp. 72–75.
111. Wegman, R.F. (1989). Surface Preparation Techniques for Adhesive Bonding, Noyes Publications, Park Ridge, NJ, pp. 66–70.
112. Baker, A.A., Chester, R.J., Davis, M.J., *et al.* (1993). Composites, **24**, p. 6.
113. Hart-Smith, L.J., Brown, D. and Wong, S. (1998). Handbook of Composites, (S.T. Peters, ed.). Chapman and Hall, London, pp. 667–685.
114. Landrock, A.H. (1985). Adhesives Technology Handbook, Noyes Publications, Park Ridge, NJ, pp. 105–106.
115. Hart-Smith, L.J., Ochsner, R.W. and Radecky, R.L. (1990). Engineered Materials Handbook, Vol. 3 Adhesives and Sealants, Brinson, H.F. (technical chairman), ASM International, pp. 840–844.
116. Hart-Smith, L.J., Redmond, G. and Davis, M.J. (1996). The curse of the nylon peel ply. *Proc. of 41st Int. SAMPE Symp.*, **41**, pp. 303–317.
117. Mazza, J.J. (1997). Advanced Surface Preparation for Metal Alloys, AGARD Report 816, February, pp. 10-1 to 10-12.
118. Blohowiak, K.Y. (2000). Sol-gel technology for space applications. *Proc. National Space and Missile Materials Symp.*, San Diego CA, 27 February–2 March.
119. Baes, C.F. and Mesmar, R.E. (1990). In Sol-Gel Science–The Physics and Chemistry of Sol-Gel Processing, (C.J. Brinker and G.W. Scherer, eds.), Academic Press, San Diego.
120. Tiano, T., Pan, M., Dorogy, W., *et al.* (1996). Functionally Gradient Sol-Gel Coatings for Aircraft Aluminum Alloys, WL-TR-96-4108 (final report for US Air Force Contract F33615-95-C-5621), October.
121. Chu, C. and Zheng, H. (1997). Sol-Gel Deposition of Active Alumina Coatings on Aluminum Alloys, WL-TR-97-4114 (final report for US Air Force Contract F33615-94-C-5605), August.
122. Blohowiak, K.Y., Osborne, J.H. and Krienke, K.A. US Patents 6,037,060 (2000), 5,958,578 (1999), 5,939,197 (1999), 5,869,141 (1999), 5,869,140 (1999), 5,849,110 (1998), 5,814,137 (1998).
123. Mazza, J., Gaskin, G., DePiero, W., *et al.* (2000). Faster durable bonded repairs using sol-gel surface treatment. *Proc. the 4th Joint DoD/FAA/NASA Conf. on Aging Aircraft*, St. Louis MO, May.
124. McCray, D.B. and Mazza, J.J. (2000). Optimization of sol-gel surface preparations for repair bonding of aluminum alloys. *Proc. 45th Int. SAMPE Symp. and Exhibition*, Long Beach CA, May, pp. 53–54.
125. Blohowiak, K.Y., Osborne, J.H., Krienke, K.A., *et al.* (1997). *DOD/FAA/NASA Conf. on Aging Aircraft Proc.*, July 8–10, Ogden UT.
126. McCray, D.B., *et al.* (2001). An ambient-temperature adhesive bonded repair process for aluminum alloys. *Proc. 46th Int. SAMPE Symp. and Exhibition*, Long Beach CA, May, pp. 1135–1147.
127. Rider, A.N. and Arnott, D.R. (2000). *Int. J. Adhes. and Adhes.*, **20**, p. 209.

Chapter 4

ADHESIVES CHARACTERISATION AND DATABASE

P. CHALKLEY and A.A. BAKER

Defence Science and Technology Organisation, Air Vehicles Division, Fishermans Bend, Victoria 3207, Australia

4.1. Introduction

The design of a bonded repair is often more demanding than the *ab initio* design of a bonded structure. For example, secondary bending in the repair, often induced by the repair patch itself, can lead to the development of detrimental peel stresses in the adhesive. Such stresses can be avoided or at least minimised in the early design stages of a bonded panel so that the adhesive is mainly loaded in shear. For bonded repair then, assuming the adhesive determines patch performance, a greater range of allowables data is needed for the adhesive from pure shear through shear/peel combinations to pure peel.

However, while the stress-strain properties of the adhesive largely determine the efficiency of load transfer into the patch, there are several possible modes of failure of the bond system, including:

- The adhesive
- The adhesive to metal or composite interface
- The adhesive to primer interface
- The surface matrix resin of the composite
- The near-surface plies of the composite.

Obviously the failure mode that occurs will be the one requiring the lowest driving force under the applied loading. Where more than two or more modes have similar driving forces then mixed mode failure will result.

In this chapter it is assumed that the primary failure mode is cohesive failure of the adhesive layer. This is a reasonable assumption for static loading for well-bonded metallic adherends, in this case with a metallic patch. However, for composites, such as boron/epoxy or graphite/epoxy, failure at low and ambient temperature is often in the surface resin layer of the composite. The tendency for

this mode of failure to occur will increase with low adhesive thickness, the presence of peel stresses, low temperatures and under cyclic loading [1].

At high temperature and particularly under hot/wet conditions, the mode may be expected to change to one of cohesive failure in the adhesive, even with composite adherends since the matrix of the one of composite is generally more temperature resistant than the adhesive.

Thus the test methods outlined here to determine the static properties of the adhesive should provide useable design allowables for static strength of representative repair joints with metallic patches and in some circumstances with composite patches. The methods are also required for determining the stress-strain properties of the adhesive and thus the reinforcing efficiency of the patch prior to failure.

Stress-strain and fracture mechanics type allowables are considered. Having identified which design allowables are needed, typical manufacturers' data, including results from the more common ASTM tests, are examined for their suitability (or lack of) for providing useful design allowables. Such data is often found wanting and more suitable test methods for obtaining allowables are suggested. Finally, a data set of some design allowables for one of the more commonly used repair adhesives is tabulated.

The best approach for fatigue and other complex loading conditions is to obtain the design allowables from representative joints, as discussed in Chapter 5.

4.2. Common ASTM and MIL tests

Manufacturers' data sheets often report a variety of ASTM, MIL and other standard test results. ASTM and MIL test specimens and methods cover the full spectrum of stress states and loading regimes that can occur in adhesively bonded joints, but most suffer from severe stress concentrations and combined stress states. Consequently, while useful for ranking the performance of adhesives, this data cannot be used for bonded repair design because it contains little or no fundamental strain-to-failure or fracture mechanics information.

For example, the data sheet for the Cytec adhesive FM300-2 contains results obtained from tests performed according to US Military Specification MIL-A-25463B and US Federal Specification MMM-A-132A (now superseded by MMM-A-132B). Tests include single-lap shear, T-peel, fatigue strength and creep rupture. For honeycomb structure applications, tests include sandwich peel, flatwise tensile, flexural strength and creep detection. The test results reported are useful for ranking adhesives but do not provide adhesive allowables. For example, stress analyses of the single-lap joint [2], reveal pronounced stress concentrations near the ends of the joint and shear and peel stresses. The "shear strength" value that is obtained by dividing the failure load of the single-lap joint by its bond area is something of a misnomer in that failure is caused by a combination of peel and shear stresses. Also, these stresses are far from uniform over the area of the bond. Other standard ASTM and MIL-A-25463B tests have similar limitations.

A useful set of test data now provided by many manufacturers and which is provided with the adhesive FM300-2 is shear stress-strain data. This data is usually obtained from the testing of thick-adherend lap shear specimens and the techniques used are now the subject of an ASTM standard: ASTM D5656. This test is described in the next section.

4.2.1. Stress-strain allowables

In situ test data for the adhesive (data obtained from testing bonded joints) is required for the generation of adhesive material allowables because of the highly constrained state of the adhesive in a joint. Neat tests, in which the adhesive is free to undergo Poisson's contraction, may yield inaccurate allowables for the performance of an adhesive in a joint, particularly on strain-to-failure. Pure shear test data is most commonly used to design adhesive joints, whereas most practical joints experience both triaxial direct stressing and shear.

4.2.1.1. Static loading

Pure shear

Test specimen types most commonly used to obtain pure shear stress-strain data include:

- Napkin ring (ASTM E229)
- Iosipescu [3]
- Thick-adherend (ASTM D5656).

The thick-adherend test, Figure 4.1, is most widely used because of its ease of manufacture and testing. Stress concentrations present in this specimen [2] are limited in range and alleviated by plastic yielding of the adhesive. Consequently, a more uniform stress field conducive to obtaining material property allowables is obtained. Allowables and design data such as strain-to-failure, ultimate shear strength, yield stress and shear modulus can be obtained from this test. The manufacturer may also provide data from tests performed at various temperatures and after saturation of the adhesive with moisture.

However, the test may not be suitable for brittle adhesives because of the stress concentrations near the ends of the bondline [4]. For most structural adhesives, however, especially those that are rubber-toughened, the thick-adherend test is more than adequate [5,6]. This technique has been adapted to provide data on the strain rate sensitivity of adhesives [7].

An international standard similar to ASTM D5656 is ISO 11003-2 "Adhesives – Determination of Shear Behaviour of Structural Bonds, Part 2: Thick-Adherend Tensile-Test Method". The ISO standard advises the use of extensometers similar to those recommended in ASTM D5656. The major difference between the two standards is in the geometry of the specimen. The specimen in ISO 11003-2 has a shorter overlap length and thinner adherends than the specimen in ASTM D5656-95. The types of design allowables that can be obtained from shear stress-strain testing depend on the design method followed. If the Hart-Smith design methodology [8] is used the adhesive is idealised as elastic/perfectly plastic. The

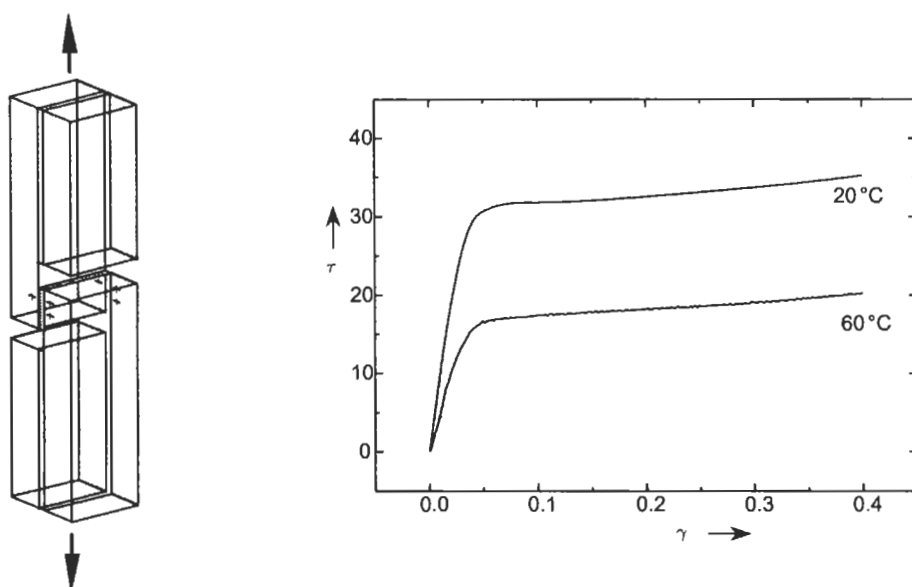


Fig. 4.1. Schematic diagram of the thick-adherend test and shear stress-shear strain curves for adhesive FM 73 at two temperatures obtained using this specimen, taken from reference [9].

advantage of this technique is that relatively simple design formulae result and that the ability of the adhesive to undergo considerable plastic flow and thus lead to higher joint strengths is incorporated. Since, as Hart-Smith argues [8], the maximum potential bond strength is determined by the ultimate adhesive strain energy in shear per unit bond area (area under the shear stress/shear strain curve), the type of idealisation is not as important as the value of the ultimate shear energy (provided this is preserved in the idealisation). The type of design allowables obtainable using this method are listed in Table 4.1.

These allowables and their relationship to an actual stress-strain curve are shown in Figure 4.2.

Table 4.1
Hart-Smith's stress-strain design allowables.

Design allowable	Symbol
"elastic" shear strain limit	γ_e
plastic shear strain	γ_p
plastic shear stress (MPa)	τ_p
modulus in shear (MPa)	G

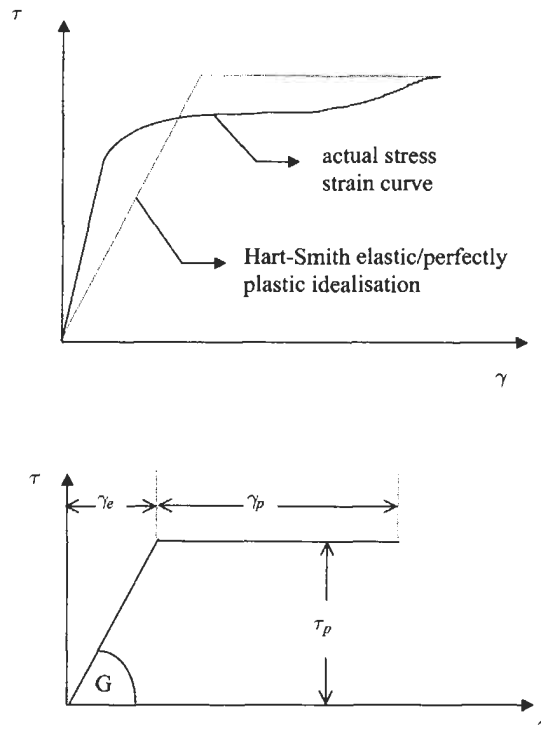


Fig. 4.2. Hart-Smith [8] type idealisation of an adhesive stress-strain curve.

Pure tension

Obtaining *in situ* measurements of the stress-strain behaviour of adhesives in bonded joints is problematic because of the triaxial stresses developed at the joint edges [10]. The stress concentration at the edges of butt joints renders the data obtained invalid for design purposes. Data can be obtained from neat adhesive specimens but care must be taken in its use. Such data can be used only in the context of a material deformation model that accounts for the highly constrained nature of the adhesive in a bonded joint (see the next section) and the strain rate. Figure 4.3 shows some neat stress-strain data obtained at two different strain rates. Similar data can be found in other work [11].

Combined shear-tension/compression

The actual stress state of the adhesive in a bonded repair is most likely to be one of combined shear and tension/compression. Repairs to curved surfaces can develop large through-thickness tensile stresses in the adhesive layer as well as shear stresses, Chapter 7. However, even repairs to flat surfaces will develop these stresses though to a lesser extent. Also, the relatively low modulus adhesive is constrained

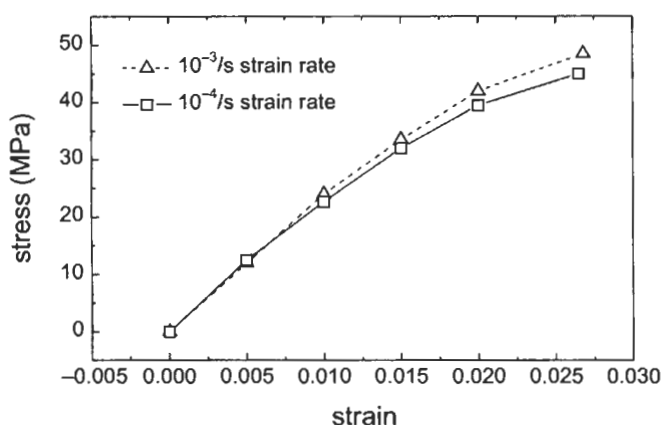


Fig. 4.3. FM73 adhesive tensile test results (specimens not taken to failure).

by stiff adherends and this imparts a triaxial constraint on the adhesive leading to the development of hydrostatic stresses within the adhesive.

The adhesives used in bonded repairs are often required to carry a high level of stress and may suffer yielding. Since the yield behaviour of many polymers is known to be sensitive to hydrostatic pressure, it is no surprise that the yield behaviour of the Cytec adhesive FM73 is also pressure sensitive. Clearly, a yield criterion that can properly account for the effect of hydrostatic stresses is needed for bonded repair studies. A recent study [12] of the *in situ* yield behaviour of the adhesive FM73 subject to combined shear-tension/compression showed that the modified Drucker-Prager/Cap Plasticity model correlated best with measured data for the adhesive FM73. The Drucker-Prager/Cap Plasticity model is more commonly associated with geological materials but performed better than more conventional models modified to include pressure sensitivity such as the modified von Mises and the modified Tresca models. The specimen used in this study was a modified Iosipescu specimen [13], which was capable of applying combined shear and peel stresses. Yield data from a range of shear and peel stress combinations were obtained. Various yield criteria, some such as von Mises and Tresca modified to include pressure-dependent yield, have been proposed [14,15] for adhesives. The Drucker-Prager criterion has also been proposed [16]. However, as shown in Figures 4.4 and 4.5 (from reference [12]), the modified Drucker-Prager/Cap Plasticity works best for the rubber-modified structural epoxy adhesive FM73 (the modified Tresca is very similar to the modified von Mises plot).

Thus for design of bonded repairs that are subject to complex loading, the multiaxial material model used should be the modified Drucker-Prager/Cap Plasticity model. This type of yield criterion can be implemented in a finite element code such as ABAQUS [17]. The parameters (for details on the physical meaning of these parameters see references [12,17]) needed for this criterion are given in Table 4.2.

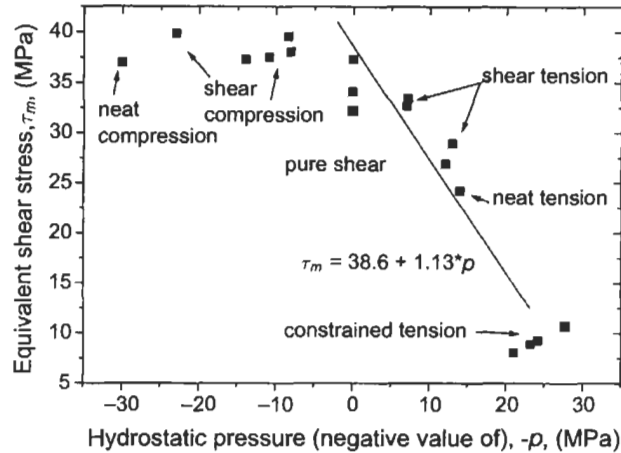


Fig. 4.4. Modified von Mises yield criterion curve fit.

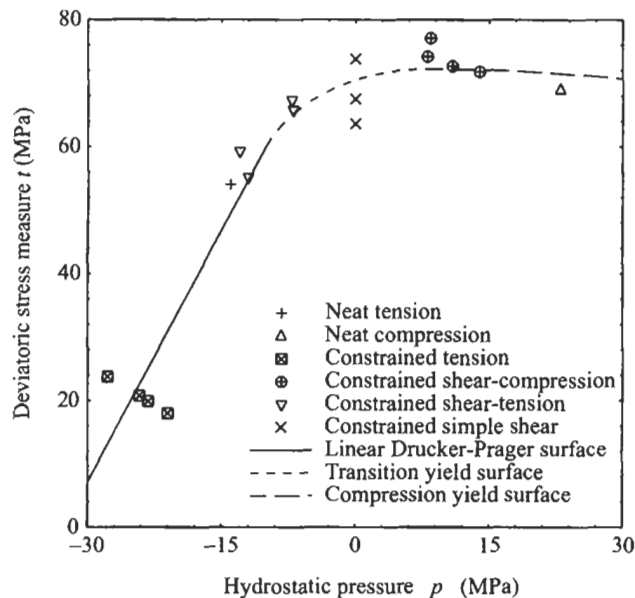


Fig. 4.5. Modified Drucker-Prager/Cap Plasticity curve fit.

Although yield stress data does exist, there is little strain-to-failure data under complex loading for adhesives. Current design practice is to knockdown pure shear data by a factor as much as one half. This is clearly an area that needs further development but is complicated by the triaxial stress states that develop in bonded joints when any stress state other than pure shear is applied.

Table 4.2
Modified Drucker-Prager/Cap plasticity parameters for FM73.

K	β (degrees)	d (MPa)	p_d (MPa)	R	α
0.778	69.3	86.5	8.0	1.0	0.18

4.3. Fatigue loading

Fatigue data ideally should be gathered from a bonded joint that is representative of the repair under design, and this approach for composite adherends is discussed in Chapter 5. However, simple endurance testing of adhesives is often undertaken using the single-overlap shear specimen. Although ASTM D3166 describes a test method using a metal-to-metal single-lap joint for investigating the fatigue strength of adhesives in shear, the actual stress state of the specimen is one of combined peel and shear and the length of the overlap is too short to properly reproduce the large strain gradients present in bonded repairs.

For the model joints (which are designed to have uniform shear in the adhesive) repeated cyclic stressing to high plastic strain levels can result in creep failure of the joint after a relatively small number of cycles [18]. This is because cyclic shear strains are cumulative. (If the cycle rate is high, full strain recovery cannot occur during the unloading cycle.) The result is an accelerated creep failure of the adhesive by a *strain ratcheting* mechanism. In practical lap joints this situation is avoided by maintaining a sufficiently long overlap, so that much of the adhesive remains elastic. The elastic region on unloading acts as an elastic reservoir to restore the joint to its unstrained state preventing the damaging strain accumulation. Fracture mechanics approaches to measuring fatigue properties can also be taken as described in Section 4.4.3.

4.4. Fracture-mechanics allowables

At present the use of fracture mechanics to evaluate the strength and durability of adhesive joints is not highly developed. Its application is complicated by factors such as geometric non-linearity in test specimens and mixed failure loci (cohesive failure of the adhesive mixed with interfacial failure). Nevertheless, high loads may induce static propagation of the disbond and similarly repeated loading can cause fatigue. Consequently fracture mechanics design allowables may become useful. The types of specimens useful for fracture mechanics studies of adhesive are shown in Figure 4.6.

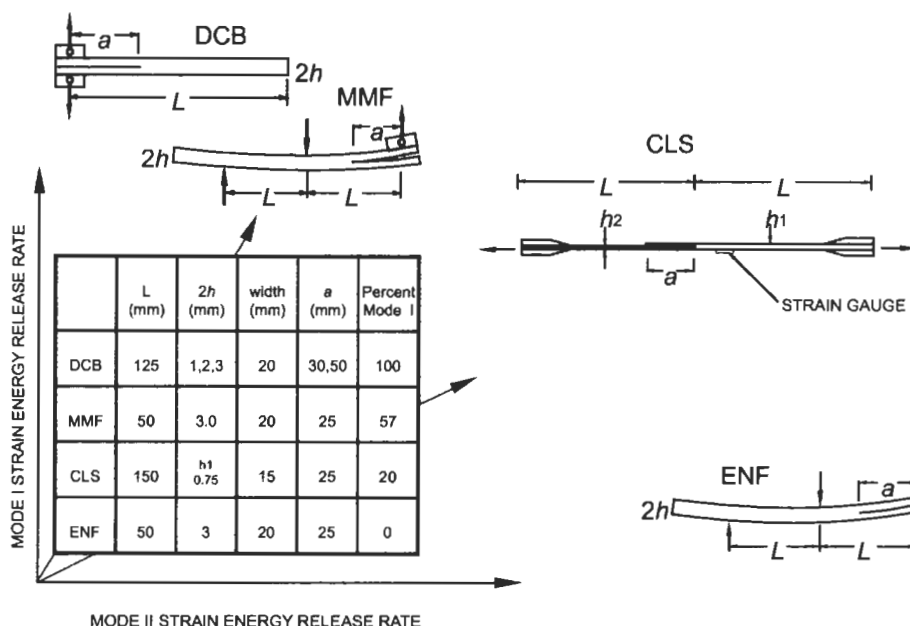


Fig. 4.6. Types of specimen used for measurement of fracture properties in laminated composites and bonded joints, showing the percentage of mode I; adapted from reference [19]. DCB = double cantilever beam, CLS = cracked Shear specimen, MMF = mixed mode flexural, ENF = edge notched flexural.

4.4.1. Static loading

If a disbond is present in a bonded repair then it is typically subject to mixed mode loading (usually a combination of Mode I and Mode II and sometimes Mode III). However, test standards only exist for Mode I loading. Since adhesives used in repair are usually very tough ($G_{IC} > 2 \text{ kJ/m}^2$) static crack propagation in the adhesive is unlikely for most repairs to composites where $G_{IC} < 150 \text{ J/m}^2$.

4.4.2. Mode I

ASTM standard D3433 covers the measurement of Mode I fracture toughness. Either flat or tapered adherend double-cantilever beam specimens can be used to measure toughness. For toughened adhesives such as FM73 the value of toughness varies with bondline thickness as shown in Figure 4.7 (tapered cantilever beam results).

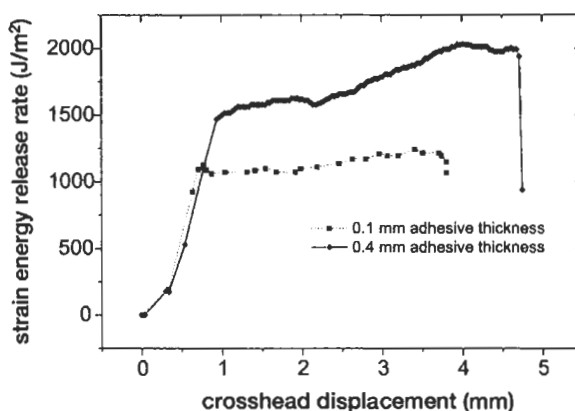


Fig. 4.7. Mode I fracture toughness of FM73 from a cantilever beam specimen (cure 8 h at 80 °C).

4.4.3. Mode II and mixed mode

Fracture mechanics testing of adhesives, from pure Mode I through mixed Mode I/Mode II through to pure Mode II can be performed using the test specimen and loading rig developed by Fernlund and Spelt [20]. Mode II tests, however, are difficult to perform for most toughened adhesives as yield of metallic adherends often occurs before the adhesive undergoes crack propagation.

4.4.4. Fatigue loading

Data on fatigue damage thresholds and crack propagation under fatigue loading are most usually obtained from the fracture mechanics-type lap-joint tests using an edge-notched flexural specimen [21] for Mode II, the double-cantilever beam specimen for Mode I and cracked lap-shear specimen for mixed mode (see Figure 4.6). In these tests the rate of crack propagation in the adhesive is usually plotted as a function of the strain-energy-release-rate range. The empirical relationship between the range of strain-energy-release rate and the crack growth rate is of the form:

$$\frac{da}{dN} = A\Delta G^n,$$

where a is the disbond or crack length in the adhesive, N the number of fatigue cycles, and ΔG the range of strain energy release rate for the relevant mode. The parameters A and n are empirically determined constants. In the mixed-mode specimens, Figure 4.8, it was found that the better correlation is with the total strain energy range ΔG_T , showing that Modes I and II contribute to damage growth. Figure 4.8 shows a typical result for the adhesive FM 300.

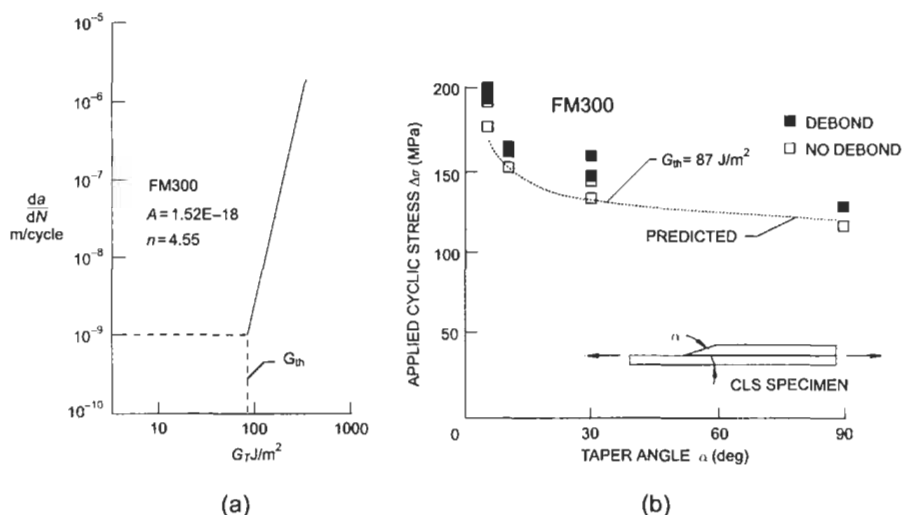


Fig. 4.8. Schematic plot of (a) da/dN versus ΔG_T based on data for adhesive FM 300 and (b) use of data to predict damage growth in CLS specimen with tapered end; taken from reference [23].

Comparative studies [22] on several joint types have shown that the values of the crack-growth parameters are similar, indicating the potential value of this approach as a design tool.

For crack growth in airframe aluminium alloys (generally tested under Mode I loading), n is of the order of 9–16, while for the typical structural film adhesive FM300 (film thickness 0.2 mm) n is close to 25, both under pure Mode I and mixed-mode loading. This indicates that disbond growth in these adhesives is rapid. Thinner bond lines due to higher constraint would probably have much higher values of n . For disbond propagation in the composite, n will also be very high because of the brittle matrix and thin effective bond line.

In general these observations strongly discourage the use of (damage-tolerant) designs based on controlled disbond growth under cyclic loading conditions. Thus, for most of the life of the joint, the design approach must be to hold ΔG below (a conservative estimate of) the threshold for crack initiation, ΔG_{Th} .

The threshold strain-energy release rate range ΔG_{Th} was used as a measure of the cyclic stress level for damage to occur in a (unidirectional) gr/ep cracked-lap specimen bonded with adhesive FM300 or a paste adhesive. The ends of the cracked-lap specimen had taper angles of 5, 10, 30 or 90°.

The estimated cyclic stress levels for the initiation of damage were compared with the observed level for the various taper angles. It was assumed that damage would grow when $\Delta G_{Th} = \Delta G_{Th}$.

A Finite-Element program was used to estimate G_{Th} for the joint, assuming the presence of a small delamination 1 mm long for the tapered end. The value for

ΔG_{Th} was taken as the strain-energy release range for a disbond propagation rate of 10^{-9} m/cycle. For FM300 the value of ΔG_{Th} was found to be 87 J/m^2 at this propagation rate.

Generally, as shown in Figure 4.8(b), the correlation was very good between the predicted and observed cyclic stress levels for disbond growth for the various taper angles, indicating the potential of this approach for fatigue-critical joints having a significant Mode I (peel) component. Sensitivity to adhesive thickness and other joint parameters remains to be demonstrated.

4.5. FM73 database

4.5.1 In situ shear stress-strain allowables

To reduce thermal residual stresses in bonded repairs or to ease application problems, a cure of 8 h at 80°C of FM73 is often used in contrast to the manufacturer's recommended 1 h at 120°C . Thus in the test specimen this was the cure temperature used and the pressure applied during cure was 100 kPa also to simulate in-field repairs. The surface treatment used was the standard solvent clean, grit blast and application of aqueous silane-coupling agent [9]. The data from testing 30 test specimens [9] at each test condition (-40°C dry, 24°C dry and 80°C wet) is shown below in Table 4.3. It is reported in both the form recommended in ASTM 5656 and in the form advocated by Hart-Smith (elastic-perfectly plastic idealisation) – the latter being the more useful for design purposes. The standard deviation is shown for the value reported.

Hart-Smith [8] type design allowables are shown in Table 4.4.

Table 4.3

FM73 stress-strain data [9] and standard deviations for three test conditions (8 h at 80°C , 100 kPa pressure cure condition).

	RT dry	-40°C dry	80°C wet
Linear limit shear stress (MPa)	27.34 ± 1.21	27.23 ± 4.72	5.97 ± 2.95
Linear limit shear strain	0.0364 ± 0.0022	0.0302 ± 0.0068	0.0207 ± 0.0054
Shear modulus (MPa)	805.47 ± 38.84	959 ± 150	278 ± 134
Knee value of shear stress (MPa)	39.22 ± 0.96	50.27 ± 2.45	8.95 ± 3.11
Knee value of shear strain	0.0739 ± 0.0028	0.0688 ± 0.0079	0.0546 ± 0.0121
Knee shear modulus (MPa)	530.7 ± 23.9	730.7 ± 91.1	163.9 ± 67.6
Ultimate shear stress (MPa)	39.14 ± 1.76	55.71 ± 2.14	21.85 ± 3.83
Ultimate shear strain	0.5774 ± 0.0475	0.1870 ± 0.0415	0.8630 ± 0.1013

Table 4.4
Hart-Smith type design allowables for FM73 cured at 80 °C for 8 h.

	RT, dry	−40 °C, dry	80 °C, wet
Elastic shear strain	0.0804 ± 0.0151	0.0723 ± 0.0082	0.6616 ± 0.1214
Shear modulus (MPa)	503 ± 88	791 ± 107	34.8 ± 13.9
Yield stress (MPa)	41.52 ± 0.97	56.46 ± 2.15	21.88 ± 3.46
Plastic shear strain	0.4970 ± 0.0468	0.1192 ± 0.0261	0.2014 ± 0.1035

4.5.2. Yield criterion

A report by Wang and Chalkley [12] details an investigation of the yield behaviour of FM73 (1 h at 120 °C cure). An experimental investigation, using the modified Iosipescu specimen loaded at various angles and various neat adhesive tests was undertaken. Yield criteria investigated include modified Tresca, modified von Mises, modified Mohr-Coloumb, modified Drucker-Prager and modified Drucker-Prager with cap plasticity. The last criterion was found to best fit the data and the resulting yield parameters are shown in Table 4.5.

4.5.3. The glass transition temperature

Studies at AMRL using dynamic mechanical thermal analysis (DMTA) have given the following estimates for the glass transition temperature of FM73 (Table 4.6).

Table 4.5
Modified Drucker-Prager/cap plasticity parameters for FM73.

K	β (degrees)	d (MPa)	p_a (MPa)	R	α
0.778	69.3	86.5	8.0	1.0	0.18

Table 4.6
Glass transition temperature data for FM73.

FM73 – 1 h at 120 °C cure	99.7 °C
FM73 – 8 h at 80 °C cure	108.5 °C

4.5.4. Fickian diffusion coefficients for moisture absorption

Althof [24] gives the following data for the diffusion coefficients of FM73 (Table 4.7).

Althof's bulk adhesive film specimens had dimensions 1 mm × 60 mm × 10 mm. This size of specimen conforms to DIN 53445 (torsion-vibration tests). The aluminium plate specimens had dimensions 5 mm × 100 mm, 10 mm × 100 mm, 20 mm × 100 mm, and 30 mm × 100 mm. The number of specimens per data point is not reported. Althof's data is also reported by Comyn [25], which is an easier reference to obtain.

Jurf and Vinson also give data for the adhesive FM73-M (FM73 having a matt scrim) and their data is given in Table 4.8.

4.5.5. Mode I fracture toughness

Fracture toughness data for the 8 h at 80 °C-cure condition (24 °C test temperature) is presented in Table 4.9.

Table 4.10 presents the fracture toughness measured for the 1 h at 120 °C cure condition.

Note that the 8 h at 80 °C cure of the adhesive results in a more brittle adhesive.

Table 4.7
Althof's [24] Fickian moisture diffusion coefficients for FM73.

Temp (°C)	Relative humidity (%)	Max. moisture content (%)	Diffusion coefficients obtained from water absorption by adhesive film experiments (m^2s^{-1})	Diffusion coefficients obtained from <i>in situ</i> absorption between aluminium plates experiments (m^2s^{-1})
20	70	1.1	2.8×10^{-13}	3.6×10^{-13}
20	95	2.0	1.7×10^{-13}	3.9×10^{-13}
40	70	1.2	8.1×10^{-13}	10.3×10^{-13}
40	95	2.5	4.2×10^{-13}	41.7×10^{-13}
50	95	2.5	11.6×10^{-13}	15.2×10^{-13}
70	95	10 ^a	—	33.3×10^{-13}

^aAlthof reports this value as an abnormal increase in moisture.

Table 4.8
Jurf and Vinson's [26] moisture diffusion coefficients for FM73-M.

Temperature (°C)	Relative humidity (%)	Diffusion coefficient (m^2s^{-1})	Saturation moisture content (%)
38	95	6.2×10^{-13}	1.55
49	95	8.0×10^{-13}	2.05
60	95	8.7×10^{-13}	2.20
71	95	9.8×10^{-13}	2.30

Table 4.9

Author's mode I fracture toughness data for FM73 cured for 8 h at 80 °C.

Adhesive thickness (mm)	Minimum fracture toughness (J/m ²)	Maximum fracture toughness (J/m ²)	Average fracture toughness (J/m ²)
0.1	1113	1230	1172
0.4	1502	1790	1646
0.9	1906	2903	2405

Table 4.10

Mode I fracture toughness data for FM73 [27] (1 h at 120 °C cure).

Temperature (°C)	Mode I fracture toughness (J/m ²)
21	3000
-40	2700

References

1. Chalkley, P.D. and Baker, A. (1999). Development of a generic repair joint for the certification of bonded repairs. *Int. J. of Adhesion and Adhesives* **19**, 121–132.
2. Anderson, G.P. (1984). Evaluation of adhesive test methods. In *Adhesive Joints – Formation, Characteristics and Testing* (K.L. Mittal, ed.) Plenum Press, New York.
3. Wycherley, G.W., Mestan, S.A. and Grabovac, I. (1990). A Method for Uniform Shear Stress–Strain Analysis of Adhesives, ASTM JOTE, May.
4. Grabovac, I. and Morris, C.E.M. (1991). The application of the Iosipescu shear test to structural adhesives. *J. of Applied Polymer Science*, **43**, 2033–2042.
5. Renton, W.J. (1976). The symmetric lap-shear test – What good is it? *Experimental Mechanics*, Nov. pp. 409–415.
6. Tsai, M.Y., Morton, J., Krieger, R.B., et al. (1996). Experimental investigation of the thick-adherend lap shear test. *J. of Advanced Materials*, April, pp. 28–36.
7. Chalkley, P.D. and Chiu, W.K. (1993). An improved method for testing the shear stress–strain behaviour of adhesives. *Int. J. of Adhesion and Adhesives*, **13**(4), October.
8. Hart-Smith, L.J. (1973). Adhesive-Bonded Double-lap Joints, NASA CR 112235, Douglas Aircraft Company, McDonnell Douglas Corporation, Long Beach, California, USA.
9. Chalkley, P.D. and van den Berg, J. (1997). On Obtaining Design Allowables for Adhesives used in the Bonded-composite Repair of Aircraft, DSTO-TR-0608, Defence Science and Technology Organisation, Melbourne.
10. Adams, R.D., Coppedale, J. and Peppiatt, N.A. (1978). Stress analysis of axisymmetric butt joints loaded in torsion and tension. *J. of Strain Analysis*, **13**(1).
11. Butkus, L.M. (1997). Environmental Durability of Adhesively Bonded Joints, Ph.D. Thesis, Georgia Institute of Technology, September.
12. Wang, C.H. and Chalkley, P.D. (2000). Plastic yielding of a film adhesive under multiaxial stress. *Int. J. of Adhesion and Adhesives*, **20**(2), April, pp. 155–164.
13. Broughton, W.R. (1989). Shear Properties of Unidirectional Carbon Fibre Composites, Ph.D. Thesis, Darwin College, Cambridge.
14. Haward, R.N. (1973). *The Physics of Glassy Polymers*, Applied Science Publishers Pty. Ltd., London.
15. Bowden, P.B. and Jukes, J.A. (1972). The plastic flow of isotropic polymers. *J. of Materials Science*, **7**, pp. 52–63.

16. Chiang, M.Y.M. and Chai, H. (1972). Plastic deformation analysis of cracked adhesive bonds loaded in shear. *Int. J. of Solids and Structures*, **31**, 2477–2490.
17. ABAQUS (1997). Theory Manual, Version 6.5. Hibbitt, Karlsson & Sorensen Inc., U.S.A.
18. Hart-Smith, L.J. (1981). Difference Between Adhesive Behaviour in Test Coupons and Structural Joints, Douglas Paper 7066, presented to ASTM Adhesives Committee, Phoenix.
19. Russell, A.J. and Street, K.N. (1985). Moisture and temperature effects on the mixed mode delamination fracture of unidirectional graphite/epoxy. *Delamination and Disbonding of Materials* (W.S. Johnson, ed.) ASTM STP 876.
20. Fernlund, G. and Spelt, J.K. (1994). Mixed-mode fracture characterisation of adhesive joints. *Composites Science and Technology*, **50**, pp. 441–449.
21. Russell, A.J. Fatigue crack growth in adhesively bonded graphite/epoxy joints under shear loading. *ASME Symposium on Advances in Adhesively Bonded Joints 1988*, MD 6 (S. Mall, K.M. Liechti and J.R. Vinson, eds.) (Book No GOO485).
22. Lin, C. and Liechti, K.M. (1987). Similarity concepts in the fatigue fracture of adhesively bonded joints. *J. of Adhesion*, **21**, pp. 1–24.
23. Johnson, K.W.S. and Dillard, D.A. (1987). Experimentally determined strength of adhesively bonded joints in joining fibre reinforced plastics (F.L. Mathews, ed.) Elsevier Applied Science pp. 105–183.
24. Althof, W. (1980). The Diffusion of Water Vapour in Humid Air into the Adhesive Layer of Bonded Metal Joints, DFVLR-FB 79-06, 1979 – RAE translation into English no. 2038, February.
25. Comyn, J. (1981). Joint durability and water diffusion. In *Developments in Adhesives – 2* (A.J. Kinloch, ed.) Applied Science Publishers, London.
26. Jurf, R.A. and Vinson, J.R. (1985). Effect of moisture on the static and viscoelastic properties of epoxy adhesives. *J. of Materials Science* **20**, pp. 2979–2989.
27. Baker, A.A., Chester, R.J., Davis, M.J., *et al.* (1993). Reinforcement of the F-111 wing pivot fitting with a boron/epoxy doubler system – Materials engineering aspects. *Composites* **24**(6), pp. 511–521.

Chapter 5

FATIGUE TESTING OF GENERIC BONDED JOINTS

P.D. CHALKLEY, C.H. WANG and A.A. BAKER

Defence Science and Technology Organisation, Air Vehicles Division, Fishermans Bend, Victoria 3207, Australia

5.1. Introduction

A certification process has been proposed [1] (see also Chapter 22) based largely on a generic approach to patch design, validation and the acquisition of materials allowables. This approach includes testing of joints representing the repaired region. This chapter reports on the development of and preliminary results for two such generic bonded joints to be used in the validation process: the double overlap-joint fatigue specimen (DOFS) and the skin doubler specimen (SDS). These two joints are selected to represent parts of the bonded repair with widely differing damage-tolerance requirements as discussed later in this chapter.

The layout of this chapter is as follows. The role of the two representative joints within the generic design and certification process is established. Then the damage-tolerance requirement for the structure that each joint represents is discussed. The specimen preparation and manufacture are outlined for each joint in turn. The stress-state of the specimen is analysed. The experimental method and test results are reported and the suitability of various fatigue-correlation parameters is discussed. Finally the suitability/limitations of the specimens for generic design and certification is discussed and further work is suggested before concluding.

5.1.1. Damage-tolerance regions in a bonded repair

Figure 5.1 shows a schematic of a bonded repair to a cracked plate for which Baker [1] proposed that two distinctly different regions exist in terms of structural integrity requirement.

The central damage-tolerant region is the zone where a significant disbond between the patch and plate can be tolerated. This is because small disbonds reduce

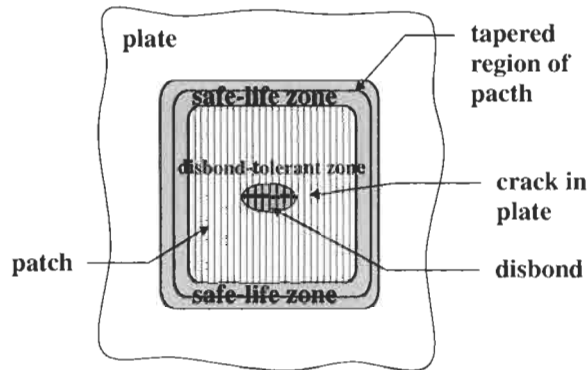


Fig. 5.1. Damage-tolerant and safe-life zones in a bonded repair.

the repair effectiveness only slightly and disbond growth under repeated loading is slow and stable. The ends of the patch are stepped, thinning down to one ply of fibre composite at the edges. In this zone disbands cannot be tolerated because as the disbond grows it moves into a region of increasing patch thickness and consequently greater driving force for disbond growth. The result may be rapid disbond growth resulting in patch separation.

To represent these two regions testing of two types of generic joint was proposed:

- The double overlap-joint fatigue specimen (DOFS), which represents the damage-tolerance region where the patch spans the crack
- The skin doubler specimen (SDS), which represents the safe-life region at the termination of the patch.

Both specimens have fibre-composite outer adherends on both sides of an aluminium inner adherend to represent bonded repairs to aircraft structural plate where there is substantial out-of-plane restraint from substructure such as stringers, stiffeners or honeycomb core.

5.1.2. The generic design and certification process

Table 5.1 places the two generic repair joints, the DOFS and the SDS, in the context of the certification process.



5.2. The DOFS

Details on the materials and geometry of the DOFS are provided in Figure 5.2.

The DOFS were manufactured by bonding the outer composite adherends to the aluminium inner adherends with adhesive FM73 and then cutting into three individual specimens. The inner adherends were made from aluminium alloy 2024-T3 (bare). Surface treatment of the aluminium plates, prior to adhesive bonding, was the solvent clean, grit blast, silane treatment described in Chapter 3. The boron/epoxy (120 °C cure system) outer adherends were cocured with a layer of

Table 5.1

Generic joint test program to obtain repair system allowables, taken from reference [1].

Requirement	Approach
To find joint static and fatigue strain allowables and confirm validity of failure criteria based on coupon test data. <i>The failure damage criteria must hold for similar geometrical configurations, e.g. adherend thickness and stiffness and adhesive thickness.</i>	<ul style="list-style-type: none"> Undertake static strength tests to: <ul style="list-style-type: none"> check strength against predictions based on coupon data Undertake fatigue tests to: <ul style="list-style-type: none"> obtain B-basis threshold for fatigue disbond growth determine disbond growth rates under constant amplitude and spectrum loading Find knockdown factors for: <ul style="list-style-type: none"> hot/wet conditions non-optimum manufacture typical damage more representative loading conditions
 <p>Double overlap-joint fatigue specimen (DOFS) representing cracked region</p>  <p>Skin doubler specimen (SDS), representing patch termination</p>	

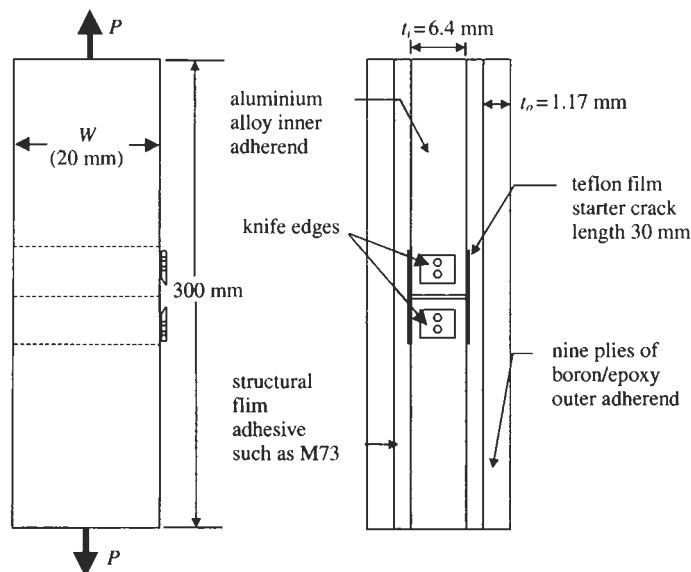


Fig. 5.2. The double-overlap-joint fatigue specimen (DOFS).

FM73 at 120 °C then grit blasted and bonded to the aluminium plates at 80 °C with another layer of FM73. The cocured adhesive layer is used to prevent damage to the boron/epoxy during the grit-blasting process and to toughen the matrix surface layer of the composite. All bonding was done in an autoclave.

5.2.1. Stress state in the DOFS

A finite element (FE) analysis of the DOFS [2] showed, as expected, that the joint is essentially in a state of shear plus transverse compression (to the plane of the adhesive), referring to Figure 5.3. The FE results were obtained based on the assumed material properties listed in Table 5.2.

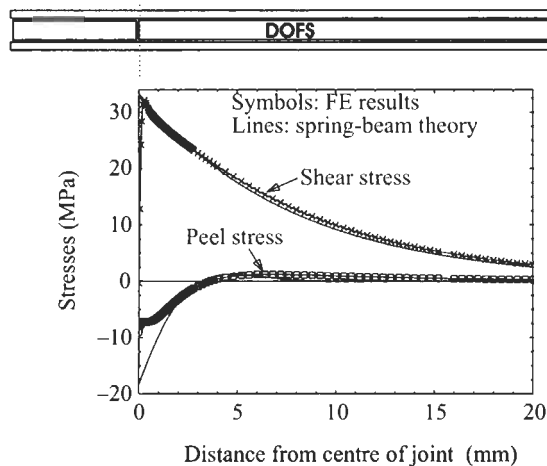


Fig. 5.3. Plot of shear and peel stresses along the mid-plane of the adhesive layer in DOFS; load/unit width = 1 kN/mm. (neglecting thermal residual stresses).

Table 5.2

Material properties used in the DOFS and SDS analyses.

Adhesive	Aluminium	Boron/Epoxy
$G_A = 800 \text{ MPa}$	$E_i = 71 \text{ GPa}$	$E_{11} = 193 \text{ GPa}$
$\nu_A = 0.35$	$\nu_i = 0.33$	$E_{22} = 19.6 \text{ GPa}$
$\alpha_A = 66 \times 10^{-6} \text{ (per } ^\circ\text{C)}$	$\alpha_i = 24 \times 10^{-6} \text{ (per } ^\circ\text{C)}$	$G_{12} = 5.5 \text{ GPa}$
		$\nu_{12} = 0.21$
		$\nu_{21} = 0.021$
		$\alpha_{11} = 4.3 \times 10^{-6} \text{ (per } ^\circ\text{C)}$
		$\alpha_{22} = 15.6 \times 10^{-6} \text{ (per } ^\circ\text{C)}$
$t_A = 0.4 \text{ mm}$	$t_i = 6.4 \text{ mm}$	$t_o = 1.1 \text{ mm}$

In the case of elastic deformation only, the maximum adhesive shear stress in a DOFS can be determined using beam-spring theories for adhesive joint [3]:

$$\tau_{\max} = \frac{\beta P}{2W} \frac{E'_i t_i}{E'_i t_i + 2E'_o t_o} , \quad (5.1)$$

with

$$\beta = \sqrt{\frac{G_A}{t_A} \left(\frac{2}{E'_i t_i} + \frac{1}{E'_o t_o} \right)} , \quad (5.2)$$

where and $E'_i = E_i/(1 - \nu_i^2)$ and $E'_o = E_o/(1 - \nu_o^2)$. The parameter P denotes the total load applied to the specimen. In the present study, the specimen width W is approximately 20 mm for all the specimens tested. For the problem depicted in Figure 5.3 with material properties being given in Table 5.2, Eq. (5.1) yields a maximum shear stress of approximately 33.3 MPa, which compares well with the finite element solution of 32 MPa as shown in Figure 5.3. The distribution of the shear stress is given by [3]:

$$\tau(x) = \tau_{\max} e^{-\beta x} \quad (5.3)$$

Although the above solutions have been derived for isotropic reinforcement, the comparison shown in Figure 5.3 suggests that these solutions can also be applied to orthotropic patch with low shear modulus, indicating that the effect of shear lag is quite small and can be ignored.

Also shown in Figure 5.3 are the results of the peel stress. It is noted that near the centre of the joint, the peel stress is compressive. According to the conventional beam-spring theories, the peel stress distribution is given by the following expression [4]:

$$\sigma(x) = -\tau_{\max} \kappa t_o e^{-\kappa x} \cos(\kappa x) , \quad (5.4)$$

with

$$\kappa = \left[\frac{E'_A}{t_A} \frac{3}{E'_o t_o^3} \right]^{1/4} , \quad (5.5)$$

where $E'_A = E_A/(1 - \nu_A - 2\nu_A^2)$ to account for the effect of triaxial stresses within the adhesive layer [5]. It can be seen that the simple beam-spring theory would over-predict the magnitude of the peel stress, which is mainly due to the non-uniformity of the stress in the thickness of the reinforcement, and cannot be captured by the simple beam-spring model.

5.2.2. Experimental method

Since the DOFS represents a section through the disbond/damage-tolerant central region of a bonded repair, disbond propagation data are required. To this end, a Teflon starter disbond was included during specimen manufacture to ensure rapid crack initiation. As discussed in the reference [2] a compliance technique was used to measure the disbond length. Essentially the compliance technique measures the relative displacement between the two inner adherends at the centre of the joint, with the aid of a crack-opening displacement (COD) gauge attached to the inner adherends as shown in Figure 5.2. Opening of the inner adherends is directly related to the disbond length via the following expression:

$$\delta = 2\gamma_{\max}t_A + 2b\epsilon_o \quad , \quad (5.6)$$

where γ_{\max} is the nominal adhesive shear strain (assuming the shear strain is uniform through the adhesive layer, i.e. ignoring the effect of crack-tip singularity), t_A is the thickness of the adhesive layer, the parameter b is the effective disbond length and ϵ_o , which is equal to $P/2wE_o t_o$, is the normal strain in the outer adherend. Equation (5.1) can be rewritten as:

$$\frac{\delta}{2\epsilon_o} = \frac{\gamma_{\max}t_A}{\epsilon_o} + b \quad (5.7)$$

The ratio $\delta/2\epsilon_o$ is calculated from the measured displacement-force pairs and is effectively the normalised compliance of the specimen. Calibration of the compliance using various lengths of Teflon starter crack gave the result shown in Figure 5.4, confirming that the compliance method provides a very good means of directly measuring the disbond length.

The slope of the fitted line shown in Figure 5.4 is 0.96, which compares well with the factor of 1.0 (coefficient of b) predicted in Eq. (5.2). It is important to note that

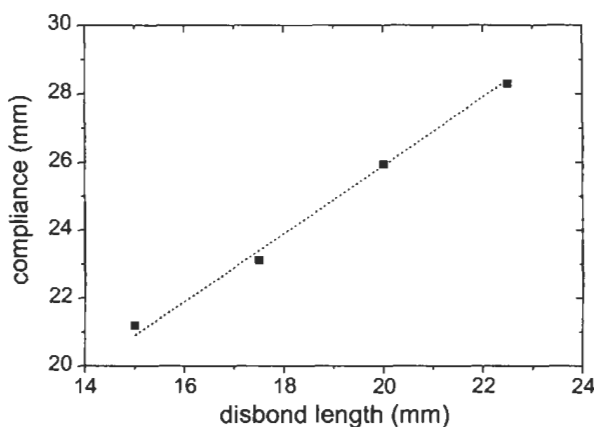


Fig. 5.4. Validation of the compliance-to-disbond length relationship.

the first term on the right-hand side of Eq. (5.2) does not change with crack length, consequently the rate of disbond growth at a given cycle db/dN , can be determined by taking the derivative of Eq. (5.2) with respect to N :

$$\frac{db}{dN} = \frac{d(\delta/2\varepsilon_o)}{dN} \quad (5.8)$$

The disbond growth rates presented in this chapter have been determined using this technique.

Since the length of the initial Teflon starter disbond is known, the nominal shear strain γ can be determined via Eq. (5.2) from the measured opening displacement. Alternatively, the adhesive shear strain can be determined using adhesive joint theory discussed earlier. Provided the adhesive does not undergo cyclic plastic deformation, i.e. the cyclic shear-strain range is less than the following value, $\Delta\gamma_Y = 2\tau_Y/G_A = 0.08$, where the subscript Y denotes the shear strain at the onset of plastic yielding, and for FM73 adhesive the shear yield stress τ_Y at room temperature is approximately equal to 32 MPa [6]. In the case of elastic deformation, the adhesive shear stress in a double-overlap joint specimen can be determined using Eq. (5.1).

Fatigue testing was carried out in an Instron testing machine at room temperature at a frequency of about 3 Hz. The load ratio (minimum value divided by the maximum value) for all cyclic loads was kept approximately zero. Damage growth in the adhesive due to the cyclic loads was measured using the above outlined compliance technique every 1000 cycles.

5.2.3. Experimental results

Two fatigue-damage criteria (correlation parameters) were investigated: the shear-strain range in the adhesive, $\Delta\gamma$, and the “global” strain energy release rate range, ΔJ . The shear-strain range was taken directly from the COD gauge measurements and the global strain energy release rate range was calculated from the load applied and constituent-material elastic properties and thicknesses. The shear-strain range was found to best correlate disbond growth rates in different specimens. Table 5.3 lists the details of the specimens. It is noted that the adhesive in specimen 2 was cured at a lower temperature than the adhesive in the other specimens and hence different adhesive material properties may have contributed to the discrepancy shown later.

Disbond growth rates for specimens 4, 5 and 6 in Table 5.3 were obtained from three structural detail specimens. Each specimen was tested under constant amplitude loading. At the end of testing the boron patches were removed and the extent of adhesive disbond measured. The disbond rate was determined by dividing the length of the disbond by the number of cycles. In all cases, for both the joints and crack-patch specimen the disbond was found to propagate along the interfaces between the first ply of the boron fibre and the cocured adhesive layer [2]. This

Table 5.3
DOFS and structural details.

Specimen no.	Spec. type	Adhesive	Adhesive thickness (mm)
1	DOFS	FM73 ^a	0.38
2	DOFS	FM73 ^b	0.30
3	DOFS	FM73 ^a	0.54
4	Crack patch specimen [7]	FM73 ^a	0.48
5	Crack patch specimen [7]	FM73 ^a	0.55
6	Crack patch specimen [7]	FM73 ^a	0.28

^a 1 h at 120 °C cure.

^b 8 h at 80 °C cure.

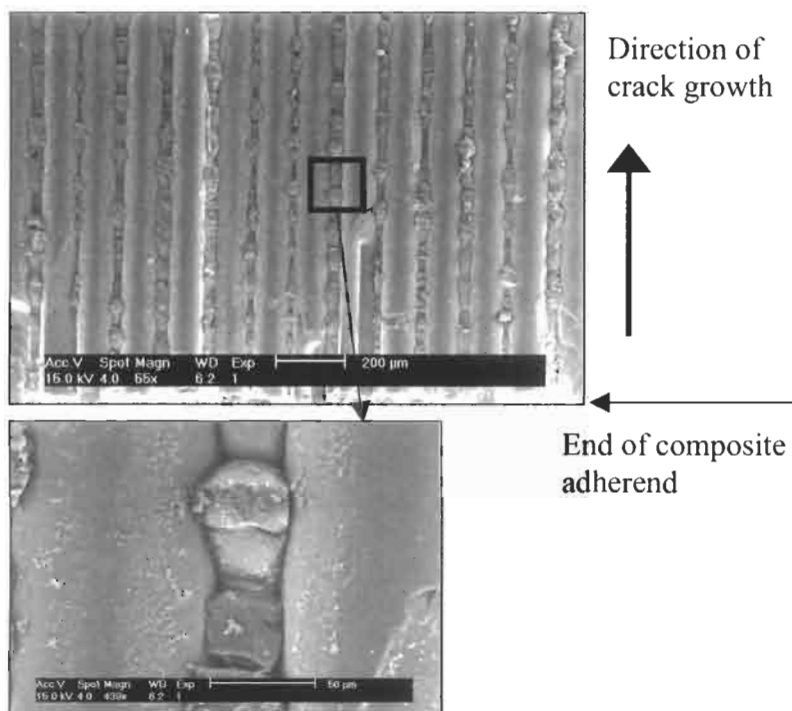
failure process involves separation of the epoxy from the boron fibres and fracture of the resin between fibres, referring to Figure 5.5.

The experimental results are plotted in Figure 5.6(a) versus the measured shear-strain range $\Delta\gamma_{\max}$ for various DOFS and crack-patching specimens. It can be seen that for a given shear-strain range, specimen 2 exhibited faster growth rates than other specimens. This is possibly due to the lower cure temperature (80 °C compared with 120 °C for the rest of the specimens; see Table 5.3) resulting in a bondline having a lower resistance to fatigue crack growth, even though crack growth was not through the adhesive. The same experimental results, excluding those of specimen 2, are re-plotted in Figure 5.6(b) against the calculated shear-strain range using Eq. (5.1). The shear-strain ranges for all the specimens are below the cyclic plastic limit, verifying the validity of the elastic solution. It can be seen in Figure 5.6(b) that all the experimental results now lie within a narrow band of $\pm 100\%$ of growth rates. The experimental results can be well correlated by the following equation:

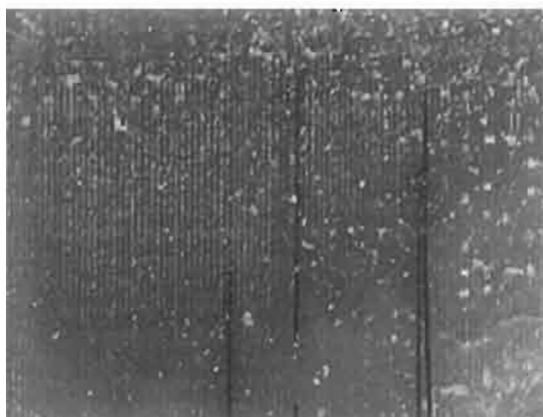
$$\frac{da}{dN} = C(\Delta\gamma_{\max})^m, \quad (5.9)$$

with $C = 37154.0$ (m/cycle) and $m = 10.1$. Similarly, the results of the 80 °C cured specimen (number 2) can be correlated by the same relation with the following constants: $C = 10^{11.4}$ and $m = 14.2$.

However, the above correlating parameter seems to contradict the conventional fracture mechanics approach [8–10], where disbond growth rates ought to be correlated by the strain-energy release rate or the J -integral [11,12]. In particular, it has been reported that under tensile mode (Mode I), disbond growth rates pertaining to different adhesive thicknesses could be well correlated by the J -integral [11]. Furthermore, the applied load ratio has been found to have negligible effect on growth rates when the cyclic strain-energy release rate is chosen as the correlating parameter [13]. To examine the applicability of the strain-energy release rate as a suitable correlating parameter for shear-dominated growth, the disbond



(a)



(b)

Fig. 5.5. SEM micrographs of (a) fracture surface on the boron/epoxy adherend and (b) on the adhesive surface showing imprint of fibres.

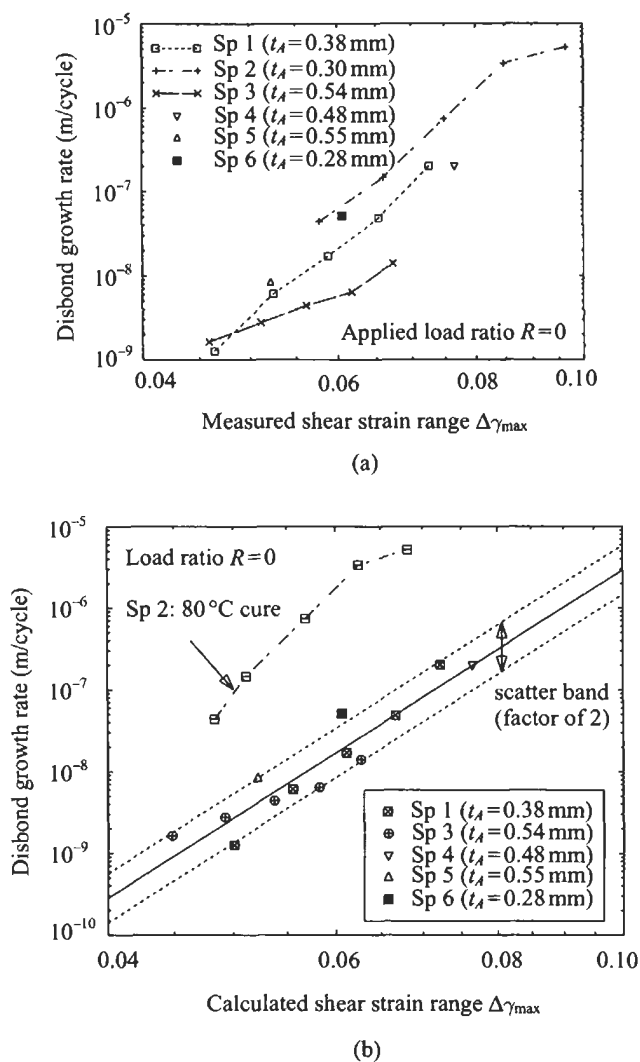


Fig. 5.6. Comparison of DOFS and generic structural detail specimen disbond growth rates versus (a) the measured shear strain range and (b) the calculated shear strain range.

growth rates are plotted against the strain-energy release rate, which is given by [12]:

$$\Delta G = \frac{(\Delta\gamma_{\max})^2 t_A}{2G_A}, \quad (5.10)$$

where G_A denotes the shear modulus of the adhesive layer. It can be shown that in the case of DOFS, the strain-energy release rate can be expressed in terms of the

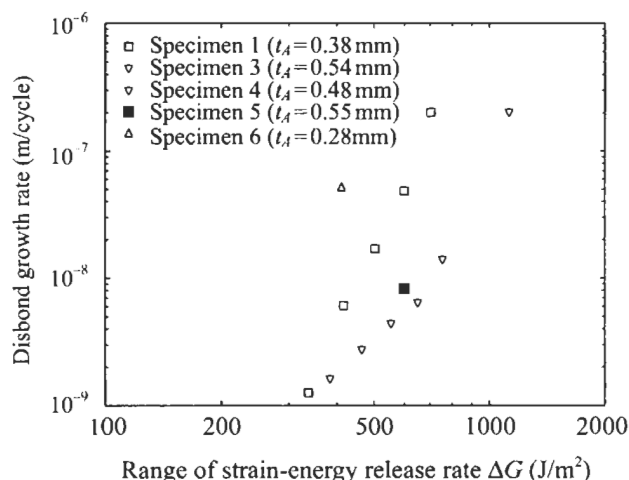


Fig. 5.7. Comparison of DOFS and generic structural detail specimen disbond growth rates using the strain energy release rate.

load applied to the specimen, noting Eqs (5.1) and (5.2):

$$\Delta G = \frac{1}{8} \left(\frac{P}{W} \right)^2 \frac{E'_i t_i}{E'_o t_o (2E'_o t_o + E'_i t_i)} \quad (5.11)$$

It is clear that, for a given applied load, the strain-energy release rate is independent of the adhesive thickness. Figure 5.7 shows the plot of disbond growth rates versus the above calculated strain-energy release rate, indicating that for the same strain-energy release rate, disbond growth rates can differ by more than a factor of ten. Therefore, for shear-dominated disbond growth, the maximum adhesive shear strain provides a better correlating parameter than the strain-energy release rate. The shear-strain range over the central region can be readily calculated in the design stage, so the data shown here are directly applicable to design. Further work needs to be done to quantify the effects of environment and temperature on disbond growth rate.

Although the strain range criterion for the adhesive appears to be of practical value as a fatigue-damage parameter, it is not yet clear why it should be relevant for the boron/epoxy specimens where, as previously noted, fatigue failure occurs largely by separation of the epoxy matrix from the fibres in the interface ply, implying that the strain-energy release rate ought to be a more suitable correlating parameter. Nevertheless, there is evidence in the literature lending support to the use of shear-strain range. Russell [14] in his work on the fatigue of adhesively bonded end-notched flexural specimens (Mode II), postulated that the magnitude of the adhesive shear modulus determines the locus of failure in graphite/epoxy joints bonded with the adhesive FM300. Presumably this is because the shear modulus and shear strain in the adhesive determine the shear stress experienced at the interface on the adhesive and surface matrix of the composite. Chai and Chiang [15] in their work on static shear fracture showed for a compression-side interface

crack in an adhesively-bonded end-notched flexural specimen (a stress state similar to that of the DOFS) that micro-disbond initiation ahead of the crack was controlled by the value of the maximum through-thickness stress (or bond-normal stress). The through-thickness stress changes from compression to tension ahead of the crack tip and reaches a maximum at a location that depends on the average shear strain in the crack tip region. Furthermore, the value of the maximum through-thickness stress depends solely on the average shear strain in the crack tip region. Clearly, the adhesive shear strain strongly influences the fracture of such joints and may influence fatigue behaviour also if the fatigue mechanism is micro-disbond initiation ahead of the crack tip. The mechanism may be a recurring micro-disbond initiation in the adhesive near the interface followed by subsequent growth into the first ply of the laminate.

5.3. The skin doubler specimen

The skin doubler specimen, which represents the ends of a repair patch, is depicted in Figure 5.8.

The materials and surface treatment used in the manufacture of the SDSs were identical to those for the DOFS. Since disbond initiation data was sought from these specimens, no Teflon starter was used. Four end-step geometries, shown in detail in Figure 5.9, were investigated.

Note that specimen type II in Figure 5.9 has ply drop-offs occurring on both the inside patch surface and the outside patch surface, i.e. two plies are added every 4-mm step. Therefore, while the step length in joint III is shorter at 3 mm, the effective taper angle is lower since only one ply is added per step. The adhesive

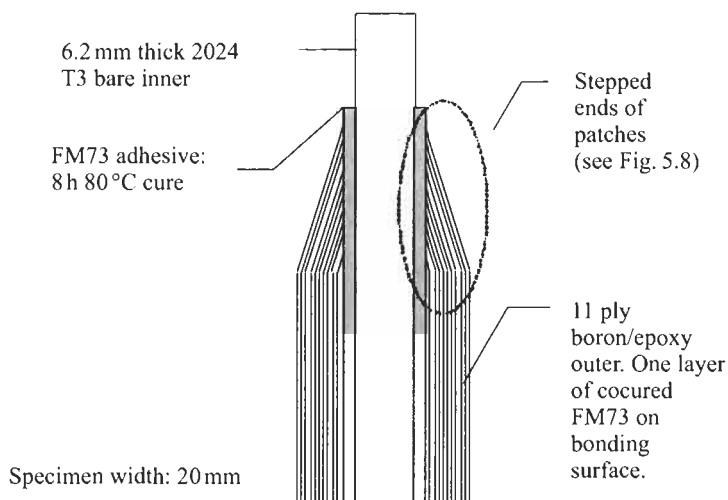


Fig. 5.8. Schematic of the skin doubler specimen (not to scale).

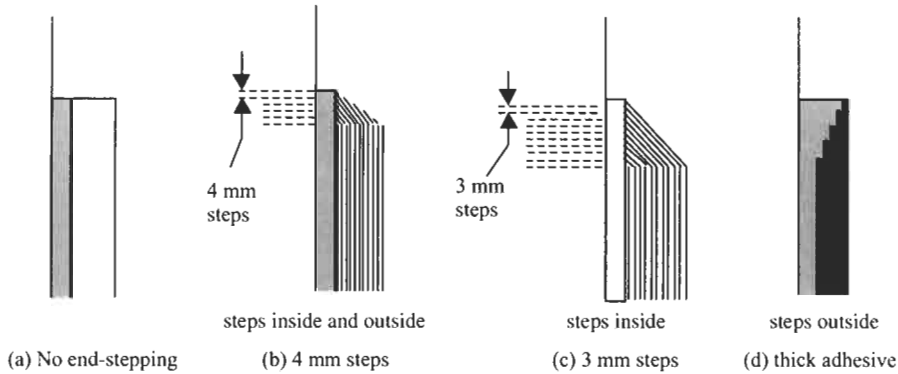


Fig. 5.9. The end step geometries investigated: (a) type I, (b) type II, (c) type III, and (d) type IV.

thickness, t_A , at the end of the overlap was typically 0.4 mm for joints I, II, and III, and 3.0 mm for joint IV.

5.3.1. Stress state in the skin doubler specimen

5.3.1.1. Block-end (no taper)

The most significant difference between the SDS and the DOFS is that the transverse stress (peel stress) in the adhesive at the patch ends is positive, as opposed to compressive in the DOFS, when the joint is subjected to tensile load. In the case of square end (no tapering at patch end) without adhesive fillet, the adhesive shear stress near the patch end is given by [3]:

$$\tau_{\max} = \frac{\beta P}{W} \frac{E'_o t_o}{E'_i t_i + 2E'_o t_o} \quad (5.12)$$

It is worth noting that the above formula is different from Eq. (5.1). However, in the case of the balanced repair ($E'_i t_i = 2E'_o t_o$), Eqs (5.1) and (5.13) become the same. For unbalanced repair, the shear stress at the centre of double overlap joint is different from that at the end of the joint. The maximum peel stress can be expressed in terms of the maximum adhesive shear stress, according to Eqs (5.4) and (5.5),

$$\sigma_{\max} = \tau_{\max} \left[3 \frac{t_o}{t_A} \frac{E'_A}{E'_o} \right]^{1/4} \quad (5.13)$$

To verify these simple solutions, a FE analysis was carried out under plane-strain conditions. The material properties used in the FE analysis are listed in Table 5.2. The FE mesh employed near the patch end is shown in Figure 5.10.

A comparison between the FE results and the predictions of the above beam-spring theory is shown in Figure 5.11, indicating a good agreement.

The mismatch in the coefficients of thermal expansion for the metallic adherend and the composite patch gave rise to thermal residual stresses after the specimens

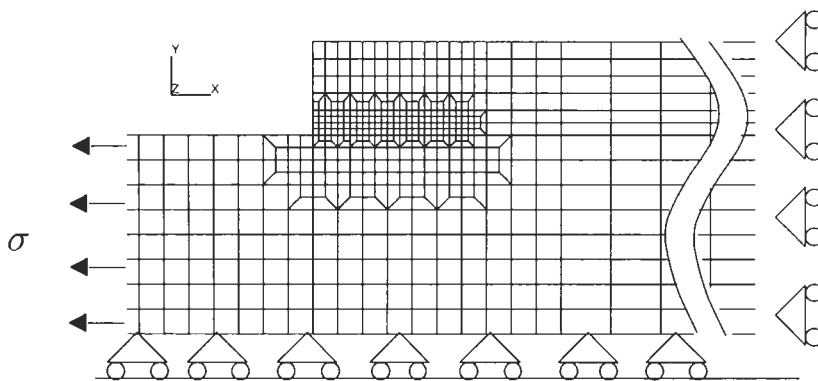


Fig. 5.10. Finite element mesh near the end of a block-end patch.

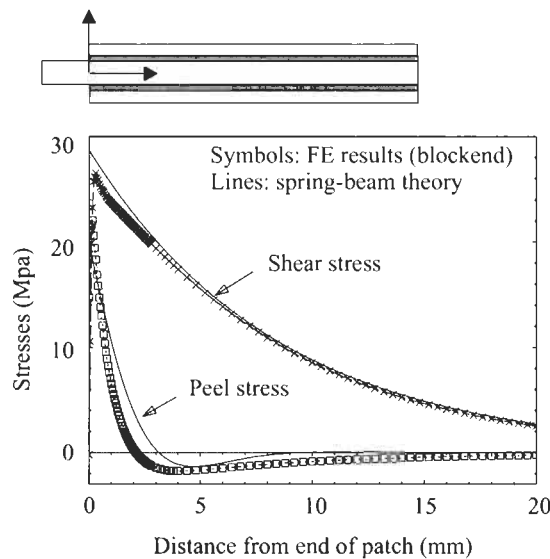


Fig. 5.11. Stress state in a SDS with block end; load/unit width = 1 kN/mm.

had been cooled to the room temperature after curing at 80 °C. The peak residual shear stress at the end of the adhesive layer can be determined [3]:

$$\tau_{\max}^T = -\beta(\alpha_i - \alpha_{11})\Delta T E_i' t_i \frac{E_{11}' t_o}{E_i' t_i + 2E_{11}' t_o} \quad (5.14)$$

where the material properties are listed in Table 5.2. The minus sign indicates that the residual shear stress at the end of patch is opposite to the shear stress induced by remote tension. For specimens cured at 80 °C, the temperature drop ΔT equals to 60 °C, which leads to a thermal residual shear stress of −17.8 MPa. This estimate compares well with the finite element solution shown in Figure 5.12, i.e. −21 MPa.

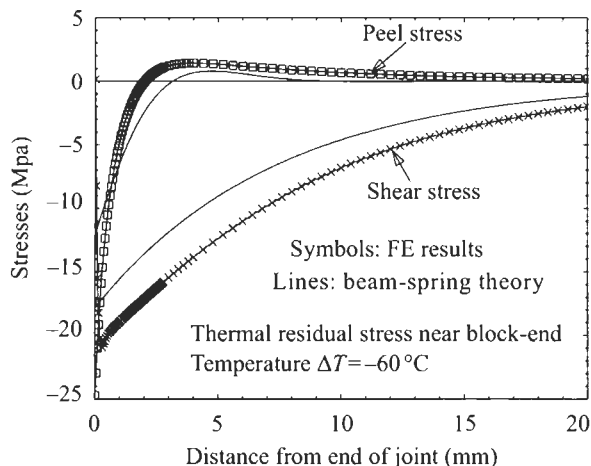


Fig. 5.12. Thermal residual stress in a SDS with block end subjected to a 60°C temperature drop.

However, the beam-spring solution considerably underestimates the magnitude of the peel stress. The reason for this discrepancy is not clear. Further study is required to develop an improved solution for the residual peel stress.

5.3.1.2. Tapered end

In practice, to enhance the fatigue resistance, patches are normally tapered at the ends so as to reduce the maximum adhesive shear and peel stresses, as illustrated in Figure 5.9(b) and Figure 5.9(c). To examine the effect of tapering on the adhesive stresses, a detailed FE analysis of the type II joint was carried out for both mechanical load and thermal load. The properties of the orthotropic reinforcement, the adhesive, and the metallic plate are given in Table 5.2. The FE mesh is shown in Figure 5.13. The adhesive bondline thicknesses for these specimens were quite large

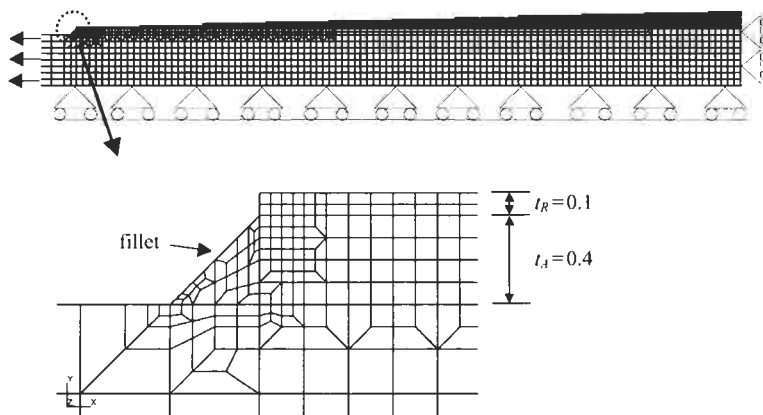


Fig. 5.13. FE mesh of half-model of type II SDS (see Fig. 5.9(b)).

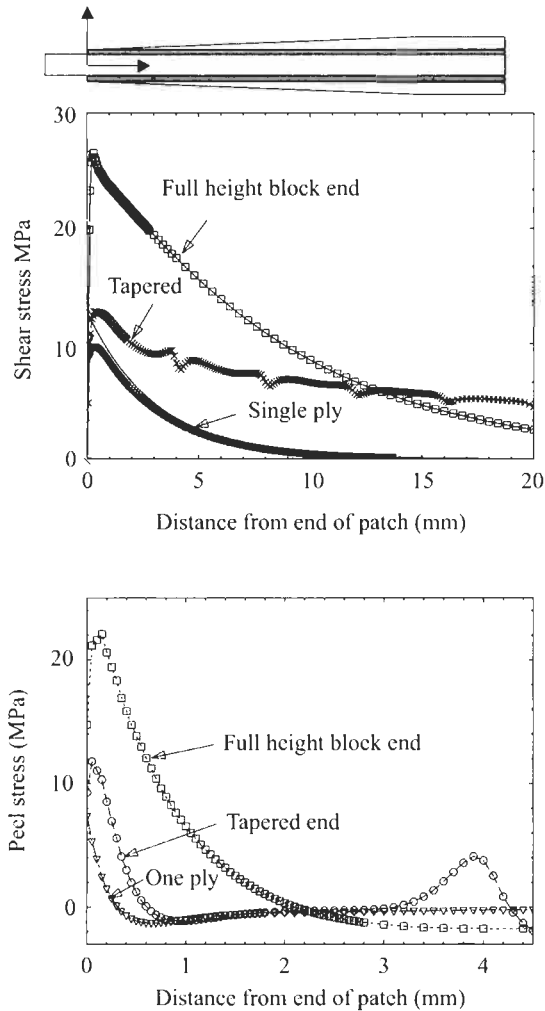


Fig. 5.14. Stress state in a tapered SDS; load/unit width = 1 kN/mm.

because effectively two layers of adhesive were present in each bondline: one co-cured with the patch and one used to secondarily bond the patch to the aluminium strips. Consequently the adhesive was thick enough for significant variations in stress to exist across the bondline width. To this end, the adhesive layer was modelled by at least four elements in the thickness direction.

Figure 5.14 shows the stresses along the mid-plane of the adhesive layer in a tapered repair (type II) subjected to an external loading, together with the estimated shear stress that would exist in a joint with a single-ply patch ($t = 0.1$ mm). The magnitude of the peak shear stress seems to be well approximated, but not the transfer distance. The actual shear stress decays more slowly than that in a single-ply patch. Perhaps the more striking finding is that

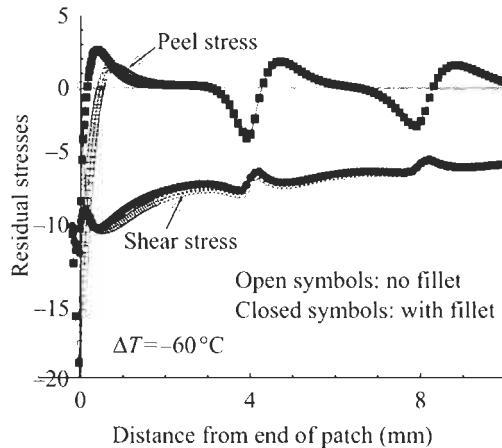


Fig. 5.15. Residual thermal stresses in a tapered SDS ($\Delta T = -60^\circ\text{C}$).

maximum peel stress is nearly equal to the maximum shear stress. Comparison with the results shown in Figure 5.11 suggest that tapering has reduced the maximum shear stress and the maximum peel stress by respectively 52% and 43%.

For a thermal loading of $\Delta T = -60^\circ\text{C}$, which corresponds to cooling the cured specimens from the curing temperature of 80°C down to the testing temperature of 20°C , the residual thermal stresses as determined using the FE method are shown in Figure 5.15. Comparison with the thermal residual stress for a block-end patch as shown in Figure 5.12 suggests that tapering the patch has reduced the maximum residual shear stress by 53%, similar to the reduction in the maximum shear stress induced by applied load. However, the maximum peel stress has been reduced only by 23%, much less than the reduction in the peel stress due to applied mechanical load.

Table 5.4 lists the results for the adhesive displacements at the joint ends for the four joint types shown in Figure 5.9. Note that the residual stresses due to thermal mismatch between the composite and metal inner adherends are negative. This is

Table 5.4
Maximum stresses for the four joints shown in Fig. 5.9.

		Joint type I ($t_A = 0.4\text{ mm}$)	Joint type II ($t_A = 0.4\text{ mm}$)	Joint type III ($t_A = 0.4\text{ mm}$)	Joint type IV ($t_A = 3.0\text{ mm}$)
Due to applied load (per kN/m)	Shear stress (MPa)	26.5	12.7	12.0	6.0
	Peel stress (MPa)	20.6	11.7	11.0	4.32
Residual stress (60°C drop from cure temp)	Shear stress (MPa)	-20.9	-9.8	-10.0	-2.57
	Peel stress (MPa)	-24.7	-19.0	-20.6	0.48

highly beneficial in offsetting the positive stresses caused by the external stresses. It is also clear that the square end joint, type (a), has the highest stresses for a given applied load and temperature change.

5.3.2. Experimental method and results

The SDS represents a section through the safe-life region of a bonded repair. Therefore the emphasis here is to obtain disbond initiation data. The technique used to determine disbond initiation load was adopted from reference [16]. Essentially it involves bonding strain gauges to the very tips of the boron/epoxy patches and monitoring strain response as a function of time as cyclic loads are applied. Disbond initiation was defined to have occurred when the amplitude of the output of one of the strain gauges dropped by 10% (see Figure 5.16). Constant amplitude loading at 3 Hertz was applied at various load ratios (ratio of maximum to minimum load). An initiation level was recorded for each load ratio. The sequence of events, starting from the small value of applied load amplitude, was

1. Select load ratio.
2. Apply 50 000 cycles at a certain load amplitude and monitor strain gauge measurement every 100 cycles.
3. If one of the strain gauge amplitudes does not drop by more than 10% then increase amplitude of cyclic load and go to step 2, otherwise go to step 4.
4. Crack initiation has occurred. Terminate test.

Figure 5.16 shows some typical strain gauge outputs for the cyclic strain response to various cyclic loads for one of the strain gauges. The initiation load for this specimen was 24.2 kN using the definition above. Since the strain gauge was installed very close to the end of patch, as illustrated in Figure 5.17, the drop in the strain gauge reading is nearly proportional to the disbond length. Therefore a 10%

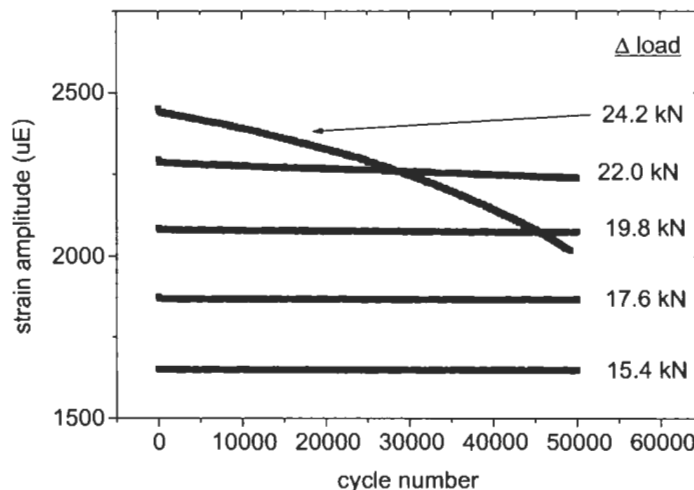


Fig. 5.16. Strain amplitude versus cycle number (dry, load ratio = -0.1) for a type II specimen.

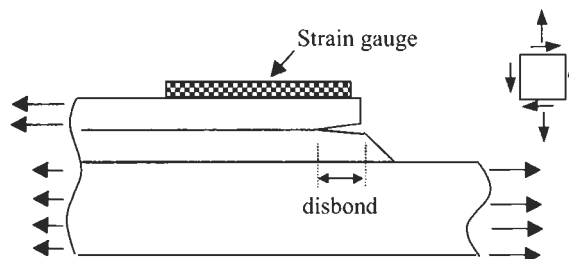


Fig. 5.17. Strain-gauge technique to detect disbond growth, showing sign conventions for positive stresses.

drop in the measured strain implies that the length of disbond would be equal to approximately 0.3 mm, considering that the strain gauge length is about 3 mm. Consequently, once disbond has been detected, the average disbond growth rate would be at least 6×10^{-9} m/cycle. This growth rate is about an order of magnitude higher than the growth rate used to define the conventional fatigue threshold.

A series of fatigue tests were conducted using type II specimens at various load ratios ranging from -0.4 to 0.4 . Using the results given in Table 5.4, the adhesive stresses are obtained by converting the applied load and the results are shown in Table 5.5, where the sign convention shown in Figure 5.17 is employed.

Table 5.5
Disbond initiation stresses for joint II.

Load ratio (min/max)	$\Delta\tau/2$ (MPa)	$\Delta\sigma/2$ (MPa)	Ignoring thermal residual stress		Considering thermal stress	
			σ_{mean} (MPa)	τ_{mean} (MPa)	σ_{mean} (MPa)	τ_{mean} (MPa)
-0.4	9.76	9.03	3.88	4.18	-16.12	5.62
-0.2	8.74	8.10	5.41	5.83	-14.59	3.97
-0.2	8.74	8.10	5.41	5.83	-14.59	3.97
-0.1	8.36	7.74	6.35	6.85	-13.65	2.95
-0.1	7.67	7.10	5.82	6.27	-14.18	3.53
0	7.60	7.04	7.05	7.61	-12.95	2.19
0	7.29	6.75	6.76	7.29	-13.24	2.51
0	7.29	6.75	6.76	7.29	-13.24	2.51
0	8.24	7.63	7.64	8.24	-12.36	1.56
0.1	7.41	6.86	8.40	9.06	-11.60	0.74
0.1	6.40	5.93	7.28	7.86	-12.72	1.94
0.2	6.14	5.69	8.40	9.06	-11.60	0.74
0.2	6.14	5.69	8.40	9.06	-11.60	0.74
0.33	5.20	4.81	9.28	10.01	-10.72	-0.21
0.33	5.52	5.11	10.16	10.95	-9.84	-1.15
0.4	4.94	4.58	10.70	11.54	-9.30	-1.74
0.4	4.56	4.22	9.87	10.64	-10.13	-0.84

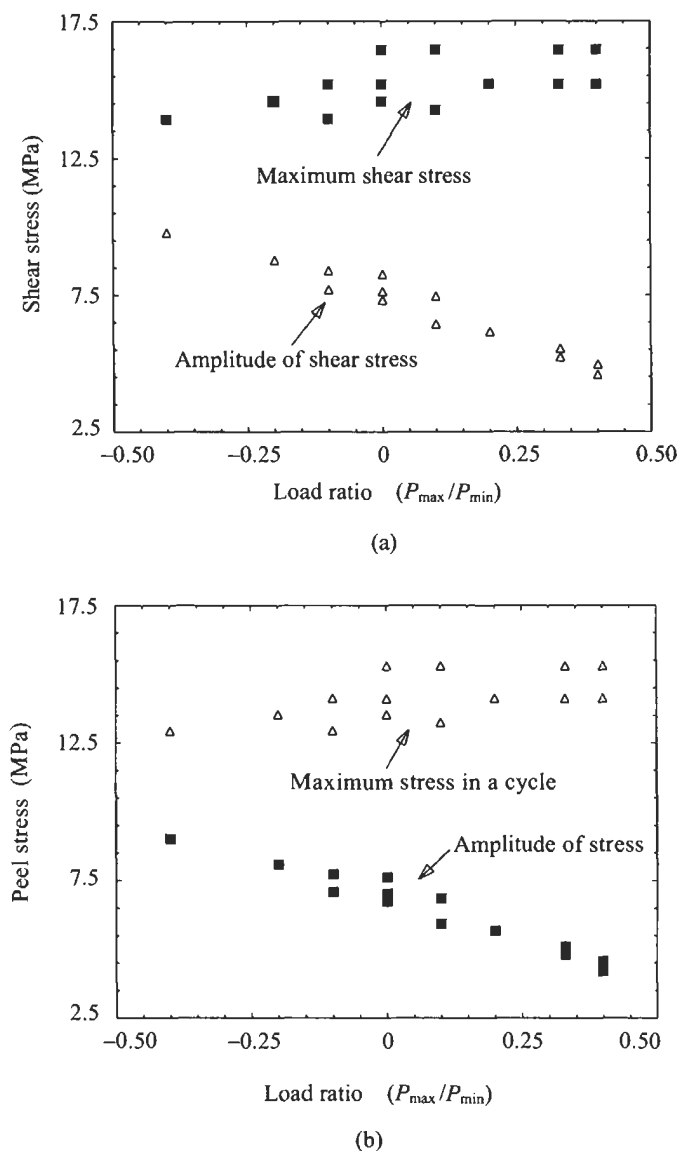


Fig. 5.18. Influence of applied load ratio on (a) adhesive shear stresses and (b) peel stresses at initiation for joint type II, ignoring thermal residual stresses.

It can be seen in Table 5.5 that the amplitudes of both the shear stress and the peel stress decrease rapidly with the increase in the applied load ratio, whereas the maximum stresses increase slightly with the increase of load ratio. This is best illustrated in Figure 5.18. Since the maximum residual peel stress is approximately -20 MPa for these specimens, inclusion of the thermal residual stress would result

Table 5.6

Initiation loads for the four joint types tested at a load ratio of zero.

	Joint type (a)	Joint type (b)	Joint type (c)	Joint type (d)
Initiation load (kN)	22.5	24	26	23

Table 5.7

Initiation loads converted to stresses considering thermal stresses.

	Joint I $t_A = 0.4 \text{ mm}$	Joint II $t_A = 0.4 \text{ mm}$	Joint III $t_A = 0.4 \text{ mm}$	Joint IV $t_A = 3.0 \text{ mm}$
Initiation load (kN)	22.5	24	26	23
Range of shear stress (MPa)	29.83	15.24	15.6	6.9
Range of peel stress (MPa)	23.18	14.04	14.30	4.97
Maximum shear stress (MPa)	8.93	5.44	5.6	9.47
Maximum peel stress (MPa)	-1.52	-4.96	-6.3	4.49

in the maximum peel stress in a cycle being compressive. This suggests that crack surface contact would occur throughout a loading cycle, rendering the peel stress largely ineffective. In this case, the disbond would be driven mainly by the cyclic shear stress. According to the crack-growth rate results shown in Figure 5.6(b) for the 80 °C cure adhesive, the disbond growth rate corresponding to an applied shear stress range of 15 MPa ($R=0$) is expected to be approximately 7.2×10^{-14} m/cycle, which is significantly lower than the detection limit (6×10^{-9} m/cycle) of the technique employed in this study.

The other three joint types, I, III and IV, were tested at a load ratio of zero only. The average initiation loads for the four joints are shown in Table 5.6. The locus of disbond initiation and subsequent propagation in joint I was within the ply of boron/epoxy adjacent to the adhesive bondline, as with the DOFS. For joints II, III, and IV, the locus of the disbond tended to be mixed: some failure within the ply of boron/epoxy adjacent to the adhesive bondline and some failure at the aluminium to adhesive interface. The loads shown in Table 5.6 are converted to stresses in Table 5.7 using the results given in Table 5.4.

It is rather surprising that the initiation loads of tapered joints (type II and III) are only slightly higher than for the untapered joint, contrary to the expectation of stress-based fatigue criteria, e.g. the maximum adhesive stresses at fatigue initiation would be a material constant. The large differences in the failure stresses indicate that the adhesive stress is not a suitable correlating parameter.

5.3.3. Fracture mechanics approach

The experimental results shown in Table 5.7 clearly suggest that the maximum stresses in the adhesive layer (either the peel stress or the shear stress) do not provide an adequate fatigue failure criterion. In particular, joint IV, which has a

Table 5.8
Initiation loads for the four joint types tested at a load ratio of zero.

	Joint I	Joint II	Joint III	Joint IV
Initiation load (kN)	22.5	24	26	23
Strain energy release rate ΔG_I (J/m ²)	37.3	18.25	18.9	17.2
Strain energy release rate ΔG_{II} (J/m ²)	222	58	60.8	89.3

much thicker adhesive layer, failed at even lower load than joints II and III with thinner bond-lines. Such a large discrepancy in the stresses to initiate disbond indicated that a fracture mechanics approach would offer a better criterion. As discussed in Section 5.2.3, the range of the strain-energy release rate ΔG due to the adhesive shear stress and peel stress are given by:

$$\Delta G_I = \frac{(\Delta \sigma_{\max})^2}{2E_A} t_A, \quad (5.15a)$$

$$\Delta G_{II} = \frac{(\Delta \tau_{\max})^2}{2G_A} t_A \quad (5.15b)$$

The results are summarised in Table 5.8, which indicates that the critical value of the Mode I strain-energy release ΔG_I seems to remain a constant for joints II, III, and IV.

Further experimental and theoretical investigations are still needed to ascertain whether the strain-energy release rate is an adequate fatigue failure criterion. In addition, the effects of load ratios, thermal residual stresses, patch tapering, and environment need to be quantified in order to develop a predictive tool for assessing the durability of bonded repairs and joints.

5.4. Discussion

If it is accepted (a) that the generic joints approach for generating basic materials allowables on fatigue resistance of the patch system is reasonable and (b) that the DOFS and SDS are appropriate specimens, then the most that can be said is that a useful start on obtaining allowables data has been made.

The first requirement is to validate fatigue-damage criteria (FDC). Some of the requirements for a suitable FDC are given in Table 5.4 where they are compared with the use of ΔK effective as an FDC for fatigue crack growth in metals.

For the DOFS the strain-range criterion is suitable for use in patch-system design, but needs much further validation. The issue of the relevance of this damage parameter to the actual interface failure mode in composites needs to be resolved. To add further to the complications, failure modes are quite likely to change to cohesive in the adhesive at elevated temperature and particularly in hot/wet conditions.

Table 5.9

Requirement of fatigue-damage criteria (FDC).

Requirements for FDC Bonded Joint/Generic Repair	E.g. ΔK_{eff} for Metal s
• FDC functionally relatable to disbond damage initiation and growth	✓ only for growth
• Invariant with geometrical parameters, such as adhesive thickness and joint geometry	✓
• Relevant also for disbond locus changes in adhesive or resin matrix	✓
– may need different FDC for totally different failure modes, e.g. peel or shear [DOFS and SDS]	
• Readily calculated from external and internal (thermal) loading	✓
• Easily measured materials parameters for initiation or db/dN as $f(FDC)$ for each failure mode	✓
• Readily incorporated into design codes	✓

For the SDS insufficient work has been done to establish any suitable FDC. There are some fundamental and contradictory issues to be resolved in relation to residual stresses and negative peel stress before this can be done. Tests on all metal specimens to separate out the issue of residual stress would seem to be required.

If FDC can be verified to be suitable for design purposes then the database on materials allowables can be generated. There is a need to obtain the basic allowables and then develop knockdown factors. Knockdown factors are factors applied to the allowables to allow for the degrading influences of, for example:

- Temperature and especially hot/wet conditions
- Environmental fluids, other than water, e.g. fuel and hydraulic oil
- Voids
- Undercure
- Spectrum loading
- Differences between the generic repair situation and the actual stressing situation

References

1. Baker, A.A. (1997). On the certification of bonded composite repairs to primary aircraft structures. *Proceedings of Eleventh International Conference on Composite Materials (ICCM-11)*, Gold Coast Australia.
2. Chalkley, P.D. and Baker, A.A. (1999). Development of a generic repair joint for certification of bonded repairs. *Int. J. of Adhesion and Adhesives*, **19**, pp. 121–132.
3. Hart-Smith, L.J. (1973). Adhesive-bonded double-lap joints. NASA CR 112235. Langley Research Centre, Hampton, Virginia, 23366, USA.
4. Hart-Smith, L.J. (1982). Induced peel stresses in adhesively-bonded joints, *MDC J9422A*, Douglas Aircraft Company.
5. Wang, C.H. and Rose, L.R.F. (1997). Determination of triaxial stresses in bonded joints. *Int. J. Adhesion and Adhesives*, **17**, pp. 17–25.
6. Wang, C.H. and Chalkley, P. (2000). Plastic yielding of a film adhesive under multiaxial stresses. *Int. J. Adhesion and Adhesives*, **20**, pp. 155–164.

7. Baker, A.A. (1996). Fatigue studies related to certification of composite crack patching for primary metallic structure. *FAA-NASA Symposium on Continued Airworthiness of Aircraft Structures*, Atlanta, August, pp. 28–30.
8. Brussat, T.R., Chiu, S.T. and Mostovoy, S. (1978). Fracture mechanics for structural adhesive bonds, Phase II, final technical report. *AFML-TR-77-163*, Wright-Patterson AFB, Ohio, 45433, USA.
9. Lin, C. and Liechti, K.M. (1987). Similarity concepts in the fatigue fracture of adhesively bonded joints. *J. Adhesion*, **21**, pp. 1–24.
10. Russell, A.J. and Jonson, D. (1990). A damage tolerance assessment of bonded repairs to CF-18 composite components, Part II: joint design, Technical Memorandum 90–3, Defence Research Establishment Pacific Victoria, Canada.
11. Wassell, G.C., Clark, J.D., Crompton, J.S., *et al.* (1991). Fatigue within adhesive bonded. *Int. J. Adhesion and Adhesives*, **11**, pp. 117–120.
12. Wang, C.H. and Rose, L.R.F. (1997). Failure analysis of adhesively bonded joints. *Advances in Fracture Research*, **6**, Pergamon Press, pp. 3057–3064.
13. Mall, S. (1987). Stress ratio effect on cyclic debonding in adhesively bonded composite joints, *Composite Structures*, **8**, pp. 31–45.
14. Russell, A.J. (1988). Fatigue crack growth in adhesively bonded graphite/epoxy joints under shear loading. *ASME Symposium on Advances in Adhesively Bonded Joints*, Chicago, Nov. 28–Dec. 2.
15. Chai, H. and Chiang, M.Y.M. (1988). Finite element analysis of interfacial crack propagation based on local shear, part II-fracture. *Int. J. Solids Structures*, **35**, pp. 815–829.
16. Baker, A.A., *et al.* (1993). Reinforcement of the F-111 wing pivot fitting with a boron/epoxy doubler system – material engineering aspects. *Composites*, **24**(6), pp. 511–521.
17. Wang, C.H. and Rose, L.R.F. (2000). Compact solutions for the corner singularity in bonded lap joints. *Int. J. Adhesion and Adhesives*, **20**, pp. 145–154.

Chapter 6

EVALUATING ENVIRONMENTAL EFFECTS ON BONDED REPAIR SYSTEMS USING FRACTURE MECHANICS

Dr L.M. BUTKUS*

*Department of Engineering Mechanics, HQ USAFA/DFEM US Air Force Academy,
CO, USA, 80840-6240*

R.V. VALENTIN

Harris Corporation, Palm Bay, FL 32905

Dr W.S. JOHNSON

*Schools of Materials Science & Engineering and Mechanical Engineering, Georgia
Institute of Technology, Atlanta, GA, USA 30332-0245*

6.1. Introduction

As discussed in Chapter 5 effective design of repairs requires detailed analyses of the mechanics of bonded joints that may be viewed as representative models of those repairs. In addition, to ensure that designs using bonded assemblies have an acceptable lifespan, the interaction of bonded joints with their service environments is required.

Bonded joint mechanics were originally analyzed using stress-based approaches [1,2]. However, fracture mechanics has also been shown to be a viable analytical tool for bonded joint evaluation and is the method described in this chapter. Adapted for use on bonded joints by Ripling, *et al.* [3], Shaw [4], and others, fracture mechanics uses the strain energy release rate, G , to characterize fracture. Research by Mall, *et al.* [5] also found that, when subjected to fatigue loading, bonded joints exhibited crack growth rates that correlated well with applied strain energy release rate levels. Johnson, *et al.* [6–8] subsequently: (1) developed a fracture-mechanics-based design approach for bonded joints, (2) examined the Mode I, Mode II, and mixed mode monotonic toughness (G_I , G_{II} , and $G_{I/II}$) of

* Previously graduate students, School of Mechanical Engineering, Georgia Institute of Technology

select aerospace adhesives and composite matrix materials, and (3) proposed using the total strain energy release rate ($G_T = G_I + G_{II} + G_{III}$ [if present]) as a design criteria for bonded joints. Johnson and Butkus [9] in their investigations of bonded metal joints exposed to aerospace service environments further examined these design criteria.

The intent of this chapter is to describe additional work that employed fracture mechanics in assessing the environmental durability of representative repair joints. The system studied, boron-epoxy bonded to aluminum, represents bonded repairs of cracked metallic aircraft structures, and has been used principally by the air forces of Australia and the US [10,11]. Prior to mechanical testing, specimens of this bonded material system were exposed to temperature and humidity levels encountered during service.

For the research presented in this chapter, monotonic and fatigue tests were conducted on double cantilever beam specimens to examine Mode I fracture toughness and fatigue behavior. Environmental effects were found to be detrimental to the toughness and threshold crack growth of the representative Al/b-ep repair system.

Although it should be understood that bonded joints are subject to significant amounts of Mode II loading in service in addition to Mode I, their fatigue and fracture behavior identified in this limited study should be carefully considered in the design of adhesively bonded repairs and components.

6.2. Materials and specimens

The bonded boron-epoxy/aluminum aerospace repair system (Al-FM[®]73M-b/ep) and its specific operating environments was examined. Fabrication was performed by an airframe manufacturer using current surface preparation, production methods, materials, etc.

6.2.1. Bonded material system and fabrication

The Al-FM[®]73M-b/ep system representing bonded airframe structural repairs, consisted of a primarily unidirectional $[0_4/90/0_3/90/0]_s$, pre-cured boron-epoxy laminate bonded to a bare 7075-T651 aluminum adherend with a toughened aerospace epoxy (Cytec's FM[®]73M containing a non-woven polyester scrim cloth). The surface of the 9.5 mm (0.375 in.) thick aluminum plate was prepared for bonding using an FPL sodium dichromate etch and BR-127 primer. Individual specimens were cut from the adhesively bonded panels.

6.2.1.1. Specimen geometry

Double cantilever beam (DCB) specimens used for this research were nominally 25 mm (1 in.) wide and 305 mm (12 in.) long. Teflon[®] release film prevented bonding and created crack initiation sites at one end of each specimen. Loading was accomplished using hinges bonded to the end of each adherend.

Due to the dissimilar adherends and a mismatch of thermal expansion coefficients ($\alpha_{AL} = 22.1 \times 10^{-6}/^{\circ}\text{C}$ [$12.3 \times 10^{-6}/^{\circ}\text{F}$], $\alpha_{b/ep} = 4.5 \times 10^{-6}/^{\circ}\text{C}$ [$2.5 \times 10^{-6}/^{\circ}\text{F}$]), the specimens were distinctly curved.

6.3. Experimental procedures

Experiments were designed to compare the behavior of as-received specimens to that of exposed specimens. Table 6.1 illustrates the combinations of pre-test conditioning and testing environments that will be described in Sections 6.3.1 and 6.3.2.

6.3.1. Pre-test environmental conditioning

Prior to mechanical testing, selected specimens were subjected to either isothermal exposure or thermal cycling. Isothermal exposure was performed using an air-circulating oven and, if necessary, a humidity chamber inside the oven. Thermal cycling was performed using a device with hot and cold chambers between which specimens were automatically shuttled. No humidity control was possible with the thermal cycling unit. No load was applied to the specimens during exposure or cycling.

Exposure conditions were based upon service conditions for the material systems. "Hot/wet" conditions simulated tropical runway operations. "Hot/dry" conditions simulated high performance operations at mid- and low altitude. A low temperature of -54°C (-65°F) used in this research represented subsonic flight at high altitudes.

Selected specimens were exposed to one of the following three environments:

1. 100 thermal cycles between -54°C (-65°F) and 71°C (160°F) following 320 h of pre-conditioning at 71°C (160°F), $> 90\%$ relative humidity (rh) (Figure 6.1)
2. 5000 h exposure to 71°C (160°F), $> 90\%$ rh (hot/wet conditions)
3. 5000 h exposure to 71°C (160°F), $> 90\%$ rh (hot/wet conditions) followed by 5000 h exposure to a desiccating environment of 22°C (72°F), 10% rh (desiccation was performed to determine if hot/wet exposure effects could be reversed)

6.3.2. Testing procedures

Monotonic tests were conducted under laboratory conditions ($22 \pm 2^{\circ}\text{C}$ [$72 \pm 4^{\circ}\text{F}$], $50 \pm 5\%$ rh) or at temperatures representing low ($-54 \pm 2^{\circ}\text{C}$ [$-65 \pm 4^{\circ}\text{F}$]) and high ($71 \pm 2^{\circ}\text{C}$ [$160 \pm 4^{\circ}\text{F}$]) service temperature limits. These tests were conducted under displacement control with a speed of 1 mm/min. (0.04 in./min.). ASTM D3433-75 and ASTM D5228-94a were used as guidelines.

Table 6.1

Pre-test conditioning and test environments used for evaluating the Al-FM[®]73M-b/ep bonded system.

Test Conditions	Pre-test conditioning			
	As-received "A"	Thermal cycling "C"	Hot/wet exposure "E"	Hot/wet exposure + dessication "E+D"
	– No pre-test conditioning	– 320 h exposure to 71 °C (160 °F), > 90% rh followed by – 100 thermal cycles between –54 °C (–65 °F) and 71 °C (160 °F)	– 5000 h exposure to 71 °C (160 °F), > 90% rh	– 5000 h exposure to 71 °C (160 °F), > 90% rh followed by – 5000 h exposure to 22 °C (72 °F), < 10% rh
<i>Monotonic Fracture Toughness</i>				
– displacement control				
– 1 mm/min. (0.04 in./min.)				
Room Temperature 22 °C (72 °F)	✓	✓	✓	✓
Low Service Temperature –54 °C (–65 °F)	✓			
High Service Temperature 71 °C (160 °F)	✓			
<i>Fatigue</i>				
– 22 °C (72 °F)	✓	✓	✓	
– displacement control, 1 Hz				
– $R_\delta = \delta_{\min}/\delta_{\max}$, of 0.1				

(✓: tests conducted under indicated combination of pre-test conditioning and test environments).

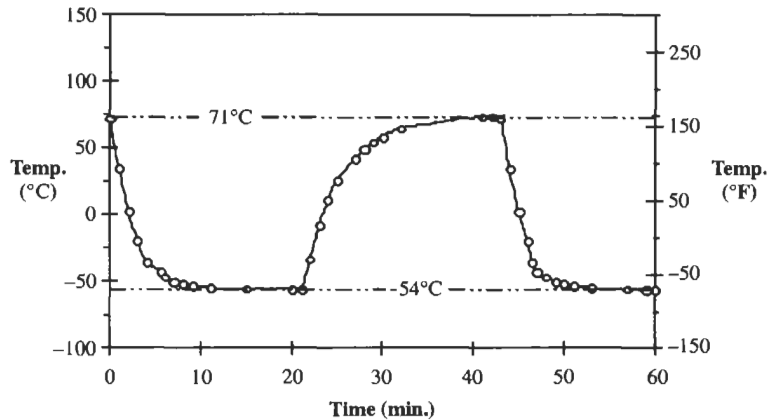


Fig. 6.1. Thermal cycling profile used for the Al-FM[®]73M-b/ep bonded system.

Crack growth was not catastrophic, so the long bond line permitted single specimens to be tested repeatedly and yield several toughness values.

Fatigue tests at laboratory conditions ($22 \pm 2^\circ\text{C}$, $50 \pm 5\%$ rh) and a frequency of 1 Hz were conducted under displacement control with a displacement ratio, $R_\delta = \delta_{\min}/\delta_{\max}$, of 0.1. This resulted in load shedding and facilitated identification of G levels at threshold growth rates of $da/dN = 10^{-6}$ mm/cycle (4×10^{-8} in./cycle), a rate based on previous work [8,12].

6.4. Analysis

Due to the Al-FM[®]73M-b/ep specimens' dissimilar adherends, residual thermal stresses produced pronounced curvature and a residual Mode II strain energy release rate (G_{II}) at the crack tip after curing. A closed-form solution could not determine G_I and G_{II} in this case, so finite element analysis was needed to understand mode mixity [13].

The ABAQUS finite element code was used to analyze a 2D model of the DCB specimen with 4927 nodes and 4658 elements. The adhesive was modeled with four rows of four-noded quadrilateral elements; the Al adherend was modeled with ten rows; and the b/ep adherend was modeled with one row per ply.

Although ABAQUS is capable of analyzing material non-linearity, it requires tensile stress-strain data. At the time this research was conducted, little was known about the tensile stress-strain behavior of the adhesives. Therefore, all materials were assumed to be linearly elastic. (More recent research [14] suggests that the adhesive's nonlinear behavior of the adhesive is important above $\sim 3\%$ tensile strain. Thus, future finite element analyses should account for this characteristic

behavior.) Plane-strain was assumed due to the large ratio of specimen width to bond line thickness.

The analysis used experimental loads and crack lengths with a reduced integration technique to provide crack tip nodal forces and displacements. The Mode I, Mode II, and total strain energy release rates were then computed using the modified crack closure technique [15].

6.5. Results and discussion

Testing revealed effects of the environment on the fracture and fatigue properties of the Al-FM[®]73M-b/ep system.

6.5.1. Fracture toughness

The specimens exhibited an average as-received fracture toughness (G_{TC}) of $\sim 815 \text{ J/m}^2$ ($4.7 \text{ in.} \cdot \text{lb./in.}^2$).

Fracture occurred in the boron-epoxy's matrix near the composite-adhesive interface (Figure 6.2). Little of the adhesive remained on the composite adherend following fracture. A few boron fibers were embedded in the FM[®]73M remaining on the aluminum adherend. The fracture paths of all specimens, regardless of pre-test conditioning or test temperature, exhibited these characteristics.

Figure 6.3 shows the effect of pre-test environmental conditioning on the fracture toughness of the system. Thermal cycling reduced the fracture toughness by $\sim 35\%$. Some of this loss may be attributed to the 320 h during which the specimens were exposed to hot/wet conditions prior to thermal cycling. However, the extent of this effect is unknown.

Hot/wet exposure for 5000 h resulted in a $\sim 50\%$ loss in toughness. Such exposure often decreases fracture toughness of bonded metals by attacking insufficiently prepared adherend surfaces and causing failure at the metal-adhesive interface.

However, the fracture surfaces of the hot/wet exposed specimens were similar to those of the as-received specimens suggesting that the hot/wet environment

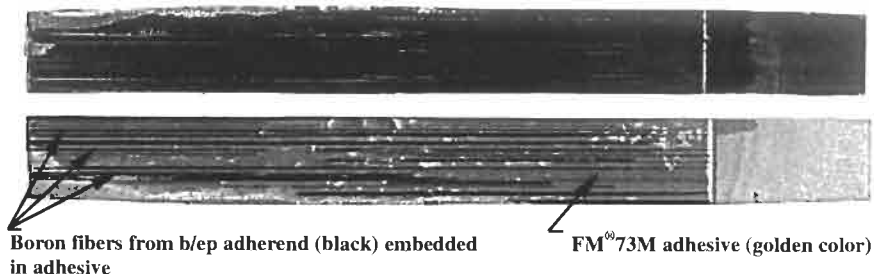


Fig. 6.2. Fracture surfaces of the Al-FM[®]73M-b/ep bonded system.

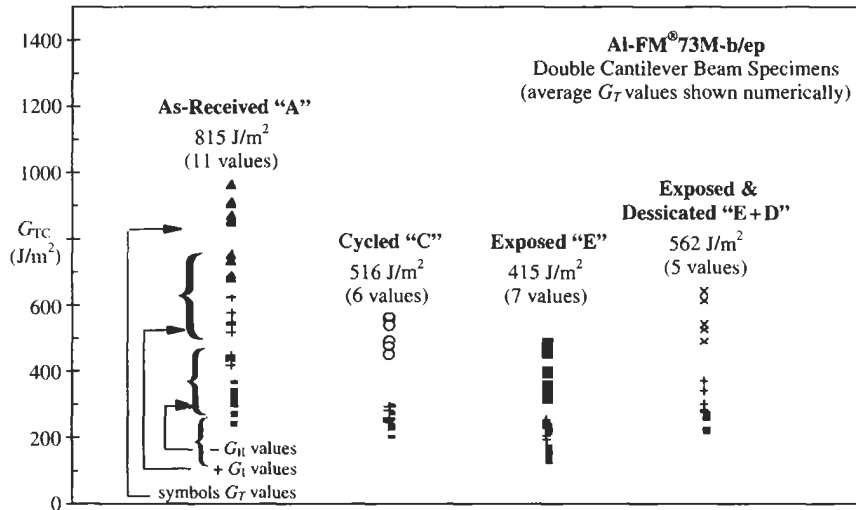


Fig. 6.3. Effect of environmental exposure on the fracture toughness of the Al-FM[®]73M-b/ep system.

adversely affected the adhesive and/or composite matrix rather than the metal-adhesive interface.

Following initial testing, one specimen used to determine the hot/wet exposure values was placed in a desiccator at room temperature for 5000 h. After desiccation, the toughness of this specimen recovered slightly but was still far below the as-received toughness.

Figure 6.4 shows the effect of test temperature on fracture toughness. The difference in adherend thermal expansion coefficients evidently magnified the

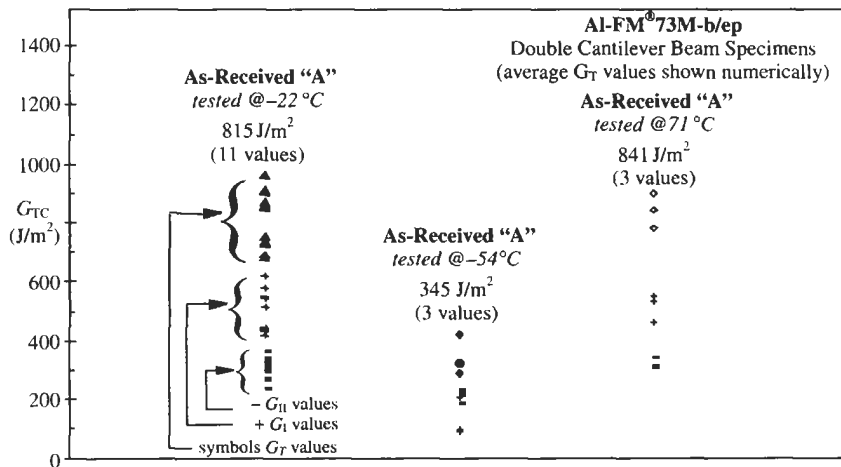


Fig. 6.4. Effect of test temperature on the fracture toughness of the Al-FM[®]73M-b/ep system.

thermally-induced strain energy release rate in the bond line at the lower test temperatures. This magnification, combined with a probable lower ductility of the adhesive at -54°C (-65°F), significantly reduced the fracture toughness.

6.5.2. Fatigue behavior

Fatigue test results are shown in Figure 6.5. Four characteristics of this data are significant.

First, the system exhibited an extremely high degree of crack growth rate sensitivity. If represented by a Paris Law relation of $da/dN = C(\Delta G_T)^n$ [16] the slope of the data (i.e. crack growth rate sensitivity) is equivalent to an exponent (n) on the order of 10. This is far above the growth rate sensitivity of metals which falls in the range of 2–3 [17].

Second, the threshold strain energy release rate range ($\Delta G_{T,th}$ at $da/dN = 10^{-6}$ mm/cycle [4×10^{-8} in./cycle]) is near 100 J/m^2 ($0.6 \text{ in.} \cdot \text{lb./in.}^2$), far below the fracture toughness, consistent with Johnson and Mall [6].

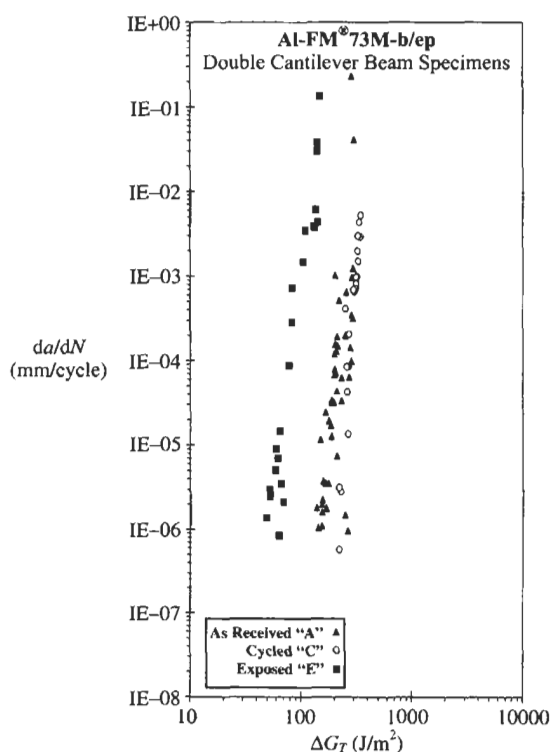


Fig. 6.5. Fatigue behavior of the Al-FM[®]73M-b/ep bonded system.

Third, hot/wet exposure reduced $\Delta G_{T,th}$, but didn't affect the crack growth rate sensitivity (n). Fourth, the fracture path in the fatigue specimens was identical to that in the fracture toughness specimens.

6.6. Summary and conclusions

Although this research was limited to investigating primarily Mode I fracture and fatigue behavior on a limited number of specimens, it highlighted potentially important trends concerning the relationship between service environments and bonded joint behavior.

As reported in this chapter, the primarily Mode I fracture and fatigue resistance of Al-FM[®]73M-b/ep can be detrimentally affected by environmental exposure. The fracture paths in this bonded system indicated that the environment appeared to have affected the adhesive and/or composite matrix materials to a greater extent than the adhesive-adherend interfaces. Additionally, the crack growth rate sensitivity of this bonded metal-composite system far exceeded that of metals. Though unaffected by long-term environmental exposure, this high sensitivity suggests that continued operation of bonded structures below the identified threshold is necessary to avoid unanticipated rapid Mode I crack growth.

The behavior of the Al-FM[®]73M-b/ep bonded aerospace material system identifies a need to carefully consider the service environment when specifying bonding for primary structures or for structural repairs. Safe and economic aerospace operations as well as modifications and protection of bonded material systems depend on an understanding of the interaction between bonded joint mechanics and operating conditions.

References

1. Goland, M. and Reissner, E.J. (1944). *J. Appl. Mech.*, **11**, pp. A17–A27.
2. Hart-Smith, L.J. and Thrall, E.W. (1985). In *Adhesive Bonding of Aluminum Alloys* (E.W. Thrall and R.W. Shannon, eds.), Marcel Dekker, New York, pp. 241–322.
3. Ripling, E.J., Mostovoy, S. and Patrick, R.L. (1963). In *Adhesion – STP 360*. Philadelphia: ASTM, pp. 5–19.
4. Shaw, S.J. (1993). In *Adhesion 7 – Proc. 20th Conf. on Adhesion and Adhesives* (K.W. Allen, ed.), Elsevier, London, pp. 173–196.
5. Mall, S., Johnson, W.S. and Everett, R.A., Jr. (1982). In *Adhesive Joints: Formation Characteristics and Testing* (K.L. Mittal ed.), Plenum, New York, pp. 639–656.
6. Johnson, W.S. and Mall, S. (1984). *Proceedings of the 5th Int'l. Congress on Experimental Mechanics Montreal: Society for Experimental Stress Analysis*, pp. 267–271.
7. Johnson, W.S. and Mall, S. (1985). In *Delamination and Debonding of Materials – STP 876* (W.S. Johnson, ed.), ASTM, Philadelphia, pp. 189–199.
8. Johnson, W.S. and Mangalgi, P.D. (1987). In *Toughened Composites STP 937* (N.J. Johnson, ed.), ASTM, Philadelphia, pp. 295–315.
9. Johnson, W.S. and Butkus, L.M. (1998). *Fat & Frac. of Engr'g. Matls. & Structs.*, **21**, pp. 465–478.
10. Belason, E.B. (1994). In *Composite Repair of Military Aircraft Structures*. AGARD, Seville, pp. 2/1–2/12.

11. Baker, A.A. (1994). In Composite Repair of Military Aircraft Structures. AGARD, Seville, pp. 1/1–1/14.
12. Marceau, J.A., McMillan, J.C. and Scardino, W.M. (1978). Adhesives Age, pp. 37–41.
13. Valentin, R.V., Butkus, L.M. and Johnson, W.S. (1998). *J. Comp. Tech. and Res.* **20**, pp. 108–119.
14. Butkus, L.M., Mathern, P.D. and Johnson, W.S. (1998). *J. Adhesion*, **66**, pp. 251–273.
15. Rybicki, E.F. and Kanninen, M.F. (1977). *Engr'g Frac. Mech.* **9**, pp. 931–938.
16. Roderick, G.L., Everett, R.A. and Crews, J.H. (1974). In Fatigue of Composites – STP 569. ASTM, Philadelphia, pp. 295–306.
17. Skinn, D.A., Gallagher, J.P., Berens, A.P., *et al.* (1994). Damage Tolerant Design Handbook. West Lafayette, Purdue Research Foundation.

Chapter 7

ANALYTICAL METHODS FOR DESIGNING COMPOSITE REPAIRS

L.R.F. ROSE and C.H. WANG

Defence Science and Technology Organisation, Air Vehicles Division, Fishermans Bend, Victoria 3207, Australia

7.1. Introduction

This chapter presents a comprehensive analysis of the mechanics of bonded repairs, with emphasis on explicit formulas and principles pertaining to the design and evaluation of repairs. Due to the multiple-layer structure of bonded repairs, which involve bonding orthotropic composite patches to cracked plates using polymeric adhesives, the stress states that exist in a bonded repair are very complex, as will be evident later in this chapter. Consequently this chapter focuses on presenting the results of recent research in such a convenient form as to be suited to the requirement of engineers and designers. Numerous references to the derivations of formulas and more detailed explanations are given, but for most part these are limited to sources that are generally available in the achieved journals and books.

The primary function of bonded repairs is to sufficiently reduce the stress-intensity factor of the crack being repaired so that (1) the residual strength has been restored to an acceptable level, and (2) the growth rate of the crack under fatigue condition is sufficiently slow to ensure an acceptable residual life, or inspection interval. Therefore the stress-intensity factor of a repaired crack will feature prominently throughout this chapter. To focus on the fundamental theoretical aspects of the mechanics of bonded repairs, we shall consider a relatively simple repair configuration, namely a centre-cracked plate being repaired by an elliptical patch, as illustrated in Figure 7.1. Since a bonded repair may fail in a number of modes, such as failure of the adhesive layer, failure of the plate near the termination of the patch, and failure of the patch, analytical formulas will be derived for the following quantities which are the primary interest in assessing the efficiency and the viability of the repair:

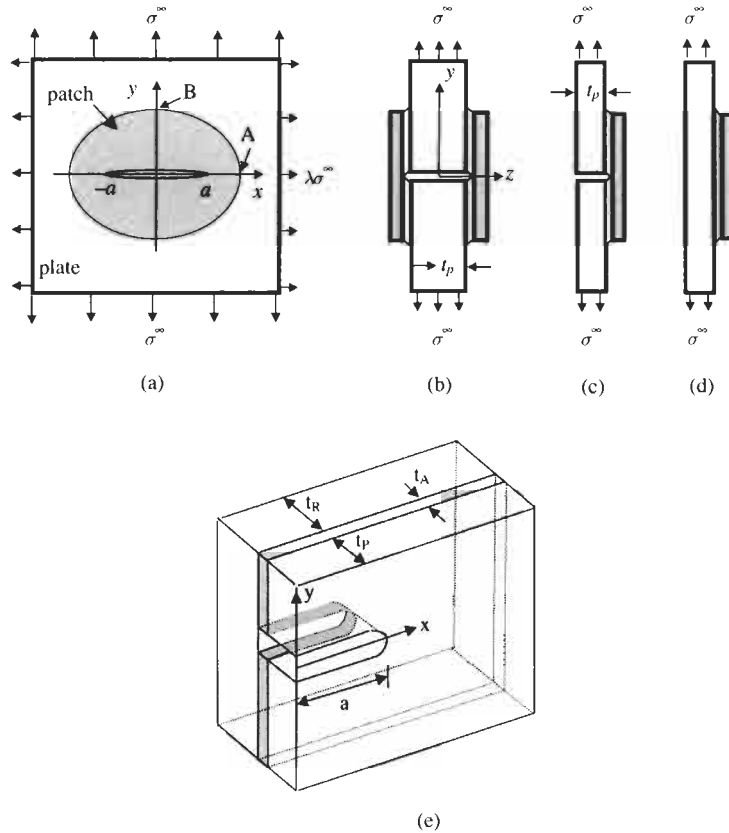


Fig. 7.1. Repair configurations and coordinates. (a) Plan view, (b) cross section along centre line ($x=0$) with no bending deflection allowed, representing two-sided repair, (c) cross section of a one-sided repair along the centre line, (d) cross section at $x \rightarrow \infty$ for one-sided repair, and (e) near crack region.

1. the *stress-intensity factor* K_r (defined below) in the repaired plate,
2. the *maximum stresses* in the adhesive, $\sigma_{\max}^A, \tau_{\max}^A$
3. the *maximum tensile stress* in the reinforcing patch, σ_{\max}^R
4. the *maximum tensile stress* in the plate near the outer boundary of the patch, σ_{\max}^P .
5. thermal residual stresses resulting from curing, σ_0^T .

The plan of this chapter is as follows. The basic problem which will be considered is formulated in Section 7.2, while Section 7.3 summaries some results of the theory of bonded joints which will be required in the sequel. An analysis of the symmetric repair, which is supported against out-of-plane deflection, is presented in Section 7.4, while Section 7.6 presents the solutions pertaining to an unsupported, one-sided repairs. The problem of residual thermal stress, which can be important in practice (see Chapter 11), is dealt with in Section 7.7.

7.2. Formulation and notation

Referring to Figure 7.1, the problem to be considered is a cracked plate with a patch adhesively bonded on one side. The plate, which has a thickness of t_P , contains a through-thickness crack of length $2a$. The thickness of the patch and the adhesive layer are respectively t_R and t_A . The cross sections in the yz and xz planes are depicted in Figure 7.1(b) and (c). The Young's modulus and the Poisson's ratio of each individual layer are denoted as E and ν ; here and in the following subscripts P , R , and A will be used to distinguish properties pertaining respectively to the plate, the reinforcement and the adhesive layer. In addition, the shear modulus of the adhesive will be denoted as μ_A . The crack is along the line segment $|a| \leq a, y = 0$, and patch is over an elliptical region defined by,

$$\left(\frac{x}{A}\right)^2 + \left(\frac{y}{B}\right)^2 \leq 1, \quad (7.1)$$

which completely covers the crack ($A > a$). After this repair, the plate is subjected to a remote stress specified by,

$$\sigma_{yy}^P = \sigma^\infty, \quad \sigma_{xx}^P = \lambda \sigma^\infty, \quad \tau_{xy}^P = \tau^\infty, \quad (x^2 + y^2 \rightarrow \infty) \quad (7.2)$$

By using the superposition principle it is easy to demonstrate that the above problem can be decomposed into a tensile mode ($\tau^\infty = 0$) and a shear mode ($\sigma^\infty = 0$). In this chapter we will focus on the tensile mode, while the shear mode [14] will be briefly discussed in Section 7.5.

From a geometrical consideration, bonded repairs as illustrated in Figure 7.2 fall into two categories: two-sided (symmetric) and one-sided (asymmetric). In the former case two identical reinforcements are bonded on the two surfaces of a cracked plate. This symmetric arrangement ensures that there is no out-of-plane deflection over the repaired region, see Figure 7.1(b), provided the cracked plate is subjected to extensional loads given by Eq. (7.2). In actual repairs, however, one-sided repair is often adopted in which composite patches are applied to only one side of the panel [12]. This is because most often, only one face of a structure to be repaired is accessible and sometimes only one side of a structure is allowed to be patched, e.g. aircraft fuselage or wing sections. Provided the structure to be repaired is well supported against out-of-plane deflection, for instance, by stiffeners attached to one side, it is acceptable to ignore the out-of-plane bending, thus permitting the problem to be treated as being symmetric. However, in the case of un-supported, one-sided repairs, the out-of-plane bending caused by the shift of the neutral plane away from that of the plate may considerably lower the repair efficiency.

By using the superposition principle it is easy to demonstrate that the problem depicted in Figure 7.1 is equivalent to solving the following perturbation problem: a patched crack subjected to an internal pressure, $-\sigma_0$, acting on the crack faces, as depicted in Figure 7.3. This allows the analysis to be divided into two stages [9]. First we consider the re-distribution of stress which would be caused by the

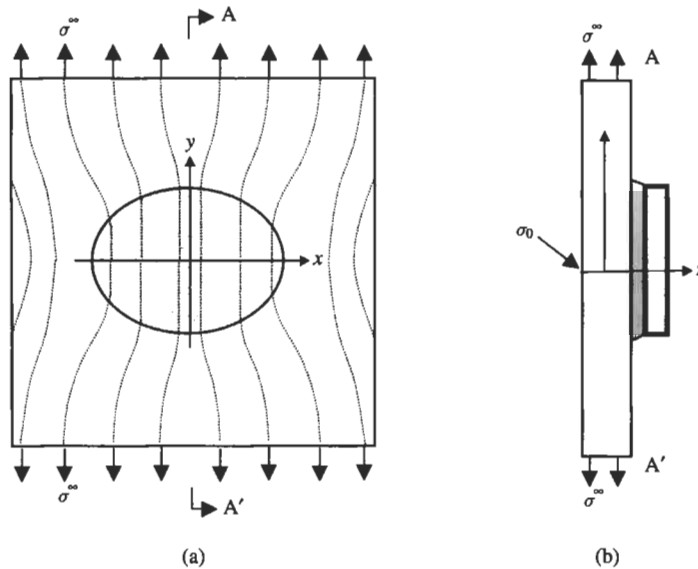


Fig. 7.2. Inclusion analogy for stage I analysis. (a) Flow of load lines into reinforced portions; (b) Cross-section along centre line.

reinforcement if it were bonded to an *un-cracked plate*, see Figure 7.2. The quantity of interest is the normal stress σ_0 along the prospective crack path in the uncracked plate. For the case of symmetric repairs (no out-of-plane bending), this *prospective* stress σ_0 is uniform through the plate thickness, whereas in the case of unsupported one-sided repairs, the prospective stress distributes linearly through the plate thickness [12], as illustrated in Figure 7.3(b) and (c). At the second stage, we determine the stress distribution around the crack subjected to an internal pressure of $-\sigma_0$. Due to the presence of the crack, a stress singularity exists at the two crack tips at $x = \pm a$. Here the stress-intensity factor K_r at the crack tip $x = a$ is defined as,

$$K_r(z) = \lim_{x \rightarrow a+} \sqrt{2\pi(x-a)} \sigma_{yy}^P(x, y=0, z), \quad (7.3)$$

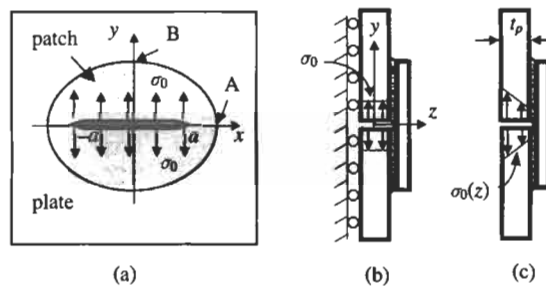


Fig. 7.3. A patched crack subjected to internal pressure.

where the stress $\sigma_{yy}^P(x, y = 0, z)$ is yet to be determined in terms of the internal stress σ_0 and the repair dimensions and constituent properties. Depending whether the repair is supported against out-of-plane bending, the stress-intensity factor may vary through the plate thickness; details will be presented in Section 7.6.

In the absence of a reinforcing patch, the normal stress σ_{xx}^P parallel to the crack would not affect the stress intensity factor, but this is no longer true for the repaired plate. After the repair, K_r will depend on the applied stress ratio λ defined by Eq. (7.2) and also on the aspect ratio B/A of the reinforcement. Provided the adhesive layer remains elastic, the main unknowns K_r , σ_{\max}^A , τ_{\max}^A , σ_{\max}^R , and σ_{\max}^P will depend linearly on the principal applied stress σ^∞ of Eq. (7.2). The analytical results which will be derived in Sections 7.4, 7.5, and 7.6 will show clearly the parametric dependence of these unknowns on the dimensions and material properties of a repair configuration.

Since a bonded repair represents a multiple layered structure with a crack being present in one layer only, an exact, analytical solution of this 3D problem is an almost intractable task. Hence it is imperative to make appropriate simplifications to enable the derivation of analytical solutions that can capture the essential features of repairs. It should be noted that there is no fundamental difficulty in employing a fully 3D finite element method to estimate the stresses and stress-intensity factors in a patched structure. It is, however, often impractical nor necessary to rely solely on time-consuming finite element computations for routine engineering designs, especially if parametric analysis is required to optimise a design and to study the sensitivities of repairs to varying geometry dimensions and material properties. In this regard, analytical solutions would be preferred over numerical solutions because the analytical solutions enable efficient optimisation of designs.

7.3. Load transfer of bonded reinforcement

To facilitate the following analysis, let us now consider first the simple reinforcement configuration shown in cross-section in Figure 7.4(a), in which a reinforcing strip of length $2B$ and thickness t_R bonded to an infinite strip of thickness t_P ; both strips are under *plane strain* conditions ($\epsilon_x = 0$). The choice of axes is designed to correspond with that used for the repair configuration in Figure 7.1.

The stresses and displacements in this reinforced strip can be calculated explicitly using the conventional 1D theory of bonded joints (see, e.g. [4,5]), which is based on the following assumptions.

- i. Each adherend is treated as an elastic continuum whose deformation under *plane strain* conditions is specified by longitudinal displacement u and a longitudinal tensile stress σ , see Figure 7.4(b). The problem of bending deformation will be considered later. The out-of-plane deformation, the stress-

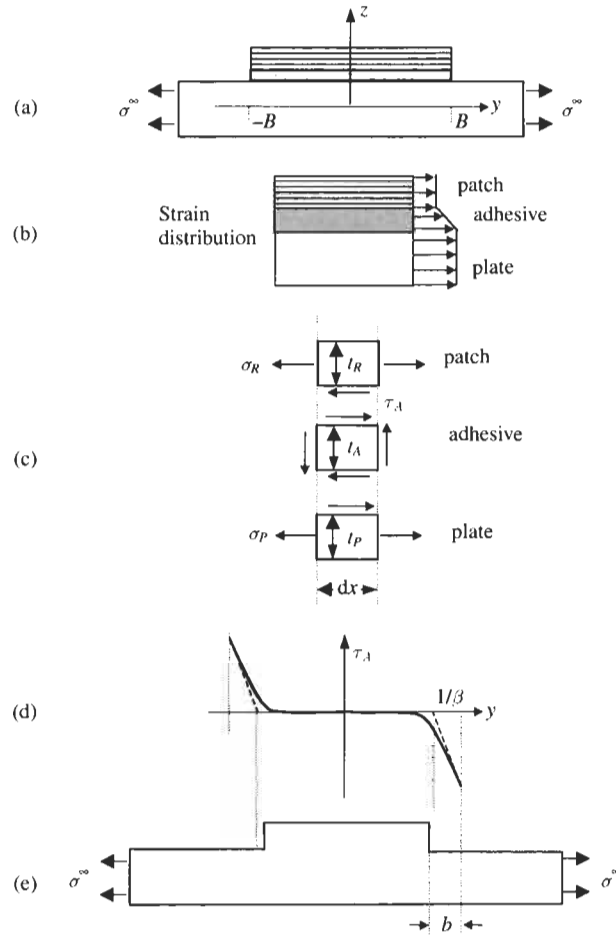


Fig. 7.4. Load transfer length for loaded reinforcement: (a) cross-section for bonded strips; (b) adhesive shear stress distribution; (c) equivalent rigid bond configuration.

displacement relations for the plate and the reinforcement respectively are

$$\sigma_P = \frac{E_P}{1 - \nu_P^2} \epsilon_P \equiv \frac{E_P}{1 - \nu_P^2} \frac{du_P}{dy}, \quad \sigma_R = \frac{E_R}{1 - \nu_R^2} \epsilon_R \equiv \frac{E_R}{1 - \nu_R^2} \frac{du_R}{dy} \quad (7.4)$$

- ii. The adhesive layer acts as a shear spring with the adhesive shear stress τ_A given by, referring to Figure 7.4(c)

$$\tau_A = \mu_A \gamma_A \equiv \mu_A \frac{u_R - u_P}{t_A} \quad (7.5)$$

- iii. The shear tractions exerted by the adhesive on the plate and the reinforcement can be replaced by an equivalent body force of X_P and X_R , respectively, i.e.

$$X_P = \frac{\tau_A}{t_P}, \quad X_R = -\frac{\tau_A}{t_R} \quad (7.6)$$

In the present case, the equilibrium equations for the plate and the reinforcement reduce to,

$$\frac{\partial \sigma_P}{\partial x} + X_P = 0, \quad \frac{\partial \sigma_R}{\partial x} + X_R = 0, \quad (7.7)$$

which lead to

$$\frac{d^2 u_R}{dx^2} - \frac{d^2 u_P}{dx^2} = \tau_A \left[\frac{1 - \nu_P^2}{E_P t_P} + \frac{1 - \nu_R^2}{E_R t_R} \right], \quad (7.8)$$

which can be rewritten as

$$\frac{d^2 \tau_A}{dx^2} - \beta^2 \tau_A = 0, \quad (7.9)$$

where

$$\beta^2 = \frac{\mu_A}{t_A} \left[\frac{1 - \nu_P^2}{E_P t_P} + \frac{1 - \nu_R^2}{E_R t_R} \right] \quad (7.10)$$

The general solution of the adhesive shear stress τ_A is given by

$$\tau_A = C_1 \sinh \beta y + C_2 \cosh \beta y, \quad (7.11)$$

where C_1 and C_2 are two integration constants yet to be determined from the boundary conditions. It should be pointed out that here the complexities of triaxial stress, stress singularity, and stress concentration in the adherends are considered in [13,15,20].

For the configuration of Figure 7.4(a) we require the adhesive shear stress τ_A to be odd in y , therefore $C_2 = 0$. The remaining constant C_1 can be readily determined from the following boundary conditions: $\sigma_P(y = \pm B) = \sigma^\infty$, $\sigma_R(y = \pm B) = 0$. Therefore,

$$\tau_A = -\sigma^\infty \frac{(1 - \nu_P^2)\mu_A}{\beta t_A E_P \cosh \beta B} \sinh \beta y \quad (7.12)$$

The important feature of this result is that for $\beta B \ll 1$, the adhesive shear stress decays exponentially from ends ($y = \pm B$) of the overlap, as sketched in Figure 7.4(d); i.e. the load transfer effectively occurs over a length of order β^{-1} at the ends of the overlap. To better elucidate this point, let us integrate Eq. (7.7) twice to derive the displacement $u_P(y)$, one can readily verify that the overall stiffness between the end points $y = \pm B$ of the reinforced strip in Figure 7.4(a) is the same as that of a strip

with a step change in stiffness from $E_P t_P / (1 - \nu_P^2)$ to $E_P t_P / (1 - \nu_P^2) + E_R t_R / (1 - \nu_R^2)$ over a central portion $|y| \leq B - b$, as indicated in Figure 7.4(e), with b given by

$$b = \frac{1}{\beta} \tanh \beta B \approx \frac{1}{\beta}, \quad (\beta B \ll 1) \quad (7.13)$$

This equivalence will be exploited in Section 7.4 to assess the redistribution of stress due to a bonded reinforcement.

The prospective stress in the plate directly underneath the reinforcing strip, $\sigma_0 = \sigma_P(x = 0)$, can be readily determined by integrating Eq. (7.4),

$$\sigma_0 = \frac{\sigma^\infty}{1 + S} \left[1 + \frac{S}{\cosh \beta B} \right] \approx \frac{\sigma^\infty}{1 + S}, \quad (\beta B \ll 1), \quad (7.14)$$

with S denoting the stiffness ratio given below,

$$S = \frac{1 - \nu_P^2}{1 - \nu_R^2} \frac{E_R t_R}{E_P t_P}, \quad (7.15)$$

which is an important non-dimensional parameter characterising a repair. As will be shown in the following section the actual prospective stress σ_0 is somewhat higher than that given by Eq. (7.14). This under-estimation is primarily due to the ignorance of the “load attraction” effect in a 2D plate associated with reinforcing.

7.4. Symmetric repairs

We return to the solution of the problem formulated in Section 7.2, assuming that the repaired structure is supported against out-of-plane bending or the cracked plate is repaired with two patched bonded on the two sides. The analysis will be divided into two stages as indicated in Section 7.2.

7.4.1. Stage I: Inclusion analogy

Consider first the re-distribution of stress in an *uncracked plate* due to the local stiffening produced by the bonded reinforcement. As illustrated in Figure 7.2(a), the reinforced region will attract more load due to the increased stiffness, leading to a higher prospective stress than that given by Eq. (7.14). The 1D theory of bonded joints (Section 7.3) provides an estimate of the load-transfer length β^{-1} for load transfer from the plate to the reinforcement. If that transfer length is much less than the in-plane dimensions A, B of the reinforcement, we may view the reinforced region as an inclusion of higher stiffness than the surrounding plate, and proceed in the following three steps.

1. Determine the elastic constants of the equivalent inclusion in terms of those of the plate and the reinforcing patch.
2. Determine the stress in the equivalent inclusion.

3. Determine how the load which is transmitted through the inclusion is shared between the plate and the reinforcement, from which the prospective stress σ_0 can be calculated.

Step (2) is greatly facilitated by the known results of ellipsoidal inclusions [3]: the stress and strain within an ellipsoidal inclusion is uniform, as indicated schematically in Figure 7.2(a). The uniform stress state can be determined analytically with the help of imaginary cutting, straining and welding operations. The results are derived in [8] for the case where both the plate and the reinforcing patch are taken to be orthotropic, with their principal axes parallel to the $x - y$ axes. We shall not repeat here the intermediate details of the analysis but simply recall the results for the particular case where both the plate and the reinforcement are isotropic and have the same Poisson's ratio, $\nu_P = \nu_R = \nu$. The prospective stress in the plate along $y = 0$ within the reinforced region ($|x| \leq A$) is

$$\sigma_0 = \phi \sigma^\infty, \quad (7.16)$$

where

$$\phi = \frac{1}{Z} \left[4 + 2\frac{B}{A} + 2\frac{A}{B} + S \left(3 + \nu + 2\frac{B}{A} \right) + S\lambda \left(1 - \nu - 2\nu\frac{B}{A} \right) \right], \quad (7.17)$$

with

$$Z = 3(1 + S)^2 + 2(1 + S)(B/A + A/B + \nu S) + 1 - \nu^2 S^2 \quad (7.18)$$

It is clear that the stress-reduction factor ϕ depends on three non-dimensional parameters: (i) the stiffness ratio S , (ii) the aspect ratio B/A , (iii) the applied stress biaxiality λ . The parameters characterising the adhesive layer do not affect σ_0 , but we recall that the idealisation used to derive Eq. (7.17) relies on $\beta^{-1} \ll A, B$, and β^{-1} is of course dependent on adhesive parameters.

To illustrate the important features of Eq. (7.17), we show in Figure 7.5(a) the variation of the stress-reduction factor ϕ with aspect ratio for two loading configurations: (i) uniaxial tension ($\lambda = 0$), and (ii) equal biaxial tension corresponding to pure shear ($\lambda = -1$), setting $S = 1$ and $\nu = 1/3$ for both cases. It can be seen that there is little variation for aspect ratio ranging from $B/A = 0$ (horizontal strip) to $B/A = 1$ (circular patch), so that for preliminary design calculations, one can conveniently assume the patch to be circular, to reduce the number of independent parameters. It is also noted from Eq. (7.17) that for $\nu = 1/3$ and a circular patch ($A/B = 1$), the stress-reduction factor ϕ becomes independent of the biaxiality ratio λ . As illustrated in Figure 7.5(a) the curves for $\lambda = 0$ and $\lambda = -1$ cross over for $B/A = 1$, indicating that, for a circular patch, the transverse stress σ_{xx}^∞ does not contribute to the prospective stress, so that this parameter can also be ignored in preliminary design estimates. In this particular case, the stress-reduction factor ϕ depends on the stiffness ratio S only, as depicted in Figure 7.5(b), together with the first-order approximation given by Eq. (7.14). It can be seen that the first-order solution ignoring the load attraction effect of composite

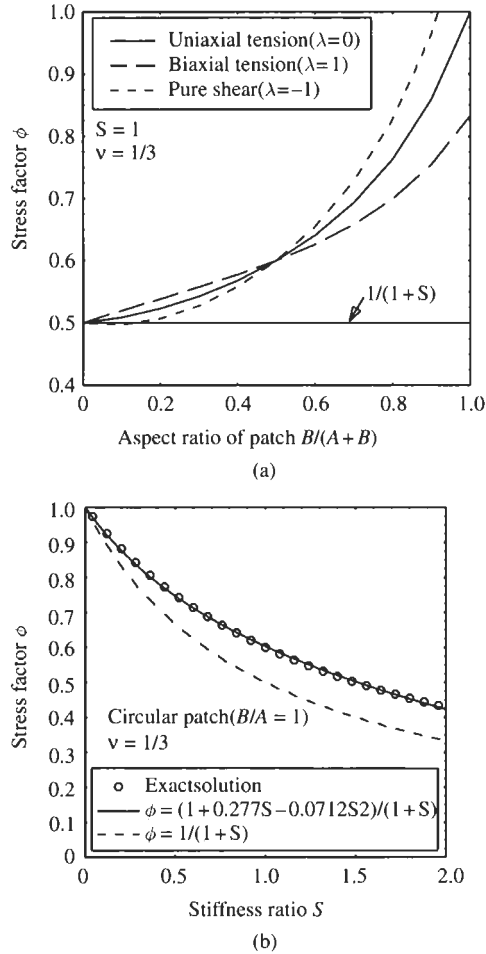


Fig. 7.5. Variation of reduced stress with (a) aspect ratio for an elliptical patch of semi-axes A and B under uniaxial tension and biaxial tension equivalent to pure shear; (b) stiffness ratio S for a circular patch.

patch overestimates the reduction in plate stress. An improved solution can be obtained by constructing an interpolating function based on the exact solution,

$$\phi = \frac{1 + 0.277S - 0.0712S^2}{1 + S}, \quad \left(\frac{B}{A} = 1, \nu = \frac{1}{3} \right), \quad (7.19)$$

which is shown by solid curve in Figure 7.5(b), indicating a very good fit to the exact solution.

The inclusion analogy also gives, as a natural by-product, the stress in the plate outside the reinforced region. The stress at the point $x = 0, y = B+$ is of particular interest, because this stress represents the increased stress due to the so-called load

attraction effect; a load attraction factor Ω_L can be defined as the ratio of the plate stress just outside the patch to the remote applied stress

$$\Omega_L = \frac{\sigma_{yy}^P(0, B+)}{\sigma^\infty} = (1 + S)\phi \quad (7.20)$$

It is clear from Figure 7.5(a) that for the case of a balanced patch ($S = 1$) under uniaxial tension, this load attraction factor ranges between 1 for patch of infinite width to 2 for patch of zero width. For the typical case of circular patch, the load attraction factor is approximately 1.2.

7.4.2. Stage II: Stress intensity factor

Once the stress at the prospective crack location is known, one can proceed to the second stage of the analysis in which the plate is cut along the line segment ($|x| \leq a, y = 0$), and a pressure equal to σ_0 is applied internally to the faces of this cut to make these faces stress-free. Provided that the load transfer to the reinforcement during this second stage takes place in the immediate neighbourhood of the crack, the reinforcement may be assumed to be of infinite extent. Thus the problem at this stage is to determine the stress intensity factor K_r for the configuration shown in Figure 7.3(a).

Without the reinforcement, the stress-intensity factor would have the value K_0 given by the well-known formula,

$$K_0 = \sigma_0 \sqrt{\pi a} \quad (7.21)$$

This provides an upper bound for K_r , since the restraining action of the patch would reduce the stress-intensity factor. However, K_0 increases indefinitely as the crack length increases, whereas the crucial property of the reinforced plate of Figure 7.3(a) is that K_r does not increase beyond a limiting value, denoted by K_∞ , as will be confirmed later. That limiting value is the value of the stress intensity factor for a semi-infinite crack. It can be determined by deriving first the corresponding strain-energy release rate as follows. Before we proceed, let us first determine the deformation of the reinforced strips shown in Figure 7.3(b). The adhesive shear stress τ_A is governed by the differential Eq. (7.9), which has the following solution for the particular case of semi-infinite strip,

$$\tau_A(y) = \tau_{A,\max} e^{-\beta y}, \quad (7.22)$$

where τ_{\max} can be determined from the simple equilibrium condition, $\sigma_0 t_P = \int_0^\infty \tau_A(y) dy$,

$$\tau_{A,\max} = \beta t_P \sigma_0 \quad (7.23)$$

Recalling Eq. (7.4), the opening displacement of the plate at $y = 0$ can be readily

determined,

$$u_y = \frac{\beta t_P t_A}{\mu_A} \sigma_0 \quad (7.24)$$

Let us denote the total opening as $\delta = 2u_y$. The above equation can be rewritten as,

$$\sigma_0 = \frac{1}{2} k E_P \delta, \quad (7.25)$$

with

$$k = \frac{\mu_A}{\beta t_A t_P E_P} \equiv \frac{S\beta}{(1+S)(1-\nu_P^2)} \quad (7.26)$$

Consider the configuration shown in Figure 7.6. If the semi-infinite crack extends by a distance da , the stress and displacement fields are simply shifted to the right by da . The change in the strain energy U_E is that involved in converting a strip of width da from the state shown as section AA' in Figure 7.6 to that shown in section BB', as depicted in Figure 7.7. Consequently the change in the potential energy Π for a crack advancement δa , which is defined as the difference between the strain energy change $U_E (= 1/2 \sigma_0 t_P \delta)$ and the work performed by the external load $W (= \sigma_0 t_P \delta)$,

$$\Pi = U_E - W = -\frac{1}{2} \sigma_0 t_P \delta \quad (7.27)$$

The crack extension force, i.e. the strain-energy release rate G_∞ is given by

$$G_\infty t_P = -\frac{\partial \Pi}{\partial a} = \frac{1}{2} \sigma_0 t_P \delta, \quad (7.28)$$

which can be re-written as, recalling Eq. (7.25),

$$G_\infty = \frac{\sigma_0^2}{k E_P} \quad (7.29)$$

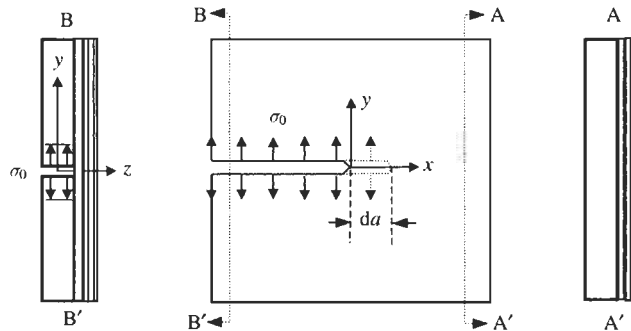


Fig. 7.6. A patched crack subjected to internal pressure.

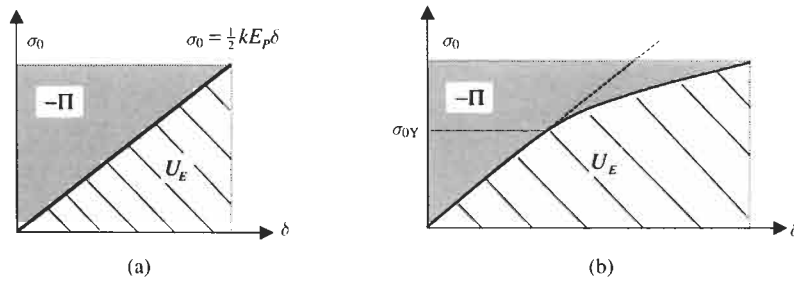


Fig. 7.7. Illustration of the interpretation of G_∞ as a complementary energy. (a) Elastic adhesive and (b) elastic-plastic adhesive.

From the above equation, assuming that the usual relation holds between the strain-energy release rate G and the stress-intensity factor K [22], we obtain,

$$K_\infty = \frac{\sigma_0}{\sqrt{k}} \quad (7.30)$$

It is clear from this derivation that K_∞ is an upper-bound for K_r . The validity of this formula will be substantiated by an independent finite element analysis to be discussed later.

7.4.3. Plastic adhesive

The stress-intensity factor solution derived in the previous section is valid only if the adhesive remains elastic. If the maximum adhesive shear stress does exceed the shear yield-stress, the relationship between σ_0 and the crack-opening displacement δ will become non-linear, as illustrated in Figure 7.7(b), which also shows the correct area corresponding to G_∞ . For an adhesive that is elastic-perfectly plastic with a shear yield-stress τ_Y , the adhesive begins to yield at the following stress,

$$\sigma_{0Y} = \frac{\tau_Y}{\beta t_P} \quad (7.31)$$

It can be shown that for $\sigma_0 \geq \sigma_{0Y}$ the crack opening-displacement δ is given by,

$$\delta = \frac{\tau_Y t_A}{\mu_A} \left[1 + \left(\frac{\sigma_0}{\sigma_{0Y}} \right)^2 \right] \equiv \frac{\sigma_{0Y}}{k E_P} \left[1 + \left(\frac{\sigma_0}{\sigma_{0Y}} \right)^2 \right], \quad (\sigma_0 \geq \sigma_{0Y}) \quad (7.32)$$

Following the method outlined in the previous section, the strain-energy release rate G_∞ can be determined,

$$G_\infty = \sigma_0 \delta - \int_0^\delta \sigma_0 d\delta = \int_0^{\sigma_{0Y}} \delta d\sigma_0 + \int_{\sigma_{0Y}}^{\sigma_0} \delta d\sigma_0 = \frac{\sigma_0^2}{k E_P} \left[\frac{P^3 + 3P - 1}{3P^2} \right], \quad (7.33)$$

$(\sigma_0 \geq \sigma_{0Y}),$

where

$$P = \frac{\sigma_0}{\sigma_{0Y}} \quad (7.34)$$

Then, the stress-intensity factor for $P \geq 1$ can be expressed as

$$K_\infty = K_{\infty,el} \left[\frac{P^3 + 3P - 1}{3P^2} \right]^{1/2}, \quad (P \geq 1), \quad (7.35)$$

where $K_{\infty,el}$ denotes the value which would be obtained from Eq. (7.30) for the stress σ_0 ignoring the plastic yielding in the adhesive. As can be seen from Eq. (7.35), the increase in K_∞ due to adhesive yielding depends only on the plasticity ratio P defined by Eq. (7.34), as shown in Figure 7.8.

7.4.4. Finite crack size

For cracks of finite size, stress-intensity factor K_r is apparently dependent on the crack length and varies between the lower-bound $K_0 = \sigma_0 \sqrt{\pi a}$ and the upper-bound $K_\infty = \sigma_0 / \sqrt{k}$. In general the stress-intensity factor K_r can be expressed as

$$K_r = F \sigma_0 \sqrt{\pi a}, \quad (7.36)$$

where F denotes the reduction in the stress-intensity factor after repair. An exact solution of the function $K_r(a)$ or F has been obtained [14] using the method developed by Keer, *et al.* [23] for the special case of an isotropic plate and reinforcement having identical Poisson's ratio. By idealising the adhesive layer as shear springs and treating the stresses in the adhesive layer as body forces acting on the mid-plane of the plate and the reinforcement, the problem can be reduced to a single integral equation. An extensive parametric study [14] revealed that the

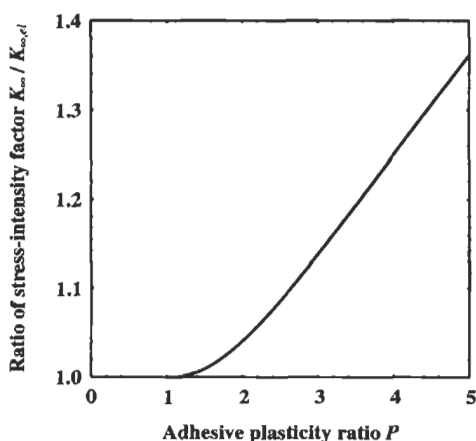


Fig. 7.8. Increase in stress-intensity factor due to adhesive yielding.

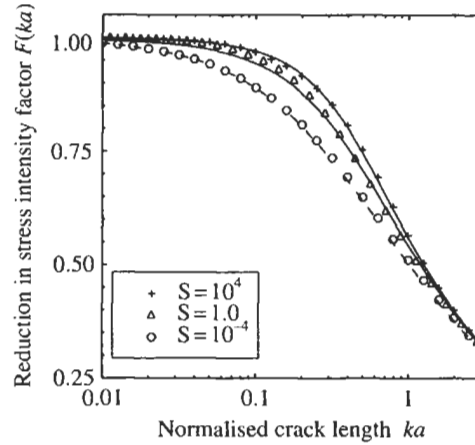


Fig. 7.9. Reduction in stress-intensity factor for various patch configurations. Symbols denote the exact solutions by the Keer method, solid curves denote the interpolating function, and dashed curve denotes the solution of crack bridging model.

reduction factor F depends strongly on the parameter k given by Eq. (7.26) and to a lesser extent on the stiffness ratio S , as shown by the symbols in Figure 7.9. Based on the solutions of the integral equation [14], the following interpolating function can be constructed,

$$F(ka) = \left[\frac{1}{\pi ka} \tanh \left(\frac{\pi ka}{1 + B\pi ka} \right) \right]^{1/2}, \quad (7.37)$$

where constant B has been determined by curve fitting the numerical solution of the integral equation, which gives $B = 0.3$ for balanced repairs ($S = 1.0$) and $B = 0.1$ for infinitely-rigid patch ($S \rightarrow \infty$).

A simple yet more versatile method of determining the reduction in stress-intensity factor after repair is the crack bridging model [10], which has been recently extended to analyse the coupled in-plane stretching and out-of-plane bending of one-sided repairs [17]. From the previous analysis it is clear that the essential reinforcing action at the second stage is the restraint on the crack opening by the bonded reinforcements. The basic idea underlying the crack bridging model is that this restraining action can be represented by a continuous distribution of springs acting between the crack faces, as illustrated in Figure 7.10. This idealisation reduces the problem at stage II to two parts: (i) determine the appropriate constitutive relation (i.e. stress-displacement relation) for the springs, and (ii) solve a one-dimensional integral equation for the crack opening,

$$\delta(x) = u_y^P(x, y \rightarrow 0+) - u_y^P(x, y \rightarrow 0-) = 2u_y^P(x, y \rightarrow 0+), |x| \leq a \quad (7.38)$$

It is assumed that distributed linear springs act between the crack faces over the

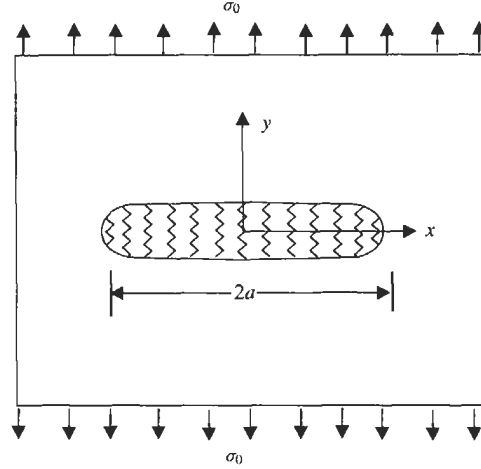


Fig. 7.10. Schematic representation of a centre-crack reinforced by distributed springs.

crack region so that the boundary conditions on $y = 0$ are

$$\sigma_{yy}(x) = kE_P u_y(x), \quad |x| \leq a, \quad (7.39a)$$

$$u_y(x) = 0, \quad |x| \geq a, \quad (7.39b)$$

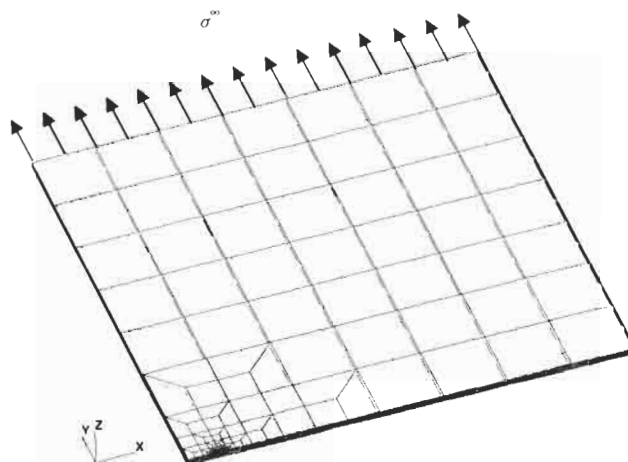
where k denotes a *normalised spring constant* which has dimension $length^{-1}$. It is worth noting that this normalised spring constant k has already been determined in Section 7.4.2 and is given by Eq. (7.26). With these boundary conditions, the problem of determining the crack opening displacement $u_y(x)$ can be reduced to that of solving the following integral equation [10,17],

$$\frac{E_P}{2\pi} = \int_{-a}^a \frac{u_y(t)}{(x-t)^2} dt = -\sigma_0 + k u_y(x) \quad (7.40)$$

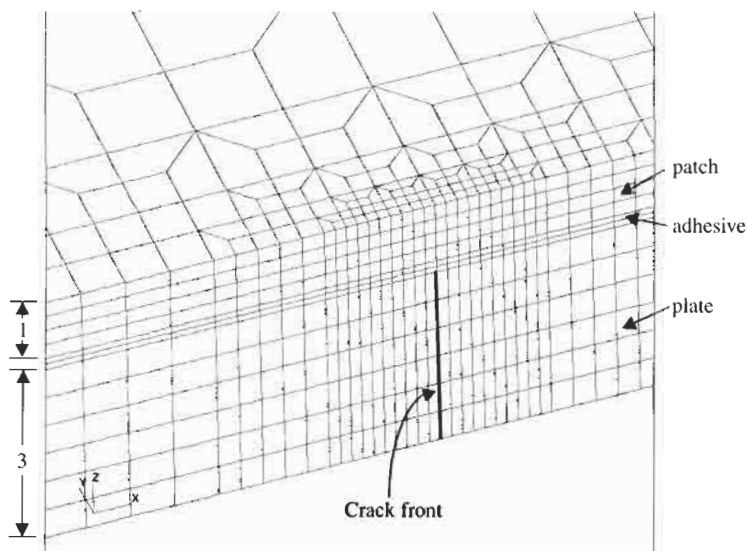
The integral in the above equation is interpreted as a Hadamard finite part [24], which can be viewed as the derivative a Cauchy principal value integral. The above equation can be efficiently solved using either Galerkin's method or collocation methods. Once the crack-opening displacement $u_y(x)$ is determined, the stress-intensity factor K_r can be calculated by

$$K_r = \lim_{x \rightarrow a} \frac{E_P \sqrt{2\pi}}{4} \frac{u_y(x)}{\sqrt{a-x}} \quad (7.41)$$

Detailed numerical results for K_r are available in reference [10], which also provided the following interpolating function constructed based on the numerical



(a)



(b)

Fig. 7.11. Finite element mesh (a) quarter model and (b) mesh near crack tip.

results,

$$F(ka) = \left[\frac{1 + 2.23ka}{1 + 4.776ka + 7(ka)^2} \right]^{1/2}, \quad (7.42)$$

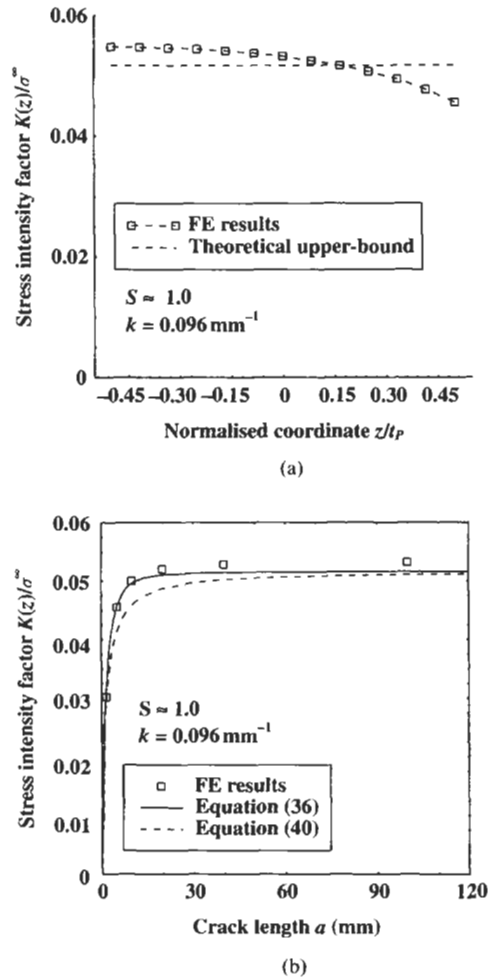


Fig. 7.12. Comparison between finite element solution and analytical predictions.

which is shown in Figure 7.12(a). As compared to the exact solutions by the Keer formulation (Eq. 7.37), the crack-bridging model (Eq. 7.42) slightly over-estimates the reduction in stress-intensity factor for balanced repair ($S = 1$) in the short crack limit. Both the two interpolating formulas, Eqs. (7.37) and (7.42) recover the asymptotic solution of Eq. (30) in the long crack limit as $a \rightarrow \infty$.

7.4.5. Finite element validation

To substantiate the theoretical solutions obtained so far, an extensive finite element analysis has been performed for various crack lengths [12]. Due to symmetry only a quadrant of the repair shown in Figure 7.1(a) was modelled. No

Table 7.1
Dimensions and material properties of a typical repair.

Layer	Young's modulus (GPa)	Poisson's ratio	Thickness (mm)
Plate	71	0.3	3.0
Reinforcement	207	0.3	1.0
Adhesive	1.89	0.3	0.2

debond between the plate and reinforcement or adhesive plasticity was considered. The finite element mesh near the crack tip region is shown in Figure 7.11. All three constituents, the patch, the adhesive, and the plate are assumed to deform elastically only, and are each modelled by 20-noded isoparametric brick elements. The dimensions and material properties of the repair configuration being considered are summarised in Table 7.1. For this repair, we have the shear stress transfer length $\beta^{-1} = 5.634$ mm, and the normalised spring constant $k = 0.096$ mm⁻¹. From the finite element results, the stress-intensity factor is calculated using Eq. (7.41), with E_P being replaced by the plane-strain value $E_P/(1 - \nu^2)$.

Figure 7.12(a) shows a comparison between the theoretical estimate and the finite element results for a long crack ($ka \approx 10$), indicating an excellent agreement within the mean stress-intensity factor through the plate thickness. It is also clear that the stress-intensity factor at the outer surface away from the adhesive layer is somewhat higher than near the adhesive layer. The asymptotic behaviour of the stress-intensity factor is shown in Figure 7.12(b) together with the two analytical estimates (37) and (42). The crack-bridging solution seems to slightly over-estimate the repair efficiency.

7.5. Shear mode

Although cracks that are likely to be encountered in practice are generally aligned in a direction perpendicular to the principal tensile stress (or strain), giving rise to mode I cracking, there are at least two circumstances where mixed mode cracking is a major concern in the context of bonded repairs. Firstly, application of bonded reinforcements, which are frequently anisotropic, may alter the local stress-state near the crack region so that the maximum principal stress may no longer remain perpendicular to the crack plane. Secondly, structures are frequently subjected to non-proportional loading in which the principal stress-strain axes rotate with time, thus cracks may experience a time-dependent mixed mode loading. If the bonded repair technique is used to repair mode II cracks, one important question that needs consideration is the effectiveness of repairs.

For simplicity let us consider the particular case of an isotropic circular patch ($A/B = 1$) with a Poisson's ratio $\nu = 1/3$. In this case, the prospective stress in the plate after repair can be determined using the general solution for biaxial tension

presented in Section 7.4.1, namely Eq. (7.19),

$$\tau_0 = \frac{1 + 0.277S - 0.0712S^2}{1 + S} \tau^\infty, \quad \left(\frac{B}{A} = 1, \nu = \frac{1}{3} \right) \quad (7.43)$$

Detailed solution of the stress-intensity factor K_r for shear loading can be found in [14]. We shall not repeat here the intermediate details of the analysis but simply recall the results for the upper-bound and the interpolating function. The upper-bound solution of K_r is given by an equation similar to that for tensile mode,

$$K_{II} = \frac{\tau_0}{\sqrt{k_{II}}}, \quad (7.44)$$

where the *normalised shear spring constant* k_{II} is given by

$$k_{II} = \frac{\lambda S}{2(1 + S)(1 + \nu)}, \quad (7.45)$$

with

$$\lambda^2 = \frac{\mu_A}{t_A} \left[\frac{1}{\mu_{P,xy} t_P} + \frac{1}{\mu_{R,xy} t_R} \right] \quad (7.46)$$

It is evident that k_{II} is lower than the spring constant pertinent to mode I. For instance, in the case of isotropic patch k_{II} is related to the spring constant k_I for mode I crack,

$$k_{II} = \sqrt{\frac{1 - \nu}{2}} k = \frac{k}{\sqrt{3}}, \quad \nu = \frac{1}{3} \quad (7.47)$$

For finite crack size, the stress-intensity factor K_r can also be expressed as [14]

$$K_r = F(k_{II}a) \tau_0 \sqrt{\pi a}, \quad (7.48)$$

with $F(x)$ being given by Eq. (7.37) or Eq. (7.42).

An important implication arising from the difference in the spring constants is that when strongly anisotropic reinforcements with low in-plane shear modulus, such as unidirectional plastic reinforced composites, are used to repair a crack under shear loading (with the fibres being perpendicular to the crack), the repair efficiency will be much lower than that could be expected on the basis of mode I analysis. It should of course be mentioned that under remote shear loading, the crack would be aligned perpendicular to the maximum tensile stress, hence aligning the fibres perpendicular to the crack is still the optimal configuration.

7.6. One-sided repairs

So far we have ignored the tendency for out-of-plane bending that would result from bonding a reinforcing patch to only one face of an un-supported plate, so that, strictly speaking, the preceding analysis is more appropriate for the case of two-sided reinforcement, with patches bonded to both faces, or one-sided repairs to fully supported structures. For the case of un-supported one-sided repairs, it is again convenient to divide the analysis into two stages. In Section 6.1 the stress reduction due to stage I will be analysed within the framework of geometrically linear elasticity [12], whereas a geometrically non-linear analysis [17] will be presented in Section 7.6.2. These two solutions will provide an upper and lower bound to the actual stress distribution. In both cases the geometrically linear analysis is all that needed for stage II. For stage I we shall consider the particular case where the reinforcement covers the entire cracked plate, ignoring the load attraction effect.

7.6.1. Geometrically linear analysis

Consider first the effect of one-sided reinforcement on an *un-cracked* plate which is subjected to a uniaxial tension. Assuming that the reinforcement is far greater than the shear stress transfer length, we treat the reinforced region as a composite plate with a rigid bondline. The stress distribution in the plate and the reinforcement can be determined using the conventional theory of cylindrical bending of plates, i.e. we shall assume that the bending deformation of the reinforced portion satisfies the usual kinetic condition that plane sections remain plane. The position of the neutral plane of the composite plate consisting of the base plate and rigidly-bonded reinforcement is denoted by \bar{z} , referring to Figure 7.13,

$$\bar{z} = \frac{S(t_P + t_R + 2t_A)}{2(1 + S)} \quad (7.49)$$

The moment of inertia of the reinforced region I_t is

$$I_t = I_P + I_R E'_R / E'_P, \quad (7.50)$$

where E' refers to the plane-strain Young's modulus ($E' = E/(1 - \nu^2)$), and

$$I_P = t_P^3/12 + t_P \bar{z}^2, \quad (7.51)$$

$$I_R = I_R^3/12 + t_R(t_P + t_R - 2\bar{z})^2/4 \quad (7.52)$$

The stress distribution in the patched plate is assumed to be linear in the thickness direction, so that it can be specified in terms of the membrane force N_0 and a bending moment M_0 per unit length in the x -direction, as depicted in Figure 7.13

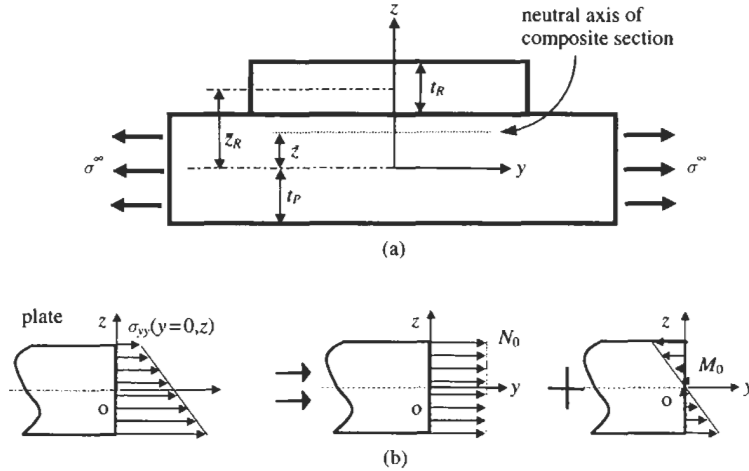


Fig. 7.13. Stress distribution in an un-cracked plate reinforced with a patch: (a) composite plate subjected to uniaxial tension; (b) stress distribution in the plate.

(see [12,17] for more details),

$$N_0 = \int_{-t_P/2}^{t_P/2} \sigma_{yy}(y=0, z) dz \equiv \frac{\sigma^\infty t_P}{1+S} + \frac{\sigma^\infty t_P^2 \bar{z}^2}{I_t}, \quad (7.53)$$

$$M_0 = - \int_{-t_P/2}^{t_P/2} \sigma_{yy}(y=0, z) z dz \equiv \frac{\sigma^\infty t_P^4 \bar{z}}{12 I_t} \quad (7.54)$$

Comparison between Eqs. (7.14) and (7.53) clearly shows that the plate in a one-sided repair is transferring more membrane stress than in an equivalent two-sided repairs. Therefore, due to out-of-plane bending induced by load eccentricity, the stress distribution along the prospective crack path before the crack appears is higher than for a corresponding two-sided reinforcement. In addition, there is a bending moment acting on the prospective crack faces. Consequently, due to the shift of neutral plane, one-sided repairs would experience not only an increase in the net force that the plate is transmitting, but also a secondary bending moment; both contributing to a considerable increase in stress-intensity factor.

In stage II, analysis of the crack-tip deformation requires the use of the shear deformation theory, which yields that the stress intensity factor varies linearly through the plate thickness,

$$K(z) = K_{\text{mean}} + K_b \frac{2z}{t_P}, \quad (7.55)$$

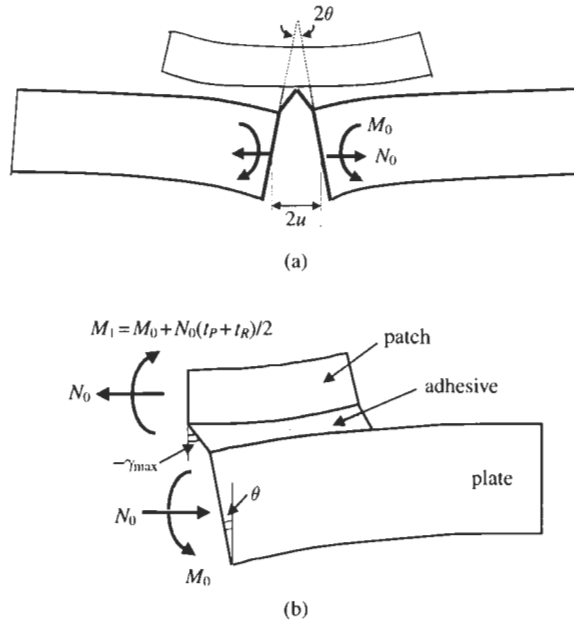


Fig. 7.14. (a) Single strap joint representing one-sided repairs subjected to membrane tension and bending moment, and (b) notations and boundary conditions.

where K_{mean} and K_b denote respectively the membrane and bending stress intensity factors. The strain-energy release rate can be determined following the method outlined in Section 7.4.2, except that the change in the potential energy now consists of two terms: work done by the membrane force and the bending moment [12], referring to Figure 7.14,

$$t_p G_{\infty}^* = N_0 u_0 + M_0 \theta_0, \quad (7.56)$$

where the superscript “*” refers to the strain-energy release rate for one-sided repair, and u_0 and θ_0 denote the opening displacement and the angle of rotation of the crack faces, which are related to the membrane force N_0 and M_0 via the following relation [17],

$$\begin{Bmatrix} u_0 \\ \theta_0 \end{Bmatrix} = \begin{bmatrix} c_{11} & c_{12} \\ c_{21} & c_{22} \end{bmatrix} \begin{Bmatrix} N_0 \\ M_0 \end{Bmatrix}, \quad (7.57)$$

with

$$c_{11} = \frac{t_P(t_P + t_R)}{4\kappa D_R} + \left[\frac{1}{E'_R t_R} + \frac{1}{E'_P t_P} + \frac{t_R(t_R + t_P)}{4D_R} \right] \left[\frac{1}{2\beta} - \frac{\mu_A t_P}{16\kappa^2 \beta t_A} \left(\frac{t_R}{D_R} - \frac{t_P}{D_P} \right) \right], \quad (7.58)$$

$$c_{12} = \frac{t_P}{2\kappa D_R} \left(1 + \frac{D_R}{D_P} \right) + \left(\frac{t_R}{2D_R} - \frac{t_P}{2D_P} \right) \left(\frac{1}{2\beta} - \frac{\mu_A t_P}{16\kappa^2 \beta t_A} \left(\frac{t_R}{D_R} - \frac{t_P}{D_P} \right) \right), \quad (7.59)$$

$$c_{21} = \frac{t_R + t_P}{2\kappa D_R} - \frac{\mu_A}{8\kappa^2 \beta t_A} \left(\frac{t_R}{D_R} - \frac{t_P}{D_P} \right) \left(\frac{1}{E'_R t_R} + \frac{1}{E'_P t_P} + \frac{t_R(t_P + t_R)}{4D_R} \right), \quad (7.60)$$

$$c_{22} = \frac{1}{\kappa D_R} \left(1 + \frac{D_R}{D_P} \right) - \frac{\mu_A}{16\kappa^2 \beta t_A} \left(\frac{t_R}{D_R} - \frac{t_P}{D_P} \right)^2, \quad (7.61)$$

$$D_P = \frac{E'_P t_P^3}{12}, \quad (7.62)$$

$$D_R = \frac{E'_R t_R^3}{12}, \quad (7.63)$$

$$\kappa^4 = \frac{E'_A}{4t_A} \left[\frac{1}{D_P} + \frac{1}{D_R} \right] \quad (7.64)$$

Therefore the total strain-energy release rate can be expressed as

$$G_\infty^* = \frac{1}{t_P} [c_{11} N_0^2 + (c_{12} + c_{21}) N_0 M_0 + c_{22} M_0^2], \quad (7.65)$$

which can be simplified to become

$$G_\infty^* = \frac{(\sigma^\infty)^2}{(1+S)^2} \frac{\omega^2}{k}, \quad (7.66)$$

where k is given by Eq. (7.26), and the term ω is well approximated by the following expression [12],

$$\begin{aligned} \omega^2 \approx & 2 + \frac{3t_P}{2t_R} + \frac{3\beta t_P}{\kappa t_R} \left(1 + \frac{t_P}{t_R} \right) + (1+S) \left(2 + \frac{3t_P}{2t_R} \right) \frac{\bar{z}^2 t_P}{I_t} + (1+S) \frac{\beta}{\kappa} \\ & \left(1 + \frac{t_P}{t_R} \right) \frac{\bar{z} t_P^3}{t_R I_t} \left(\frac{3\bar{z}}{t_P} - 1 \right) \end{aligned} \quad (7.67)$$

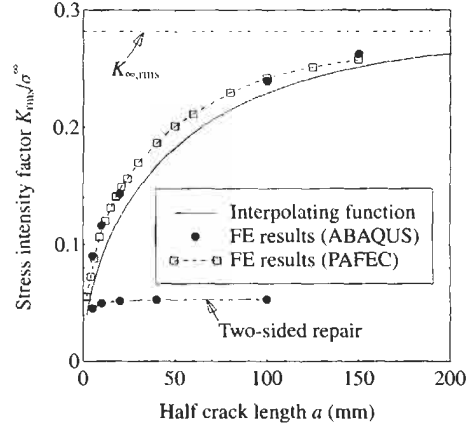


Fig. 7.15. Comparison between analytical solution and finite element results for one-sided repairs. Symbols denote the results of three-dimensional finite element analysis and the curves indicate the theoretical formulas.

Consequently the root-mean-square stress-intensity factor $K_{\infty,rms}$ for one-sided repair can be expressed as,

$$K_{\infty,rms} = \frac{\sigma^\infty}{1+S} \frac{\omega}{\sqrt{k}} \quad (7.68)$$

It is now possible to define a spring constant for one-sided repairs,

$$k^* = \frac{k}{\omega^2} \quad (7.69)$$

With this spring constant, the stress intensity factor for a one-sided repair can be expressed in a similar form as for two-sided repairs,

$$K_{rms}(a) = \frac{\sigma^\infty}{1+S} \sqrt{\pi a} F_1(k^* a), \quad (7.70)$$

where F_1 is given by Eq. (7.37). Figure 7.15 shows a comparison between Eq. (7.70) and the results of 3D finite element analyses. The repair configuration being considered is the same as that analysed in Section 7.4.4. The same problem has been analysed using two different finite element codes, namely ABAQUS [26] and PAFEC [25]; both yielded approximately the same result. It can be seen that the above formula is in good correlation with the finite element results. It is also worth noting that the results confirm that the stress-intensity factor K_{rms} for a one-sided repair is much higher than that for an equivalent two-sided repair, indicating the importance of out-of-plane bending.

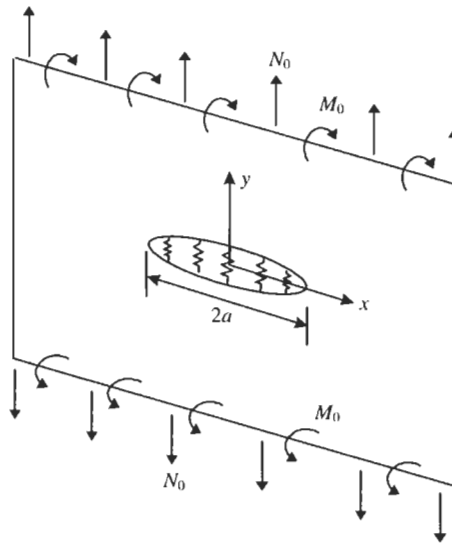


Fig. 7.16. A plate with a through crack reinforced with tension and bending springs.

The root-mean-square stress-intensity factor K_{rms} is related to the membrane and bending stress intensity factors [12],

$$K_{\text{rms}}^2 = K_{\text{mean}}^2 + \frac{1}{3} K_b^2 \quad (7.71)$$

Although the root-mean-square of the stress intensity factor has been derived, the maximum and minimum stress intensity factors still remain unresolved. It is apparent that the energy method alone is insufficient to determine the membrane and bending stress intensity factors, as an additional equation is required to partition K_{rms} into membrane and bending components. To this end, let us now briefly discuss a crack-bridging model which is capable of analysing the combined tensile stretching and bending of one-sided repairs.

7.6.2. Crack bridging model

The perturbation problem of stage II for a one-sided repair can be reduced by representing the patch by distributed springs bridging the crack faces [17], as illustrated in Figure 7.16. The springs have both tension and bending resistances; their stiffness constants are determined from a 1D analysis for a single strap joint, representative of the load transfer from the cracked plate to the bonded patch. The spring constants are given by Eq. (7.57). For the purpose of parametric investigation, we introduce the following non-dimensional variables,

$$h_1(x) = \frac{u(x)}{a}, \quad h_2(x) = \frac{1}{6} \theta t_P / a \quad (7.72)$$

By using Reissner's plate theory, the normalised crack face displacement h_1 and normalised crack face rotation h_2 are solutions of the following coupled integral equations [17],

$$-\frac{1}{2\pi} = \int_{-1}^1 \frac{h_1(\eta)}{(r-\eta)^2} d\eta + (k_{tt}a)h_1(r) + (k_{tb}a)h_2(r) = \frac{N_0}{E_P t_P}, \quad (7.73a)$$

$$-\frac{3}{2\pi} = \int_{-1}^1 \frac{h_2(\eta)}{(r-\eta)^2} d\eta - \frac{15}{(1+\nu_P)2\pi} \left(\frac{a}{t_P}\right)^2 \int_{-1}^1 L(\sqrt{10}\frac{a}{t_P}|r-\eta|)h_2(\eta)d\eta \quad (7.73b)$$

$$+ (k_{bt}a)h_1(r) + (k_{bb}a)h_2(r) = \frac{6M_0}{E_P t_P^2},$$

where

$$k_{tt} = \frac{c_{22}}{E_P t_P (c_{11}c_{22} - c_{12}c_{21})}, \quad k_{tb} = -\frac{6c_{21}}{E_P t_P^2 (c_{11}c_{22} - c_{12}c_{21})}, \quad (7.74)$$

$$k_{bt} = -\frac{6c_{12}}{E_P t_P^2 (c_{11}c_{22} - c_{12}c_{21})}, \quad k_{bb} = \frac{36c_{11}}{E_P t_P^3 (c_{11}c_{22} - c_{12}c_{21})}, \quad (7.75)$$

$$L(s) = -\frac{48}{s^4} + \frac{4}{s^2} + 4[K_2(s) - K_0(s)] + \frac{24}{s^2} K_2(s), \quad (7.76)$$

with K_0 and K_2 are the modified Bessel functions of the second kind. The integral equations can be readily solved by expanding the unknowns using Chebyshev polynomials of the second kind. The membrane and bending stress intensity factors K_m and K_b are directly related to the values of h_1 and h_2 at $\eta \rightarrow 1$.

With the prospective membrane force N_0 and bending moment M_0 are given by Eqs. (7.53) and (7.54), respectively, the membrane and bending stress intensity factors can be solved. For the repair configuration specified by Table 7.1, the results are shown in Figure 7.17 together with the finite element results. Considering the approximate nature of the crack bridging model and the finite element method, the reasonably good correlation between the predictions and the finite element results confirms the validity of the above theoretical model.

7.6.3. Geometrically non-linear analysis

The geometrically linear analysis presented in the preceding section is strictly speaking applicable only when the out-of-plane deflection is negligible relative to plate thickness, i.e. when the applied stress σ^∞ is very low. Otherwise the geometrically non-linear deformation, as indicated in Figure 7.18, has to be taken

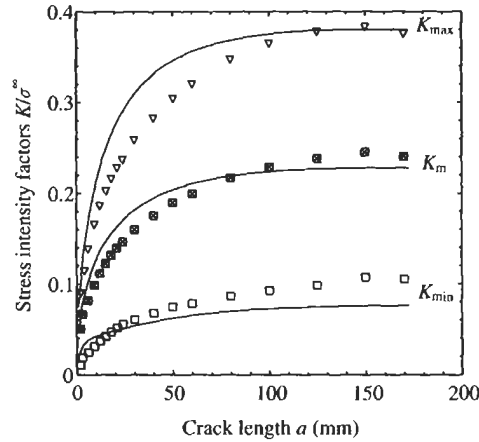


Fig. 7.17. Theoretical predictions and finite element results for a typical one-sided repair assuming geometrically linear deformation.

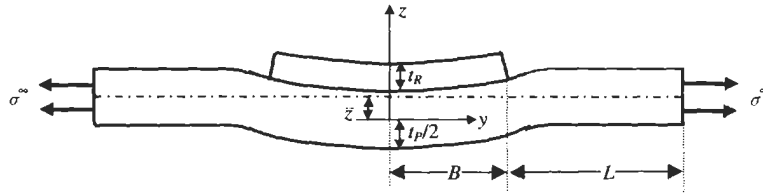


Fig. 7.18. Geometrically non-linear deformation of a single strap joint representing one-sided repairs.

into account. We shall use the rigid-bond approximation and denote the deflection of the plate as w . The governing equation for the deflection of the beam inside and outside the repaired region is,

$$E_P I_t \frac{d^2 w}{dy^2} = \sigma^\infty t_P (w + \bar{z}), \quad |y| \leq B, \quad (7.77a)$$

$$E_P I_P \frac{d^2 w}{dy^2} = \sigma^\infty t_P w, \quad a \leq |y| \leq B + L, \quad (7.77b)$$

where I_t and I_P are given by Eqs. (7.50) and (7.51) respectively. The boundary condition is

$$w(y = B + L) = 0 \quad (7.78)$$

The general solution of the deflection w is

$$w = \begin{cases} C_1 \cosh \chi y + C_2 \sinh \chi y - \bar{z} & (|y| \leq B), \\ C_3 \cosh \chi_P y + C_4 \sinh \chi_P y & (a \leq |y| \leq B + L), \end{cases} \quad (7.79)$$

where

$$\chi = \left[\frac{\sigma^\infty t_P}{E_P I_t} \right]^{1/2}, \quad \chi_P = \left[\frac{\sigma^\infty t_P}{E_P I_P} \right]^{1/2}, \quad (7.80)$$

and constants C_1 , C_2 , C_3 , and C_4 can be determined from the boundary condition (78) and the following continuity and symmetry conditions,

$$w'(y = 0) = 0, \quad (7.81)$$

$$w(y = B-) = w(y = B+), \quad (7.82)$$

$$w'(y = B-) = w'(y = B+) \quad (7.83)$$

After some derivation the following constants are determined,

$$C_1 = \frac{\bar{z}}{\cosh \chi B \left[1 - \frac{\chi [\tanh \chi_P B - \tanh \chi_P (B+L)] \tanh \chi B}{\chi_P [1 - \tanh \chi_P B \tanh \chi_P (B+L)]} \right]}, \quad (7.84a)$$

$$C_2 = 0, \quad (7.84b)$$

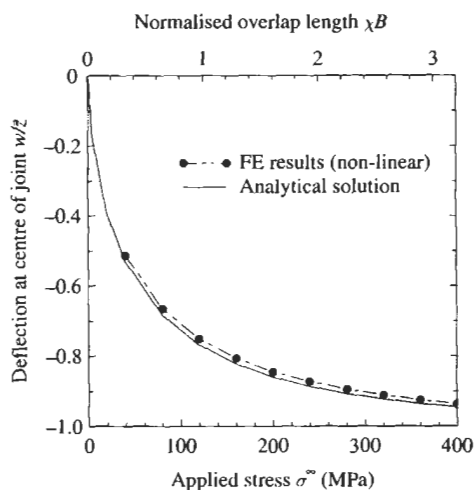
$$C_3 = -C_1 \frac{\chi \sinh \chi B \tanh \chi_P (B+L)}{\chi_P \cosh \chi_P B [1 - \tanh \chi_P B \tanh \chi_P (B+L)]}, \quad (7.84c)$$

$$C_4 = -\frac{C_3}{\tanh \chi_P (B+L)} \quad (7.84d)$$

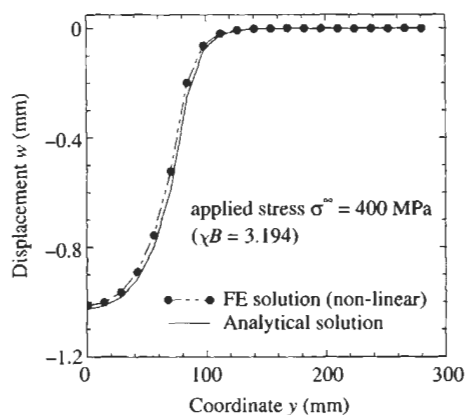
The deflection at the centre of the reinforcement is given by

$$w(y = 0) = C_1 - \bar{z} \quad (7.85)$$

The above solution has been verified for a particular strap-joint representing the one-sided repair specified in Table 7.1. In the finite element analysis, the lengths B and L are taken to be 80 and 200 mm. The results for the deflection at the centre of the joint $y = 0$ are shown in Figure 7.19(a) together with the analytical prediction (85), indicating the accuracy of the beam theory solution. Similarly the finite element results for the deflection along the joint and the analytical solution are shown in Figure 7.19(b), together with the analytical solution (79), indicating a good agreement. From the above analytical solution it is clear that the displacement w at the centre of the strap joint w depends on three non-dimensional parameters, χB , χ_P/χ , and L/B . It is easy to show that w approaches $-\bar{z}$ as $\chi_P B \rightarrow \infty$, provided $L/B \neq 0$. This limiting case corresponds to when the neutral axis of the patched region is aligned perfectly with the path of the applied load.



(a)



(b)

Fig. 7.19. Deflection of a one-sided strap joint accounting for geometrically non-linear: deformation: (a) centre of overlap, and (b) along the joint.

Since the bending moment at the centre of the overlap is

$$M(y=0) = C_1 \sigma^\infty t_P, \quad (7.86)$$

the prospective membrane force and bending moment can now be determined,

$$N_0 = \frac{\sigma^\infty t_P}{1+S} + \frac{C_1 \sigma^\infty t_P^2 \bar{z}}{I_t}, \quad (7.87a)$$

$$M_0 = C_1 \frac{\sigma^\infty t_P^4}{12 I_t} \quad (7.87b)$$

With the prospective force and bending moment given by Eqs. (7.87), the coupled Eqs. (7.73) can then be solved numerically. The superposition principle used in the previous section to reduce the problem of a one-sided repair subjected to remote tension to a simple perturbation problem where the crack is internally pressurised is, strictly speaking, not valid should the structure undergo geometrically nonlinear deformation. However, an upper bound solution can be obtained by a hybrid method, in which the prospective stress distribution is solved using geometrically nonlinear elasticity theory, the stage II analysis is carried out using the geometrically linear theory, i.e. the crack bridging method developed in Section 7.5.2. A proof that this hybrid method will provide a conservative prediction of the stress intensity factors can be found in [17]; a validation using the geometrically non-linear finite element method will be presented later.

For a given repair configuration, the prospective membrane force (Eq. (87a)) increases with the load σ^∞ while the bending moment (Eq. (87b)) decreases, resulting in a net increase in the stress intensity factors, although the rate of increase is slower than that expected from geometrical linear considerations. This is illustrated in Figure 7.20(a) for the case of half crack length a of 20 mm. It is seen that the minimum stress-intensity factor K_{\min} determined by the hybrid method correlates very well with the finite element results. However the hybrid method over-predicts the maximum stress-intensity factor, K_{\max} , confirming that the hybrid method is an upper-bound solution [17]. A similar trend can be observed in Figure 7.20(b) which shows the asymptotic behaviour of the stress-intensity factors as the crack length increases. The remote applied stress σ^∞ is kept to be 400 MPa. Again the minimum stress-intensity factor K_{\min} determined by the hybrid method correlates very well with the finite element results, whereas the maximum stress-intensity factor K_{\max} determined by the hybrid method is greater than that obtained from finite element analysis.

7.7. Residual thermal stress due to adhesive curing

The process of adhesive bonding using high-strength structural adhesives (thermal-plastics) generally requires curing the adhesive above the ambient temperature. For instance, in a typical repair applied to aircraft structures the reinforced region is initially heated to a temperature of 120 °C, under pressure, for approximately one hour (the precise curing cycle depends on the adhesive being used). Upon cooling the fully cured, patched structure to the ambient temperature, thermal stress will inevitably develop in both the plate and the reinforcement, due to cooling a locally stiffened structure, especially when the reinforcing patch has a lower coefficient of thermal expansion than the plate being repaired. Thermal stresses may also arise when the patch structure experiences thermal cycling in service. Therefore thermal residual stresses represent a major concern to the repair efficiency of a repair. This is because the resulting thermal residual stresses post cure in the metal plate are inevitably tensile, owing to the increase in the stiffness of the patched region and the lower coefficient of thermal expansion of the composite

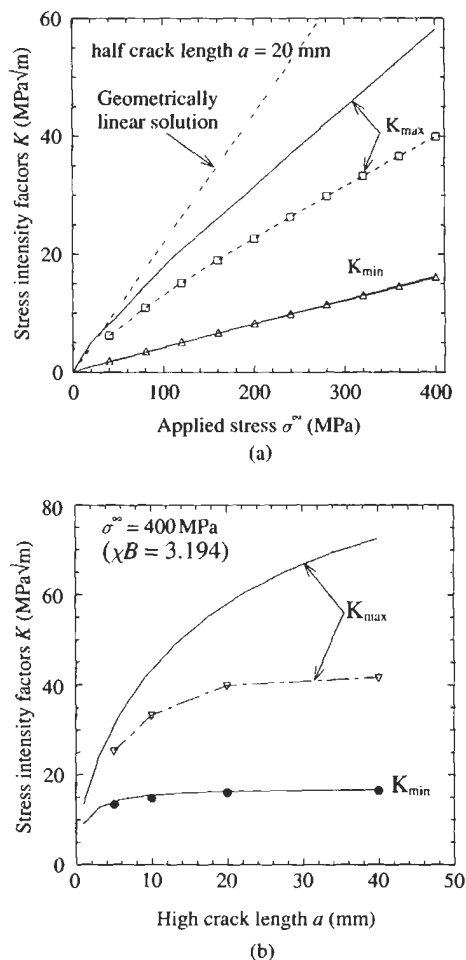


Fig. 7.20. Geometrically non-linear deformation of a single strap joint representing one-sided repairs.

patches. This tensile residual stress will increase the maximum stress-intensity factor of the crack after repair, hence may enhance fatigue crack growth rate (see Chapters 11 and 12).

7.7.1. Temperature distribution

Solutions of the thermal residual stresses in symmetric repairs and one-sided repairs have been developed in [18] and [19], respectively. In the following, only the results pertaining to symmetric repairs will be presented; details of solution for one-sided repairs can be found in reference [19]. Consider the configuration shown in Figure 7.21(a), in which an isotropic plate is reinforced by a circular patch of radius R_i . The coordinate system xy is chosen so that the principal axes of the orthotropic

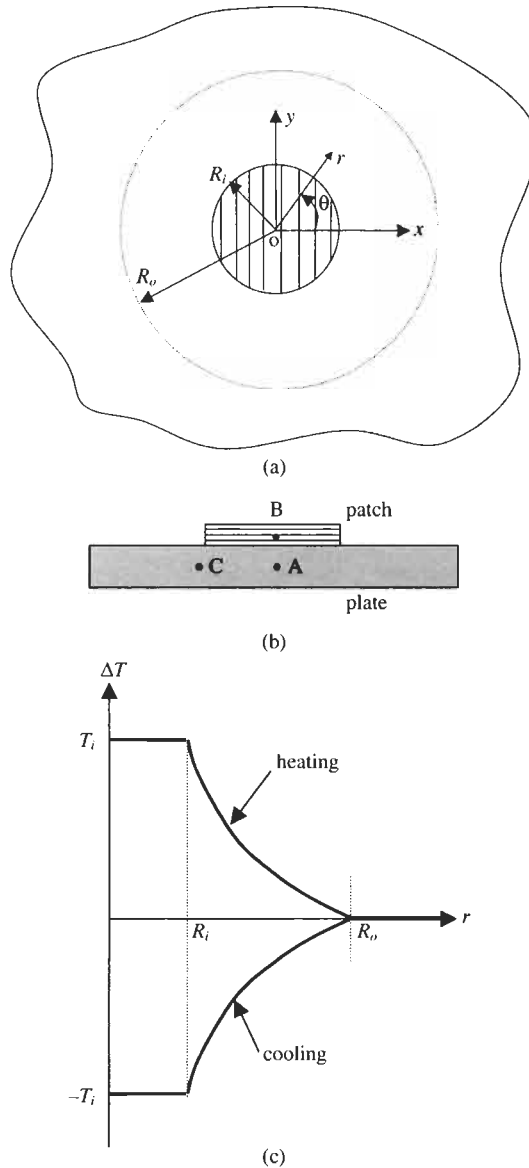


Fig. 7.21. An infinite plate reinforced with a circular composite patch. (a) Configuration and (b) temperature distribution during heating and cooling.

patch are aligned and parallel to the x, y axes, with the major direction along the y -axis. The objective here is to determine the thermal stresses in the patch, in the plate both inside the bonded region and just outside the patch.

During the first step of bonding, suppose that the inner portion ($r \leq R_i$) is heated to a temperature T_i during the curing process, with the usual convention that the

ambient temperature is taken as the zero of temperature. The temperature field satisfies the Laplacian Eq. (7.88) [21],

$$\nabla^2 T = 0 , \quad (7.88)$$

which has the following solution,

$$\Delta T^H(r) = \begin{cases} T_i & r \leq R_i \\ T_i \frac{\ln(r/R_o)}{\ln(R_i/R_o)} & R_i < r \leq R_o \\ 0 & r > R_o \end{cases} \quad (7.89)$$

where the superscript H denotes the temperature change corresponding to the first step: heating. A schematic of the temperature distribution is shown in Figure 7.21(c).

7.7.2. Residual stress due localised heating

Due to this non-uniform temperature distribution given by Eq. (7.89), thermal stresses (equal biaxial) develop in the plate, which can be readily derived [21],

$$\sigma_0^H = -\frac{1}{2} \alpha_P E_P \Delta T , \quad (7.90)$$

where $\Delta T = T_i - T_o$, α_P and E_P denote the thermal expansion coefficient and Young's modulus of the plate. Since $T_i - T_o > 0$ during heating, the above thermal initial stress is compressive. It should be noted that this thermal stress arises only in the case of localised heating of a large structure; for the case of a finite size specimen being uniformly heated to T_i , no thermal stress will develop. This stress distribution serves as the initial stress that will be added to the thermal stress induced by cooling the patched region down to the ambient temperature.

Now consider the case of a circular plate of radius R_o whose outer edge $r = R_o$ is constrained by a continuous distribution of springs of stiffness Θ according to the following relation,

$$\sigma_{rr}(r = R_o) = -\Theta E_P u_r(r = R_o) \quad (7.91)$$

The cases of free edge and a clamped edge $r = R_o$ can be recovered by setting $\Theta = 0$ and $\Theta \rightarrow \infty$, respectively. In this case, the thermal stress can be determined from Eq. (7.96), to be discussed in the next section, by setting $S = 0$,

$$\sigma_0^H = -\alpha_P E_P \Delta T \frac{1 - e/\alpha_P}{1 + \lambda + \lambda \nu_P - \nu_P} , \quad (7.92)$$

where

$$e = \frac{\alpha_P \beta}{1 - \beta R_i^2/R_o^2} \left\{ -\frac{R_i^2}{R_o^2} - \frac{1 - R_i^2/R_o^2}{2 \ln(R_i/R_o)} \right\}, \quad (7.93)$$

$$\lambda = \frac{1 + \nu_P + \beta(1 - \nu_P)R_i^2/R_o^2}{(1 + \nu_P)(1 - \beta R_i^2/R_o^2)}, \quad (7.94)$$

$$\beta = \frac{1 - (1 + \nu_P)\Theta R_o}{1 + (1 - \nu_P)\Theta R_o} \quad (7.95)$$

It can be shown that with the following spring stiffness Θ ,

$$\Theta_{\text{inf}} = \frac{1}{(1 + \nu_P)R_o}, \quad (7.96)$$

the solution for an infinite plate, Eq. (7.90), can be recovered as a special case by setting $\beta = 0$, $\lambda = 1$, and $e = 0$.

7.7.3. Residual stresses after cooling from cure

For the second step of adhesive bonding we assume that there is no shear stress in the adhesive layer during curing, so that the reinforcing patch expands freely without developing any stresses. After the adhesive is fully cured, the patched plate is then cooled down to the ambient temperature. In other words, the temperature change over the entire patched plate is subjected to the following temperature field, referring to Figure 7.21(c),

$$\Delta T^C(r) = -\Delta T^H(r), \quad (7.97)$$

where the superscript C denotes the temperature change corresponding to the second step: cooling. Now the problem is to determine the thermal stress σ_0^C on cooling to ambient temperature after curing. The final stress in the plate

$$\sigma_0^T = \sigma_0^H + \sigma_0^C \quad (7.98)$$

During this cooling process, it is assumed that the adhesive bond between the composite patch and the metal plate is absolutely rigid, so that the same strain-state prevails in both the patch and the plate directly beneath the patch. Details of a general solution for orthotropic patch are given in [18]. It is interesting to note that even for an orthotropic patch, the thermal residual stress σ_0^C in the plate is well approximated by the solution for an isotropic patch, which takes the major properties of the orthotropic patch [18]. Therefore in the following we will present

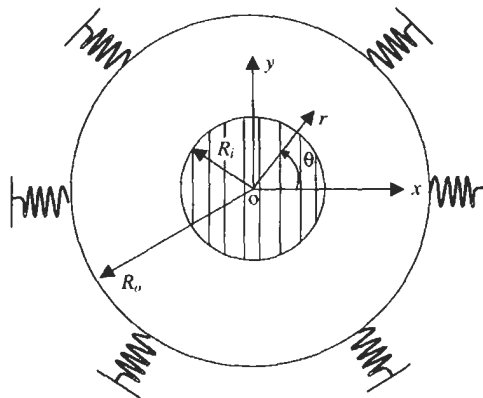


Fig. 7.22. Spring representation for simulating finite size effect.

only the solution for an isotropic patch with a coefficient of thermal expansion α_R ,

$$\sigma_0^C = -\alpha_P E_P \Delta T \frac{1 - \nu_R + (1 - \alpha_R/\alpha_P)(1 + \nu)S}{2(1 - \nu_R) + (1 - \nu_P^2)S} \quad (7.99)$$

The above solution applies strictly for an infinite plate. In practice, however, structures to be reinforced may be finite in size or constrained by the surrounding structure. To quantify the effect of this constraint, consider the configuration shown in Figure 7.22, in which an un-cracked circular plate of radius R_i is reinforced by a concentric patch of radius R_o . The outer edge $r = R_o$ is constrained by a continuous distribution of springs according to the following relation (91). In this case the thermal residual stress due to the cooling is given by [18],

$$\sigma_0^C = -\alpha_P E_P \Delta T \frac{(1 - \nu_R)(1 - e/\alpha_P) + (1 - \alpha_R/\alpha_P)(1 + \nu_P)S\lambda}{(1 - \nu_R)(1 + \lambda + \lambda\nu_P - \nu_P) + (1 - \nu_P^2)S\lambda}, \quad (7.100)$$

where the parameters e , λ , and β are given by Eqs. (7.93–7.95).

For the special case of an infinite patch ($R_i/R_o \rightarrow 0$, $\Theta_{inf} = 1/(1 + \nu_P)R_o$), one can further show that the residual thermal stress in the plate, point A in Figure 7.21(b), reduces to, noting $\lambda = 1$ and $e = 0$,

$$\sigma_0^C = -\alpha_P E_P \Delta T \frac{1 - \nu_R + (1 - \alpha_R/\alpha_P)(1 + \nu_P)S}{2(1 - \nu_R) + (1 - \nu_P^2)S} \quad (7.101)$$

It is evident that in the special case of isotropic patch, the final solution is dramatically simplified, providing a simple estimate of the residual stress in the plate. The thermal stress in the plate just outside the patched region, point C in Figure (7.21b), is

$$\sigma_P = -\alpha_P E_P \Delta T \frac{1 - \nu_R + S(1 - \nu_P)\alpha_R/\alpha_P}{2(1 - \nu_R) + (1 - \nu_P^2)S} \quad (7.102)$$

Similarly, the stresses in the patch, point B in Figure 7.21b, can be derived,

$$\sigma_R^T = \alpha_P E_R \Delta T \frac{1 + \nu - 2\alpha_R/\alpha}{2(1 - \nu_R) + (1 - \nu_P^2)S} \quad (7.103)$$

7.7.4. Thermal stress due to uniform temperature change

Often it is necessary to determine the thermal stresses in a patched structure undergoing uniform temperature change, such as changes in operating temperature. In this case, the temperature is essentially uniform. However, since the patch region has a higher stiffness than the surround area, thermal stress would occur. Omitting the details of derivation, expressions of the thermal stresses in the plate and the patch are

$$\sigma_P^T = \begin{cases} -\alpha_P E_P \Delta T \frac{(1+\nu_P)(1-\alpha_R/\alpha_P)S}{2(1-\nu_R)+(1-\nu_P^2)S} & \text{inside patch} \\ \alpha_P E_P \Delta T \frac{(1-\nu_P)(1-\alpha_R/\alpha_P)S}{2(1-\nu_R)+(1-\nu_P^2)S} & \text{outside patch ,} \end{cases} \quad (7.104)$$

$$\sigma_R^T = \alpha_P E_R \Delta T \frac{2(1 - \alpha_R/\alpha_P)}{2(1 - \nu_R) + (1 - \nu_P^2)S} \quad (7.105)$$

Verification of the above presented formulae will be discussed in the next section.

7.7.5. Validation

To validate the present theory and to examine the accuracy of the solution for finite size plate, a detailed finite element analysis is carried out for both an isotropic patch and an orthotropic patch, simulating a cross-ply laminate composite patch. The properties and dimensions of the isotropic patch and the orthotropic patch are summarised in Tables 7.2 and 7.3. The ratios of the outer radius to inner radius, R_o/R_i , will be varied to investigate the size effect. A comparison of the stresses in the plate as obtained using the finite element method and the analytical solutions is shown in Figure 7.23. It is seen that the closed-form solution [18] is in very good agreement with the finite element results. More importantly the solution based on an equivalent isotropic reinforcement, which takes the major properties of the orthotropic reinforcement, provides a reasonably good correlation with the finite element results.

Table 7.2
Properties and dimensions of isotropic reinforcement.

Material	Young's modulus (GPa)	Poisson's ratio	Thickness (mm)	Thermal coefficient
Plate	71	0.3	1.0	23×10^{-6}
Reinforcement	156	0.3	0.5	6.24×10^{-6}

Table 7.3
Properties and dimensions of orthotropic reinforcement.

Material	Young's modulus (GPa)	Poisson's ratio	Thickness (mm)	Thermal coefficient
Plate	71	0.3	3.0	23×10^{-6}
Reinforcement	$E_1 = 156$ $E_2 = 29.7$	$\nu_{21} = 0.1097$ $\nu_{12} = 0.5762$	1.5	$\alpha_1 = 6.24 \times 10^{-6}$ $\alpha_2 = 16.96 \times 10^{-6}$

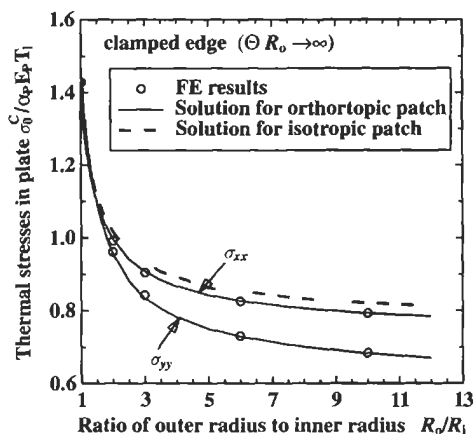


Fig. 7.23. Thermal residual stress resulting from cooling a circular patch over a concentric plate with outer edge being clamped.

References

1. Baker, A.A. and Jones, R. (ed.) (1988). *Bonded Repair of Aircraft Structures*, Martinus Nijhoff Publishers.
2. Baker, A.A. (1993). Repair efficiency in fatigue-cracked aluminium components reinforced with boron/epoxy patches. *Fatigue Fract. Engng. Mater. Struct.*, **16**(7), pp. 753–765.
3. Eshelby, J.D. (1957). The determination of the elastic field of an ellipsoidal inclusion, and related problems. *Proceedings of Royal Society of London*, **A241**, pp. 376–396.
4. Goland, M. and Reissner, E. (1944). The stresses in cemented joints. *J. Appl. Mech.*, **11**, pp. A17–A27.
5. Hart-Smith, L.J. (1982). Induced peel stresses in adhesively bonded joints, Douglas Aircraft Company, MDC J9422A.
6. Jones, R. (1988). Crack patching: design aspects, in *Bonded Repair of Aircraft Structures* (A.A. Baker and R. Jones, eds.). Martinus Nijhoff Publishers, pp. 40–76.
7. Ratwani, M.M. (1979). Cracked, adhesively bonded laminated structures. *AIAA Journal*, **17**(9), pp. 988–994.
8. Rose, L.R.F. (1981). An application of the inclusion analogy for bonded reinforcements. *Int. J. Solids and Structures*, **17**, pp. 827–838.
9. Rose, L.R.F. (1982). A cracked plate repaired by bonded reinforcements. *Int. J. Fracture*, **18**(2), pp. 135–144.
10. Rose, L.R.F. (1987). Crack reinforcement by distributed springs. *J. Mech. Phys. Solids*, **35**(4), pp. 383–405.

11. Rose, L.R.F. (1988). Theoretical analysis of crack patching, in *Bonded Repair of Aircraft Structures* (A.A. Baker and R. Jones, eds.). Martinus Nijhoff Publishers, pp. 77–105.
12. Wang, C.H., Rose, L.F.R. and Callinan, R. (1998). Analysis of out-of-plane bending in one-sided repair. *Int. J. of Solids and Structures*, **35**, pp. 1653–1675.
13. Wang, C.H. and Rose, L.R.F. (1997). Determination of triaxial stresses in bonded joints. *Int. J. of Adhesion and Adhesive*, **17**, pp. 17–25.
14. Wang, C.H. and Rose, L.F.R. (1998). Bonded repair of cracks under mixed mode loading. *Int. J. of Solids and Structures*, **35**, pp. 2749–2773.
15. Wang, C.H., Heller, M. and Rose, L.R.F. (1998). Substrate stress concentrations in bonded lap joints. *J. of Strain Analysis*, **33**, pp. 331–346.
16. Wang, C.H., Heller, M. and Rose, L.R.F. (1998). Substrate stress concentrations in bonded lap joints. *J. of Strain Analysis*, **33**, pp. 331–346.
17. Wang, C.H. and Rose, L.R.F. (1999). A crack bridging model for bonded plates subjected to tension and bending. *Int. J. of Solids and Structures*, **36**, pp. 1985–2014.
18. Wang, C.H., Rose, L.R.F., Callinan, R., et al. (1999). Thermal stresses in a plate with a circular reinforcement. *Int. J. of Solids and Structures*, **37**, pp. 4577–4599.
19. Wang, C.H. and Erjavec, D. (1999). Geometrically linear analysis of the thermal stresses in one-sided composite repairs. *J. of Thermal Stresses*, **23**, pp. 833–851.
20. Wang, C.H. and Rose, L.R.F. (2000). Compact solutions for the corner singularity in bonded lap joints. *Int. J. of Adhesion and Adhesives*, **20**, pp. 145–154.
21. Timoshenko, S.P. and Goodier, J.N. (1970). *Theory of Elasticity*, McGraw-Hill Book Company.
22. Lawn, B.R. and Wilshaw, T.R. (1975). *Fracture of Brittle Solids*, Cambridge University Press, Cambridge, UK.
23. Keer, L.M., Lin, C.T. and Mura, T. (1976). Fracture analysis of adhesively bonded sheets. *J. of Applied Mechanics*, **98**(4), pp. 652–656.
24. Hadamard, J. (1952). *Lectures on Cauchy's Problem in Linear Partial Differential Equations*, Dover Publications Inc., New York.
25. PAFEC Users' Manual (1995). PAFEC Limited, Strelley Hall, Nottingham, United Kingdom.
26. ABAQUS (1997). User's manual, Version 5.6, Hibbitt, Karlsson and Sorensen, Inc., Rhode Island.

Chapter 8

RECENT EXPANSIONS IN THE CAPABILITIES OF ROSE'S CLOSED-FORM ANALYSES FOR BONDED CRACK PATCHING¹

Dr. L.J. HART-SMITH

Phantom Works, The Boeing Company, Mail Stop H013-A316, 5301 Bolsa Ave, Huntington Beach, California 92647-2099, U.S.A.

8.1. Introduction

In the beginning, there was the "Blue Book" [1]. This now classic work, commonly referred to as the "Bible" on the subject, contains the outline [2] by Dr. Francis Rose of the analytical methods he developed for bonded crack-patching repairs a long time ago, at what was then known as the Aeronautical Research Laboratory in Fishermans Bend, Melbourne, Australia. These tools provided the understanding that led to the fleet-wide application of composite patches on the C-130 and C-141 metallic wings, making it possible to keep the aircraft flying when riveted repairs would have been ineffective, or possibly even harmful. The techniques were also applied to many other aircraft, some such repairs being described in reference [3] by Dr. Alan Baker, leader of the team at what is now known as AMRL. The present paper shows how these pioneering analyses have been expanded, as part of the Composite Repairs of Aircraft Structures (CRAS) program 1 being conducted at Boeing, in Long Beach, California, under contract to the USAF Research Laboratories at WPAFB, Ohio.

Rose's original analyses were for linearly elastic adhesives. They have been extended to non-linear adhesive behavior in the form of an elastic-plastic adhesive model [4] developed by this author at an even earlier date. Rose's original analyses were for isotropic patches. They have been extended to orthotropic elliptical patches

¹ Several engineers are involved in this program, addressing many issues beyond the coverage of this paper. What *is* addressed here is the portion of the CRAS program focussed on deriving closed-form analyses of the type employed by Dr. Francis Rose, but with a far greater range of applicability than originally envisaged. Also, there are some additional variables not covered in the original work, on which everything presented here is based.

by new analyses that account for both patch material anisotropy and thermal mismatch. Rose's original solution was limited to isotropic patches. (It is surprising how similar the predictions are throughout most of the design domain.) Rose's analyses had erroneously been believed to be limited in applicability to simple flat-plate configurations. It is shown here that they are equally applicable to integrally stiffened structures like wing skins. The introduction of the concept of a "negative-thickness" patch has enabled Rose's solutions to be applied directly to the assessment of the load redistribution associated with local corrosion cavities. Patches over corrosion damage can now be designed using the same tools developed earlier for patching through cracks. These methods, once devised for patching structures that had cracked in service, can also be used to design local reinforcement to be applied at the time of initial manufacture, with the goal of *preventing* the initiation of cracks in service. The methods can even quantify the severe stress concentrations associated with poorly designed stiffener run-outs, which are often terminated short of the ends of integrally stiffened panels in order to simplify the splice plates. In short, Rose's original analyses have opened a veritable Pandora's box of additional capability with which to maintain existing aircraft structures and to design better ones in the future.

(This is not to imply that there are no remaining problems to solve in this discipline. On the contrary, work on new analyses continues in America, England, and Australia, to expand the application of bonded crack patching. But it is unlikely that the impact of Rose's novel use of the inclusion model to generate closed-form solutions for the stresses in and under bonded patches will ever be surpassed by later work.)

8.1.1. Rose's use of the inclusion model to establish stress fields

The issue of interest here, in the simple form analyzed by Rose, in reference [5], is a local perturbation in an otherwise uniformly loaded infinite plate, as shown in Figure 8.1, when the perturbation is in the form of an elliptical inclusion with axes parallel to the principal remote stresses. Rose was able to establish an analogy between this problem, for which an exact solution existed, and the situation of a bonded patch over a local crack in a very large skin.

In the special case of a homogeneous elliptical inclusion of constant thickness in a constant-thickness skin, the stresses in the inclusion are uniform and parallel to the remote stresses. Perhaps the most comprehensive set of solutions for stresses in and around the inclusions, for isotropic inclusions, at least, is to be found in reference [6], where expressions are given for the stresses in and under the patch, and for the radial and tangential stresses just outside the extremities of the patch. Rose's specific solution, for the stress in the skin just outside the ends of the patch, is

$$k_t = \frac{\sigma_y|_{y=B+}}{\sigma_\infty} = \left\{ 1 + \frac{S}{D} \left[1 + 2(1+S) \frac{B}{A} (1-\nu\Sigma) + (1+S-\nu S)(\Sigma-\nu) \right] \right\}, \quad (8.1)$$

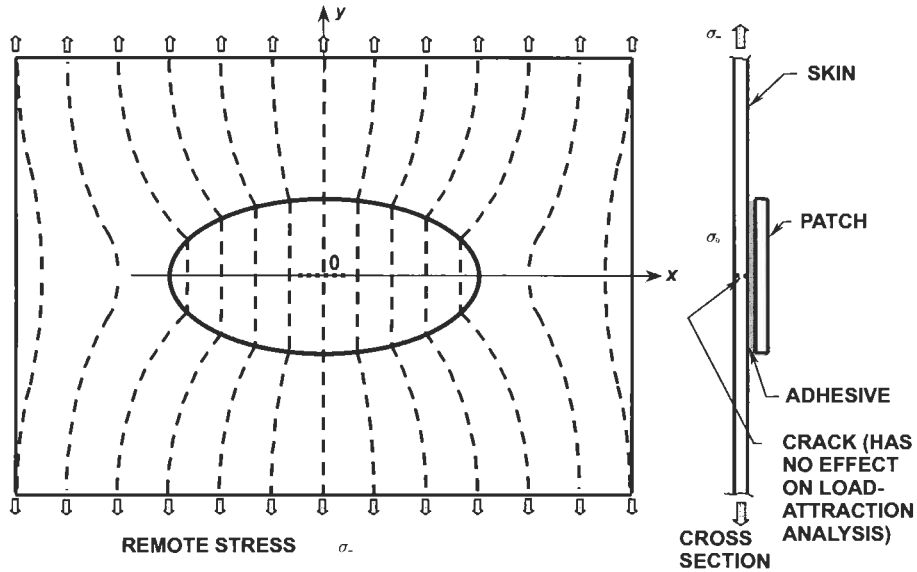


Fig. 8.1. Inclusion model as the basis of analyzing patches and stress concentrations.

in which

$$D = 3(1 + S)^2 + 2(1 + S) \left[\frac{B}{A} + \frac{A}{B} + \nu S \right] + 1 - \nu^2 S^2, \quad (8.2)$$

The stress in the patch, under the skin, is related to the remote stress perpendicular to the crack by

$$\frac{\sigma_0}{\sigma_{y\infty}} = \frac{k_t}{(1 + S)}, \quad (8.3)$$

Yes, this powerful solution is no more complicated than these simple explicit expressions. Here σ defines a variety of stress components, ν is the Poisson's ratio that is taken to be common for both skin and patch, $\Sigma = \sigma_{x\infty}/\sigma_{y\infty}$ is the ratio of the remote stress parallel to the crack, in the x direction, to the dominant stress component perpendicular to the crack, in the y direction. The width and length of the elliptical patch are $2A$ and $2B$, in the x and y directions, respectively, and S is the patch stiffening ratio $(Et)_{\text{patch}}/(Et)_{\text{skin}}$. The location of the crack and locations remote from the crack are identified by the subscripts 0 and ∞ , respectively, along the y axis. The crack extends for a total distance of $2a$ in the x direction, as shown in Figure 8.1, symmetrically about the y axis.

The brilliance of Rose's analysis is that, even though the load transfer through the bonded joint around the periphery of the patch is *not* instantaneous in the manner of the inclusion model, it is so close to it that the differences have no effect in the vicinity of the crack. Similarly, a crack, no matter how long it is, has no

significant width, as long as the skin on each side of it remains bonded to the patch. Rose was able to *separate* the two steps of his analysis without any significant loss of accuracy. The first stage, referred to as the load-attraction analysis, establishes the stress in and under the patch, and in the skin just outside each end of the patch, by neglecting the presence of the crack (or other local damage). This leads to the establishment of one uniform set of stresses in the skin, parallel to the axes of the elliptical patch, and a parallel second set of uniform stresses in the patch. The analysis of the immediate vicinity of the crack, which constitutes the second stage, then proceeds as if the patch extended uniformly to infinity.

8.1.2. Rose's solution for stress-intensity factor K at the crack tips

The second stage in Rose's analysis establishes the crack-tip stress-intensity factor K , as affected by the bonded patch, from which it is possible to establish the reduced (or zero) rate of subsequent crack growth. This is customarily referred to as the constant- K solution, which is discussed below. As long as the crack does not progress to the sides of the patch, any subsequent crack growth will be at a constant rate – provided, in addition, that there are no disbonds adjacent to the crack.² This has been confirmed by tests, but it had already been explained by Rose's analysis. When a long crack in the skin is covered by an adhesively bonded patch, it is effectively reduced to two very short half-cracks, each of length Λ , separated by a bonded joint throughout which the crack opening is constant. Rose's result for this characteristic length is

$$\Lambda = \frac{1}{\pi\lambda} \left(1 + \frac{1}{S} \right), \quad (8.4)$$

in which λ (Rose uses the symbol β for this purpose) is the exponent of the adhesive shear stress distribution given by

$$\lambda^2 = \frac{G}{t_a} \frac{1}{E_{\text{skin}} t_{\text{skin}}} \left(1 + \frac{1}{S} \right), \quad (8.5)$$

in which the additional terms are G for the adhesive shear modulus, t_a for the thickness of the adhesive layer, t_{skin} for the thickness of the skin, and E_{skin} for the Young's modulus of the skin.

Rose's expression for the crack-tip stress-intensity factor, which determines crack growth rates once the crack has grown long enough for the bonded-joint load path to limit any further crack opening, is

$$K_{\infty} = \sigma_0 \sqrt{\pi\Lambda}, \quad (8.6)$$

²There is a further exception, for very "short" cracks. If a crack is so short, in relation to governing parameters, that its crack growth rate has not yet built up to its stable value, an initially increasing crack rate would be followed by a long period of constancy.

Were it not for the bonded patch, the crack would grow at an ever increasing rate governed by the solution for an unpatched crack:

$$K_0 = \sigma_0 \sqrt{\pi a} . \quad (8.7)$$

Rose's characteristic length is typically very short, so the reduction in stress intensity is very important. Indeed, it is now apparent that the residual thermal stresses induced by hot bonding of composite patches are so severe that bonded crack patches would be relatively ineffective were it not for this particular mechanism.

The total length $2a$ of the crack does not then control any subsequent crack growth rate, unless the patch or bond is broken. The physics of these phenomena are depicted in Figure 8.2.

Rose's mathematical explanation of these phenomena is shown in Figure 8.3, in which his two asymptotic equations are portrayed. The first, for very short cracks, assumes that the adhesive is so flexible that the patch cannot restrain the crack opening. The second is in the form of a plateau, established by Rose's bonded-joint analogy. The point at which these two independent solutions cross defines the effective crack length 2Λ . This characteristic length, which Rose defined in terms of adhesive, skin, and patch properties, reliably represents the crack growth rate once the crack has grown beyond that length, which is usually extremely short and far less than critical lengths for unrepaired cracks. If the skin is thin enough, and the adhesive strong enough, the value of K can be reduced below the threshold for any subsequent crack growth, completely "killing" the crack. If not, the rate of growth will be retarded, in accordance with the difference between the patched K , shown in non-dimensionalized form as unity, and the projection of the curve shown for unrepaired cracks.

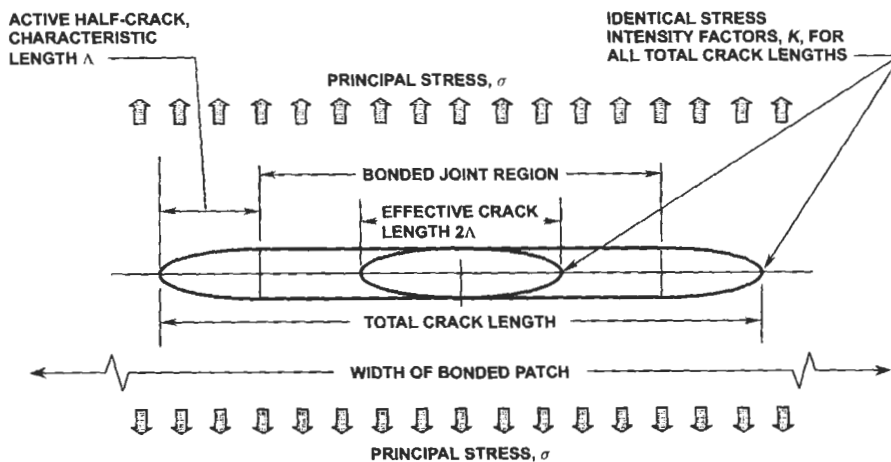


Fig. 8.2. Patched crack model as bonded joint separating two short fixed-length half-cracks.

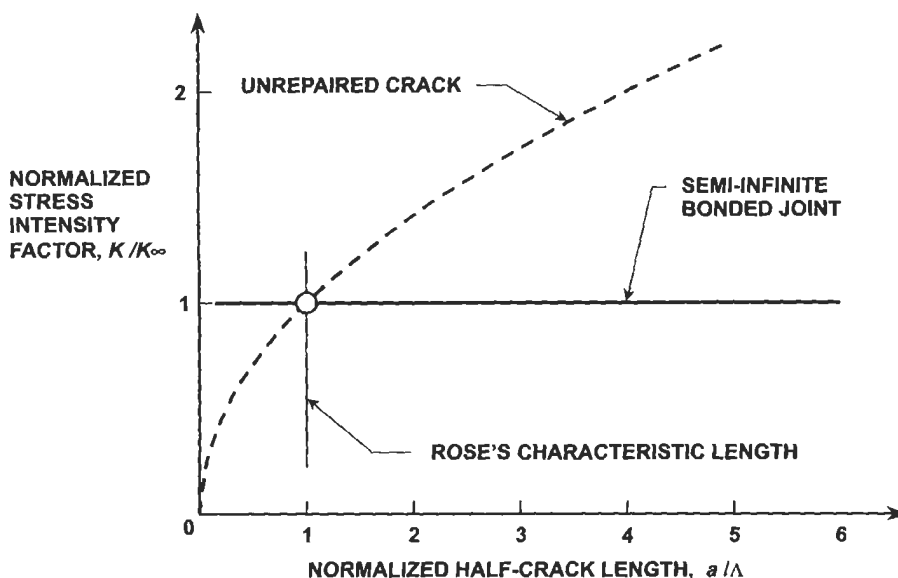


Fig. 8.3. Rose's solution for crack-tip stress-intensity factor under bonded patch.

Whereas the overall understanding of these phenomena has been cleverly explained by Rose, there is an inherent problem in his transitional formula. This is of no numerical consequence if the adhesive remains linearly elastic regardless of the crack length. However, it is simply not possible, according to his Eq. (5.23a) in reference [2] for the crack to ever grow long enough to exceed the elastic capability of the adhesive. In reference [7], the present author added a compatibility-of-deformations analysis to those by Rose and established a slightly different transitional formula in which K reached its limiting value (for elastic behavior) at a crack length exactly four times as long as that defined by Rose's characteristic length 2Λ . This modification, which does not change the significance of Λ in relation to the plateau level of K , is shown in Figure 8.4.

While the values of the two solutions are not all that different, because they are both governed by the same two limiting equations, this modification is necessary as a *prelude* to being able to analyze for the effects of adhesive non-linearity (plasticity) that are discussed later.

Although not discussed here, Rose's analyses do address the stresses in the adhesive as the load is transferred through very narrow zones adjacent to the crack and the periphery of the patch. In addition, there is an explanation of the thermal stresses induced by bonding composite patches that are thermally dissimilar to the underlying metallic skins, resulting in the crack often being preloaded in the opening mode before any mechanical load is applied. Rose and his colleagues have improved upon this aspect, in reference [8]. The effects of the constraint provided by surrounding structure that is not heated during the cure process are discussed later, now that the CRAS team has developed a model that can be compared to

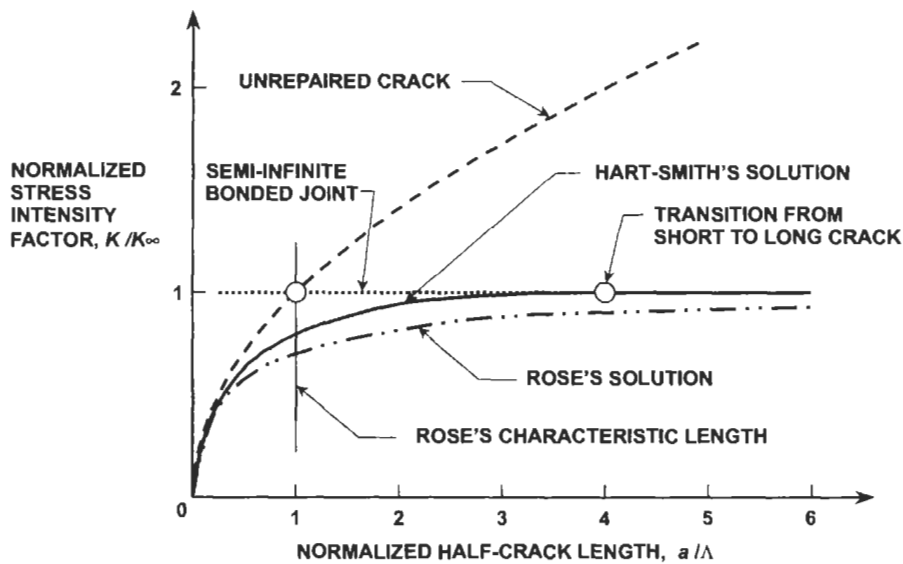


Fig. 8.4. Hart-Smith's refinement of Rose's solution for crack-tip stress-intensity factors.

those of Rose and his colleagues. The original analysis in reference [2] also includes an accounting of the geometrically non-linear out-of-plane bending associated with one-sided patches, an issue also addressed in reference [9]. In short, while they left room for others to improve upon their work, Rose and his colleagues made *the* major contribution to this field by developing explicit comprehensible models governing the dominant variables in the design of bonded patches for cracked metallic structures.

8.2. Universal efficiency charts for isotropic patches

Rose's original analyses are in closed form, making it easy to perform parametric studies of the effects of the governing variables. This is an attribute inevitably lost whenever total reliance is placed on finite-element analysis, no matter what *other* benefits may be added in the form of being able to analyze non-standard geometries for which no closed-form solution exists. The CRAS team took visualization of the results one stage further when it was recognized that Rose's Stage I equations could be plotted in the form of an almost universal preliminary design chart.

This chart, presented in Figure 8.5, makes it easy to understand the effects of patch stiffening ratio and of the aspect ratio of elliptical patches. There is no universal "best" point design, but it is clear that excessive stiffening ratios are to be avoided because they dump so much load into the skin at the ends of the patch. In the terminology of Figure 8.5, k_t is then too high. Long, skinny, patches (high B/A ratios) are also to be avoided, for the same reason. Long patches are also seen to be

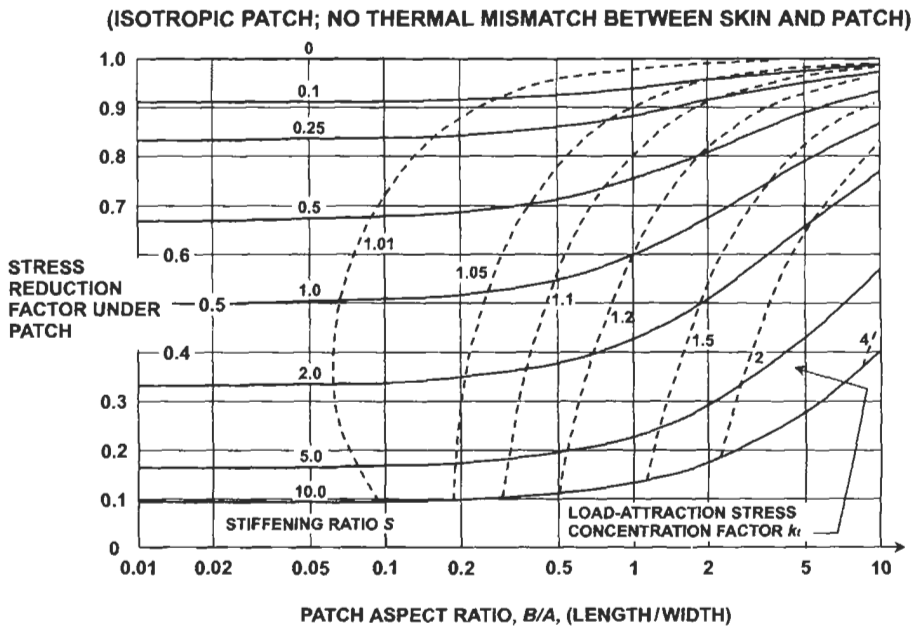


Fig. 8.5. Patch design chart for isotropic patches, showing stress reduction under patch and load attraction at ends of patch as functions of patch stiffening ratio and shape.

less effective than wide patches in reducing the stress level beneath the bonded patch, in the skin around the crack, as defined by the ratio σ_0/σ_∞ , where the stress in the denominator is the remote stress at infinity, perpendicular to the crack.

This same informative depiction of the analyses is used here, later, to show the effects of corrosion cavities and of orthotropic composite patch materials. The specific solutions in Figure 8.5 are effectively restricted to isotropic patches made from the same material as in the basic structure, because they omit consideration of residual thermal stresses induced by bonding or co-curing thermally dissimilar skins and patches together. Nevertheless, it will be seen that these are still a useful approximations for practical composite patch fiber patterns, which are not all -0° plies, despite the fact that these are the only plies to contribute appreciably to holding the crack tip shut. The Warner Robins team in Georgia, led by Bill Schweinberg, has found that composite patches are prone to longitudinal splitting if too few transverse plies are included in the design. The latest CRAS analyses for orthotropic patches include provision for assessing this phenomenon.

8.3. Equivalence between octagonal and elliptical patch shapes

The closed-form analyses of the type pioneered by Francis Rose are restricted to elliptical patches only because this is the only shape for which explicit closed-form

solutions are possible. Most of the patches actually applied are octagonal in shape because it is difficult to trim boron-epoxy patches to an elliptical shape. The CRAS team has approached this issue from two directions. A power-series solution was developed by Duong, in reference [10], for octagonal patches. This overcame the restriction, albeit at the expense of considerable added complexity and the introduction of mathematical singularities at each corner of the patch. These are not physically significant, however, because the flexibility of the adhesive there would eliminate them from more detailed analyses. More significantly in the present context, another CRAS member, J.J. Wang, used this analysis to establish that, while the stress surrounding the crack under typical octagonal patches is not absolutely uniform, as it would be for truly elliptical patches, it is very close to uniform until the crack length $2a$ approaches the width $2A$ of the patch. It was also shown to be within a few percent of the Rose's solution for an elliptical shape that circumscribed the octagon. This author approached the same problem from a different perspective, reasoning that the stress field outside the patch would be determined by the *volume* of the patch, which is uniformly stressed in Rose's solution. Therefore, there should be an *equivalent* elliptical patch for each octagonal patch – one that would create both the same nominally uniform stress around the crack and the same intensity of load attraction at the end of the patch. The ideal equivalent elliptical and octagonal shapes for uniformly thick patches are identified in Figure 8.6, which also presents Wang's solution. The designs are seen to be very similar, confirming that analyses for elliptical patches *can* be applied as reasonable approximations to *some* octagonal patches. The restriction to elliptical patch shapes may not be a serious limitation on the applicability of Rose's analyses, after all.

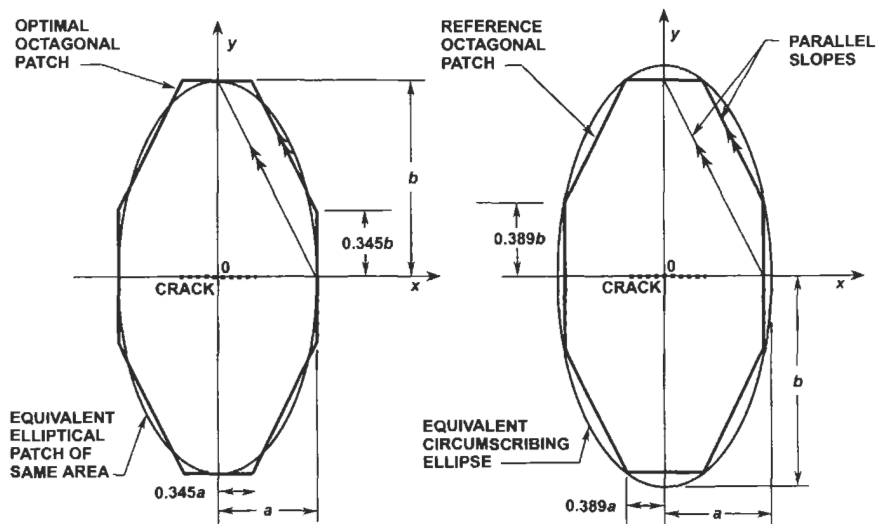


Fig. 8.6. Equivalence between elliptical and octagonal bonded patches of uniform thickness.

If the trimming of the corners of the octagonal patch does not match that shown in Figure 8.6, one could use the (as yet unverified) techniques suggested in reference [11] to deduce an equivalent elliptical patch shape on which to base the present level of analyses. It should be noted, however, that the use of an octagonal shape with far more or far less trimmed off the corners than is suggested in Figure 8.6 will result in less effective stress reduction under the patch or in more severe load attraction at the ends of the patch.³

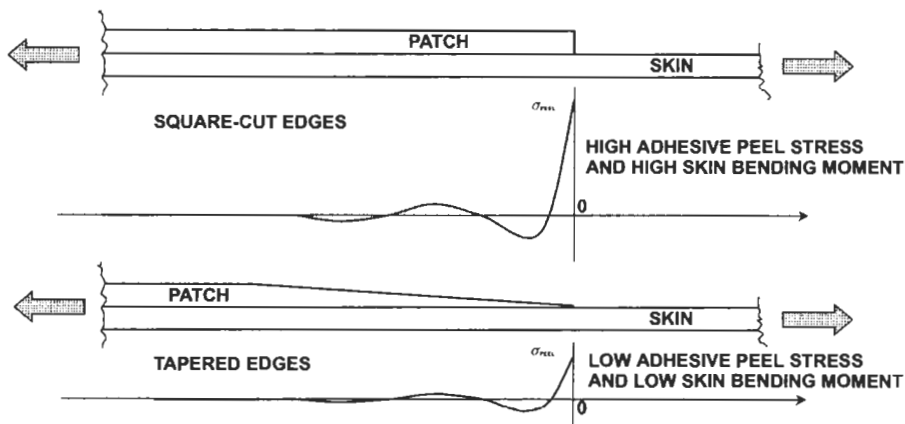
8.4. Effects of patch tapering on the adhesive stresses

The nature of load transfer through adhesive bonds whereby virtually all of the transfer is confined to the immediate vicinity of any discontinuity in load patch, such as at a crack and at the ends of the patch, means that the exact distribution of the adhesive stresses and strains has little effect on the skin and patch stresses outside those immediate areas. Therefore, Rose's sequential approach to independent analyses can be employed in this context, too.

In the area immediately adjacent to the crack, the governing conditions will be the stress σ_0 in the skin, reduced with respect to the remote stress σ_∞ , that is interrupted by the crack and diverted through the adhesive into the patch and back to the skin again on the other side of the crack. Even though it is customary not to taper the skin on the back side of the crack to reduce the severity of the adhesive bond stresses, there is significant relief with respect to what a unit-strip analysis along the middle of the patch would predict. In the absence of *any* tapering of the patch at its ends, the adhesive there would be subject to a combination of intense peel stresses, whether for a one-sided patch with out-of-plane bending or for a two-sided symmetric patch with no apparent bending deformations, and shear stresses aggravated by the locally *higher* than nominal skin stresses. It is essential, at least, to apply *local* tapering of the ends of the patch, to reduce the induced peel stresses to a tolerable level. It is customary to reduce the severity of all of these adhesive stresses by far more widespread tapering of the kind shown in Figure 8.7. A slope on 1-in-50 is typical for boron-epoxy patches.⁴ There has been no indication of any problems associated with such tapered patches other than for compressive remote loads or very thick patches – and the problem then is caused by residual thermal stresses, not the tapering.

³ It is intended to publish an assessment of the constant-volume analogy for off-optimum octagonal patches with confirmation of the underlying skin stresses by finite-element analyses at some future date. It is also common practice to use rectangular patches in which the thickness at the ends of the patch have been tapered very gently, to dramatically reduce both the shear and peel stresses in the adhesive at those locations. Whether or not the sharp corners still presented a load-attraction problem after tapering would be established by these same systematic numerical analyses.

⁴ The magnitude of adhesive stresses associated with extensively tapered patches is another issue to be covered by CRAS analyses. The issue of adhesive stresses is not in doubt; the tapering really does work. What has yet to be confirmed is the magnitude of any relief with respect to load attraction, particularly for patches with sharp corners.



NOTE: THE SAME TECHNIQUE ALLEVIATES THE PEAK ADHESIVE SHEAR STRESSES, TOO

Fig. 8.7. Tapering of bonded patches to prevent premature failures at the ends of the overlap.

Even though the process of transferring load through the adhesive is confined to very narrow bands adjacent to the crack or to untapered edges of the patch, there is a minimum overlap needed for the bond to ensure that the adhesive will not fail by creep rupture under sustained loads. There must be a long elastic trough in the adhesive shear-stress distribution to ensure that the minimum adhesive shear stress is sufficiently low to prevent creep in at least *some* of the bonded overlap. An estimate for this length was prepared during the PABST program [12] for bonded double-lap joints that were free from bending effects. This simple formula is

$$\lambda = \frac{P}{\tau_p} + \frac{6}{\lambda}, \quad \text{where} \quad \lambda^2 = \frac{G_a}{t_a} \sqrt{\frac{1}{(Et)_{\text{skin}}} + \frac{1}{(Et)_{\text{patch}}}}. \quad (8.8)$$

Here, P is the load transferred per unit width, per bond layer, τ_p is the peak adhesive shear stress, G_a is the adhesive shear modulus, t_a is the thickness of each adhesive layer, and E and t are the Young's modulus and thickness of the skin and patch, as appropriate. The exponent λ defines the distribution of the adhesive shear stresses. (Rose uses the symbol β for that purpose, but β is already customarily used for other purposes in the context of stress-intensity factors at cracks.) The load P in this equation has traditionally been taken as the remote load $\sigma_\infty t_{\text{skin}}$ in establishing minimum patch lengths. This formula is still good for bonded splices, even though the factor six could be reduced to five as explained below. However, for bonded patches, it is now apparent that this value for P is unnecessarily conservative for the adhesive adjacent to the crack and too low to account for the load attraction at the ends of the patch, where the skin stress is boosted to $(1+S) \sigma_\infty t_{\text{skin}}$, where

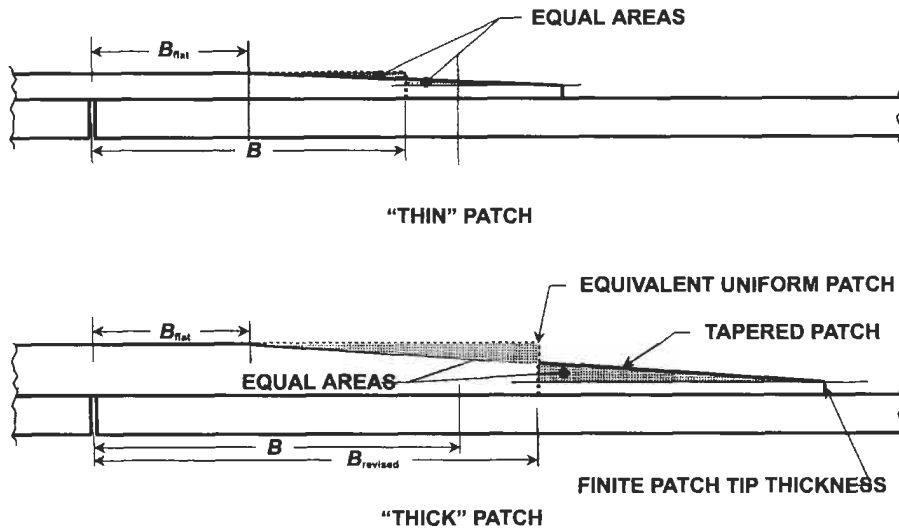


Fig. 8.8. Calculation of equivalent tapered patch length, with respect to nominal length for uniformly thick patch.

$S = [(Et)_{\text{patch}} / (Et)_{\text{skin}}]$ is referred to as the stiffening ratio for the patch. In addition, the process of deducing the bonded overlap λ in Eq. (8.8) as the sum of the lengths of the load-transfer zone(s) and that of the elastic trough has been refined by taking account of the small increment of load transferred through the elastic trough. It is now recommended by the CRAS team to use the formula

$$\lambda = \frac{\sigma_{0\text{skin}} t_{\text{skin}}}{\tau_p} + \frac{5}{\lambda}, \quad \text{where} \quad \lambda^2 = \frac{G_a}{t_a} \sqrt{\frac{1}{(Et)_{\text{skin}}} + \frac{1}{(Et)_{\text{patch}}}}, \quad (8.9)$$

based on conditions in the adhesive adjacent to the crack. If only what is referred to as anti-peel tapering were employed at the ends of the patch, the $\sigma_{\infty} t_{\text{skin}}$, in Eq. (8.9) would be increased by the factor k_t to account for the load attraction.

A taper angle as low as even 1-in-30 is assumed to be sufficient to ensure that the adhesive is more critical adjacent to the crack than at the ends of the patch. The manner in which the tapering extends the length of the patch, for a constant-volume model, is explained in Figure 8.8. The patch width $2A$ is related to the *equivalent* uniformly thick patch length $2B$ in Figure 8.5, not with the *actual* larger tapered patch length.

The manner in which the adhesive shear stresses are influenced by tapering the patch thickness is illustrated schematically in Figure 8.7. With sufficient tapering, the adhesive will always be more critical adjacent to the crack than around the periphery of the patch. The criticality of the adhesive adjacent to the crack can be alleviated by employing a patch on both sides of the cracked skin, or by tapering

the skin on the side opposite the patch as suggested in reference [7]. Obviously, either of these approaches relies on there being access to both sides of the skin. A slight tapering on the patch side, to thicken the adhesive layer locally in the manner commonly used to relieve induced peel stresses, would also add to the flexibility of the patch across the crack, resulting in a higher value of the stress intensity factor K . Consequently, tapering the skin on the patch side would be counterproductive. In the absence of access to both sides of the patch, the only way to enhance the effectiveness of the bonded patch in restraining the opening of the crack is to use a stepped patch like that shown in reference [7], after the manner employed by the RAAF for damage to skins too thick to be repaired by standard one-sided patches.

8.5. Universal charts for the effects of corrosion

If Rose's calculations for the load attraction caused by an inclusion that was stiffer than the basic skin were extended to one that was *less* stiff, it would be possible to characterize the effects of local loss of material due to corrosion. This can be done simply by replacing the customary positive patch thickness and stiffening ratio by negative values. No changes are needed in Rose's equations because, in this case, the "patch" material really is isotropic, and the same as the material in the skin. Figure 8.9 shows the results of such calculations, for varying depths of corrosion, which is modeled as a uniformly deep elliptical corrosion cavity with axes aligned with the principal remote stresses. As before, the *volume* of the corrosion damage is the same as for the actual loss of material. Thus, the plan

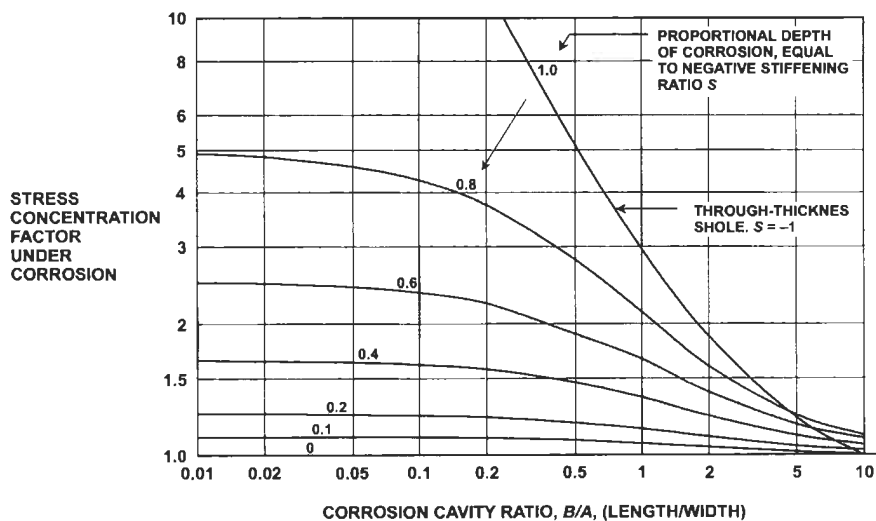


Fig. 8.9. Universal design charts with which to characterize the effects of local corrosion.

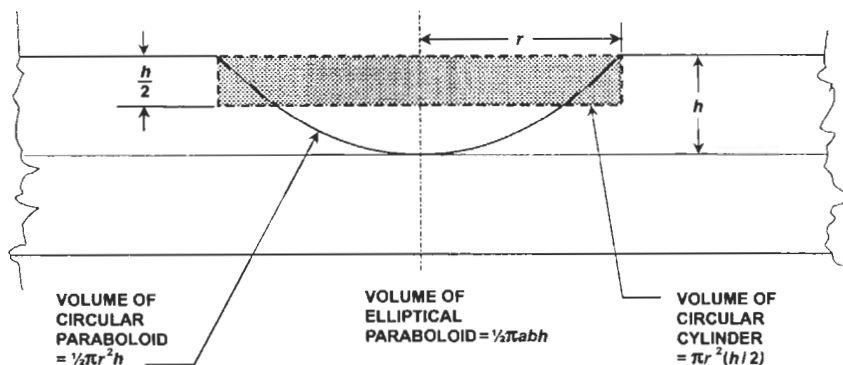


Fig. 8.10. Geometric details of the actual and as-modeled corrosion cavity.

form of the idealized corrosion cavity is an ellipse, with axes oriented parallel to the remote principal stresses, with an area roughly equal to that of the actual corrosion.

In contrast with the bonded patches, there is no increase in skin stress at the ends of the cavities. Indeed, there is a reduction in *average* longitudinal stress there, although, in reality, the peak value remains constant at the ends of the patch. This stress diffuses into the uniform lower value a slight distance outside the cavity. With the cavity, including the extreme case of a through-thickness hole, the stress concentration of concern is the tangential skin stress just beyond the sides of the patch, in the area for which the classical stress concentration factor of three applies for circular holes interrupting a uniform uniaxial load. Of course, if the corrosion damage is not blended out smoothly, there can also be concern about stresses at the sharp corners around the base of the corrosion cavity, as indicated in Figure 8.10. In any event, while analysis is for a uniformly deep approximation to the actual variable damage, finite-element analyses have confirmed the expected still higher value at the thinnest section below the cavity. The present method of analysis can be applied a second time, as explained in reference [4], to refine the estimate from the present analysis.

Figure 8.9 appears to confirm the classic stress-concentration factor of three for a full-thickness circular hole. Actually, this is not so. The formula for the tangential stress *outside* the cavity is slightly different from that for the stress *under* the cavity, as is shown in reference [4].

Experience has often shown that the best thing to do about local corrosion damage is to blend it out smoothly, removing the corroded material, and *not* to repair it, since repairs will raise the stress level by attracting more load. The analysis embodied in Figure 8.9 confirms these findings. Whereas a short wide patch is better than a long skinny patch over a crack in a skin, as indicated in Figure 8.5, the converse is true for minimizing the interruption of a uniform uniaxial stress by a corrosion cavity, as shown in Figure 8.9. (In both cases, of course, a closer to circular shape would be best for equal biaxial remote stresses.)

8.6. Design of patches to compensate for corrosion damage

In the event that corrosion has been sufficiently extensive that repairs are needed, an adhesively bonded patch can be the best option, since it requires no holes through the original structure. Nevertheless, for widespread surface corrosion rather than isolated deep cavities, it can be necessary to take a small surfacing cut to level out sufficient of the area to be bonded that the adhesive can effectively transfer loads between the skin and the patch. If the adhesive layer is too variable in thickness, virtually all of the load will be transferred through the thinnest bond areas. Worse, the load that *should* have been transmitted through the thicker bond areas will be diverted and overload the thin bonds even more. If the underlying structure is metallic, which is likely since composites do not corrode, and there are no sharp cracks in the damage, the *best* patch material is more of the *same* metal, to avoid generating residual thermal stresses that would be tensile if a composite patch were bonded to a metallic skin. (Likewise, if a patch were being bonded over impact damage to a composite skin, the patch material should be the same composite material and fiber pattern for precisely the same reason.⁵)

The process for designing a patch over a small finite area of damage is much the same as for a patch over a skin crack, except that the use of Rose's two-stage analysis now ought to require that the patch dimensions be about three times larger than the damaged area. If this is not possible, because the corrosion is too widespread, there will be a small error caused by following this procedure, but not as great an error as would ensue from totally neglecting the load-attraction aspects of the patch. The one refinement that has been incorporated in reference [13] is to allow for a decrease in load attraction because of the added flexibility created by the corrosion in the skin, as explained in Figure 8.11. The effect on the total inclusion, skin *and* patch, would be proportionally less, and would require

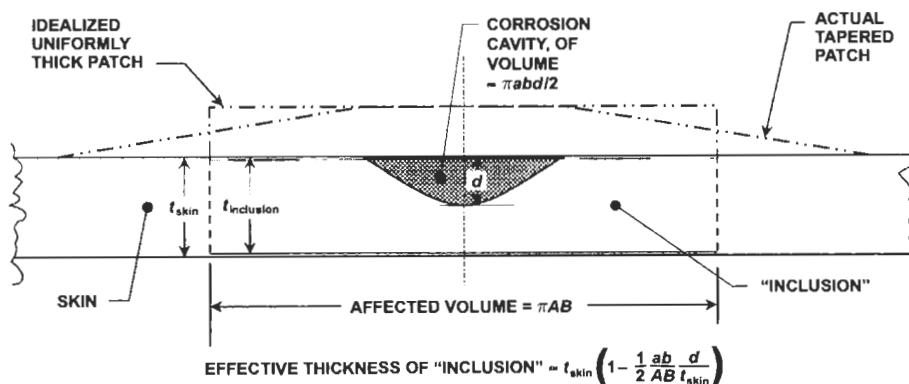


Fig. 8.11. Refinement included in the process of designing patches over corrosion cavities.

⁵ For cosmetic (non-structural) repairs to fibrous composite structures, it is common practice to use low-modulus glass fibres throughout the patch to limit the load it will attract.

accounting for any different elastic properties between the two. Otherwise, the new analysis and that by Rose are identical, except for the absence of critical adhesive conditions at the crack that is not there. With gently tapered patches, it is unlikely that the adhesive will ever become critical in such a case. With no crack from which to establish a crack-tip stress-intensity factor K or an effective crack tip half-length Λ , life predictions for the patched structure are based on the reduced stress level σ_0 created under the patch.

Again we see a previously unrecognized field of application of Rose's analysis that can assist in keeping even more aircraft airworthy while adding to existing damage far less than conventional riveted repairs would.

8.7. Analysis of patches over cracks in stiffened panels

It is a commonly held, but totally erroneous, belief that Rose's methods of analysis are restricted to simple *unstiffened* skins, probably because the application of the method was first reported in that context. However, as shown in reference [14], the original formulation is directly applicable to many of the most common stiffened-panel problems, too. Whenever there is a primary unidirectional load parallel to the stiffeners, as with wing skins under bending loads, for instance, the area in the stiffener can simply be flattened out and added to the skin, as if by unfolding the original structure, as shown in Figure 8.12, or by refolding it as shown in Figure 8.13.

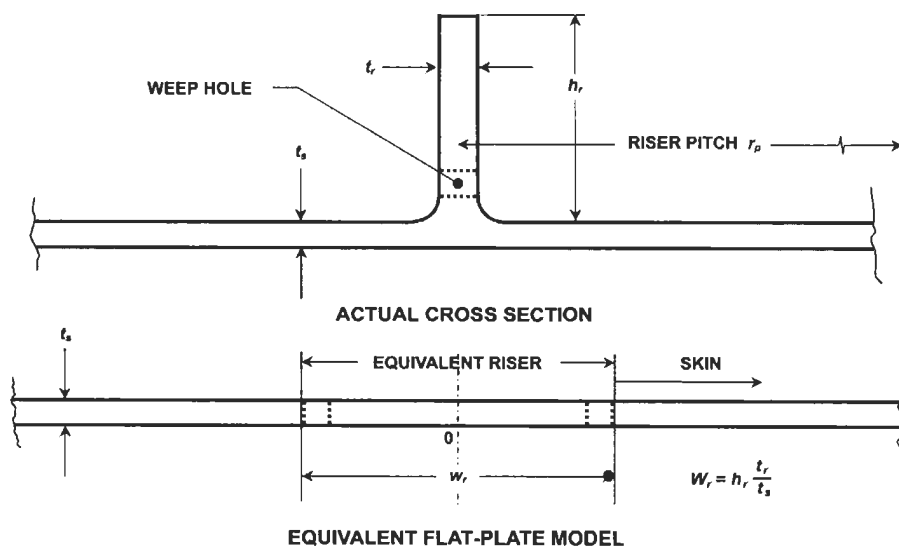


Fig. 8.12. Conversion of stiffened skin construction into equivalent infinite uniform flat plate.

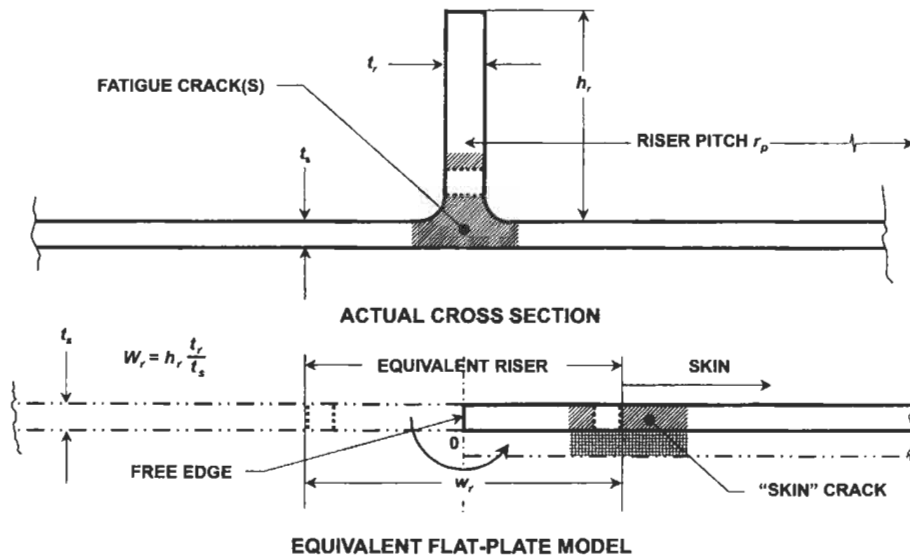


Fig. 8.13. Conversion of stiffened skin construction into equivalent semi-infinite uniform flat plate.

The choice between these two approaches depends on the location of the initial damage, and whether or not a crack has developed in the skin or in a stiffener. With a cracked stiffener and an intact skin, the approach in Figure 8.12 would be preferable because the transformed damage is a simple single crack in the middle of an infinite sheet. A crack in the skin, with the stiffeners intact, is better represented by the model in Figure 8.13, with a crack near the edge of a semi-infinite plate, because of the complexity of the process for computing crack-tip stress-intensity factors for two disconnected cracks in proximity. Either model would work equally well for Step I of Rose's analysis to establish the stress fields near the damage. It is only in Stage II that the right choice needs to be made.

Figure 8.14 shows the design of a sample patch to limit further growth of cracks initiating at weep holes in stiffened wing skins. Such cracks have been found in service on both the C-141 and F-111 aircraft. The derivation of this design is reported in reference [14], using only Rose's equations to assess the load attraction and the skin stress under the patch. When flattened out, the aspect ratio B/A for the equivalent single total patch is far smaller than for each individual patch segment.

The same approach is equally applicable for repair of damage from local corrosion, too. This technique is most obviously applicable for spanwise stresses caused by a dominant wing-bending load case. If the primary load were one of torsion, the stiffeners would be far less effective. Indeed, in a case of pure in-plane shear loading, there would be no significant stress in the stringers at all. Their influence would therefore be minimal and it would then be appropriate to omit them from such an analysis.

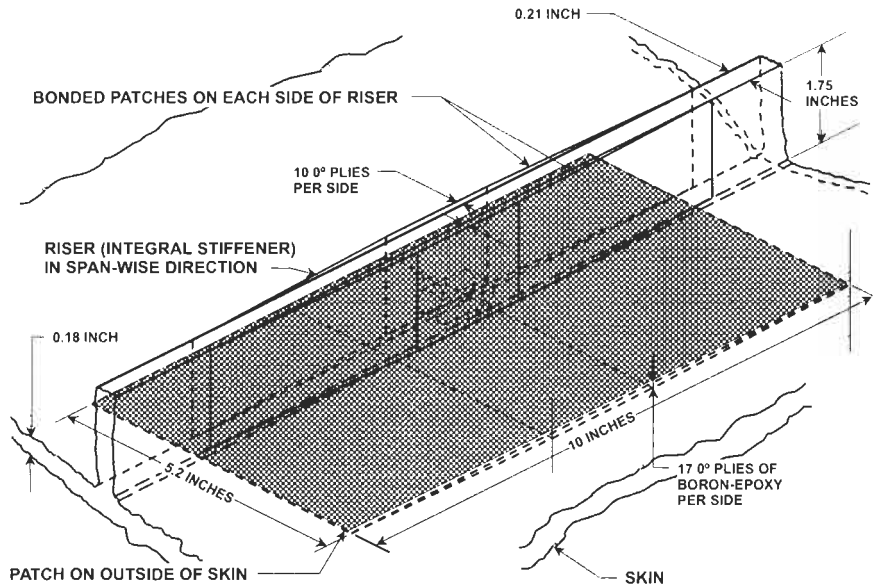


Fig. 8.14. Typical design of bonded repairs for cracks in stiffened structures.

8.8. Designing to avoid crack initiation

The very same analyses could also be used to establish how much local reinforcement would be needed to *prevent* the occurrence of cracks at such local stress concentrations. Exactly the same analysis would be used, since no allowance was made in Stage I of the analysis for any adhesive flexibility. Consequently, the same result would be predicted if there were not any adhesive and the “patch” was now part of the original structure. Such local reinforcement obviously attracts more load than would be present in the absence of any local reinforcement, and Rose’s adaptation of the inclusion model is the perfect tool for assessing the situation. Figure 8.15 shows the result of the analysis/design process corresponding to that in Figure 8.14. The integral reinforcement can be more compact because there is no need to consider any load-transfer lengths through an adhesive layer that is far weaker than the metal in an integral patch.

Yet again, it should be noted that this design was prepared with no analysis/design tools other than those developed by Rose in reference [2].

As noted earlier, stress concentrations caused by holes in integrally stiffened structures are usually far less of a problem than inappropriately designed stiffener run-outs – because the latter are only rarely recognized as such, no matter how many times such problems had been encountered in the past. Now, at last, it will be possible to reliably and simply estimate such stress concentrations. In the limit, for very long stiffeners terminated too abruptly inside the edges of any panel subjected to in-plane loads around its boundary, the associated stress concentration factor is

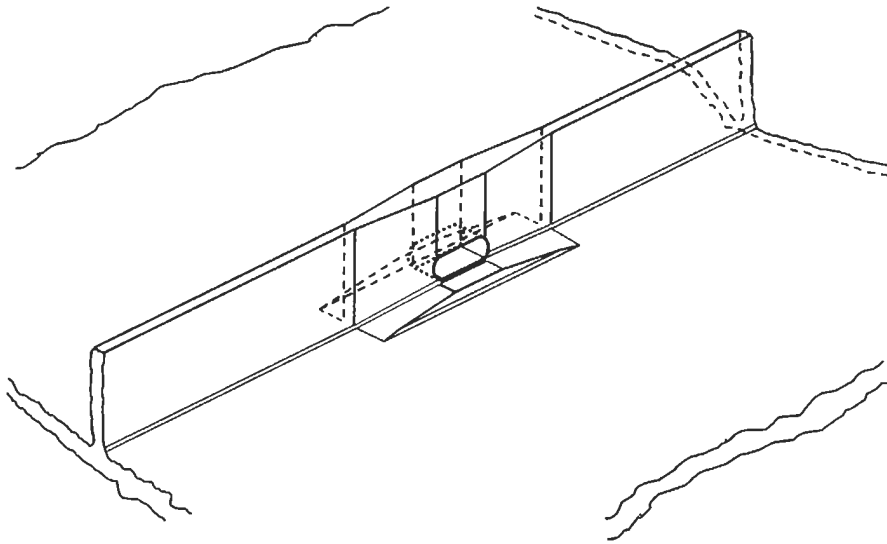


Fig. 8.15. Typical design of integral local reinforcement to prevent cracks in stiffened structures.

given by

$$k_t = 1 + \frac{A_{\text{stringer}}}{t_{\text{stringer}} \times t_{\text{skin}}} \quad \text{in general ,} \quad (8.10)$$

$$k_t = 1 + \frac{h_{\text{stringer}}}{t_{\text{skin}}} \quad \text{for blade stiffeners .}$$

Here, h is the depth of the blade stringer, assumed to be of locally constant thickness. The effective height would be greater if the stringer included an interrupted inner flange as well. Stress concentrations in excess of 10 from this source are not at all uncommon. Rivet holes usually generate stress concentration factors of only about three – lower if the holes have been cold-worked and somewhat higher if designed to excessive bearing stresses. However, the cure for the stringer run-out problem is *not* local reinforcement; it is continuing the stiffeners uninterrupted from one end of the panel to the other, as shown in Figure 8.16, even if doing so does complicate skin splices and frame/stringer intersections.

An exactly analogous situation arises with the traditionally segmented shear ties between frames and fuselage skins. The end rivets of each segment act as hard points, attracting considerable load and sometimes initiating fatigue cracks. Again, the load on these end rivets can be estimated reliably without the need for complex finite-element models by simply assuming a common circumferential strain and sharing the interrupted load in the shear ties between the skin and the frame. Experience has shown that the frame can suffer from the same problem; it need not be confined to the skin.

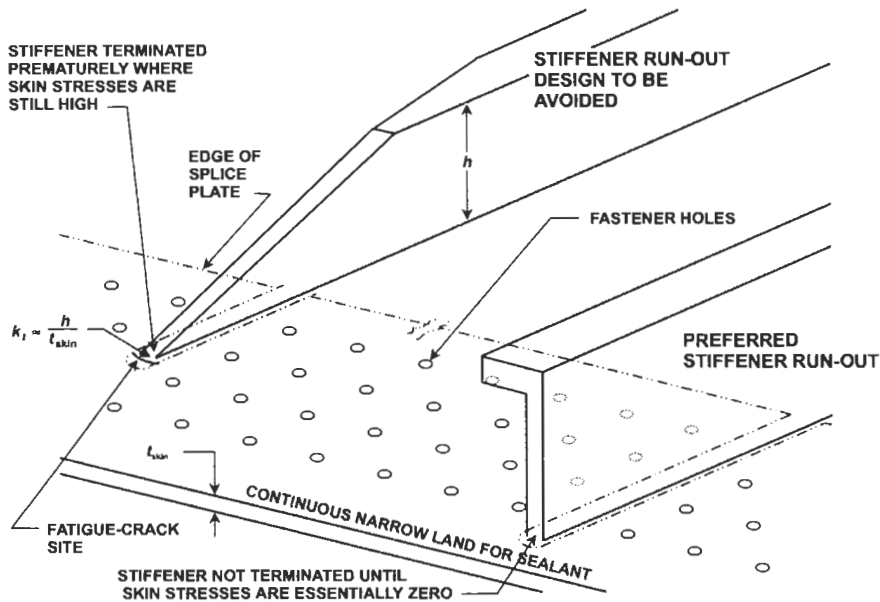


Fig. 8.16. Preferred and undesirable stringer run-outs.

8.9. Universal efficiency charts for orthotropic patches

So far, attention has focussed on mainly further applications of Rose's original analysis methods. This section, and the next, addresses *extensions* of Rose's pioneering work, using the same *kind* of analyses. Rose's solution in Eqs. (8.1) through (8.3) has been simplified by the assumption of an isotropic patch as well as an isotropic skin, for a common Poisson's ratio throughout. In a new derivation reported in reference [15], these limitations have been lifted, even though the new solutions are still formulated in terms of elliptical patches. These analyses include biaxial remote loads aligned with the axes of the patch and crack, orthotropic patch properties, thermal dissimilarity between skin and patch, and the effects of constraints from surrounding structure as the area to be patched is hated to cure the adhesive. For the special case of a unidirectional composite patch, it is reasonable to set the transverse patch stiffness to zero. In this case, for a uniaxial remote load perpendicular to the crack and parallel to the fibers in the patch, Rose's solution is replaced by

$$\frac{\sigma_{y0}}{\sigma_{y\infty}} = \frac{(1-\nu^2)}{D} \left\{ \left[1 + 2\left(\frac{A}{B}\right) \right] \left[\left[1 + 2\left(\frac{B}{A}\right) \right] (1-\nu^2) + \nu(1-\nu)S_y \right] - (1-\nu^2) - 2\nu\left(\frac{A}{B}\right)S_y \right\}, \quad (8.11)$$

while the stress concentration in the skin, just outside the ends of the patch, would likewise *not* be the simplistic approximation $(1+S_y)(\sigma_{y0}/\sigma_{y\infty})$ but would be

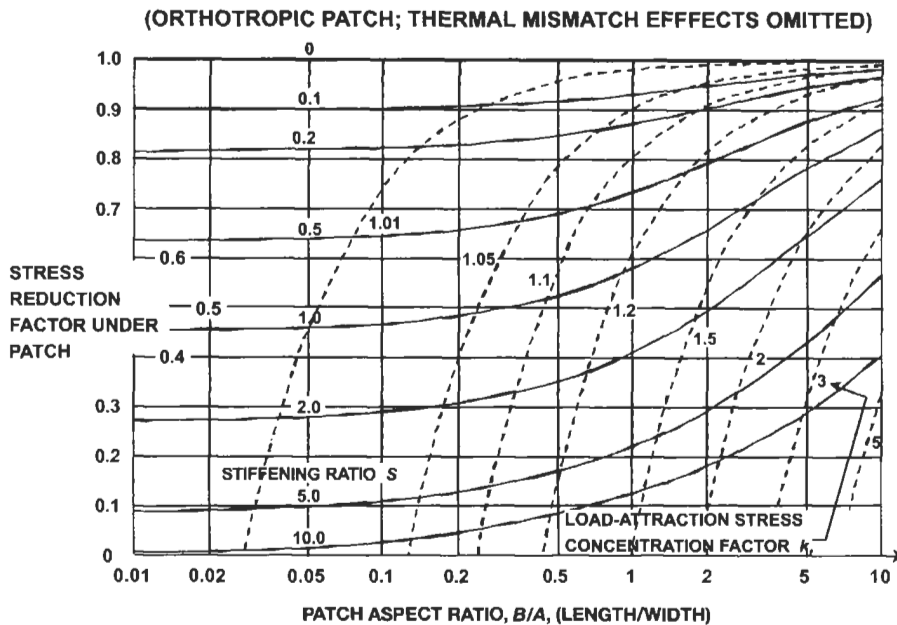


Fig. 8.17. Patch design chart for unidirectional composite patches, showing stress reduction under patch and load attraction at ends of patch, as functions of patch stiffening ratio and shape.

determined by adding the forces, in the y direction, in the skin and patch, in accordance with the new solution. This result is plotted in Figure 8.17, which shows both striking similarities with respect to Figure 8.5 for isotropic patches (both diagrams omitting thermal effects) as far as the stress reduction under the patch is concerned and some unexplained differences with respect to the constant load-attraction contours for thin (soft) patches.

The predictions of these two analyses are so similar that either could be used with confidence, as appropriate. The differences arise in the relative capabilities with respect to thermal mismatch and induced stress effects. Both researchers have accounted for this effect, subject to specified limitations, and both have used quite different approaches to the problem, which is so severe that it must not be overlooked.

8.10. Effects of residual thermal stresses on bonded repairs

Residual thermal stresses develop whenever the patching material has a much lower coefficient of thermal expansion than does the skin, as is always the case with fibrous composite patches for conventional aluminum structures. The problem is not removed even by the use of room-temperature-curing adhesives, because the absence of thermal stresses is lost whenever the operating temperature is lowered,

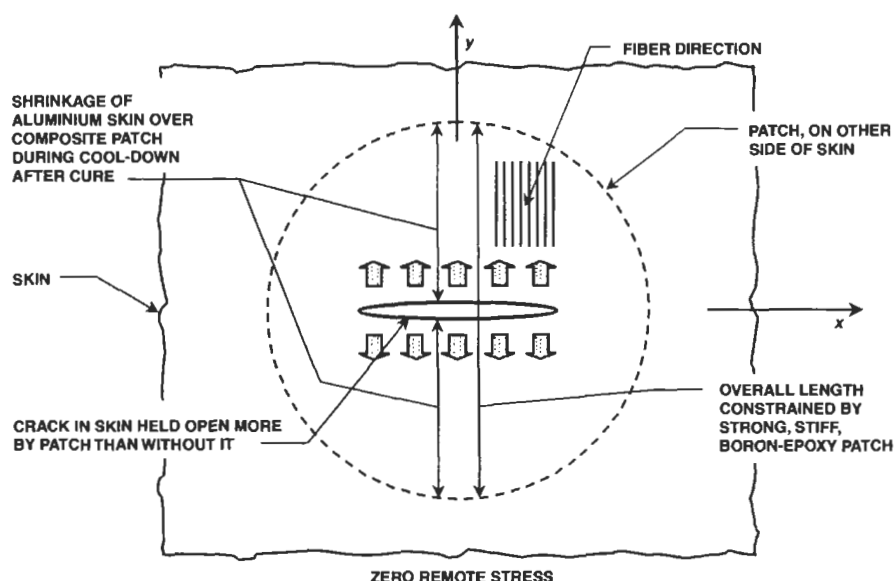


Fig. 8.18. Effect of residual thermal stresses associated with composite patches bonded to metallic structures.

as for high-altitude flight of aircraft. In any event, most room-temperature-curing adhesives are either softer or weaker than heat-cured adhesives, so that approach could entail a reduction in effectiveness of the bonded patch to hold the crack shut. The origin of these stresses is as follows. At high temperature, while the adhesive is uncured and still liquid, the adhesive does not transfer loads so the patch and the structure can expand independently of each other. The skin will normally have expanded appreciably, but the length of a composite patch will be virtually unchanged in any direction for which there are fibres. Consequently, after the adhesive has set and the heat source is removed, the skin under the patch wants to contract – away from the edges of the patch and away from the crack, thereby pre-stressing the crack in the open position, as shown in Figure 8.18. This is aggravated by further reductions in operating temperature. Nevertheless, as long as the bond remains intact, a long crack will still behave like two separated half-cracks in the manner of Eq. (8.4), only the half-crack lengths Λ will be larger than they would in the absence of thermal effects. Consequently, the crack-tip stress-intensity factor K_{∞} would also increase, in accordance with Eq. (8.6), and so would the crack growth rates.

If the structure being repaired is stiff enough, and flat enough too, some of the thermally induced stresses in the skin under the patch will be reduced by compressive stresses that develop during the cure if the surrounding structure, which is not heated, constrains the patch area. The AMRL team has quantified these phenomena in reference [8] for circular composite patches. The CRAS team has recently done the same for elliptical composite patches. (Rose's original

analysis in reference [2] had omitted any effects of orthotropy.) It is now apparent that, even under the best of circumstances, the relief provided by restraint during cure will typically amount to only some 25% of the total thermal stresses at the minimum operating temperatures. Nevertheless, such a reduction in operating stress levels has a pronounced effect on fatigue lives. What is more concerning is that it is now evident that these thermal stresses, for boron- or carbon-epoxy patches will have roughly the same effect on the stresses in the skin under the patch as the remote mechanical loads do. This provides considerable support for the advocates of the use of Glare[®] patches which, despite their lower stiffness than for composite patches, have virtually no thermal mismatch with respect to aluminum alloy structures.

Another significant effect of the thermal mismatch is that it seriously affects the adhesive stresses developed between the skin and the patch. At the ends of the patch, the adhesive is pre-loaded in the *opposite* direction to what a *tensile* remote load would cause. Consequently, this is a benign effect for the adhesive, and the ends of the patch, for tensile mechanical loads, but is an adverse effect for compressive mechanical loads. Cracks grow only when opened up by tensile loads, so this is not always a problem. However, some structures dominated by tensile loads, like lower wing skins, are also subjected to lesser compressive loads, from gusts and from inertia on the ground. This effect of the thermal stresses has an insidious effect on the fatigue life of adhesive bond. When loaded monotonically, at the adhesive level, the adhesive can tolerate a certain level of cracking that occurs when it is strained beyond its elastic limit, as shown in Figure 8.19. Apart from a reduction in macro-level stiffness, most adhesives are remarkably tolerant of such damage, tolerating much higher loads until failure finally occurs.

However, a very different set of circumstances applies if the adhesive bond is subjected to *reversed* loads. The hackles would try to develop in *both* directions

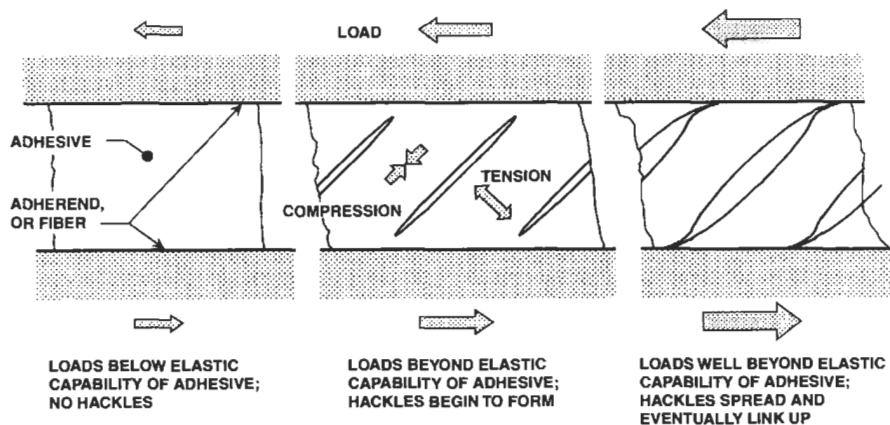


Fig. 8.19. Hackles that develop in adhesive bonds loaded beyond their proportional limit.

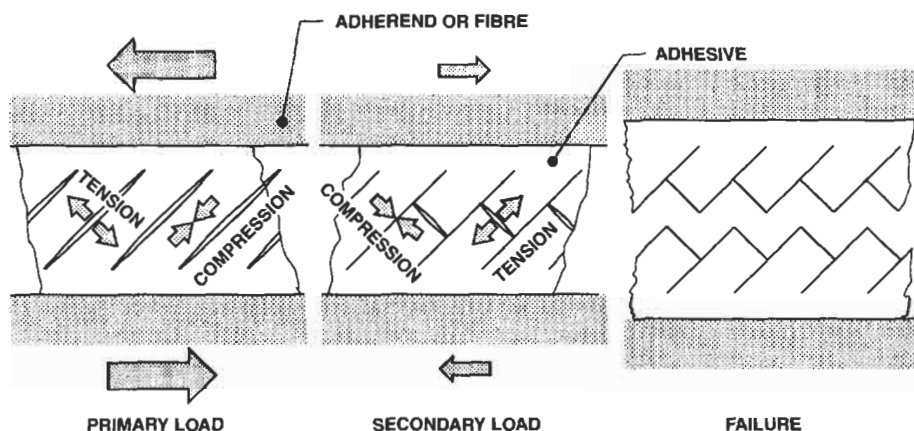


Fig. 8.20. Saw-tooth fractures developed in adhesive bonds subject to severe reversed loading.

then, resulting in a complete saw-tooth surface separating the two adherends, as shown in Figure 8.20.

Although the remote loads may appear to be monotonic, the adhesive is usually subjected to reversed loads when the residual thermal stresses are accounted for, with an associated reduced fatigue life. This potential problem is a total non-issue for thin structures, for which the adhesive *cannot* be loaded beyond the proportional limit, but may explain some of the troubles experienced with some bonded repairs to *thick* bonded structure – defined as such, regardless of actual dimensions, by the ability to overload the adhesive. As if to confirm the analyses in this regard, no such problems have ever been encountered in service or test for what really are patches over obviously thin structure.

8.11. Effects of adhesive non-linearity and disbands on crack-tip stress-intensity factors

Rose's original Stage II analysis is restricted in applicability to linearly elastic behavior of the adhesive. As part of the CRAS program, this limit has been removed by modifying his solution to account for an elastic-plastic adhesive model. This simple model is defined in Figure 8.21.

Since the load that can be transferred through an adhesive bond between two nominally uniformly thick adherends is limited by the square root of the adhesive strain-energy, it is clear that the added area under the extended stress-strain curve in Figure 8.21 is very significant, in spite of the concerns expressed in the previous section. The further along the stress-strain curve that the adhesive is loaded, the more micro-damage will be done in the form of micro-cracks that may eventually link up. (Figure 8.21 is a very useful macro-level model for analysis, but it does not

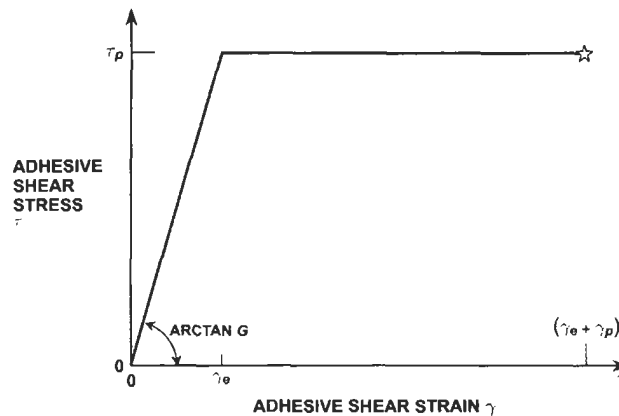


Fig. 8.21. Elastic-plastic representation of adhesive non-linear behavior in shear.

mean that the adhesive actually behaves like a ductile metal. If it did, it would unload with a permanent offset; actually, it unloads with hysteresis but almost to the origin.)

The results of the new elastic-plastic analysis, documented in reference [7], are depicted in Figure 8.22, in the same non-dimensionalized form as for Rose's elastic solution in Figure 8.3. The value 1 on the ordinate of Figure 8.22 represents the elastic solution.

It is clear that the added strain energy of ductile adhesives, with respect to brittle ones with no non-linear capacity, is to reduce the stiffness of the load over the

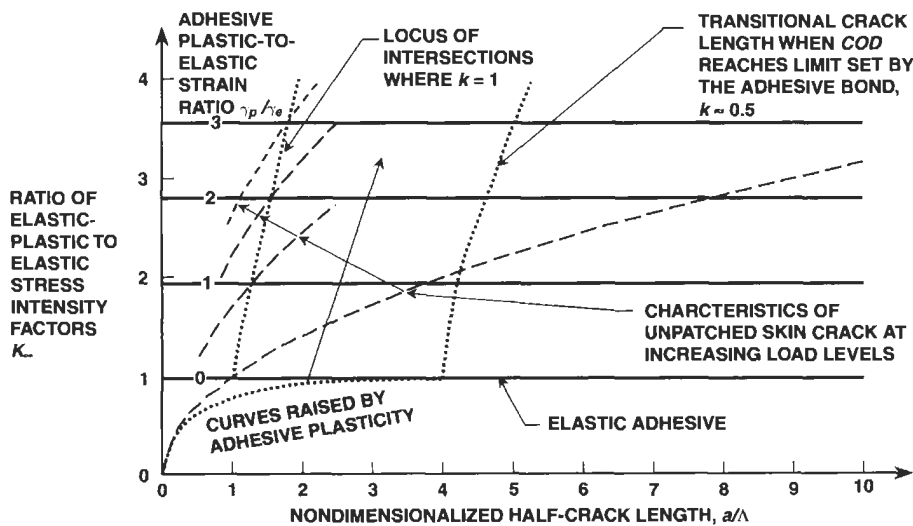


Fig. 8.22. Effect of elastic-plastic adhesive behavior on crack-tip stress intensity factors underneath bonded patches.

crack, for sufficiently high loads. This, of course, is undesirable, since it increases the stress intensity K . On the other hand, the same added flexibility goes hand-in-hand with increased joint strength, enabling bonded patches to be applied to thicker cracked structure than can be repaired with elastic adhesives – unless one is willing to employ stepped patches to decrease the load transferred per step and, at the same time, decrease the eccentricity in load patch for one-sided patches.

The new, longer, effective half-crack tips and higher stress-intensity factors have been derived in [7] as

$$\Lambda_{e-p} = \Lambda_e \frac{\left\{ 1 + \frac{2}{3} \left[\left(1 + 2 \frac{\gamma_p}{\gamma_e} \right)^{3/2} - 1 \right] \right\}}{\left(1 + 2 \frac{\gamma_p}{\gamma_e} \right)}, \quad (8.12)$$

$$K_{\infty e-p} = K_{\infty e} \sqrt{1 + \frac{2}{3} \left[\left(1 + 2 \frac{\gamma_p}{\gamma_e} \right)^{3/2} - 1 \right]},$$

where the elastic values are defined in Eqs. (8.4) and (8.6).

Reference [7] also contains an assessment of the effects of disbonds adjacent to the crack. It is predicted there that these disbonds cannot initiate until the crack has grown sufficiently and that, thereafter, any shear-dominated disbonds will grow in a stable manner, *in concert* with further crack extension. In other words, the *width* of any disbond is limited by, and eventually proportional to, the *length* of the crack. (The behavior of peel-induced disbonds has yet to be examined by closed-form analysis.) Disbonds render bonded patches far less effective; avoiding them justifies the use of more complex stepped patches let into stepped recesses cut into the skin around the crack. The choice between nominally uniform (or linearly tapered) patches on a uniform substrate or stepped patches bonded into a stepped recess cut from the structure seems to be difficult to establish, because so many factors have been omitted from older analyses that the patches have often out-performed the predictions. Nevertheless, the distinction is exceedingly simple to grasp; patches with complex geometries are *needed* whenever the structure is so thick *and* so highly loaded that the simple patches cannot do the job.

8.12. Out-of-plane bending effects with one-sided patches

Rose's original analysis includes the necessary geometrically non-linear bending analyses for the effects of the eccentricity in load patch inherent in one-sided bonded patches. He correctly established that the so-called Stage I correction factor is very small. Analyses under the CRAS program, reported in reference [16], have confirmed this need. Indeed, the tendency for the centroid of the skin/patch combination to align itself with the plane of action of the remote load is so great that, in the worked example in reference [16], a linear bending analysis would have

over-estimated the deflection in the patch, over the crack, by a factor of 18-to-1. Linear analyses are totally inappropriate for this class of problem.

The author's analyses in reference [16] include an improvement with respect to the model used by Goland and Reissner in their classical analysis of bonded single-lap joints. This model assumes that plane sections remain plane, even though the overlap area is treated as a single layer twice as thick as the individual adherends. Such an approximation is obviously unrealistic immediately adjacent to the ends of the overlap or, in the present context, immediately adjacent to the skin crack. The author removed this constraint by adding a flexible adhesive layer *only* in narrow zones adjacent to the ends of the patch and on each side of the crack. The analyses were made more accurate because of this refinement, but it was shown that, numerically, the Goland and Reissner level of model is sufficiently accurate. Rose relied upon these same phenomena when he modeled the load transfer between skin and patch as being instantaneous. It really isn't – but a more precise derivation often does not change the answer significantly.

Such simplifications are not *always* valid, however. No matter how precise the Stage I bending analysis, it is going to predict almost zero bending moment in the patch over the crack, provided that the lengths are long enough to allow the transverse deflections to occur. Nevertheless, both Rose's original analysis, and the more recent one in reference [17], have included Stage II bending analyses in the immediate vicinity of the crack. The reason for this is that there is a local abrupt eccentricity in load path too short to effect the global bending. The same phenomenon is described in reference [16]. It would be fair to say that this aspect of the problem is not yet adequately characterized. It is clearly *not* a classical plane-sections-remain plane linear bending analysis, because finite-element analyses performed as part of the CRAS program have confirmed the absence of curvature in that region, even with five elements through the thickness. So most of the eccentricity must be accommodated by shear-lag, as Wang, Rose, and Callinan recognized in preparing their reference [17] based on Reissner's plate-bending analysis. However, it seems to the present author that the whole issue might be moot. The only interest in this particular bending moment is possible unequal crack opening across the thickness of the skin. But, surely this is more dominated, at the crack tips, by the uncracked and unbent very stiff laminate of skin and patch just *ahead* of the crack tips. It is obvious that the crack opening will vary from the patch side to the unrepaired side of the skin in the "bonded joint" zone of Figure 8.2, and that this might impart a slightly greater displacement than developed in the adhesive alone, but this seems to be far from the dominant effect at the crack tip. It must be remembered that only those portions of the crack within the very short length Λ are important here.

Curiously, shear lag *is* known to be important in the patch, directly over the crack in the skin. Composite patches have very little transverse shear stiffness, in comparison with that of aluminum alloy skins, because all such load must be transmitted through the resin matrix. Consequently, those layers of fibers closest to the skin are locally loaded far more highly than those located far away on the outside of a thick patch. (The same phenomenon was observed at Douglas Aircraft

during the PABST program, where the splice plates in double-strap metal-to-metal joints were far more prone to fatigue failures, where the skins butted together, than the nominally equally stressed portions of the skins.)

8.13. Remaining challenges involving closed-form analyses

Despite the abundance of Rose's work, and that of the whole team led by Alan Baker, as well as the more recent contributions by the CRAS team, there are still challenges waiting to be addressed. Some may never be solved in this manner because it will be found that finite-element analyses are absolutely necessary. Nevertheless, some of the remaining tasks that will be attempted by the CRAS team include the following.

1. Adhesive stresses associated with patches with very long tapers.
2. Load transfer between the skin and the patch for thick structures (and patches to match).
3. Further studies of disbonds, particularly those associated with adhesive peel stresses.

Other investigations will continue with ways to improve or facilitate finite-element analyses, and these are no less important than the closed-form solutions discussed here. However, they lie beyond the scope of this article.

8.14. Concluding remarks

It is hoped that, more than a decade after the publication of Rose's classical treatise on this subject, and the thousands of bonded patches that have been successfully applied by the RAAF and USAF, in particular, that it is now clear what a vital analysis it was. Also, as this paper shows, the techniques used have spawned a large number of refinements and expansions that retain the original simplicity while enabling the effects of far more parameters to be assessed parametrically.

One must wonder whether or not Rose knew, at the time, that the precise transverse stiffness of composite patches was not to have a dominant influence on his Stage I analysis for the load attraction at the ends of the patch and the stress in the skin under the patch, where the crack existed. Certainly, it is *now* apparent that orthotropic composite patches designed with his analysis for isotropic patches would not be all that different if the composite patch analysis had been derived earlier.

Rose's foresight in recognizing the importance of a uniform stress surrounding the crack under the patch means that the restriction he accepted to elliptical patches to achieve that goal was sensible. Although octagonal patches are easier to make, it is important that the trimming of their corners lead to a patch that is *equivalent* to some elliptical patch. Otherwise, there will be regions of higher-than-average stress

for the crack to grow into. Again, what others have mistaken for a restriction on applicability is now revealed as good design advice.

It is known that Rose had not anticipated the direct application his analysis to corrosion damage, simply by using a negative patch thickness. Nevertheless, once the idea had been suggested he was able to help the present author complete that task, so that Rose's original analysis can be applied to a whole further class of problems. It should also be noted that the original analysis, intended for the analysis of repairs to structures damaged in service, can also be applied to yet another task – that of designing optimally sized local integral reinforcement to be left in place when the parts are first machined, so that they will not develop fatigue cracks in service. These very same tools can also be applied to prevent further instances of poorly designed stringer run-outs, which have been a chronic source of fatigue cracks in the past. Now there are simple closed-form analyses available to quantify potential hot spots *before* the designs are frozen.

It is also now known that the idea of being able to directly apply Rose's model to integrally stiffened structures is sound, and that, henceforth, they need not always be limited to the simple flat-plate geometries that formed the basis of the idealized model Rose first analyzed.

It would take remarkable insight to predict where all of the extensions of Rose's work will end. The author will make no such attempt. However, he will state the obvious, that much of the CRAS closed-form analysis work would not have been possible had Rose not taken that first giant step so many years ago.

References

1. Baker, A.A. and Jones, R. (1988). Bonded Repairs of Aircraft Structures (A.A. Baker and R. Jones, eds.). Martinus Nijhoff Publishers.
2. Rose, L.R.F. (1988). Theoretical analysis of crack patching. In *Bonded Repairs of Aircraft Structures* (A.A. Baker and R. Jones, eds.). Martinus Nijhoff Publishers, pp. 77–106.
3. Baker, A.A. (1988). Crack patching: experimental studies, practical applications. In *Bonded Repairs of Aircraft Structures*, (A.A. Baker and R. Jones, eds.). Martinus Nijhoff Publishers, pp. 107–173.
4. Hart-Smith, L.J. and Rose, L.R.F. Characterizing the Effects of Corrosion Damage Using Analytical Tools Developed for Bonded Composite Crack Patching. Boeing Paper MDC 00K00100, in preparation.
5. Hart-Smith, L.J. (1973) Adhesive-Bonded Double-Lap Joints. NASA Langley Contract Report NASA CR-112235, January.
6. Rose, L.R.F. (1981). An application of the inclusion analogy for bonded reinforcements. *Int'l. J. Solids and Structures*, **17**, pp. 827–838.
7. Hart-Smith, L.J. (1999). On the relative effectiveness of bonded composite and riveted patches over cracks in metallic structures. Boeing Paper MDC 99K0097, *Proc. 1999 USAF Aircraft Structural Integrity Program Conf.*, San Antonio, Texas, 30 November–2 December.
8. Wang, C.H., Rose, L.R.F., Callinan, R., *et al.* Thermal stresses in a plate with a circular reinforcement. *Int. J. Solids and Structures*, **37**, pp. 4577–4599.
9. Hart-Smith, L.J. (2000). Analyses of bending deformations in adhesively bonded one-sided doublers and patches over skin cracks, Boeing Paper MDC 00K0024, *Proc. of the 4th Joint DoD/FAA/NASA Conf. on Aging Aircraft*, St. Louis, Missouri, 15–18 May.

10. Duong, C.N., Wang, J.J. and Yu, J. An approximate algorithmic solution for the elastic fields in bonded patched sheets. *Int. J. of Solids and Structures*, Vol. 38, 2001, pp. 4685–4699.
11. Hart-Smith, L.J. (1999). Nonlinear closed-form analyses of stresses and deflections in bonded on-sided splices and patches. Boeing Paper MDC 99K0069, *Proc. of the 3rd Joint FAA/DoD/NASA Conf. on Aging Aircraft*, Albuquerque, New Mexico, 20–23 September.
12. Hart-Smith, L.J. (1983). Adhesive bonding of aircraft primary structures, Douglas Paper 6979, presented to SAE Aerospace Congress and Exhibition, Los Angeles, California, 13–16 October, 1980; SAE Trans. 801209; reprinted in *High Performance Adhesive Bonding*, (L. De Frayne, ed.). Society of Manufacturing Engineers, Dearborn, Michigan, pp. 99–113.
13. Hart-Smith, L.J. and Duong, C.N. Use of bonded crack-patching analysis tools to design repairs for non-crack-like (Corrosion) damage, Boeing Paper MDC 00K00101, in preparation.
14. Hart-Smith, L.J. (2001). A demonstration of the versatility of Rose's closed-form analyses for bonded crack-patching, Boeing Paper MDC 00K0104, presented to *46th International SAMPE Symposium and Exhibition*, Long Beach, California, 6–10 May.
15. Hart-Smith, L.J. (2001). Extension of the Rose bonded crack-patching analysis to orthotropic composite patches, also accounting for residual thermal stresses, Boeing Paper MDC 00K0102, to be presented to *5th Aging Aircraft Conference*, Kissimmee, Florida, 10–13 September, 2001.
16. Hart-Smith, L.J. and Wilkins, K.E. (2000). Analyses of bending deformations in adhesively bonded one-sided doublers and patches over skin cracks, Boeing Paper MDC 00K0024, presented to the *Fourth Joint DoD/FAA/NASA Conf. on Aging Aircraft*, St. Louis, Missouri, 15–18 May.
17. Wang, C.H., Rose, L.R.F. and Callinan, R. (1998). Analysis of out-of-plane bending in one-sided bonded repair, *Int. J. of Solids and Structures*, 35, pp. 1653–1675.

Chapter 9

NUMERICAL ANALYSIS AND DESIGN

R. JONES

*Department of Mechanical Engineering, Monash University, Wellington Rd,
Clayton, Victoria 3168, Australia*

9.1. Analysis and design

This chapter describes a number of complementary approaches to the analysis and design of bonded repairs. First, an approach based on the two dimensional finite element method is presented and illustrated by an application to an actual repair. An analytical approach for the design parameters for repairs to rib stiffened panels is then presented. Section 4 subsequently compares the predictions with both experimental and numerical results. Design studies for repairs to thick sections are described in Sections 9.5–9.8. Section 9.9 presents a methodology for allowing for adhesive non-linearities and visco-plasticity. Section 9.10 discusses how to extend existing design methodologies to allow for variable adhesive thickness. Section 11 presents the solution for composite repairs to cracked fastener holes or corrosion damage under bi-axial loading. Section 9.12 summarises the findings for repairs to primary structures, and also discusses the applicability of a range of commercially available finite element programs.

There are several methods available for designing composite repairs to cracks in thin metallic skins, i.e. typical thickness less than 3 mm. The finite element method was the first to be developed [1], and has been used to design several complex repair schemes, such as the repair of fatigue cracks in the lower skin of Mirage aircraft [2], and cracks on the upper surface of the wing pivot fitting of F111C aircraft in service with the Royal Australian AirForce (RAAF), see [3]. Following the development of this approach the work presented in [4] revealed that the stress intensity factor for a patched crack approached a constant value as the crack length increased, thus simplifying the initial design process. This approach was based on the premise that, for a sufficiently long crack in a structure which is subjected to a remote uniform stress field, the central region of the patch, over the

crack, behaves like an overlap joint. From this premise it follows that the stress distribution in this central region should be independent of crack length, see Chapter 7 for more details.

As a result of this analogy the problem of a bonded symmetric lap joint can be used in the initial design process. The analytical formulae are particular easy to use and provide a first estimate for the patch design. In some cases, this first estimate is sufficient. However, there are situations in which the repair is critical and a long life is required. In these cases, a full finite element analysis is necessary. As a result, the finite element approach will be discussed first and illustrated by considering the design of a repair to the lower wing skin of a Mirage III aircraft. At this stage it should be noted that whilst much of the initial impetus for composite repairs arose from the need to maintain the structural integrity of military aircraft [1–4] the concepts, analysis and design tools are also applicable to repairs to civilian aircraft [5–10].

9.2. The 2D finite element formulation

A variety of numerical techniques are now available for analysing composite repairs. These include 2D finite element techniques [1], boundary element formulations [11], finite element techniques using of Mindlin plate bending elements [12], 2D and 3D finite element alternating techniques [13] and fully 3D finite element analysis [3]. Of the various techniques the 2D finite element and 2D alternating finite element techniques are the simplest to apply. When a more detailed analysis is required or it is necessary to determine the interlaminar stresses in the repair then it is best to use 3D finite element analysis since Mindlin plate bending elements cannot capture the true three dimensional stress states at the patch adhesive interface. The current 3D finite element alternating technique has a similar shortcoming. However, recent, as yet unpublished, work has shown that it is possible to use the 3D alternating technique to obtain a sub-structure like model of the cracked region and combine this with a standard finite element model for the remaining region and the repair. A detailed discussion of the relative applicability of a range of commercial finite element analysis programs is given in Section 9.12. In general the best results are obtained using 21 noded hex elements or cubic iso-parametric elements. Variants of these elements are available in a range of commercial finite element programs, viz: PATRAN, NE-NASTRAN and PAFEC. Standard quadratic iso-parametric elements can also be used but care must be taken to avoid ill conditioning.

When analysing bonded repairs to cracked metallic sheets it is first necessary to develop a realistic mathematical model for the behaviour of the adhesive layer bonding the patch to the sheet. Under in plane or transverse loading, shear stresses are developed in the adhesive. If we define the x and y axes to lie in the plane of the sheet with the z axis in the thickness direction, then these shear-stresses can be

expressed in terms of the displacements in the sheet and the patch, viz:

$$\begin{aligned}\tau_{xy} &= K_1(u_R - u_p) + K_3(v_R - v_p) + K_4 \frac{\partial w}{\partial x} + K_6 \frac{\partial w}{\partial y} \\ \tau_{yx} &= K_3(u_R - u_p) + K_2(v_R - v_p) + K_6 \frac{\partial w}{\partial x} + K_5 \frac{\partial w}{\partial y}\end{aligned}\quad (9.1)$$

Here τ_{xx} and τ_{yy} are the values of the shear stresses in the adhesive K_1, K_2, K_3, K_4, K_5 and K_6 are spring constants whose values depend on the material properties and thickness of the adhesive, skin and composite patch. The terms u_R, v_R and u_p, v_p are the displacements at the mid-surface of the patch and the skin respectively while w is the vertical deflection. It is often a reasonable assumption that for the composite patch, which from here on will be considered to be unidirectional with the fibres perpendicular to the crack, $G_{13} = G_{23} = G_{12}(G_R)$, i.e. the interlaminar shear moduli are equal. This assumption is unnecessary and the full form for the K_1 's is contained in [1]. However, it dramatically simplifies the analysis and has little effect on any quantities of interest. With these assumptions we obtain, in the case of a patch on one side of the skin:

$$\begin{aligned}K_1 &= K_2 = \frac{1}{(t_A/G_A + 3t_R/8G_R + 3t_R/8G_p)} \\ K_3 &= K_6 = 0 \\ K_4 &= K_5 = \left(\frac{t_A + t_R}{2} + \frac{t_p}{2}\right) K_1,\end{aligned}\quad (9.2)$$

where t_A, t_R and t_p are the thicknesses of the adhesive, patch (composite overlay) and skin respectively and G_A, G_R and G_p are the shear moduli of the adhesive, patch and skin.

These formulae were presented in [1] and make full allowance for the shear deformation which occurs throughout the composite patch and skin. With this approach, the u and v displacements through the patch, adhesive and skin are given by:

$$u = u_R + \tau_{xx} \frac{[z(t_p + t_A + t_R - z/2) - (t_p + t_A + t_R/2)(t_p/2 + t_A/2 + 3t_R/4)]}{G_R t_R}$$

in the patch

$$\begin{aligned}
u &= \frac{(u_R - 3\tau_{sx}t_R/8G_R)(z - t_p)}{t_A} \\
&+ \frac{(u_p + 3\tau_{sx}t_p/8G_p)(t_p + t_A - z)}{t_A} \quad \text{in adhesive} \\
u &= \frac{u_p + \left(z^2 - t_p^2/4\right)\tau_{sx}}{2G_pt_p} \quad \text{in the sheet}
\end{aligned} \tag{9.3}$$

and a similar expression for v .

If the patch is placed on both sides of the skin, then the term $3t_p/8G_p$ appearing in the above equations is replaced by $t_p/4G_p$. These assumptions result in a shear stress profile which is piece wise linear.

9.2.1. Element stiffness matrix

Having obtained the nature of the stress field in the adhesive we can now derive the stiffness matrix for the adhesive layer. When there is no bending, the sheet is assumed to be in a state of plane stress and it is usually modelled by isoparametric membrane elements while the patch is modelled by isoparametric membrane elements with an orthotropic stress strain law. The adhesive is also assumed to only carry the shear stresses τ_{xz} and τ_{yz} . As a result, the total strain energy of an element of the repaired structure is:

$$V = \frac{1}{2}\delta K_p \delta^T + \frac{1}{2}\delta K_R \delta^T + \frac{1}{2} \int \int \int (\tau_{xz}\gamma_{yz}) dx dy dz, \tag{9.4}$$

where K_p and K_R are the stiffness matrices of the skin and patch respectively. The last term in this expression is the contribution due to shear deformation. To be completely accurate, the z integration should be over the total thickness of the skin, adhesive and patch, whilst the x, y , integration is over the surface area of the element.

We first define a vector \mathbf{f} such that:

$$\mathbf{f} = (u_R, v_R, u_p, v_p) = (N\delta)^T, \tag{9.5}$$

where the components of N are generalised functions of position and

$$\delta^T = (\delta_1^T, \delta_2^T \dots \delta_m^T) \tag{9.6}$$

Here the element is considered to be an arbitrary shape with m nodes and

$$\delta_1^T = (u_{Ri}, v_{Ri}, u_{pi}, v_{pi}) \tag{9.7}$$

The strain vector may be expressed as:

$$\gamma^T = (\gamma_{xz}, \gamma_{yz}) = (D\tau)^T, \tag{9.8}$$

where the matrix D is a function of z and where:

$$\tau^T = (\tau_{xx}, \gamma_{xy}) , \quad (9.9)$$

It thus follows that τ can be written as:

$$\tau = AN\delta , \quad (9.10)$$

where

$$A = \begin{bmatrix} 1 & 0 & -1 & 0 \\ 0 & 1 & 0 & -1 \end{bmatrix} \left(\frac{t_A}{G_A} + \frac{3t_p}{8G_p} + \frac{3t_R}{8G_R} \right) \quad (9.11)$$

As previously mentioned, the assumed deformation profile results in a quasi-linear shear stress. The shear stresses τ_{xz} and τ_{yz} vanish at the top of the patch, increase linearly to the values of τ_{xx} and τ_{yy} respectively in the adhesive and then decay linearly to zero at the free surface of the skin (or plane of symmetry in the case of a patch on both sides of the skin). This results in the matrix D having the form:

$$\begin{aligned} D &= \frac{f(z)}{G_p} \begin{bmatrix} 1 & 0 \\ 0 & 1 \end{bmatrix} \text{ in the skin, i.e. } 0 \leq z \leq t_p \\ &= \frac{f(z)}{G_A} \begin{bmatrix} 1 & 0 \\ 0 & 1 \end{bmatrix} \text{ in the adhesive } t_p \leq z \leq t_p + t_A \\ &= \frac{f(z)}{G_R} \begin{bmatrix} 1 & 0 \\ 0 & 1 \end{bmatrix} \text{ in the patch } t_p + t_A \leq z \leq t_p + t_A + t_R , \end{aligned} \quad (9.12)$$

with the term t_p being replaced by $t_p/2$ in the case of a patch on both sides of the skin.

Here:

$$\begin{aligned} f(z) &= z/t_p \text{ in the skin } z \leq t_p \\ &= 1 \text{ in the adhesive } t_p \leq z \leq t_p + t_A \\ &= \frac{(t_p + t_A + t_R - Z)}{t_R} \\ &\text{ in the patch } t_p + t_A \leq z \leq t_p + t_A + t_R , \end{aligned} \quad (9.13)$$

Making use of the expression for τ_{xz}, γ_{xz} , etc. we now find that:

$$\begin{aligned} &= \frac{1}{2} \int \int \int (\tau_{xz} \gamma_{yz}) dV \\ &= \frac{1}{2} \int \int \int (AN\delta)^T \left(\int f(z) D dz \right) AN\delta dx dy \end{aligned} \quad (9.14)$$

As a result, we find that the stiffness matrix K^e for the adhesive layer, plus the shear

coupling in the skin and patch, is given by:

$$\begin{aligned} K^e &= \int \int (AN)^T \left(\int f(z) D dz \right) AN \delta dz dy \\ &= \left(\frac{t_A}{G_A} + \frac{t_R}{3G_R} + \frac{t_p}{6G_p} \right) \int \int (AN)^T \begin{bmatrix} 1 & 0 \\ 0 & 1 \end{bmatrix} AN dx dy \end{aligned} \quad (9.15)$$

For a patch on both sides of the skin, the stiffness matrix for both layers of adhesive and the shear coupling in the skin and patch is:

$$K^e = 2 \left(\frac{t_A}{G_A} + \frac{t_R}{3G_R} + \frac{t_p}{6G_p} \right) \int \int (AN)^T \begin{bmatrix} 1 & 0 \\ 0 & 1 \end{bmatrix} AN dx dy \quad (9.16)$$

A more general expression for K^e including bending effects is given in [1].

Having thus obtained the stiffness matrix for adhesive layer, it is now possible to analyse complex repair schemes.

To illustrate the versatility of this approach, we will consider the boron fibre repair to fatigue cracks in the lower wing skin of Mirage III aircraft in service with the RAAF. This problem highlights the recommended approach to designing bonded repairs to cracked metallic wing skins.

9.2.2. Repair of cracks in aircraft wing skin

In the late 1970s a boron fibre patch was developed for cracks in the lower wing skin of a number of Mirage III aircraft. These cracks were pre-dominantly found at an angle of 45° to the main spar. To investigate the feasibility to a b/ep repair, a design study was undertaken into the repair of a crack whose tips were 111 mm apart and which lay at 45° to the spar (see Figure 9.1). This crack represented the longest crack which had been found in service.

As a first step in the design of the repair, a study of the cracked, but unpatched, region was undertaken. A detailed finite element model of the area surrounding the drain hole region was developed. The loads applied to this model were obtained directly from the stress distribution which resulted from a previous finite element model of this region and which correspond to a 7.5 g load case. The study gave the values of the stress intensity factors to be $K_1 = 72 \text{ MPa m}^{1/2}$ and $K_2 = 3.3 \text{ MPa m}^{1/2}$ at the tip closest the spar and $K_1 = 68 \text{ MPa m}^{1/2}$, $K_2 = 0.5 \text{ MPa m}^{1/2}$ at the tip closest to the root rib. These values were consistent with a fractographic examination of the crack which showed that the crack was essentially growing as a mode I fracture and that of the two crack tips the tip closest to the spar was growing the faster. Indeed, the tip closest to the spar was found to be very close to final failure.

Having thus obtained a reasonable model for the unpatched crack, we add to this a finite element representation of the repair. Six boron epoxy patch configurations were considered, each with the same plan form, see Figure 9.1. Each patch was modelled using approximately 380 of the "bonded" elements described in Section 9.2.

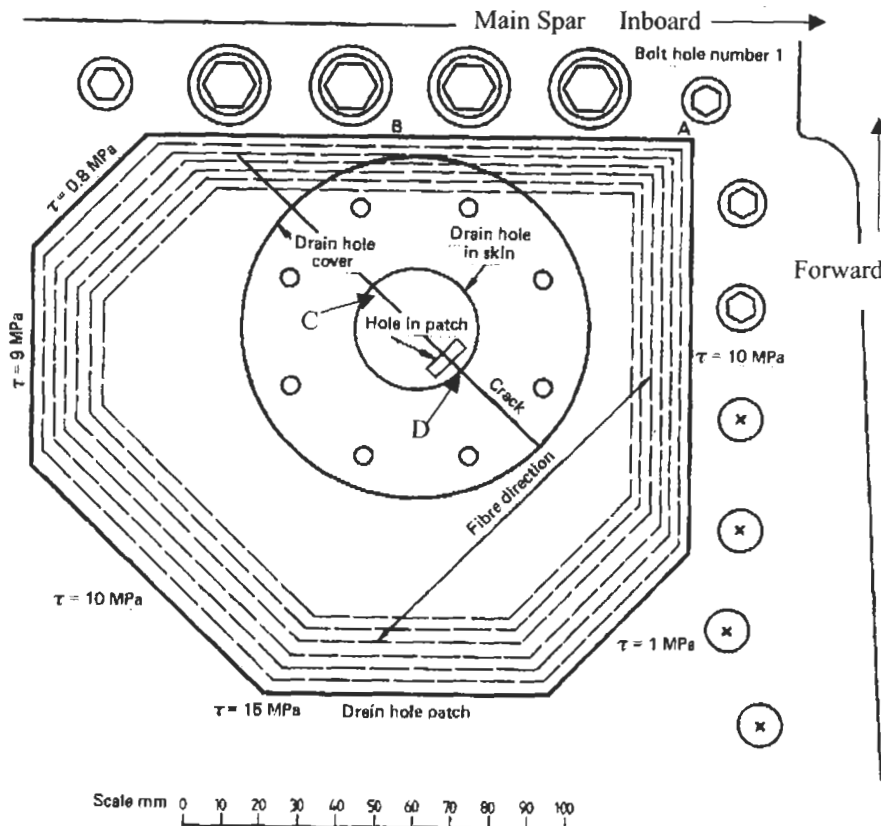


Fig. 9.1. Geometry of cracked drain hole region and patch.

All of the six patches considered were unidirectional laminates and were internally stepped, i.e. with the longest ply on the outside. The fibre direction was at ninety degrees to the crack.

Initially, it was uncertain if carrying the fibres over the drain hole was necessary, or how frequently the drain hole was used in service. As a result, in three of the patches considered a hole was left so as not to interfere with the draining of the wing. In the other three patches, varying amounts of the hole were covered. In one case, one third of the total area of the hole was covered, while in the other cases virtually all of the hole was covered.

For each of the patches, the maximum shear stresses in the adhesive bonding the patch to the wing skin occurred at points A, B, C and D (see Figure 9.1). The maximum stresses in the fibres occurred at point D for the patches with a hole in the patch, and in the fibres over the hole in the patches with the hole partially covered. The values for these stresses, along with the percentage reduction of the stress intensity factor K_I at each tip, achieved by each patch are shown in

Table 9.1
Effect of drain hole patch: 7.5 g load case.

Patch number	1	2	3	4	5	6
Maximum patch ² Thickness (mm)	0.762	0.762	0.776	0.889	0.889	0.889
Adhesive thickness (mm)	0.102	0.102	0.102	0.203	0.203	0.203
Thickness of first layer (mm)	0.127	0.254	0.127	0.254	0.254	0.127
Covering of drain	Open	open	1/3 covered	open	substantially covered	substantially covered
Adhesive shear stress (MPa) at points:						
A	29	43	29	31	26	18
B	55	79	55	58	42	30
C	181	179	164	120	63	64
D	153	153	131	98	50	51
Maximum fibre stress (MPa)	953	930	760	911	450	455
Reduction in stress intensity factor K_I , i.e. $1 - K_{Ip}/K_{Iu}$, at:						
1. Spar tip	91%	91%	91%	91%	92%	91%
2. Root rib tip	99%	99%	99%	99%	99%	99%

Table 9.1. Here K_{Iu} and K_{Ip} are the values of the stress intensity factors before and after patching respectively.

We see that all of the six patches achieve a reduction in the stress intensity factor K_I of at least 91%. Consequently, they would all significantly retard growth. Similarly for all of the patches, the fibre strains are below the maximum working levels of 0.005 which corresponds to a stress of 1 GPa, although of the six patch numbers, 5 and 6 have by far the greatest factors of safety. As a result, the patch design was finally chosen primarily on the basis of the magnitude of the shear stresses developed in the adhesive. On the basis, patch numbers 1, 2, 3 and 4 were rejected. The two remaining patches are patch numbers 5 and 6. Of the two, Table 9.1 shows that the adhesive shear stresses along the edges of the patch, are substantially higher for patch number 5 than for patch number 6, although both are below the threshold value for fatigue damage. As a result, patch 6 is much less likely to suffer fatigue damage to the adhesive bond. Hence, patch number 6 was adopted as the final repair.

Consulting Table 9.1, we see that at locations C and D in patch 6 the shear stress in the adhesive is sufficiently high so as to cause concern over the possibility of fatigue damage occurring in the adhesive. However, these high values occur in the interior of the patch at the intersection of the crack with the drain hole, and are very localised. As a result, any damage which does occur should not spread and should have virtually no effect on the stress intensity factors at the crack tips or on the fibre stresses.

Let us now summarise the criteria which were used to finalise the patch design.

1. The peak fibre stresses must be less than the maximum permissible tensile strength. For boron epoxy this is approximately 1 GPa.
2. The peak adhesive stress must be less than its fatigue threshold value. For the AF126 epoxy nitrile adhesive used, this is approximately 40 MPa.
3. A significant reduction in the stress intensity factor K_{I_p} must be achieved. Wherever possible, it is desirable to reduce K_{I_p} to below the fatigue threshold limit of the wing skin.

Let us now consider the effect that the difference between the coefficients of thermal expansion of the boron patch and the aluminium alloy wing skin has on the residual stresses left in the skin after the patch has been applied. Patching the skin involved heating the area to be repaired to approximately 120 °C. The patch which also been heated to 120 °C, is then attached and the patched structure is allowed to cool to ambient temperature. It is during this cooling phase that the difference in the coefficients of expansion between the patch $\alpha_1 = 4.5 \times 10^{-6}$ per °C and $\alpha_2 = 20 \times 10^{-6}$ per °C, and the wing skin, $\alpha = 23 \times 10^{-6}$ per °C, causes a residual thermal stress to be left in the structure. (Note that α_1 is the coefficient of expansion in the fibre direction and α_2 is that perpendicular to the fibre direction.)

In order to analyse this phenomenon the shear modulus of the adhesive was taken as zero at 120 °C and was assumed to increase linearly, as the temperature decreased, to a value of 0.965 MPa at ambient temperature, i.e. 40 °C. At each step decrease in temperature the adhesive layer was modelled using the finite element method described above. As a result of this analysis, it was found that when the skin was assumed to be restrained from in plane movement by the spar and root rib attachments, the mean residual stress left in the skin under the patch was a tensile stress of 8.7 MPa. This stress should not significantly alter fatigue behaviour of the patched panels.

A more detailed discussion of the effects of thermal mismatch is given in [2].

Following patch design a series of fatigue tests were then performed both under constant amplitude loading and using a detailed flight spectra. The results of this test program are shown in Figure 9.2 where it can be seen that the patch essentially stopped crack growth.

9.3. Initial design guidelines

As mentioned in Section 9.1 externally bonded composite patches have proved to be an effective method of repairing cracked, or damaged, structural components, [1–10]. A variety of approaches are now available for the design of composite repairs to cracks in thin metallic skins, i.e. typical thickness less than ~3 mm. One such technique is based on the fact that the stress intensity factor for a patched crack approaches a constant (limiting) value, defined as K_∞ , as the crack length increases. This approach was based on the premise that, for a sufficiently long crack in a structure which is subjected to a remote uniform stress field, the central region of the patch, over the crack, behaves like an overlap joint [4]. From this premise it

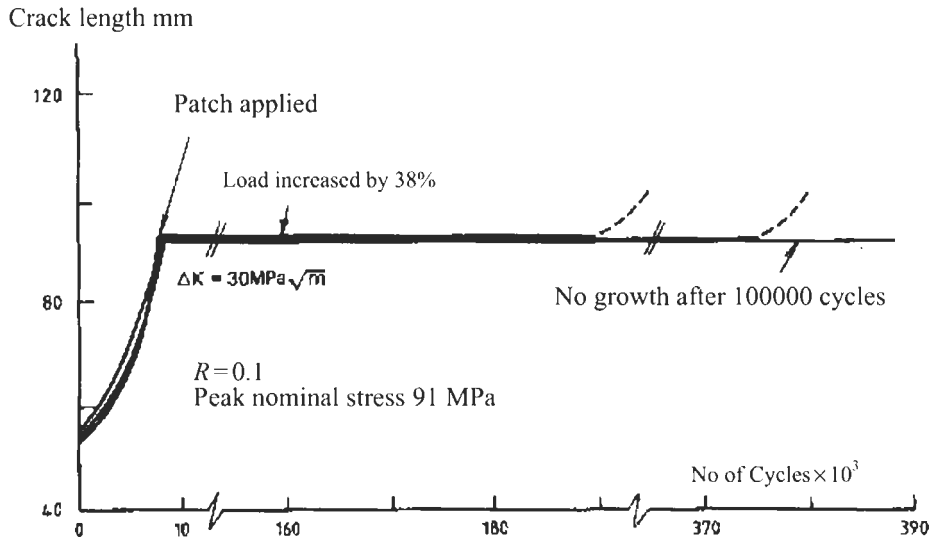


Fig. 9.2. Effect of patch on crack growth rate.

follows that the stress distribution in this central region and the stress intensity factor should become independent of crack length.

As a result of this analogy it has been found that the problem of a bonded symmetric lap joint can be used in the initial design process. Indeed, the resultant analytical formulae are particularly easy to use and provide a first estimate for the patch design.

It is possible to increase the accuracy of the current approximate 2D formulae, initially developed by Rose in [4], for the limiting stress intensity factor K_{∞} for a crack repaired with an externally bonded composite repair, by (partially) accounting for through-the-thickness effects. To this end the value of K_{∞} can be approximated, see Chapters 7, 8 and 12, by the formulae:

$$K_{\infty} = Y\Omega_L\sigma_o\sqrt{\pi\hat{\lambda}}, \quad (9.17)$$

where

$$\sigma_o = \frac{\sigma E_p t_p}{(E_p t_p + E_r t_r)} \quad (9.18)$$

Y is a geometry factor, which accounts for repairs to center or edge cracks;

$$\begin{aligned} Y \text{ is a geometry factor} &= 1 \text{ for a repair to a center crack} \\ &= 0.9 \text{ for a repair to an edge crack} \end{aligned}$$

and Ω_L is the load attraction factor. For long uni-directional fibre patches it has

been found that the term Ω_L can be approximated as follows

$$\Gamma = 3/8 \cdot 1. / (1 + X E_r t_r / (B E_p t_p)) - (E_p t_p / (E_r t_r + E_p t_p)) , \quad (9.19)$$

$$\Omega_L = \frac{(E_p t_p / (E_r t_r + E_p t_p) + \Gamma)}{\sigma_o} , \quad (9.20)$$

$$\pi \lambda = \sqrt{E_p t_p / \beta (1 + t_p E_p / E_r t_r)} \quad (9.21)$$

and

$$\beta = \frac{(t_a / G_a + t_r / 3 G_r + t_p / 3 G_p)}{(t_a / G_a + 3 t_r / 8 G_r + 3 t_p / 8 G_p)^2} \quad (9.22)$$

Here X is the width of the patch, B is the width of the plate/skin, t_a , t_p and t_r are the thickness' of the adhesive, plate, and patch respectively, G and E denote the shear and Young's modulus and the subscripts a , p and r denote their values for the adhesive, plate, and patch respectively.

Until now we have ignored bending effects. However, even if the wing skin is in a state of plane stress, the location of the neutral axis of the patch-adhesive-skin section will differ from the neutral axis of the wing skin itself. Hence, forces applied to the skin will result in an out of plane bending which will reduce the efficiency of the repair.

There are several methods that can be used. One approach, developed at Northrop see [14] for more details, can be used to account for this out of plane bending. Other more precise methods are discussed in Chapters 7 and 12. In the Northrop method, the apparent stress intensity factor K_p^* at the mid surface of the sheet is given by:

$$K_p^* = (1 + BC) K_p , \quad (9.23)$$

where BC is a bending correction factor. Here,

$$BC = a y_{\max} (1 - K_p / K_s) (t_p + t_r) / I , \quad (9.24)$$

where K_s is the value of the stress intensity factor before patching, t_p and t_r are the thicknesses of the sheet and patch respectively, y_{\max} is the distance of the lower unpatched surface of the plate from the neutral axis of the section (i.e. sheet plus patch). I is the moment of inertia of the section and a is the crack half length. This formulation has several analytical shortcomings and more recent, and exact, developments are presented in Chapters 7 and 12.

The value of K_p^* can be related to J , the energy release rate for self similar crack growth, in the usual way, viz:

$$J = \frac{K_p^{*2}}{E} \quad (9.25)$$

If growth is non self-similar with the maximum growth occurring at the lower free surface, then it may be best not to use K_p^* or J but to design on the basis of the maximum stress intensity factor K_p^{\max} which is given by:

$$K_p^{\max} = (1 + 2BC)K_p \quad (9.26)$$

These formulae have been validated by comparison with in excess of 2400 different numerical examples solved using 3D finite element analysis.

If the adhesive is behaving plastically then the asymptotic solution $K_{\infty e-p}$, where the subscript $e-p$ indicates that it is the elastic plastic solution, can be related to $K_{\infty e}$, where the subscript e indicates that it is the elastic solution, as follows, see [29].

$$K_{\infty e-p} = K_{\infty e} \sqrt{1 + \frac{2}{3} \left[\left(1 + 2 \frac{\gamma_p}{\gamma_e} \right)^{\frac{1}{2}} - 1 \right]} \quad (9.27)$$

Here γ_p and γ_e are the elastic and the plastic components of the peak shear strain acting over the crack, see Chapter 8 and [29], and $K_{\infty e}$, is as given in Eq. (9.17). In this case it is essential to have an accurate representation of the elastic plastic behaviour of the adhesive. The formulation given in [29] and in Chapter 8 treats the adhesive as being rate independent. Unfortunately this simplification is invalid. Most commonly used structural adhesives are highly visco-plastic and exhibit extensive strain rate dependency, see Section 9.8. As a result when calculating γ_p and γ_e , for use in Eq. (9.27), a more realistic visco-plastic formulation is required. One such formulation is given in Section 9.8. Sections 9.8 and 9.9 also show how to use Glinka's hypothesis [19] plus valid visco-plastic formulation for the adhesive to obtain accurate values for γ_p and γ_e without the need for a fully non-linear finite element analysis. An extension of these formulae to account for cracks at holes and load biaxiality is given in Section 9.10.

To illustrate the accuracy of these formulae let us first consider an externally bonded composite repair (patch) to a center crack in a 3 mm thick aluminium panel with $E = 72000$ MPa and $\nu = 0.33$. Two patch thicknesses were analysed viz: 1.0 and 1.85 mm, and the patch was assumed have the following mechanical properties: $E_{11} = 208000$ MPa, $E_{22} = 25432$ MPa, $\nu_{12} = 0.183$, and $G_{12} = G_{13} = G_{23} = 7241$ MPa. The plate was assumed to have dimension of 200 (length) \times 290 (width) \times 3 mm and the patch was assumed to have a plan form of 100 (length) mm \times 82 (width) mm. The adhesive was taken to be 0.25 mm thick with a shear modulus of 375 MPa and $\nu = 0.33$. The analysis used 20 noded isoparametric 3D brick elements with two layers of elements through each of the

plate, patch and adhesive. The plate was subjected to a remote uniform stress of 229.8 MPa and global bending, after patching, was prohibited.

In this analysis symmetry was used and only a quarter of the structure was modelled. The resultant mesh consisted of 4889 nodes and 1132 elements and, to simulate the crack tip singularity, the near tip elements had the mid side nodes moved to the 1/4 points. The resultant solution was well conditioned and the accuracy of the solution was evaluated by performing two separate analyses. The first used optimum integration, i.e. $2 \times 2 \times 2$ Gaussian quadrature points, to form the stiffness matrices of the elements whilst the second used full integration, i.e. $3 \times 3 \times 3$ Gaussian quadrature points, to form the stiffness matrix. These analyses gave results which agreed to within 1%.

Following this analysis the composite repair to edge notch cracks in a 200 (length) \times 145 (width) \times 3 mm plate was then considered. In this study the patch was assumed to be 1.85 mm thick and have a plan form of 100 (length) mm \times 41 (width) mm. The results both these repair configurations are presented in Tables 9.2–9.5.

The third study involved similar repair configurations where skin thicknesses of 2 mm, 3.15 and an adhesive shear moduli of 700 MPa were also considered. For the first two repair configurations the differences between the present approximation

Table 9.2

K values for a repaired edge notch panel, patch thickness 1.85 mm.

Crack length	5 mm	6 mm	7 mm	10 mm	20 mm
Patched surface	10.6	10.8	10.9	10.9	10.4
Middle	11.6	11.7	11.9	12.1	12.9
Bottom	11.7	11.9	12.0	12.2	12.7

Table 9.3

K values for repaired center notch panel, patch thickness 1.85 mm.

Crack half length	5 mm	6 mm	7 mm	10 mm	20 mm
Patched surface	11.2	11.5	11.8	12.0	11.6
Middle	11.9	12.4	12.7	13.3	14.3
Bottom	12.0	13.16	12.9	13.4	14.1

Table 9.4

K values for a repaired center notch panel, patch thickness 1 mm.

Crack half length	5 mm	6 mm	7 mm	10 mm	20 mm
Patched surface	14.6	15.2	15.6	16.1	15.7
Middle	15.5	16.3	16.8	17.8	19.4
Bottom	15.6	16.4	17.0	17.9	19.1

Table 9.5

Comparison of solutions for K_{∞} for a patch thickness 1.85 mm.

Crack configuration	Crack length	Predicted	K finite element
Center crack	20 mm	14.1	~ 14.1 to 14.3
Edge crack	20 mm	12.7	~ 12.7 to 12.9

and the finite element results are summarised in Table 9.5. The differences for the third study are summarised in Table 9.6. In each case the agreement is shown to be quite good. The analytical formulae are also quite accurate for the case when bending is allowed, see Tables 9.7–9.9. However, in this case the accuracy of the simple analytical formulae decreases when the crack length approaches a half of the patch width (X).

For repairs to rib stiffened panels the bending correction factor BC must be modified. This modification involves a parameter, which we will call the stiffener correction factor, SCF.

$$\text{SCF} = \frac{(P \times \ln(10^{12} I_s) - Q)}{10^2}, \quad (9.28)$$

where, to a first approximation, P and Q are only functions of the ratio $E_r t_r / E_p t_p$.

Table 9.6

Comparison of prediction for K_{∞} for various patch configurations.

Crack configuration	Crack length	Configuration	Predicted	K finite element
Edge crack $\sigma = 344.8$ MPa	20 mm	Skin ^A 2 mm, patch = 0.75 mm $G_a = 375$ MPa $t_a = 0.25$ mm	21.6	17.8–22.4
Center crack $\sigma = 344.8$ MPa	20 mm	Skin ^A 2 mm, patch = 0.75 mm $G_a = 375$ MPa $t_a = 0.25$ mm	23.6	19.8–24.0
Center crack $\sigma = 229.8$ MPa	20 mm	Skin ^A 3 mm, patch = 1.00 mm, $G_a = 375$ MPa $t_a = 0.25$ mm	19.2	15.7–19.1
Center crack $\sigma = 229.8$ MPa	20 mm	Skin ^B 3 mm, patch = 0.889 mm, $G_a = 750$ MPa $t_a = 0.165$ mm	16.2	15.7–15.8

^A The planform of the skin and patch were as previously described.

^B Planform of plate was 320 mm \times 150 mm (wide) with a semi-circular patch, radius = 80 mm.

Table 9.7
Comparison of prediction for bending problems, Case 1.

K_{max} MPa m ^{1/2}	Edge center	a mm	t_p mm	E_p MPa	t_r mm	G_r MPa	t_a mm	G_a MPa	σ MPa	X mm	B mm
	Center	40	3.16	72000	1	208030	0.2	375	158	200	200
predicted	48.3										
f.e.	47.4										

Table 9.8
Comparison of prediction for bending problems, Case 2.

K_{max} MPa m ^{1/2}	Edge center	a mm	t_p mm	E_p MPa	t_r mm	G_r MPa	t_a mm	G_a MPa	σ MPa	X mm	B mm
	Edge	20	2	72000	0.75	208030	0.25	375	345	200	200
predicted	85.2										
f.e.	83.4										

Table 9.9
Comparison of prediction for bending problems, Case 3.

K_{max} MPa m ^{1/2}	Edge center	a mm	t_p mm	E_p MPa	t_r mm	G_r MPa	t_a mm	G_a MPa	σ MPa	X mm	B mm
	Center	20	3	71000	0.89	208000	0.17	750	230	41	145
predicted	62.7										
f.e.	59.2										

Stiffness ratio $E_r t_r / E_p t_p$	"P"	"Q"
0.73	2.8	10
0.91	2.4	12
1	2.7	18
1.15	1.9	13
1.28	2.2	18
1.3	2.5	23
1.62	1.6	17
1.65	1.9	22
2.1	1.4	21

The new stress intensity factor, which included stiffener effects, for rib stiffened panels thus becomes:

$$K_p = (1 - SCF)K_p \quad (9.29)$$

This approximation has been validated by comparison with more than 2000 different 3D numerical examples, see Figure 9.4.

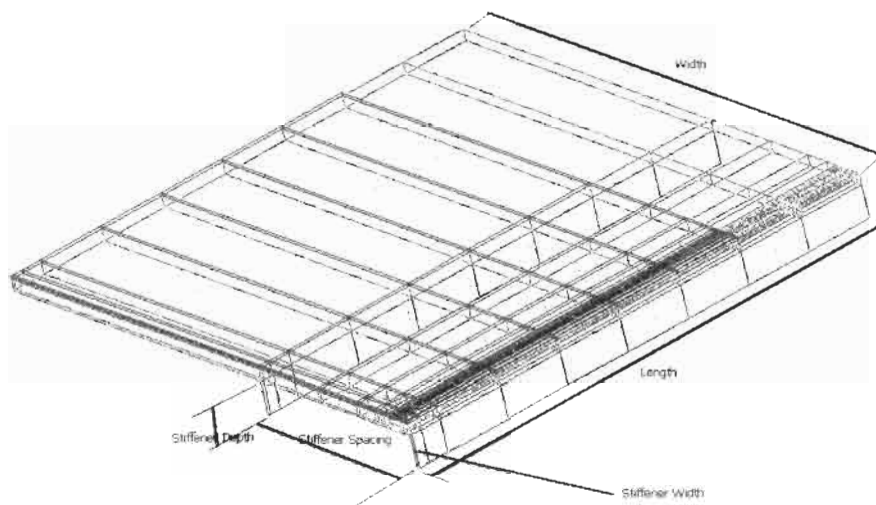


Fig. 9.3. Schematic of three dimensional 1/4 finite element model of stiffened panel.

To illustrate the accuracy of this formulae a 3D finite element study for the composite repair of cracked rib stiffened panels was undertaken. In this study the stiffeners were assumed to be riveted to the skin. Symmetry considerations enabled only a 1/4 of the structure to be modelled. The typical geometries investigated is shown in Figure 9.3. In this study the crack length, patch thickness, skin thickness,

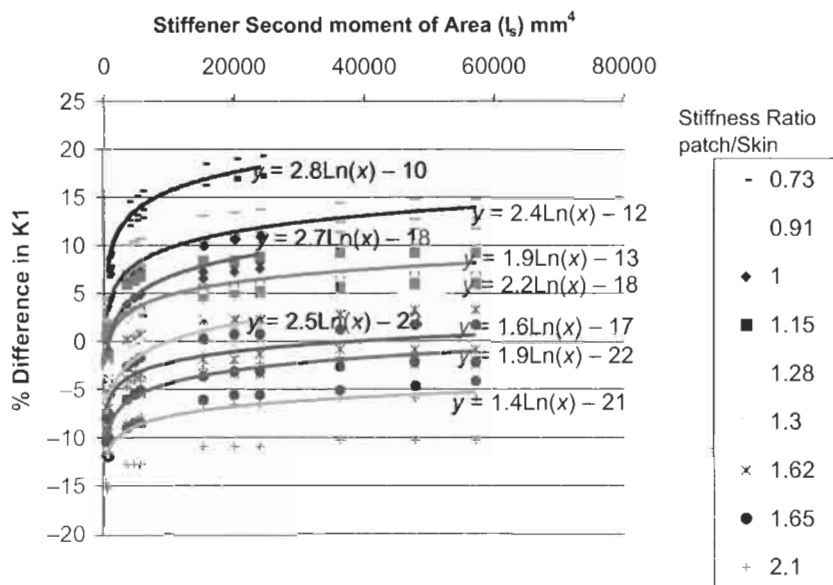


Fig. 9.4. Plot of percentage difference in the value of K_{1max} , defined as y , of numerical analysis from closed form solution v 's x , the second moment of areas (I_s) for a range of stiffness ratios.

stiffener width, stiffener spacing, and stiffener depth were varied to determine their effects on the stress intensity factors.

The difference between the predicted, using Eqs. (9.17), (9.23) and (9.24), and the computed values of K_{\max} are summarised in Figure 9.4. From this we see that even without allowing for effect of the stiffener and the predicted values lie within 18% of the numerical values. When allowing for the stiffeners using the stiffener correction factor (SCF), i.e. Eq. (9.29) the approximate formulae was accurate, for all (200+) test cases, to within 5%.

To confirm the accuracy of these formulae an experimental study into the composite repair of cracked rib stiffened panels was also undertaken. The test geometry, for which bending was not restrained, was as shown in Figure 9.5.

Test matrix			
Case and number of specimens	Skin thickness	Stiffener broken or unbroken	Crack length
Case 1: 3	1.25	Unbroken	40 mm
Case 2: 3	1.25	Broken	40 mm

In each test case the loads were adjusted to give a peak stress in the skin of 120 MPa. In the first test case we had a skin thickness of ~ 1.25 mm and a width of 133 mm. The area of the skin A_p was thus:

$$\begin{aligned} A_p &= [133 \times 10^{-3} \text{ m}] \times [1.25 \times 10^{-3} \text{ m}] \\ &= 1.665 \times 10^{-4} \text{ m}^2 \end{aligned}$$

For this test configuration the cross sectional area of the stiffener A_s was

$$\begin{aligned} A_s &= [50 \times 10^{-3} \text{ m}] \times [2.2 \times 10^{-3} \text{ m}] + [23 \times 10^{-3} \text{ m}] \times [2.2 \times 10^{-3} \text{ m}] \\ &= 1.606 \times 10^{-4} \text{ m}^2 \end{aligned}$$

This gave a total cross sectional Area (A_t) of $3.271 \times 10^{-4} \text{ m}^2$. In this case the maximum F_{\max} force needed to be applied was

$$F_{\max} = \sigma \times A_t = 39.5 \text{ kN}$$

The fatigue test program was performed with an R ratio of 0.5. Consequently, the loads applied in the fatigue test were $F_{\min} = 1.96 \text{ kN}$ and $F_{\max} = 39.5 \text{ kN}$. The exception to this was the first test specimen where the minimum and maximum loads applied were $F_{\min} = 2.0803 \text{ kN}$ and $F_{\max} = 41.6 \text{ kN}$ respectively. In this case the stress amplitude, rather than the maximum stress, was $\sim 120 \text{ MPa}$.

From the results of the first test sample (Sample 2/40.1), see Figure 9.7, which had an intact stiffener we found that the crack growth rate was constant and that

$$\frac{da}{dN} = 5.578 \times 10^{-4} \text{ mm/cycle} = 21.96 \times 10^{-6} \text{ in/cycle}$$

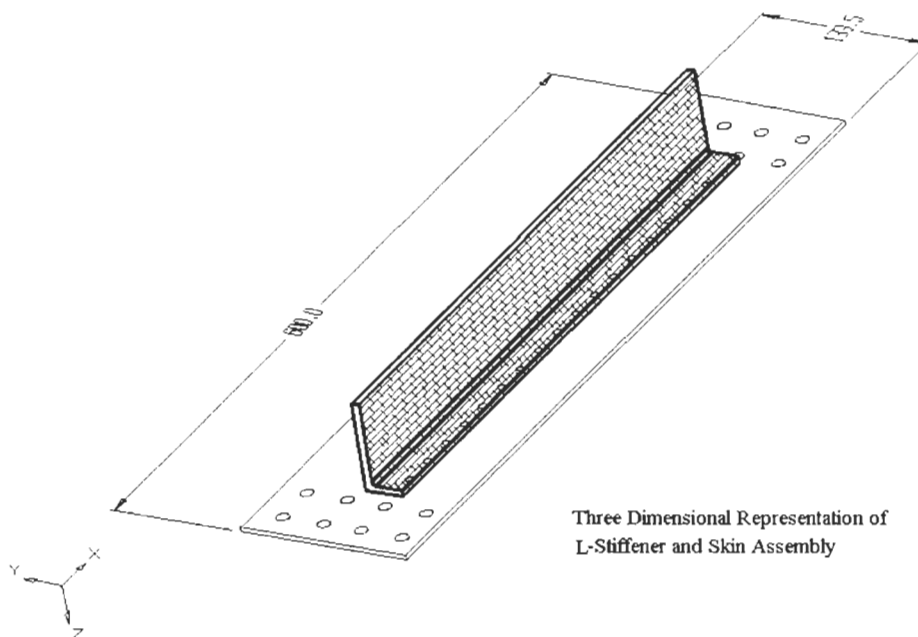


Fig. 9.5. Schematic representation of the panel test geometry.



Fig. 9.6. View of patched surface and underside of the test configuration with cracked stiffener.
Note adhesive seepage through the rivets.

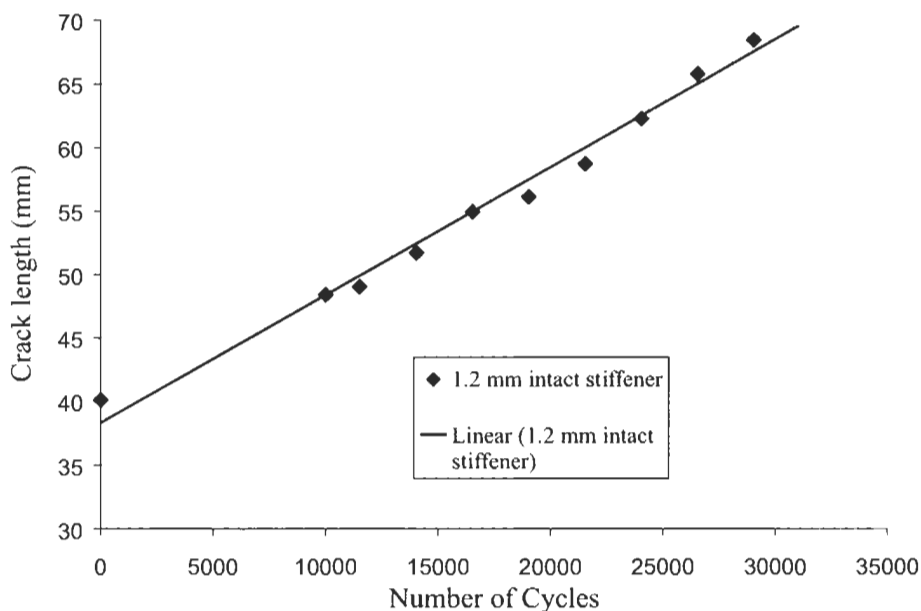


Fig. 9.7. Crack growth for a 1.25 mm thick specimen (intact stiffener) $\Delta\sigma = 120$ MPa.

In this case from the results¹ given in [31], page 8.9-84, for an R ratio of 0.02 and a plate thickness of between 0.02" to 0.2", we found that the experimental crack growth rate corresponds to an (experimental) value of ΔK of $\sim 11 \text{ MPa m}^{1/2}$. This compares quite favourably with the values of ΔK of $12.2 \text{ MPa m}^{1/2}$, obtained using the semi-analytical formulae, and $\sim 12.5 \text{ MPa m}^{1/2}$ obtained via a detailed 3D finite element analysis². For the subsequent tests the stress amplitude was ~ 11.4 MPa. The growth rate again was constant and da/dN of $\sim 3.72 \times 10^{-4} \text{ mm/cycle}$, see Figure 9.8. The experimental crack growth rate corresponded to an (experimental) value of ΔK of $\sim 10.0 \text{ MPa m}^{1/2}$ compared with a predicted value of $11.5 \text{ MPa m}^{1/2}$ and $11.8 \text{ MPa m}^{1/2}$ obtained using 3D finite element analysis.

When the stiffener was broken the stress in the skin under the stiffener increased to ~ 238 MPa. In this case we obtained a predicted value of ΔK of $23.9 \text{ MPa m}^{1/2}$, obtained using the semi-analytical formulae, and a value of $21.2^3 \text{ MPa m}^{1/2}$ obtained via a 3D finite element analysis. From the experimental test results, see Figure 9.9, we again obtained a constant growth rate with a da/dN of $\sim 2.39 \times$

¹ In this case the growth law can be approximated as $da/dN \cong 1.64 \times 10^{-9} (\Delta K)^{2.35}$.

² This value was obtained for a 40 mm (tip to tip) crack. For a 14 mm crack the value obtained was $\sim 11.5 \text{ MPa m}^{1/2}$.

³ This value was obtained for a 40 mm (tip to tip) crack. For a 14 mm crack the value obtained was $\sim 22.6 \text{ MPa m}^{1/2}$.

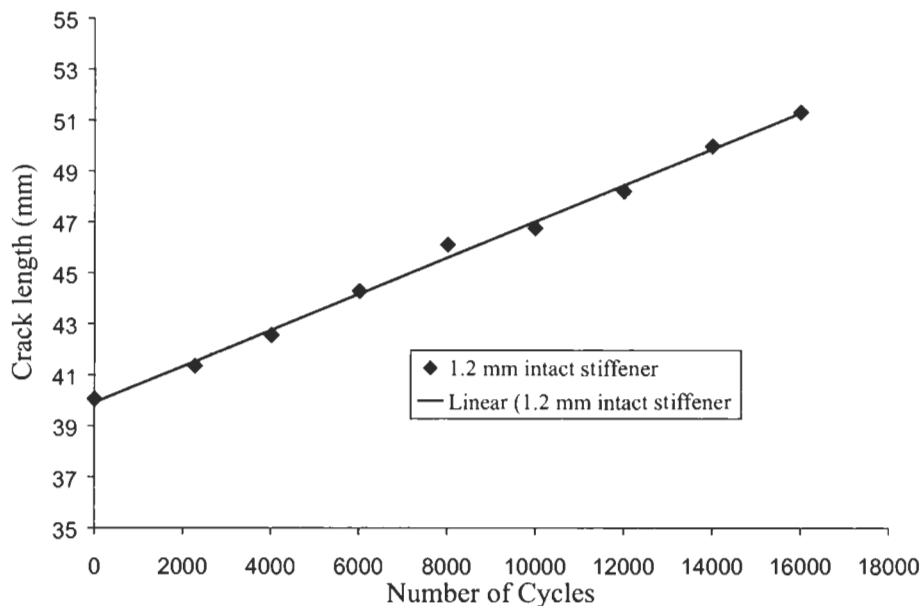


Fig. 9.8. Crack growth for a 1.25mm thick skin specimen with an intact stiffener, max stress of 120 MPa.

10^{-3} mm/cycle. In this case using the results given in [31] this growth rate gave a ΔK of $\sim 22.3 \text{ MPa m}^{1/2}$, which is in reasonable agreement with the numerical predictions. The tests results were extremely repeatable, as can be seen from Figure 9.9.

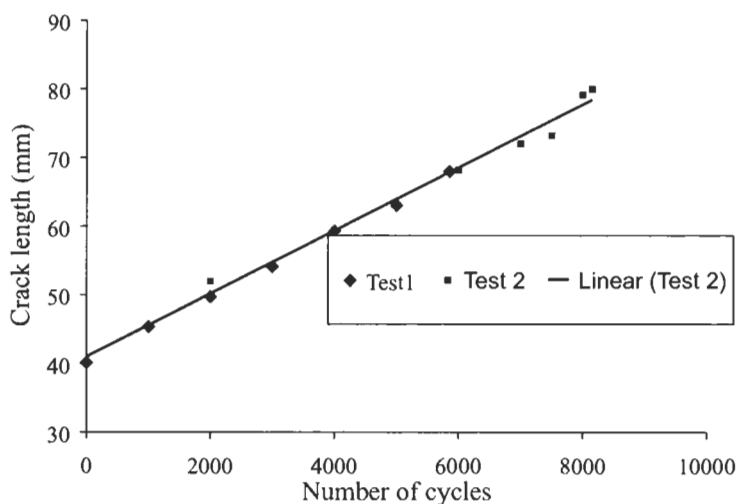


Fig. 9.9. Crack growth for a 1.25mm thick skin specimen with a broken stiffener.

During the fatigue tests it was found that failure generally initiated at rivet holes outside of the patched area. The location of the initiation site was essentially random and appeared to associated with the initial fabrication of the specimen.

9.4. Comparison with experimental results for non rib stiffened panels

To further illustrate the accuracy of these simple formulae let us consider a centrally located crack, 38 mm long, in a rectangular sheet of aluminium alloy with dimensions $300\text{ mm} \times 320\text{ mm} \times 2.29\text{ mm}$. The crack is patched, on one side only, with a uni-directional boron epoxy laminate with dimensions $160\text{ mm} \times 160\text{ mm} \times 0.889\text{ mm}$ and bending is prohibited, see Figure 9.10. The adhesive is 0.1651 mm thick and has a shear modulus of 700 MPa. The aluminium alloy has a Youngs modulus E of 7.2.86 GPa and a Poisson's ratio of 0.3, whilst the

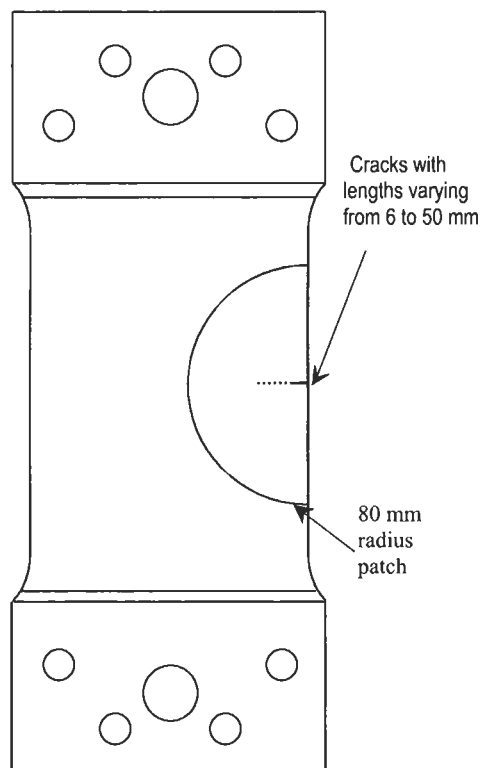


Fig. 9.10. Geometry of edge cracked edge notch test specimen.

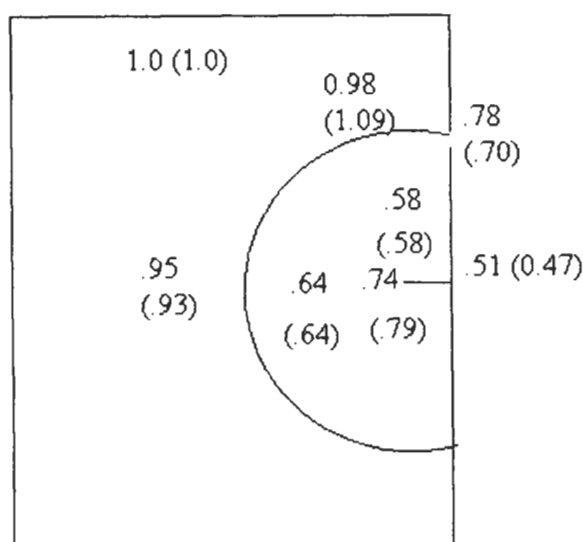


Fig. 9.11. View of the repaired region showing the ratio of measured strains to the far field strain, finite element values in brackets.

moduli of the boron epoxy laminate are taken as

$$E_{11} = 208.3 \text{ GPa}, E_{22} = 24.5 \text{ GPa}, \nu_{12} = 0.1667, G_{12} = 7.24 \text{ GPa}$$

We first analyse this problem, making use of symmetry using a fully 3D finite element model. The aluminium sheet is modelled by forty-one twenty-noded isoparametric bricks and thirteen of the fifteen-noded isoparametric elements whilst the composite patch is represented by twenty-one of the twenty-noded isoparametric bricks and thirteen of the fifteen-noded isoparametric elements.

The elements at the crack tip are triangular in plan form and have the midpoint nodes moved to the quarter points in order to simulate the $r^{-1/2}$ singularity at the crack tip. The elements at the crack tip are triangular in plan form and have the midpoint nodes moved to the quarter points in order to simulate the $r^{-1/2}$ singularity at the crack tip. To avoid problems with numerical ill conditioning and the use of elements with large aspect ratios, reduced integration, or preferably directionally reduced integration, must be used whenever a full 3D analysis is undertaken. In addition, on 32 bit machines the formulation of the stiffness matrices and the solution must be done using double precision.

Let us now compare these results with those obtained experimentally for this repair configuration. Figure 9.11 shows a comparison of the numerically predicted surface strains with those measured strains on the surface of the patch at four locations. The clip gauge openings measured near the mouth of the crack are given in Table 9.10 as are those predicted numerically and those using the analytical approach.

Table 9.10
Clip gauge opening.

	Clip gauge opening (mm)
Predicted using F.E.M.	0.037 mm
Predicted analytically (overlap joint analogy)	0.032 mm
Measured	0.041 mm

This clearly shows that the finite element approach is capable of accurately representing realistic repairs and that the analytical formulae provide a good first estimate of the clip gauge opening and hence the adhesive stresses/energy.

9.5. Repair of thick sections

In recent years, a number of boron epoxy patches have been used to repair surface flaws in thick sections, e.g. the repairs to the Macchi and Mirage main landing wheels and the repair to the console truss in F111 aircraft (see [10]). In each case, the crack section was ~ 12 mm thick.

In the case of the Mirage and Macchi landing wheels, the repairs are installed when the crack reaches a total length of 24 mm. In each case, the cracks were found to be nearly semi-elliptical in shape with a surface length of 24 mm and a maximum depth of 6 mm. In order to study the effect on such a crack, an investigation was undertaken on the repair of a similar semi-elliptical crack centrally located in a rectangular block of aluminium with dimensions as shown in Figure 9.12, (in this figure, only one quarter of the structure is shown). The block was subjected to a uniform uniaxial stress, and the effect that various boron fibre patches had on the crack were calculated using a detailed 3D finite element analysis. Table 9.11 shows the calculated values of the stress intensity factors at point d , the point of deepest penetration, and s , the point at which the crack intersects the free surface. The fibre stresses σ_f are a maximum over the crack and vary through the thickness of the

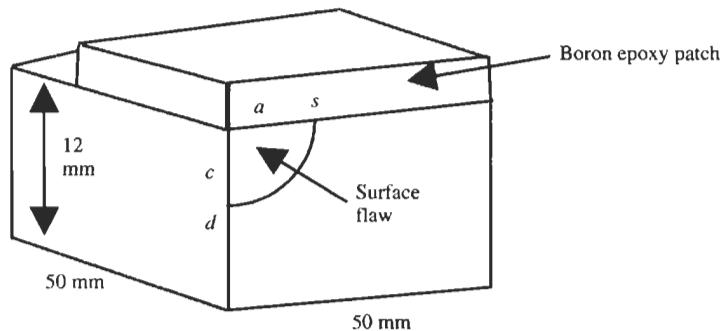


Fig. 9.12. Repair of surface flaw (1/4 structure modelled).

Table 9.11

Semi-elliptical flaw $A = 12$ mm; $C = 6$ mm; unpatched values at d , $K_I = 12.45 \text{ MPam}^{1/2}$, at s , $K_I = 12.5 \text{ MPam}^{1/2}$.

Number layers boron	Stress intensity factor K_I at:		Fibre stress over crack σ_f / σ at points			Adhesive shear stress over crack τ/σ
	d	s	1	2	3	
5	8.33	4.396	3.481	4.256	5.293	0.451
10	7.222	3.3463	1.918	2.572	3.670	0.353
15	662	2.979	1.271	1.810	2.907	0.304
20	365	2.709	0.874	1.364	2.488	0.277
25	211	2.588	0.587	1.073	2.244	0.262

Table 9.12

Semi-circular flaw $A = C = 6$ mm

Number layers boron	Stress intensity factor at K_I at:		Fibre stress over crack σ_f / σ at points:			Adhesive shear over crack τ/σ stress
	d	s	1	2	3	
5	882	5.412	3.333	3.966	4.811	0.402
10	232	4.552	2.113	2.672	3.615	0.337
15	5.842	4.035	1.541	2.005	2.972	0.300
20	5.605	3.712	1.153	1.576	2.582	0.276
25	5.465	3.509	0.852	1.276	2.337	0.261

patch. These values are also shown in Table 9.12 along with the peak adhesive stresses over the crack. In this study, the adhesive was taken to be AF126, an epoxy nitrile, 0.1016 mm thick with a shear modulus of 0.7 GPa. Table 9.12 also shows the corresponding values of stress intensity factors, fibre stresses and adhesive stresses for the case when the surface flaw is semi-circular, rather than semi-elliptical, with a surface length of 12 mm.

As a second example let us consider the problem of a 40.12 mm (surface crack length) by 5.71 mm (crack depth) surface flaws in rectangular aluminium alloy section with dimensions 300 mm \times 128 mm \times 11.2 mm, see Figure 9.13. This section is subjected to a remote uniform stress σ of 68.9 MPa acting at right angles to the crack plane. The structure is assumed to be repaired using a ten ply boron epoxy laminate, i.e. 1.27 mm thick, bonded over the crack with using the, 0.106 mm thick, structural film adhesive FM73.

To illustrate the effect of surface crack length three different surface lengths were considered; viz: 10.066, 20.066 and 30.66 mm and the values of K_a , at the surface, and K_c at the point of maximum depth computed, see Table 9.13. To illustrate the effect of crack depth a case when the surface length was 10.066 and the crack depth was 3.0 mm was also considered.

From Table 9.13 it is apparent that the stress intensity factors are dependent on the surface crack length and the depth of the crack. However, the value of maximum stress intensity factor K_c increases only slightly as the surface crack

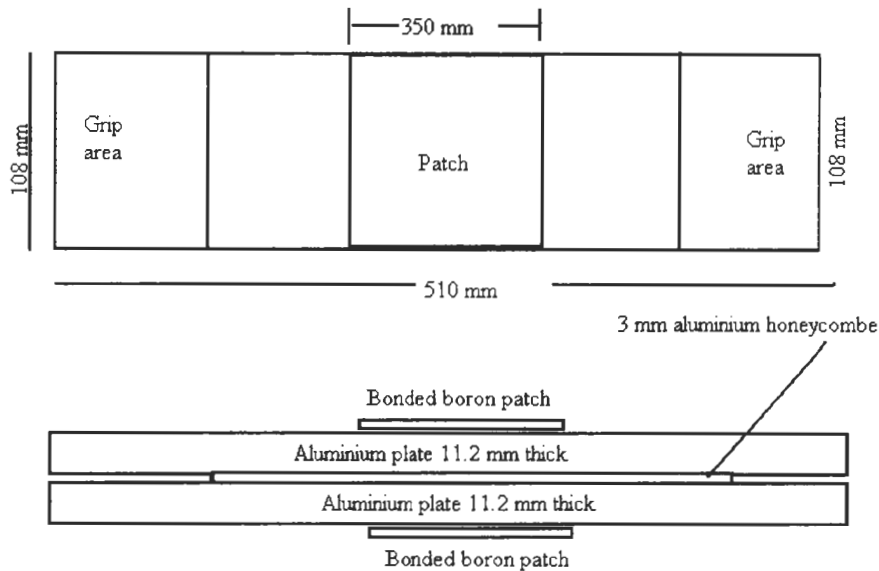


Fig. 9.13. Geometry of the surface flaw specimen.

Table 9.13

Stress intensity factors for a semi-elliptical surface flaw after repair.

Surface crack half length mm	K_a MPa m ^{1/2}	K_c MPa m ^{1/2}
10.066	1.4	4.5
20.066	0.73	5.3
30.066	0.48	5.46
10.066 surface length by 3.0 mm deep crack	0.68	3.56

length increases from 20.66 mm to 30.66 mm. This “asymptotic” phenomenon was discussed previously. However, for 3D surface flaws it should be stressed that the value of the maximum stress intensity factor, in this case K_c , will depend on the depth of the crack.

9.5.1. Experimental results

To illustrate the significant reductions in the stress intensity factors and hence in the rate of crack growth, a series of fatigue tests were performed. The specimens were 2024 T4 aluminium alloy, 11.1 mm thick, 108.3 mm wide and 304 mm long, and contained a centrally located surface crack. The surface length of the crack was 37 mm and it was 6 mm deep, see Figure 9.13. A 3D finite element analysis was performed and the ratio of the patched stress intensity factor to the unpatched

value was found to be 0.22, at the upper surface, and 0.44 at the deepest point in the aluminium. Five specimens were tested under a constant amplitude stress of 65 MPa and $R=0.01$. A further six specimens were repaired with a ten ply thick boron fibre patch. In confirmation of our previous results, the unpatched specimens lasted an average of 22.450 cycles whilst the patched specimens lasted an average of 527000 cycles.

From Tables 9.11 and 9.12 we see that the peak fibre and adhesive stresses are relatively insensitive to the surface lengths of the crack. Consequently, we can estimate the peak values of these stresses in the specimens, viz:

$$\sigma_f = 3.67 \times 65 \text{ MPa} = 238 \text{ MPa and}$$

$$\tau_{\max} = 0.353 \times 65 \text{ MPa} = 22.94$$

These values are considerably lower than their critical design values. Several specimens were also loaded at 130 MPa with no evidence of fibre breakage or patch debonding.

Tests were also performed using FALSTAFF loading with a peak stress of 138.9 MPa. The fatigue lives of these test specimens are given in Table 9.14.

This illustrates that under FALSTAFF loading the repair has increased the fatigue life of the component by a factor of approximately 5.8. This is significantly lower than the value of ~ 22 obtained using constant amplitude loading. This was due to a variety of effects:

- Fatigue damage in the adhesive due to the higher loads.
- Growth of disbond/delamination directly over the crack.
- Plastic strain of the adhesive which results in a higher K , see Eq. (9.27).
- Load history effects due to the visco-plastic nature of the adhesive.

Although there was adhesive disbonding during the tests, final failure was in the boron epoxy composite and was due to delamination of the upper nine plies from the (1st) ply next to the adhesive boron interface, see Figure 9.14. Indeed, this failure mechanism has been observed in a range of composite repairs and

Table 9.14
Fatigue of repair to thick section under FALSTAFF loading.

Patched/unpatched	Specimen	Cycles to failure
Unpatched	9/22U	344039
	5/6U	326560
	3/4U	411595
	7/8U	334778
	mean	354117
Patched	14/15P	1954783
	18/19P	2699357
	16/17P	1923680
	12/13P	1632406
	mean	2052557

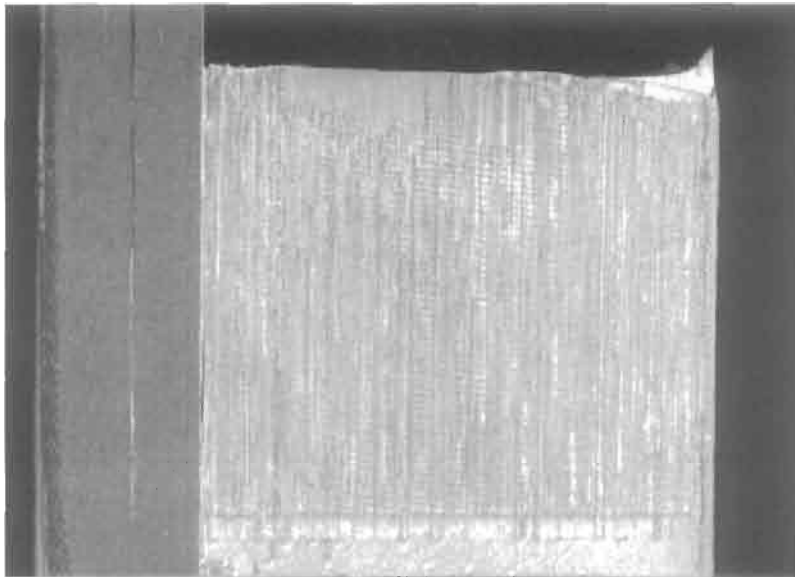


Fig. 9.14. Close up of failure surface showing 1st layer of repair still attached to the specimen.

composite joints [3,15]. Consequently when designing repairs to primary structural components this highlights the need to:

1. Allow for interlaminar failure in the composite repair.
2. Allow for the visco-plastic behaviour of the epoxy.

At the moment this level of analysis can only be done using advanced finite element tools. Hence for primary structures repairs need to be designed using 3D finite element analysis. A methodology for allowing for material non-linearities without the need to perform a fully non-linear finite element analysis will be given in the following sections.

9.6. Repair of cracked holes in primary structures

Let us now consider the repair of corner flaws, with a surface length of c and a depth of a , at a through the thickness holes of radius r , see Figure 9.15. The material is a 2024-T4 aluminium alloy with $E=72.4$ GPa and $\nu=0.33$. The thickness of the structure was taken to be $t=11.2$ mm, its width $w=72$ mm and the total length to be $2h=200$ mm. Two repair cases are considered. In the first we use a 1.27 mm, i.e. a 10 ply, patch with an adhesive thickness of 0.1016 mm and where the fibres are orientated perpendicular to the crack. In the second we augment the patch with a 1 mm thick steel sleeve which is assumed to be bonded into the hole. The structure is subjected to a uniform remote stress of 68.9 MPa. The resultant values for the stress intensity factors at point s on the crack front nearest the patch and at point d down the bore of the hole are given in Table 9.15.

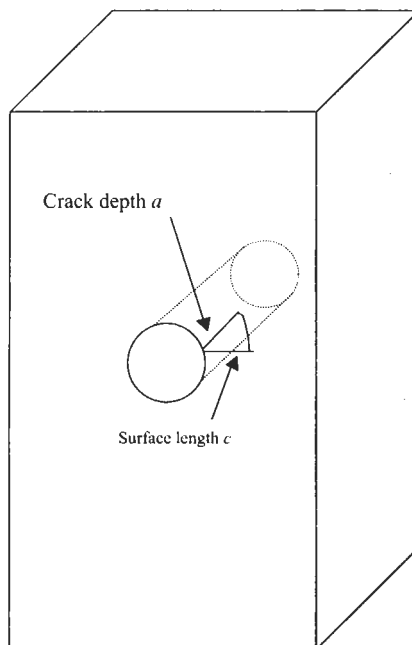


Fig. 9.15. Geometry of cracked hole.

Table 9.15
Stress intensity factors $\text{MPa m}^{1/2}$ for patched specimens.

Case	Location	Unrepaired value	Case 1: Patch only	Case 2: Patch and steel sleeve
$a = c = 3 \text{ mm}$, $r = 3 \text{ mm}$	S	74	3.17	2.43
	D	10.61	7.97	3.66
$a = c = 3 \text{ mm}$, $r = 5 \text{ mm}$	s	7.89	3.8	2.96
	d	12.63	9.7	4.7
$a = 3 \text{ mm}$, $c = 6 \text{ mm}$, $r = 3 \text{ mm}$	s	3.62	1.77	1.02
	d	10.8	7.89	3.48
Through crack $r = 3 \text{ mm}$, $c = 3 \text{ mm}$	s	9.42	4.0	3.06
		11.5 at the mid-surface	11.1 on the unpatched surface	68 on the unpatched surface

The point to note here is that, as we saw in the previous cases, the patch alone has only a relatively small reduction in K at the point d deepest into the structure. To reduce K at this point requires further action. In this case the use of a steel sleeve bonded into the hole.

To obtain a first estimate of the worst (highest) value for K it is possible to use the solution for a through crack. Table 9.15 allows us to predict the effect of the patch on fatigue life. For the case of a patch only with $a = c = 3$ mm we see that the ratio of the unpatched stress intensity factor to unpatched value is 10.6/7.97. As a first approximation the rate of crack growth can be related to ΔK the stress intensity range during cycling by the Paris growth law,

$$\frac{da}{dN} = C(\Delta K)^n,$$

where for aluminium alloys $n \sim 3$. Thus as a first approximation the increase in life due to patching can be estimated as:

$$L_r = \frac{\text{repaired fatigue life}}{\text{repaired fatigue}} = \frac{(\Delta K_{\text{unpatched}})^n}{(\Delta K_{\text{patched}})^n},$$

which for the case when $a = c = 3$ mm and $r = 3$ mm this gives a value of 2.35. For the case when $a = c = 3$ mm and $r = 5$ mm we obtain a value of 2.21.

To illustrate the effectiveness of this approach a series of constant amplitude fatigue tests were performed for each of the two repair cases listed in Table 9.15. The results of this investigation are shown in Table 9.16. Table 9.17 compares the

Table 9.16
Fatigue test results for repair of cracked holes.

Specimen configuration	Number	Fatigue life cycles	Average cycles
$a = c = 3 \text{ mm}, r = 3 \text{ mm}$			
Un-repaired	A1	94240	113537
	A2	104150	
	A3	137830	
	A4	117930	
Repaired Case 1	A5	119800	215405
	A6	179160	
	A7	277310	
	A8	285351	
Repaired Case 2	A9	623630 ⁺	N/A
	A10	2,347300 ⁺	
	A11	2,253500 ⁺	
	A12	5,078200 ⁺	
$a = c = 3 \text{ mm}, r = 5 \text{ mm}$			
Unrepaired	B1	97600	94967
	B2	86600	
	B3	100700	
Repaired with patch only	B5	162500	203900
	B6	147000	
	B7	258000	
	B8	248100	

⁺Specimens failed in grips.

Table 9.17
Comparison of fatigue life increase due to patch only.

Case	Predicted	Measured
$a = c = 3 \text{ mm}, r = 3 \text{ mm}$	2.35	1.9
$a = c = 3 \text{ mm}, r = 5 \text{ mm}$	2.21	2.1

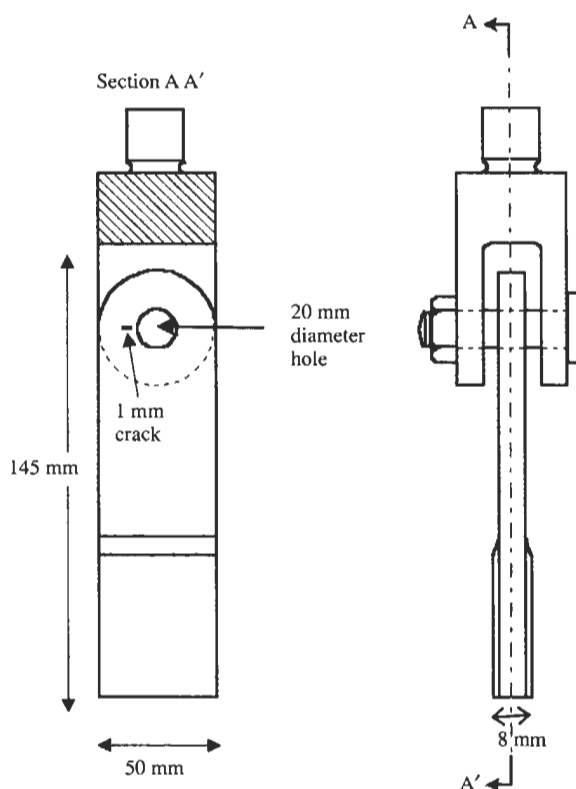


Fig. 9.16. Schematic diagram of lug with 20 mm diameter hole.

predicted increase in life with that obtained experimentally and as can be seen the agreement is quite good.

9.7. Repair of cracked lugs

Let us now consider the repair of an aluminium (7075-T651) lug, see Figure 9.16, which was designed to be representative of a cracked, load-bearing, fastener hole. The specimen was 8 mm thick, 145 mm long and 50 mm wide and contained a

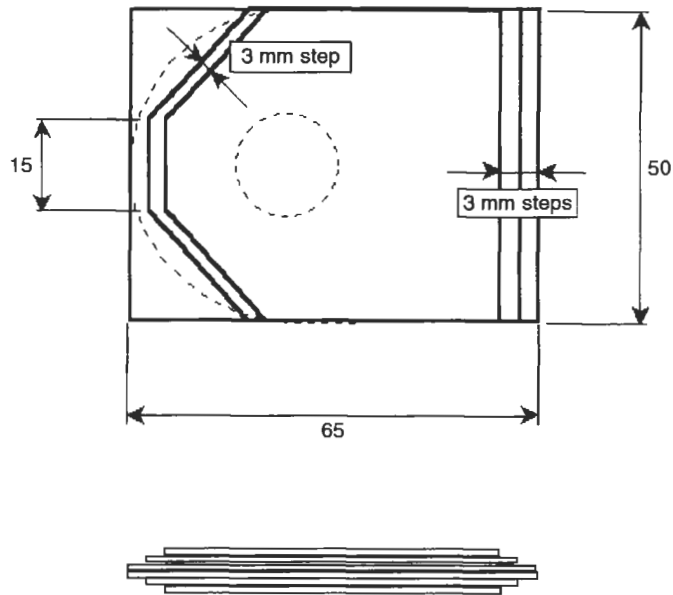


Fig. 9.17. Schematic diagram of lug repair, all dimensions in mm.

20 mm diameter hole, see Figure 9.17. In this investigation the specimen also had a 1 mm notch machined on one side of the loading hole. A fatigue crack was initiated from this notch and grown an average length of 1 mm to give a total crack length of 2 mm.

The traditional approach to the design of a bonded composite repair is to restore the local stiffness. For the present problem this would require a 2.8 mm thick (or 22 ply) boron/epoxy doubler. However, the available specimen load transfer and taper lengths restricted the repair thickness to 0.8 mm (or 6 ply) per side, see Figure 9.17. A doubler was applied to each side of the specimen giving a total repair material thickness of 1.6 mm. Thus only a 55% stiffness restoration was possible. The doublers were made from boron/epoxy prepreg tape and bonded to specimens using an epoxy-based structural-film adhesive in an autoclave.

In an effort to further reduce the stress intensity at the crack front, two specimens were also repaired with a combination of composite doublers and a 1 mm thick steel-sleeve insert was then bonded into the fastener holes using a two-part acrylic structural paste adhesive. A test matrix outlining the specimen configurations is given in Table 9.18.

To ensure accurate bonding of the sleeves in the holes a bonding jig was used to locate both the sleeve and specimen. This ensured that the bondline thickness was constant around the circumference of the sleeve. The adhesive was allowed to cure at room temperature and atmospheric pressure prior to removal of the repaired specimens from the bonding jig.

Table 9.18

Test matrix for lug repair specimens.

Specimen Number	Description
1	Spare
2	Repaired with doublers
3	Repaired with doublers and a sleeve
4	Repaired with doublers
5	Repaired with doublers and a sleeve
6	Unrepaired, as reference
7	Unrepaired, as reference

9.7.1. Numerical analysis

A 3D numerical analysis of the pin-loaded specimen was performed using symmetry in the z direction. The structure was loaded to 36 MPa, which was equivalent to applying a load of 14.4 kN to the end of the specimen (Figure 9.16). The load transfer at the hole is a complex problem which was modelled using a non-linear gaps analysis.

Two repair configurations, as described above, were analysed. The first configuration was modelled with 3D iso-parametric brick elements representing both the adhesive layer and the boron/epoxy laminate. The second configuration was analysed in the same way, except that the pin size was reduced and the adhesive layer and steel sleeve were also modelled.

In each case the finite-element analysis needed to be 3D and used both 20-noded iso-parametric brick elements and 15-noded iso-parametric prism elements. To avoid problems associated with the use of large aspect ratios, reduced integration was used. At the crack tip, triangular elements were used with their mid-side nodes relocated to the quarter point location closest to the crack tip. For increased accuracy the size of the crack-tip elements should be set at $\sim 1/15$ the length of the crack.

For each specimen configuration five crack lengths were analysed and an analysis of the un-cracked specimen was also performed. The crack lengths examined were 2 mm, 4 mm, 6 mm, 8 mm and 10 mm. In each case the crack was assumed to grow directly towards the outer edge of the specimen. The finite element meshes used for this analysis are shown in Figure 9.18. In all cases the boron/epoxy laminate was uni-directional, 0.8 mm thick (6 plies).

For each crack length the stress intensity factors (K) were calculated at the surface and at the mid-point of the specimen. The results for all three configurations can be seen in Figure 9.19. The results for the repaired configuration show that the stress intensity factor reduces to an asymptotic value. This phenomena has been discussed earlier. The effect of the idealised sleeve in the hole is to further reduce the stress intensity factor.

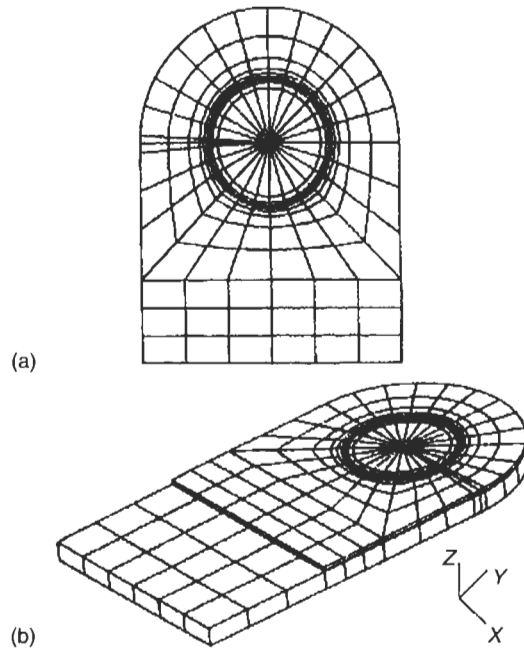


Fig. 9.18. Schematic diagram of finite element mesh.

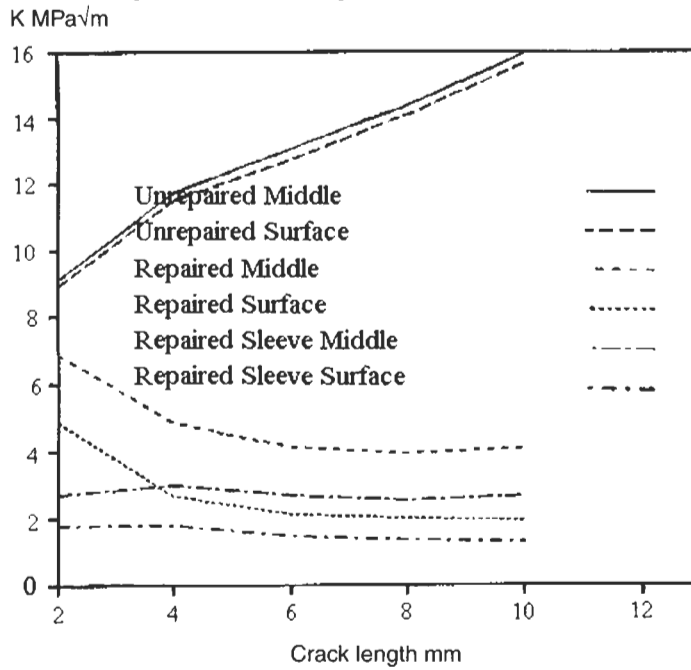


Fig. 9.19. Stress intensity factors for the various repair configurations.

9.7.2. Experimental test

To assess the effectiveness of the repair a total of six specimens were fatigue tested at constant-amplitude load. The three specimen configurations, as described in Table 9.18. The specimens were loaded from 1.0 kN to 14.4 kN using a sinusoidal wave-form at a frequency of 5 Hz.

In the case of Specimens 6 and 7 (the unrepaired group) the length of the crack was measured on both sides of the specimen using a travelling vernier microscope. The crack length of the remaining repaired specimens was measured non-destructively through the boron/epoxy repair using an eddy-current instrument. For the repaired specimens it was not possible to monitor the crack for more than approximately 10–11 mm of growth due to interference from the outer edge of the specimen as crack growth progressed.

The loading mechanism consisted of a 100 kN static (50 kN dynamic) load cell attached to the upper crosshead of a servo-hydraulic testing machine. Each specimen was loaded using a simple pin and clevis grip with the unreinforced lower end of the specimen clamped in flat hydraulic grips. To avoid premature fatigue failure of the specimen within the test-machine grips, end tabs, as shown in Figure 9.11, were bonded to the unreinforced end of the specimen.

The results of this test program are shown in Table 9.19 and in Figure 9.20. For the unrepaired specimens the failure was due to complete failure of the ligament containing the crack and subsequent inability to sustain load. For the repaired specimens, failure was defined as the appearance of the crack on the outer edge of the ligament running from one face to the other. At this stage the mean load (7.7 kN) was still sustainable. To evaluate the residual strength a subsequent static test was carried out on Specimen 2. This specimen failed at a load of 25.29 kN and a far field strain of 930 $\mu\epsilon$.

The average crack growth rate versus crack length relationship for the three specimen types is shown in Figure 9.20. From this figure it can be seen that a composite repair is capable of significantly increasing the fatigue lives of cracks in an 8 mm thick aluminium alloy.

Table 9.19
Fatigue test results for repaired lug.

Specimen	Unrepaired	Boron patch only	Patch plus steel sleeve
6	11900		
7	12500 ⁺		
2		168034	
4		130000*	
3			213000
5			176000

⁺ Test was stopped immediately prior to failure.

* Test was stopped and doubler removed to confirm crack length.

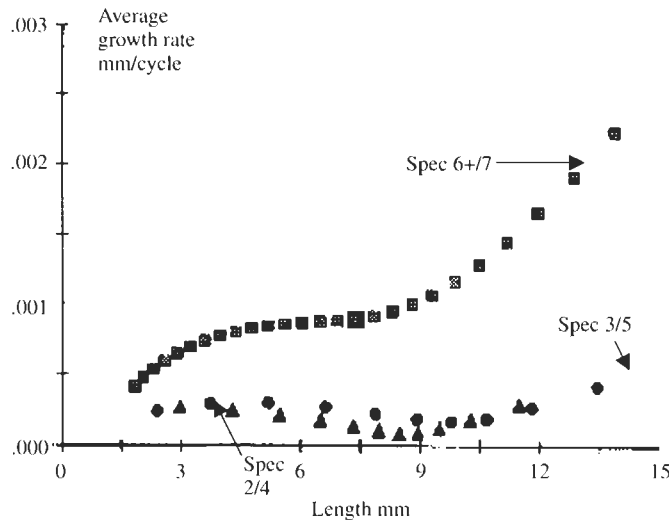


Fig. 9.20. Comparison of crack growth rates.

9.7.3. Discussion

The numerical analysis predicted that the boron/epoxy repair was capable of reducing K by approximately 60%, see Figure 9.19. A further 15% reduction of K was predicted if the specimen was repaired with a combination of a composite doubler and a steel-sleeve insert. For the repaired cases, the analysis again shows that K reduces asymptotically to a constant value implying that during constant amplitude loading, as the crack length increases, the crack growth rate should rapidly become constant.

In the region of constant crack growth rate, at a crack length of more than 6 mm, using the predicted value of K from Figure 9.20 and interpolating the K versus da/dN curve for the specimen material, for the crack growth rate for the repaired specimens was predicted to be between 1.7×10^{-4} to 2.2×10^{-4} mm per cycle. (This range of crack growth is a result of the scatter band in the experimental crack growth data for the material). This compares favourably with the experimentally obtained value, this crack length, of 2.5×10^{-4} mm per cycle.

An average fatigue life of 12200 cycles was achieved by the unrepaired specimens. The repaired specimens on average, discounting specimen 4 where cycling was stopped prior to specimen failure, achieved a fatigue life of 185000 cycles (a 15 times increase in life expectancy).

The numerical and experimental results again illustrate that the stress-intensity factors, and hence the crack growth rate, for a bonded composite repair to a cracked lug rapidly approach an asymptotic value as the crack length increases. Additionally a substantial reduction in crack growth rate was obtained. This implies that the crack growth may be arrested by an optimum choice of the thickness of the repair. In this case the thickness of the repair should be such that

the resultant asymptotic value of stress intensity factor is below the threshold value for crack growth.

Given that the maximum life to failure of the two un-repaired specimens was in the vicinity of 12200 cycles, under the loading conditions applied, the bonded-boron/epoxy repaired specimens revealed at least a 10 fold increase in the fatigue life. Furthermore a static test to failure of a repaired specimen containing fatigue failure of the ligament demonstrated that the specimen was capable of sustaining a load of approximately 25 kN, which is nearly twice the applied fatigue load, before total structural failure.

9.8. Repairs to interacting surface flaws

The phenomenon of aging structures has focused attention on the problem of multiple-site damage (MSD) and wide spread fatigue damage (WFD). In isolation each flaw or crack may be safe. However, the cumulative effect of multiple, interacting cracks may significantly degrade the damage tolerance of the structure. In the civilian arena the importance of understanding and managing ageing structures was highlighted by the failure of the Aloha 737 on April 28, 1988. This failure was essentially due to the linking, into one large crack, of numerous small cracks at a number of fastener holes, see [7]. Although the phenomenon of MSD was first observed in civilian aircraft, MSD and WFD also play a major role in determining the fatigue life military aircraft.

To illustrate the mechanism by which composite repairs reduce crack interaction and improve the damage tolerance of structures containing MSD let consider the problem shown in Figure 9.8. In this case there are two 40.12 mm (surface crack length) by 5.71 mm (crack depth) surface flaws in the rectangular aluminium alloy section, which has dimensions 300 mm \times 128 mm \times 11.2 mm. As previously this section is subjected to a remote uniform stress σ of 68.9 MPa acting at right angles to the crack plane. The structure is again assumed to be repaired using a ten ply boron epoxy laminate, i.e. 1.27 mm thick, bonded over the crack with using the, 0.106 mm thick, structural film adhesive FM73. In this case the associated solutions, for different surface distances between the adjacent surface crack tips, are given in Table 9.20.

From these results we see that, when using a composite repair, even when the crack tips are 5 mm apart the interaction between the cracks was less than 10% at the surface. At the point deepest into the body, which in this case is the point with

Table 9.20
Stress intensity factors for two interacting semi-elliptical surface flaws.

	One crack only	Two cracks: Distance between tips = 5 mm	Two cracks: Distance between tips = 10 mm
K_a MPa m ^{1/2}	0.73	0.79	0.79
K_c MPa m ^{1/2}	5.3	5.3	5.3

the maximum stress intensity factor, the interaction was negligible. It should be noted that slightly different meshes had to be used in each case and that the slight difference in the solution for the one crack and the crack case may well be due to the difference in the meshes. Consequently, when performing a damage tolerance assessment of this repair each crack could be considered separately. A more detailed study of repairs to MSD is given in [6–8,12].

9.9. Material nonlinearities

When designing bonded repairs, or adhesively bonded joints, the stress/strain response of the adhesive plays a central role in determining both the load carrying capacity and the fatigue performance of the repair or joint, see [16–18]. We have also seen in Section 9.2 and Chapter 8 that the formulae for K_p depends on the level of plastic strain in the adhesive. To this end we need a test methodology capable of accurately and consistently reproducing this behaviour. In this context Chiu, *et al.* [16] have developed a variant of the ASTM thick-adherend short over-lap adherend test specimen for characterising the stress/shear behaviour of thin film adhesives, see Figure 9.21. The results revealed that the properties of the film adhesive FM73 exhibited significant visco-plasticity, even at room temperature, see Figures 9.21 and 9.22. Chiu, *et al.* [16] also developed a unified constitutive model to describe this visco-plastic behaviour.

This section assesses the structural significance of this visco-plastic behaviour, in a realistic symmetric double lap joint/repair, via a detailed finite element analysis. Here we show that the stress/strain behaviour of the adhesive in a bonded joint is dependent on both the loading rate and the load history. We also see that when the joint is subjected to monotonic loading, with a constant loading rate, the energy density, which is the primary adhesive design variable in a bonded repair, at the worst point in the joint is essentially time independent. This is very important as it allows the existing design tools to be used even though the adhesive exhibits significant visco-plastic behaviour, and as a result is strongly rate dependent. However, in order to estimate the stress intensity factor after patching $K_{\infty e-p}$, see Eq. (9.27), it is necessary to correctly account for these visco-plastic effects.

Unfortunately, the peak adhesive shear stresses and strains are strongly effected by the loading history, and hence this can significantly effect the stress intensity factor $K_{\infty e-p}$. Since the shear stresses are continuous across the interface an accurate knowledge of the interlaminar stresses in the composite repair requires these visco-plastic effects to be incorporated in the analysis. To this end a simple methodology

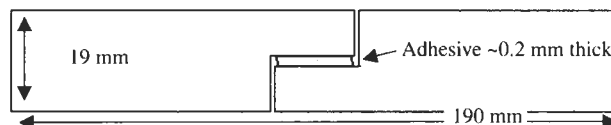


Fig. 9.21. Schematic diagram of the ASTM D 1002 thick adherend test specimen.

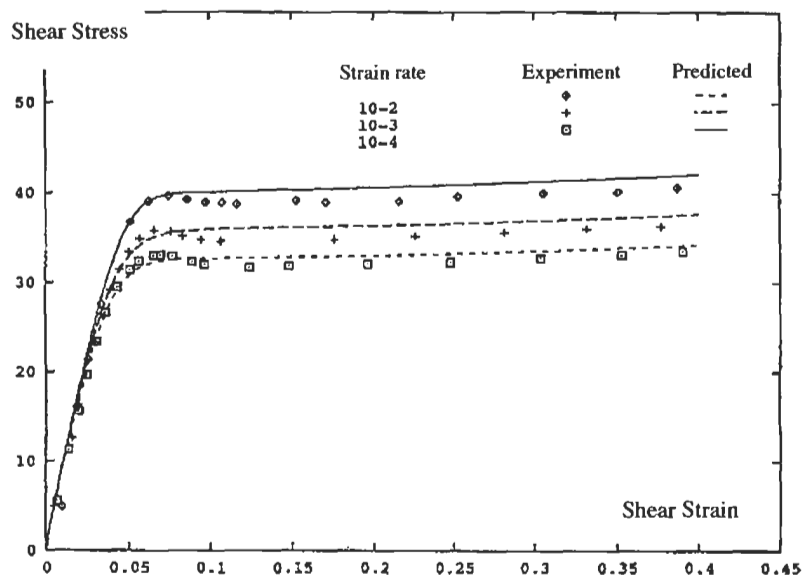


Fig. 9.22. Stress strain curves for FM73 at room temperature, from [16].

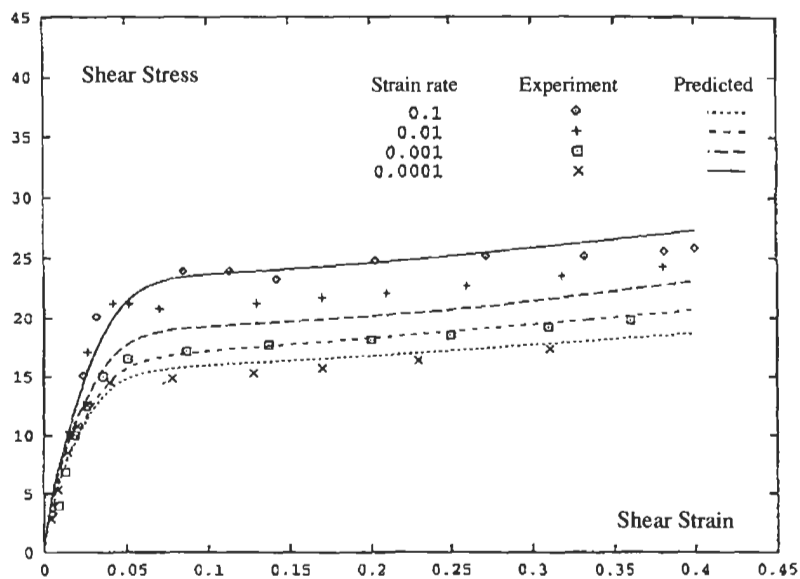


Fig. 9.23. Stress strain curves for FM73 at 60°C, from [16].

will now be presented which uses the Glinka hypothesis [16] and which negates the need for a complex non-linear finite element analysis. Details of the analytical methodology enabling this time-dependent inelastic deformation of the adhesive to be included in the design process are given below.

9.9.1. Governing differential equations for bonded joints/repairs

In the previous section we have seen that thin film adhesives exhibits significant visco-plastic effects. The question thus arises:

How do we account for this in both the analysis and design of a composite repair/joint?

To this end let us consider a symmetric double lap joint, see Figure 9.24, subjected to a remote load P where the lower and the upper adherend thicknesses and Moduli are T_1 , E_1 and T_2 , E_2 respectively and where the adhesive has a thickness t and an elastic shear modulus of G_a . The governing differential equations relating the stresses in the adherends σ_1 , σ_2 , where the subscript differentiates between the lower and the upper adherend, to the adhesive shear stress τ , in the joint are:

$$\frac{\partial \sigma_1}{\partial x} - \frac{\tau}{T_1} = 0, \quad (9.30)$$

$$\frac{\partial \sigma_2}{\partial x} + \frac{\tau}{T_2} = 0 \quad (9.31)$$

If the adherends are elastic then Hooke's law applies and the displacements in the lower and the upper adherends, defined as u_1 and u_2 respectively, are related to the stresses through the Young's moduli; viz:

$$E_1 \frac{\partial u_1}{\partial x} = \sigma_1, \quad (9.32)$$

$$E_2 \frac{\partial u_2}{\partial x} = \sigma_2, \quad (9.33)$$

whilst the shear strain γ in the adhesive is related to the relative displacements in the

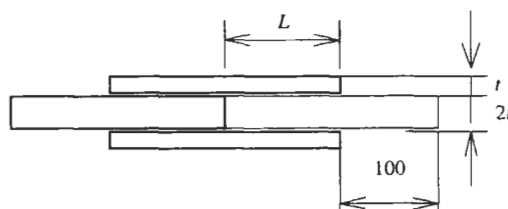


Fig. 9.24. A schematic diagram of a symmetric double lap joint.

adherends; viz:

$$\gamma = \frac{(u_1 - u_2)}{l} \quad (9.34)$$

This system of equations results in the following relationship between the adhesive shear stresses and shear strains; viz:

$$\frac{\partial^2 \gamma}{\partial x^2} = \tau \left(\frac{1}{lE_2T_2} + \frac{1}{lE_1T_1} \right), \quad (9.35)$$

where from equilibrium considerations the load P applied to the upper adherend must equal the integral of the adhesive shear stresses; viz:

$$P = \int_0^l \tau dx, \quad (9.36)$$

where l is the overlap length of the joint. To complete this system of equations it is necessary to prescribe the relationship between the adhesive shear strain γ and the adhesive shear stress τ . Since this relationship is usually in-elastic it best to consider a general functional form; viz:

$$\dot{\gamma}^I = f(\tau, \dot{\gamma}^I), \quad (9.37)$$

where the inelastic shear strain rate $\dot{\gamma}^I$ is considered to be an arbitrary function, $f(\tau, \dot{\gamma}^I)$ of the shear stress τ and the shear strain rate $\dot{\gamma}^I$.

This formulation extends the approach, used by Hart-Smith [18], to allow for the visco-plastic response of the adhesive. At this stage it should be stressed that it is well known that the computed values of peak stresses and strains in a simple joint are strongly dependent on the mesh density, and in particular the number of elements used through the adhesive, and the element type used in the analysis [20]. On the other the peak value of the strain energy density ($W = \int \sigma_{ij} d\epsilon_{ij}$) is relatively insensitive to these variables, see [17] for a more detailed summary of this phenomena. This means that, as recommended by Hart-Smith [15], it is best to use the strain energy density as the primary design variable.

The solution to this set of non-linear time dependent equations can be quite messy and time consuming. To overcome this we use Glinka's [19] technique for estimating the peak stresses and strains in the adhesive.

Structural components, albeit composite repairs, bonded joints or stiffener runnouts, are frequently subjected to complex loading spectra. These alternating loads tend to initiate fatigue cracks at notches and at other regions of high stresses. Historically the field of fatigue has been classified into a number of specific areas; viz: high-cycle and low-cycle fatigue; fatigue of notched members; the initiation and propagation of cracks and fatigue life extension techniques. Fatigue initiation and crack growth programs require an accurate knowledge of the local notch tip stresses

and strains. These quantities can be determined in several ways, viz: via direct strain gauge measurements, using finite element analysis or by using approximate methods, such as the Glinka's approach [19], that relate local stresses and strains to their remote values. To this end we will first briefly outline the Glinka approach for calculating the peak shear stresses and shear strains. Attention is then focused on developing a simple method which combines modern constitutive theory with the Glinka approach to calculate the peak (visco-plastic) adhesive stresses and strains.

Let us first define the peak adhesive shear stresses and strains obtained via an elastic solution as τ and $\gamma (= \tau/G)$ respectively. Let us next define the peak adhesive shear stresses and strains obtained via an in-elastic solution as τ and γ respectively. In this case, Hooke's law cannot be used to relate the peak shear stress, τ , to the peak strain, γ . Instead Glinka's rule [19] can be used to compute the peak stresses and strains. According to this hypothesis the peak in the strain energy density field obtained via in an elastic plastic analysis is the same as the peak strain energy obtained via a purely elastic analysis; viz:

$$\frac{1}{2} \tau \gamma = \frac{\tau^2}{2G} = \int \sigma_{ij} d\epsilon_{ij} = \int \tau d\gamma \quad (9.38)$$

It should be noted that this relationship also follows from the Hart-Smith solution [18]. As such the Hart-Smith solution is contained as a special case of Glinka's hypothesis. However, in [15] visco-plastic effects were not considered.

The solution process required to determine the true visco-plastic response thus involves first solving for the peak elastic stresses and strains in the repair. Once a valid stress strain relationship for the epoxy is known we then use Eq. (9.35) together with the elastic solution to determine the peak (in-elastic) adhesive stresses and strains.

In the past few years there has been an increasing interest in the use of unified constitutive models for predicting the inelastic response of structural materials, i.e. visco-plasticity, creep, stress relaxation etc. These models overcome many of the deficiencies of the classical approaches to the inelastic behaviour of materials. The present work uses the formulation presented in [16] to represent the visco-plastic response of thin film adhesives.

This formulation uses two internal state variables, back stress Ω_{ij} (deviatoric) tensor and drag stress Z to define the state of the material. Here the inelastic deformation is driven by the over stress which is defined as $(S_{ij} - \Omega_{ij})$. Similar types of theories have been widely used to describe the behaviour of thermoplastics.

In this approach, the flow equation is defined as:

$$\dot{\epsilon}_{ij}^i = D \exp \left[\frac{-A}{2} \left(\frac{Z^2}{3K_2} \right)^n \right] \frac{(S_{ij} - \Omega_{ij})}{\sqrt{K_2}} \quad (9.39)$$

where $\dot{\epsilon}_{ij}^i$ is the inelastic strain rate tensor, S_{ij} is the deviatoric stress and $K_2 = \frac{1}{2} (S_{ij} - \Omega_{ij})(S_{ij} - \Omega_{ij})$. Here D , A and n are material constants. The term $(S_{ij} - \Omega_{ij})/\sqrt{K_2}$ in Eq. (9.39) is the normalised over stress and defines the straining

direction. The drag stress is history dependent and evolves with the effective inelastic strain ϵ^i . The initial drag stress is Z_0 , final Z_1 , and m_0 controls the rate of evolution. The “growth” of the drag stress is defined by Eq. (9.40).

$$Z = Z_1 + (Z_0 - Z_1)e^{-m_0\epsilon^i} \quad (9.40)$$

The back stress is initially zero and its evolution is controlled by an evolution equation, viz:

$$\dot{\Omega}_{ij}^2 = f_2 S_{ij} + f_1 \dot{\epsilon}_{ij}^i - \frac{3}{2} f_1 \frac{\Omega_{ij}}{\Omega_{\max}} \dot{\epsilon}_{ij}^i \quad (9.41)$$

where $\epsilon^i = \sqrt{\frac{2}{3} \epsilon_{ij}^i \epsilon_{ij}^i}$ is the effective inelastic strain rate. Here, f_1 , f_2 and Ω_{\max} are material constants. The effective inelastic strain rate is defined in the normal fashion.

Illustration

Consider the symmetric double lap joint shown in Figure 9.25. This joint has an overlap length of 90 mm, and consists of two identical aluminium adherends with an elastic modulus $E = 70000$ MPa, and $t = 1.5$ mm. The aluminium adherends and doublers were assumed to be bonded together using FM73. The adhesive, FM73 film, was 0.2 mm thick and had a shear modulus G of 750 MPa. Its visco-plastic behaviour is described using the state variable formulation described above. The material parameters for the constitutive law for FM73 at room temperature are given in Table 9.21.

This joint was analysed using both the Glinka approach, described above, and the ABAQUS finite element analysis program together with the associated UMAT material subroutine. In each case a remote stress of 401 MPa was assumed to be monotonically applied to the ends of the inner adherend with the load increasing from 0 to its maximum load in either 0.1 s, 1 s, 10 s or 100 s. A comparison of the calculated peak shear strains γ in the joint is shown in Table 9.22.

Application to the analysis of double lap joints

Having thus validated the Glinka approximation a further series of finite element analysis of various double lap joints (Figure 9.25) were then performed. The joints

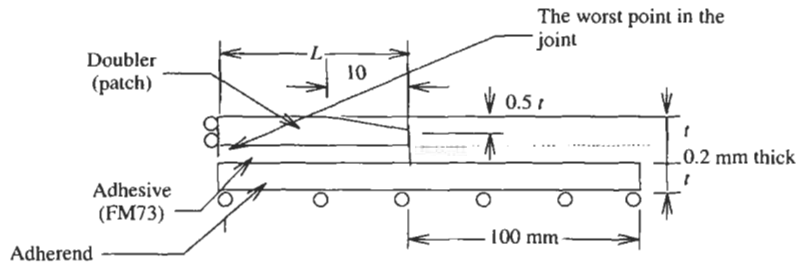


Fig. 9.25. A quarter of a symmetric double lap joint.

Table 9.21

Typical material parameters for FM73 film at room temperature.

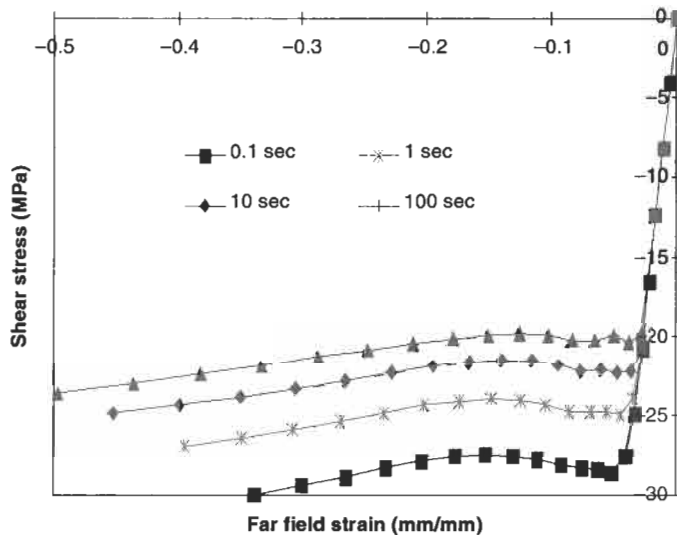
	A	D	f_1 (MPa)	f_2	n	m_0	Ω_{\max}	Z_0 (MPa)	Z_1 (MPa)
Room temp.	1	10000	800	0.2	0.85	10	12.5	120	350

Table 9.22

Comparison of peak shear strain γ with 1D Glinka formulation, $L/2t = 15$.

Dimension	Loading time (sec)			
	0.1	1	10	100
1D algorithm	0.143	0.152	0.163	0.177
Finite element 2D/3D	0.152	0.165	0.179	0.189
% Diff	5.9	7.9	8.9	6.3

analysed in this paper had ($L/2t$) ratios of 7.5 and 15 and a range of load histories were evaluated. These joints had overlap lengths of 90 mm (for $L/2t = 15$), and 45 mm (for $L/2t = 7.5$) respectively. The elastic modulus of the adherends was $E = 70000$ MPa. The thicknesses were 3 mm (for the inner adherend) and 1.5 mm (for the doubler). The aluminium adherends and doublers were assumed to be bonded together using FM73. The FM73 adhesive was 0.2 mm thick and had a shear modulus of 750 MPa. These joints were loaded to a maximum remote stress of 401 MPa, with the load going from 0 load to its maximum value in either 0.1 s, 1 s, 10 s or 100 s. The stress-strain relationship at the worst (critical) point in the adhesive layer during these load up sequences is shown in Figure 9.26 ($L/2t = 15$) and 9.27 ($L/2t = 7.5$).

Fig. 9.26. Adhesive shear stress-strain curves at a critical point in the joint, $L/2t = 15$.

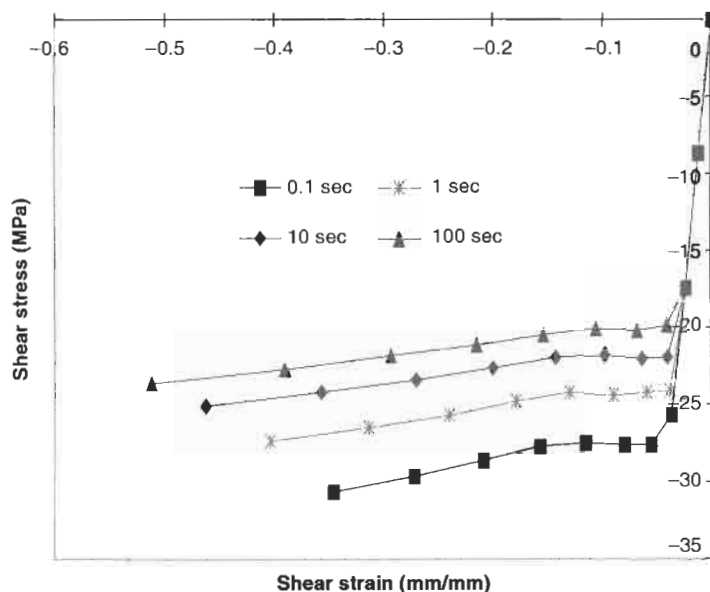


Fig. 9.27. Adhesive shear stress-strain curves at a critical point in the joint, $L/2t = 7.5$.

These figures illustrate that the stress/strain behaviour of the adhesive exhibits significant visco-plasticity and, as a result, is dependent on the loading rate (the higher the loading rate, the higher is the apparent yield stress). The maximum stress level (apparent yield stress) in the adhesive is higher when the joint is loaded more rapidly. These figures also show that the strain level in the adhesive is dependent on the loading history. Here the higher loading rate resulted in lower adhesive strain levels.

In contrast to the stress or strain based approaches Hart-Smith's [18] analysis of a double lap joint revealed that the load carrying capacity of the bond can be estimated from the energy density at the worst point in the adhesive. This design methodology was based on the assumption that the adhesive behaviour can be approximated using a single bi-linear stress/strain curve. This simplification is not necessary. With the extended analysis given in this report the adhesive can be allowed to undergo both creep and visco-plastic behaviour. As shown in Figs 9.26 and 9.27 the stress/strain relationship at any location along the adhesive layer will be governed by the local adhesive strain rate (i.e. the higher the local adhesive strain rate, the larger will be the apparent yield stress of the adhesive).

To determine how the visco-plastic behaviour of the adhesive affects the load carrying capacity of the joint the energy density at the worst point in the adhesive layer was also calculated. The results are shown in Table 9.23. The first observation, apparent from this table, is that the energy density at the worst point is slightly higher when the $L/2t$ ratio is 7.5. Hence one would expect the joint with a lower ($L/2t$) ratio to have a slightly lower load carrying capacity. More importantly we find that, whilst the local stress/strain behaviour of the adhesive are largely dependent on

Table 9.23

Effect of loading rate on energy density both $L/2t = 7.5$ and 15 at room temp.

Energy Density (MPa)	$L/2t$	Loading Time (sec)	0.1	1	10	100	% Diff
	7.5	Adhesive layer	42.6	44.4	46.1	47.1	9.5
	15	Adhesive layer	41.6	43.7	44.9	45.1	7.8

the loading rate, the energy density at the worst point in the adhesive is relatively independent of the loading rate. There is only approximately 8% variation, refer to Table 9.23, in the energy density from the slowest to the fastest loading rate.

This work thus confirms that the design hypothesis first presented by the Hart-Smith [18] for estimating the load carrying capacity of a double lap joint can be used for thin film adhesives, such as FM73 and FM300, which exhibit significant visco-plastic effects provided that failure occurs in the adhesive.

Traditional design approaches [18] do not cover interlaminar failure in the composite patch. In this case, since the shear stresses are continuous across the patch adhesive interface it is necessary to determine the stress state in the adhesive which, as we have seen, requires an allowance for the visco-plastic response of the adhesive.

Remarks

This analysis reveals that, even at room temperature, when the loading history is simply monotonic the visco-plastic nature of the adhesive in the double lap joint has limited effects on the strain energy density, and thus on the load carrying capacity of the adhesive bond (repair). In contrast the peak adhesive shear stresses and strains are strongly effected. Consequently, since the shear stresses are continuous across the composite patch-adhesive interface, for an accurate knowledge of the interlaminar stresses in the composite repair it is important that these visco-plastic effects to be incorporated in the design. Similarly when estimating the effect of yield in the adhesive on K it is important that these visco-plastic effects to be allowed for. This can easily be achieved by using Glinka's approach.

9.10. Effect of variable adhesive thickness

Let us now address the problem of variable adhesive thickness. In this section we will show that the Glinka extension to the Hart Smith design formulae can be used for those cases when the adhesive thickness is not constant. However, before examining the inelastic behaviour of joints with variable adhesive thickness let us first consider the elastic response.

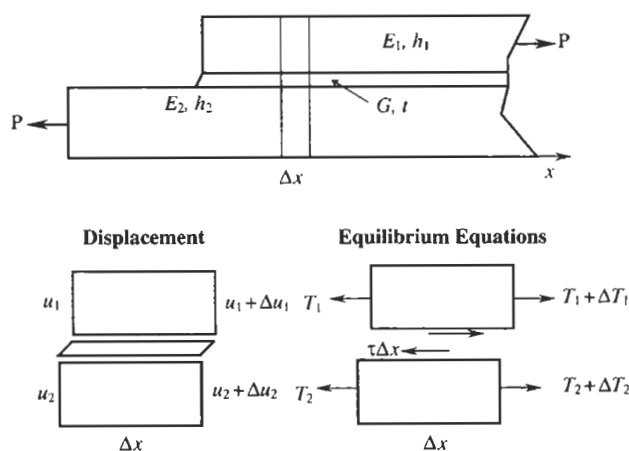


Fig. 9.28. Schematic of the adhesive joint.

Consider the joint as shown in Figure 9.28, the governing equations for this joint are:

$$T_{1,x} = \tau, \quad (9.42)$$

$$T_{2,x} = -\tau, \quad (9.43)$$

and

$$u_1 - u_2 = t\gamma \quad (9.44)$$

From Hooke's law for the adherends we find that:

$$T_1 = E_1 h_1 u_{1,x}, \quad (9.45)$$

$$T_2 = E_2 h_2 u_{2,x}, \quad (9.46)$$

and for adhesive

$$\tau = G\gamma \quad (9.47)$$

where $E_{1,2}$ and $h_{1,2}$ are Young's modulus and thicknesses of adherends, G and t are the shear modulus and thickness of the adhesive. Other parameters are as shown in Figure 9.28.

Let us consider the case when the adhesive thickness is variable i.e. $t = t(x)$. In this case Eqs. (9.42) to (9.47) produce the resultant differential equation, viz:

$$(\gamma t)_{xx} = \beta^2(x) \gamma t, \quad (9.48)$$

where $\beta^2(x) = \frac{G}{t(x)} \left((E_1 h_1)^{-1} + (E_2 h_2)^{-1} \right)$.

In the case of a constant adhesive thickness Eq. (9.48) reduces to the well-known equation for the shear stress in adhesive, viz

$$\tau_{xx} = \beta^2 \tau, \quad (9.49)$$

where $\beta^2 = \frac{G}{t} \left((E_1 h_1)^{-1} + (E_2 h_2)^{-1} \right)$.

For a constant thickness adhesive joint the concept of a characteristic length λ is commonly used. This distance λ is given by the formulae:

$$\lambda = \frac{3}{\beta}, \quad (9.50)$$

and represents the length of the adhesive playing the major role in the load transfer process transferring the loading.

Equation (9.48) has no general analytical solution. However by using the transformation $z = (\gamma t)_x / \gamma t$ it can be reduced to the special Riccati Eq. (9.27):

$$z_x + az^2 = \beta^2(x), \quad (9.51)$$

with $a = 1$. This Eq. (9.14) can be solved for a wide class of function $\beta(x)$, particularly when this function has the form $\beta^2(x) = bx^m$.

Consider the following example. Let the adhesive thickness in the vicinity of the edge is distributed as $t(x) = t_0 x^4$. In this case $\beta^2 = \beta^2(x)$ has the form

$$\beta^2(x) = b^2 x^{-4}, \quad (9.52)$$

where $b^2 = \frac{G}{t_0} \left((E_1 h_1)^{-1} + (E_2 h_2)^{-1} \right)$.

We thus require a solution to the following equation:

$$(\gamma t)_{xx} = bx^{-4} \gamma t \quad \text{at} \quad x_0 \leq x \leq \infty \quad (9.53)$$

The solution of this equation results in the following expression for the adhesive shear stresses

$$\tau(x) = \frac{G}{t_0 x^3} \left(c \cdot \cosh\left(\frac{b}{x}\right) + a \sinh\left(\frac{b}{x}\right) \right) \quad (9.54)$$

The constants a and c in this solution can be found from the boundary conditions, which can be taken in the following form

$$\frac{PE_1 h_1}{E_1 h_1 + E_2 h_2} = \int_{x_0}^{\infty} \tau(x) dx, \quad (9.55)$$

which represents the balance of forces acting on the adherends and

$$-\frac{P}{E_2 h_2} = (\gamma t)_x \big|_{x=x_0} \quad (9.56)$$

From the boundary conditions we find that

$$c = \frac{PE_1h_1}{E_1h_1 + E_2h_2} b^2 \frac{t_0}{G} - \frac{P}{E_2h_2}, \quad (9.57)$$

and

$$a = \frac{-\frac{P}{E_2h_2} + \frac{bc}{x_0} \sinh(b/x_0) - c \cdot \cosh(b/x_0)}{\sinh(b/x_0) - b/x_0 \cosh(b/x_0)} \quad (9.58)$$

In the special case when $E_1h_1 = E_2h_2 = Eh$ we have $c = 0$ and

$$a = -\frac{P}{Eh} \left(\sinh\left(\frac{b}{x_0}\right) - b/x_0 \cosh\left(\frac{b}{x_0}\right) \right)^{-1}, \quad (9.59)$$

and the expression for the shear stresses becomes

$$\tau(x) = \frac{P}{Eh} \frac{G}{t_0x^3} \frac{\sinh(b/x)}{b/x_0 \cosh(b/x_0) - \sinh(b/x_0)} \quad (9.60)$$

The criterion proposed by Hart-Smith for failure of adhesive joints, see Chapter 9, can be written in the form

$$W_{\max} \geq W_{\text{cr}}, \quad (9.61)$$

where W_{\max} is the maximum value of the strain energy density in the adhesive, and W_{cr} is the critical value for the energy determined from standard materials tests.

In this problem the maximum strain energy density occurs at the edge of the joint, i.e. $x = x_0$, where the shear stress

$$\tau(x_0) = \tau_{\max} = \frac{P}{Eh} \frac{G}{t_0x^3} \frac{1}{b/x_0 \coth(b/x_0) - 1}, \quad (9.62)$$

where $\coth(b/x_0)$ is the hyperbolic cotangent.

Consider the case when the value of $b/x_0 \gg 1$, this corresponds to small changes of the thickness of the adhesive on the characteristic length of the stress distribution, then

$$\frac{1}{b/x_0 \coth(b/x_0) - 1} \approx \frac{x_0}{b} \quad (9.63)$$

In this limiting case the solution for W_{\max} reduces to

$$W_{\max} = \frac{1}{4} \frac{P^2}{Eht_0x_0^4} = \frac{1}{4} \frac{P^2}{Eht} \quad (9.64)$$

This formula, which is independent of the stress-strain relationship for the adhesive, coincides with the maximum strain energy density for an adhesive with a constant equal to the thickness at the edge $x = x_0$. This means that the present

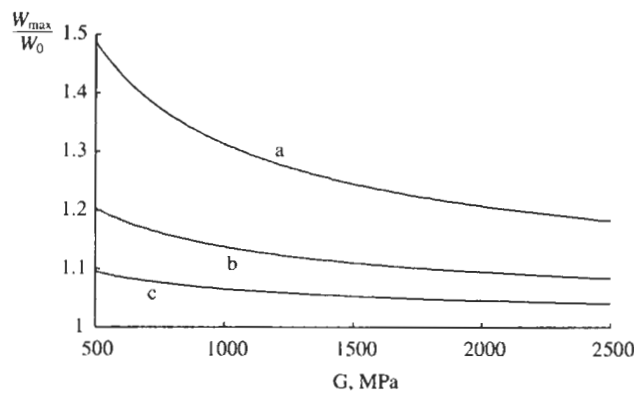


Fig. 9.29. Dependence of the maximum strain energy density on the adhesive shear modulus.

solution asymptotes to the solution for the constant thickness of the adhesive as x_0 reduces to zero.

Let us now we consider the case when the adherends are an equal thickness aluminium alloy with $h_1 = h_2 = 3$ mm, and $E_1 = E_2 = 73$ GPa. The thickness of the adhesive is distributed in accordance with a power law in the following form $t(x) = t_0 x^4$ where the thickness at the edge is 0.1 mm and increases to 0.2 mm after a distance of (a) 5 mm, (b) 10 mm, and (c) 20 mm from the edge. In this study the shear modulus of the adhesive was allowed to vary from 500 MPa to 2500 MPa. This range covers most practical situations.

The ratio of maximum strain energy density, for the non-uniform adhesive thickness, to the maximum strain energy for the case when the joint has a constant adhesive thickness of 0.1 mm is shown in Figure 9.29. From this figure we see that the maximum strain energy is now dependent on the shear modulus of the adhesive. However, for cases (b) and (c), where the rate of change of the adhesive thickness with respect to distance is relatively small, this dependence is rather weak. Even for case (a) where the adhesive thickness doubles over a distance of 5 mm the variation in extreme values of the energy density is approximately 25%. Since the load carrying capacity of the joint is proportional to the square root of the maximum energy density this corresponds to a variance in the failure load of approximately 10%.

This figure also reveals that the energy density is a function of the local geometry of the joint. As such the Hart-Smith formulation cannot be used to predict the strength of the joint. In this case we must use the Glinka extension to the Hart-Smith formulation. Indeed, a feature of the solution, for a constant adhesive thickness is that the maximum strain energy W_{\max} , obtained using the elastic-perfectly-plastic solution, is exactly equal to that obtained via a purely elastic solution W_{\max}^e . In the present case the elastic plastic solution reveals that, as a first estimate, Glinka's hypothesis is valid, i.e. $W_{\max} / W_{\max}^e \cong 1$, see Figure 9.30.

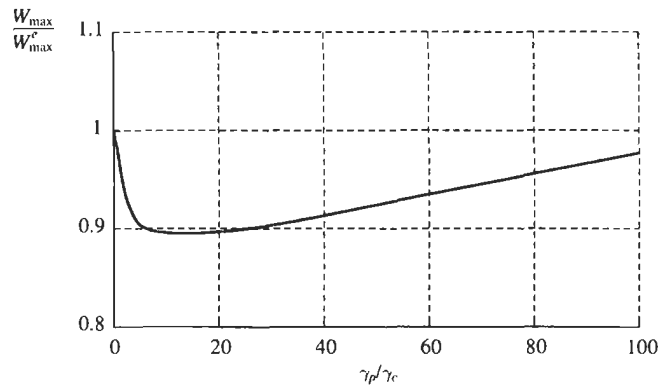


Fig. 9.30. Ratio of the maximum strain energy for the elastic-perfectly-plastic solution to value obtained via an elastic analysis for a non-uniform adhesive thickness.

9.10.1. The effect of variable adhesive thickness and material non-linearity

Having established the Glinka hypothesis to be applicable to bonded joints with global bending prohibited let us now consider the effect of both variable adhesive thickness adhesive plasticity. We have seen that the energy density is a weak function of the adhesive shear modulus. It should thus follow that the hypothesis will also hold if the adhesive thickness is variable.

To evaluate this effect let us consider a symmetric double lap joint with a lower adherend (half)thickness T_1 of 3 mm, an upper adherend thickness T_2 of 2 mm, and $E_1 = E_2 = 73000$ MPa. The adhesive, which was assumed to be FM73, was allowed to be either one or two layers thick, i.e. 0.1 mm or 0.2 mm thick, and had a Young's modulus of 1890 MPa and a Poisson's ratio of 0.35. Whilst the adhesive was assumed to have a post yield slope E' of 250 MPa and the yield stress of the adhesive was allowed to vary, see Table 9.24. Furthermore, at the critical end of the

Table 9.24

Percentage difference in W and values of W , $\sigma = 360$ MPa.

Yield stress and adhesive thickness	A (mm), the local increase in the adhesive thickness.		
	0.025	0.05	0.075
$\sigma_y = 40$ MPa	18.1	17.0	15.5
$t_a = 0.2$ mm	$W = 13.27$	$W = 11.54$	$W = 10.22$
$\sigma_y = 68$ MPa	13.9	11.5	9.5
$t_a = 0.2$ mm	$W = 14.65$	$W = 13.12$	$W = 11.78$
$\sigma_y = 40$ MPa	25.0	22.7	20.5
$t_a = 0.1$ mm	$W = 16.95$	$W = 14.80$	$W = 12.87$
$\sigma_y = 68$ MPa	21.6	17.7	15.33
$t_a = 0.1$ mm	$W = 18.76$	$W = 16.75$	$W = 14.59$

joint the thickness t_a^1 was assumed to vary according to the following equation

$$\begin{aligned} t_a^1 &= t_a + A \cos(\pi x / 2x_1) \quad \text{for } 0 < x < x_1 \\ t_a^1 &= t_a \quad \text{for } x > x_1, \end{aligned} \quad (9.65)$$

where t_a , A , x , and x_1 are the nominal adhesive thickness, the amplitude of the perturbation of the thickness, the distance from the end of the joint and a characteristic length. In this initial study we chose, on the basis of past experience, x_1 to be 3 mm, and varied the values of A . At this stage only monotonic loading was considered and to increase the amount of yielding the remote stress, in the lower adherend, was taken to be 360 MPa. The results of this analysis are summarised in Table 9.24.

To further illustrate the validity of Glinka's hypothesis for variable adhesive thickness let us consider the case when the adhesive is two layers thick, i.e. $t_a = 0.2$ mm, and $A = 0.05$ mm. This corresponds to a perturbation in the adhesive thickness equal to 25% of the base line thickness. In this case the distance over which the perturbation occurred, i.e. x_1 , was varied from 1.5 to 5 mm and the results are shown in Table 9.25.

In the previous section we saw that for a variable thickness adhesive the analytical solution for the peak in the energy density field W_{\max} was a weak function of the adhesive shear modulus. This contrasts with the analytical solution for a constant thickness joint where W_{\max} is independent of the shear modulus. From this we would expect that, for repairs with a variable thickness adhesive, Glinka's hypothesis may be less accurate as the plasticity becomes more extensive. The present finite element results appear to support this conjecture. Nevertheless, for monotonic loading, Glinka's hypothesis still appears to be a reasonable first approximation with error levels consistent with those for notched isotropic bodies. Indeed, Tables 9.24 and 9.25 also show that, even for joints with a variable adhesive

Table 9.25
Percentage difference in \sqrt{W} and values of W (MPa), $A = 0.05$ mm.

Yield stress and post yield slope	Remote stress σ (MPa)				
	144	200	240	288	360
$\sigma_y = 68$ MPa	0.0	0.4	2.5	6.0	11.1
$t_a = 0.2$ mm, $x_1 = 1.5$ mm	$W = 2.58$	$W = 4.90$	$W = 6.81$	$W = 9.11$	$W = 12.7$
$\sigma_y = 40$ MPa	8.7	5.5	2.2	9.0	16.7
$t_a = 0.2$ mm, $x_1 = 1.5$ mm	$W = 3.05$	$W = 5.49$	$W = 6.85$	$W = 8.53$	$W = 11.1$
$\sigma_y = 68$ MPa	0.0	0.5	2.8	6.4	11.5
$t_a = 0.2$ mm, $x_1 = 3$ mm	$W = 2.68$	$W = 5.08$	$W = 7.03$	$W = 9.39$	$W = 13.12$
$\sigma_y = 40$ MPa	7.3	4.3	3.5	9.4	17.0
$t_a = 0.2$ mm, $x_1 = 3$ mm	$W = 3.09$	$W = 5.59$	$W = 7.08$	$W = 8.80$	$W = 11.54$
$\sigma_y = 68$ MPa	0.0	0.8	3.2	6.9	12.1
$t_a = 0.2$ mm, $x_1 = 5$ mm	$W = 2.80$	$W = 5.28$	$W = 7.28$	$W = 9.70$	$W = 13.53$
$\sigma_y = 40$ MPa	6.6	3.7	3.0	9.9	17.5
$t_a = 0.2$ mm, $x_1 = 5$ mm	$W = 3.18$	$W = 5.75$	$W = 7.32$	$W = 9.09$	$W = 11.91$

thickness, W_{\max} is also a (relatively) weak function of the yield stress of the adhesive.

This finding infers that, for bonded composite repairs, even if there is variability in the thickness of the adhesive bond the energy field and hence the strength of the joint, provided failure is due to failure of the adhesive, can be estimated from a purely linear elastic analysis of the joint. This has the potential to significantly simplify the design/assessment process particularly in the case where fabrication problems, or the inability to control the local localised flow or cure temperatures, can give rise to a variable adhesive thickness repair.

We thus see that, for monotonic loading, although variable adhesive thickness changes the stress and the energy fields Glinka's hypothesis is still valid. This means that, for the present class of problems, even if there is variability in the thickness of the adhesive bond the energy field W_{\max} can be computed using only the elastic solution. The strength of the joint, provided failure is due to failure of the adhesive, can be then estimated from a purely linear elastic analysis of the joint. This will occur at the load level when

$$W_{\max} = W_{\text{crit}} \quad (9.66)$$

This finding has the potential to significantly simplify the design process for repairs with a variable thickness adhesive.

9.11. Repairs to cracked holes under bi-axial loading

The problem of composite repairs to cracks at a hole or notch was first studied by Baker, *et al.* [2], which deals with repairs to cracks a fuel decant hole in Mirage III aircraft, and later by Atluri, *et al.* [12]. For this problem as the crack length (l) gets larger, i.e. $l \rightarrow \infty$, the solution should approach that of a patched crack without a hole. Hence when l/ρ is large, the stress intensity factor should tend to an asymptotic value K_{∞} , which is independent of the size of hole.

Let us begin by considering the problem of a crack emanating from a notch, see Figure 9.31. Schijve [30] presented an excellent review of the existing literature and proposed that the stress intensity factor could be expressed in the form, viz:

$$K = F\sigma_{\max}\sqrt{\pi l} \quad (9.67)$$

where σ_{\max} is the peak stress at the notch. In this work he also proposed that the geometry factor F was only a function of the ratio l/ρ .

Using this technique we can present an approximate solution, for the problem of a composite repair to a cracked hole subjected in the form, viz:

$$K = F(l/\rho)W(l/2\pi\lambda)K \quad (9.68)$$

Here K is the solution to the problem of a center notch crack $2l$ long, i.e. an embedded crack, in an infinite plate acted upon by the same stress field (σ_y , τ) as

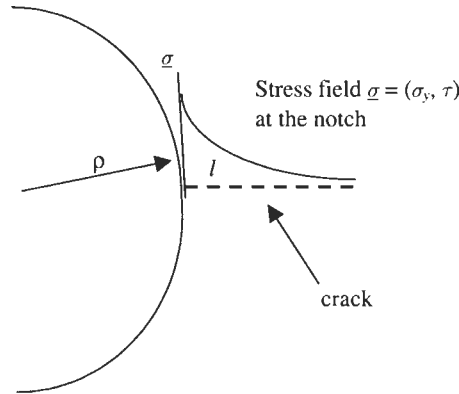


Fig. 9.31. Schematic diagram showing notch, crack and the stress field at the notch.

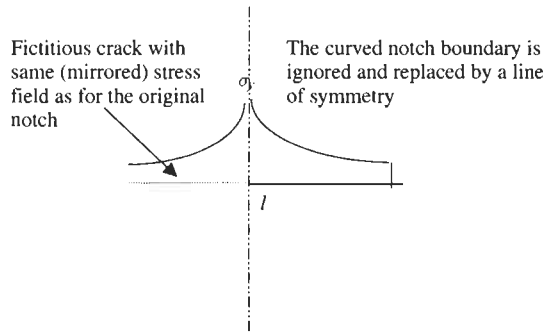


Fig. 9.32. Schematic picture of the problem used to determine K .

found at the notch, see Figure 9.32. In this formulation we create a fictitious crack of equal length and the stress field is mirrored across the boundary of the notch, see Figure 9.32. Since K is the starting solution in the finite element alternating solution this formulation can be thought of as a marriage of the alternating solution and the method, see [32]. The values for F are given in Table 9.26. It is often convenient to express F as an analytical function of l/ρ . The function F can be approximated as:

$$F = \frac{1}{\sqrt{2}} - (1.12 - \frac{1}{\sqrt{2}}) \exp(-\alpha l/\rho) , \quad (9.69)$$

which satisfies the requirements that $F \rightarrow 1.12$ as $l/\rho \rightarrow 0$, and $F \rightarrow 1/\sqrt{2}$ as $l/\rho \rightarrow \infty$, so that the expression for K has the correct asymptotic limits at both $l/\rho \rightarrow 0$, i.e. for short cracks, and $l/\rho \rightarrow \infty$, i.e. for long cracks. The functional form used in this work, which agrees with the values presented in Tables 9.26 to within $\sim 5\%$, was:

$$\alpha = 0.8(1.0 - 0.3l/\rho + 0.13(l/\rho)^2) \quad (9.70)$$

Table 9.26
Recommended values for F .

l/ρ	F_1
0.0	1.12
0.04	1.10
0.1	1.063
0.12	1.053
0.16	1.033
0.2	1.015
0.3	0.977
0.4	0.948
0.5	0.924
0.75	0.882
1	0.854
1.5	0.820
2	0.800
3	0.778
4	0.765
5	0.757
∞	$1/\sqrt{2}$

Here the function W describes the transition from the small crack solution $l \rightarrow 0$ to the long crack solution $l \rightarrow \infty$. Here l is the half length of the crack. At this stage we will use the functional form given by Wang and Rose [32].

$$W(l/\pi\lambda) = \sqrt{\left[\frac{(1 + 2.23l/\pi\lambda)}{(1 + 4.77l/\pi\lambda + 7(l/\pi\lambda)^2)} \right]} \quad (9.71)$$

This solution has the correct bounds for the stress intensity factor for both short and long cracks at a cracked hole repaired with an externally bonded composite patch.

The accuracy of this approach can be illustrated by considering the problem of a crack at a centrally located hole in an infinite sheet subjected to a either remote uniform stress (σ) or a remote (equal) bi-axial stress $\sigma_1 = \sigma_2 = \sigma$. The predicted K 's for this case are shown in Figure 9.33, along with the analytical solutions due to Tweed and Rooke [33]. Here $K_0 = \sigma\sqrt{(\pi l)}$, where σ is the remote stress acting perpendicular to the crack.

To illustrate the ease of application of this solution let us consider the case of a crack of length l emanating from a hole with a radius R of 3 mm, this size was chosen to represent a typical fastener hole, in an infinite Aluminium alloy plate (skin) subjected to a uniform remote stress of 100 MPa. The plate is repaired using a uni-directional boron epoxy patch that covers its entire width. The patch also contains a 3 mm radius hole and the fibres are orientated perpendicular to the crack, i.e. in the direction of the load. The moduli of the aluminium skin (plate) are $E = 72000$ MPa and $\nu = 0.33$. The patch was assumed to have the following

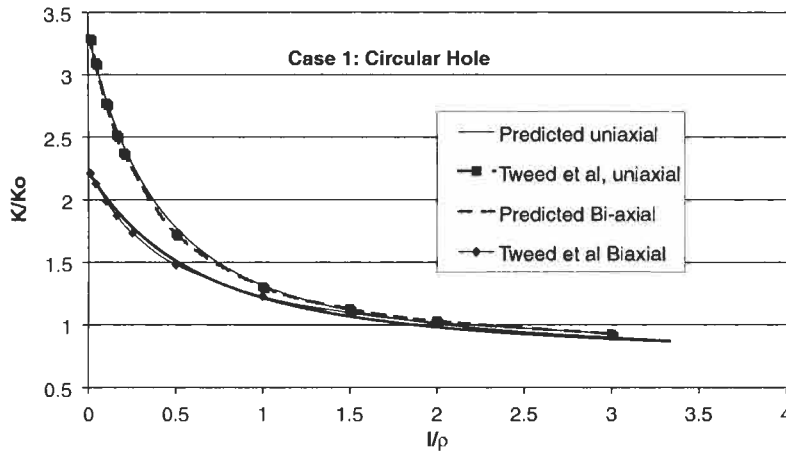


Fig. 9.33. Comparison of the predicted and analytical solutions for a crack at a circular hole.

mechanical properties: $E_{11} = 208000$ MPa, $E_{22} = E_{33} = 25432$ MPa, $\nu_{12} = 0.183$, and $G_{12} = G_{13} = G_{23} = 7241$ MPa. The adhesive was taken to be FM73 and was 0.2 mm, i.e. two layers, thick with a shear modulus of 750 MPa and $\nu = 0.35$.

Two different plate and patch thicknesses were considered:

Case (i) A plate thickness of 1.2 mm and a patch thickness of 0.52 mm, i.e. approximately four plies thick.

Case (ii) A plate thickness of 3 mm and a patch thickness of 0.889 mm, i.e. approximately seven plies thick.

The first case was chosen to approximate a crack at a fastener hole in the fuselage skin of a wide-bodied transport aircraft. The second case was chosen to approximate a crack at a fastener hole in the wing skin of a military fighter aircraft. In each case the patch thickness was chosen to approximate the stiffness, i.e. the product of the modulus and the thickness, of the plate (skin). The resultant stress intensity factors are presented in Figure 9.34.

This section has used the formulae, for the function W , developed by Wang and Rose [32]. However, recent work by Hart-Smith [29] has produced a slightly different formulae. The difference between these two approaches is shown in Figure 9.35, which shows how the stress intensity factor approaches the asymptotic value.

When performing fatigue life calculations for unrepaired structures it is often sufficient to only consider the stress field acting perpendicular to crack. For small cracks at holes this simplification can lead to erroneous results. This is because the load bia-axiality ratio can have a significant effect on K , see Figure 9.33. Consequently, when designing repairs to cracked holes, or to cut outs resulting from the removal of corroded material, load bi-axiality needs to be considered. This effect is discussed in more detail in [31].

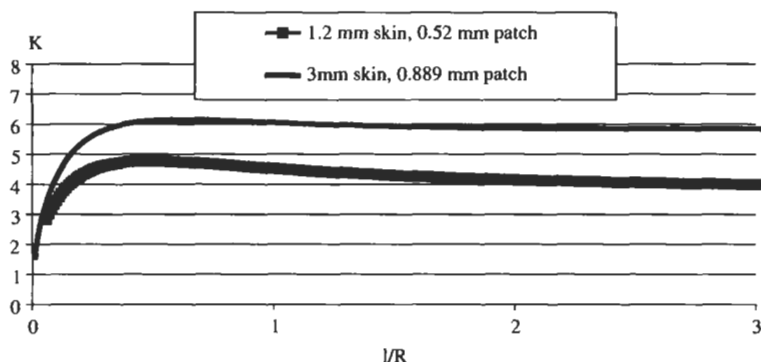


Fig. 9.34. Composite repairs to cracked holes.

9.12. Findings relevant to thick section repair

As a result of this chapter we find that the major design considerations are, viz:

1. The maximum stress intensity factor, allowing for the visco-plastic nature of the adhesive, should be as low as possible and preferably below the critical value K_{th} for fatigue crack growth in the material. For cracks at holes or notches, or repairs to corrosion damage load bi-axiality should be accounted for in the design process.
2. The maximum adhesive stresses/energy should be below the value at which fatigue damage accumulates in the adhesive, see [8,16,21]. For FM73 this

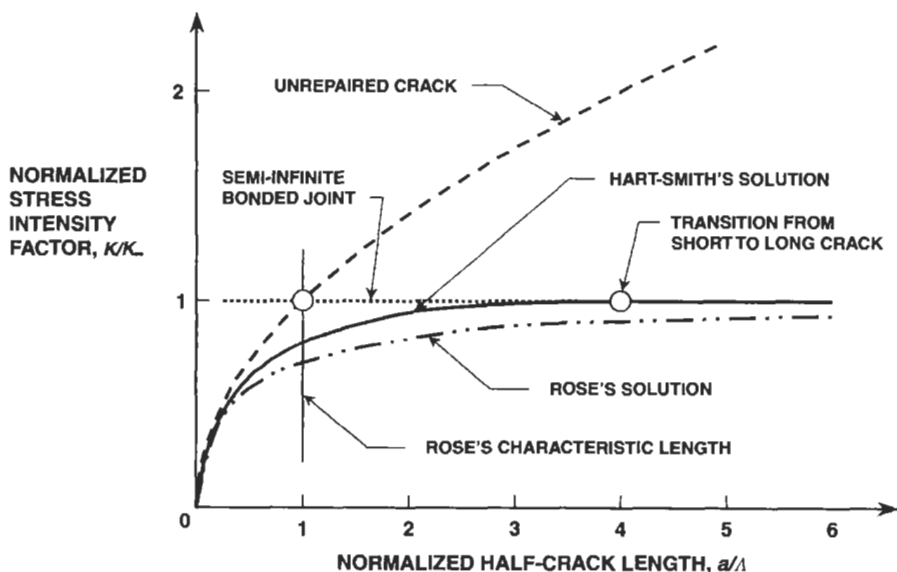


Fig. 9.35. Crack-tip stress-intensity factors for "short" and "long" cracks, from [29].

value is ~ 25 MPa. However, to minimise errors in measuring and computing the adhesive stresses and allowables, see [20], it is best to compute and measure the energy in the adhesive $W = 1/2 \sigma_{ij} \epsilon_{ij} = \int \sigma_{ij} d\epsilon_{ij}$. These measurements are best performed using the ASTM thick adherend test, ASTM D 1002, see [16].

3. The composite patch must not experience failure by interply delamination. This can be checked by ensuring that the polynomial failure criteria is not greater than one. The commonly used failure criteria are: Tsai-Hill, Hoffman and Tsai-Wu. These failure criteria are generally written in the form:

Tsai-Hill criterion: Failure is assumed to occur when

$$\frac{\sigma_1^2}{X^2} - \frac{\sigma_1 \sigma_2}{X^2} + \frac{\sigma_2^2}{Y^2} + \frac{\tau_{12}^2}{S^2} = 1 \quad (9.72)$$

Here the material is assumed to have equal strengths in tension and compression, i.e. $X_t = X_c = X$ and $Y_t = Y_c = Y$

Hoffman criterion: Failure is assumed to occur when

$$\left(\frac{1}{X_t} - \frac{1}{X_c}\right)\sigma_1 + \left(\frac{1}{Y_t} - \frac{1}{Y_c}\right)\sigma_2 + \frac{\sigma_1^2}{X_t X_c} + \frac{\sigma_2^2}{Y_t Y_c} + \frac{\sigma_{12}^2}{S^2} - \frac{\sigma_1 \sigma_2}{X_t X_c} = 1 \quad (9.73)$$

Tsai-Wu criterion: Failure is assumed to occur when

$$\left(\frac{1}{X_t} - \frac{1}{X_c}\right)\sigma_1 + \left(\frac{1}{Y_t} - \frac{1}{Y_c}\right)\sigma_2 + \frac{\sigma_1^2}{X_t X_c} + \frac{\sigma_2^2}{Y_t Y_c} + \frac{\sigma_{12}^2}{S^2} + 2F_{12}\sigma_1\sigma_2 = 1 \quad (9.74)$$

The coefficient F_{12} is experimentally determined from test specimens under biaxial loading and F_{12} must satisfy a stability criterion of the form

$$\left[\frac{1}{X_t X_c}\right] \left[\frac{1}{Y_t Y_c}\right] - F_{12}^2 > 0, \quad (9.75)$$

creates some complication in the use of this theory. It has been suggested that F_{12} be set to zero.

The symbols used in Eqs. (9.76) to (9.79) are defined as:

X_t Allowable tensile stress in the principal x (or 1)-direction of the material

X_c Allowable compressive stress in the principal x (or 1)-direction of the material

Y_t Allowable tensile stress in the principal y (or 2)-direction of the material

Y_c Allowable compressive stress in the principal y (or 2)-direction of the material

S Allowable shear stress in the principal material system

At the moment one shortcoming in the certification process for composite joints/repairs and rib stiffened panels is the lack of understanding of the matrix dominated failures. The vast majority of the analysis tools assume that the composite is behaving in the linear elastic regime. However, there are instances, see [22–24] when material nonlinearities, in the composite adherends, play a significant

role in these failures. Unfortunately, it is currently uncertain as to when these effects need to be considered, for more details see [22–24].

4. The average stress, over any one ply through the thickness of the boron patch, should not exceed 1000 MPa.

It must be stressed that for repairs to primary structures a full 3D finite element analysis must be performed. (Even for repairs to thin skins the stresses and strain fields are dependent on the mesh density and element type used in the analysis, see Section 9.9.1 and [20] for a more detailed summary of this phenomena.) This analysis should include a damage tolerant assessment of both the structure and the composite repair performed in accordance with the current FAA procedures for damage tolerant assessment, as given in [25]. As discussed in [26] this analysis should be supported by test evidence in the appropriate environment, unless (as stated in [25]) “it has been determined that the normal operating stresses are of such a low order that serious damage growth is extremely improbable”, that:

- (a) The repaired structure, with the extent of damage established for residual strength evaluation, can withstand the specified design limit loads (considered as ultimate loads); and
- (b) The damage growth rate both in the structure, the adhesive and the composite repair, allowing for impact damage, interply delamination and adhesive debonding under the repeated loads expected in service (between the time the damage becomes initially detectable and the time the extent of damage reaches the value for residual strength evaluation) provides a practical basis for development of the inspection program.

The analysis/testing program should allow for impact damage, interply delamination and adhesive debonding under the repeated loads expected in service (between the time the damage becomes initially detectable and the time the extent of damage reaches the value for residual strength evaluation) provides a practical basis for development of the inspection program.

9.12.1. Comparison of commercial finite element programs for the 3D analysis of repairs

A variety of commercial finite element programs can now be used to design composite repairs. The most widely used programs are: MSC-Nastran, NE-Nastran, ABAQUS, PAFEC, and ANSYS. To obtain the necessary accuracy, and to assess all possible failure modes, the finite element analysis of most composite repairs needs to be 3D. Since the adhesive bond line is typically 0.2 mm thick this means that it is often necessary to work with elements with large aspect ratios. As a result any analysis should use elements with at least one mid-side node. With this in mind the relative advantages and disadvantages of these programs are presented below.

Program Name	Advantages	Disadvantages
ANSYS	Widely used for mechanical design.	Cannot cope with very large aspect ratio elements.
ABAQUS	ABAQUS is recognised as being an excellent non-linear program.	Cannot cope with very large aspect ratio elements. If the aspect ratio is large it can yield poor results when the adhesive yields.
PAFEC	Can automatically link 2D and 3D models. Can use cubic as well as parabolic elements.	Requires the use of the PAFEC graphics pre and post processor.
MSC-Nastran	The Nastran data structure is very widely used and many structural models are MSC-Nastran based.	Cannot cope with very large aspect ratio elements. When using 3D parabolic elements, i.e. 20 noded bricks <i>etc.</i> the analysis options are quite severely reduced.
NE-Nastran	The data structure is compatible with MSC-Nastran. Has the ability to use enriched 3D elements, i.e. 21 noded bricks <i>etc.</i> As such it can tolerate very large aspect ratio elements. Can model both material and geometric non-linearities using both 20 and 21 noded elements.	Limited number of pre and post processors available. On PC's it uses the same pre and post processor, i.e. FEMAP (SDRC), as MSC-Nastran. Essentially limited to mechanical and aeronautical structural analysis.

In 3D elasticity the displacements u , v and w must satisfy the differential Eq. (9.34)

$$\nabla^4 u = 0, \quad \nabla^4 v = 0, \quad \text{and} \quad \nabla^4 w = 0 \quad (9.76)$$

The use of P-element based finite element analysis can violate this fundamental requirement, if the order is greater than three, and as such the use of P-element based analysis is not recommended for 3D problems. As pointed out by Liebowitz, *et al.* [35] this means that “the basic equilibrium conditions of the basic f.e. equations is violated”. Furthermore, the use of high order P elements can result in localised oscillations in the solution, see Zenkiewicz, *et al.* [36] for more details. As such the use P-element formulations for fracture and composite repair analysis should be avoided.

When performing a 2D analysis of a joint the best results are obtained using nine noded elements, which have a node at the centroid, or the CQUADR element, or the equivalent element with drilling degrees of freedom. The advantage of these elements is that they can accommodate large aspect ratio's and extensive mesh distortion.

References

1. Jones, R. and Callinan, R.J. (1979). A design study in crack patching. *J. of Structural Mechanics*, **1**(7), pp. 107–130.
2. Baker, A.A., Callinan, R.J., Davis, M.J., *et al.* (1984). Repair of mirage iii aircraft using BFRP crack patching technology. *Theoretical and Applied Fracture Mechanics*, **2**(1), pp. 1–16.
3. Molent, L., Callinan, R.J. and Jones, R. (1989). Structural aspects of the design of an all boron/epoxy reinforcement for the F-111C wing pivot fitting – Final report. Aeronautical Research Laboratory, Research Report 1, ARL-RR-1, November 1992. See also *Composite Structures*, **11**(1), pp. 57–83.
4. Rose, R.F. (1942). A cracked plate repaired with bonded reinforcements. *Int. J. of Fracture*, **18**, pp. 135–144.
5. Bartholomeus, R.A., Paul, J.J. and Roberts, J.D. (1991). Application of bonded composite repair technology to civilian aircraft – 747 demonstrator program. *Proc. Int. Conf. on Aircraft Damage Assessment and Repair* (R. Jones and N.J. Miller, eds.). Published by The Institution of Engineers Australia, ISBN (BOOK) 85825 537 5, July.
6. Jones, R., Bartholomeusz, R., Kaye R., *et al.* (1994). Bonded-composite repair of representative multi-site damage in a full-scale fatigue-test article. *J. Theoretical and Applied Fracture Mechanics*, **21**, pp. 41–49.
7. Jones, R., Molent, L. and Pitt, S. (1999). A study of multi-site damage in fuselage lap joints. *Theoretical and Applied Fracture Mechanics*, **32**, pp. 81–100.
8. Molent, L., Bridgford, N., Rees D., *et al.* (1992). Environmental evaluation of repairs to fuselage lap joints. *Composite Structures*, **21**(2), pp. 121–130.
9. Jones, R. (1991). Recent developments in advanced repair technology. *Proc. Int. Conf. on Aircraft Damage Assessment and Repair*, Melbourne, August 1991, Published by Institution of Engineers Australia, ISBN (BOOK) 85825 5375, July.
10. Baker and Jones, R. (1988). Bonded repair of aircraft structures, Martinus Nijhoff, The Netherlands.
11. Dowrick, G., Cartwright, D.J. and Rooke, D.P. (1980). The effects of repairs patches on the stress distribution in a cracked sheet, Royal Aircraft Establishment Technical Report 80098, August.
12. Atluri, S.N., Park, J.H., Punch, E.F., *et al.* (1993). Composite repairs of cracked metallic aircraft, Federal Aviation Administration, Contract Report, May, DOT/FAA/CT-92/32.
13. Sun, C.T., Klug, J. and Arendt, C. (1996). Analysis of cracked aluminium plates repaired with bonded composite patches. *AIAA Journal*, pp. 369–374.
14. Ratwani, (1981). Development of bonded composite repairs for cracked metal structure. *Proc. Int. Workshop on defence applications of repair technology*, NRL, Washington D.C., 22–24th July, 1981, pp. 307–403.
15. Jones, R., Chiu, W.K. and Hanna, S. (1994). Potential failure mechanisms of bonded composite repairs for metal and concrete. *Theoretical and Applied Fracture Mechanics*, **21**, pp. 107–119.
16. Chiu, W.K., Chalkley, P.D. and Jones, R. (1994). Effects of temperature on the stress/strain behaviour of film adhesives FM73, Computers and Structures, pp. 1–7.
17. Thrall, E.W. (1979). Primary adhesively bonded structure technology (PABST): Design handbook for adhesive bonding, USAF Technical Report, AFFDL-TR-79-3119.
18. Hart-Smith, L.J. (1973). Adhesively bonded double lap joints, NASA Langley Research Center Report NASA CR-112235, January.
19. Glinka, G. (1985). Calculation of inelastic notch-tip strain-stress histories under cyclic loading. *Engineering Fracture Mechanics*, **22**(5), pp. 839–854.
20. Chiu, W.K. and Jones, R. (1992). A numerical study of adhesively bonded joints. *Int. J. of Adhesion and Adhesives*, **12**(4), pp. 219–225.
21. Chiu, W.K., Rees, D., Chalkley P., *et al.* (1994). Designing for damage tolerant repairs. *J. of Composite Structures*, **28**(1), pp. 19–38.
22. Mignery, L.A. and Schapery, R.A. (1991). Viscoelastic and nonlinear adherend effects in bonded composite joints. *J. of Adhesion*, **34**3, pp. 17–40.

23. Wang, S., Srinivasan, S., Hu, H.T., *et al.* (1995). Effect of material nonlinearity on buckling and postbuckling of fiber composite laminated plates and cylindrical shells. *Composite Structures*, **33**, pp. 7–15.
24. Jones, R., Alesi, H. and Mileshekin, N. (1998). Australian developments in the analysis of composite structures with material and geometric nonlinearities. *J. Composite Structures*, **41**, pp. 197–214.
25. Damage Tolerance and Fatigue Evaluation of Structure, Federal Aviation Administration Advisory Circular, 25.571-1A, (1986).
26. Composite Aircraft Structure, Federal Aviation Administration Advisory Circular, 20-107A, (1984).
27. Korn, G. and Korn, T. (1961). Mathematical handbook for scientists and engineers, Second, enlarged and revised edition, McGraw-Hill Book Company, New York.
28. Damage Tolerance Design Handbook, Volume 4, December.
29. Hart-Smith, L.J. (1999). On the Relative Effectiveness of Bonded Composite and Riveted Patches over Cracks in Metallic Structures, Boeing Paper MDC 99K0097, *Proc. of The 1999 USAF Aircraft Structural Integrity Program Conference*, San Antonio, Texas, 30 November–2 December.
30. Schijve, J. (1982). The stress intensity factor of small cracks at notches. *Fatigue of Engineering Materials and Structures*, **5**(1), pp. 77–90.
31. Jones, R. (2001). Effect of load bi-axiality on composite repairs. *Proc. 12th Int. Conf. on Composite Structures*, Melbourne 2001, to be reprinted in *Journal of Composite Structures*.
32. Wang, C.H. and Rose, L.R.F. (1999). A crack bridging model for bonded plates subjected to tension and bending. *Int. J. of Solids and Structures*, **36**, pp. 1985–2014.
33. Tweed, J. and Rooke, D.P. (1973). The distribution of stress near the tip of a radial crack at the edge of a circular hole. *Int. J. of Engineering Science*, **11**, pp. 1183–1195.
34. Filenko-Borodich, M. (1959). Theory of Elasticity, Foreign Languages Publishing House, Moscow.
35. Liebowitz, H., Sandhu, J.S., Menandro S.C.M., *et al.* (1995). Smart computational fracture of materials and structures. *Engineering Fracture Mechanics*, **50**(5–6), pp. 639–651.
36. Zenkiewicz, O.C., De, J.P., Gago, S.R., *et al.* (1983). The hierarchical concept in finite element analysis. *Computers and Structure*, **16**(1–4), pp. 53–65.

Chapter 10

SHAPE OPTIMISATION FOR BONDED REPAIRS

M. HELLER and R. KAYE

Defence Science and Technology Organisation, Air Vehicles Division, Fishermans Bend, Victoria 3207, Australia

10.1. Introduction

Bonded repairs function by transferring some portion of the load from the reinforced component through the adhesive bond layer, thereby reducing the range and mean of the cyclic stresses in the repaired component. The relative stiffness of the reinforcement, as compared to the repaired component, determines not only the portion of load attracted, but also the level of peak stresses in the adhesive layer, and the intensity of associated stress concentrations in the repaired component. Hence a key technical objective addressed in this chapter is the use of automated numerical procedures to determine optimised repair designs, which reduce the magnitude of these critical stresses. There are essentially two load paths for a plate with a bonded repair/reinforcement, where each can be approximated by a distinct 2D idealisation. The first is through-thickness load transfer, where the repair configuration can be represented as a single or double lap joint [1]. Secondly we can refer to in-plane load transfer, where a finite width patch can be approximated as an inclusion, which locally attracts load in excess of the load based on nominal remote stress. The finite element stress analysis approach [2–5] is ideally suited to investigate such load transfer and the estimation of the induced internal stresses for these types of problems. It is important to note that due to airworthiness considerations, when applied to primary structural components, bonded repairs are typically used as a measure to prevent crack initiation and retard crack growth. It is generally required that the component has adequate static strength with or without the bonded repair. Hence, in some cases it is necessary to restore residual static strength before application of a bonded repair. This can be achieved by precise rework shape optimisation [6–11], which has recently been shown to be a highly effective procedure for concurrently removing any pre-existing cracks and reducing

local stress concentrations (thereby increasing residual strength) in metallic components, prior to application of a bonded repair. Such optimal reworking also helps to further increase the fatigue life extension benefits provided by bonded repairs.

10.1.1. Context for finite element based shape optimisation

Early applications of bonded reinforcements were to thin section components such as skin panels. These skin panels were usually stiffened by internal structure such that there was no out-of-plane bending present. Here the theoretical stress analysis has usually been based on an analogy with a one-dimensional lap-joint analysis, where 100% of the load is carried by the reinforcements, [1,12]. A key quantity of interest being the adhesive stress concentrations at the extremities of load transfer regions, [13,14]. Often yielding of the adhesive can occur at these locations, and this can possibly lead to premature adhesive failure depending on the severity of the in-service loading history. Some more recent practical problems have been concerned with reinforcement to thick section airframe components. These cases are usually complicated by the presence of curvature of the surface to be bonded and the need to transfer more load into the reinforcement because of the thick sections (i.e. 3D solid type components) [15,16]. Here unacceptably high adhesive stresses can occur (shear and peel) in the adhesive layer, which can compromise the integrity of the adhesive layer. This also leads to an unfortunate associated trade off, where the stiffness of the patch needs to be lowered to enable a reduction in peak adhesive stresses, thereby limiting the amount of stress reduction in the repaired component that can be achieved. It is important to note that for both thin and thick section reinforcements to practical applications theoretical solutions are not available, and hence trial and error finite element analyses have typically been used to arrive at a suitable practical design. However, for thin section cases (with no bending), the analytical formulations given in [1], provide useful initial design estimates. It should also be noted that all practical applications to date have essentially used a constant adhesive thickness, as well as a constant reinforcement thickness (except for tapering at the ends of the reinforcement).

Published work on the optimal design of bonded repairs/lap joints to reduce adhesive stress is very limited. However, some investigations of specific scope have been undertaken, such as the consideration of optimal tapering at the ends of a continuous reinforcement/repair. For example, an analytical treatment of the optimal tapering at the ends an isotropic reinforcement for a uniaxial loaded lap joint is provided is given by Ojalvo [17]. In other work given by Heller, *et al.* [6,7], the same problem is considered by using a 2D gradientless FE method. Groth and Nordland [18] have used FE based design sensitivity methods to also optimise essentially the same configuration. In all three references above, the analyses are confined to the consideration of reinforcement tapering and do not consider variation in adhesive thickness. More recently at Air Vehicles Division (AVD) sensitivity based methods have been used for 2D optimal through thickness shaping of both the reinforcement and adhesive layer, [8,19].

10.1.2. Finite element modelling considerations

The finite element method [2–5] is ideally suited for meeting two essential requirements for design optimisation of bonded reinforcements. Firstly, accurate stresses can be obtained for realistic practical geometries, and loading conditions, (which analytical methods cannot provide), and secondly the method is amenable to automation as an iterative process, which can improve an initial non-optimal design. For all FE work presented in this chapter, the analyses were conducted using a Hewlett-Packard K series 9000 computer at AVD. One of two codes were used, MSC.NASTRAN Version 70 for sensitivity based shape optimisation, (with MSC.PATRAN level 7.5 code used for pre and post processing of the models) or PAFEC level 8, which has been extended with AVD code to undertake gradientless shape optimisation. For all analyses presented, linear elastic material properties were used, with elements being eight noded isoparametric rectangles or six noded triangles unless noted otherwise. For the through-thickness analyses plane strain conditions were assumed, while for the in-plane analyses plane stress was assumed.

10.1.3. Outline of chapter

It appears that there is very little work on optimisation relating to bonded reinforcements, hence by necessity most of the work presented is focused on work undertaken in the last few years in AVD. Here the focus is on through-thickness optimisation for minimising adhesive stress, since it is considered that this a key technical issue, which offers significant scope for improvement. Also, some preliminary work on in-plane shaping effects is given. In Section 10.2 a 1D analytical formulation is provided for a simple configuration of a double lap joint. This leads to strategies for minimisation of adhesive shear stresses in the tapered/stepped region of a typical patch, where each step is allowed to be of arbitrary height, modulus and length. Finite element analyses, which demonstrate reductions in peak adhesive stresses and plate stress concentrations, for the improved configurations discussed in Section 10.2, are given in Section 10.3. Automated through thickness optimisation using a free-form gradientless finite element method is then considered in Section 10.4, for typical taper region. In Section 10.5 the automated sensitivity based free-form shape optimisation is discussed, for single and double sided joint configurations, where both typical taper and crack regions are considered. Specific aspects of the finite element optimisation procedure are given in some detail as the key features are also used in the subsequent Sections 10.6 and 10.7. Section 10.6 gives the application of the sensitivity-based approach for determining optimal reinforcement/adhesive configurations for minimising adhesive stresses. Section 10.7 then presents the application of precise rework shape optimisation (to remove cracking) in combination with subsequent bonded reinforcement for the life extension of F/A-18 inboard aileron hinges. The reworking is essential from an airworthiness perspective, to restore initial surface stress as discussed above in the first paragraph. The subsequent reinforcement stepping is then designed using an iterative approach to minimise peak adhesive

stresses. Finally in Section 10.8 the issue of improved in-plane shaping of patches, for reducing plate stress concentrations is investigated using finite element analysis.

10.2. Analytical formulation for improved stepping in patch taper region

The large peak in adhesive shear strain, which occurs near the end of a typical stepped patch can potentially cause failure of the adhesive system. To reduce the severity of this peak, uniform stepping of multi-layer patches is currently used for bonded repairs on RAAF aircraft, with the typical step length being 3 or 4 mm per lamina ply. However, having uniform step lengths is not optimal (in terms of minimising peak adhesive shear strain). One possible approach for reducing the peak adhesive strains is to increase the length of the uniform steps of the composite patch, where each step consists of one unidirectional lamina [13]. However to achieve a significant benefit as compared to a standard patch configuration, the length of the stepped region needs to be much increased, hence resulting in an undesirable increase in the overall length of the patch. It is interesting to note that for the non-linear continuous (i.e. not stepped) tapering of the patches, it has been shown that it is possible to maintain the shear strain at a minimised and constant level. [6,17]. Hence this is what is desirable for stepped taper regions. Rees, *et al.* [20] have undertaken a finite element analysis of a practical repair application for a multi-layer composite patch, where the step length was allowed to be non-uniform, and this was shown to be beneficial. However no analytical formulation or attempt to optimise the stepping scheme was presented. Hence it is desirable to further investigate the stress behaviour analytically, for minimising the peak adhesive shear strain where each step is allowed to be of different height and modulus, and of non-uniform step length.

10.2.1. General configuration for symmetric stepped patches

The general configuration of the problem under study is shown in Figure 10.1(a). A thin plate of uniform thickness t_i is subjected to a uniaxial remote load P (per unit width in the z direction). Each side of this plate is reinforced with an identical adhesively bonded patch, thereby symmetry is retained with respect to the plate mid-plane $y = 0$, where the origin of the axis system is at the left hand end of the patch. The adhesive thickness is uniform and is denoted η . Each patch has a maximum length of L , and is stepped at each of its ends identically, with symmetry being retained with respect to the line $x = L/2$. Its maximum thickness is denoted t_o . The geometry and notation for the stepping arrangement is shown in Figure 10.1(b). There are n steps at the end of each patch which are allowed to be of different thickness, modulus and of non-uniform length. For an arbitrary step k , the thickness is denoted t_o^k , the modulus is E_o^k , and the position of the beginning of the step is denoted $x_{(k-1)}$. It should be noted here that the step height is defined as the difference in total step thickness from one step to another, i.e. $t_o^k - t_o^{k-1}$ is the height for step k .

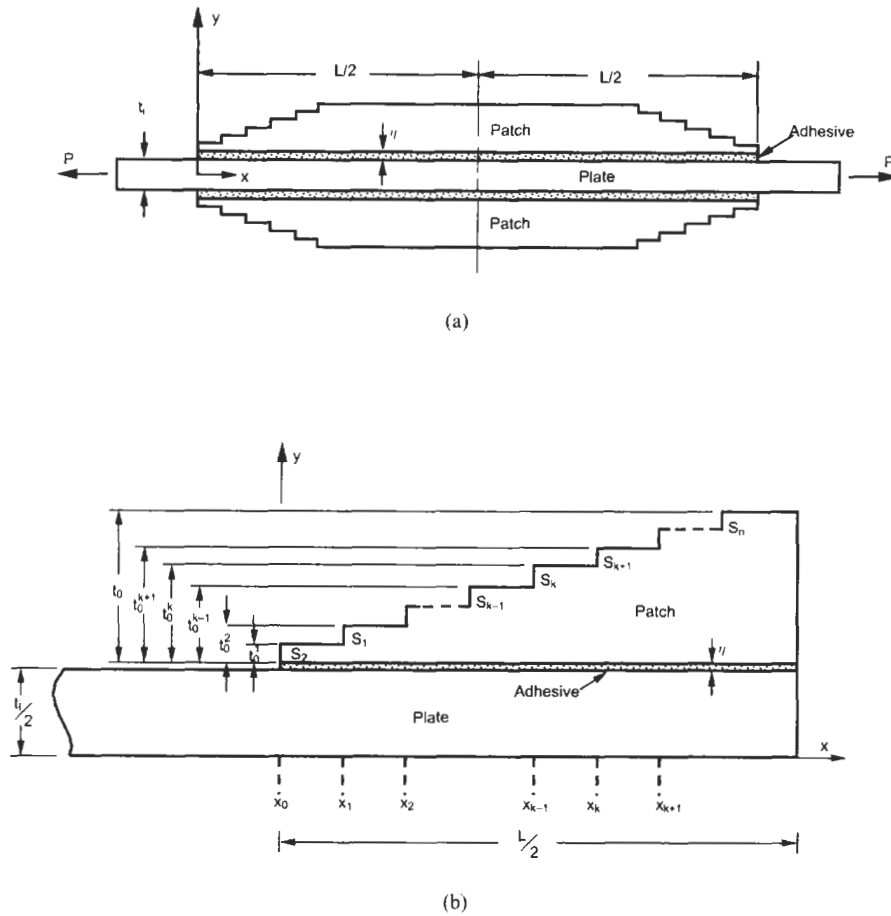


Fig. 10.1. Plate with bonded symmetric stepped patches: (a) general arrangement, and (b) notation and geometric definitions for stepped regions.

10.2.2. Analysis for single step case

The standard elastic adhesive shear lag formulation [12,21,22], for this case is given here, as it provides relevant expressions required subsequently for the multi-step analysis and bounding case. A 1D idealisation is taken, for a thin vertical slice of width Δx through the patch and plate, so that displacements in the inner and outer adherends are assumed to be constant across their thicknesses respectively. For the adhesive a uniform shear deformation is assumed across its thickness. For any position x , the tensile forces per unit width of the inner adherend (plate) and outer adherend (patch) are denoted T_i and T_o respectively, and τ is the shear stress in the adhesive layer per unit depth. Also δ_i and δ_o are the displacements in the x direction of the inner and outer adherends respectively. For the thin vertical slice,

the equilibrium of forces in the x -direction for the outer and inner material respectively, gives the following two equations

$$\frac{dT_o}{dx} - \tau = 0 \quad \text{and} \quad \frac{dT_i}{dx} + 2\tau = 0 \quad (10.1)$$

Assuming 1D linear elastic stress-strain relations, we can write the strains ϵ_o , and ϵ_i for the outer and inner adherends respectively as

$$\epsilon_o = \frac{d\delta_o}{dx} = \frac{T_o}{E_o t_o} \quad \text{and} \quad \epsilon_i = \frac{d\delta_i}{dx} = \frac{T_i}{E_i t_i}, \quad (10.2)$$

where E_o and E_i are the elastic moduli of the outer and inner adherends respectively. Since the shear strain γ in the adhesive is assumed to be constant across its thickness is given by

$$\gamma = \frac{\delta_o - \delta_i}{\eta} \quad (10.3)$$

Differentiating Eq. (3) with respect to x and substituting from Eq. (2) gives

$$\frac{d\gamma}{dx} = \frac{1}{\eta} \left(\frac{T_o}{E_o t_o} - \frac{T_i}{E_i t_i} \right) \quad (10.4)$$

Differentiating again, substituting from Eq. (1), and writing in terms of strain gives

$$\frac{d^2\gamma}{dx^2} - A^2\gamma = 0, \quad \text{where} \quad A = \left[\frac{G}{\eta} \left(\frac{1}{E_o t_o} + \frac{2}{E_i t_i} \right) \right]^{\frac{1}{2}}, \quad (10.5)$$

and G is the shear modulus. The general solution to Eq. (10.5) is

$$\gamma = C_1 e^{-Ax} + C_2 e^{+Ax}, \quad (10.6)$$

where C_1 and C_2 can be determined from the boundary conditions. At the end of the patch, we have from equilibrium the conditions $T_i(0) = P$, $T_o(0) = 0$, while at the centre of the patch, we have the condition $\gamma(L/2) = 0$. From these conditions, and Eqs. (10.4) and (10.6) we have the adhesive shear strain as

$$\gamma(x) = \frac{-P \sinh(Ax - AL/2)}{\eta E_i t_i A \cosh(AL/2)} \quad (10.7)$$

10.2.3. Analysis for patch with multiple steps

For the case where the patch has multiple steps, Eqs. (10.4) to (10.7) given above are appropriate when interpreted as representing the shear strains in each step separately. However the boundary conditions at the ends of each step are now different to those presented previously. Referring to the geometry and notation

given in Figure 10.1(b), we can consider an arbitrary step, k for which we have from Eq. (10.6)

$$\gamma^k = C_1^k e^{-A^k x} + C_2^k e^{+A^k x} \quad (10.8)$$

From force equilibrium, we have the condition, $2T_o^k + T_i = P$, at any section x through the patched plate. Hence differentiating Eq. (10.8), and using this condition with Eq. (10.4), gives the load in the step, T_o^k , as

$$T_o^k = \left(\frac{1}{E_o^k t_o^k} + \frac{2}{E_i t_i} \right)^{-1} \left(-A^k \eta C_1^k e^{-A^k x} + A^k \eta C_2^k e^{+A^k x} + \frac{P}{E_i t_i} \right) \quad (10.9)$$

Due to equilibrium we require that the force T_o^k is continuous where one step ends and another begins. Also, the shear strain γ has to be continuous at this location from kinetic considerations. Hence at the beginning of step k , (i.e. at $x = x^{k-1}$), we have $\gamma^{k-1} = \gamma^k$ and $T_o^{k-1} = T_o^k$, while at the end of step k , (i.e. at $x = x^k$), we have $\gamma^k = \gamma^{k+1}$ and $T_o^k = T_o^{k+1}$. Two further boundary conditions are also known, namely $T_o(0) = 0$ and $\gamma(L/2) = 0$. Using these continuity and boundary conditions, in conjunction with Eqs. (10.8) and (10.9), yields a set of linear simultaneous equations which can be solved for the coefficients C_1^k and C_2^k for $k = 1, \dots, n$. The adhesive shear strain distribution can be readily evaluated once the coefficients are determined from Eq. (10.8). A useful iterative numerical procedure to solve for adhesive shear strains has been given in [14]. In this approach we start in the first step, and use the condition $T_o(0) = 0$, and take an arbitrary assumed value of $\gamma(0)$. From these two initial values, C_1 and C_2 are estimated for the first step using Eqs. (10.8) and (10.9) and consequently the values of T_o and $\gamma(x)$ at the other end of the first step are determined from these two equations. Then using the above conditions for T_o and γ , Eqs. (10.8) and (10.9) give C_1 and C_2 in the next step. The whole process is repeated for every subsequent step until an estimated value for $\gamma(L/2)$ is found at the centre of the patch. If the required condition $\gamma(L/2) = 0$ at the centre of the patch is not satisfied, then another value of $\gamma(0)$ is assumed and the process repeated to determine a new estimate of $\gamma(L/2)$. By using an interval halving technique to determine improved estimates for $\gamma(0)$ the method is repeated until the correct value of $\gamma(L/2) = 0$ is obtained. A suitable upper bound first estimate for $\gamma(0)$ can be obtained assuming the patch has uniform thickness, and typically a converged solution is obtained after approximately 60 iterations with a typical accuracy in shear strain of 10^{-6} .

10.2.4. Estimate for optimal first step length

It is helpful here to obtain an estimate of a suitable first step length, x_1 , which can be used in the numerical solution method. We wish to determine approximately the distance from the beginning of the first step such that the peak shear strain has decayed to almost zero (assuming there are no other steps). Hence if the next step was started here, its presence would have minimal effect on the magnitude of the

peak at the end of the patch. To determine the required length we make use of the single step formulation as given in Section 10.2.1. At the beginning of the first step, and at the position, $x = x_1$, we have the respective shear strains from Eq. (10.7) as

$$\begin{aligned}\gamma(0) &= \frac{P \sinh(A^k L/2)}{\eta E_i t_i A^k \cosh(A^k L/2)} \quad \text{and} \\ \gamma(x_1) &= \frac{-P \sinh(A^k x_1 - A^k L/2)}{\eta E_i t_i A^k \cosh(A^k L/2)}\end{aligned}\quad (10.10)$$

Choosing the case where the strain value $\gamma(x_1)$ has reduced to 1% of the peak value, $\gamma(0)$, we have from Eq. (10.10)

$$0.01 = \frac{-(e^{(A^k x_1 - A^k L/2)} - e^{-(A^k x_1 - A^k L/2)})}{e^{A^k L/2} - e^{-A^k L/2}} \quad (10.11)$$

Rearranging Eq. (10.11) and setting $e^{-A^k L/2} = 0$, we have since $x_1 \ll L/2$, that the required length of the first step is

$$x_1 = \frac{5}{A^k} \quad (10.12)$$

10.2.5. Minimum bound for peak shear strain due to patch length

It is convenient here to consider one theoretical lower bound on adhesive shear strain. This bound equates to the case where the shear strain is uniform along the patch (except for a region close to $x = L/2$, where the strain must vanish to zero). Equilibrium of forces gives the relation

$$P = 2T_o + T_i \quad (10.13)$$

In this case for a patch of sufficient length, the load transferred to the patch at the centre of its length is given by combining Eq. (10.13) with (10.2)

$$T_o = P \left(\frac{E_o t_o}{E_i t_i + 2E_o t_o} \right) \quad (10.14)$$

This is also the load that the adhesive must transmit by shear deformation over the half length of the patch. Hence for a constant adhesive shear stress over this length we have

$$\tau = \frac{T_o}{L/2} \quad (10.15)$$

Hence from Eqs. (10.14) and (10.15) we have one lower bound for a uniform shear

strain distribution as

$$\gamma = \frac{2P}{GL} \left(\frac{E_o t_o}{E_i t_i + 2E_o t_o} \right) \quad (10.16)$$

10.2.6. Minimum bound for peak shear strain due to stiffness of first step

Another key bound equates to the peak value of shear strain corresponding to the case where there is a long first step, which can be estimated by putting $x = 0$ in Eq. (10.7) and letting L tend to infinity. This gives the estimated lower bound as

$$\gamma = \frac{-P}{\eta E_i t_i A^{k=1}} \quad (10.17)$$

10.2.7. Numerical examples

In this section the proceeding formulation presented in Section 10.2.3 is applied to a number of illustrative problems. It is important to make clear here that each step can consist of one or multiple laminae. Hence the value of the effective stiffness, $E_o^k t_o^k$, as used in the formulation of Section 10.2.3 will be different for each step, and will depend on the properties of the individual lamina within the step. For a particular step, the effective stiffness is given by

$$E_o^k t_o^k = \sum_{l=1}^{l=m} E_l t_l, \quad (10.18)$$

where the subscript l refers to an individual lamina, and m denotes the number of laminae in the step. To provide a meaningful comparison for the various patch configurations presented, a number of parameters and boundary conditions were kept the same for all cases, namely: (i) remote loading (ii) plate properties, (iii) the adhesive shear stress has reduced to zero at the centre of the patch, $x = L/2$, and (iv) the maximum effective stiffness $E_o t_o$ for the patch is equivalent to that for ten unidirectional boron/epoxy laminae. Hence the same amount of load was transferred to the patch for each analysis case, where the plate remote loading was $P = 2000 \text{ kN/m}$. The material and geometric properties were as follows: (i) for the aluminium plate Young's modulus was 71000 MPa and the thickness was 6 mm , (ii) for the boron/epoxy lamina used to compose multi-layer patch Young's modulus in the unidirectional orientation was $E_o = 208000 \text{ MPa}$, Young's modulus in the cross-ply orientation was $E_o = 20800 \text{ MPa}$, thickness $t = 0.13 \text{ mm}$, and the maximum length was $L = 80 \text{ mm}$, and (iii) for the typical structural adhesive, the shear modulus was $G = 590 \text{ MPa}$, and thickness $\eta = 0.1 \text{ mm}$.

In Figure 10.2(a) the adhesive shear strain distribution is shown for the case where each patch consists of one step only. The solution for this case provides an upper bound to the value of the peak adhesive shear strain for multiple stepped

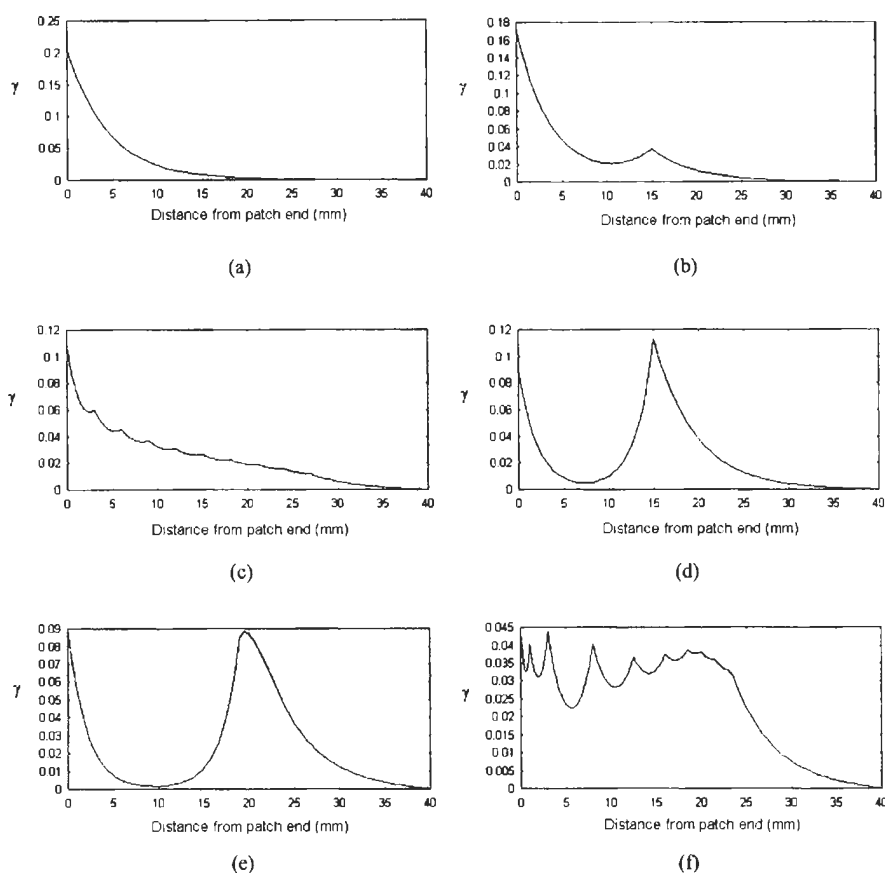


Fig. 10.2. Comparison of adhesive shear strain results for bonded symmetric stepped patches: (a) patch with one unidirectional step, (b) patch consists of two unidirectional steps, each of same height, (c) unidirectional patch consists of ten steps of equal height with uniform step length of 3 mm, (d) patch consists of two unidirectional steps, the first of one lamina thick, (e) unidirectional patch consists of ten steps of equal height with non-uniform step lengths, (f) patch consists of 11 unequal step heights, and a combination of cross-ply and unidirectional laminae.

patches. The peak and exponential decay, in the adhesive shear strain distribution at the end of the patch can be readily seen. The adhesive shear strain distribution for the case where there are two steps of equal length and height is shown in Figure 10.2(b). It can be seen that this configuration provides a significant improvement as compared to the single step case. The adhesive shear strain distribution for the case of 10 equal step heights, and a uniform step length of 3 mm is given in Figure 10.2(c). Results for this patch case are also given in [13], and the present results are in very close agreement with those finite element and analytical results. This stepping scheme is typical of that recommended by the RAAF Engineering

Standard on Bonded Repairs [23]. It is important to note that while the peak shear strain is significantly reduced as compared to the single step case, the highly localised peak in adhesive shear strain at the end of the patch is still evident and there is significant interaction between the first and second stress peaks. Also, the maximum shear strain in the adhesive is significantly greater than the lower bound of $\gamma = 0.0237$ determined from Eq. (10.16) for the given length of the patch. Hence it is evident that there is scope for minimising the magnitude of the peak strain.

One obvious approach for minimising the interaction of the first and second peak, for a patch comprising unidirectional laminae is to use a longer first step. Figure 10.2(d) shows the adhesive shear strain distribution when the patch has two steps, where the first step is very thin, of thickness 0.13 mm (typical of one lamina), and 15 mm long. It can be seen that there is now minimal interaction between the two peaks at each step, hence the first peak has been reduced to its limiting value for the given load and relative material properties. Clearly, splitting the second step into multiple steps would further reduce the value of the second peak. We now consider the case where we again have a long first step but the second step is further split into nine steps. The adhesive shear strain distribution for such a case is given in Figure 10.2(e). Here the patch has a thin long first step of length 19 mm consisting of one lamina. Subsequent steps each consist of one lamina and have equal lengths of 0.5 mm, (except for the last step which has a length of 17 mm to take up the remaining half length of the patch). It is evident that this method of having maximal length for the first thin step gives a reduction of about 20% in the peak shear strain at the edge of the patch, as compared to the standard method given, represented in Figure 10.2(c).

To reduce the magnitude of the peak further the value of the effective stiffness E_{ot_o} of the first step must be lowered. One possible method of achieving this is to replace the unidirectional lamina in the first step with a cross-ply, so that the new E_{ot_o} value is equivalent to about one tenth of that for a typical unidirectional lamina. Hence one possible general stepping arrangement can be proposed where the first step consists of one cross-ply lamina, and a combination of cross-ply and unidirectional lamina are used for the remaining steps, with non-uniform step lengths. To allow a direct comparison with the previous cases, the maximum value of E_{ot_o} for the patch is kept the same as previously. One way of meeting this requirement easily is to replace the first unidirectional step, used in the previous cases, with ten cross-ply laminae further split into three steps, while keeping the step heights of the remaining 9 steps unchanged (each consisting of one lamina). Hence this patch consists of 11 steps, with a combination of 19 unidirectional and cross-ply lamina with the geometric details as given in Table 10.1. Here the step lengths were chosen such that the highest shear strain was minimised. The resulting shear strain distribution is shown in Figure 10.2(f), and it can be seen that the peak strain value has been reduced by about 60% from that given by Figure 10.2(c). Due to the dominant effect of the stiffness of the first step, it is believed that a similar reduction can be achieved by adding just one extra layer of cross ply lamina, underneath a typical DSTO unidirectional patch, which would only require 11 lamina in total.

Table 10.1

Geometric details for patch on one side of plate for non-uniform stepping case.

Step number	Step length (mm)	Lay-up order of laminae within step (C refers to cross-ply laminae) (U refers to unidirectional laminae)
1	1.0	1C
2	2.0	3C
3	5.0	6C
4	4.5	10C,1U
5	3.5	10C,2U
6	2.5	10C,3U
7	1.5	10C,4U
8	1.5	10C,5U
9	1.5	10C,6U
10	0.5	10C,7U
11	16.5	10C,9U

For the case shown in Figure 10.2(f) the value of maximum shear strain has been lowered to be approximately twice the theoretically lowest bound as given by Eq. (10.15), (where the total patch length has been constrained to 80 mm). If this lower bound for the maximum shear strain is to be approached, E_{ot_o} of the first ply step must be further reduced, and more gradual changes in E_{ot_o} across step interfaces would be desirable. A patch composed of different materials, using appropriate step lengths, offers this possibility.

10.2.8. Discussion

Without recourse to increasing the overall patch length, the formulation given in this section has shown that an improved stepping arrangement can significantly reduce the peak adhesive shear strain, as compared to standard patch with 3 mm length uniform stepping. For the case where the patch material is of one type and all lamina thicknesses are the same, the best stepping procedure is to have a relatively long first step (Eq. (10.17)) while successive steps can be quite close together. Significant further reductions can be achieved for such a patch, by making use of cross-ply laminae in the first two steps. Clearly, the use of a patch composed of different laminae materials offers the potential of further improvement, via a reduction and more gradual change in E_{ot_o} . This would theoretically enable a stress distribution approaching the lower bound as given by Eq. (10.17) to be achieved. Here the minimum attainable value of peak shear strains will depend primarily on E_{ot_o} of the first step and secondly on the total permissible length of the patch. It should also be noted that there may be practical difficulties in the manufacture/application of a patch with cross-ply laminae of the different materials, and this needs to be investigated.

10.3. FE analysis for adhesive stress and plate stress concentration

It is clear from the results presented in Section 10.2, that minimising the adhesive strain is essentially equivalent to smoothing the load transfer from the plate to the patch. It is reasonable to expect that minimising the adhesive shear strains will naturally lead to a reduction in the detrimental stress concentration outside the patch [24], as has been postulated in [14]. Inspection of the results given in [20] gives evidence supporting this conjecture, as does recent analytical work [25] and two dimensional finite element stress analysis [26]. In [25], an analytical formulation is given to describe the stress concentration in the plate and to determine what type of shear stress distribution in the adhesive gives the best reduction in the plate stress concentration. It has also been determined in [27] that the combination of adherend tapering, and the inclusion of an adhesive fillet at the edge of the overlap produced a significant increase in joint strength, due to a reduction in adhesive stresses. In this section, results from finite element (FE) analyses are given to highlight the influence on the plate stress concentration for a bonded repair specimen of the following: (i) modification of the shear stress distribution in the adhesive by changing the distribution of the patch stiffness and stepping arrangement, and (ii) introduction of an adhesive fillet at the end of the patch.

10.3.1. Configuration and finite element analysis method

Analyses were undertaken for the three key patching cases indicated in Section 10.2, (i) patch with one step, i.e. a uniform thickness patch comprising 10 unidirectional laminae, (ii) patch with 10 steps, each consisting of one unidirectional lamina, where the first nine steps are each 3 mm long (i.e. standard AVD approach), (iii) patch with multiple non-uniform step lengths, unequal step heights and different lamina moduli via unidirectional and cross-ply orientations. This lay-up is the same as indicated in Table 10.1 of Section 10.2. In view of the symmetry, only one quarter of the actual specimen was modelled. An existing finite element model of a cracked plate repaired with a one step patch was used as a starting point for the current investigation [26]. It was assumed here that the end of the patch was sufficient distance from the crack, so that interaction between these two regions was not a dominant effect. Typical patch geometries with and without fillets are shown schematically in Figure 10.3. Typical finite element meshes for each of the three cases without fillets are shown in Figure 10.4, while Figure 10.5 shows the highly refined mesh around the region near the end of the patch with a full height rectangular adhesive fillet. Unless otherwise noted, the following material and geometric properties and loading conditions were used in all the analyses undertaken: (a) For the aluminium plate: (i) Young's modulus, $E = 71$ GPa, (ii) Poisson's ratio, $\nu = 0.33$, (iii) assumed length, $l = 104$ mm, (iv) thickness, $t_i = 6$ mm and (v) remote stress, $\sigma_o = 71$ MPa. (b) For the adhesive: (i) shear modulus, $G = 590$ MPa, (ii) Poisson's ratio, $\nu = 0.35$ and (iii) thickness, $\eta = 0.1$ mm. (c) For a given unidirectional boron lamina: (i) Young's modulus, $E_1 = 208$ GPa and $E_2 = E_3 = 20.8$ GPa, (ii) Poisson's ratio, $\nu = 0.3$, (iii) maximum length, $L = 80$ mm

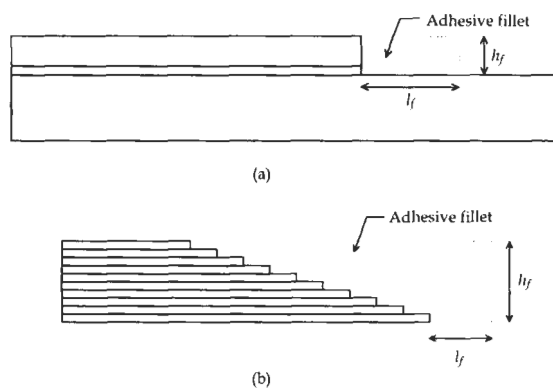


Fig. 10.3. Typical patch geometries with and without rectangular adhesive fillets: (a) single step patch case, (b) typical multiple stepping arrangement.



Fig. 10.4. Typical finite element meshes for three patch stepping cases: (a) single step case, (b) uniform stepping case, (c) non-uniform stepping case.

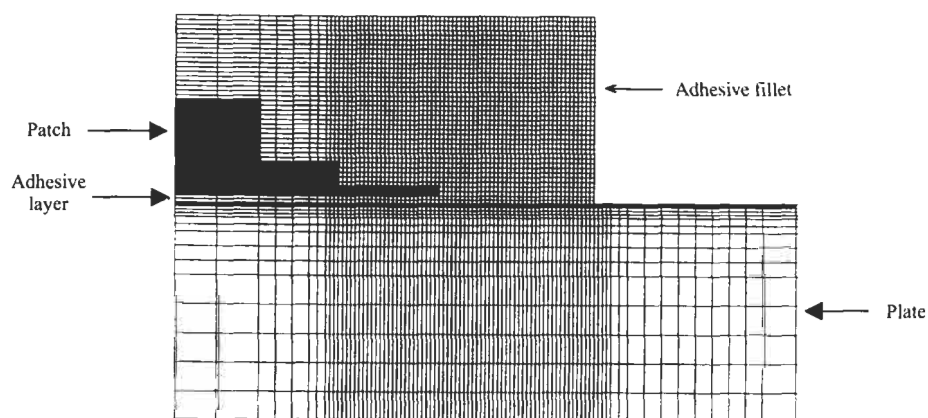


Fig. 10.5. Typical finite element mesh around region at the end of patch for full height rectangular adhesive fillet.

and (iv) thickness $t = 0.13$ mm. It should be noted that for all analyses, the adhesive shear stress results are presented along the mid-surface of the adhesive layer. For the presentation of direct stresses in the plate, the results are given at the interface with the adhesive layer.

10.3.2. Results for no-fillet case

Results for the shear stress distribution for all three stepping cases, without an adhesive fillet, are shown in Figure 10.6(a). The dominant peak stress at the start of the patch is clear for the single step case, and this then decreases to a minimum at the centre of the half patch length and, as expected, increases to another peak as it approaches the crack and dips down to zero at the crack location. For the patch with multiple uniform steps there is a significant reduction in the adhesive stress at the start of the patch, as compared to the single step case. The large reduction in adhesive stress for the non-uniform stepping case is clearly seen. A comparison of results for the plate direct stresses on the patched surface, near the start of the patch (i.e. at $x = 40$ mm), is given in Figure 10.6(b). The highly localised peak for the single step case is apparent, along with the significant advantage of the non-uniform stepping case over the uniform stepping case. The results given in Figures 10.6(a) and 10.6(b) are consistent with the expectation that the non-uniform patch stepping arrangement serves to make the transfer of load from the plate to the patch less abrupt as compared to the previous no-fillet cases. A summary of stress results is given in Table 10.2.

10.3.3. Results for fillet case

Initially the influence of different sizes of a rectangular adhesive fillet, on the stress distribution in the region of concern, was investigated for a patch of one step. For convenience, the length of the fillet (l_f) from the end of the patch was varied, as shown in Figure 10.3(a) for the following cases; (i) 0.4 mm, (ii) 1 mm, (iii) 2 mm and

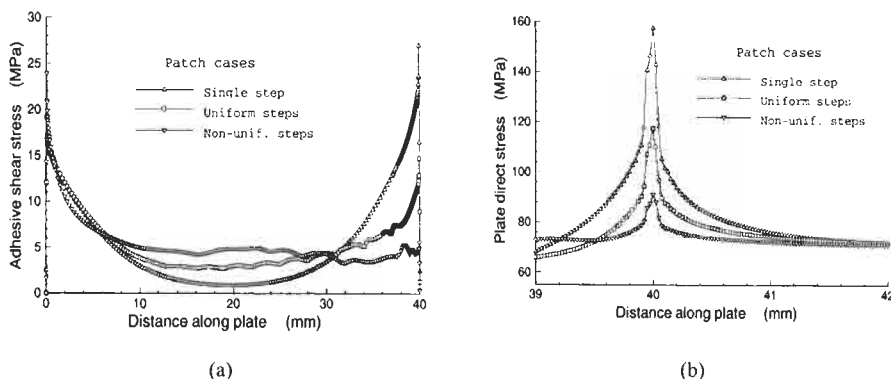


Fig. 10.6. Stress distributions for no fillet cases: (a) shear stresses in adhesive layer, (b) plate direct stresses on patched surface.

Table 10.2
Adhesive shear stress and plate stress concentrations.

Cases considered	Adhesive shear stress (MPa)	Plate stress concentration
Patch with single step		
<i>No fillet</i>	26.9	2.22
<i>Rectangular fillet cases</i>		
0.4 mm length	20.9	1.76
1 mm length	20.3	1.45
2 mm length	20.0	1.42
12 mm length	19.6	1.42
Patch with uniform stepping		
<i>No fillet</i>	14.7	1.65
<i>Rectangular 2 mm fillet length</i>		
Adhesive level fillet height	11.8	1.34
First step fillet height	11.2	1.26
Second step fillet height	11.1	1.24
Every step fillet height	11.0	1.21
Patch with non-uniform stepping		
<i>No fillet</i>	5.6	1.28
<i>Rectangular 2 mm fillet length</i>		
Every step fillet height	4.9	1.17

(iv) 12 mm. The values obtained are given in Table 10.2, where it is seen that for both the adhesive shear and plate direct stress peaks, there exists a similar trend whereby with the increase in fillet length, a subsequent reduction in the peak value occurs. However it can be seen that the values of the peaks near the end of the patch, for both distributions, do not change significantly for fillet lengths greater than about 2 mm. It is also interesting to note, as expected, there are stress peaks (relatively low in magnitude) in the adhesive and the plate near the end of the adhesive fillet. (these have not been tabulated). The adhesive shear stress distributions determined from the detailed 2D finite element analyses are in good agreement with the analytical predictions from the 1D stress analysis for the various no-fillet cases given in Section 10.2.

Next the effect of fillet heights (h_f), as shown in Figure 10.3(b), was investigated for multiple step patches, all with 2 mm length rectangular fillets. For the uniform step patch, adhesive fillet heights were varied, ranging from (i) adhesive level fillet height – here the layer of adhesive between the patch and the plate was extended to 2 mm outside the bonded patch, to (ii) every step fillet height – in this instance the height of the adhesive fillet was extended from the adhesive level right up to the very top of the stepped patch. The adhesive stress distributions for the first step and every step fillet height cases are plotted in Figure 10.7(a), where it can be seen that there is no significant reduction in the peak adhesive shear stress values for different fillet heights. With the plate direct stress distributions, see Figure 10.7(b), there are also two peaks in the vicinity of the end of the patch, one under and just past the end of the patch, and the second (smaller) at the end of the fillet. For the patch with non-uniform stepping an adhesive fillet was used that covered the entire height of

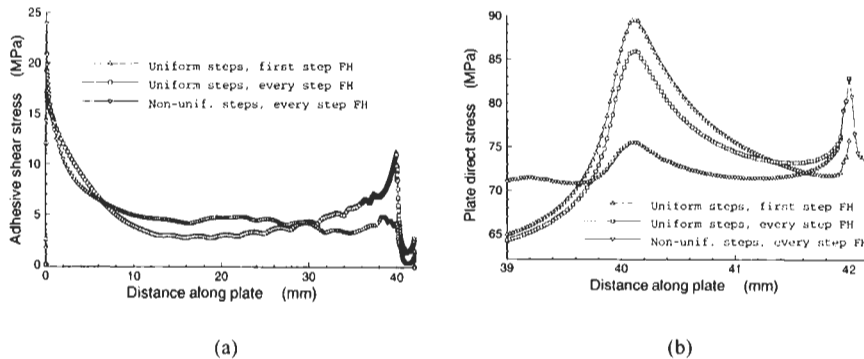


Fig. 10.7. Stress distributions for multiple step cases with rectangular fillets: (a) shear stresses in adhesive layer, (b) plate direct stresses on patched surface.

the patch. Figures 10.7(a) and 10.7(b) display the adhesive and plate stress results obtained. Here the adhesive shear stress distribution remains virtually the same as for the no-fillet case, except for a small reduction in the peak value at the end of the patch, and the occurrence of a second smaller peak at the end of the fillet. As for the other patch configurations, there are two peak locations for the plate direct stresses, one just beyond the end of the patch, and the other at the end of the fillet. However, this is the first case where the peak at the end of the fillet is greater than that at the end of the patch. Clearly tapering the fillet profile, and also extending the fillet length if needed could reduce the peak at the end of the fillet.

10.3.4. Discussion of results

A summary of all results for all cases is given in Table 10.2. The finite element results provide confirmation that the plate stress concentration is integrally related to the magnitude of the shear stress peak within the adhesive layer. Minimising the adhesive stress peak reduces the plate stress concentration. The type of stepping arrangement significantly influences the plate stress concentration. A non-uniform stepping combined with cross-ply yields a significantly greater reduction than a uniform stepping (with no cross-ply) configuration, as compared to the single step case. The addition of an adhesive fillet to the end of a patch, with or without stepping, can significantly reduce peak adhesive shear stresses, and plate stress concentrations.

10.4. Gradientless FE method for optimal through-thickness shaping

In the case of bonded repairs, the initial design has typically been based on simplified analytical formulations, and then finalised by undertaking standard finite element analyses. Often the design of the bonded repairs has been confined to rectangular patches of constant thickness with linear tapering around the patch

boundary. FE based optimisation methods offer the potential to determine improved designs, in an automated manner. In this section, results obtained using a simple yet efficient computational gradientless optimisation method are given. The aim of the method is to achieve constant (or near constant) stresses at region of stress concentration, by correctly moving boundary nodes. The method was initially developed for minimising stresses at stress concentrators in metallic components, however it is also well suited to minimising adhesive stresses in bonded reinforcements. First we consider the continuous shaping of a patch end, and then the continuous shaping of the adhesive layer for a bonded reinforcement [6,7].

10.4.1. Optimal adherend taper profile at the end of a bonded joint

Figure 10.8 shows the configuration under study, which is representative of a 2D idealisation of a bonded repair to a cracked plate. The inner adherend is a plate of 4 mm thickness, which is loaded by a remote stress of 100 MPa. An outer adherend (i.e. patch) is bonded to each side of this plate by an adhesive layer having a uniform thickness of 0.15 mm. Thereby, symmetry is retained with respect to the plate mid-plane ($y=0$), and hence plate bending is eliminated. The thickness of each patch is denoted t_o and is 2 mm. As is commonly advocated, an initial linear taper with a 1:10 slope was used at the ends of each patch to reduce the magnitude of the adhesive stress concentration at the end of the patch. The material properties for both the plate and the patch were taken as Young's modulus $E=70$ GPa, and Poisson's ratio $\nu=0.32$. For the adhesive, a Young's Modulus of 840 MPa and a Poisson's Ratio of 0.3 was used. In this optimisation the aim is to alter the shape of the tapered region of the patch, so as to achieve as closely as possible a constant adhesive stress distribution. The procedure used was to reduce the patch thickness (at a given x co-ordinate) where the adhesive stresses were high, while increasing patch thickness where adhesive stresses were low. Here an iterative procedure is used, where for each iteration, each node on the free boundary of the patch was moved by an amount dependent on its stress value in relation to a reference (i.e.

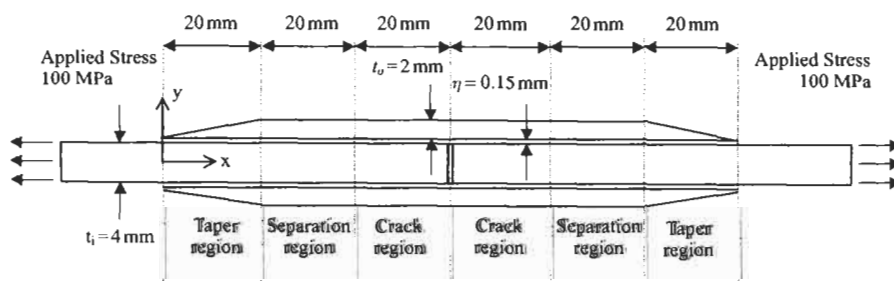


Fig. 10.8. Dimensions and loading arrangement for uniaxially loaded double lap-joint, with initial linear taper profile of the outer adherend.

threshold) stress. The amount to move each node is then given by

$$d_i = -\left(\frac{\tau_i - \tau_{th}}{\tau_{th}}\right)rs, \quad (10.19)$$

where positive d_i indicates material addition to the patch outer boundary, τ_i is the shear stress at the adhesive mid-plane node i , τ_{th} is a threshold shear stress at the adhesive mid-plane, r is an arbitrary characteristic dimension and s is an arbitrary step size scaling factor. It is clearly evident that movements are less for locations having stresses closest in value to the threshold stress.

The finite element mesh of the initial geometry, making use of quarter symmetry, is shown in Figure 10.9(a). A very dense mesh was used near the end of the patch to accurately model the high stress gradients in this region. The optimisation procedure was applied with the parameters $r=2$ mm and $s=0.1$. One further practical constraint was introduced such that the patch thickness could not be less than 0.01 mm, corresponding to a minimum thickness that can be reliably machined, and not greater than 2 mm (i.e. original thickness). The solution geometry obtained after 89 iterations is shown in Figure 10.9(b). As a comparison, a 1D theoretical analysis given in [17] was found to give the profile shown in Figure 10.9(c), where the thickness in the tapered region as a function of position is given by

$$t = \frac{t_o x}{2l - x}, \quad (10.20)$$

where x is the distance from the start of the tapered region, t_o is the maximum thickness of the patch, and l is the length of the tapered region. In Figure 10.10 the

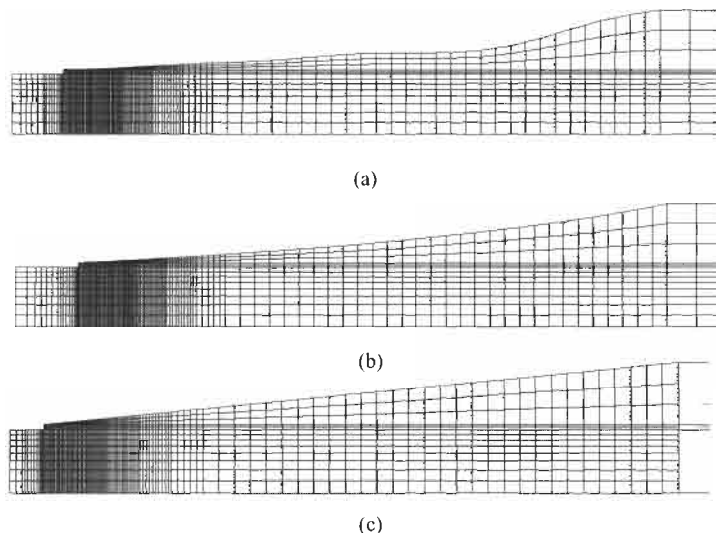


Fig. 10.9. Comparison of various taper profiles for bonded double lap joint. (a) linear taper, (b) numerically optimised taper, and (c) analytically optimised taper.

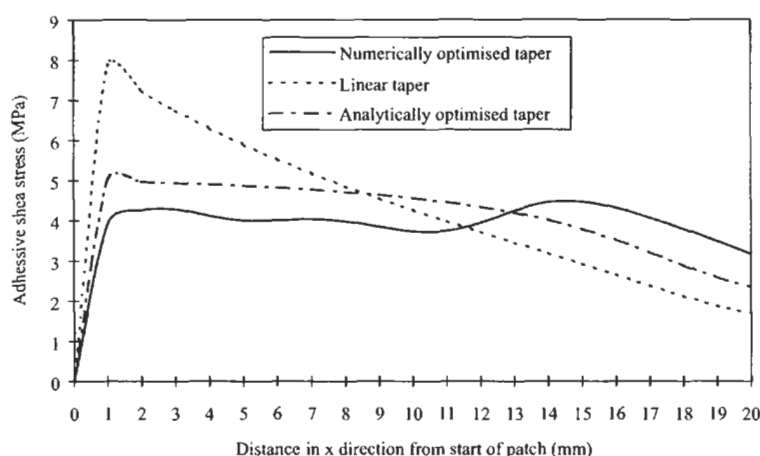


Fig. 10.10. Adhesive shear stress distributions for bonded double lap-joint with a unidirectional applied stress for various taper profiles (for taper region only).

adhesive shear stresses are plotted for the following three taper profiles: (i) linear taper, (ii) numerically optimised taper, and (iii) analytically optimised taper [17]. It can be seen that the process provided a good result in reducing the initial peak shear stress of 8.2 MPa by about 30%, and rendering the shear stress distribution relatively uniform. The 1D analysis gives almost as large a reduction in the peak adhesive stress. It must be noted that the advantage of the finite element method is that key parameters such as loading type and material properties are easily changed.

10.5. Sensitivity FE method for optimal joint through-thickness shaping

In this section an automated sensitivity-based shape optimisation procedure is presented for the optimal design of free-form bonded reinforcements, with the aim of achieving reduced adhesive stresses [19]. The approach is demonstrated through application to a number of single and double sided configurations. Particular features of the present approach include: (i) free form shapes, where the outer adherend and/or the adhesive thicknesses are allowed to be non-uniform, and are optimised, (ii) a “least squares” objective function is used to obtain a true optimal for the specified constraints, and (iii) multiple shape-basis vectors from the analysis of an auxiliary model are used to specify allowable shape changes. In this investigation, the finite element meshes consisted of mostly four noded elements in preference to eight noded elements. This was done since the four noded elements are more convenient to use with the NASTRAN two noded beam elements, which were an important part of the modelling for optimisation.

10.5.1 Initial geometry, materials and loading arrangement

For all analyses the initial configuration under study was a typical bonded double lap joint as defined in Figure 10.8. The geometry is also representative of the 2D idealisation of a bonded repair to a cracked plate [1,12], as discussed in the previous sections. For all cases, the inner adherends have a thickness of 4 mm and are subjected to a remote uniaxial stress of 100 MPa. The outer adherends are bonded to the inner adherends by an adhesive layer having a nominal thickness of $\eta = 0.15$ mm. The outer adherends are both 120 mm in length and have a thickness of 2 mm if aluminium, or 0.67 mm if boron/epoxy. As is commonly advocated, an initial linear taper with a 1:10 slope was used at the ends of the outer adherends to reduce the magnitude of the adhesive stress concentration at the end of the patches. As indicated on Figure 10.8, the joint has been divided into three load transfer regions on each side of the symmetry line $x = 60$ mm, having an arbitrary length of 20 mm each. In the taper and joint regions most of the load transfer takes place between the patches and the plate, and this is where the shape changes were undertaken. It is common practice to have a region in between where there is no load transfer, termed here as the separation region. This region is essentially a safety buffer zone (i.e. potential load carrying region), should there be adhesive debonding in the nominal load transfer regions.

For all analyses the following material properties were used as appropriate: (i) for aluminium, isotropic material behaviour was assumed with Young's Modulus, $E = 70000$ MPa, and Poisson's Ratio, $\nu = 0.35$, (ii) the isotropic epoxy adhesive had Young's Modulus $E = 840$ MPa, and Poisson's Ratio, $\nu = 0.3$, and (iii) the unidirectional boron/epoxy adherend was taken as 2D orthotropic with $E_{11} = 210000$ MPa, $E_{22} = 25400$ MPa, $\nu_{12} = 0.18$, and $G_{12} = 7200$ MPa where the subscript 1 refers to the direction of the fibres and 2 is the through thickness direction. Here the 1 and 2 directions are aligned with the x and y axes respectively.

10.5.2. Optimisation method

Shape optimisation was achieved using the general sensitivity-based optimisation technique available in the MSC/NASTRAN code [28]. In broad terms, the approach involves changing the position of nodes defining a boundary shape, based on the computation of rates of change of nodal stresses with respect to shape changes. Hence the general problem definition for shape optimisation can be stated as

minimise/maximise : objective function
 subject to : constraint functions
 where : design variables

The software allows for very wide scope as to how to define the quantities above, which is left to the analyst to determine. The objective function used in this work has been termed the least squares objective function in prior AVD work. It seeks to

minimise the deviations from the average von Mises adhesive stress value in both the joint region and the taper region, and is given in equation as

$$\text{minimise : } f_{\text{obj}} = \sum_{i=n}^{i=1} (\sigma_{\text{avt}} - \sigma_i)^2 + \sum_{j=k}^{j=1} (\sigma_{\text{avj}} - \sigma_j)^2, \quad (10.21)$$

where i and j are the number of an individual adhesive element in the taper and joint regions respectively, n and k are the total number of adhesive elements in the taper and joint regions respectively, and σ_{avt} and σ_{avj} are the average adhesive element stresses in the taper and joint region respectively. The adhesive was modelled using three rows of elements and the stress values are taken at the centroids of centre row elements. This objective function takes advantage of the constant stress characteristic of optimal geometries, and uses responses in both load transfer regions simultaneously, as indicated by the first and second summations in the equation above. This function appears to achieve better convergence than using the peak stress as the quantity to be minimised, avoiding local minima. It is interesting to note that for typical sectional stress values across the adhesive thickness and away from corner singularities, the variation is less than 10% with the centre row having the highest values. This applies for the thick adhesive regions of the solution shapes as well as for the initial configurations. A key feature of the optimisation process is the way that shape changes are defined as design variables. Here, a set of displacement fields was generated by using an auxiliary model with a set of dummy loads applied normal to the movable boundary. This auxiliary model must have the same geometry and node numbers as the primary model however, the material and element properties can be varied so as to give suitable shapes. These fields are called basis shape vectors in NASTRAN and can be considered as a set of vectors \mathbf{T}_j as follows:

$$\mathbf{T}_j = \begin{bmatrix} \Delta G_{1x}, \Delta G_{1y} \\ \dots\dots\dots \\ \Delta G_{Kx}, \Delta G_{Ky} \end{bmatrix}, \quad (10.22)$$

where j is the basis shape vector number, ΔG_x and ΔG_y are the nodal displacement in the x and y direction respectively, and K is the total number of nodes (same in both models). Typically, for the analysis cases, 25 load-cases were used to generate 25 displacement fields and consequently 25 design variables were defined in the optimisation data file. These load application points, along the movable part of the boundary or interface, are shown in Figure 10.11. While the auxiliary model provides absolute displacements which are dependent on the size of the applied dummy load, the whole displacement field is scaled up or down as required by the optimisation process. At each iteration $i+1$, the new shape comes from taking the nodal positions at iteration i , and adding the displacements from all of the basis

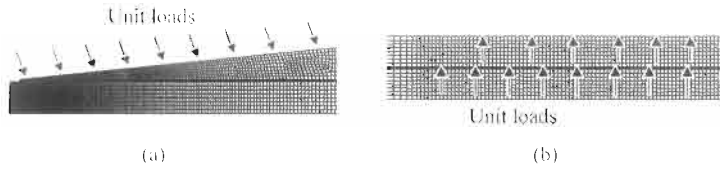


Fig. 10.11. Finite element mesh and loading arrangement for generating basis shape vectors in auxiliary model: (a) taper region, and (b) crack/joint region.

shape vectors multiplied by their scaling factors, as given by Eq. (10.23) below:

$$\begin{aligned}
 \begin{bmatrix} G_{1x}^{i+1}, G_{1y}^{i+1} \\ \dots \\ G_{Kx}^{i+1}, G_{Ky}^{i+1} \end{bmatrix} &= \begin{bmatrix} G_{1x}^i, G_{1y}^i \\ \dots \\ G_{Kx}^i, G_{Ky}^i \end{bmatrix} + \sum_{j=1}^J X_j^* \mathbf{T}_j, \quad \text{where} \\
 \begin{bmatrix} X_1^{i+1} \\ \dots \\ X_J^{i+1} \end{bmatrix} &= g \left(\begin{bmatrix} \delta f / \delta X_1^i \\ \dots \\ \delta f / \delta X_J^i \end{bmatrix} \right)
 \end{aligned} \tag{10.23}$$

Here G_x and G_y are the x and y coordinates respectively of nodes $k=1$ to K (all nodes in model), i is the iteration number, j is the design variable number in the range $j=1$ to J , X is a design variable (i.e. multiplier applied to \mathbf{T}), $\delta f / \delta X$ is the sensitivity of the objective function with respect to a design variable, and g is a function to represent the search algorithm described in [28].

The scaling factors X_j , (one per basis shape) are the unknown design variables to be found by the optimisation process. As it is only the nodal displacements that are used from the auxiliary model, the elements and their properties can be selected so as to give a smooth deformation over a suitable region. In the cases presented circular beam elements have been added along the boundaries (using the existing nodes only). The stiffness of the beam elements in relation to the neighbouring 2D elements was chosen to give a suitable shape and region of deflection. Hence circular beam elements of 25 mm radius were used in conjunction with plate elements of 0.5 mm thickness, noting that both had the same elastic modulus. The beam elements were typically 0.25 mm in length and the dummy load points were typically 3 mm apart. It should be noted that, three and four noded 2D elements in the structural and auxiliary model were not up-graded to six and eight noded elements, as three noded beam elements were not available. Clearly, an important requirement of the numerical approach is the appropriate choice of the basis shapes and particular care must be taken. However, if a poor choice has been made, it would be evident in the final boundary stress distribution (i.e. non-uniformity) and remedial action could be taken. Certain constraints are dependent on the particular configuration case and are discussed in the following sections. A constraint on minimum adhesive thickness of 0.15 mm was consistent across all analyses.

10.5.3. Analysis for symmetric crack repair with aluminium patch

Here the aim is to optimise the repair shape to minimise peak von Mises adhesive stresses, such that the repair effectiveness was unchanged as compared to a nominal geometry. For the initial configuration, the maximum thickness of the patch has been selected to be equivalent to that of the plate. The finite element mesh used in the quarter symmetric analysis is shown in Figure 10.12(a). A very dense mesh refinement was used to obtain accurate stress results, as well as represent small geometric changes in the subsequent optimisation analyses. The stresses obtained from this analysis are presented in Figure 10.13, and are as expected. For the taper region they agree with those presented in [6,7] where the finite element code PAFEC was used. For the joint region they also agree well with other published FE results. For example the predicted adhesive stress peak is 25.8 MPa as compared to 24.0 MPa given in reference [26]. More importantly, for the present context, the opening displacement of the centreline node, half way through the plate thickness in the x direction was 0.0086 mm (equivalent to the total opening of 0.0172 mm in the full configuration). For the idealisation of 2D crack patching, the stress

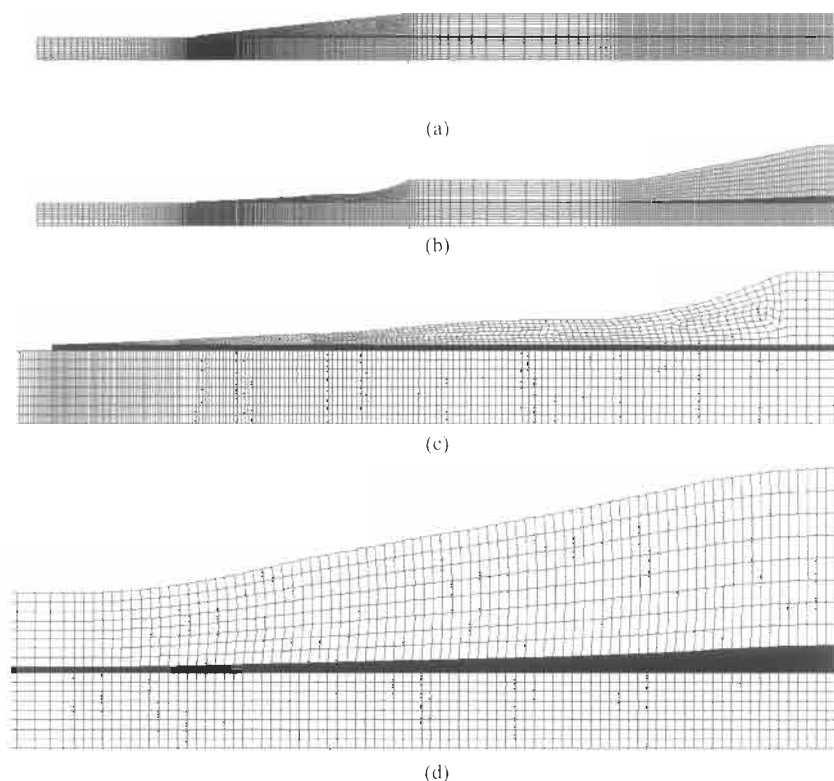


Fig. 10.12. Optimal shape for symmetric crack repair with aluminium patches: (a) initial arrangement (b) optimised arrangement, (c) detail in taper region, and (d) detail in joint/crack region.

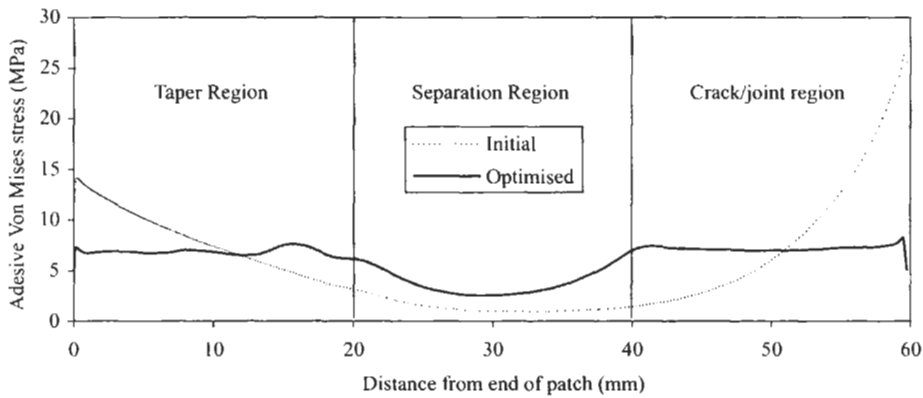


Fig. 10.13. Von Mises stress distribution in adhesive for symmetric crack repair with aluminium patches.

intensity factor in the inner adherend is directly related to the opening displacement by the following equation from [1]

$$K_T = \sqrt{\frac{1}{2} E_p \phi \sigma \Delta} , \quad (10.24)$$

where K_T is an upper bound stress intensity factor for a long crack under a patch, E_p is the elastic modulus of patch, ϕ is the stress reduction in the uncracked plate due to the patch (factor less than 1) at the prospective crack location, σ is the remote applied stress, and Δ is the crack opening due to the remote applied stress.

For the optimisation analyses all 25 design variables were active (but restrained from going negative). For the taper region the patch was allowed to vary in thickness while the adhesive thickness was kept constant at 0.15 mm. This choice was made to allow direct comparison with some existing published solutions. In the crack region, both the patch and the adhesive thickness were allowed to vary. A constraint on crack opening was applied at the centreline node, half way through the plate thickness, to maintain the same repair effectiveness as the nominal repair. Hence the constraint applied was $|\Delta/2| < 0.0086$ mm, where: $|\Delta/2|$ is the displacement in the x direction at the node described above. The overall solution shape obtained after seven iterations for the total geometry is shown in Figure 10.12(b). Figures 10.12(c) and 10.12(d) show more detail for the taper and crack/joint regions respectively. The resultant von Mises adhesive stress results are given in Figure 10.13. For the taper region the shape obtained is very similar to the 2D FE solutions given in other investigations [6,18]. Here there is a rapid reduction in patch thickness at the start of the taper leading to a very fine tip at the end of the patch. In the taper region the process has arrived at a good result, in reducing the initial peak stress of 14.4 MPa by about 50%, and achieving a relatively uniform stress distribution. The slight deviations from complete uniformity of these adhesive stresses are mainly due to the fact that there are low sensitivity values between the patch shape and the adhesive stresses as the

Table 10.3

Adhesive shear peel and Von Mises stress components for symmetric loading case with aluminium alloy patches.

Shape and location	Peel stress (MPa)	Shear stress (MPa)	Von Mises stress (MPa)
Initial shape, taper region ($x = 0.1$ mm)	2.5	7.2	12.7
Initial shape, crack region ($x = 59.5$ mm)	- 3.6	- 14.4	25.1
Optimised shape, taper region ($x = 0.1$ mm)	1.0	3.7	6.5
Optimised shape, crack region ($x = 59.5$ mm)	- 3.6	4.1	7.8

optimal solution is approached. Obviously, if the taper region was increased in length the adhesive stresses would have been further reduced as the same load transfer would take place over a longer region.

The solution stress plot given in Figure 10.13 also shows a good result in the crack/joint region with a near constant von Mises stress in the adhesive. A very large stress reduction of about 70% is evident in this linear elastic analysis (in practice, for this load level, the stress peak for the initial shape would be smaller due to local yielding of the adhesive). In Table 10.3 results for von Mises, shear and peel stresses are given near the ends of the two load transfer regions respectively. These indicate that the reduction in von Mises stress come about mainly by reduction in the shear component. Both the adhesive thickness and the patch thickness have increased to meet the optimisation objective and constraint requirements. Here the load transfer through the adhesive has been diverted away from the joint symmetry line at $x = 60$ mm, to be distributed more evenly over the 20 mm length comprising the crack/joint region. An optimisation analysis for this case with boron/epoxy patches has also been undertaken [19], with very similar results, except the patch thickness is about one-third as expected.

10.5.4. Analysis for non-symmetric crack repair with boron/epoxy patch

In this case the patch is bonded to one side of the plate only. Application of the remote stress will cause secondary bending, and hence a more severe adhesive stress distribution will result (particularly for peel). Again the aim is to optimise the repair shape to minimise peak adhesive stress such that the repair effectiveness is unchanged as compared to the nominal geometry.

For the analysis of the initial geometry the finite element mesh is virtually the same as that given for the preceding case except that the through-thickness symmetry restraint, along the line $y = 0$ has been removed. Hence there is no support to eliminate the out-of-plane bending induced by the presence of the single patch. Also, at the stress application region, out-of-plane rotation has been restrained to represent a plate which is globally flat but able to deflect near the crack/joint region. In this analysis, the patch is now of thickness 0.67 mm. The von

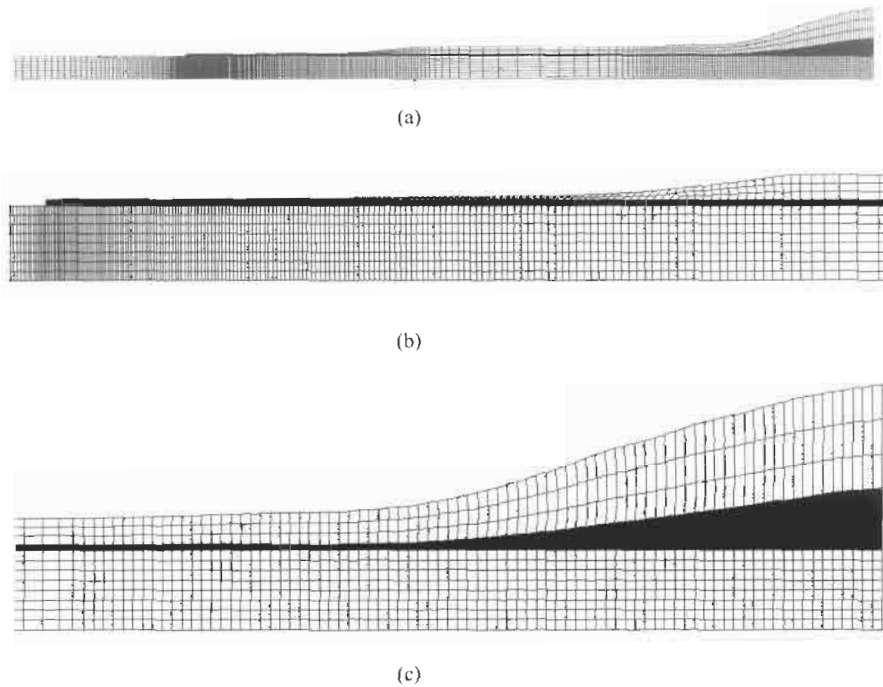


Fig. 10.14. Optimal shape for non-symmetric crack repair with a boron/epoxy patch: (a) general arrangement, (b) detail in taper region, and (c) detail in joint/crack region.

Mises stresses obtained from this analysis are presented in Figure 10.15. It can be seen that in the taper region the stresses are significantly higher as compared to the previous case. For example the peak here is 30.0 MPa as compared to 14.4 MPa previously. Also in the joint region the adhesive stresses are higher, with a peak of

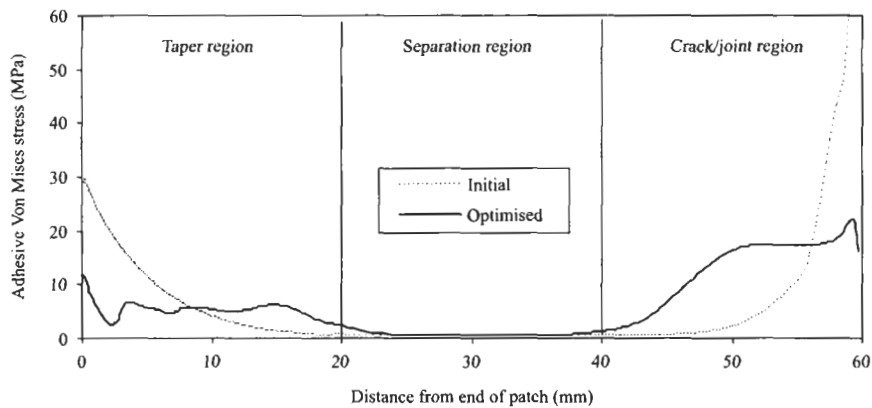


Fig. 10.15. Von Mises stress distribution in adhesive for non-symmetric crack repair with boron/epoxy patch.

64.0 MPa as compared to 26.2 MPa previously. The opening displacement of the centreline node half way through the plate thickness in the x direction was 0.096 mm, as compared to 0.0086 mm previously.

For the optimisation analysis the same solution procedure was used as before except that basis shapes were modified to allow non-zero movable boundary slopes at the centreline. This was necessary because of the very large initial stress concentration, however it produces a discontinuous slope over the crack. The solution shape for the total geometry obtained after seven iterations is shown in Figure 10.14(a), while the von Mises stresses are given in Figure 10.15. In the taper region the optimal patch profile is similar to that of the previous section (scaled by 1/3), although the adhesive stress range is 2.6 to 11.9 MPa, which is marginally higher than that of the previous section due to the effects of bending. In the joint region the optimisation has produced a radical change of shape due to the very high initial adhesive stresses. The adhesive and patch thicknesses have increased by a factor of three. For the joint region the optimisation process has provided stress reductions, which are larger than for the previous example. Here the stress reduction is approximately 78%. The results given in Table 10.4 highlight the extent to which the presence of bending has changed the adhesive stresses in both load transfer regions. All values are higher and while the shear stress component is still dominant for the initial shape in the taper region, the peel component is larger in the crack region. The optimisation process has reduced both components in both regions. In this case, the large variation in adhesive stress in the taper region is due to this solution having an excessively long fine taper with thickness less than 0.01 mm for much of its length. It is clear that if desired, with an increased number of basis shapes, a more uniform stress solution could be determined. In practice it is expected that the effective stiffness of the long fine taper region will need to be achieved by using a lower modulus first ply, possibly a cross ply of boron/epoxy.

Table 10.4
Adhesive shear, peel and Von Mises stress components for non-symmetric loading case with orthotropic boron patches.

Shape and location	Peel stress (MPa)	Shear stress (MPa)	Von Mises stress (MPa)
Initial shape, taper region ($x = 0.1$ mm)	3.9	15.3	26.8
Initial shape, crack region ($x = 59.5$ mm)	61.1	42.6	90.1
Optimised shape, taper region ($x = 0.1$ mm)	0.9	7.5	14.5
Optimised shape, crack region ($x = 59.5$ mm)	17.7	5.0	20.0

10.6. Optimal through-thickness shaping for F/A-18 bulkhead reinforcement

In this section the automated sensitivity-based shape optimisation for the bonded reinforcements for a realistic practical problem is presented. The practical problem under consideration is a major structural component of an F/A-18 aircraft, namely the F/A-18 470 Bulkhead [8]. Particular features of the present approach include: (i) free form shapes, (ii) a “least squares” objective function is used to obtain a true optimal for the specified constraints (i.e. constant stresses at critical region), (iii) multiple shape-basis vectors from the analysis of an auxiliary model are used to specify allowable shape changes, and (iv) both the adhesive thickness and the reinforcement thickness are allowed to be non-uniform and are optimised. Results for two distinct configurations for an optimal reinforcement for an optimal reinforcement are given, depending on the selected adhesive stress to be minimised (i.e. shear or peel). Both reinforcement configurations are constrained to be equivalent in effectiveness (stress reduction in the metal) to a nominal constant thickness reinforcement.

10.6.1. Initial geometry, materials and loading arrangement

The 2D finite element mesh shown in Figure 10.16 indicates the in-plane geometry of the F/A-18 470 Bulkhead. The bulkhead is an aluminium alloy frame made up of flanges and webs of thicknesses ranging from 6–81 mm. It is a highly loaded component since it supports the attachment of the wings. The initial MSC/NASTRAN model is semi-symmetric about the y-axis (i.e. vertical centreline) and consists of three noded and four noded plane stress elements. The bulkhead is aluminium alloy and isotropic material behaviour was assumed with Young's modulus $E = 72000$ MPa, and Poisson's ratio $\nu = 0.35$. Also, the isotropic epoxy adhesive had Young's Modulus $E = 840$ MPa and Poisson's ratio $\nu = 0.3$, while the unidirectional boron/epoxy reinforcement was taken as 2D orthotropic with $E_{11} = 207000$ MPa, $E_{22} = 25400$ MPa, $\nu_{12} = 0.18$ and $G_{12} = 7200$ MPa where the

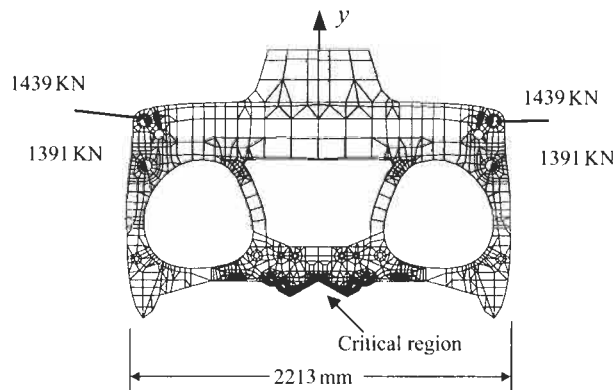


Fig. 10.16. F/A-18 470 bulkhead finite element mesh and dominant loading.

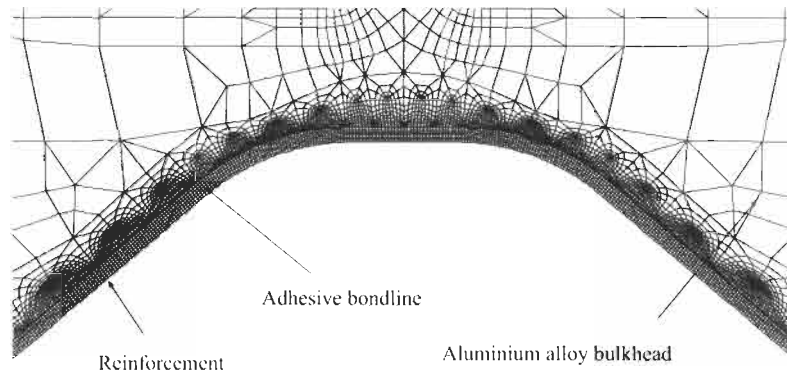


Fig. 10.17. FE mesh for analysis of standard rework with nominal 18 layer reinforcement.

subscript 1 refers to the direction of the fibres and 2 and 3 are the transverse fibre directions. All solutions are for the design ultimate load case. For this example problem, the local curved region has been re-profiled locally to a shape termed ECP [29]. This shape provides a reduction in the local bulkhead stresses of about 15%, before reinforcement. Before considering an optimised reinforcement, a standard finite element analysis was undertaken with a nominal constant thickness 18-layer reinforcement. This has a uniform thickness of 2.34 mm (except at its ends remote from the region of interest) and a uniform thin adhesive layer of 0.13 mm thickness is used. The geometry is shown in Figure 10.17 for the standard reinforcement case, which provides a reduction in the peak bulkhead boundary stress of 25% against the un-reinforced case.

10.6.2. Parameters for reinforcement optimisation analyses

For the optimisation analyses, the aim is to achieve the same reinforcement effectiveness as before (via a constraint), with a reduction in the peak adhesive stresses. For these runs there are consequently three boundaries under consideration with the following features (i) the interface between the bulkhead and the adhesive is fixed in location and is where the effectiveness of the reinforcement is determined by the bulkhead nodal stress values, (ii) the interface between the adhesive and the reinforcement is a boundary that has been made variable in position and has ultimately been located by the optimisation process, and (iii) the outer free boundary of the reinforcement has also been made variable and has been located by the optimisation process. The boundary mesh density (as compared to that described in Section 10.6.1) has again been increased in the region of interest, to better model the adhesive using lower aspect ratio elements. Three rows of elements are used across the initial adhesive thickness of 0.13 mm. A similar optimisation strategy as was used in Section 10.5 is implemented and hence the

objective function used is

$$f = \sum_{i=n}^{i-1} (\sigma_i - \sigma_{av})^2, \quad (10.25)$$

where: σ_i is the stress at element i (i.e. structural response), σ_{av} is the arithmetic average of element stress values over a selected bond line segment (i.e. reference stress), and n is the number of elements included in objective function evaluation. Here the stresses used in the above equation are the mid-layer element centroid stresses, and these are also the ones presented in the subsequent figures. Reducing the number of stress points in the objective function by including only every fifth element enhanced numerical performance. The regions of bond line that were included in the analyses for the two distinct cases are given in Figure 10.18. Outside this region the bulkhead boundary stresses and adhesive load transfer were negligible. The peak stress on the bulkhead boundary has been constrained to the value of 380 MPa, which was given by standard reinforcement. Constraint bounds were applied to design variables to prevent the adhesive reducing in thickness. Also, for the minimum shear stress solution the peel stress was constrained from rising above its peak value for the nominal reinforcement. Similarly for the minimum peel stress solution the adhesive shear stress was constrained from rising above its peak value for the nominal reinforcement. Figure 10.18 also shows the loading arrangement in the auxiliary model for generating the 23 basis shapes. It should be noted that the auxiliary model loads are applied to the interface between the adhesive and the reinforcement and the free edge of the reinforcement. In the

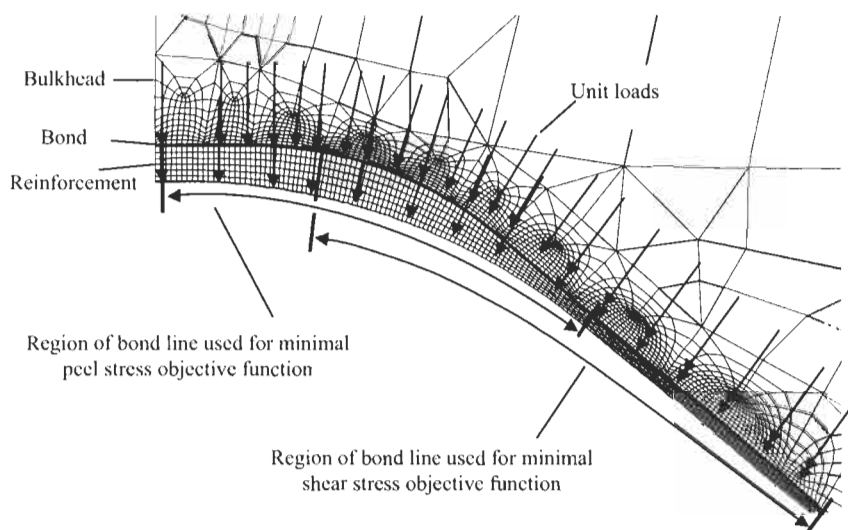


Fig. 10.18. Finite element mesh and loading arrangement for generating basis shapes, also showing bond line regions for objective function calculation.

auxiliary model, beam elements of 25 mm diameter were applied along both edges of the reinforcement to smooth the deflections caused by the point loads. All materials in the auxiliary model were changed to aluminium alloy and all 2D elements were reduced in thickness to 0.5 mm.

10.6.3. Stress results for optimal reinforcement designs

The resulting shape and the adhesive stresses for the minimum shear stress solution are shown in Figure 10.19. The solution was obtained after seven iterations. It can be seen that the shear stress has been made more uniform by the increase in adhesive thickness at the high stress region near the curved part of the boundary. The initial stresses plotted in Figure 10.19 are those of the nominal 18-layer reinforcement and show that the 20% reduction in shear stress has been achieved without an increase in adhesive peel stress. It can be seen that the adhesive has been made thicker in the regions of high initial shear stress near the curved parts of the boundary. The resulting shape and adhesive stresses for the minimum peel stress solution are shown in Figure 10.20. The main difference from the previous result is that the increase in thickness occurs near the centreline region where the initial peel stresses were highest. The size of the reduction in peel stress is brought about by the reinforcement bridging the concave region and comes without increase in shear stress. A feature of this solution is that the peaks in shear and peel are now at different locations, where the high shear stresses have been moved outboard (in the x direction). This is advantageous since experience with bonded joints indicates they are more prone to failure when both peel and shear are high at the same location.

10.6.4. Discussion

It is important to note that with both these solutions the constraint on reinforcement effectiveness has been met, that is, the adhesive stress reductions have not come at the expense of an increase in hoop stress in the parent material of the bulkhead. The capability of the optimisation process to move both the adhesive and patch boundaries simultaneously to arrive at the desired solution is also significant.

10.7. Optimisation for F/A-18 aileron hinge reinforcement

This section presents the numerical stress analysis undertaken to design an appropriate reinforcement for the aft strut of the aileron hinge which has experienced in-service cracking, (further background information is given in [11]). The fundamental approach followed is to first remove existing cracks with a suitable precise rework shape before reinforcement. This precise rework shape is determined using structural optimisation procedures, to minimise the peak stresses for an un-reinforced hinge. The optimisation of the reworking is essential from an

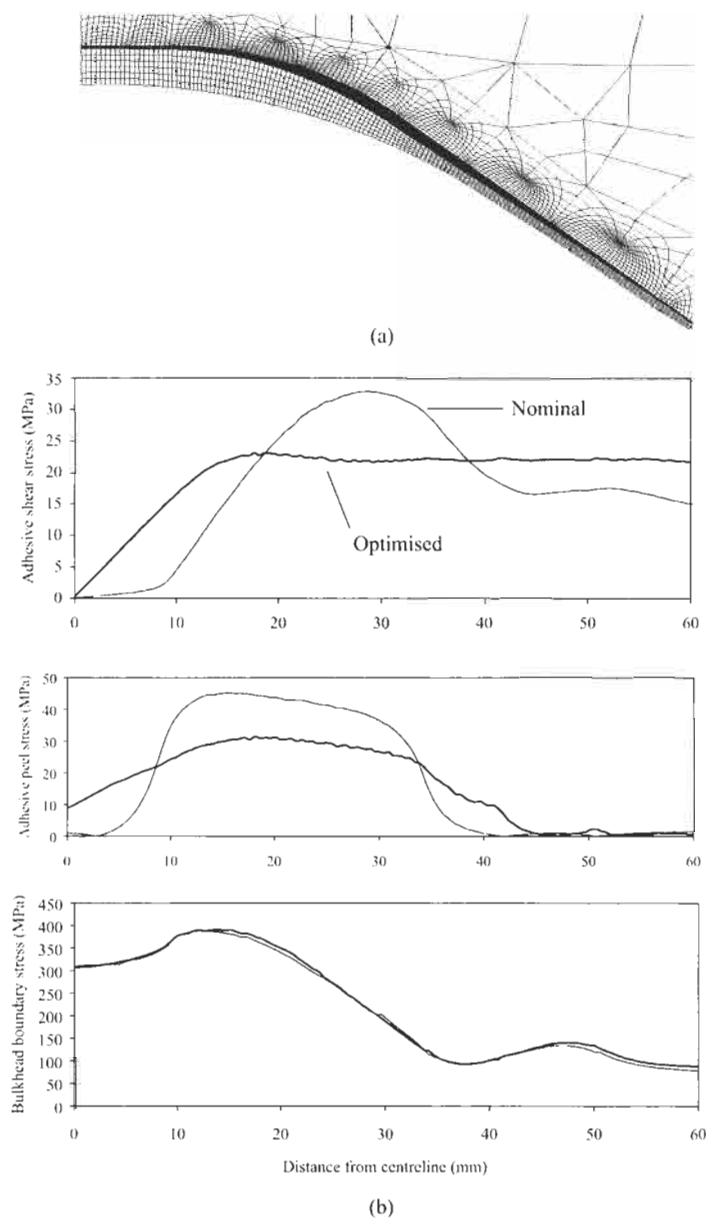


Fig. 10.19. Results for optimal 470 bulkhead reinforcement with minimal adhesive shear stress: (a) shape solution, (b) stress solution.

airworthiness perspective, to restore the boundary stresses to about the same peak values as for the uncracked, un-worked hinge. The subsequent reinforcement stepping is then designed using an iterative approach to minimise peak adhesive

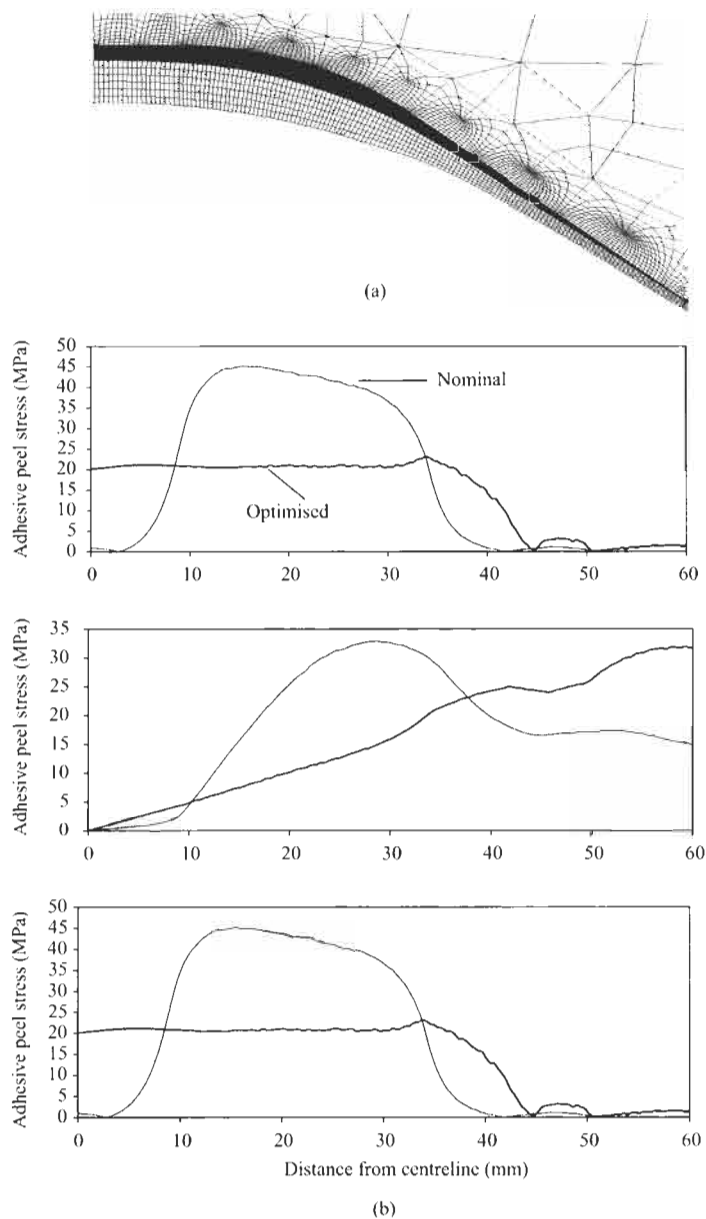


Fig. 10.20. Results for optimal 470 bulkhead reinforcement with minimal adhesive peel stress: (a) shape solution, (b) stress solution.

stresses. Since in practice various crack depths will exist before possible enhancement, it is proposed here to explain in detail the limiting case where the rework depth is 2 mm at the crack location.

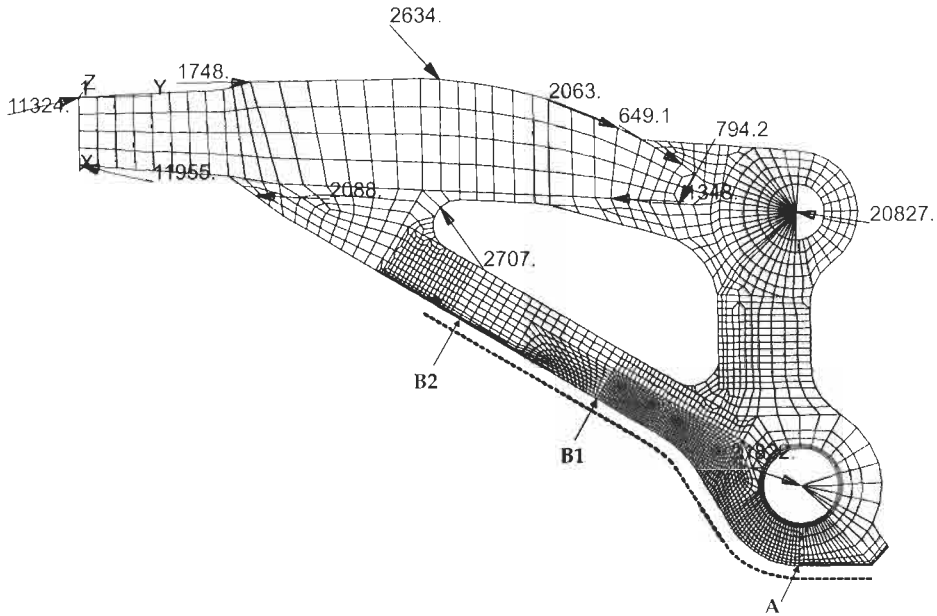


Fig. 10.21. Finite element mesh and loading (KN) for the nominal un-worked hinge analysis, where the dotted line represents the prospective patch location.

10.7.1. Initial geometry, materials and loading arrangement

The initial plane stress finite element mesh, in the MSC.NASTRAN, code is shown in Figure 10.21 with dominant loads corresponding to the WO 39 case. For all analyses isotropic material behaviour under ambient conditions was assumed for the aluminium hinge, the steel bearing, and the FM73 adhesive layer. Conversely for the elements comprising the boron/epoxy reinforcement the material was taken as orthotropic. The material properties were as follows; (i) for the aluminium hinge the Young's modulus, E , was taken as 70.38 GPa, Poisson's ratio, ν , was taken as 0.33; (ii) for the steel bearing and pin in the lower lug, Young's moduli were taken as $E=213.90$ GPa, and Poisson's ratio was $\nu=0.30$; (iii) for FM73 adhesive, $E=1.43$ GPa, $\nu=0.35$; (iv) for the boron, $E_{11}=208.95$ GPa, $E_{22}=E_{33}=19.18$ GPa, $\nu_{12}=0.21$, $\nu_{23}=0.3$ and $\nu_{31}=0.02$ where 1 refers to the direction of the fibres and 2 and 3 are the transverse fibre directions.

10.7.2. Shape optimisation before reinforcement

Rework shape optimisation (with or without subsequent reinforcement) to minimise notch stresses in metallic airframe components has been a focus of recent work in AED [6–11]. In the present example the design sensitivity approach using MSC.NASTRAN code, as discussed in Sections 10.5 and 10.6, is used. In the

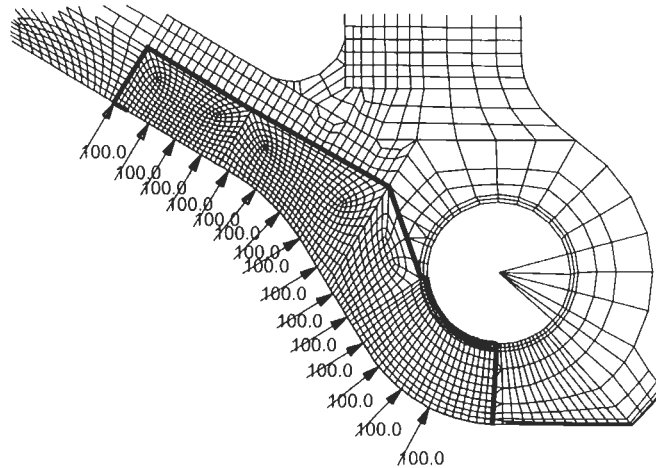


Fig. 10.22. Typical auxiliary model used in the shape optimisation procedure for F/A-18 aileron hinge, showing point loads (KN) for generating shape basis vectors with fully restrained nodes indicated by dark line.

present case the aim is to remove material from the prospective crack location while still achieving a minimised notch stress. Hence the objective function used is

$$f = \frac{\sum (\sigma_i - \sigma_{av})^2}{k^2}, \quad (10.26)$$

where σ_i are the nodal hoop stress along the along boundary to be moved, σ_{av} is the average nodal hoop stress around boundary, and k is number of boundary nodes to be moved. As discussed in the preceding sections, meeting this objective effectively means that a more constant hoop stress is achieved along a boundary region being optimised, which corresponds to minimising the peak stress in that region. In this work the objective function convergence was defined when two consecutive optimisation iterations produced the same objective function result within a 1% tolerance. For all analyses the constraints employed are nodal movement constraints which effectively limit allowable boundary shape changes per iteration (i.e. to a maximum rework of about 2mm). A typical auxiliary model used in the shape optimisation procedure, for generating the shape basis vectors, is shown in Figure 10.22.

The resultant finite element mesh shape obtained after seven iterations of the rework optimisation is shown in Figure 10.23(a) for the 2mm rework. The shape obtained (termed the “O” profile) is compared to the initial boundary in Figure 10.23(b) while the corresponding stresses are given in Figure 10.23(c). It can be seen that the stresses for the rework have been rendered constant in the critical region, and are essentially the same magnitude as those for the nominal geometry, even though 2mm of material depth has been removed. If a typical non-optimal rework shape had been used instead, the peak strut stresses could be

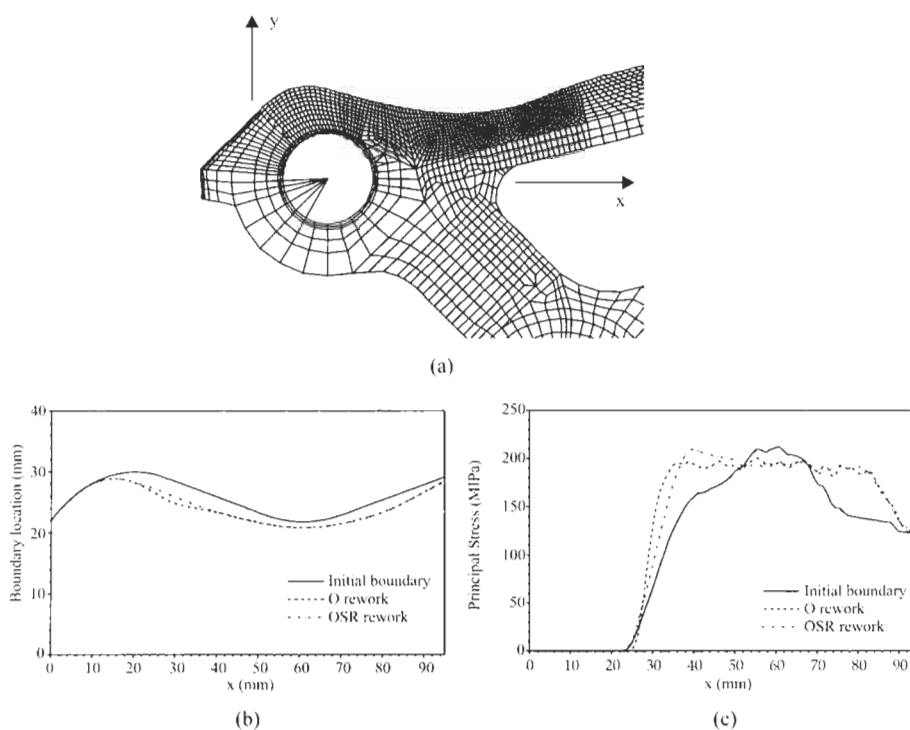


Fig. 10.23. Typical results for optimal reworking. (a) local detail of finite element geometry after reworking to 2 mm depth, (b) comparison of rework shapes for 1 mm rework depth, and (c) comparison of hoop stresses along strut edge for 1 mm rework depth.

expected to be about 20% higher. If a reinforcement is applied directly to the optimised rework, there is a local peak stress in the adhesive, at the location near $x = 40$ mm (the peak is due to the local change in curvature of the optimal profile shape at $x = 40$ mm) which would be greater than the adhesive yield stress, at DLL. Hence this rework profile can be further developed to meet the needs of minimal peel and shear stress in the adhesive, in addition to minimising the peak stress in the strut. To achieve this, the slight curvature discontinuity in the O rework profile (near $x = 38$ mm) is manually smoothed, which then resolves this problem regarding this adhesive stress peak. Of course as expected, the trade off due to this profile change is a 9% increase in the strut stresses if the patch were to be removed. This effect is clearly shown in Figure 10.23(c) by comparing strut stresses for the “O” and “OSR” profiles.

10.7.3. Iterative reinforcement design

As discussed in Section 10.1, for the design of a typical bonded reinforcement to a component, there are two particular regions of concern for the adhesive layer. These

are respectively; (i) near the end of the reinforcement where shear stresses can be very high, and (ii) locations under the reinforcement where it is desired to reduce the stress concentration in the repaired component; typically shear and/or peel stresses are high here. Clearly, due to load transfer, the reinforcement effectiveness increases with increasing numbers of plies, while simultaneously the adhesive stresses at the two key locations also increase. Hence a suitable final reinforcement design will be a compromise between these two requirements, i.e. adequate reinforcement effectiveness for reasonable adhesive stress magnitudes. In view of the above, it was decided to undertake a ply-by-ply interactive design procedure for the multi-ply reinforcement. This enabled firstly the relationship between the number of plies and the peak adhesive stresses and the associated reductions in plate stresses to be determined. Secondly, it enabled the best non-uniform stepping of reinforcement plies near the end of the reinforcement to be designed to minimise peak adhesive shear strains. It should be noted that the position of the ends of the reinforcement were selected to be adequately remote from the critical strut region, such that they would not compromise the ability of the reinforcement to reduce the stress in the critical region. The patch location is shown by the dotted line in Figure 10.21. Also, due to the higher stresses at the strut end of the reinforcement, the non-uniform stepping was only applied to this end of the reinforcement. The region at the lug end of the reinforcement has low stresses, and hence the step lengths at this end were simply made constant at 2 mm, except for the step length from the first to the second ply, which was 4 mm. These step lengths are summarised in Table 10.5.

The initial FE model used an adhesive layer thickness of 0.4 mm, consisting of two layers of elements through the thickness of the adhesive. The strut end of the adhesive layer began 153 mm from the centre of the lower lug and continued to the end of the “horizontal” section around the lug, as indicated in Figure 10.24. The first ply of the boron/epoxy reinforcement was then applied where one layer of elements was used to represent each layer of boron/epoxy. The shear stress in the adhesive (in the local element axes) and the principal stress reduction in the strut were noted. An estimate of an appropriate first step length (17.8 mm) was made using the Eq. (10.12) given in Section 10.2 and the second ply of boron/epoxy was added to the model and the stress results recorded. The step length was then slightly altered (and the analysis

Table 10.5
Step lengths at strut end of patch as determined from interactive FE design method.

Layer	Step length at strut end (mm)
1st ply (from the start of the adhesive layer)	1.7
2nd ply	18.6
3rd ply	15.8
4th ply	11.8
5th ply	7.9
6th ply	3.9
7th ply	3.9
8th ply	3.9

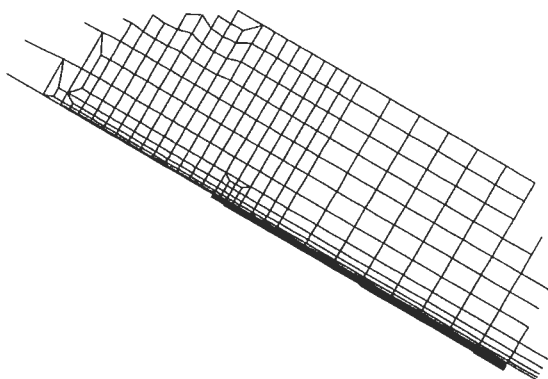


Fig. 10.24. Mesh refinement in the region at the beginning of the strut end of the F/A-18 aileron hinge patch.

re-run) such that the addition of the second ply did not increase the previous peak value of the adhesive shear stress at the start of the first ply. This process was then repeated, with step lengths being obtained such that the adhesive shear stress peaks at the beginning of each new step were well below the peak at the start of the first step. The addition of boron/epoxy plies was then stopped when adequate stress reductions in the critical region of the radius were achieved while also keeping the shear stress in the adhesive (at DUL) below the “knee” value. This corresponded to an eight-ply reinforcement. Figure 10.25(a) summarises results for each successive addition of non-uniform boron/epoxy plies, while Figure 10.25(b) gives a comparison between non-uniform optimised and uniform 4 mm stepping arrangements. The step lengths determined from this procedure are listed in Table 10.5. The advantages of the non-uniform stepping are clearly evident. It is noted that the addition of the full patch provides approximately a 20% stress reduction along the strut edge for the optimal reworks. Similar reductions are provided by the patch for the 1 mm depth rework and 0.2 mm depth reworks [11].

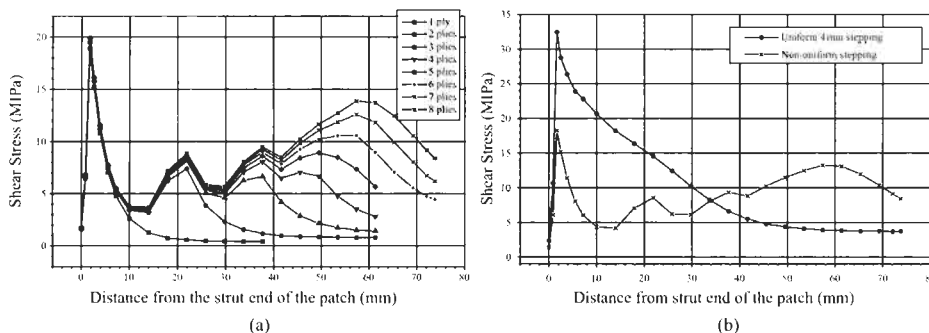


Fig. 10.25. Shear stresses in the adhesive for the optimised stepping near the strut end of the F/A-18 aileron hinge patch: (a) results for each successive additions of non-uniform boron/epoxy plies, and (b) comparison between non-uniform optimised and uniform 4 mm stepping arrangements.

10.7.4. Discussion

The benefits of rework shape optimisation before reinforcement are clearly demonstrated by this practical application. Also, when used in conjunction with FE, the iterative ply addition approach for determining an appropriate reinforcement stepping arrangement, is highly convenient and effective for obtaining minimised adhesive stresses.

10.8. In-plane shaping effects

Previous sections in this chapter all relate to advances in through-thickness shaping or tapering of patches. These improved shapes are shown by mathematical or numerical analysis to alleviate stress concentrations in the adhesive and/or parent material. For all these cases there was no stress variation across the width of the patch, the assumption being that the patch covered the full width of the component. While this can be the case when a patch is applied to the edge of a thick component or to a slender component such as a spar cap, when a patch is applied to a large flat surface such as a wing or fuselage skin load is drawn in from the width direction as well as up through the repaired component. This creates a region of higher stress immediately outside the ends of the patch. Historically, rectangular patches have been the most common for practical applications. In this section, the aim is to investigate the extent to which alternate shapes may give reduced stress concentrations, and to provide candidate configurations to be used as initial estimates for possible subsequent shape optimisation. Hence these issues are addressed by conducting exploratory numerical analyses, where the in-plane load attraction effect of a patch is approximated as a 2D inclusion in a relatively large plate. For comparative purposes a full 3D model of a one layer patch, including an adhesive layer, on a large rectangular plate is also presented.

10.8.1. Geometry, loading and modelling considerations

The 2D geometry under consideration is shown in Figure 10.26 and consists of a flat square plate of 3 mm thickness with 400 mm sides. The plate was modelled taking advantage of quarter symmetry and using only 2D plane stress elements. Here the patch was confined to a design space of 80 mm by 80 mm at the centre of the plate and was represented as an inclusion by a region of elements with an increased thickness of 3.381 mm. This thickness gives an increase in stiffness approximately equivalent to one layer of boron. A remote unidirectional stress of 100 MPa was applied in the y direction along the edges $y = \pm 200$ mm. Isotropic aluminium alloy properties of $E = 71000$ MPa and $\nu = 0.3$ were used throughout the model. Initial analyses for rectangular patches indicated that patches of the same shape give better results as they get wider. Hence to compare shape effects alone it was necessary to consider only patches with the same overall aspect ratio, which is

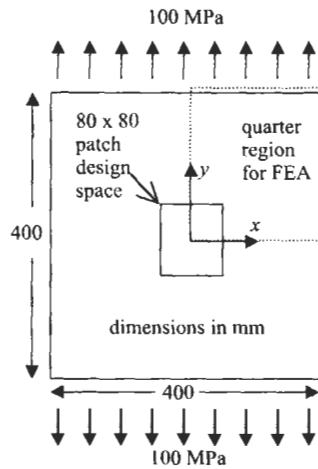


Fig. 10.26. Geometry and loading arrangement for in-plane analysis of patch on plate using inclusion analogy.

defined as the maximum length of the patch in the y direction divided by its maximum width in the x direction.

The 3D model of a one layer patch represents a $\frac{1}{8}$ portion of a plate with length 400 mm, width 120 mm and thickness 6 mm. A centrally located patch of length 80 mm and width 40 mm had a thickness of 0.13 mm and was joined to the plate by a 0.13 mm thick layer of adhesive. The plate is subjected to a unidirectional stress in its length direction of 100 MPa. Material properties used are as follows: For the plate Young's modulus, $E = 71000$ MPa and Poisson's ratio $\nu = 0.32$, for the adhesive, Young's modulus, $E = 2190$ MPa and Poisson's ratio $\nu = 0.3$, and for the unidirectional boron/epoxy, $E_{11} = 203836$ MPa, $E_{22} = 18468$ MPa, $E_{33} = 18468$, $\nu_{12} = 0.18$, $\nu_{23} = 0.3$, $\nu_{31} = 0.0208$, $G_{12} = 5582$ MPa, $G_{23} = 7098$ MPa and $G_{31} = 5582$ MPa, where the subscripts 1, 2 and 3 refer to longitudinal, transverse and through-thickness directions respectively. In order to achieve 1% convergence in peak stress it was necessary to use 3D elements of P (polynomial) formulation. These elements allow for a complex stress variation to be accurately represented within the element and reduce the need for mesh transition near a stress concentration. The bulk of the model consisted of 3D P elements of order 2. The region near the end of the patch was modelled with P elements of order 4.

10.8.2. Determination of K_t from FEA output

Numerical values of element centroid major principle stresses were extracted for all elements in the high stress region, and the stress concentration K_t is expressed in percentage terms of the largest value as compared to the applied remote stress of 100 MPa. The major principle stress term was used as this is the quantity that would determine fatigue life if a defect was located in this region. Typically, the

orientation of the major principal stress is very slightly different to the applied remote load direction due to the patch drawing in load sideways. Element size in the high stress region was kept to about 1/12000 of patch size. To give an indicative result, accuracy of the peak stress value was checked for convergence and finite width effect for the 3:4 aspect ratio patches and total error in stress was found to be less than 0.3%. For this work the K_t (stress concentration) values are provided only for comparing shapes. While the absolute values may have some small error the authors believe that for comparison purposes only, the K_t values can be quoted to the nearest 0.1%. This is because the same process and mesh was used in each case, the only variation being the shape of the patch.

10.8.3. Uniaxial loading and patches with aspect ratios of 2:1

Results obtained for this aspect ratio are summarised in Figure 10.27. The first observation is that the raised stress region is distributed evenly across the end of the rectangular patch as seen in Figure 10.27(a). This is an indication of optimality. A small perturbation in the slope of the end of the patch was then made, which gave worse K_t values and made the stresses less uniform as shown in Figures 10.27(b) & (c). Results for elliptical and diamond shape patches are then given in Figure 10.27(d) & (e). From these results it is clear that the rectangular shape is very close to being fully optimal for this aspect ratio, although it is possible that further study may show slight improvement. As a useful comparison, Figure 10.27(f) shows the stress distribution for a 3D analysis of the rectangular patch. Accurate modelling of such a localised high stress region in 3D (for a bonded repair configuration) has only recently become possible through the availability of more computer power and the use of variable order P elements. In this 3D analysis both the through-thickness and in-plane load attraction effects are captured. For this single layer case, the through-thickness effect dominates with a small rise attributable to the in-plane effect. It can be seen that the high stress region modelled in 3D is also spread evenly along the end of the patch, as in the 2D in-plane analysis case. Further details regarding the full 3D stress distributions are given in [30].

10.8.4. Uniaxial loading and other patch aspect ratios

For the aspect ratio of 1:1, all K_t values are lower than the 2:1 aspect ratio case, with the rectangular patch being better than the ellipse, as shown in Figure 10.28. For the recent case it can be seen that the raised stress region is not as evenly spread in the rectangular case suggesting that some improvement could be made through an optimisation process, such as the gradientless method presented above in Section 10.3. For the wider patch of 1:2 aspect ratio, the results are also given in Figure 10.28, where it can be seen that the ellipse performs better than the rectangle, and has an evenly spread raised stress region along the part of its boundary nearest the centreline. Wider ellipses (not shown in the figures) give further reductions in K_t and longer boundaries with even stress distribution.

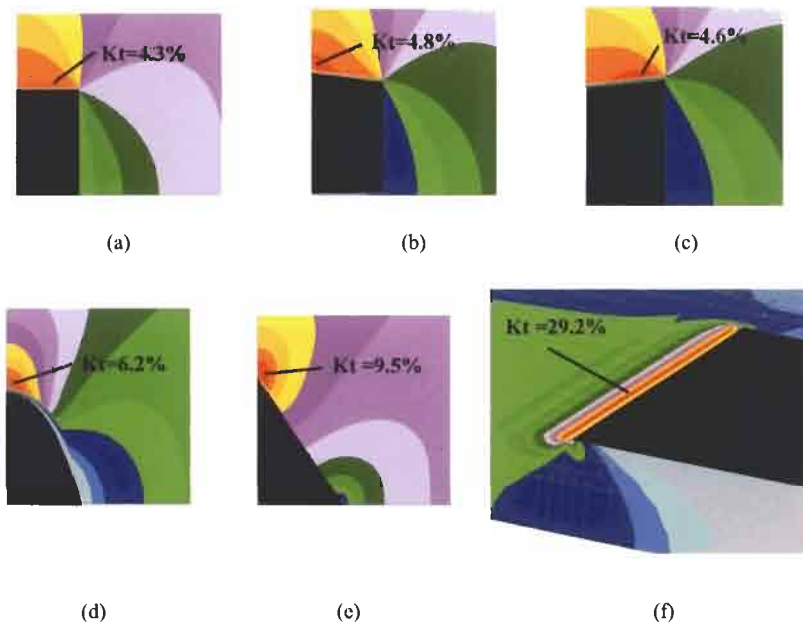


Fig. 10.27. K_t values and major principal stress plots for doublers with aspect ratio 2:1 (a) rectangle, (b) sloped end, (c) reverse sloped end, (d) ellipse, (e) diamond, (f) rectangle in 3D model.

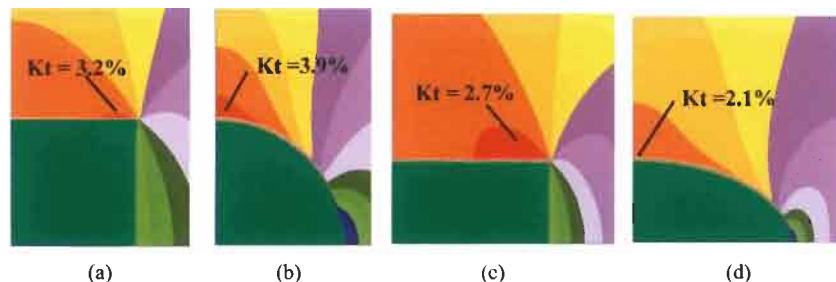


Fig. 10.28. K_t values and major principal stress plots for doublers with aspect ratios: (a) 1:1 rectangle, (b) ellipse, (c) 1:2 rectangle and (d) 1:2 ellipse.

10.8.5. Analogy with hole-in-a-plate problem

It is well known that for a uniaxially loaded plate with an elliptical hole, K_t reduces with increasing aspect ratio (i.e. ratio of length to width) of the hole. The results above suggest that wide elliptical patches (i.e. low aspect ratio) are better in the same remote uniaxial stress field. Since a hole is a represents region of reduced stiffness and a patch is a region of increased stiffness, it appears that the problems are complementary in some way, and the solution of one gives an indication as to the solution of the other.

10.8.6. Stress reduction at the centre of the patch for uniaxially loaded plate

The purpose of applying a patch is to bypass some of the load away from a defect, usually located near the patch centre. For patches that draw in load from the sides this plate stress reduction varies with patch shape as well as with patch thickness. The present results indicate that this stress reduction in the direction of remote loading (at the prospective defect location) is less than that predicted by a 1D analysis based on comparing the stiffness's of the plate and patch with that for the plate alone. For example the 1D analysis predicts a plate stress reduction of 50%, while the present 2D FE for a 2:1 aspect ratio rectangular patch gives a 32.5% reduction at the patch centre, and the 2:1 aspect ratio elliptical patch gives a 33.1% stress reduction throughout the patched region.

10.8.7. Summary of results and discussion

The K_t values are plotted for rectangles and ellipses at different aspect ratios in Figure 10.29. It shows that rectangular patches perform better than ellipses at aspect ratios larger than 3:4. Because of the need for long load transfer lengths and space limitations most real patch applications have to be at least twice as long as their width. Hence this work suggests that the commonly used rectangular shapes are good if not optimal (for aspect ratios of 2:1 and higher) in terms of in-plane shape. However if for a practical application the opportunity arose to implement a wide patch some benefit could be gained by using an elliptical shape. The results stated here are for one layer only and the actual benefit would be larger for a typical multi-layer patch.

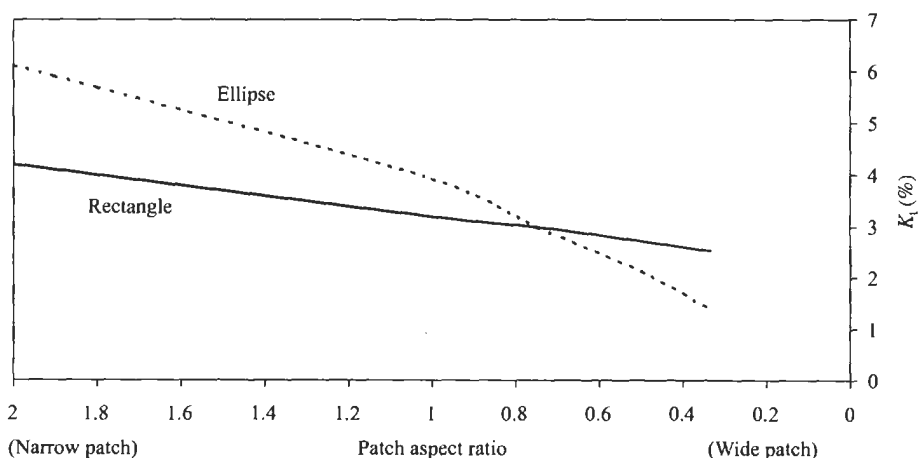


Fig. 10.29. In-plane plate K_t values of rectangular and elliptical shaped 1 layer patches with various aspect ratios.

10.9. Conclusions

Optimal stepping and tapering of the ends of bonded repairs has been investigated in detail by analytical and numerical means in Sections 10.2 to 10.5. All methods give as one conclusion that by transitioning the effective stiffness of the repair in the taper region large stress reductions can be achieved using realistic configurations. However to fully realise the potential maximum improvements at the very ends of the patch, it is desirable to reduce the effective stiffness of the first ply to below that of a typical unidirectional single layer of boron/epoxy layer. Hence the use of cross-ply boron layers or of other more compliant materials has been suggested and it is envisaged that such options will soon be investigated by further modelling and laboratory testing at DSTO. Throughout these sections effort has been focused on the adhesive stresses under the patch. The authors are aware that adhesive cracking often starts in the adhesive fillet region outside the end of the patch and that the modelling has shown significant adhesive stress concentrations in this region regardless of fillet shape. The use of a more compliant first layer would relieve these stresses as well.

Sections 10.5 and 10.6 show the benefits of using numerical shape optimisation techniques to define variation of adhesive thickness (as well as reinforcement thickness) such that the load transfer through the adhesive can be more evenly spread along the bond line. This results in significant reductions in peak stress. These improvements are demonstrated near a crack or joint for the case of a lap joint, or over a curved region in the case of the F/A-18 470 bulkhead. Hence the optimal variation of adhesive thickness has been shown numerically to be an effective method in reducing adhesive stress concentrations. The benefits of combining optimal rework shaping with a boron/epoxy reinforcement have been discussed in Section 10.7 for the case of an F/A-18 aileron hinge. Here the use of an optimal rework prior to reinforcing has the double benefit of keeping the surface stresses to their initial un-cracked and un-reworked values and reducing adhesive stresses when the reinforcement is applied. It is important to note that a 2 mm deep rework of some form was required for crack removal and the use of a standard circular shaped rework would have significantly raised the peak surface stress, as compared to the optimal rework.

Investigation of repair in-plane shaping in Section 10.8 has led to the conclusion that the standard rectangular shape is good if not optimal for the typical repair aspect ratios of 2:1 or higher. The exception is for unusually wide patches where an elliptical shape gives better results for the stress concentration in the repaired component. Hence for such wide patches the opportunity exists to apply numerical procedures to determine the optimal shapes. It is expected that future work will need to be directed at the inclusion of temperature curing effects as part of the optimisation process.

References

1. Rose, L.F.R. (1988). Theoretical analysis of crack patching, in Chapter 5 – Bonded repair of aircraft structures (A.A. Baker and R. Jones, eds.), Martinus Nijhoff.
2. Zienkiewicz, O.C. and Taylor, R.L. (1991). The Finite Element Method (4th ed.), New York, McGraw-Hill.
3. Bathe, K.J. (1982). The Element Procedures in Engineering Analysis. New Jersey, Prentice-Hall.
4. Spyrakos, C.C. and Raftoyiannis, J. (1997). Linear and Non-Linear Finite Element Analysis, Algor Publ. Div., Pittsburgh, PA.
5. Rockey, K.C., Evans, H.R., Griffiths, D.W., *et al.* (1983). The Finite Element Method (2nd ed.), John Wiley & Sons, New York.
6. Kaye, R. and Heller, M. (1997). Structural Shape Optimisation by Iterative Finite Element Solution, DSTO-RR-0105, Defence Science and Technology Organisation, Department of Defence, Australia, June.
7. Heller, M., Kaye, R. and Rose, L.R.F. (1999). A gradientless finite element procedure for shape optimisation. *J. Strain Analysis*, **34**(5), pp. 323–336.
8. Kaye, R. and Heller, M. (2000). Design of life extension options for an F/A-18 bulkhead using shape optimisation. *J. of Strain Analysis*, **35**(6), pp. 493–505.
9. Waldman, W. and Heller, M. (1999). Shape optimisation of PC9/A lower wing skin rework in vicinity of undercarriage bay door up-lock mechanism mounting holes, Defence Science and Technology Organisation, Department of Defence, Australia, File B2/129, April.
10. Heller, M., McDonald, M. and Burchill, M. (2001). Shape optimisation of critical stiffener run-outs in the F-111 Wing pivot fitting. DSTO-TR-1119, Defence Science and Technology Organisation, Department of Defence, Australia, April.
11. Heller, M., Kaye, R., Whitehead, S., *et al.* (1999). Design and Stress Analysis, Chapter 3 – Life extension of F/A-18 inboard aileron hinges by shape optimisation and composite reinforcement (Editor R. Chester.), Defence Science and Technology Organisation, Australian Department of Defence, DSTO-TR-0699.
12. Hart-Smith, L.J. (1973). Adhesive Double Lap Joints, NASA CR-112235.
13. Chalkley, P.D. (1993). Mathematical Modelling of Bonded Fibre-Composite Repairs to Aircraft, Defence Science and Technology Organisation, Australian Department of Defence, Aeronautical Research Laboratory, Research Report, ARL-RR-7.
14. Tran-Cong, T. and Heller, M. (1997). Reduction in Adhesive Shear Strains at the Ends of Bonded Reinforcements, Defence Science and Technology Organisation, Australian Department of Defence, DSTO-RR-0115, September.
15. Chester, R.J., Walker, K.F. and Chalkley, P.D. (1999). Adhesively bonded repairs to primary aircraft structure. *Int. J. of Adhesion and Adhesives*, **19**, pp. 1–8.
16. Bartholomeusz, R., Searl, A., Baker, A., *et al.* (1999). Bonded composite repair of F/A-18 Y470.5 bulkhead – applications with through-thickness stresses. *Proc. of the Int. Aerospace Congress (IAC 97)*, 1, Sydney, February, pp. 24–27.
17. Ojalvo, I.U. (1985). Optimisation of bonded joints. *AIAA J.*, **23**(10), January, pp. 1578–1582.
18. Groth, H.L. and Norlund, P. (1991). Shape optimisation of bonded joints, *Int. J. of Adhesion and Adhesives*, **11**(4), pp. 204–212.
19. Kaye, R. and Heller, M. (2001). Through thickness shape optimisation of bonded repairs and lap-joints, *Int. J. of Adhesion and Adhesives*, Vol **22**, pp. 7–21.
20. Rees, D. and Molent, L. (1993). Analysis of Candidate Bonded Repairs for Cracks in Weep Holes of USAF C141 Aircraft, Defence Science and Technology Organisation, Australian Department of Defence, Aeronautical Research Laboratory, Technical Note, ARL-TN-62.
21. Goland, M. and Reissner, E. (1999). The stresses in cemented joints. *J. of Applied Mec.*, **7**, A17.
22. Volkerson, O. Die Nietkraftverteilung in Zugbeanspruchten Nietverbindungen mit Konstanten Laschenguerschnitten, *Luftfahrtforschung*, **15**, pp. 41–47.
23. Anon. (1995). Composite Materials and Adhesive Bonded Repairs, RAAF Engineering Standard, No. C5033, Issue 1, Department of Defence, Australia.

24. Boykett, R. and Walker, K. (1996). F-111C Lower Wing Skin Bonded Composite Repair Substantiation Testing, Technical Report, DSTO-TR-0480.
25. Wang, C.H., Heller, M. and Rose, L.R.F. (1998). Substrate stress concentrations in bonded lap joints. *J. of Strain Analysis*, **33**(5), pp. 331–346.
26. Shah, L.P., Heller, M., Wang, C.H., *et al.* (1997). Reduction of plate stress concentration factors due to bonded reinforcements. *Int. Aero. Conf.*, **2**.
27. Adams, R.D., Comyn, J. and Wake, W.C. (1997). *Structural Adhesive Joints in Engineering*, Chapman and Hall, (2nd ed.).
28. Moore, G.J. (1994). *Design Sensitivity and Optimisation*, The MacNeal-Schwendler Corporation.
29. Martin, P. (1995). ECP 365 Y470 bulkhead beef-up, SES DI 0942, Defence Systems Division, Canadair Group, Bombardier Inc.
30. Kaye, R. and Heller, M. (2000). Comparative Assessment of Local Adhesive and adherend Stress Concentrations for Full 3D Bonded Repairs (in preparation).

Chapter 11

THERMAL STRESS ANALYSIS

R.J. CALLINAN

Defence Science and Technology Organisation, Air Vehicles Division, Fishermans Bend, Victoria 3207, Australia

11.1. Introduction

Accurate computational thermal stress analysis is particularly important for assessment of the viability of bonded repairs to aircraft. Thermal stresses arise due to the different coefficients of thermal expansion of the plate and patch involved and may be significant at the extremes of the operating temperatures of these aircraft. Furthermore the bonding process involves heating to approximately 100 °C for several hours before curing and cooling to room temperature. The resulting residual thermal stresses due to the bonding process may be significant in affecting fatigue crack growth rate. In this section closed form solutions are considered and verified using F.E. analysis. In particular, 1D closed form solutions [1,2,3] and 2D solutions [4,5,6,7,8] for circular repairs on circular plates are considered. This involves computation of thermal stresses due to heating and thermal stress in both isotropic and orthotropic repairs, and have been found to be accurate in comparison to F.E. results. Both thermal and residual stresses are considered in this analysis. It is found that this solution can be used for bonded repairs to large structures such as aircraft wings provided that a suitable edge restraint factor is applied. A relatively simple closed form solution is applied for the thermal analysis of one dimensional strip joints. A simplification of the problem is made by assuming that bending is restrained as shown in Figure 11.1. This assumption is applicable to integral stiffened skins or thick skins supported by multiple spars. The approach to the residual stress problem involves a two stage process, firstly heating the structure up to the curing temperature, and secondly cooling down to ambient temperature.

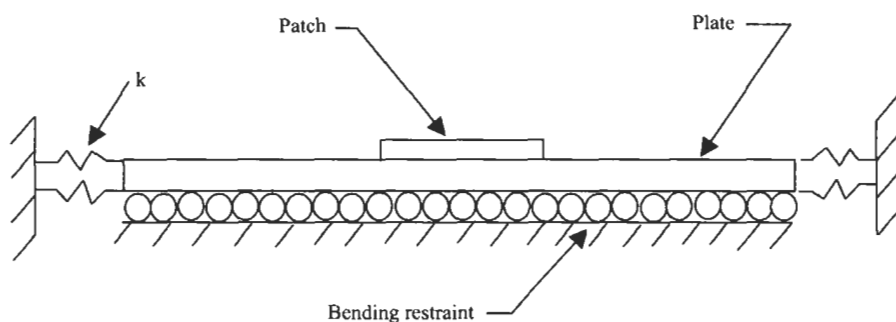


Fig. 11.1. Bending restraint provided to repaired skin.

11.2. Analytical expression for initial stresses in a circular plate due to heating

Circular repairs on circular plates are useful for the derivation of a closed form solution which contains a bi-axial stress/strain field and has relevance for actual repairs. Consider now a circular plate shown in Figure 11.2. This plate is uniformly heated within a radius $r = R_i$ equal to a temperature T_i , while the temperature at the boundary is T_o . The temperature solution given in [5] which satisfies the Laplacian operator:

$$\nabla^2 T = 0, \quad (11.1)$$

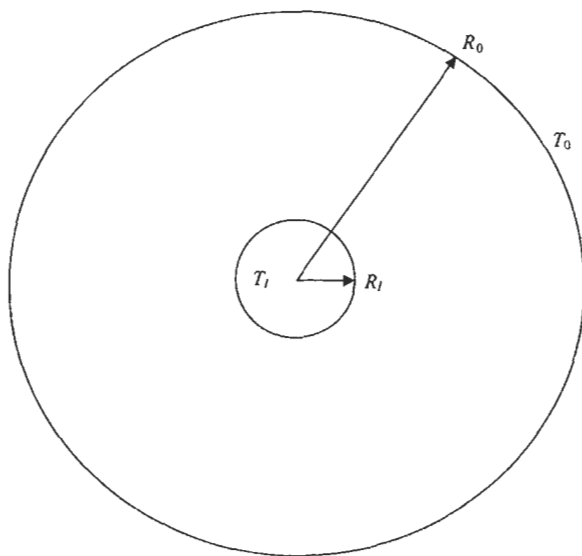


Fig. 11.2. Circular plate, definition of temperatures and radii.

is given by:

$$\begin{aligned} T &= T_O + \frac{(T_I - T_O) \ln(r/R_O)}{\ln(R_I/R_O)} && \text{for } R_I \leq r \leq R_O \text{ and} \\ T &= T_I, && \text{for } r \leq R_I \end{aligned} \quad (11.2)$$

For this temperature distribution, the following differential equation is applicable for the elastic displacement, assuming plane stress:

$$\frac{d}{dr} \left(\frac{1}{r} \right) \frac{d(ru)}{dr} = \alpha(1 + \nu) \frac{dT}{dr}, \quad (11.3)$$

where:

r is the radius

u is the radial displacement

ν is Poisson's ratio

α is the coefficient of thermal expansion

T is the temperature.

For the case of plane stress, and fixed edges the strain can be defined as:

$$\varepsilon_r = \alpha_{\text{eff}}(T_I - T_O), \quad (11.4)$$

where α_{eff} is the effective coefficient of thermal expansion and is given by:

$$\alpha_{\text{eff}} = \frac{\alpha(1 + \nu)}{R_O(T_I - T_O)} \left[R_O T - \left(\frac{R_O}{r^2} \right) \int_0^r r T dr - \left(\frac{1}{R_O} \right) \int_0^{R_O} r T dr \right] \quad (11.5)$$

The explicit solution given by [5] for the case of fixed edges for $r \leq R_I$ is:

$$\alpha_{\text{eff}} = \frac{\alpha(1 + \nu)}{2} \left\{ 1 + \frac{1 - R_I^2/R_O^2}{2 \ln(R_I/R_O)} \right\} \quad (11.6)$$

As expected, the expression is dependent on the geometry only and not temperature.

As mentioned in [9] the calculation of the effective coefficient of expansion in a structure is important in determining the residual stresses in a bonded structure. The effective coefficient of expansion of the plate structure is very much lower than the value α in the asymptotic limit $R_I/R_O = 0$, i.e.

$$\alpha_{\text{eff}} = \frac{\alpha(1 + \nu)}{2} \quad (11.7)$$

From Eq. (11.6) the asymptotic value for an aluminium plate is 14.95×10^{-6} while the 1D value is $23 \times 10^{-6}/^\circ\text{C}$. The lower value of the coefficient of thermal expansion, in this example, is firstly due to the circumferential restraints applied to the edge of the plate and secondly is the result of the resistance of the surrounding

colder structure. This occurs, for example, in the bonding of a high strength repair to the wing of an aircraft in which a high temperature, over a local area, is required to cure the adhesive.

In this section the derivation of an expression for residual stresses essentially follows that given by [5,6]. In a bonded repair both the patch and plate are heated to the cure temperature T . In the case of a plate in which the edges are restrained, the heating gives rise to an initial stress in the plate before curing of the adhesive and cooling takes place. In the case of the patch no restraint exists and the initial stress is negligible. To compute the initial stress in the plate we have the following expressions for displacement, obtained by integrating Eq. (11.3), and radial stress from [10]:

$$u = \frac{\alpha_1(1+\nu)}{r} \int_0^r T r dr + C r, \quad (11.8)$$

$$\sigma = -\frac{\alpha_1(1+\nu)}{r^2} \int_0^r T r dr + \frac{E_1}{(1-\nu)} C, \quad (11.9)$$

from the boundary condition that $u = 0$ at $r = R_O$ we obtain the integration constant C . From this the general form for the radial displacements and stresses is:

$$u = \frac{\alpha_1(1+\nu)}{R_O} \left\{ \frac{R_O}{r} \int_0^r T r dr - \frac{r}{R_O} \int_0^{R_O} T r dr \right\}, \quad (11.10)$$

$$\sigma = -\alpha_1 E_1 \left\{ \frac{1}{r^2} \int_0^r T r dr + \frac{1+\nu}{(1-\nu)R_O^2} \int_0^{R_O} T r dr \right\} \quad (11.11)$$

Specifically for $r = R_I$ the displacement is given by:

$$u = \frac{\alpha_1(1+\nu)}{2} R_I (T_I - T_O) \left\{ 1 + \frac{1}{2 \ln(R_I/R_O)} \left(1 - \frac{R_I^2}{R_O^2} \right) \right\} \quad (11.12)$$

Specifically for $r \leq R_I$ we have a constant state of stress given by:

$$\sigma = -\frac{\alpha_1 E_1}{2} \left\{ T_I + \frac{(1+\nu)}{(1-\nu)} \left[T_O + \frac{(T_I - T_O)}{2 \ln(R_I/R_O)} \left(\frac{R_I^2}{R_O^2} - 1 \right) \right] \right\} \quad (11.13)$$

Equation (11.13) gives the required initial stress. The second part to the solution of residual stresses involves the analysis of the plate and patch. We require the state of stress corresponding to a cooling of the plate and patch. If we start at a temperature 0°C corresponding to zero initial stress, then cooling to a negative temperature equal in magnitude to the cure temperature ($-T$) will give the required stress components. A summation with the initial stresses will give the residual stress state.

In this analysis, the adhesive will not be considered, and the patch is assumed to be rigidly connected to the plate. Radial stresses and displacements will be obtained for the skin and patch. The skin is hereafter referred to as the plate. Consider a plate shown in Figure 11.3, which has properties E_1, α_1, t_1 for $r \geq R_I$ and overall properties E_0, α_0, t_0 for $r \leq R_I$. Again the temperature boundary conditions are given by T_I being constant for $r \leq R_I$ and $T = T_O$ at $r = R_O$. The displacements are given by:

for $r \geq R_I$

$$u_1 = \frac{\alpha_1(1+\nu)}{r} \int_{R_I}^r T r dr + C_2 r + \frac{C_3}{r}, \quad (11.14)$$

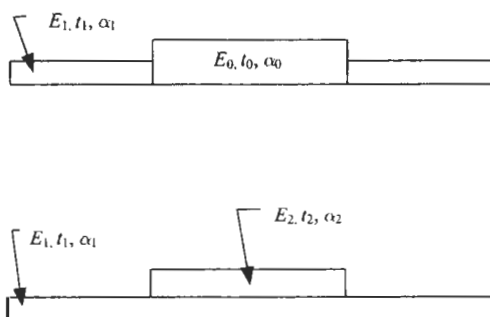
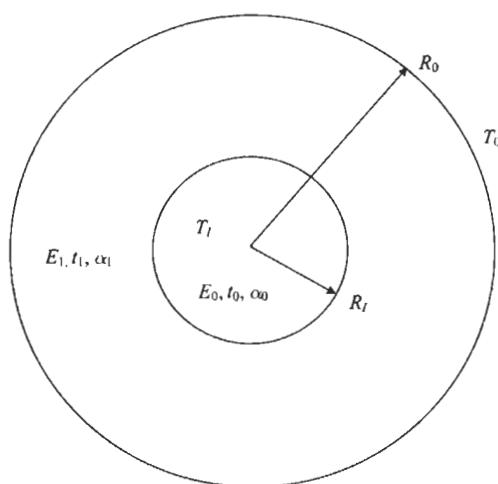


Fig. 11.3. Idealised bonded repair.

for $r \leq R_I$

$$u_o = \frac{\alpha_o(1+\nu)}{r} \int_0^r T r dr + C_1 r \quad (11.15)$$

The stresses are given by:

for $r \geq R_I$

$$\sigma_1 = -\frac{\alpha_1 E_1}{r^2} \int_{R_I}^r T r dr + \frac{E_1}{(1-\nu^2)} \left[C_2(1+\nu) - \frac{C_3(1-\nu)}{r^2} \right], \quad (11.16)$$

for $r \leq R_I$

$$\sigma_o = -\frac{\alpha_o E_o}{r^2} \int_0^r T r dr + \frac{E_o}{(1-\nu^2)} C_1(1+\nu) \quad (11.17)$$

The solution of these equations must satisfy the following conditions:

- (a) The displacement u_1 and u_o is equal at $r = R_I$, hence from Eqs. (11.14) and (11.15):

$$C_2 r + \frac{C_3}{r} = \frac{\alpha_o(1+\nu)}{R_I} \int_0^{R_I} T r dr + C_1 R_I \quad (11.18)$$

- (b) Equilibrium must be maintained across the boundary at $r = R_I$, using Eqs. (11.16) and (11.17):

$$\frac{E_1 t_1}{(1-\nu^2)} \left[C_2(1+\nu) - \frac{C_3(1-\nu)}{R_I^2} \right] = -\frac{\alpha_o E_o t_o}{R_I^2} \int_0^{R_I} T r dr + \frac{E_o t_o}{(1-\nu)} C_1 \quad (11.19)$$

- (c) Also we have the further boundary condition that at $r = R_o$:

$$u_1 = 0 = \frac{\alpha_1(1+\nu)}{R_o} \int_{R_I}^{R_o} T r dr + C_2 R_o + \frac{C_3}{R_o} \quad (11.20)$$

At this stage we have enough information for the evaluation of the constants C_1 , C_2 and C_3 .

It is more convenient to have the equations in the form that represent a patch over the plate for $r \leq R_I$ as shown in Figure 11.3. As before, the plate has the properties E_1, t_1, α_1 while the patch has the properties E_2, t_2, α_2 . It is necessary to

derive an expression for α_o in terms of these quantities. From equilibrium considerations we have:

$$E_o t_o \alpha_o = (E_1 t_1 + E_2 t_2) \alpha_o = E_1 t_1 \alpha_1 + E_2 t_2 \alpha_2 , \quad (11.21)$$

hence:

$$\alpha_o = \frac{(\alpha_1 + s \alpha_2)}{(1 + s)} , \quad (11.22)$$

where:

$$s = \frac{E_2 t_2}{E_1 t_1} \quad (11.23)$$

The expression for the stress state in the plate just outside the patch is given by Eq. (11.16) for $r = R_I$:

$$\sigma = E_1 \left[\frac{C_2}{(1 - \nu)} - \frac{C_3}{(1 + \nu) R_I^2} \right] \quad (11.24)$$

We will now derive the expressions for the stress state in the plate beneath the patch and in the patch. From Eq. (11.15) with $r \leq R_I$, under a uniform temperature, the displacement is given by:

$$u = \left[\frac{(1 + \nu) \alpha T_I}{2} + C \right] r \quad (11.25)$$

Since the displacement is the same in both the patch and plate we have:

$$\frac{(1 + \nu) \alpha_1 T_I}{2} + C_1 = \frac{u}{R_I} , \quad (11.26)$$

$$\frac{(1 + \nu) \alpha_2 T_I}{2} + C_2 = \frac{u}{R_I} , \quad (11.27)$$

where the displacement u corresponds to the location $r = R_I$.

The radial stresses for the plate and patch are given by:

$$\sigma_1 = -\frac{\alpha_1 E_1}{r^2} \int_0^r T_I r dr + \frac{E_1 C_1}{(1 - \nu)} , \quad (11.28)$$

$$\sigma_2 = -\frac{\alpha_2 E_2}{r^2} \int_0^r T_I r dr + \frac{E_2 C_2}{(1 - \nu)} \quad (11.29)$$

Using Eqs. (11.26–11.29) we have the expressions for the radial stresses in the plate

beneath the patch and in the patch:

$$\sigma_1 = \frac{E_1}{(1-\nu)} \left[-\alpha_1 T_I + \frac{u}{R_I} \right], \quad (11.30)$$

$$\sigma_2 = \frac{E_2}{(1-\nu)} \left[-\alpha_2 T_I + \frac{u}{R_I} \right] \quad (11.31)$$

To obtain the residual stress in the plate beneath the patch it is necessary to sum Eqs. (11.13) and (11.30), but with $T_I = -T_I$ in Eq. (11.30). Hence the final expression for the residual stress beneath the patch is:

$$\begin{aligned} \sigma = & -\left(\frac{\alpha_1 E_1}{2}\right) \left\{ T_I + \frac{(1+\nu)}{(1-\nu)} \left[T_O + \frac{(T_I - T_O)}{2 \ln(R_I/R_O)} \left(\frac{R_I^2}{R_O^2} - 1 \right) \right] \right\} \\ & + \frac{E_1}{(1-\nu)} \left(\alpha_1 T_I + \frac{u}{R_I} \right) \end{aligned} \quad (11.32)$$

Since the initial stress in the patch is zero, then the residual stress in the patch is given by Eq. (11.31), but again with $T_I = -T_I$ hence:

$$\sigma = \frac{E_2}{(1-\nu)} \left(\alpha_2 T_I + \frac{u}{R_I} \right), \quad (11.33)$$

and the final expression for the residual stress just outside the patch is given by the summation of Eqs. (11.13) and (11.24), hence:

$$\begin{aligned} \sigma = & -\frac{\alpha_1 E_1}{2} \left\{ T_I + \frac{(1+\nu)}{(1-\nu)} \left[T_O + \frac{(T_I - T_O)}{2 \ln(R_I/R_O)} \left(\frac{R_I^2}{R_O^2} - 1 \right) \right] \right\} \\ & + E_1 \left[\frac{C_2}{(1-\nu)} - \frac{C_3}{(1+\nu)R_I^2} \right] \end{aligned} \quad (11.34)$$

These equations now give the residual stress in terms of the cure temperature T . The displacement u at $r = R_I$ for Eqs. (11.17, 11.18) and integration constants C_2 , C_3 are given in the appendix.

These equations now give the residual stress in terms of the cure temperature T . For operating temperatures different from room temperature, Eqs. (11.24), (11.30) and (11.31) can be used to calculate the stresses. In this case $T_I = T_O =$ uniform temperature change from room to operating temperature. The final stresses are obtained by superimposing these stresses on the residual stresses.

11.2.1. Comparison of F.E. and analytic results

The solution of these equations has been carried out for $\Delta T = 100^\circ\text{C}$, and the following quantities have been evaluated for the comparison with F.E. results, the mesh is shown in Figure 11.4:

1. residual stress just outside the patch at $r = R_I$

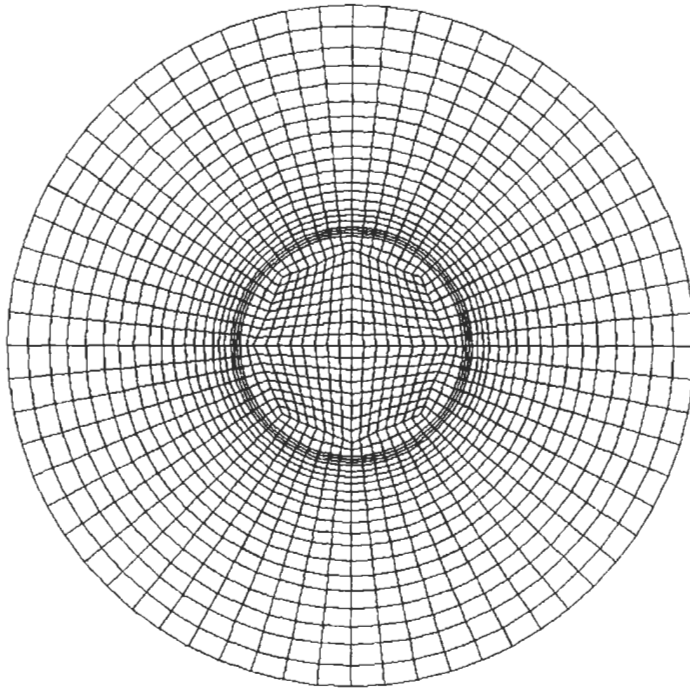


Fig. 11.4. Finite element mesh of circular patch on circular plate. Here $R_I = 162$ mm and $R_O = 500$ mm.

2. residual stress in the skin beneath the patch (σ_1)
3. residual stress in the patch (σ_2)

As an example a circular patch and plate are considered whose mechanical properties are shown in Table 11.1. These properties are representative of a quasi-isotropic boron patch reinforcement of an aluminium plate (although the value of α used here for boron corresponds to uni-directional boron and should have been

Table 11.1

Material properties used for study of circular repairs on circular plates, $\Delta T = 100^\circ\text{C}$.

Component	Thickness (mm)	Young's modulus (MPa)	Poisson's ratio	Coefficient of thermal expansion ($1/^\circ\text{C}$)	Conductivity ($\text{J/ms}^\circ\text{C}$)
Plate(Aluminium)	1.0	71016	0.3	23×10^{-6}	13.2
Patch(boron)	0.5	156000	0.3	$^{**}4.1 \times 10^{-6}$	0.294
*Adhesive (FM300)	0.254	3460	0.35		

* Only used for a 3D run.

** In this instance the value for the laminate is taken to be equal to the unidirectional value.

3.76×10^{-6} for the laminate). While this is not a perfect representation of an actual repair it is acceptable for estimating residual stresses. Also this assumes that bending is restrained, e.g. by stiffeners or thick plates, and also the edge restraint exists when the repair is bounded by structural elements such as spars and ribs. Consider the case in which the plate edge is restrained in the radial direction. Firstly consider the heating up process to the cure temperature, given by Eq. (11.13) and shown in Figure 11.5. The comparison between theory and F.E. results is in agreement to four significant figures. In the case of no edge restraint the initial stresses would be zero.

The second stage of the process involves cooling down from the cooling temperature alone. The analytical and F.E. results are shown in Figure 11.6 where the curves are from Eqs. (11.24), (11.30) and (11.31), and the points on the curves are F.E. results. In all cases very good agreement between analytical and F.E. results are obtained, (to four significant figures). The final solution for the residual stresses is given by Eqs. (11.32–11.34) in Figure 11.7 with the corresponding F.E. results. Again very good agreement between analytical and F.E. results is obtained. Note that the residual stresses in the plate shown in Figure 11.7 are significantly lower than those during the cooling process, Figure 11.6. This is simply due to the lack of initial stresses which arise as a result of the restrained edges of the plate when heated up to the cure temperature. The assumption of edge restraints is important. Typically a repair to an aircraft wing plate can be considered as fully restrained in the radial direction if the repair is bounded by significant structural elements such as spars and ribs.

Returning to the residual stresses shown in Figure 11.7. It is evident that for large values of R_0/R_1 asymptotic values occur for all stress components and may be considered as limiting values.

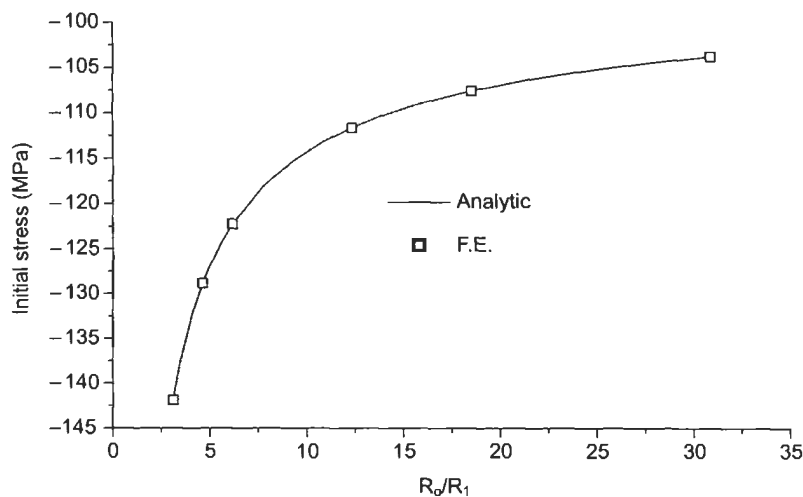


Fig. 11.5. Initial stresses in plate due to heating to cure temperature.

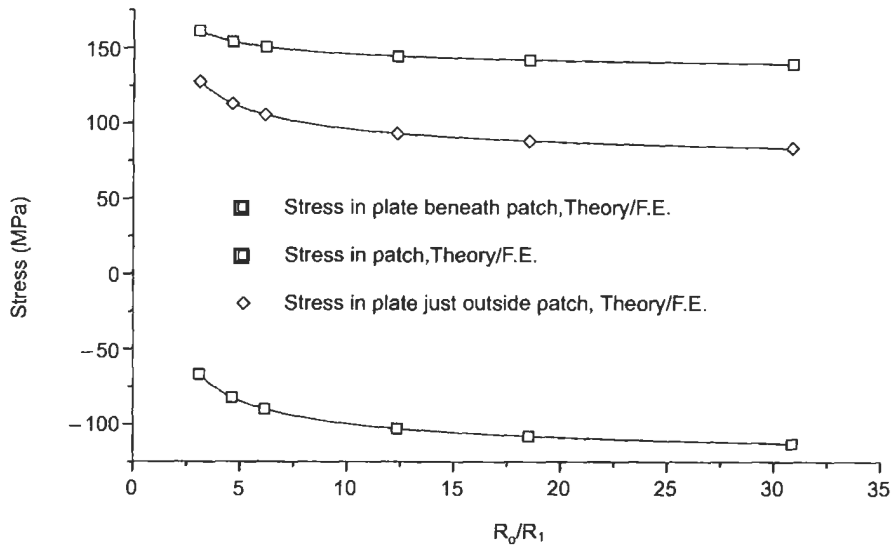


Fig. 11.6. Comparison of theory and F.E. results for cooling down process only.

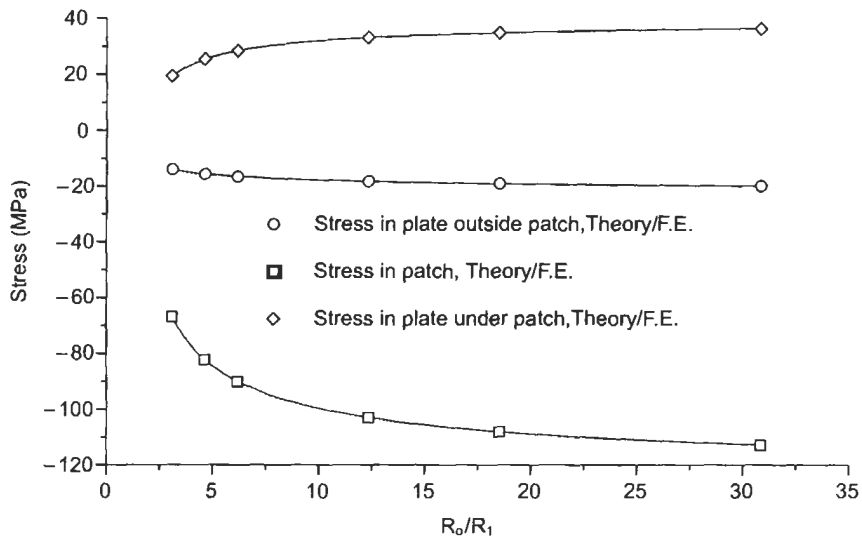


Fig. 11.7. Residual stresses in bonded repair: sum of heating and cooling stresses.

So far, the adhesive has not been considered in the analysis. However F.E. results have been obtained in which the patch and plate have been coupled using 3D adhesive elements. To make a useful comparison with the previous analytical work the bending of the plate has had to be restrained. The introduction of the adhesive has

Table 11.2

2D isotropic circular plate, patch and 3D adhesive elements. Residual displacements and stresses, $\alpha_1 = 23 \times 10^{-6}/^\circ\text{C}$, $\alpha_2 = 4.1 \times 10^{-6}/^\circ\text{C}$ (analytic values in parenthesis), [5].

R_0 (mm)	Displacement at edge of patch (mm)	Residual stress just outside patch (MPa)	Residual stress in skin beneath patch (MPa)	Residual stress in patch (MPa)
500	-0.11551 (-0.11499)	128.31 (127.92)	161.91 (161.33)	-65.532 (-66.813)

resulted in an error of only 2% in direct stresses, shown in Table 11.2, and indicates that the use of a closed form solution is sufficiently accurate for patch design.

The main concern in this chapter is the equations for direct stresses in the repair. It is important to know the direct stress in the plate beneath the patch in order to predict crack growth rate or simply the residual strength of the repaired structure. The adhesive itself has no effect on the maximum value of the direct stresses.

Some F.E. programs have the capability in which the material properties can be temperature/time dependent. In this case a simulation of the bonding process can be carried out. The adhesive properties change during the curing process. At the end of the curing process the adhesive has developed a shear stiffness and as the repair is cooled to room temperature residual stresses develop. If the simulation capability is available, then residual stresses are directly obtained from the analysis.

If this capability is not available then a superposition procedure can be used. The analysis is carried out in two steps. The first analysis is equivalent to heating up of the plate to the curing temperature (without the patch, since the adhesive has no stiffness at this stage). Secondly, another analysis is carried out with the patch included, subject to a cooling temperature equal to the cure temperature. ($T_f = -T_f$). In the work presented here this two stage procedure has been shown to be very accurate. The superposition of these two analyses gives the residual stresses in the repair. Since the adhesive shear modulus is temperature dependent, an arithmetic average value of the shear modulus should be used during the cooling process.

11.2.2. Orthotropic solution

Recent work by [7,8] has extended the analysis of residual stresses to circular orthotropic patches on isotropic plates. The solution of this problem is based on an inclusion analogy, which refers to the inner region of the repair where $r \leq R_f$ in which equivalent properties of the inclusion can be made without altering the stress or displacement state. Exact solutions are presented for both residual stresses and thermal coefficients of expansion.

Results of this work are shown in Figures 11.8 and 11.9 for stresses due to cooling only. For plate stresses beneath the patch both σ_{xx} and σ_{yy} are predicted, as shown in Figure 11.8 and correspond to clamped edge conditions. As a comparison, the isotropic solution is included and gives close results when

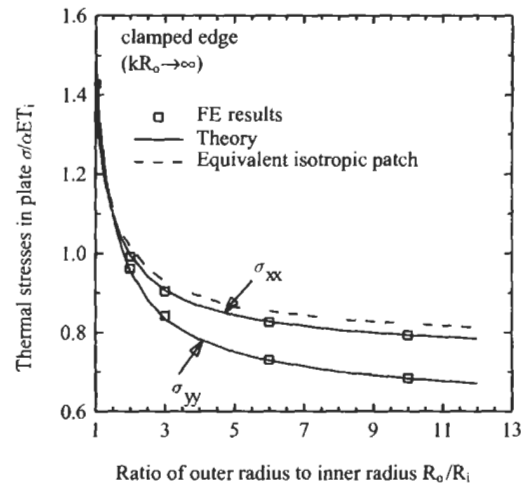


Fig. 11.8. A circular patch over a concentric plate with outer edge being clamped: cooling induced stresses in the plate. [7]

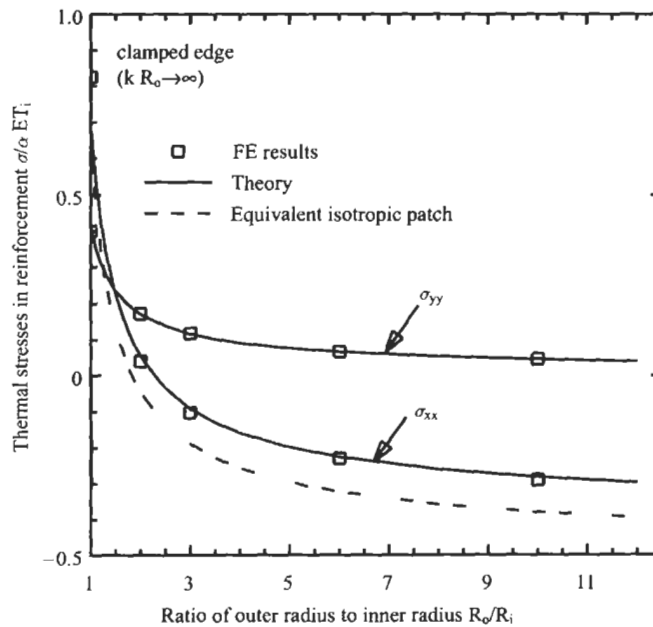


Fig. 11.9. A circular patch over a concentric plate with outer edge being clamped: cooling induced stresses in the orthotropic reinforcement. [7]

compared with σ_{xx} stresses, however the isotropic solution predicts $\sigma_{xx} = \sigma_{yy}$ where in fact $\sigma_{yy} < \sigma_{xx}$.

In the case of the reinforcement shown in Figure 11.9, the isotropic stress is slightly higher than the σ_{xx} stress, but while the isotropic solution predicts $\sigma_{xx} = \sigma_{yy}$, where in fact the absolute value of the stresses, $|\sigma_{yy}| < |\sigma_{xx}|$. Note that for $R_O/R_I \geq 1.5$ the sign of the σ_{yy} stress is opposite in sign to the σ_{xx} stress. For the cases of both the plate and reinforcement stresses, the isotropic solution is conservative.

11.2.3. Thermal stresses in a one-dimensional strip

11.2.3.1. Shear stresses. In a bonded joint in which two materials are bonded together, thermal stresses may develop as a result of the difference in thermal coefficients of expansion. The following equations will be given for a simple double overlap joint whose geometry is given in Figure 11.10 together with the location of the origin of the x axis. It is assumed that all the load transferred by the lap joint is by adhesive shear. Also, in this symmetrical joint it is assumed that no bending takes place [5].

The constitutive equations are:

$$\frac{du_1}{dx} = \frac{\sigma}{E_1} + \alpha_1 \Delta T, \quad \frac{du_2}{dx} = \frac{\sigma_2}{E_2} + \alpha_2 \Delta T, \quad (11.35)$$

where:

u_1 and u_2 are the displacements in the components of the joint

α_1 and α_2 are the thermal coefficients of expansion

E_1 and E_2 are the Young's moduli of the two materials

ΔT is the change of temperature $= T_C - T_A$

T_C is the cure temperature

T_A is the initial temperature

σ_1 and σ_2 are the stresses in the components of the joint.

The equilibrium equations are:

$$\frac{d\sigma_1}{dx} + \frac{\tau}{t_1} = 0, \quad \frac{d\sigma_2}{dx} - \frac{\tau}{t_2} = 0, \quad (11.36)$$

where:

t_1, t_2 are the different thicknesses of the two components and

τ is the shear stress in the adhesive.

Compatibility requires that the shear stress is given by:

$$\tau = \frac{G_a}{t_a} (u_2 - u_1), \quad (11.37)$$

where:

t_a is the thickness of the adhesive

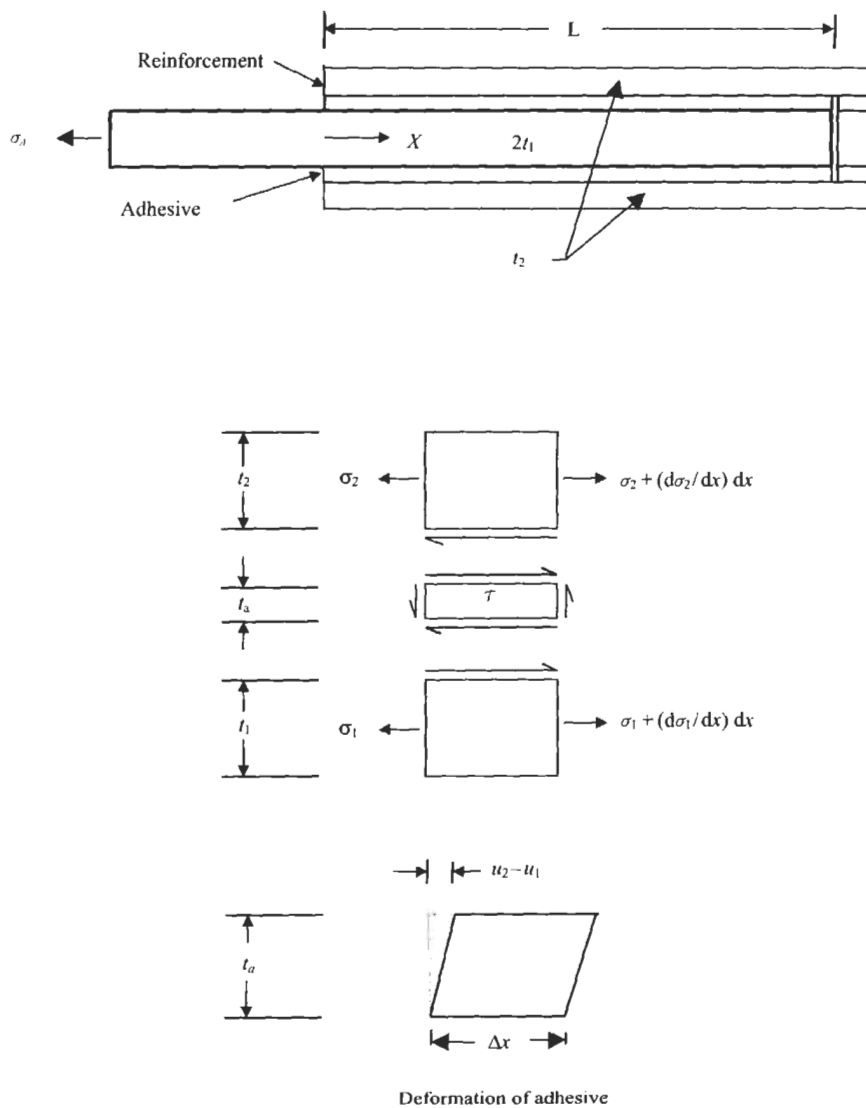


Fig. 11.10. One dimensional equation, definition of parameters.

G_a is the shear modulus of the adhesive.

From these equations the result is obtained:

$$\tau_{\max} = \frac{G_a l}{t_a} \left[\frac{\sigma_A}{E_l} + (\alpha_1 - \alpha_2) \Delta T \right], \quad (11.38)$$

where:

$$l = \left[\frac{t_a E_1 E_2 t_1 t_2}{G_a (E_1 t_1 + E_2 t_2)} \right]^{1/2} \quad (11.39)$$

For thermal stresses only $\sigma_A = 0$ and:

$$\tau = \frac{G_a l}{t_a} (\alpha_1 - \alpha_2) \Delta T e^{-x/l} \quad (11.40)$$

The direct stress for component 1 given by:

$$\sigma_1 = \frac{G_a}{t_a t_1} \left[\frac{\sigma_1}{E_1} + (\alpha_1 - \alpha_2) \Delta T \right] \left(e^{-x/l} - 1 \right) \quad (11.41)$$

At $x=0$, $\sigma_1 = 0$, and σ_1 rises to a maximum value when x is large which is given by:

$$\sigma_1 = -\frac{G_a}{t_a t_1} \left[\frac{\sigma_1}{E_1} + (\alpha_1 - \alpha_2) \Delta T \right] \quad (11.42)$$

If we consider a single lap joint in which bending is restrained and if the thickness of the skin is t_s , then $t_1 = t_s$.

11.2.4. Peel stresses

Comparisons of the F.E. are made with the d.e. expression, given by [11]. This expression can be used for a single lap joint but with no bending and is a function of the shear stress τ :

$$\sigma_p = -w_o E_c / t_a, \quad (11.43)$$

where

$$w_o = (A/2) \left(e^{\chi(x-1/2)} + e^{-\chi(x+1/2)} \right) \sin \chi x \\ + (B/2) \left(e^{\chi(x-1/2)} - e^{-\chi(x+1/2)} \right) \cos \chi x, \quad (11.44)$$

where

$$\chi = (E_c / (4D t_a))^{0.25}$$

$$A = (\tau(t_a / 2D) \sin \chi l / 2) / \chi^3$$

$$B = -(\tau(t_a / 2D) \cos \chi l / 2) / \chi^3$$

E_c = effective tensile modulus of the adhesive

τ = shear stress (normally taken to be the plastic value τ_p)

$D = E_o t_o^3 / 12(1 - \nu^2)$ and is the bending stiffness of boron

In this case the location of the coordinate system is at the midpoint of the joint, and $x = \pm l/2$ corresponds to the ends of the joint.

11.2.5. Coefficients of thermal expansion of a laminate

The material properties of the basic unidirectional laminate of boron/epoxy used in the 3D analysis are given in Table 11.8. For a thermal analysis of a multi-ply laminate it is necessary to compute the effective coefficients of thermal expansion in the material symmetry axes. Usually manufacturers' data will provide the longitudinal (α_1) and transverse (α_2) coefficient of thermal expansion for a unidirectional laminate. In this case the longitudinal coefficient of thermal expansion is a measure of the fibre property while the transverse coefficient is a measure of the resin property. The starting point for the derivation of overall coefficients of thermal expansion in a laminate is the well known stiffness matrices corresponding to in-plane stiffness, bending stiffness and coupling between in-plane and bending respectively:

$$[A] = \sum_{i=1}^k [\bar{Q}](z_i - z_{i-1}) \quad (\text{in-plane}) , \quad (11.45)$$

$$[B] = \frac{1}{2} \sum_{i=1}^k [\bar{Q}](z_i^2 - z_{i-1}^2) \quad (\text{coupling}) , \quad (11.46)$$

$$[D] = \frac{1}{3} \sum_{i=1}^k [\bar{Q}](z_i^3 - z_{i-1}^3) \quad (\text{bending}) , \quad (11.47)$$

where

$[\bar{Q}]$ is the reduced stiffness matrix of the laminate

$z_i - z_{i-1}$ is the thickness of each ply

k is the total number of plies in the laminate

If the analysis is restricted to symmetric laminates then it can be shown that the coefficient of thermal expansion is restricted to in-plane extensional stiffness only with no bending effects. The expression for the overall thermal expansion of the laminate is given by [12] as:

$$\{\alpha_x\} = -\frac{1}{\Delta T} [A]^{-1} \{N^T\} , \quad (11.48)$$

where:

$$\{N^T\} = \int_{-h}^h \sigma_x dz , \quad (11.49)$$

where the thermal contribution is given by:

$$\{\sigma_x\} = -[\theta][Q]\{\alpha_l\}\Delta T , \quad (11.50)$$

where $[\theta]$ is a 3×3 transformation matrix defined by:

$$\{\varepsilon_x\} = [\theta]\{\varepsilon_l\} , \quad (11.51)$$

where x denotes the laminate axis and l the ply axis. The individual terms are given by: $\theta_{11} = m^2$, $\theta_{12} = n^2$, $\theta_{13} = -2mn$, $\theta_{21} = n^2$, $\theta_{22} = m^2$, $\theta_{23} = 2mn$, $\theta_{31} = mn$, $\theta_{32} = -mn$, $\theta_{33} = m^2 - n^2$, $m = \cos \theta$, $n = \sin \theta$. The angle θ is from the laminate axis to the ply axis.

where $[Q]$ is a 3×3 elasticity matrix defined by:

$$\{\sigma_x\} = [Q]\{\alpha_l\} , \quad (11.52)$$

where x refers to the laminate axis and l to the ply axis. The individual terms are given by:

$$\begin{aligned} Q_{11} &= E_1/(1 - \nu^2 E_2/E_1) , \quad Q_{12} = \nu_{12} E_2/(1 - \nu^2 E_2/E_1) = Q_{21} , \\ Q_{13} &= Q_{23} = Q_{31} = Q_{32} = 0 , \quad Q_{22} = E_2/(1 - \nu^2 E_2/E_1) , \end{aligned}$$

$$\text{where } \{\alpha_l\}^T = \{\alpha_1, \alpha_2, 0\} , \quad (11.53)$$

finally integrating through the thickness:

$$\{N^T\} = -\Delta T \sum_{i=1}^k [\theta][Q]\{\alpha_l\}(z_i - z_{i-1}) \quad (11.54)$$

Hence substituting in Eq. (11.48) gives the overall laminate coefficient of thermal expansion.

In order to demonstrate the effect of ply lay-up on the effective coefficient of thermal expansion, an angle ply has been considered in which the $\pm\theta$ plies have been varied from 0 to $\pm 90^\circ$. The value of α_x is shown in Figure 11.11. Starting from a value of zero degrees α_x continually reduces until approximately 33 degrees, after which it continually increases to a maximum at 90 degrees. This corresponds to $19.1 \times 10^{-6}/^\circ\text{C}$ which is the transverse value for the unidirectional laminate. The resulting shape of the curve is dependent on both poisson's ratio effects (that are continuously changing), and plies values of α_1 .

The coefficients of thermal expansion, α_1 and α_2 , are the effective coefficients of thermal expansion for a unidirectional laminate. For a 3D laminate the out of plane coefficient of thermal expansion may be taken as being equal to the value α_2 in the unidirectional lay-up.

In Table 11.3 a comparison has been made between the coefficients of thermal expansion for a unidirectional laminate and a lay-up consisting of $\{0_2, \pm 45, 0_3\}_S$. The overall effect of the Poisson's ratio and the lay-up is to produce an effective coefficient in the longitudinal direction (α_L) higher than the unidirectional lay-up and a transverse coefficient (α_T) lower than the unidirectional lay-up.

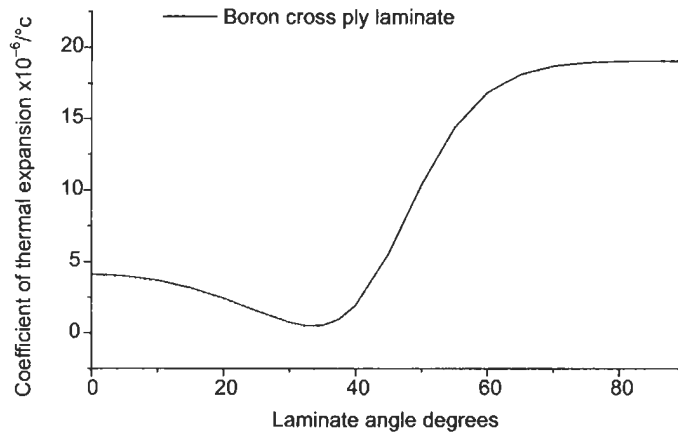


Fig. 11.11. Cross ply laminate coefficient of thermal expansion, α_x , versus laminate angle.

11.3. Finite element thermal stress analysis

As a result of the increasing trend towards computational stress analysis it is worthwhile looking at the equations used by F.E. analysis. A thermal stress analysis is usually carried out with the intention to calculate thermally induced stresses, strains or displacements. Thermal stresses may arise, for example, in a bonded joint consisting of materials with different thermal coefficients of thermal expansion. Thermal stresses may occur in a heated structure which is rigidly constrained, and also in a structure with temperature gradients. As previously mentioned, a thermal stress analysis is usually carried out in two steps, the first being the thermal analysis which will calculate temperatures at each node, and the second to calculate the corresponding stresses and displacements.

The governing equation for heat flow problems is:

$$\nabla^2 T = Q, \quad (11.55)$$

where Q is the heat flux.

Table 11.3

Thermal expansion coefficients for unidirectional boron/epoxy, and values computed for a Boron/epoxy laminate.

Coefficient of expansion	Unidirectional [19]	$[0_2, \pm 45, 0_3]_s$
α_L (longitudinal)	4.1×10^{-6}	3.76×10^{-6}
α_T (transverse)	19.1×10^{-6}	12.29×10^{-6}

For F.E. analysis the equations that govern the non-linear heat transfer analysis are given in matrix form by [13]:

$$[C]\{T\} + [R]\{T + T_{\text{ABS}}\} = \{Q\} + \{N\} , \quad (11.56)$$

where:

$[C]$ is the conductivity matrix

$[R]$ is the radiation exchange matrix

$\{T\}$ is the nodal temperature vector

$\{Q\}$ is the heat flux vector

$\{N\}$ is the non-linear heat flux vector that depends on temperature

T is the temperature

T_{ABS} is the absolute temperature

For steady state conduction and where the radiation losses are insignificant the equations are linear and reduce to:

$$[C]\{T\} = \{Q\} \quad (11.57)$$

The boundary conditions may be specified as temperatures or heat flux at nodes. A partitioning of Eq. (11.57) is carried out into unknown and known temperatures. If the heat flux is known at a node, then the temperature is treated as being unknown at that node. The thermal solution carried out by NASTRAN, PAFEC and ABAQUS use elements whose properties are dependent on the geometry and thermal conductivity for that material. This analysis solves for the temperature vector and writes it to an output file for use in the structural analysis that follows.

The static structural solution involves the matrix equations:

$$[K]\{d\} = \{P\} + \{P_T\} , \quad (11.58)$$

where:

$[K]$ is the structure stiffness matrix

$\{d\}$ is the displacement vector

$\{P\}$ is the applied load

$\{P_T\}$ is the thermal load vector and is given by:

$$\{P_T\} = \int [B][D][\alpha]\{T\} dv , \quad (11.59)$$

where:

$[B]$ relates strains to displacements

$[D]$ is the elasticity matrix

$[\alpha]$ are the coefficients of expansion

$\{T\}$ is the temperature vector from the thermal solution

dv integration is taken over the volume.

The thermal load vector is added to any applied loads that exist, and the usual displacement solution is obtained. This corresponds to the second NASTRAN,

PAFEC and ABAQUS run in which the previously calculated temperatures in the output file are read back in.

11.3.1. Two-dimensional strip joints

A 2D F.E. (plane stress) analysis has been carried out for a bonded joint whose geometry is shown in Figure 11.10. Only 2D isotropic, 8 noded quadrilateral elements are used in the analysis, and all lie in the xy plane. While Figure 11.12 is a diagram only, the area which is refined is indicated. The temperature throughout the joint is set at 100°C with a reference temperature of 0°C . The relevant coefficients of thermal expansion are shown in Table 11.5, which may be derived from figures in Tables 11.3 and 11.4.

In the structural analysis that follows, the corresponding structural properties used, are shown in Table 11.6. While the adhesive also has a coefficient of thermal

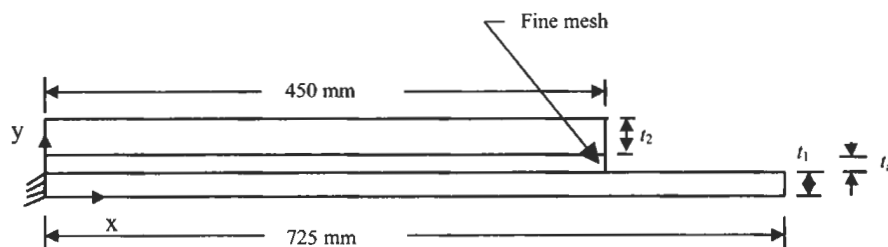


Fig. 11.12. Two dimensional strip joint subject to temperature change, with bending restrained.

Table 11.4
Properties of unidirectional Boron/epoxy, [14].

E_{11} (MPa)	E_{11}/E_{22}	ν_{12}	G (MPa)
207000	10.89	0.21	4800

Table 11.5
Thermal properties in 2D isotropic joint.

Component	Coefficient of thermal expansion 1°C
α_1 (Aluminium)	23×10^{-6}
α_2 (Boron laminate)	3.76×10^{-6}

Table 11.6
Mechanical properties of 2D strip.

t_1	t_2	t_a	ν_1	ν_2	ν_a	E_1	E_2	G_a
3.6	1.778	0.254	0.3	0.3	0.35	71016.0	156000.0	842.0

expansion it is neglected in order to make the best comparison with the 1D d.e. given by Eq. (11.40). In the analysis the restraints used are:

1. restraints are used in the x direction for all nodes located on component 1 with co-ordinates of $x=0$
2. restraint in the y direction for all nodes in component 1 with the co-ordinate of $y=0$.

The restraints in the y direction have been applied to prevent bending of component 1, so that a direct comparison can be made with the 1D d.e. The d.e. results are based on Eq. (11.40). Also in this analysis no non-thermal loads have been applied.

A comparison of the shear stress is made on the basis of shear stress taken directly from the F.E. results corresponding to the midplane of the adhesive are shown in Figure 11.13. The F.E. results for the 2D isotropic case are about 2.5% lower than the 1D d.e.

Overall the difference in results between the 2D F.E. and 1D d.e. do not necessarily indicate the existence of an error in either solution. Factors that may influence results are firstly the Poisson's ratio effect which is not considered in the 1D d.e. Secondly, in the F.E. analysis shear deformation occurs in all components of the joint, while in the 1D d.e. it only occurs in the adhesive. Furthermore, the F.E. analysis of bonded repairs in general shows a considerable variation in shear stress from the patch/adhesive interface to the plate/adhesive interface as shown in Figure 11.13.

To achieve good results in the F.E. analysis a very fine mesh of 0.05 mm increments has been required to pick up the rise from $\tau=0$ to a maximum at up to

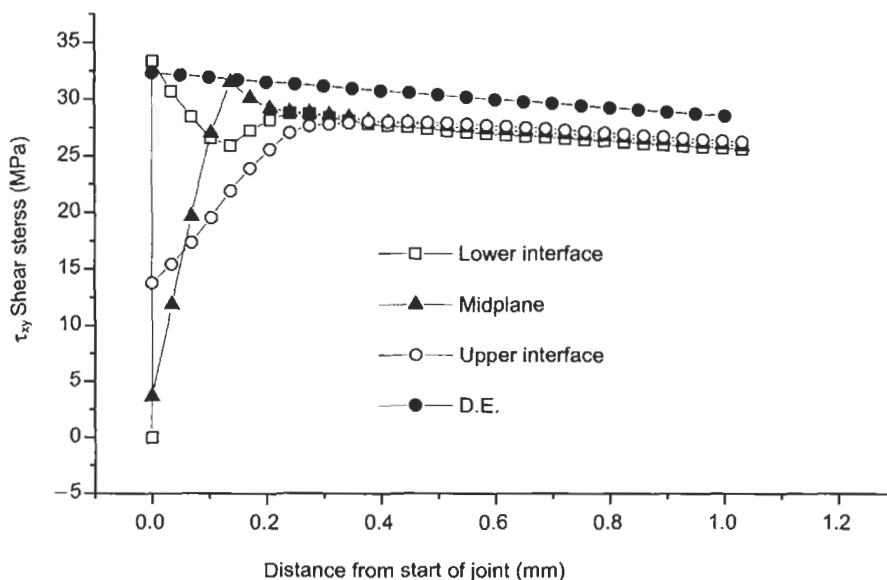


Fig. 11.13. Thermal adhesive shear stresses in 2D bonded strip joint.

0.25 mm away from the end of the joint. This distance is approximately equal to the thickness of the adhesive. In the case of the d.e. the formulation is such that the maximum value occurs at the end of the joint. Also the decay of the F.E. and d.e. results are the same.

In the case just considered the F.E. analysis was confined to the analysis of isotropic materials. Now consider the case in which component 2 has orthotropic properties. Composite materials are orthotropic and bonded joints are often comprised of such materials. In the repair of cracked metallic structures, materials such as boron/epoxy laminates are used as reinforcement. Consider a 2D analysis in which E_X is the major modulus of the laminate and E_Y represents the modulus perpendicular to the laminate. In this case the shear modulus is taken as that for a unidirectional layer of boron/epoxy. Using typical properties for the boron/epoxy and making a comparison with the 1D d.e. on the basis of $E_2 = E_X$ gives the results shown in Figure 11.13. The isotropic solution was found to give almost identical results and have has not been plotted. Comparison of the shear stresses obtained by the F.E. and 1D d.e. show that the midplane 2D orthotropic results are about 2.5% lower than the 1D d.e.

11.3.2. Three-dimensional strip joints

A 3D F.E. thermal analysis, using 20 noded brick elements, has been carried out for the structure defined in Figure 11.14, which is fully restrained at the right hand end. Also, bending in the y direction has been restrained. To simplify matters the $[0_2, \pm 45^\circ, 0_3]$ laminate is assumed to be homogenous orthotropic, where the principal material symmetry axis is in the x direction. The mechanical properties of the laminate are derived from the uni-directional properties in Table 11.3 and are shown in Table 11.7. The coefficients of thermal expansion are calculated using Eqs. (11.48) and (11.54) and are also shown in Table 11.3. The mesh used for the width of the patch involves 0.05 mm increments at both the free edge and centreline. The overall effect of the Poisson's ratio and angle ply layup is to produce an effective coefficient in the longitudinal direction (α_L) lower than the uni-directional lay-up and transverse coefficient (α_T) also lower than the uni-directional lay-up. The value used by the 1D d.e. is α_L .

This joint is subject to a uniform temperature of 100 °C. The resulting τ_{XY} shear stresses have been evaluated at points A and B which are located as shown in Figure 11.14. It was found that the τ_{XY} shear stresses were 13% higher at location A than location B and these are plotted in Figure 11.15. The 3D results are the most accurate computation of the shear stresses and exceed that predicted by the d.e. by 15%. Again shear stresses considered are those in the midplane of the adhesive. Although results are not presented, if transverse coefficients of thermal expansion are ignored and set to zero, this may result in 8% higher shear stresses. It is evident that an interaction is occurring between the Poisson's ratio effect and the two coefficients of thermal expansion. Clearly a 3D analysis is significantly different to a 1D analysis when both longitudinal and transverse coefficients of thermal expansion exist. While the 1D d.e., Eq. (11.40), provides a close estimate shear

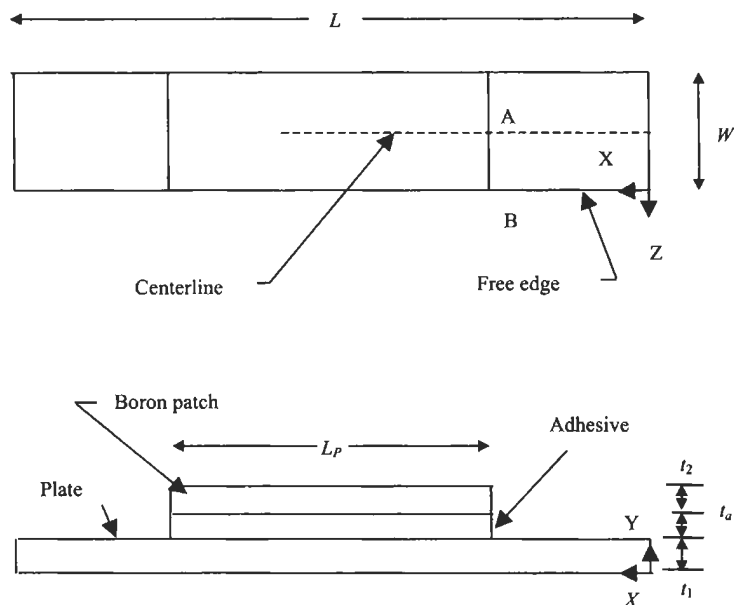


Fig. 11.14. Three dimensional bonded joint subject to uniform temperature change.

Table 11.7

Overall properties of the Boron patch for patch lay-up of $[0_2, \pm 45, 0_3]_s$.

$$E_{XX} = 156107. \quad E_{YY} = 29781. \quad \nu_{XY} = 0.574884 \quad \nu_{YX} = 0.109675 \quad G_{XY} = 190651.$$

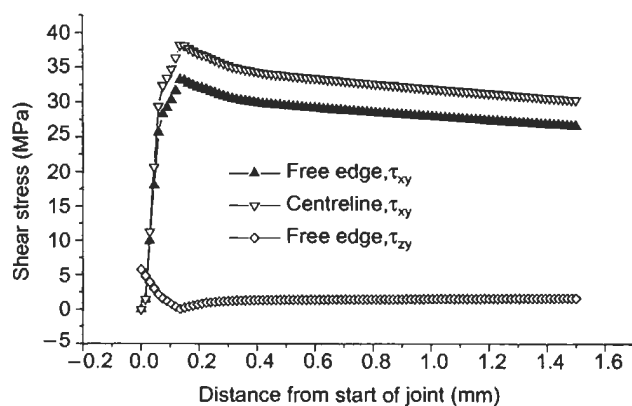


Fig. 11.15. Solutions for 3D bonded strip joint on the centre line and very close to the free edge.

stresses at the free edge it under-predicted the maximum value by 15%. Note that at the free edge a τ_{ZY} shear stress component exists with maximum value of 6 MPa, Figure 11.15.

11.4. Application of analysis to large repairs of aircraft wings

The object of this section is to determine the applicability of a closed form solution to the large repair of an aircraft wing, whose cross section is shown in Figure 11.16. In this case the repair covers one spar and two of the cells. While the application of closed form solutions to repairs bounded by spars and ribs is reasonable, the application of closed form solutions to large repairs presents difficulties. In this section a simplified multi-spar wing FE model is considered and has properties at the repaired site similar to an F-111 wing. The wing is only constrained at the wing root and a repair is considered over the middle spar. A similar repair has been carried out on an F-111 wing, [15]. In this case the repair considered was rectangular of size 450 mm in the spanwise direction and 300 mm in the chordwise direction with the repair centred over the forward auxiliary spar, rather than the middle spar. Since heat losses to the surrounding air will occur due to convection, the actual temperature distribution was determined during a simulation of the curing cycle, [16], and are shown in Figures 11.17 and 11.18. This has been adjusted for a cure cycle of 100 °C and a room temperature of 25 °C and will be applied to the FE wing model. The alternative procedure is to specify a convection heat transfer coefficient, h , in the thermal analysis, in which the rate of

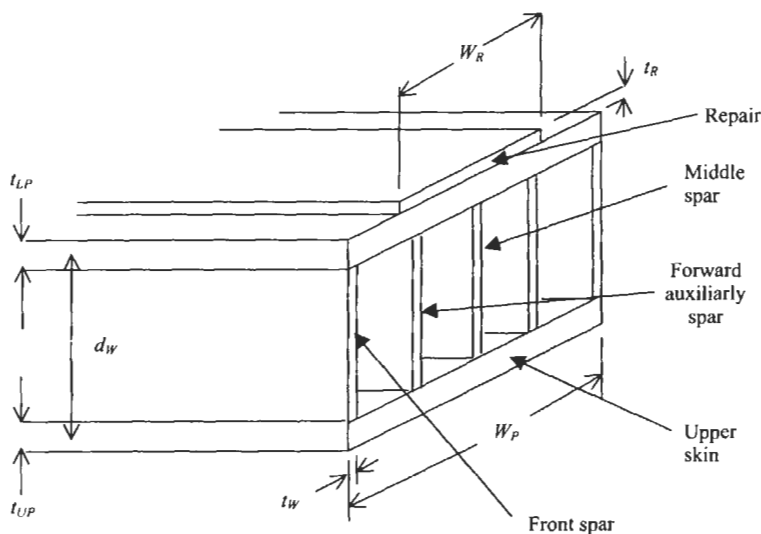


Fig. 11.16. Cross-section of multi-spar wing (up-side down), flanges not shown.

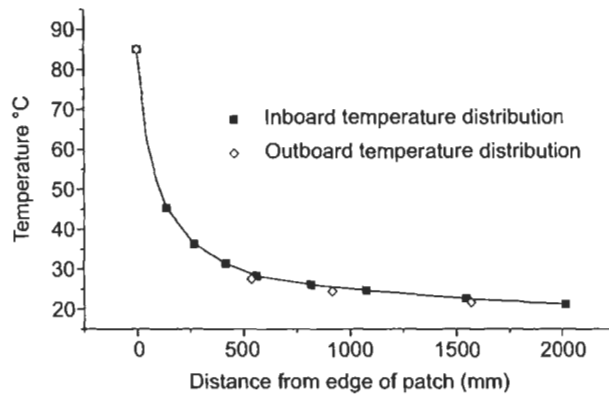


Fig. 11.17. Spanwise variation of temperature for simulated curing.

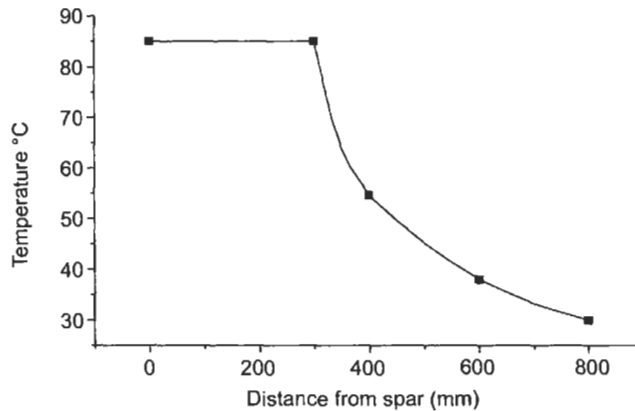


Fig. 11.18. Chordwise variation of temperature for simulated curing.

heat transfer is, in its simplest form, given by [17] as:

$$Q = hA(T_S - T_f) , \quad (11.60)$$

(This is also known as heat flux, as shown in Eq. (11.56))

where

T_S is the temperature of the surface

T_f is the air temperature

where h is the heat transfer coefficient and needs to be experimentally determined.

This wing model is idealised using shell elements for the skins (plates) and spar webs, and rod elements for the spar flanges. The dimensions are shown in Table 11.8. Also the adhesive has been ignored and the boron fibre patch is considered to be welded to the plate, i.e. composite shell elements overlay the plate. In other words, it is assumed that bending is fully restrained. In this analysis we will

Table 11.8
Dimensions of wing box in mm.

Overall length	4300.0
Distance of patch centre to wing tip	2300.0
w_p	800.0
d_w	185.0
w_r	400.0
t_{UP}	3.6
t_{LP}	3.6
t_W	2.5
l_p	400.0
t_R	1.778
Flange areas	200.0 mm ²

consider a repair using both a uni-directional boron laminate and an angle ply laminate.

11.4.1. F.E. analysis

The first step in the F.E. analysis is to determine the initial stresses with no repair. In this case the temperature distribution is determined in the complete structure. Known temperatures are input into the model and the unknown temperatures are found during the thermal analysis as shown in Figure 11.19. The corresponding structural analysis then determines the distribution of initial stresses throughout the F.E. model as shown in Figure 11.20. These stresses are spanwise components. Note that tensile stresses on the edge of the wing box exist to restore the equilibrium. The next step in the analysis involves the cooling down of the F.E. model which in this case also contains the boron patch. In this case the sign of the temperatures is changed (Figure 11.21), and the thermal and corresponding structural analysis is run, with results shown in Figures 11.22 and 11.23. In Figure 11.22 the spanwise stresses in the plate of a repaired wing are shown, while Figure 11.23 shows the spanwise stresses in the patch, and plate outside the repair. Significant variations of stress occur from the centre and edges of the repair, and also plate stresses beneath the repair. The stresses shown in the patch are the final residual stresses, while the residual stresses in the plate are a sum of the initial stresses and stresses due to cooling. In both Figures 11.22 and 11.23 stresses exist on the top edges of the wing box to restore equilibrium. Initially, only the stresses in the centre of the plate and patch are considered, Tables 11.9 and 11.10.

For the heating up of the F.E. model spanwise displacements have been computed in the area that is to be repaired. From these results it is possible to compute the effective coefficient of thermal of expansion of the aluminium wing in this region. A slight variation occurs across the patch in a chordwise direction and an average spanwise value of $16.76 \times 10^{-6}/^{\circ}\text{C}$ is obtained. This is comparable with Eq. (11.7) where $\alpha_{\text{eff}} = 14.95 \times 10^{-6}/^{\circ}\text{C}$ for a bi-axial stress state in a circular repair on a circular plate, fully restrained at the edges.

The F.E. results for the $[0_2, \pm 45, 0_3]_S$ and $[0_7]_S$ laminates are contained within Tables 11.9 and 11.10 respectively. These tables contain results corresponding to

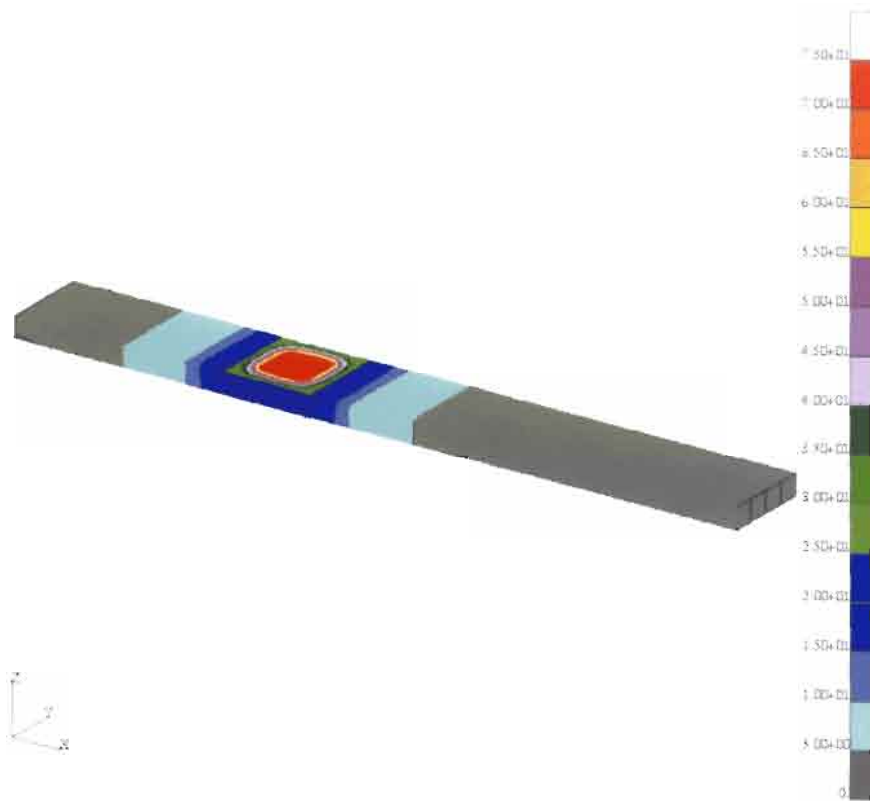


Fig. 11.19. Distribution of temperature for heating process only. The repair is closest to the wing tip, the wing being completely restrained at the root end only.

the initial stresses, stresses due to cooling and residual stresses for both F.E. and closed form solutions.

The first closed form solution is that from [2]. In this case the residual stresses are obtained directly. The first equation for the residual stress under the patch is given by:

$$\sigma_1 = \frac{E_1 s \Delta T (\alpha_1 - \alpha_2)}{(1 + s)} \quad (11.61)$$

The equation for the residual stress in the patch is given by:

$$\sigma_B = \frac{-\sigma_1 t_A}{t_B} \quad (11.62)$$

The results for these equations are based on the direct value of $\alpha_1 = 23 \times 10^{-6} / ^\circ\text{C}$. The results over predict the residual stress in the plate, but does give a close value for the residual stress in the patch. Although not shown, results based on $\alpha_1 =$



Fig. 11.20. Spanwise stresses corresponding to thermal loading as a result of heating. (This model does not include the patch). Note the tension stresses on the top edge of the wing.

$14.95 \times 10^{-6}/^{\circ}\text{C}$ do more accurately predict the residual stress in the plate but significantly under predict the stress in the patch.

The 2D closed form solutions derived from circular patches on circular plates will now be considered, the first being the isotropic solution and the second the orthotropic solution. Application of a closed form solution to the repair of an aircraft wing requires an assumption of the value of R_O to be used. Previous results have shown limiting stress values are obtained for large R_O/R_I ratios, hence these are the results shown in Tables 11.9 and 11.10.

Consider now the residual stresses predicted by the 2D isotropic solution. From both Tables 11.9 and 11.10 these values show conservative agreement for residual stresses in the plate beneath the patch, slightly un-conservative stresses in the patch and un-conservative values in the plate just outside the patch.

The 2D orthotropic solution, shown in Table 11.9, gives much the same results as the 2D isotropic solution except that it can predict both stress components for the orthotropic patch material. However the stress perpendicular to the spanwise axis has been found to be much lower than the spanwise component and hence is not as important.

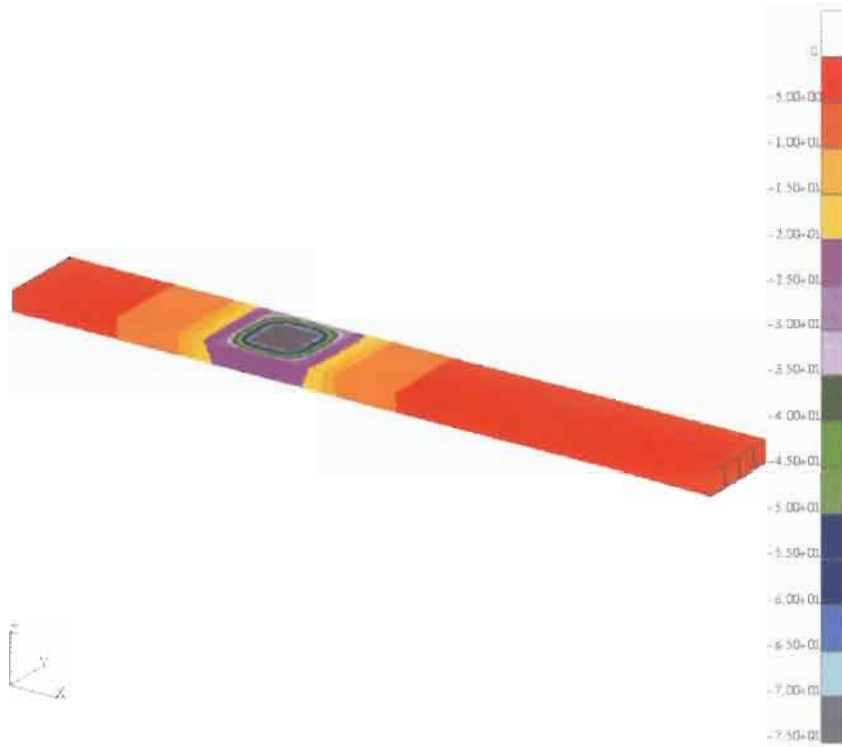


Fig. 11.21. Distribution of temperature for cooling down process only. The repair is closest to the wing tip, the wing being completely restrained at the root end only.

Overall the 1D solution compares more favourably with the F.E. than 2D solutions, since with the wing tip unrestrained the problem is closer to a 1D problem. The main reason for the difference of 2D and FE solutions is that the analytical models do not take into account the stiffness and temperature distributions of the spar webs and upper skin structure. It is clear that for accurate thermal stress analysis of a large repair to a wing structure the FE method is the most suitable.

11.4.2. Edge restraint factor

If a suitable edge restraint factor, k , can be found, see Figure 11.1, then it may be possible to more accurately predict stresses in the wing using 2D closed form solutions. Returning to Eq. (11.13) if the boundary condition $u = 0$ at $r = R_O$ is changed to $u = \bar{u}$ then Eq. (11.13) can be written as:

$$\sigma = -\frac{\alpha_1 E_1}{2} \left\{ T_I + \frac{(1+\nu)}{(1-\nu)} \left[T_O + \frac{(T_I - T_O)}{2 \ln(R_I/R_O)} \left(\frac{R_I^2}{R_O^2} - 1 \right) \right] \right\} + \frac{E_1 \bar{u}}{(1-\nu)R_O} \quad (11.63)$$

This represents the initial stress as a result of displacement of the outer edge of the plate which has stiffness k .

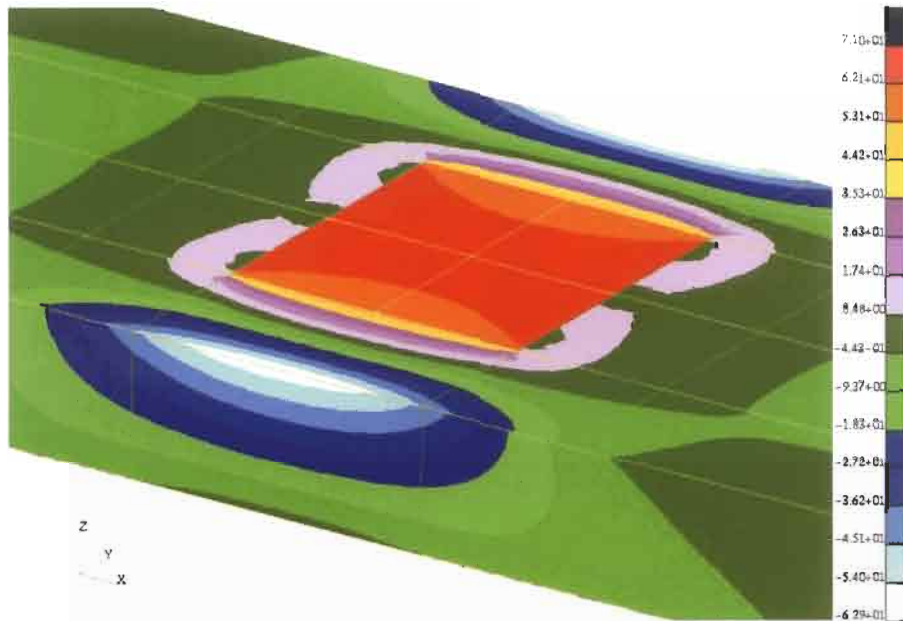


Fig. 11.22. Spanwise stresses, shown in the plate only, corresponding to a cooling thermal loading. The repair lay-up is $[0_2, \pm 45, 0_3]_S$. Note the compressive stresses on the top edge of the wingbox.

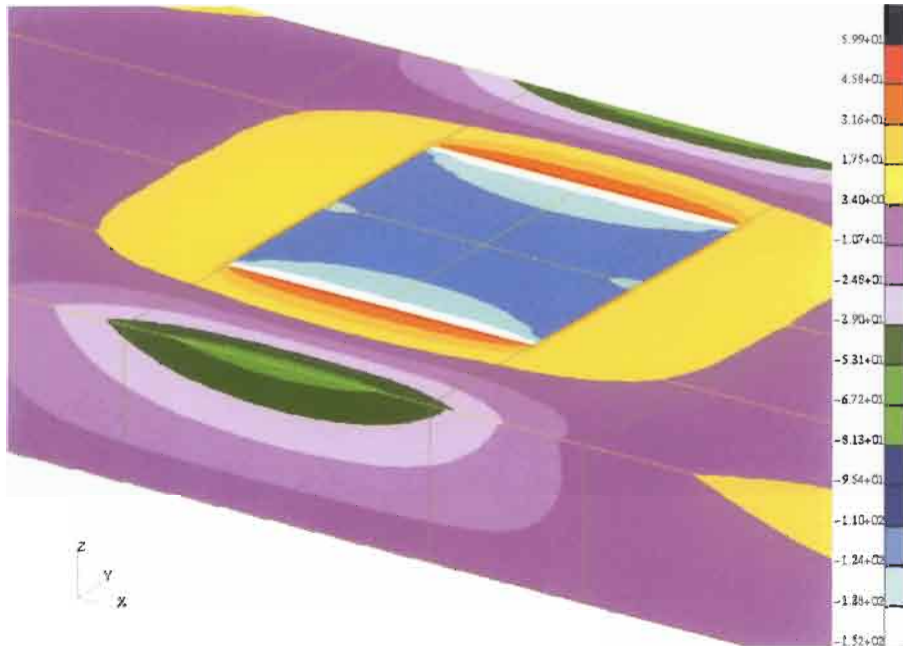


Fig. 11.23. Spanwise stresses in boron patch and stresses in plate surrounding the repair, corresponding to a cooling thermal loading for a repair with a lay-up of $[0_2, \pm 45, 0_3]_S$.

Table 11.9

Stresses predicted in wing box corresponding to a geometric symmetric repair; layup $[0_2, \pm 45, 0_3]_S$ boron repair $\Delta T = 75^\circ\text{C}$.

Thermal loading	Centre of plate under repair (MPa)				Centre of patch (MPa)				Plate just in/outboard of patch (MPa)	
	F.E.	1D	2D (iso.)	2D (orth.)	F.E.	1D	2D (iso.)	2D (orth.)	F.E.	2D (isot.)
Heating	-11.6	-	-68.6		0		0		-11.6	-68.6
Cooling	67.3	-	111.0		-113.0	-	-64.3	-63.3	9.2	57.6
Residual	55.7	46.5	42.4		-113.0	-94.2	-64.3	-63.3	-2.4	-11.0

Table 11.10

Stresses predicted in wing box corresponding to a geometric symmetric repair; $[0_{14}]$ boron repair. $\Delta T = 75^\circ\text{C}$.

Thermal loading	Centre of plate under repair (MPa)				Centre of patch (MPa)				Plate just in/outboard of patch (MPa)	
	F.E.	1D	2D (iso.)	2D (orth.)	F.E.	1D	2D (iso.)	2D (orth.)	F.E.	2D (isot.)
Heating	-11.6	-	-68.6		0		0		-11.6	-68.6
Cooling	58.4*	-	95.0		-131.0	-	-91.9	-	13.6	50.7
Residual	46.8*	52.8	26.4		-131.0	-107.0	-91.9	-	1.8	-17.9

Table 11.11

Stresses predicted in wing box corresponding to a geometric symmetric repair; layup $[0_2, \pm 45, 0_3]_S$ boron repair. $\Delta T = 75^\circ\text{C}$, $k = 4.42 \times 10^6 \text{ N/mm}$.

Thermal loading	Plate under repair (MPa)		Patch (MPa)	
	F.E. (centre/edge)	2D (iso)	F.E. (centre/edge)	2D(iso)
Heating	- 11.6/-13.2	- 9.7		
Cooling	54.7/67.8	65.8	- 113.0/- 139.7	- 154.0
Residual	43.1/54.6	56.1	- 113.0/- 139.7	- 154.0

Also Eq. (11.20) becomes:

$$\bar{u} = \frac{\alpha_1(1+\nu)}{R_O} \int_{R_I}^{R_O} Trdr + C_2 R_O + \frac{C_3}{R_O}, \quad (11.64)$$

at $r = R_O$ the stresses due to cooling at the boundary are given by Eq. (11.16):

$$\sigma_R = \frac{\alpha_1 E_1}{4} \left[\frac{T_I}{\ln(R_I/R_O)} \right] + \frac{E_1}{(1-\nu^2)} \left[C_2(1+\nu) - \frac{C_3(1-\nu)}{R_O^2} \right] \quad (11.65)$$

The constants of integration C_2 and C_3 are now found from the solution of Eqs. (11.18, 11.19, 11.63). If the edge restraint factor is denoted by k then the displacement \bar{u} is given by:

$$\bar{u} = 2\pi R_O t_1 \sigma_R / k. \quad (11.66)$$

Furthermore if R_O is chosen to be approximately 2000mm on the basis of temperature measurements, then it is possible to choose a value k which when incorporated in the analysis will give better agreement, as shown in Table 11.11. However it is clear that these results still involve some error, and as a result F.E. analysis is still recommended. Also as mentioned previously the F.E. method has also shown some variation, see Table 11.11, of stress under the patch and in the patch where in both cases the closed form solution predicts uniform stress. In Table 11.11 the edge of the plate is defined by the following. Consider the axis system shown in Figure 11.23 to be translated to the centre of the patch. The particular edge considered is defined by $x=0$, $y = \pm 200 \text{ mm}$.

11.5. Conclusions

In this chapter some proposed closed form solutions for direct residual stresses in bonded repairs have been considered. 2D solutions considered are for direct stresses in the plate beneath the repair, stresses in the repair and stresses in the plate just outside the repair. These solutions are restricted to steady state heat conduction, and are for both isotropic and orthotropic circular patches on circular

plates. Validation of these solutions has been carried out using F.E. analysis. The applicability of these equations is restricted to repairs which are bounded by structural members such as spars or ribs.

Adhesive shear stresses have been evaluated in 1D strip joints subject to a uniform temperature. In this case results have been considered from the simple differential equation, and also 2D and 3D F.E. models. It has been found that the simple d.e. gives results which exceed 7.5% of the results given by 3D F.E.

A multi-spar wing box containing a very large repair in which bending is restrained has also been considered. In this case the temperature field was based on a simulation cure on a F-111 wing. The results have been obtained using a F.E. model in which the repair site is similar to an F-111 wing. Comparison with predictions using 1D and 2D closed form solutions have shown that 1D solutions give better agreement than 2D solutions. However when an appropriate edge restraint factor is used then the 2D solution improves. Only small differences occur between the 2D isotropic and orthotropic results, except that isotropic solution will over-predict the stresses in the minor material symmetry axis.

While the effective coefficient of thermal expansion used for biaxial stress state has given good agreement with the geometrically symmetric multi-spar wing repair, the asymmetric repair results in lateral bending and an average effective coefficient of expansion which exceeds the closed solution value. It is evident that more analytical work is required in this area.

Acknowledgment

The author would like to thank Mr S. Sanderson for assistance with the F.E. work carried out in this chapter.

References

1. Baker, A.A., Hawkes, G.A. and Lumley, E.J. (1978). Fibre composite reinforcement of cracked structures – thermal – stress and thermal – fatigue studies. *ICCM2 Proceedings of the 1978 Int. Conf. on Composite Materials* (B. Noton, R. Sigorelli, K. Street, eds.). April, Toronto, Canada.
2. Rose, L.R.F. (1982). A cracked plate repaired by bonded reinforcements. *Int. J. Fracture*, **18**, pp. 135–144.
3. Baker, A.A. (1988). Crack patching: experimental studies, practical applications. *Bonded Repair of Aircraft Structures* edited by (A.A. Baker and R. Jones, eds.). Martinus Nijhoff Publishers, Dordrecht, pp. 107–173.
4. Rose, L.R.F. (1988). Theoretical analysis of crack patching. *Bonded Repair of Aircraft Structures* (A.A. Baker and R. Jones, eds.). Martinus Nijhoff Publishers, Dordrecht, pp. 77–106.
5. Callinan, R.J., Sanderson, S., Tran-Cong, T., *et al.* (1997). Development and validation of a Finite element based method to determine thermally induced stresses in bonded joint of dissimilar materials, *DSTO RR-0109*, Aeronautical and Maritime Research Laboratory, Melbourne, Australia.

6. Callinan, R.J., Ton Tran-Cong, Sanderson, S., *et al.* (1998). Development of an Analytical Expression and a Finite Element Procedure to Determine the Residual Stresses in Bonded Repairs. Paper A98-31608 21st ICAS Congress, 13-18 Sept. Melbourne, Australia.
7. Wang, C.H., Rose, L.R.F., Callinan, R.J., *et al.* (2000). Thermal stresses in a plate with circular reinforcement. *Int. J. Sol. and Structures*, **37**, pp. 4577-4599.
8. Wang, C.H. and Erjavec, D. (2000). Geometrically linear analysis of the thermal stresses in one sided composite repairs. *Journal of thermal stresses*, **23**, pp. 833-852.
9. Jones, R. and Callinan, R.J. (1981). Thermal considerations in the patching of metal sheets with composite overlaps. *J. of Structural Mechanics*, **8**.
10. Timoshenko, S.P. and Goodier, J.N. (1970). *Theory of Elasticity*, Third edition, McGraw-Hill.
11. Hart-Smith, L.J. (1973). Adhesive-Bonded Double-Lap Joints. NASA CR 112235, January.
12. Humphreys, E.A. and Rosen, B.W. Properties analysis of laminates. *Composite Materials and Design*, pp. 218-230.
13. Blakely. MSC/NASTRAN, basic dynamics analysis, user's guide. The MacNeal-Schwendler Corporation, Dec. 1993.
14. Hadcock, R.N. (1969). Table 24.3, Boron-Epoxy Aircraft Structures Handbook of Fibreglass and Advanced Plastic Composites. Editor G.Lubin, Van Nostrand Reinhold Company.
15. Callinan, R.J., Sanderson, S. and Keeley, D. (1997). Finite element analysis of an F-111 Lower Wing Skin Crack Repair. DSTO-TN-0067, January.
16. Mirabella, L. and Callinan, R.J. Temperature Simulation of Boron/epoxy Patch Repair Site on a F-111 Outer Lower Wing Skin. Draft report.
17. Rohsenow, W.M., Hartnett, J.P. and Cho, Y.I. (1998). Handbook of Heat Transfer, McGraw-Hill.

Appendix

The displacement at $r = R_I$ is given by:

$$u = \frac{(1 + \nu)}{2} R_I \times \frac{2((\alpha_O T_I - \alpha_I T_O) + \alpha_I R_I^2 (T_I - T_O) / (R_O^2 - R_I^2)) + \alpha_O T_I s + \alpha_I (T_I - T_O) / (\ln R_I / R_O)}{2R_O^2 / (R_O^2 - R_I^2) + s(1 + \nu)}$$

The integration constants are given by:

$$C_2 = -\frac{(1 + \nu)}{4} \frac{D_1 + D_2}{2R_O^2 + s(R_O^2 - R_I^2)(1 + \nu)}$$

where

$$D_1 = 2(T_O s(R_O^2 - R_I^2)\alpha_I(1 + \nu) + 2\alpha_O T_I R_I^2(1 + s)) - (R_O^2 - R_I^2)s\alpha_I(T_I - T_O) \times (1 + \nu) / (\ln R_I / R_O)$$

and

$$D_2 = (2s\alpha_1 R_I^2(1+\nu)(T_O - T_I) + 4\alpha_1(T_O(R_O^2 - R_I^2) - R_I^2(T_I - T_O))) \\ - 2\alpha_1(R_O^2 - R_I^2)(T_I - T_O)(1+\nu)/(\ln R_I/R_O) \\ C_3 = \frac{(1+\nu)}{4} R_I^2 \frac{F_1 + F_2}{2R_O^2 + s(1+\nu)(R_O^2 - R_I^2)}$$

where

$$F_1 = 2(s\alpha_1(1+\nu)(T_O R_O^2 - T_I R_I^2) + 2\alpha_O T_I R_O^2(1+s))$$

and

$$F_2 = -(R_O^2 - R_I^2)s\alpha_1(T_I - T_O)(1+\nu)/(\ln R_I/R_O).$$

Chapter 12

FATIGUE CRACK GROWTH ANALYSIS OF REPAIRED STRUCTURES

C.H. WANG

Defence Science and Technology Organisation, Air Vehicles Division, Fishermans Bend, VIC 3207, Australia

12.1. Introduction

The primary function of composite repairs is to restore or improve the damage tolerance of the repaired structure. To this end, it is essential to demonstrate by analysis and/or test that the repair can meet the residual strength and damage tolerance requirements. This means that the stress-intensity factor after repair has been sufficiently reduced so that (i) the residual strength has been restored to an acceptable level, and (ii) the growth rate of the crack under fatigue condition is sufficiently slow to ensure an acceptable residual life, or inspection interval. In this regard, theoretical and numerical analyses of repair efficiency are respectively discussed in Chapters 7 and 9, while experimental investigations of the fatigue crack growth are described in Chapter 13. The aim of this chapter is to present an analytical method for predicting the growth rates of patched cracks, and hence the residual life or inspection interval. Emphasis will be given to the modelling of the crack closure behaviour of patched cracks under constant amplitude and variable amplitude loading. Comparison with experimental results will be made whenever possible to validate the proposed methodology.

Extensive experimental studies, see Chapter 13 of this book and References [1–3], have demonstrated the effectiveness of bonded repairs as a cost-effective means of repairing cracked structures, in terms of restoring the residual strength to the design level and significantly reducing fatigue crack growth rate. However, it remains a challenging task to predict the growth rate of patched cracks using the crack growth data obtained from un-patched specimens, especially under spectrum loading. For un-patched cracks, it is now possible to obtain satisfactory predictions of the effects of stress ratio and variable amplitude loading on fatigue crack growth rate using crack-closure models [4]. The aim of this chapter is to establish a

correspondence principle between patched cracks and un-patched cracks, with particular emphasis on the crack-closure behaviour under steady-state (constant amplitude loading) and transient conditions (spectrum loading). The effect of thermal residual stress resulting from the mismatch between the coefficients of thermal expansion for the composite patch and the parent metallic material will also be considered.

A repaired crack can be viewed as being bridged by a series of distributed springs sprang between the crack faces [5,6]. Under fatigue loading, these springs restrain the opening of the crack, and thus reducing the stress-intensity factor. To analyse the effect of this bridging mechanism on the residual plastic wake behind the crack tip, the crack bridging theory [6] is employed together with a crack-closure model [7] to analyse the steady-state closure of patched cracks subjected to constant amplitude loading. The analytical consideration proves that under small-scale yielding condition (the applied stress is far smaller than the material's yield stress), the steady-state crack closure level depends only on the applied stress ratio and is almost identical to that corresponding to un-repaired cracks subjected to the same applied stress ratio. This finding has been verified by a finite element analysis. Furthermore, the transient crack closure behaviour following an overload, which is the main mechanism responsible for crack growth retardation, has also been investigated by the finite element method. The results reveal that patched cracks exhibit the same transient decrease/increase in the crack-closure stress as un-patched cracks. Based on these findings, a correspondence principle relating the transient crack-closure behaviour of patched cracks to that of un-patched cracks is proposed. It is finally shown that predictions based on this method are in good agreement with the experimental results obtained using two aircraft loading spectra.

12.2. Crack-closure analysis of repaired cracks

12.2.1. Small-scale yielding

A schematic of a patch repair is shown in Figure 12.1, where it is assumed for simplicity that the cracked plate is restrained from out-of-plane deflection. The problem to be considered is a cracked plate repaired by a patch adhesively bonded on one side of the cracked plate. The plate, which has a thickness of t_P , contains a through crack of length $2a$. The thickness of the patch and the adhesive layer are respectively t_R and t_A . The front view in the xy plane and the cross-section in the yz plane are depicted in Figure 12.1(a) and (b). The Young's modulus and the Poisson's ratio of each individual layer are denoted as E and ν ; here and in the following subscripts P , R , and A will be used to distinguish properties pertaining respectively to the plate, the reinforcement and the adhesive layer.

As discussed in Chapter 7, the elastic problem has been analysed using a crack bridging model [5,6], and an integral equation method [8,9]. For isotropic reinforcement having the same Poisson's ratio as the cracked plate, the stress-

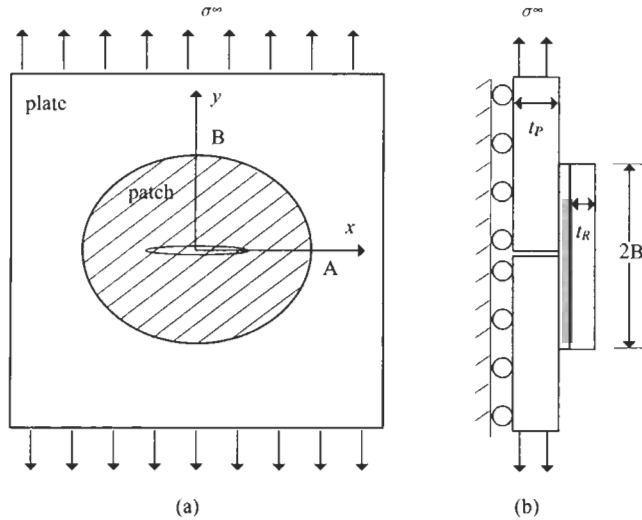


Fig. 12.1. Repair configuration: (a) plan view, (b) cross-section along centre line.

intensity factor range can be expressed as [9], assuming that the adhesive remains elastic,

$$\Delta K = \Delta \sigma_0 \sqrt{\pi a} F(\pi k a, S), \quad (12.1)$$

where the parameter $\Delta \sigma_0$ denotes the stress range which would prevail at the prospective location of the crack for a patched but un-cracked plate, which can be related to the remotely applied stress $\Delta \sigma^\infty$ [10],

$$\Delta \sigma_0 = \phi \Delta \sigma^\infty, \quad (12.2)$$

where the factor ϕ depends on several non-dimensional parameters for an elliptical reinforcement having the same Poisson's ratio as the plate; see Chapter 7 for details. The parameters k and S denote respectively the spring stiffness and stiffness ratio,

$$k = \frac{\beta S}{(1 - \nu^2)(1 + S)}, \quad (12.3)$$

where $\beta = [G_A/t_A((1 - \nu_P^2)/E_P t_P + (1 - \nu_R^2)/E_R t_R)]^{1/2}$ and $S = E_R t_R/E_P t_P$. The function F can be well approximated (within an error less than 0.5%) by

$$F(\pi k a, S) = \left[\frac{1}{\pi k a} \tanh \frac{\pi k a}{1 + B(S) \pi k a} \right]^{1/2}, \quad (12.4)$$

where the parameter $B(S)$ has been obtained by curve fitting the numerical solution of integral equation [8,9] representing patch repairs, e.g. $B = 0.3$ for balanced repairs ($S = 1$) and $B = 0.1$ for thick patch ($S \rightarrow \infty$).

In the long crack limit ($\pi ka \gg 1$), the stress intensity factor of patched cracks (see Eq. 12.4) asymptotes to the following upper limit, in the absence of disbonding and plastic deformation in the adhesive layer,

$$\Delta K = \frac{\Delta \sigma_0}{\sqrt{k}} \quad (\pi ka \gg 1) \quad (12.5)$$

This near constant stress-intensity factor suggests that under constant amplitude loading, a patched crack would grow at an approximately constant rate, indicating a steady-state condition. In this case, it is not unreasonable to postulate that patched cracks ought to experience the same crack-closure as un-patched cracks subjected to the same stress ratio (as the amplitude of the stress-intensity factor does affect crack closure, provided small-scale yielding prevails at the crack tip). In this case the plastic zone size and the crack-tip opening displacement are given by the following well-known relationship,

$$\omega_K = \frac{\pi}{8} \left(\frac{K}{\sigma_Y} \right)^2, \quad (12.6)$$

$$CTOD_K = \frac{K^2}{E\sigma_Y} = \frac{8\sigma_Y}{\pi E} \omega_K, \quad (12.7)$$

where ω_K and $CTOD_K$ denote the plastic zone size and the crack-tip opening displacement estimated based on stress-intensity factor K .

The fatigue crack growth rate can be correlated using the effective stress intensity factor,

$$\Delta K_{\text{eff}} = \frac{\Delta K}{1 - R} \left(1 - \frac{\sigma_{\text{op}}}{\sigma_{\text{max}}} \right), \quad (12.8)$$

where R denotes the applied stress ratio ($= \sigma_{\text{min}}/\sigma_{\text{max}}$), which is strongly influenced by the thermal residual stresses [11,12] present in the plate induced by curing; further in discussion will be presented later in Section 4. The crack-opening stress σ_{op} can be obtained by simplifying the expressions constructed by Newman [13],

$$\frac{\sigma_{\text{op}}}{\sigma_{\text{max}}} = \begin{cases} A_0 & R < 0 \\ A_0 + A_2 R^2 + A_3 R^3 & R > 0 \end{cases}, \quad (12.9)$$

where the constants A_0 , A_2 , A_3 are

$$\begin{aligned} A_0 &= 0.825 - 0.34\alpha + 0.05\alpha^2, \\ A_2 &= 2 - 3A_0, \\ A_3 &= 2A_0 - 1 \end{aligned} \quad (12.10)$$

The plastic constraint factor α depends parametrically on only one non-

dimensional parameter: the ratio of plastic zone size to plate thickness [14],

$$\alpha = \frac{1 + 0.64([\omega_K/t_P]^{1/2} + 2[\omega_K/t_P]^2)}{1 - 2\nu + 0.54([\omega_K/t_P]^{1/2} + 2[\omega_K/t_P]^2)}, \quad (12.11)$$

which is illustrated in Figure 12.2 together with the finite element results obtained by Newman, *et al.* [15].

12.2.2. Large-scale yielding solution for a stationary crack

The above method is valid in the limiting case of small-scale yielding, i.e., the applied stress is far smaller than the material's yield stress, the plastic zone size is far smaller than the crack size and the plate thickness. In practice, however, such conditions are not always met, especially when repairs are applied to fatigue cracks in highly stress regions. To evaluate the range of the validity of the method presented in the previous section, the influences of large-scale yielding on the crack-tip plastic deformation and plasticity-induced crack closure will now be addressed. To this end, a model for patched cracks will be presented, which extends the complex function method of Budiansky and Hutchinson [7] to include crack bridging effect.

For simplicity, let us consider the long crack limit, i.e. $\pi ka \geq 1$, so that the stress-intensity factor under maximum load can be considered as approximately constant. Since the crack-tip opening displacement (CTOD) is proportional to the square of the stress-intensity factor, the residual plastic stretch attached to the crack faces would be approximately constant in thickness. A simple schematic of the deformed

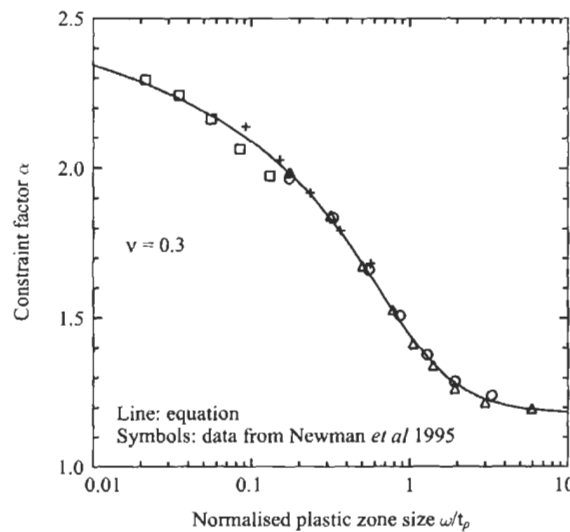


Fig. 12.2. Constraint factor versus normalised plastic zone size.

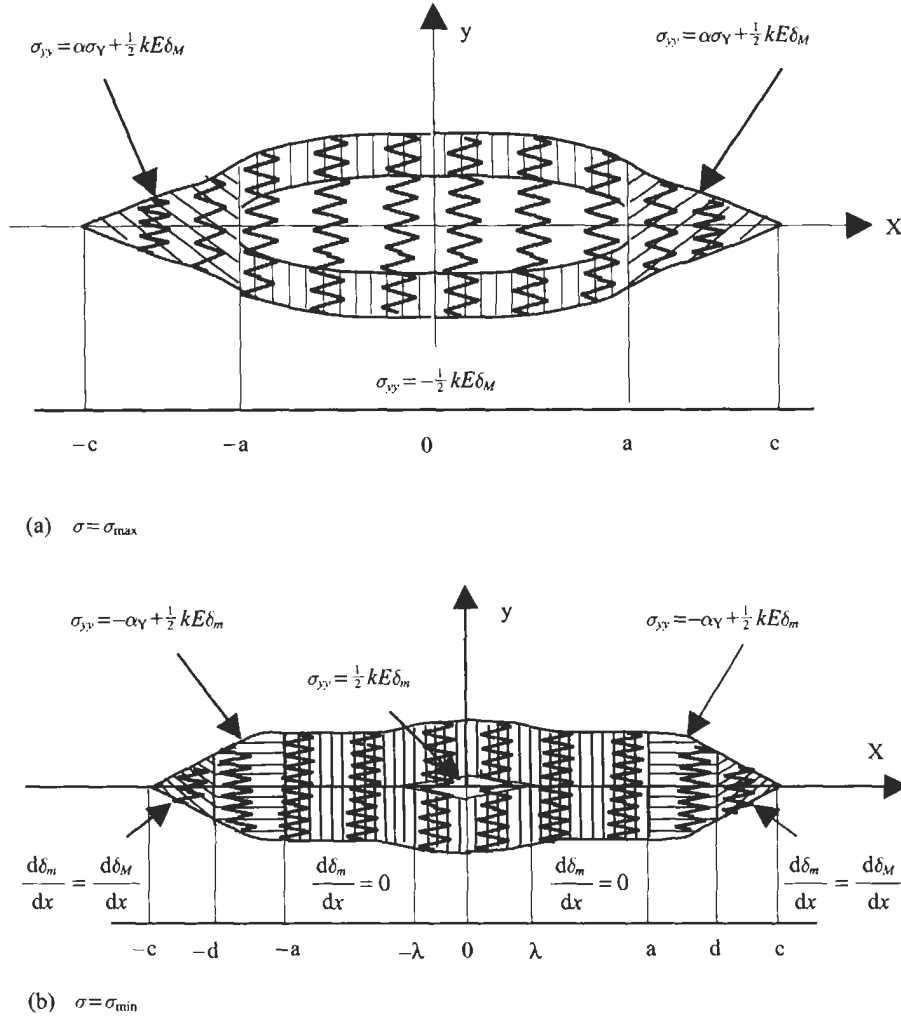


Fig. 12.3. Crack closure model for short cracks.

profile of a bridged crack at maximum stress is shown in Figure 12.3(a), while the boundary conditions upon unloading to the minimum stress are shown in Figure 12.3(b). Here the difference between a patched crack and an un-repaired crack is that the crack faces of a patched crack are bridged by a series of distributed springs. As will be seen later, this bridging mechanism will affect the plastic deformation ahead of the crack tip.

Adopting the Dugdale model, plastic deformation ahead of the crack tip is assumed to occur within the region $a < |x| < c$, where $c = a + \omega$. Here ω denotes the plastic zone size. The problem depicted in Figure 12.3(a) can be mathematically

expressed as [6]

$$-\frac{E_P}{2\pi} \int_{-c}^c \frac{u(t)}{(x-t)^2} dt + kE_P u(x) = \begin{cases} \alpha\sigma_0 & |x| < a \\ \alpha\sigma_0 - \sigma_Y & a < |x| < c \end{cases}, \quad (12.12)$$

where u denotes the crack face displacement, σ_Y the material's yield stress, and α the plastic constraint factor discussed in Section 12.2.1. The first term in the left-hand side of Eq. (12.12) represents the resistance of material to crack opening and the second term represents the resistance of springs.

The above hyper-singular integral equation can be solved using a Galerkin method: the unknown crack-face displacement u is expanded in terms of Chebyshev polynomials [6]. The plastic zone size ω is determined so that the stress just outside the plastic zone $x = c^+$ is non-singular, i.e.,

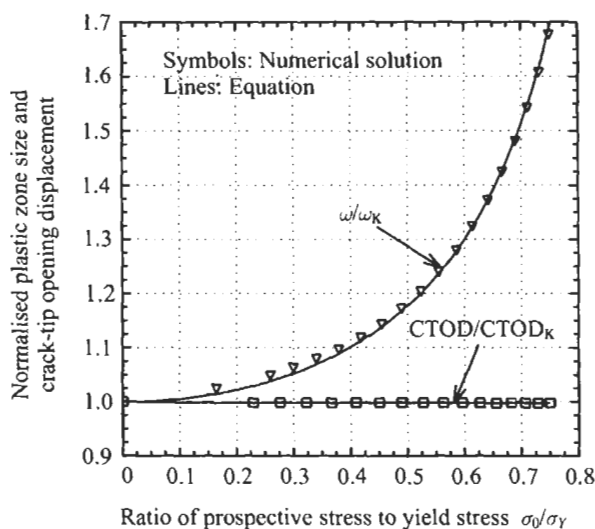
$$K = \lim_{x \rightarrow c^+} \frac{E_P \sqrt{\pi a}}{2} \frac{u(x)}{\sqrt{c^2 - x^2}} \equiv 0, \quad (12.13)$$

which furnishes the necessary condition for determining the plastic zone for a given applied stress. Solution of ω can be determined by iteration: Eq. (12.12) is first solved for a trial ω , then check whether Eq. (12.13) is satisfied. If this is the case, then convergence is achieved. The numerical results are presented in Figure 12.4. It is evident that provided the prospective stress is less than 40% of the material's yield stress, the plastic zone size is approximately equal to the estimate by the stress-intensity factor. At high stress levels, the prospective stress has a significant effect on the plastic zone size. As shown in Figure 12.3(a), the ratio of the plastic zone size for large-scale yielding to the values from K solution can be well approximated by the following expression,

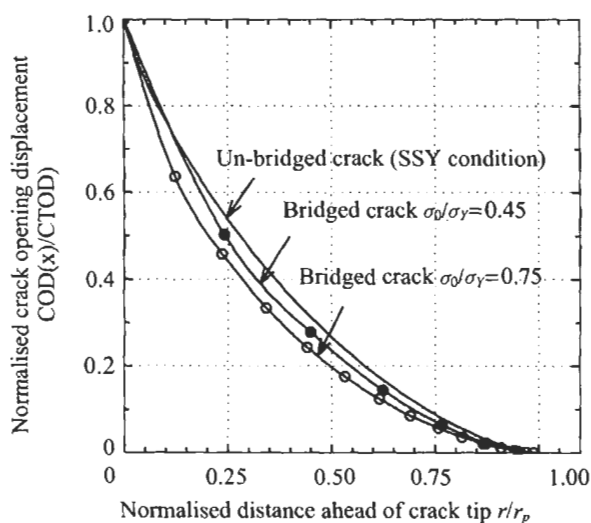
$$\frac{\omega}{\omega_K} = 1 + A \cdot \left[\sec\left(\frac{\pi}{2} \frac{\sigma_0}{\sigma_Y}\right) - 1 \right], \quad (12.14)$$

where the coefficient A is determined by a least square method, $A = 0.4272$. By contrast, the crack-tip opening displacement remains the same as that estimated based on the stress-intensity factor, for prospective stress up to 70% of the yield stress. Furthermore, it is interesting to note that the normalised plastic stretch variation ahead of the crack tip, as shown in Figure 12.4(b) seems to be reasonably insensitive to the level of applied stress. Therefore the plastic stretch variation is approximately given by a universal relation identical to that pertaining to unpatched cracks under small-scale yielding conditions. This is best illustrated by the ratio of the crack opening displacement to the maximum opening at the crack tip,

$$\frac{\delta(x)}{CTOD_K} = g(x/\omega), \quad (12.15)$$



(a)



(b)

Fig. 12.4. Influence of applied stress on (a) plastic zone size and (b) crack-tip opening displacement.

where the function g is [7]

$$g(x/\omega) = \sqrt{1 - x/\omega} - \frac{x}{2\omega} \ln \left| \frac{1 + \sqrt{1 - x/\omega}}{1 - \sqrt{1 - x/\omega}} \right| \quad (12.16)$$

This important result provides a basis to extend existing crack closure model for un-patched cracks to analyse patched cracks.

12.2.3. Plasticity induced crack closure under large-scale yielding solutions

Having now determined the crack-tip plastic deformation at the maximum applied stress, it is now possible to characterise the plasticity-induced crack closure. Denote the crack opening at the maximum stress at δ_M and the crack opening at the minimum stress at δ_m . Upon unloading to the minimum stress, referring to crack surface contact is assumed to occur within the intervals $\lambda < |x| < a$, where λ denotes the as-yet-unknown size of the contact-free region. The upper and lower crack surfaces are now attached with a layer of plastically stretched material of as-yet-unknown size $\delta_R/2$. There is also a region ahead of the crack tip, of unknown length $d - a$, that has gone into reverse plastic flow, leading to a total crack-tip residual stretch equal to δ_R . Here d denotes the coordinate of reversed plastic zone. Between $x = d$ and $x = c$ the plastic stretch is equal to the plastic stretch that existed at the maximum stress that remains unchanged. The boundary-value problem depicted in Figure 12.2(b) can be analysed using the complex function method [7,16,17]. In particular, the boundary conditions can be expressed as,

$$\left. \begin{aligned} \sigma_{yy} &= \frac{1}{2} k E \delta_m(x) & |x| < \lambda \\ \frac{d\delta_m}{dx} &= 0 & \lambda < |x| < a \\ \sigma_{yy} &= -\sigma_Y \left(1 - \frac{k E \delta_R}{2\sigma_Y}\right) & a < |x| < d \\ \frac{d\delta_m}{dx} &= \frac{d\delta_M}{dx} & d < |x| < c \\ \frac{d\delta_m}{dx} &= 0 & |x| > c \end{aligned} \right\} \quad (12.17)$$

For low prospective stress, we have, noting $\delta_R \leq CTOD$ and Eq. (12.5),

$$\frac{k E \delta_R}{2\sigma_Y} \leq \frac{k E \cdot CTOD}{2\sigma_Y} = \frac{1}{2} \left(\frac{\sigma_0}{\sigma_Y} \right)^2 \leq 0.125, \quad (\sigma_0 \leq 0.5\sigma_Y), \quad (12.18)$$

therefore the term $k E \delta_R / 2\sigma_Y$ can be neglected without appreciable loss of accuracy. In this case the boundary conditions for the minimum stress can be reduced to those corresponding to un-bridged cracks. The resulting equations can be solved in a manner similar to that employed by Wang and Rose [17]. Consequently the known solutions for un-repaired cracks, as described in Section 12.2.1, can be extended without modifications to bridged cracks.

12.3. Overload effect and validation using finite element method

To verify the above analytical solutions, a finite element analysis was performed. The finite element model will also be employed to investigate the transient crack-closure behaviour of patched and un-patched cracks subjected to variable

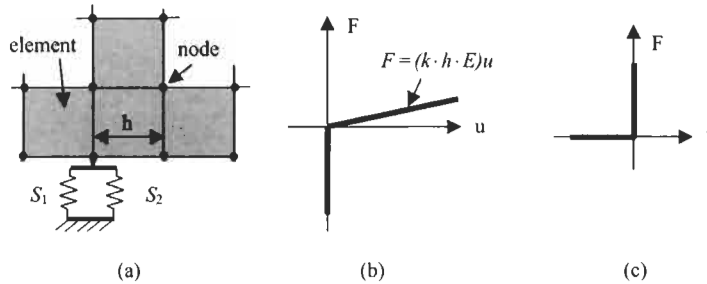


Fig. 12.5. Spring elements (a) attached to one node, constitutive relations for (b) bi-linear spring S1, and (c) tension-only spring S2.

amplitude loading. The fatigue crack opening and closure stresses were obtained using a spring element release method, which involves introducing two sets of bi-linear spring elements along the crack plane, as illustrated in Figure 12.5(a). One set of spring elements, which are attached to all the nodes, are used to simulate the patch in restraining the opening of the crack as well as to maintain the zero displacement condition under compression. This series of spring elements have a force-displacement relationship to give the spring constant given by Eq. (12.3), and an almost infinite compressive stiffness, as illustrated in Figure 12.5(b). For an element of width h , The force-displacement of this bi-linear spring attached to a corner node is

$$F = (k \cdot h \cdot E)u, \quad (12.19)$$

where F and u are the force and displacement pertaining to the spring element, and E is the Young's modulus of the parent plate material. In addition, a series of tension-only spring elements are also attached to each node ahead of the crack tip to maintain the zero displacement condition ahead of the crack tip under tension, see Figure 12.5(c). Crack-growth was simulated by releasing, at the maximum load, one tension-only spring-element every two cycles. The emphasis here is to determine the stabilised crack-closure stress, assuming that the crack will take many cycles to grow one element distance.

The finite element model was developed using a general-purpose finite element code, ABAQUS. A quarter model of centre-crack panel is modelled using plane-stress quadrilateral elements; the size of the initial crack, a_i , was 5 mm. The material is assumed to have Young's modulus of 72 GPa, a Poisson's ratio of 0.3, and a yield stress of 400 MPa, typifying an aluminium alloy. The half panel width was 101 mm. For the patched crack, the spring elements are chosen to simulate a spring constant of $k = 120 \text{ m}^{-1}$, and the applied stress is repeated tension with a maximum value of 150 MPa. For the un-patched centre-crack, the applied stress is also repeated tension but with a maximum value of 100 MPa to ensure the patched crack and the un-patched crack are subjected to approximately the same stress intensity factor. Shown in Figure 12.6 are the contours of the y -stress plotted on the deformed geometry of the patched crack after the crack has grown 0.8 mm under constant

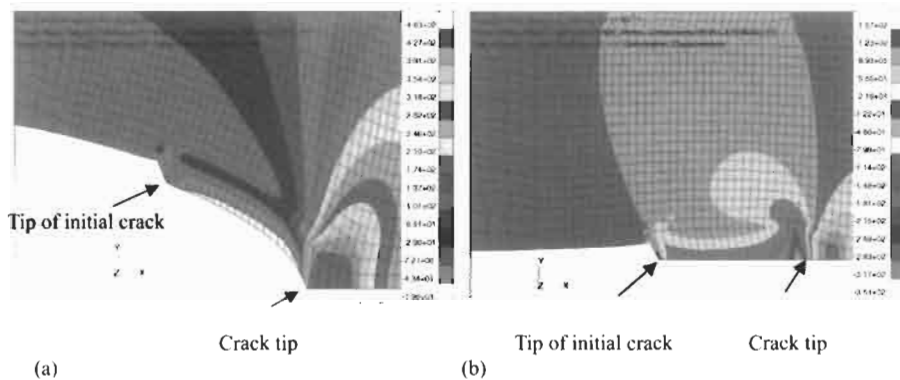


Fig. 12.6. Finite element solution of a patched crack growing under constant amplitude loading with $R=0$; (a) at the maximum stress showing the residual plastic stretch and (b) at minimum stress showing crack surface closure.

amplitude loading. As it can be seen in the figure, the residual plastic stretch at the crack tip caused the crack surface to close before the minimum stress is reached, similar to that observed in un-repaired cracks. In fact, the crack-closure stresses correspond to the patched crack and the unpatched crack agree well with each other, and are in close correlation with the theoretical solution [7] of un-repaired cracks subjected to the same stress ratio. Therefore, under constant amplitude loading, the crack-closure stress of patched cracks can be determined from the known results of un-repaired cracks. It is also noted that under steady-state condition, the crack-closure stress depends solely on the applied stress ratio, and is independent of the level of the applied stress intensity factor. As discussed later, this is in sharp contrast with the transient crack closure under variable amplitude loading.

The same finite element model has been used to further investigate the transient crack closure behaviour of patched cracks subjected to variable amplitude loading, with a view to identifying an equivalence between patched cracks and un-patched cracks. A simple overload sequence as shown in Figure 12.7 is applied to both an un-repaired crack and a patched crack. The maximum stress of the overload is about 30% higher than that of the background constant loading (150 MPa for patched crack and 100 MPa for un-patched crack). The patched crack experienced the same stress-intensity factor history as the un-repaired crack. Figure 12.8 shows

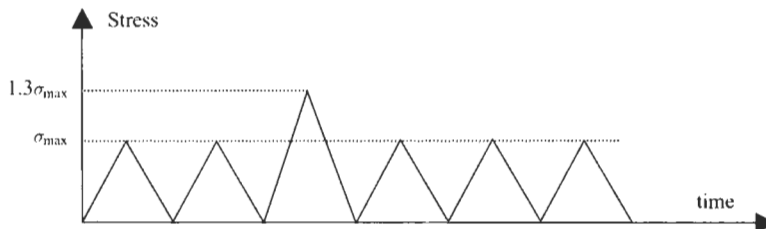


Fig. 12.7. A single overload superimposed on a constant amplitude loading sequence.

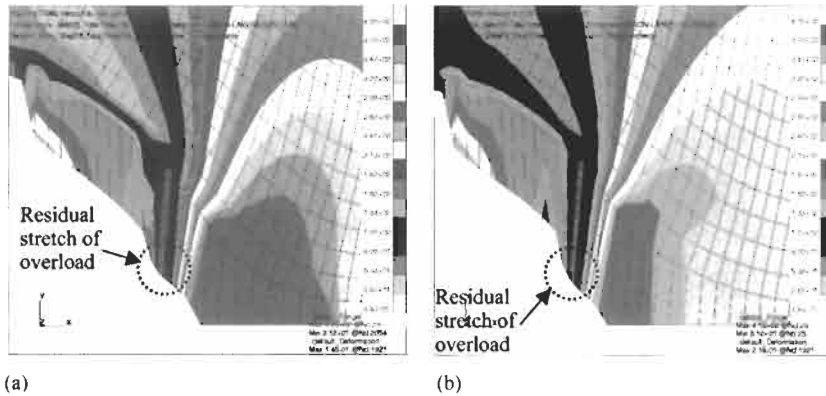


Fig. 12.8. Plastic wake induced by an overload for (a) an un-patched crack and (b) a patched crack subjected to approximately the same stress-intensity factor history.

the plastic wake created by the overload for an un-patched crack and a patched crack. It is evident that there is no discernible difference between the patched crack and the un-patched crack. A fundamental difference between the crack closure behaviour under steady-state condition (see Figure 12.6) and variable amplitude loading is that the crack-closure stress is independent of the magnitude of the residual plastic stretch under steady-state condition. By contrast, the transient crack-closure behaviour after an overload is dictated by the residual stretch created by the overload relative to that induced by prior constant amplitude loading. A schematic of the residual plastic wake associated with a single overload is shown in Figure 12.9. The ratios of the crack-closure stress (and crack-opening stress) to the maximum stress are calculated from the finite element results and shown in Figure 12.10, for both the patched and the un-patched crack. The crack advance is normalised by the distance between the plastic zone boundaries for the overload and the constant amplitude loading. Two important observations can be made from the results shown in Figure 12.10. First, following the overload, an initial

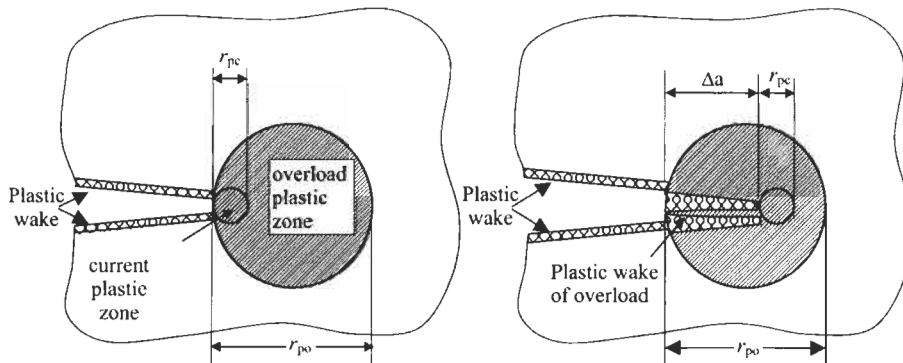


Fig. 12.9. Schematic of transient crack closure for a single overload.

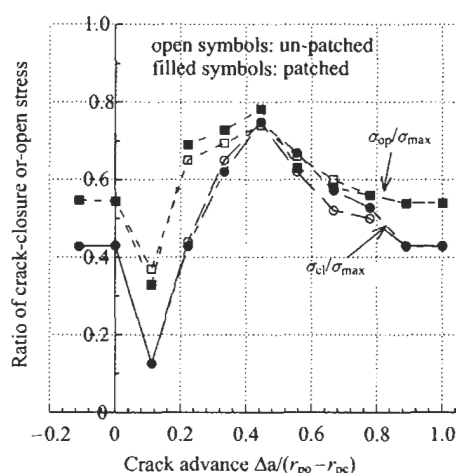


Fig. 12.10. Effect of overload on the crack-closure stress of patched and un-patched crack.

sharp drop occurred in the crack-closure and crack-opening stresses, for both the patched and un-patched cracks. After the initial drop, the crack-closure stress attained a higher value and it was only after considerable crack growth did the crack-closure stress return to the same level as prior to the overload. The fact that the higher (than steady-state value) crack-closure stress occurred over a crack advance greater than that over which the lower crack-closure stress occurred is a clear indication of net retardation in fatigue crack growth rates. Secondly, and more importantly, there is little difference between the transient evolution of the crack-closure stress for the patched crack and the un-patched crack. This implies that the crack closure behaviour of patched crack can be well approximated by that corresponding to an un-patched crack subjected to the same stress intensity factor. Therefore, the crack-closure behaviour of a patched crack can be obtained by analysing an un-patched, centre crack subjected to the same stress-intensity factor history as the patched crack, or the equivalent crack method [18]. In this regard, it is worth noting that the under-prediction of the fatigue crack growth rates of patched crack as reported in [18] is due to ignorance of the thermal residual stress in the earlier analysis, an issue to be discussed in more detail in the next section.

12.4. Thermal residual stresses and comparison with experimental results

12.4.1. Thermal residual stresses

Since composite patches generally have a lower thermal expansion coefficient than the metallic component to be repaired, thermal residual stresses would occur upon cooling the fully cured repair from elevated temperature (typically around 80–120 °C for structural adhesives) to either the ambient temperature or the

operating temperature. In particular, the residual stress in the metallic plate is generally positive, which may enhance fatigue crack growth rate due to increased stress ratio. Other complicating factors affecting fatigue crack propagation include possible changes in the patching efficiency resulting from adhesive plastic yielding (referring to Chapter 7 for more details) and debonding (referring to Chapter 13 for more details). In the following, we will focus our attention on the influence of thermal residual stress only.

For an orthotropic composite patch bonded to an isotropic plate, the resulting thermal residual stresses can be determined using the method developed in [11]. For a patched specimen being cured in a uniform temperature field (e.g. an oven), an approximate solution of the thermal stress in the plate can be derived by treating the patch as isotropic [11],

$$\sigma_0^T = \alpha E \Delta T \frac{(1 + \nu)(1 - \alpha_R/\alpha)S}{2(1 - \nu_R) + (1 - \nu^2)S}, \quad (12.20)$$

where α , E , ν denote the coefficient of thermal expansion, Young's modulus and Poisson's ratio. As before, the subscript R is used to distinguish parameters pertaining to the patch. The temperature change is given by ΔT . For a typical balanced repair with $S = 1$ and $\nu = \nu_R = 0.3$, the above equation yields a thermal stress about 12.6% higher than that estimated based on 1D idealisation [1].

In practical applications to actual aircraft structures, bonding a composite patch requires a localised heating of the repair area followed by cooling to the ambient temperature (or the operating temperature). In this case the constraint imparted by the surrounding structure induces additional thermal residual stresses. Upon heating of a circular region in an infinite plate from the room temperature T_r to the curing temperature T_c , the following compressive thermal residual stress σ_h^T develops in the structure when the adhesive is being cured [11],

$$\sigma_h^T = -\frac{1}{2}\alpha E(T_c - T_r) \quad (12.21)$$

Cooling of the patched structure to the operating temperature T_o , which may be the same as the room temperature, results in a tensile thermal residual stress σ_c^T ,

$$\sigma_c^T = \alpha E(T_c - T_o) \frac{1 - \nu_R + (1 - \alpha_R/\alpha)(1 + \nu)S}{2(1 - \nu_R) + (1 - \nu^2)S} \quad (12.22)$$

Consequently the total thermal residual stress σ_0^T in the plate is the sum of the above two stresses,

$$\sigma_0^T = -\frac{1}{2}\alpha E(T_c - T_r) + \alpha E(T_c - T_o) \frac{1 - \nu_R + (1 - \alpha_R/\alpha)(1 + \nu)S}{2(1 - \nu_R) + (1 - \nu^2)S}, \quad (12.23)$$

which is generally a tensile stress for Boron patches with a coefficient of thermal expansion being far smaller than that of the metallic material $\alpha_R \ll \alpha$.

For a constant amplitude loading, the presence of the residual thermal stress implies that the patched crack experiences a stress intensity factor R_{tip} different from the applied stress ratio,

$$R_{tip} = \frac{K_{min}}{K_{max}} = \frac{\phi\sigma_{min}^{\infty} + \sigma_0^T}{\phi\sigma_{max}^{\infty} + \sigma_0^T} = R + \frac{1 - R}{1 + \phi\sigma_{max}^{\infty}/\sigma_0^T}, \quad (12.24)$$

where R denotes the ratio of the applied stress $R = \sigma_{min}^{\infty}/\sigma_{max}^{\infty}$. Since $\sigma_0^T \geq 0$, the actual stress intensity factor ratio is higher than the applied stress ratio. This difference needs to be considered when comparing the fatigue crack growth rates of patched and un-patched cracks. In this regard, a rational approach would be to adopt the effective stress intensity factor as the correlating parameter for fatigue crack growth. Take the example of aluminium alloy 2024-T3, the fatigue crack-growth rates obtained using an un-patched, edge cracked panel are plotted in Figure 12.11(a) against the applied stress-intensity factor range. It is evident that the stress ratio has a considerable effect on the crack-growth rates for a given applied stress-intensity factor range. By re-plotting the crack growth rates against the effective stress-intensity factor range determined using Eq. (12.8), as shown in Figure 12.11(b), the crack-growth rate data corresponding to three different stress ratios fall within a narrow band ($\pm 100\%$), consistent with the crack growth rates independently obtained for the same material [19]. The plastic constraint factor α employed in the analysis is equal to 1.8. The following expression provides the best fit to all the experimental data,

$$\frac{da}{dN} = C(\Delta K_{eff})^m, \quad (12.25)$$

where $C = 2.234 \times 10^{-10}$ and $m = 3.135$, in SI unit.

12.4.2. Experimental results under spectrum loading

In light of the above success in correlating the crack-growth rates of the un-patched cracks, the experimental results of patched cracks reported in [12] are re-analysed, taking into account of the residual thermal stress. The results are shown in Figure 12.12. It can be seen that the experimental results of patched cracks also fall within the same band as the un-patched cracks. Here the stress-intensity factors for the patched cracks are calculated using Eq. (12.1), assuming that the adhesive remains elastic. With the actual stress ratio being determined from Eq. (12.24), the crack-opening stress is evaluated by Eq. (12.9), and the effective stress-intensity factor range is calculated via Eq. (12.8). The good correlation between the patched and un-patched cracks as observed in Figure 12.12 confirms that growth rates of patched cracks and un-patched cracks are uniquely characterised by the effective stress-intensity factor range. Therefore, the growth behaviour of patched cracks and un-patched cracks, under constant amplitude loading, can be successfully rationalised by the concept of fatigue crack closure. This enables the crack growth rates of patched cracks to be predicted using the growth rates of un-patched cracks.

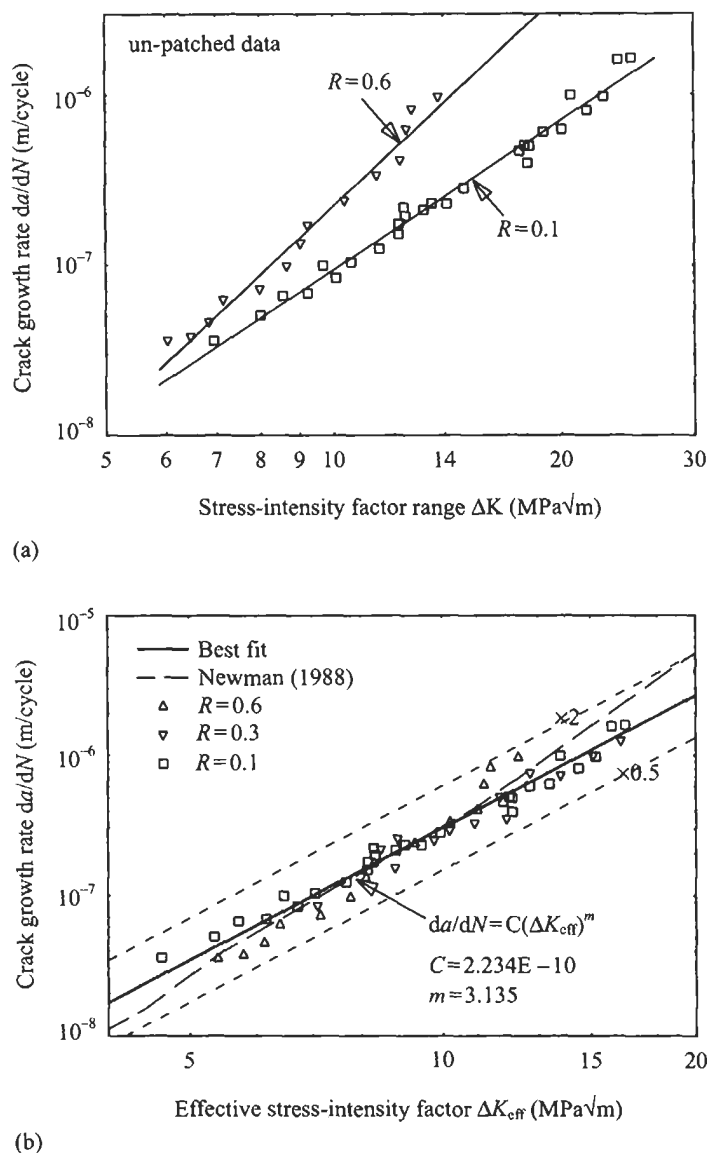


Fig. 12.11. Fatigue crack growth rates in 2024-T3 aluminium alloy (un-repaired) plotted against (a) the applied stress-intensity factor range ΔK and (b) the effective stress-intensity factor range ΔK_{eff} .

Under variable amplitude or spectrum loading, it is important to analyse the transient crack closure, especially the retardation effects associated with overloads. As already discussed in the previous section, after the application of an overload, a patched crack experiences nearly the same transient crack closure behaviour as un-

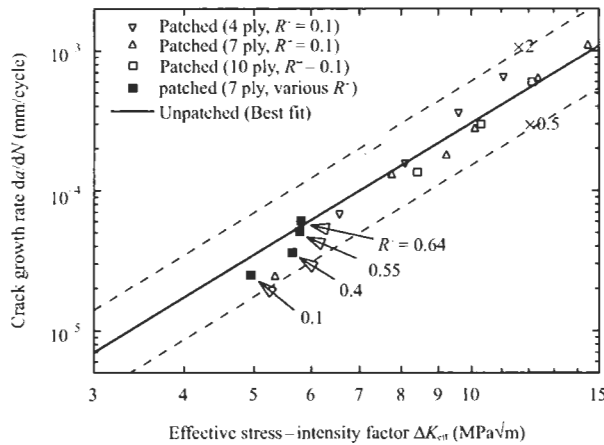


Fig. 12.12. Growth rates of patched and unpatched cracks under constant amplitude loading with various stress ratios.

patched crack subjected to the same stress intensity factor. Therefore the crack closure of patched cracks can be determined by analysing the crack closure of a centre-cracked panel subjected to a reference stress, as illustrated in Figure 12.13. The reference that the centre-cracked panel is subjected to is determined to ensure

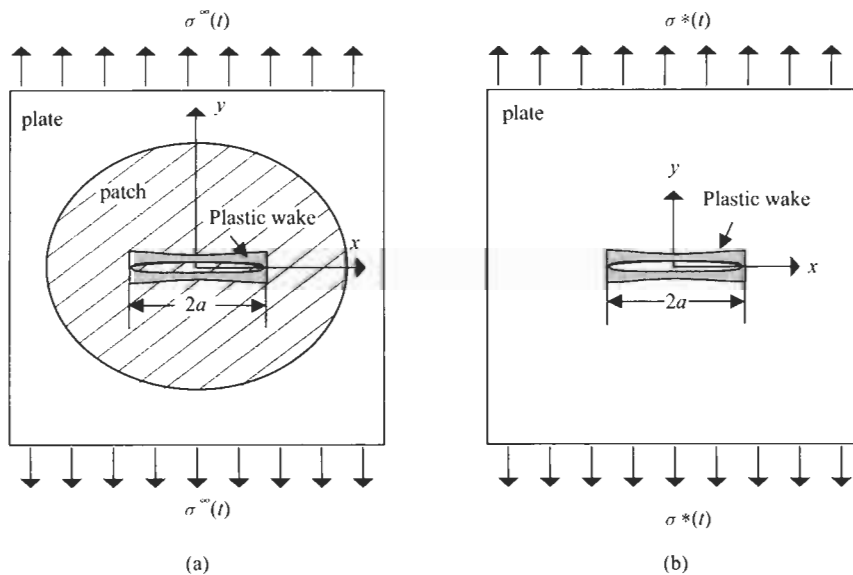


Fig. 12.13. Correspondence between a patched crack and an un-patched crack subject to an equivalent stress.

that the stress intensity factor is the same as the patched crack, viz,

$$\sigma^*(t)\sqrt{\pi a} = [\phi\sigma^\infty(t) + \sigma_0^T]\sqrt{\pi a}F(\pi ka, S), \quad (12.26)$$

which leads to

$$\sigma^*(t) = [\phi\sigma^\infty(t) + \sigma_0^T]F(\pi ka, S) \quad (12.27)$$

Since the factor F decreases as the crack size increases, the equivalent stress $\sigma^*(t)$ would become a progressively smaller fraction of the applied stress, to ensure that the cyclic plastic deformation at the tip of the equivalent crack remain the same as that for the patched crack.

A comparison with some experimental results [20] is shown in Figure 12.14. The test specimens, which were made of 2024-T851 aluminium alloy panels having a thickness of 3.7 mm, were repaired with a boron composite patch after being pre-cracked to give a half crack size equal to 20 mm. Patches were made from Boron/Epoxy pre-preg fibre composites to form a 14-ply laminate; the lay-up is $[0_s, \pm 45]_s$. The patched specimens were subjected to a load spectrum (to be denoted as F-111) consisting of 36273 turning points per block, with the ratio of the minimum to the maximum equal to -0.278 . The maximum applied stress, as listed in Table 12.1, was equal to 217 MPa, giving rise to a maximum plate stress (in a block) about 112 MPa. The geometry and material properties of the patched specimen (denoted as F111) are summaries in Tables 12.1 and 12.2. The patches were bonded to the plate using a FM-73 adhesive and cured at 80°C , resulting in a thermal residual stress of 67.35 MPa. The base-line fatigue crack-growth data for the material were taken from the literature [21], which were then converted to obtain the crack-growth rate against effective stress-intensity factor range relationship. This allows

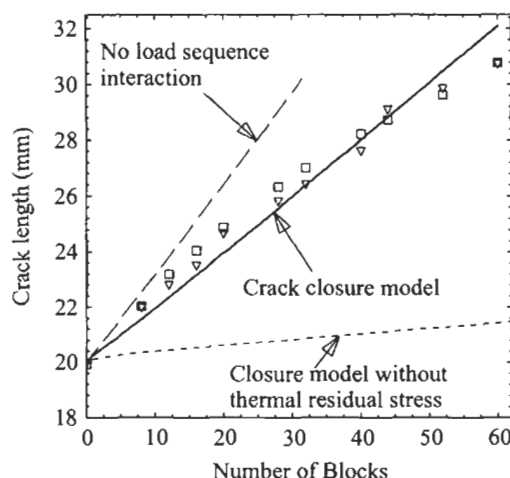


Fig. 12.14. Comparison between experimental and predicted growth behaviour of patched cracks under F-111 spectrum. Symbols denote experimental data.

Table 12.1
Geometry and material properties of specimens.

Specimen	E_P GPa	T_P mm	E_R GPa	t_R mm	G_A GPa	t_A mm	ϕ	k 1/m	σ_{\max}^α MPa
F-111	72	3.7	156	1.82	0.57	0.25	0.52	58.0	217
FALSTAFF	72	3.14	200	0.91	0.54	0.2	0.55	65.5	248

Table 12.2
Thermal properties and temperature change.

Specimen	α (plate)	α_R (patch)	ΔT (°C)	σ_0^T (MPa)
F-111	2.40E-05	4.00E-06	60	67.35
FALSTAFF	2.40E-05	4.00E-06	100	70.67

the experimental results from various stress-ratio tests to be collapsed within a single scatter band. The converted data can be well correlated using the standard Paris relationship, giving rise to the following constants $C = 7.4 \times 10^{-10}$ and $m = 2.93$. As seen in Figure 12.14, the predictions based on the equivalent crack method are in good agreement with the experimental results. It is also interesting to note that, due to the increased mean stress resulting from the thermal residual stress, simple predictions based on simply integrating the crack growth equation on a cycle-by-cycle basis, using the steady-state crack opening stress given by Eq. (12.9), are slightly conservative. This implies that the retardation effect of the loading spectrum is also not very significant due to the high mean stress. Also shown in Figure 12.14 are the predictions based on the crack closure model, without considering the thermal residual stress. It is evident that the calculated crack growth rate is far lower than the experimental results, demonstrating the importance of the thermal residual stress in enhancing the fatigue crack-growth rates. This also highlights the need to minimise the thermal residual stress.

The experimental results of another series of tests involving FALSTAFF spectrum [3] are plotted in Figure 12.15, together with predictions made using equivalent crack method. The test specimens, which were made from 3.2 mm thick 2024-T3 aluminium sheets, were first fatigue pre-cracked under constant amplitude loading to two prescribed crack lengths: 5 mm and 25 mm. The test panels were then repaired with boron/epoxy using three different adhesive systems. Two edge-cracked face-sheets were bonded to an aluminium honeycomb core to form a sandwich panel to avoid out-of-plane bending. A total of six such panels were tested. The thermal residual stress, as listed in Table 12.2, was estimated based on Eq. (12.20) to be approximately 70.67 MPa. This thermal residual stress is significant as the maximum plate stress $\phi\sigma^\infty$ is about 136 MPa. The spectrum used was a “clipped” FALSTAFF spectrum, in which the negative loading has been removed. As seen in the figure, the predictions based on the crack closure model, when thermal residual stress is taken into account, are in good correlation with the experimental data. As indicated by the dashed lines in Figure 12.15, predictions

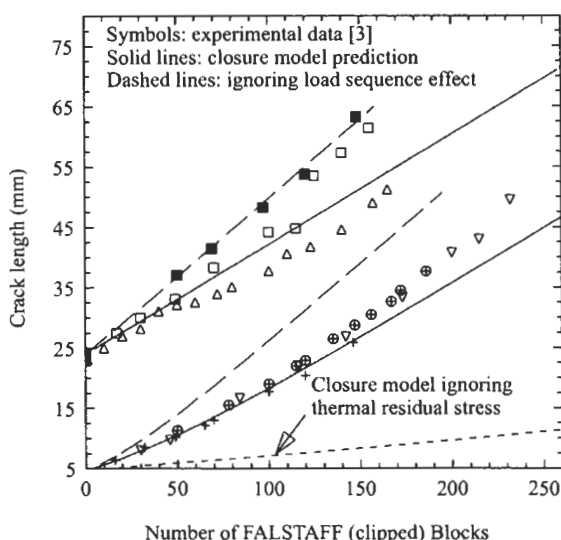


Fig. 12.15. Comparison between experimental and predicted growth behaviour of patched cracks under FALSTAFF spectrum.

made by integrating the crack growth rate equation, with the crack-opening stress for each reversal being taken to be the steady-state value, are slightly on the conservative side. Similar to the results shown in Figure 12.14, this behaviour indicates that, due to the high thermal residual stress, the spectrum loading does not have a strong retardation effect. Also plotted in Figure 12.15 are the predictions made by neglecting the thermal residual stress. Again, much slower crack-growth rates are predicted. This confirms the observations made earlier regarding the importance of the thermal residual stresses and the need to minimise residual stresses in order to achieve lower crack-growth rates. It should be noted that the effects of disbond and adhesive plasticity have not been considered in this chapter. Further work is required to account for the interaction between of fatigue crack growth and disbond.

12.5. Conclusions

It has been shown that under constant amplitude loading with the prospective stress much lower than the material yield stress, the closure behaviour of repaired cracks is nearly identical to that corresponding to un-patched cracks subjected to steady-state loading. Under variable amplitude loading, the crack closure behaviour of a patched crack has also been shown to be identical to that corresponding to an un-patched crack subjected to the same stress-intensity factor history.

An equivalent crack method has been developed, which enables the fatigue crack closure of patched cracks to be determined by analysing a centre-cracked panel subjected to an equivalent stress given by

$$\sigma^*(t) = [\phi\sigma^\infty(t) + \sigma_0^T]F(\pi ka, S) \quad (12.28)$$

Predictions based on this method have been found to correlate well the experimental results obtained under two aircraft loading spectra. It has also been found that the ignorance of the thermal residual stress would lead to significant under-prediction of the crack growth rate.

References

1. Baker, A.A. (1988). Crack patching: experimental studies, practical Applications, Chapter 6. in *Bonded Repair of Aircraft Structures*, (A.A Baker and R. Jones, eds.), Martinus Nijhoff, pp. 107–173.
2. Baker, A.A. (1993). Repair efficiency in fatigue-cracked panels reinforced with boron/epoxy patches. *Fatigue and Fracture of Engineering Materials and Structures*, **16**, pp. 753–765.
3. Raizenne, M.D., Heath, J.B.R. and Benak, T. (1988). TTCP PTP-4 Collaborative test program – variable amplitude loading of thin metallic materials repaired with composite patches, Laboratory Technical Report, LTR-ST-1662, National Aeronautical Establishment, Ottawa, Canada.
4. Newman, J.C. Jr. (1992). FASTRANII – A fatigue crack growth structural analysis program, NASA Technical Memorandum 104195, NASA Langley Research Centre.
5. Rose, L.R.F. (1988). Crack reinforcement by distributed springs. *Journal of Mechanics and Physics of Solids*, **35**, pp. 383–405.
6. Wang, C.H. and Rose, L.R.F. (1999). A crack bridging model for bonded plates subjected to tension and bending. *Int. J. of Solids and Structures*, **36**, pp. 1985–2014.
7. Budiansky, B. and Hutchinson, J.W. (1978). Analysis of closure in fatigue crack growth. *J. of Applied mechanics*, **45**, pp. 267–275.
8. Keer, L.M., Lin, C.T. and Mura, T. (1976). Fracture analysis of adhesively bonded sheets. *J. of Applied Mechanics*, **98**(4), pp. 652–656.
9. Wang, C.H. and Rose, L.F.R. (1998). Bonded repair of cracks under mixed mode loading. *Int. Solids and Structures*, **35**(21), pp. 2749–2773.
10. Rose, L.R.F. (1981). An application of the inclusion analogy for bonded reinforcements. *Int. J. Solids Structures*, **17**, pp. 827–838.
11. Wang, C.H., Rose, L.R.F., Callinan, R., et al. (1999). Thermal stresses in a plate with a circular reinforcement. *Int. J. of Solids and Structures*, **37**, pp. 4577–4599.
12. Baker, A.A. (1996). Fatigue studies related to certification of composite crack patching for primary metallic structure. *Proc. of the FAA/NASA Symposium on Continued Airworthiness of Aircraft Structures*, Atlanta, USA, pp. 313–330.
13. Newman, J.C., Jr. (1984). A crack-opening stress equation for fatigue crack growth. *Int. J. of Fracture*, **24**, pp. R131–R135.
14. Guo, W., Wang, C.H. and Rose, L.R.F. (1998). On the influence of cross sectional thickness on fatigue crack growth. *Fatigue and Fracture of Engineering Materials and Technology*, **22**, pp. 437–444.
15. Newman, J.C. Jr., Crews, J.H. Jr., Biglew, C.A., et al. (1995). Variations of a global constraint factor in cracked bodies under tension and bending loading, Constraint Effects in Fracture Theory and Applications: Second Volume, ASTM STP 1244, M. Kirk and A. Bakker, eds., American Society for Testing and Materials, Philadelphia.

16. Tanaka, K. and Nakai, Y. (1983). Mechanics of growth threshold of small fatigue cracks, *Fatigue Crack Growth Threshold Concepts*, (D.L. Davidson and S. Suresh, eds.). The Metallurgical Society of AIME, pp. 497–516.
17. Wang, C.H. and Rose, L.R.F. (2001). Closure analysis of small fatigue cracks with a self-similar plastic wake. *J. of the Mechanics and Physics of Solids*, **49**, pp. 401–429.
18. Wang, C.H., Rose, L.R.F. and Baker, A.A. (1998). Modelling of the fatigue growth behaviour of patched cracks. *Int. J. of Fracture*, **88**, pp. L65–L70.
19. Edwards, P.R. and Newman, J.C. Jr. (1990). An AGARD supplemental test programme on the behaviour of short cracks under constant amplitude and aircraft spectrum loading, *AGARD Report* 767.
20. Boykett, R. and Walker, K. (1996). F-111C lower wing skin bonded composite repair substantiation testing, *DSTO-TR-0480*, Aeronautical and Maritime Research Laboratory, Melbourne, Australia.
21. DTDH (1972). Damage Tolerant Design Handbook, a compilation of fracture and crack-growth data for high-strength alloys, Metals and Ceramics Information Centre, MCIC-HB-01.

Chapter 13

BORON/EPOXY PATCHING EFFICIENCY STUDIES

A.A. BAKER

Defence Science and Technology Organisation, Air Vehicles Division, Fishermans Bend, Victoria 3207, Australia

13.1. Introduction

As discussed in Chapters 1 and 2, the fibre-composite boron/epoxy (b/ep) is well suited for use as a patching or reinforcing material for metallic structures. Briefly the attributes of b/ep include:

- High Young's modulus (three \times aluminium for unidirectional b/ep) and static and fatigue strength, which minimises the required patch thickness
- Good formability, which allows formation of complex shapes
- Low electrical conductivity, which facilitates use of eddy-current non destructive inspection for monitoring the patched cracks and eliminates concerns with galvanic corrosion.

However, b/ep is not suited for repairs of regions with small radius of curvature, because of the large diameter of the boron fibres (125 micrometres compared to 8 micrometres for graphite). Graphite/epoxy (gr/ep) would be chosen for such applications.

Because of its attributes, b/ep was chosen for most Australian [1,2] bonded composite repair applications. The patches are generally bonded with an aerospace-grade structural epoxy-nitrile film adhesive, currently Cytec[®] FM 73 a 120 °C curing adhesive. This adhesive has the additional advantage that it can be cured at temperatures as low as 80 °C. However, FM 73 is limited to applications below about 80 °C so Cytec FM 300-2, a 120 °C curing adhesive is chosen for applications at over 80 °C to around 100 °C. A modified acrylic, such as Flexon 241, is chosen for applications below 50 °C where curing temperatures even as low as 80 °C are not acceptable.

To develop a capability to predict patching efficiency of b/ep patched fatigue cracks, studies were made to assess the effect of important variables on crack-

growth rate under constant amplitude fatigue. The variables studied included (a) patch disbond size, (b) applied stress, (c) patch thickness, (d) stress ratio R (e) test temperature and (f) panel thickness variation. The parameter used to assess crack-growth behaviour is the stress intensity K . This study is based on estimations of K using Rose's [3] analysis for patched cracks.

13.2. Stress intensity analysis of patched cracks

One important aim in the analysis of patch repairs is to estimate the stress intensity of the patched crack as a function of the various geometrical, physical and stress parameters.

The parameters other than applied stress σ_∞ in determining K for a patched crack are:

- Metallic structure: thickness t_p , Youngs modulus E_p , shear modulus G_p and thermal expansion coefficient α_p
- Reinforcement: thickness t_R , Youngs modulus E_R , and thermal expansion coefficient α_R
- Adhesive: thickness t_A , shear modulus G_A , shear yield stress τ_p under the service conditions of temperature, humidity and loading rate.
- Disbonds (if any) over the cracked region: length normal to the crack, $2b$.

13.2.1. Model for estimating stress intensity

In the model developed by Rose [3] in the patched crack a two-step approach is used to estimate stress intensity, as illustrated in Figure 13.1.

Briefly, in step 1, Figure 13.1, the patch is modelled as an inclusion in a large panel and the presence of the crack (assumed to be relatively very small) is neglected. The stress in the metallic component in the prospective region of the crack is then given by $\phi\sigma_\infty$, where ϕ is a factor which accounts for the stiffness and shape of the patch. Because the patch attracts load, the stress reduction may be significantly less than predicted simply on the basis of ratio of patch stiffness to plate stiffness. Calculation of ϕ is described in reference [1].

For full width reinforcement ϕ is given by $(1 + E_R t_R / E_p t_p)^{-1}$. For the patch and plate properties used here, assuming full width reinforcement $\phi = 0.6$, while for a circular patch as used in these experiments $\phi = 0.68$, estimated from inclusion theory.

In step 2, Figure 13.1 the crack is assumed to be semi-infinite and fully covered by the patch. The stress in the panel containing the crack is $\phi\sigma_\infty$. The *upper-bound* stress intensity K_∞ is then as given by:

$$K_\infty = \left[\frac{1}{2} E_p \Phi \sigma_\infty \delta \right]^{1/2}, \quad (13.1a)$$

where δ is the "crack" opening displacement; δ is estimated from the overlap joint

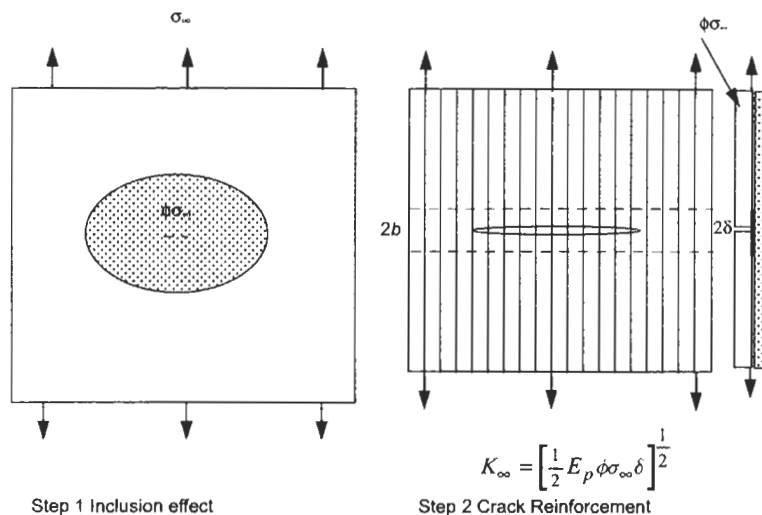


Fig. 13.1. Schematic illustration of the analytical approach to crack patching. The dotted parallel lines represent a disbond, width $2b$.

that would be obtained by cutting a strip through the panel normal to the crack. Equation (13.1a) is strictly correct only for linear behaviour (no yielding of the adhesive) but provides a reasonable estimate of ΔK_{∞} provided yielding of the adhesive is small.

The use of K_{∞} to assess the stress intensity in the cracked component allows considerable simplification in crack-growth analysis, since as seen in Eq. (13.1a) K_{∞} is independent of crack length a .

The use of K_{∞} is justified in Figure 13.2, which plots K_R the predicted stress intensity (based on Rose's model and the more recent Rose-Wang model [4]) versus a . The parameters used are those of the b/ep patched panels tested in these studies, described in Section 13.3. This plot shows that K_R becomes close to K_{∞} for crack lengths above 20 mm. Thus at least to a good first approximation, the assumption that K_R is equal to K_{∞} for a above 20 mm is reasonable for these specimens. Experiments to measure K_R for comparison with the predicted K_R are described in Chapter 18. The results of these experiments provide some confidence in the model and in particular the use of K_{∞} as the key patch design parameter.

Under the cyclic stress range $\Delta\sigma_{\infty}$ the stress-intensity range ΔK_{∞} is given by:

$$\Delta K_{\infty} = \left[\frac{1}{2} E_p \Phi \Delta\sigma_{\infty} \Delta\delta \right]^{1/2} \quad (13.1b)$$

The displacement range $\Delta\delta$ is dependent on the thicknesses and stiffnesses of the patch and of the cracked component, and on the thickness, shear modulus and effective shear yield stress of the adhesive. It is important to note that the adhesive

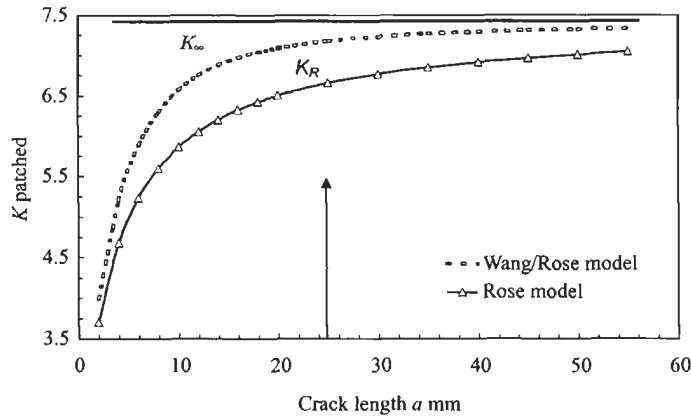


Fig. 13.2. Plot of predicted variation of stress intensity of the patched crack K_R versus crack length, based on Rose's model and the more recent Rose-Wang model. K_∞ is the upper bound estimate used in these studies.

properties are highly temperature- and strain-dependent and strain-rate dependent and also dependent on the amount of absorbed moisture. The displacement $\Delta\delta$ is also dependent on the residual stress, σ_T , resulting from the difference in thermal expansion coefficient between the patch and parent structure, since this affects the level of external stress at which the adhesive will yield. The estimation of δ is as described in reference [1]; for the elastic adhesive case it is given by the following relationship:

$$\delta = \frac{2\sigma_\infty t_p}{(\beta E_R t_R)} \quad , \quad (13.1c)$$

$$\text{where} \quad \beta = \left\{ \left(\frac{G_A}{t_A} \right) \left(\frac{1}{t_p E_p} + \frac{1}{t_R E_R} \right) \right\}^{1/2} \quad , \quad (13.1d)$$

β is the exponent of the elastic shear strain distribution (β^{-1} is called the characteristic load transfer length).

13.2.2. Use of model to estimate crack growth

It is assumed for simplicity that, as for unpatched cracks, a Paris-type relationship holds:

$$\frac{da}{dN} = f(\Delta K, R) = A_R \Delta K^{n_R} \quad , \quad (13.2)$$

where a is crack size, N is the number of constant amplitude cycles and A_R and n_R are assumed to be constants for a given minimum to maximum stress ratio R .

If this assumption is reasonable (for practical purposes) a should be found experimentally to be linearly related to N , at least to a reasonable first approximation. This is found to be the case, as shown later.

Finally, the relationship between crack length a and the number of cycles N can be obtained from:

$$a = A_R \int_0^N (\Delta K_\infty)^{n_R} dN \quad (13.3)$$

As ΔK_∞ is constant, it can be moved outside of the integration sign; however, ΔK_∞ is not constant where disbonding occurs, as discussed in the next section.

13.2.3. Extension of the model for growth of disbond damage

Experimentally and practically it is found that local disbonds develop in the high shear-stress regions around the crack in the parent structure. It is thus necessary to modify the model to account for this behaviour.

It is assumed for a simple extension to the basic model [5] that a parallel disbond, size $2b$, traverses the specimen, as illustrated in Figure 13.1.

Then the opening of the gap is increased by $2be$, where e is the estimated strain in the reinforcement.

Equation (13.1a) then becomes:

$$\Delta K_\infty = \left[\frac{1}{2} E_p \Phi \Delta \sigma_\infty (\delta + 2be) \right]^{1/2} \quad (13.4)$$

If it is assumed as a first approximation (based on early fatigue tests on double-overlap joints [6]) that db/dN is a constant for given stressing conditions, then:

$$b = N \left(\frac{db}{dN} \right) \quad (13.5)$$

Thus, the effect of disbond growth on crack-growth behaviour can be estimated approximately using Eq. (13.4). Because of the disbond growth ΔK_∞ then no longer remains constant but follows a square-root relationship as a function of b . Finally, from Eqs (13.3) and (13.4) a non-linear relationship between a and N is predicted.

13.3. Experimental approach

Fatigue crack propagation tests were conducted on 2024 T3 specimens 3.14 mm thick having starting cracks about 5 mm long repaired with unidirectional boron/epoxy (Textron 5521/4) patches which (unless otherwise mentioned) were 7 plies (0.9 mm) thick. In most studies a layer of FM 73 adhesive was first cocured onto the boron/epoxy-bonding surface. This is current Australian practice since patches

with the cocured layer of adhesive are much less prone to disbond damage during fatigue and the adhesive provides a less sensitive surface for grit blasting. However, in some specimens representative of our previous practice (in the disbond study) to encourage the growth of disbonds, the cocured layer was not used.

The patches were then bonded with adhesive FM 73 at 120 °C, following surface treatment of the metal using the silane process [1,7] and the boron/epoxy patches by blasting with alumina grit, either directly onto boron/epoxy or onto the cocured adhesive layer.

In the fatigue tests, two similar panels are simultaneously tested, joined together as a honeycomb sandwich panel, as shown in Figure 13.3. There are two reasons for using this configuration. The first is to minimise bending curvature following patching due to the residual stress σ_T which, as mentioned earlier, arises from the mismatch in thermal expansion coefficient between the patch material and the metal panel. Thus, the patches were bonded to the panels at the same time as the panels were bonded to the honeycomb core. The second reason is to minimise the secondary bending of the panels, which would otherwise occur during testing. The bending moments arise from the displacement of the neutral plane by the patch. The resistance to bending resulting from the honeycomb core (substantial but not perfect) is considered a reasonable simulation of the level of support that would be provided by typical military aircraft structure. In almost all tests, similar rates of crack growth were observed for the two panels in the combination.

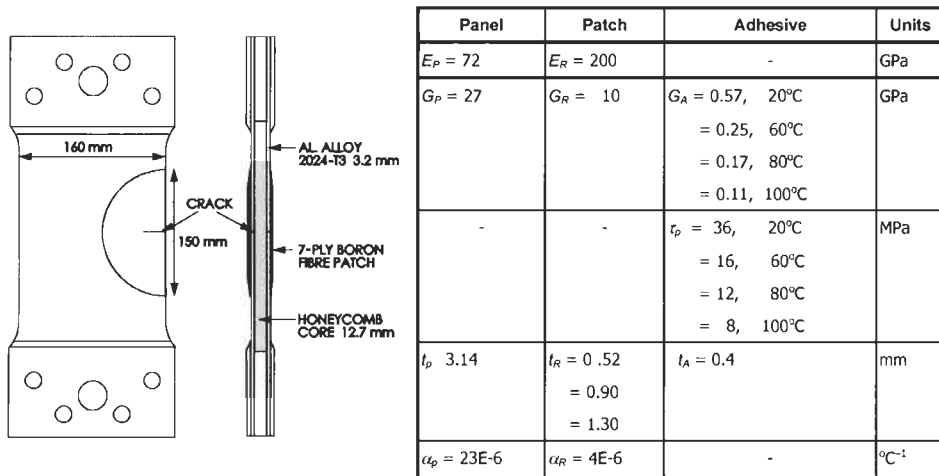


Fig. 13.3. Illustration of the test configuration used to evaluate patching efficiency in patched panels. Note that two cracked-patched panels are tested simultaneously in this configuration. A 7 ply patch is standard but 4 and 10 ply patches were also evaluated. The table provides properties assumed in the calculations based on Cytec short-overlap shear data.

Tests were conducted under constant amplitude stressing to a maximum of 240 MPa at a range of temperatures up to 100 °C and applied R values to 0.64. However, a stress of 138 MPa and an applied R of 0.1 and ambient temperature were the standard conditions. The length of the crack under the patch was measured within about ± 0.5 mm using standard eddy-current NDI.

After testing, the patches were heated to 190 °C for 2 h and stripped from the test specimen (at the elevated temperature). This process discolours any disbonded regions by oxidation, making them clearly visible.

13.4. Fatigue studies

13.4.1. Disbond damage in the patch system

In these studies [2] the aim was to evaluate the effect of disbands on the rate of crack growth. A series of specimens was made with artificial disbands (using thin PTFE sheet inserts) of length $2b$ ranging from 10 mm to 60 mm. Tests were conducted at the standard conditions of 138 MPa and $R=0.1$. The crack-growth results, Figure 13.4(a), show that, as expected, patching efficiency falls dramatically with increasing disbond size.

Tests were also conducted on patched specimens having a single adhesive layer, which are more prone to disbond growth. However, in all specimens, disbands if they occur propagate almost totally within the surface layer of the boron/epoxy, which consists of a very light scrim of glass cloth, impregnated with the matrix epoxy resin. The locus of failure is in the matrix resin between the scrim and the boron fibre surface.

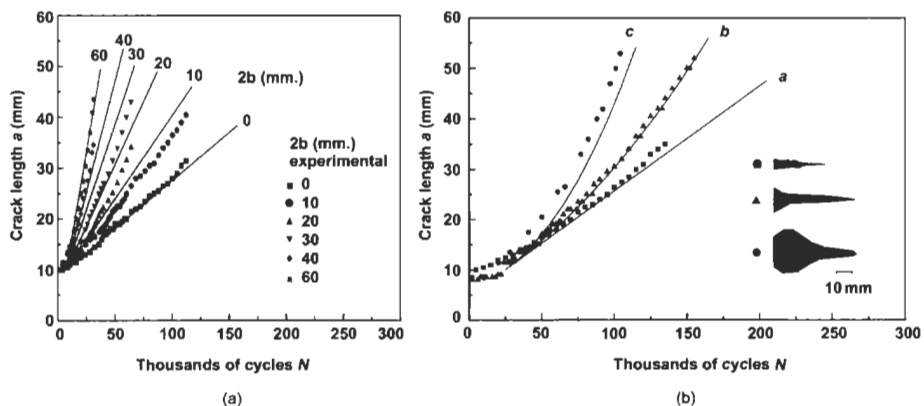


Fig. 13.4. (a) Plot of crack length (a) versus cycles (N) for a patched specimen having artificial disbands of various lengths; solid lines are theoretical estimates, based on estimated A_R and n_R . (b) Plot of crack length (a) versus cycles (N) for patched panels tested at a peak stress of 138 MPa and nominal $R = 0.1$.

Figure 13.4(b) plots crack length a versus N at a peak stress of 138 MPa and $R = 0.1$ for three test panels. The observed final disbond shapes ($2b$) are shown inset in the figure. As seen in Figure 13.4(b), the greater the final disbond size the greater the crack-growth rate and the more strongly parabolic the curve of a versus N . These observations are in qualitative agreement with predictions of the patching model described in Section 13.2.3.

Figure 13.4(b) also shows, as solid curves labelled a to c, the predicted behaviour based on the analysis in Section 13.4 assuming disbond growth rates, db/dN , respectively of 0, 6×10^{-5} and 20×10^{-5} mm/cycle. To produce these curves an Excel spreadsheet was developed to estimate da/dN and thus a versus N based on Eqs (13.2–13.5); where A_R and n_R for Eq. (13.2) were determined from the experiments on patched panels with artificial disbonds.

The approach used to find A_R and n_R was:

- Estimate the theoretical value for the ratio R_{K_I} the relative rates of crack propagation for disbonded and no disbond at the various disbond sizes $2b$. This is defined as:

$$R_{K_I} = \left(\frac{\Delta K_{\infty}(b)}{\Delta K_{\infty}(b=0)} \right) \quad (13.6)$$

Then find an experimental value for n_R using the measured crack growth ratio R_{K_e} :

$$R_{K_e} = \left[\frac{(da/dN)_b}{(da/dN)_{b=0}} \right]^{n_R}, \quad (13.7)$$

where the da/dN values are determined from the crack-growth rates for different disbond rates in the specimen with the artificial disbonds. Assuming $R_{K_I} = R_{K_e}$, the value of n_R was found to be around 3.

- Finally, the experimental value for A_R was obtained from:

$$A_R = \frac{(da/dN)}{(\Delta K_{\infty})^3} \quad (13.8)$$

Using this approach A_R was thus found to be around 5×10^{-11} , which with n_R of around 3 is reasonable for 2024 T3 compared with unpatched results at similar ΔK levels.

Estimates for the disbond growth rates, db/dN , for use in Eq. (13.5) were obtained from the observed *maximum* disbond size observed in the tests divided by N .

On the basis of the results provided here, the tentative conclusion reached is that the model outlined in Section 13.2.3 can reasonably account for the influence of disbond growth in the patch system on patching efficiency.

A major input to this model is the relationship between db/dN and cyclic stress or strain level. This relationship can be obtained empirically from tests on equivalent double-overlap joint specimens representing the repair configuration, Chapter 5.

However, to estimate db/dN generically from repair design data, stress patch geometry *etc.* a suitable damage criterion for the adhesive is required. In the preliminary tests on representative joints [1], the effective shear-strain range in the adhesive ($\Delta\gamma_A$) was used as the damage criterion. An alternative criteria based on strain energy release rate is discussed in Chapter 5.

13.4.2. Influence of stress range

Figure 13.5(a) plots the results for a versus N for a 7 ply specimen for $R=0.1$ at σ_{\max} levels ranging from 80 to 244 MPa. The highest stress level corresponds to typical design limit load capability (DLL) for this alloy. This stress level is nominally experienced only once in the life of an aircraft.

The plots in Figure 13.5 at the low stress levels are quite linear, suggesting that the experimental value of K_R is effectively constant. The increase in K_R with a at small crack lengths as expected from the predictions plotted in Figure 13.2 may be too small to show up in these experiments.

The change from an approximately linear relationship to a more parabolic relationship occurs above $\sigma_{\max}=138$ MPa and results from the development of disbond damage in the bond layer, indicated as a $2b$ value in the figure. For the standard 138 MPa stress level, damage in the adhesive system is negligible so, as expected, patching efficiency is comparable to the best of the previous series, Figure 13.4.

A linear least-squares fit was used to obtain da/dN for all the stress levels, despite the disbond damage found at the two highest stresses. The high stress values at

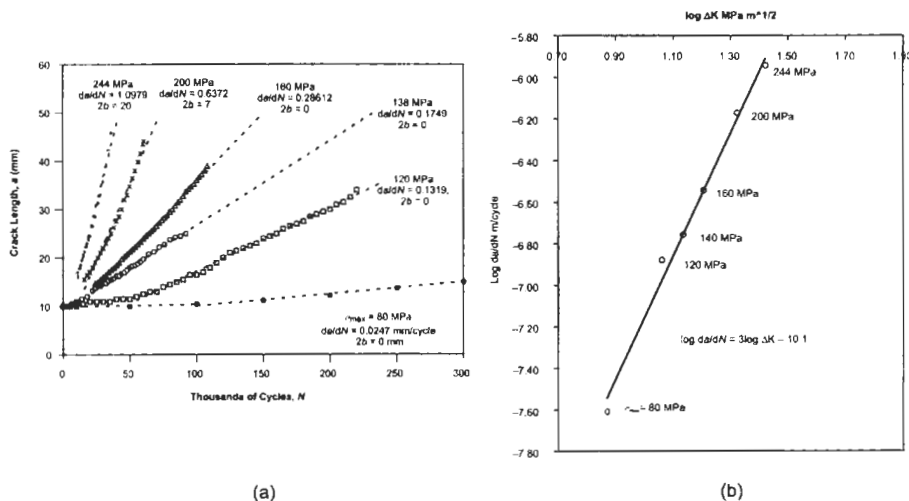


Fig. 13.5. (a) Plots of crack length a versus cycles N for a standard 7-ply patched specimen for applied $R=0.1$. (b) Plot of $\log da/dN$ versus $\log \Delta K_{\infty}$ for the results in (a).

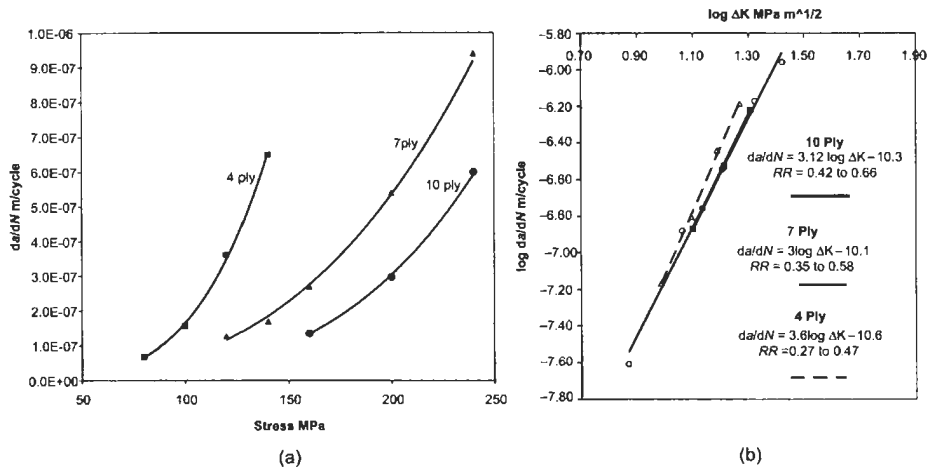


Fig. 13.6. Plots (a) of da/dN versus $\Delta\sigma$ and (b) $\log da/dN$ versus $\log \Delta K_\infty$ for test panels having 4-, 7- or 10-ply patches. R is 0.1, R_R is as indicated on (b) and l_A is about 0.5 mm.

small crack lengths are included since they fit well with the other results; however, if only the large crack da/dN values at these high stresses are considered, these lie well to the left of the curve, as expected for damage. Using these results, Figure 13.5(b) plots $\log da/dN$ versus $\log \Delta K_\infty$ for these test specimens. The relationship thus obtained is $da/dN = 7.9 \times 10^{-11} \Delta K_\infty^3$ m/cycle, which is reasonably close to the results for the damage series mentioned in the previous section.

13.4.3. Influence of patch thickness

Figure 13.6 plots $\log da/dN$ versus $\log \Delta K_\infty$ for test panels with 4-, 7- or 10-ply thick patches, at an R value of 0.1. The results for the 7-ply panel are as plotted in Figure 13.5(b); the results for the 4- and 10-ply panels were obtained from single test panels stressed at several levels.

It can be seen from Figure 13.6 that the model using the da/dN relationship for the 7-ply panel would have given quite reasonable predictions for the 4- and 10-ply panels. However, the values obtained are 4 ply: $n_R = 3.6$, $A_R = 2.3 \times 10^{-11}$; 7 ply: $n_R = 3$, $A_R = 7.7 \times 10^{-11}$; 10 ply: $n_R = 3.12$, $A_R = 5 \times 10^{-11}$.

13.4.4. Influence of R ratio

For an unpatched specimen $R = \sigma_{\min}^\infty / \sigma_{\max}^\infty$, whereas for a patched specimen due to residual stress R_R the effective ratio is given by:

$$R_R = \frac{(R\phi\sigma_\infty + \sigma_T)}{(\phi\sigma_\infty + \sigma_T)}, \quad (13.9)$$

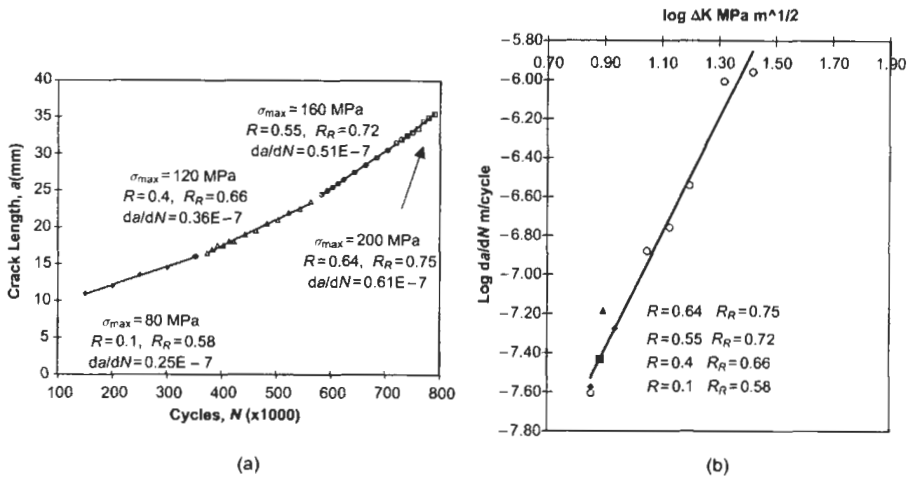


Fig. 13.7. (a) Plot of a versus N for R values as shown for a standard 7-ply test specimen and (b) Plot of $\log da/dN$ versus $\log \Delta K_{\infty}$ for the data from the 7-ply specimen ($R=0.1$) of Fig. 13.6(b), including, as solid data points the corresponding results for different R ratios from (a).

where σ_T is the thermal residual stress, which has a maximum value of:

$$\sigma_T = \frac{t_R E_R E_P \Delta T (\alpha_P - \alpha_R)}{(t_P E_P + t_R E_R)}, \quad (13.10)$$

where $\Delta T = (\text{adhesive cure temperature} - \text{operating temperature})$.

Thus $R_R > R$ and varies with stress level for a constant R . For the standard 7-ply patched panel at $\sigma_{\max} = 138$ MPa and $R = 0.1$, $R_R = 0.58$.

To evaluate the effect of R , standard 7-ply panel tests were conducted at R values of 0.1 (standard), 0.4, 0.55 and 0.64 at $\Delta\sigma = 72$ MPa. Stresses were kept fairly low to avoid adhesive damage, which would have complicated the outcome of the tests. Figure 13.8 shows the results of (a) a versus N and (b) $\log da/dN$ versus $\log \Delta K_{\infty}$.

As seen in Figure 13.7(b), the data points for $R > 0$ fall close to the curve for $R = 0.1$. This is unexpected since a higher crack-growth rate would be expected at the higher R level so that these data points should lie to the left of the curve. However, earlier studies at low temperatures [2] (-40°C) where R_R is very high, (0.55) showed no observable change in crack-growth rate compared to ambient, which also suggests an insensitivity to R .

A possible explanation is that the crack does not experience closure due to the presence of high tensile residual stresses in the patched panel so that the effective ΔK is insensitive to mean stress.

If the behaviour of composite patched cracks turns out to be insensitive to R , prediction of crack-growth behaviour under spectrum loading will be greatly simplified.

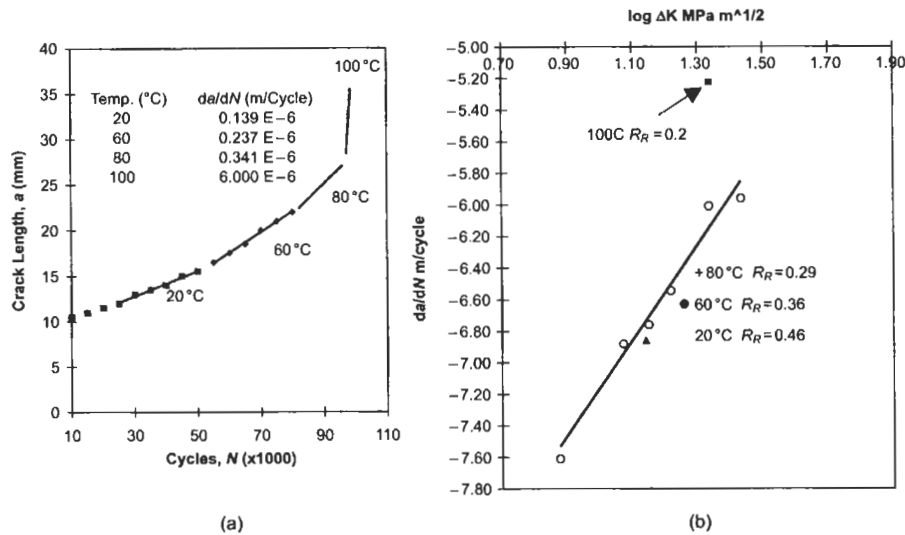


Fig. 13.8. (a) Plot of a versus N at various temperatures and (b) Plot of $\log da/dN$ versus $\log \Delta K_{\infty}$ for the data from the standard 7-ply specimen of Fig. 13.6 ($R=0.1$ at 20 °C), including, as separate data points, the corresponding results from (a).

13.4.5. Influence of temperature

The influence of temperature on crack propagation behaviour in patched specimens is quite complex [2] since several changes occur including:

- A change in R since residual stress reduces as temperature increases
- A change in patching efficiency:
 - ΔK_{∞} is increased as temperature increases because of a decrease in adhesive shear modulus G_A and shear yield stress τ_p ,
 - ΔK_{∞} is increased if the rate of disbond damage increases with increasing temperature.
- A change in the crack propagation properties of the aluminium alloy panel.

To investigate the influence of temperature, tests were conducted on a standard 7-ply specimen at a stress level of 138 MPa at 20, 60, 80 and 100 °C. Estimations of ΔK_{∞} for the log plots against da/dN were based on the temperature values of G_A and τ_p provided in the table with Figure 13.3. Figure 13.8 shows the results of (a) a versus N and (b) $\log da/dN$ versus $\log \Delta K_{\infty}$.

Based on these approximate values Figure 13.8(b) shows that the data points for temperatures up to 80 °C lie below those for the standard 7-ply specimen, suggesting that the patching model or the input data is in error. The main difficulty with the model is to know what values to take for the adhesive properties at elevated temperature because both temperature and strain rate have to be taken into account; the values used (Table in Figure 13.3) for G_A and τ_p were based on

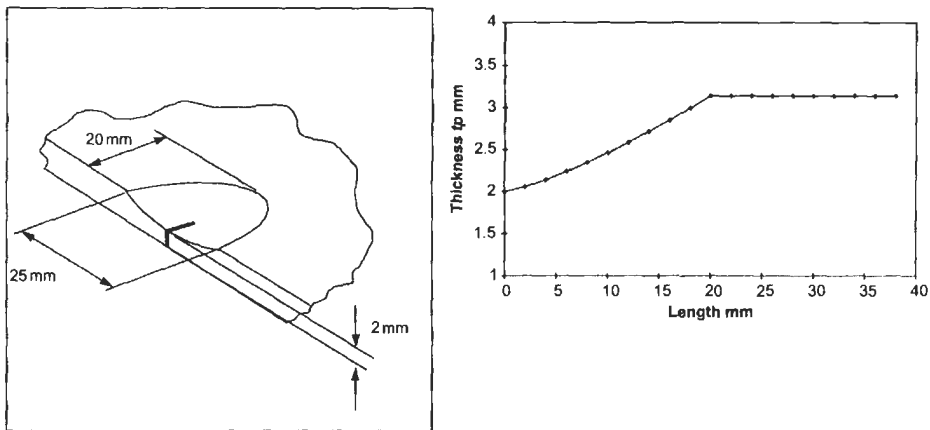


Fig. 13.9. (a) Geometry and (b) profile of the grind-out region.

static measurements and so will be low compared to dynamic values appropriate to the fatigue test conditions.

13.4.6. Influence of panel thickness variation

In these experiments [8] to simulate repair after the removal of corrosion damage, a ground-out region was produced, as shown in Figure 13.9(a), having the profile shown in Figure 13.9(b). Fatigue tests were conducted under constant amplitude stressing to a maximum of 120 MPa and nominal R of 0.1 and ambient temperature. Plots of crack growth versus cycles are shown in Figure 13.10.

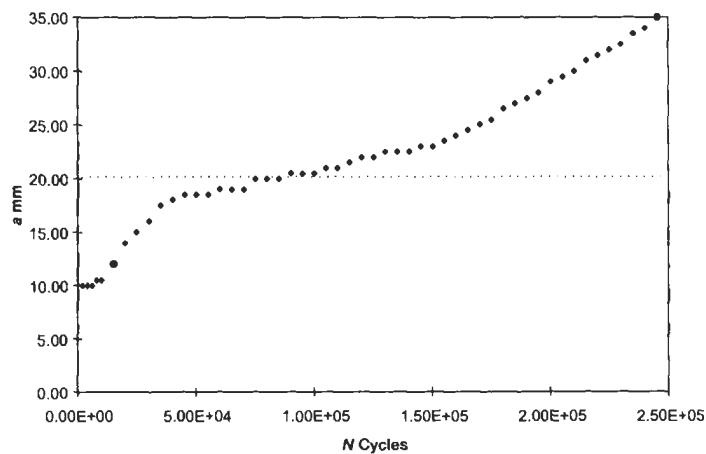


Fig. 13.10. Plot of crack length versus cycles for the specimen with the grind-out.

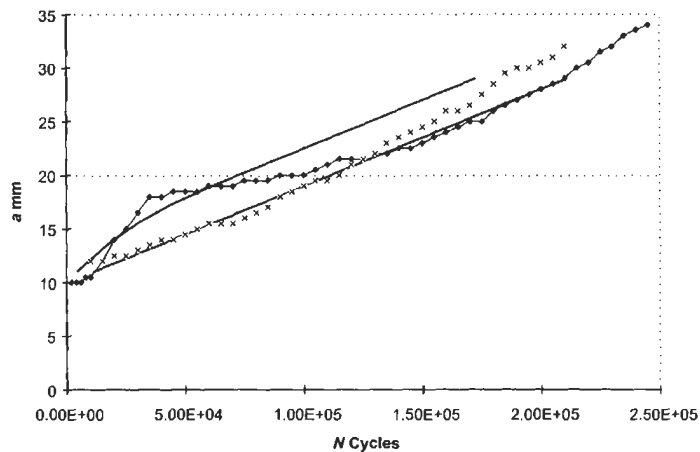


Fig. 13.11. Plots of crack size a versus cycles N for both the standard and the specimen with the simulated corrosion grind out. The predicted curves for both cases are shown as solid lines.

In contrast to the standard panels, the crack-growth behaviour of the panel with the simulated corrosion grind out is highly non-linear. However, once the crack emerges from the grind-out region growth becomes reasonably linear.

The main reasons for this are that over the grind-out zone (a) there is a reduction in patching efficiency (even though the patch is relatively stiffer), due to the increased adhesive thickness and (b) there is an increased stress, due to the local thinning. Thus ΔK_{∞} varies along the grind-out region.

To simplify the analysis, the increased stress in the grind-out zone is assumed to be simply due to the thinning of the panel, with zero stress concentration factor assumed because of the large grind-out radius. Also the panel was arbitrarily divided into 2-mm wide slices normal to the crack (in which tp is assumed constant), each considered as a separate joint with constant load equal to that for the full 3.14 mm thickness.

The parameters A_R and n_R used to estimate crack growth were obtained from the study on crack propagation in the standard panels at varying stress levels, Figure 13.4.

The predicted curves of a versus N are shown superimposed on the experimental curves in Figure 13.11 where it can be seen that, as expected, the predicted behaviour over the constant thickness zone appears in good agreement with the experimental observations. Although agreement over the grind-out zone is only fair, it seems reasonable considering the highly simplified approach taken. The model predicts a smoothed out version of the actual behaviour. However, the rather complex crack-growth behaviour observed, particularly near the edge of the grind-out is difficult to explain and would not be expected to be matched by this simple patching model.

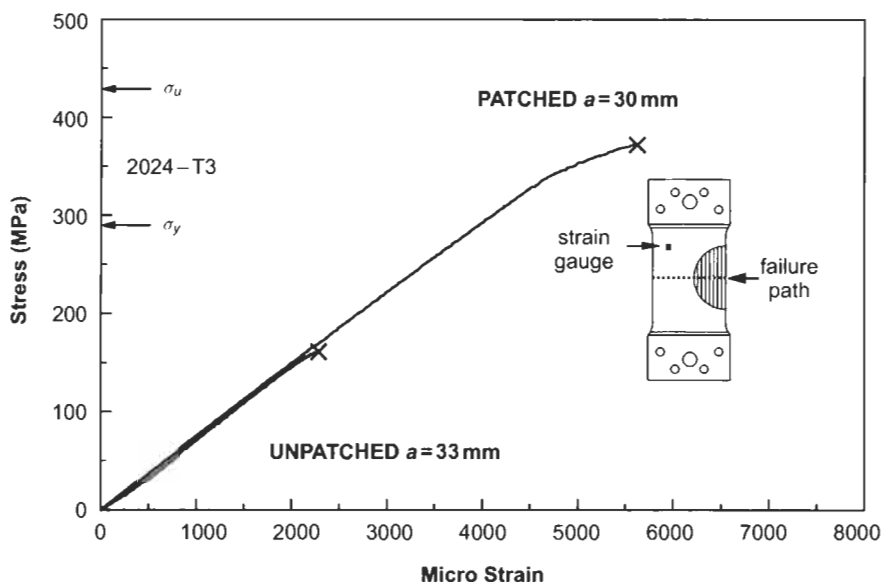


Fig. 13.12. Plot of stress versus strain to failure for (a) a fatigue cracked unpatched panel and (b) a panel initially fatigue cracked unpatched and then patched; strain readings are taken from the gauge position indicated.

13.4.7. Residual strength of patched panels

No prior fatigue

Figure 13.12 plots the stress-strain behaviour to failure of (a) unpatched and (b) patched panels [9]. The strain plotted is measured from the strain gauge shown on the diagram inset. In this test the residual strength in the patched panel exceeded the nominal yield stress σ_y of 2024T3 (B allowable value, Mil Handbook 5C), indicated on Figure 13.12. However, significant yielding was observed at a higher stress level, as shown by the stress at departure from linearity.

Failure of the patched panel, shown schematically in Figure 13.12 inset, occurred as a fracture through the patch above the crack with no evidence of any disbond. This mode of failure could be caused by either:

- (a) exceeding the strain capacity of the patch when the crack grew under the patch, or
- (b) exceeding the strain capacity of the patch over the existing crack.

Stress intensity analysis

The first mechanism requires that the critical stress intensity K_{crit} of the crack under the patch be exceeded. From the failure stress σ_{max} of unpatched panel, K_{crit} can be obtained using the standard relationship for an edge-cracked panel

(assumed to apply for this specimen configuration):

$$K_{\text{crit}} = 1.1 \sigma_{\text{max}} \sqrt{\pi a} \quad (13.11)$$

Since, from Figure 13.12, σ_{max} is around 160 MPa and a is 33 mm, K_{crit} is estimated to be about $56 \text{ MPa m}^{1/2}$. Similar results for K_{crit} were obtained from several other unpatched panels. These values for K_{crit} are in reasonable agreement with published values for 2024T3 panels of this thickness.

For the patched panel, patching theory suggests that K_{∞} is approximately $53 \text{ MPa m}^{1/2}$. Although K_{∞} is fairly close to K_{crit} , the former is an upper-bound estimate of stress intensity so it is tentatively concluded that crack propagation in the metal was not the cause of the failure.

Strain capacity analysis

A direct estimate, using joint theory, of *net strain* in the patch over the crack indicates a value of 7100 microstrain. However, if the extra load attracted to the patch (as a result of the inclusion effect) is considered, the strain could be as high as 9500 microstrain. Since strain capacity of the boron/epoxy is measured to be about 7300 microstrain, the conclusion is that failure was probably a result of initial failure of the patch.

Furthermore, as discussed in reference [1] for the patch configuration employed, the ratio (inner-surface strain)/(outer-surface strain) in the patch is significantly greater than unity. In this case it is estimated to be about 2.5. On this basis the inner strain could have exceeded 12 000 microstrain; however, the strain elevation would be very localised.

The conclusion is thus reached that failure in the patched panels resulted from initial failure of the patch, possibly associated with the strain concentration at its inner surface.

This failure mode may change where significant disbond growth occurs during fatigue cycling for two reasons:

- Stress intensity K_{∞} may exceed K_{crit} allowing the crack to grow catastrophically under the patch.
- The strain concentration in the patch over the crack will be reduced if even minor disbonding occurs.

Thus, for a small disbond, say a few mm, residual strength is likely to increase because of the reduced stress concentration in the patch.

Increasing the thickness of the patch, say to nine layers (the current patch is seven layers), should provide some increase in residual strength. However, at higher stress levels, plastic yielding of the metal around the patch (exacerbated by stress concentrations at the ends of the patch) will limit this increase. The failure mode is then expected to change from patch failure to disbonding from at the ends of the patch.

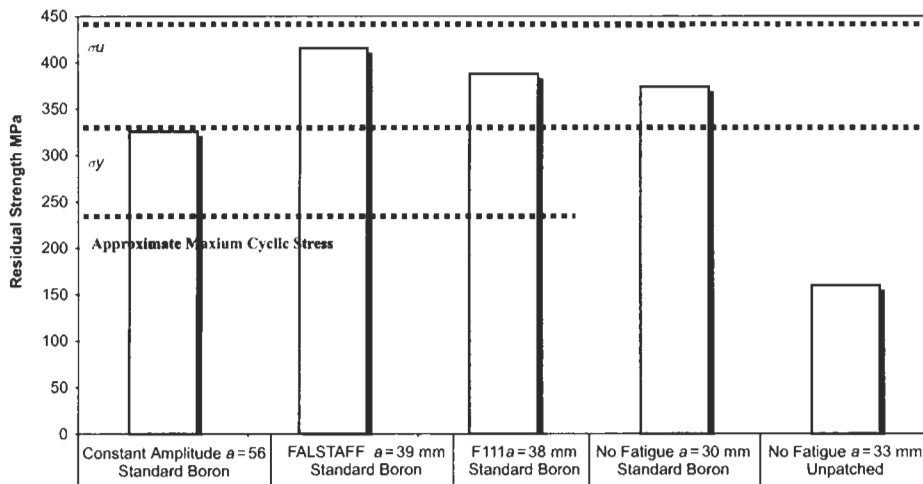


Fig. 13.13. Histogram showing residual strengths for patched panels with or without prior fatigue testing and for an unpatched panel. The results for the panels with no prior fatigue are plotted in Figure 13.12.

Residual strength following fatigue testing

Tests were also conducted on panels after fatigue testing under (a) constant amplitude, (b) F-111 spectrum loading-representative of the F-111 lower wing skin or (c) FALSTAFF spectrum, representative of a standard fighter lower wing skin.

Figure 13.13 depicts the results together with those patched after fatigue cracking. Thermographic NDI was used in an attempt to detect disbond damage over the crack region in the fatigue-tested specimen; however, damage could only be detected in the FALSTAFF specimen as a relatively small ~ 2 mm ellipse centred on the crack. This does not imply that the other specimens had not suffered damage, only that the disbonds were probably smaller or for some reason less detectable by thermography.

The first conclusion is that the residual strength has not been reduced by cyclic loading for cracks in the 30–40 mm range. Indeed the strength may have actually increased due to the reduction of stress concentration around the crack caused by any local disbonding. In the case of the 56-mm crack residual strength was clearly reduced compared to the others. Since this crack is approaching the boundary of the patch, it is possible that in this case the critical stress intensity for the crack in the panel was exceeded, rather than the failure stress of the boron/epoxy. In all test panels the strength equalled or exceeded σ_y – although, with no margin in the case of the panel with the 56-mm crack.

As discussed later, there is a case for equating σ_y with DUL. If this case is accepted it can be concluded that the patched panels had adequate residual strength to satisfy most certification requirements.

13.5. An approach to b/ep patch design

13.5.1. Cyclic loading

Assuming that environmental degradation of the adhesive is not an issue (through good quality control), the margin of safety, efficiency and durability of a repair to a cracked component can be assessed from estimates of the following:

- The stress intensity range ΔK and R in the repaired region. This determines patching efficiency through the crack-growth parameters A_R and n_R .
- The tensile strain e_R in the b/ep patch which allows estimation of the margin of safety for failure of the patch. It is assumed for a composite patch that fatigue is not an issue; if it were then the range of strain Δe_R and R ratio would have to be considered.
- A (validated) damage parameter in the adhesive system (including the composite interface). Possible parameters are the shear strain range $\Delta\gamma$ or Mode II energy release rate ΔG_{II} . This allows estimation of the fatigue durability of the adhesive system. It is best, if feasible, to design the repair so that the damage threshold of the adhesive system over the crack is not exceeded; however, if it is not feasible the disbond growth rate, db/dN (Section 13.2.3) must be included in the analysis, using Eq. (4). Limited disbond growth over the crack is acceptable, however, and within limits will not dramatically reduce patching efficiency.

Another important factor needed for design of the repair system is the length L^* available for the patch between obstructions (Figure 13.14), since this can limit the allowable patch thickness. The length L_R required for efficient load transfer depends on the patch and adhesive parameters (Figure 13.3) including patch thickness t_p and the taper rate at the outer ends of the patch.

Assuming largely elastic conditions in the adhesive (as required to avoid patch system fatigue), a conservative estimate of the patch length [1] is given by:

$$L_R = \frac{6}{\beta} + \text{length of the taper} , \quad (13.12)$$

where β is given by Eq. (1d), The taper rate for b/ep we use is around 3 mm per ply.

Finally, the residual stress σ_T , resulting from patch and component thermal expansion mismatch, must be included in the analysis, since this influences $\Delta\gamma$, e_R and R_R . Residual stress σ_T depends on $\Delta T = (T_{\text{operating temperature}} - T_{\text{cure temperature}})$, typically 100 °C for a 120 °C curing adhesive and, $\Delta\alpha = (\alpha_{\text{patch}} - \alpha_{\text{component}})$. The length between thermal expansion constraints in the component structure (see Figure 13.13) influences $\alpha_{\text{component}}$ which for full constraint is $0.5\alpha_p$.

Based on Rose's analysis described earlier, the author [1] developed a simple algorithm for estimating the minimum thickness patch that could be applied within the installation constraints that would survive the external cyclic loading.

It is generally desired to use the thinnest patch feasible for several reasons, including (a) to minimise the residual stress problems, (b) to maintain aerodynamic

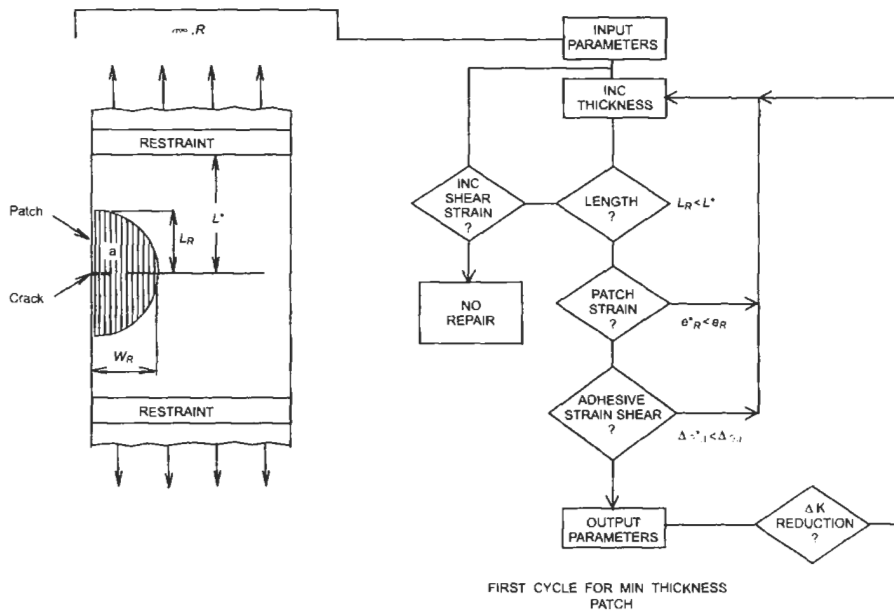


Fig. 13.14. Outline of algorithm for designing the minimum thickness patch.

acceptability, for example to minimise disturbance to the airflow when repairs are made to an external surface, (c) to minimise balance problems; for example, when repairs are made to a control surface, and (d) to comply with installation restraints, for example, not to exceed available fastener lengths when fasteners must pass through the patch for system requirements, or to maintain clearance between moving surfaces.

The logic for the design approach is shown in flow chart form in Figure 13.14, which is based on comparison of the following, as the patch is increased in thickness one ply at a time:

- The computed patch length L_R with the allowable (available) length L^*
- The computed strain in the patch compared with the experimentally determined allowable strain e_R^* ; a value of 5000 microstrain was found to be reasonable for b/ep.
- The computed shear-strain range compared with experimentally determined allowable $\Delta\gamma^* = 0.18$ was originally used for FM73, but current work suggests that 0.10 may be more appropriate for long life repairs.

These patch and adhesive allowables were obtained from tests on representative bonded joints. Increasing patch thickness increases L_R but reduces e_R and $\Delta\gamma$.

Assuming constant amplitude fatigue at $\Delta\sigma_\infty$ and R , Figure 13.15, shows the outcome of a calculation based on the parameters listed.

EXAMPLE

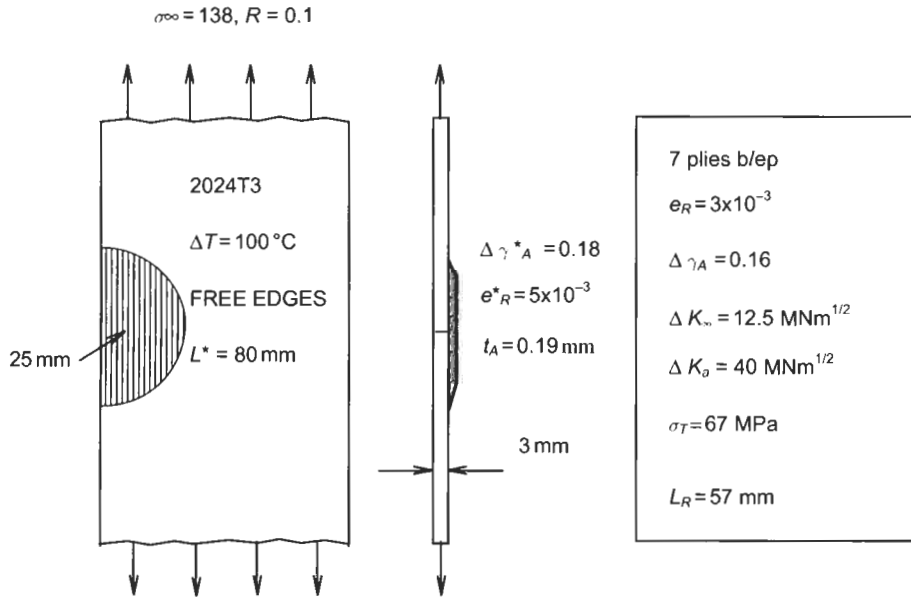


Fig. 13.15. Outcome of an analysis for the minimum patch thickness, ΔK_{u} is the stress intensity for the unpatched case.

Once ΔK_{∞} is estimated the inspection interval N can be determined from Eq. (13.2) and (1a) or (if disbonding is a consideration) from Eq. (13.4) as:

$$N = \int_{a_i}^{a_X} \frac{da}{A_R} (\Delta K_{\infty})^{n_R}, \quad (13.13)$$

where a_i is the initial crack size and a_X is the size chosen for inspection. Typically a_X would be less than one third patch width to provide at least three chances of finding the crack before it grows out from under the patch.

As shown in Figure 13.14, if the inspection interval is too short, (the ΔK reduction is inadequate) there is an option to increase the thickness of the patch providing it can still fit within the allowable length.

13.5.2. Spectrum loading

Crack-growth analysis is significantly more complex under spectrum loading. It is feasible to assess crack growth for the cracked component and damage growth in the adhesive system on a cycle-by-cycle basis for the various values of effective $\Delta K \sigma_{\infty}$ and R .

If the spectrum is unknown, design can be based on a standard spectrum: FALSTAFF or TWIST for fighter or large transport aircraft respectively. If the peak stress in the spectrum (the design limit stress, σ_{DLL}) is unknown, an estimate can be made based on the material yield stress σ_y as described in the next section.

The patch length L_R can then be estimated for the estimated patch thickness t_p to obtain the required K reduction. However, this may be over-conservative since by definition σ_{DLL} is expected to occur only once (although in fighter aircraft it can occur many times) in the life of the aircraft. Thus L_R could be based on say 0.5 or $0.6 \sigma_{DLL}$ – and still provide acceptable residual strength at say $1.2 \times \sigma_{DLL}$ (see final section).

A simplified estimate of patching efficiency could be obtained by increasing stresses in all cycles in the spectrum *above the threshold for crack growth* to the peak stress σ_{DLL} . As this is a severe assumption for both the cracked component and patch system, it provides an over-conservative estimate. A complication with using this approach is that the threshold stress will reduce with disbond growth.

13.5.2.1. Estimating the design limit stress

There are several options to estimate the σ_{DLL} :

- The most conservative is to equate it with material yield σ_y . Thus the nominal stress at the design ultimate load DUL is $1.5\sigma_y$, which marginally exceeds the material ultimate strength σ_u . For example for 2024T3 and 7075T6, respectively, $\sigma_u/\sigma_y = 1.4$ and 1.3 .
- A less conservative but (in the author's opinion) more reasonable assumption [2] is to equate the stress at DUL with σ_y . Thus in accord with the requirements for DLL, where limited yielding is allowed at stress concentrations but no large-scale yielding leading to permanent deformation. As an example, Table 13.1 provides σ_{DLL} and σ_y values for the F-111 lower wing skin, which is made of aluminium alloy 2024 T581. This shows that the ratio σ_y/σ_{DLL} exceeds 1.5 , as required. Use of approach A would result in a 30–40% overdesign.
- By direct strain measurement, either from a static calibration or in flight.
- From a knowledge of the external aerodynamic loads and the availability of a full F-E model of the aircraft and local region to estimate internal loads.

Table 13.1

Data on design limit stress σ_{DLL} for F-111 for several (DADTA) data points in the lower wing made of aluminium alloy 2024 T581, compared with the yield stress σ_y .

DADTA Item No.	σ_{DLL}	σ_y	σ_u	σ_u/σ_y	$\sigma_y/1.5$	σ_y/σ_{DLL}	σ_u/σ_{DLL}
67	202.9	400.2	462.3	1.2	266.8	1.97	2.28
70	167.0	400.2	462.3	1.2	266.8	2.40	2.77
70a	204.2	400.2	462.3	1.2	266.8	1.96	2.26
78	149.7	400.2	462.3	1.2	266.8	2.67	3.09
154	171.8	400.2	462.3	1.2	266.8	2.33	2.69
194	165.6	400.2	462.3	1.2	266.8	2.42	2.79

Approach (c) is very time consuming and likely to be prohibitively expensive in most repairs. Approach (d) depends on having the loads and F-E model available, and even then will be costly and time consuming. However, this is the preferred approach for critical repairs and was the procedure adopted in a bonded composite repair developed for the F-111 lower wing skin [10].

Of the two simple approaches the result of assuming approach (a) is that a thick repair would be designed resulting, in the case of composite patches, in large residual stresses and in large parasitic stress concentrations. This is not a major concern for thin-skin components (skin thickness $< 2\text{ mm}$) where approach (a) is probably quite acceptable.

13.5.3. Check on residual strength

It is most important to check that residual strength of the repaired region will exceed σ_{DLL} by an acceptable factor F generally between 1.2 and $1.5 \times$ (the latter being the design ultimate). If this is not the case the thickness of the patch will need to be increased beyond that required for the fatigue stress level.

The residual strength of the patched cracked component appears to be dependent on the strain capability of the reinforcement (including strain concentration) and the adhesive rather than on the stress intensity in the patched crack. However, a first test should be made to check that at $F \times \sigma_{DLL}$, $K_R < K_Q$ the effective critical stress intensity for the cracked material. If this is not the case then the patch thickness must be increased.

The main test check is to ensure that the patch static-strength allowables, obtained from tests on representative bonded joints, are not exceeded. For the adhesive the allowable shear strain will be greatly increased (for FM73, $\Delta\gamma^* = 0.5$); however, the allowable patch strain e_R^* is unchanged, since for b/ep the static strength allowable is the about same as the fatigue allowable.

At the ultimate load the adhesive yield shear stress will be greatly exceeded so, in principle, a much longer length than predicted by Eq. (13.12) would be required. However, since the ultimate load case is a check load (where large-scale yielding in both the metallic structure and adhesive is acceptable, as long as failure does not occur) the length given by Eq. (13.12) for the fatigue case should still provide an adequate strength margin.

References

1. Baker, A.A. (1988). Crack patching: Experimental studies, practical applications. Chapter 6 in *Bonded Repair of Aircraft Structures*, (A.A. Baker and R. Jones, eds.) Martinus Nijhoff, pp. 107–173.
2. Baker, A.A. (1994). Bonded composite repair of metallic aircraft components, Paper 1 in AGARD-CP-550 Composite Repair of Military Aircraft Structures.
3. Rose, L.R.F. (1988). Theoretical analysis of crack patching. Chapter 5 in *Bonded Repair of Aircraft Structures*, (A.A. Baker and R. Jones, eds.), Martinus Nijhoff, pp. 107–173.

4. Wang, C.H. and Rose, L.R.F. (1998). Bonded repair of cracks under mixed mode loading. *Int. J. of Solids*, **35**, pp. 2748–2773.
5. Baker, A.A. (1993). Repair efficiency in fatigue-cracked panels reinforced with boron/epoxy patches. *Fatigue and Fracture of Engineering Materials and Structures*, **16**, pp. 753–765.
6. Chalkley, P.D. and Baker, A.A. (1999). Development of a generic repair joint for certification of bonded composite repairs. *Int. J. Adhesion and Adhesives* **19**, pp. 121–132.
7. Baker, A.A. and Chester, R.J. (1992). Minimum surface treatments for adhesively bonded repairs. *Int. J. of Adhesives and Adhesion*, **12**, pp. 73–78.
8. Baker, A.A. and Beninati, O. (1997) Repair efficiency in composite patched panels after removal of corrosion damage. *Proc. of Int. Aerospace Conf. 1997*, Sydney, Australia, pp. 53–60.
9. Baker, A.A. (1997). On the certification of bonded composite repairs to primary aircraft structure. *Proc. of ICCM 11*, Gold Coast Australia, July, Volume 1, pp. 1–24.
10. Baker, A.A., Rose, L.R. and Walker, K.F. (1999). Repair substantiation for a bonded composite repair to F-111 lower wing skin, *Applied Composite Materials*, **6**, pp. 251–267.

Chapter 14

GLARE PATCHING EFFICIENCY STUDIES

R. FREDELL and C. GUIJT

Department of Engineering Mechanics, Center for Aircraft Structural Life Extension, US Air Force Academy

14.1 Introduction

Most bonded composite crack patching has been accomplished on small areas of thick structures using high-modulus boron/epoxy composites. Extending the lives of aging transport fuselage structures, however, may involve repairs to large areas of thin fuselage skins and lap joints. These structures often see their highest mechanical stresses (due to pressurization) at the low temperatures encountered at cruise altitude. Hence, more attention to the thermal properties of composite materials may be needed when fuselage structures are being repaired.

This chapter presents the results of detailed parametric studies of thermal effects on bonded repairs to cracked pressurized transport fuselage structures. The hybrid glass/epoxy/ aluminum materials known as GLARE are offered as an alternative to boron/epoxy for this special crack patching application. Experiments performed at room temperature, and at the low temperatures encountered at high altitudes, show that bonded GLARE 2 patches can out-perform boron-epoxy in selected repairs to thin skins. These results are discussed with the conclusion that, under certain circumstances, thermal compatibility can be the driving factor in repair material selection in pressurized fuselage skin repairs.

14.1.1. Overview and background of fibre metal laminates

The Fiber metal laminate (FML) GLARE 2 is a hybrid material of moderate modulus, combining 2024-T3 aluminum with high-strength unidirectional S-glass/epoxy composite in a sheet like laminate [2–3]. It is known for its excellent fatigue resistance due to the “crack-bridging” effect of the fibers and its high residual

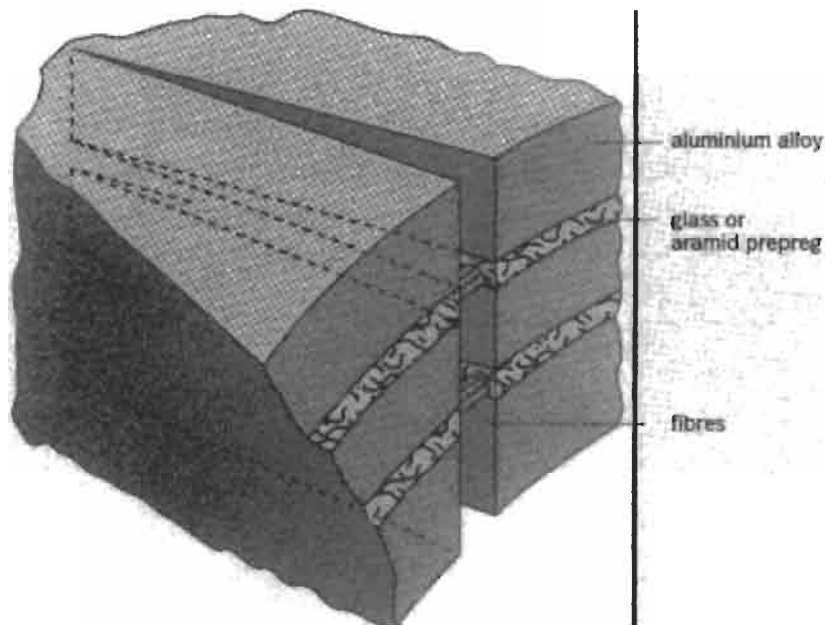


Fig. 14.1. Schematic of glass/epoxy/aluminum laminate GLARE 2.

strength. Figure 14.1 shows a schematic of GLARE 2 with a crack in the aluminum layers and “crack-bridging” fibers.

GLARE and the ARALL family of FMLs were developed by Delft University, the Netherlands, with the support of AKZO and Alcoa. FMLs have the high strength and excellent fatigue resistance of advanced composite materials, while retaining the machinability and cold-formability of aluminum alloys. In addition, the GLARE laminates approach the performance of titanium alloys as fire barrier materials. Fiber metal laminates are in service on the C-17 Globemaster III (aft cargo door), Boeing 777 (cargo floors and liners) aircraft, and as bonded repairs on a USAF C-5A. Airbus Industrie will use GLARE as a fuselage skin material for the A-380 aircraft.

14.2. Parametric studies of various patch materials

When one focuses on pressurized fuselage skin repairs, the following special conditions must be considered:

- The damaged structure is relatively thin (up to 2 mm/0.079"). An extremely stiff patch is not required, or even desirable, as load attraction to the repaired region could cause secondary damage to the relatively thin skin.
- The adhesive is cured at a temperature ranging from 80 to 120 °C (180 to 250 °F), and the fuselage sees service temperatures ranging from perhaps 60 °C (140 °F)

(unloaded, hot day on the ground) to -54°C (-65°F) (maximum internal pressure, temperature at cruise altitude). This increases the likelihood of thermal mismatch problems.

Because the transport fuselage experiences its greatest internal pressure loads at its minimum service temperature, thermally-induced stresses in a fuselage bonded repair can be a more significant consideration than in, say, a fighter wing skin repair.

Reduction in stress intensity factor, K , to slow or stop crack growth, is not the only design criterion for effective crack patching. The significant variables to be considered in a crack patching design include (see Figure 14.2):

- slow down or stop crack growth
- acceptably low stresses in the patch to avoid patch failure
- avoidance of excessively high stresses in the skin adjacent to the repair to preclude new fatigue problems in the skin
- tolerably low peel and shear stresses in the bond line
- prevention of adhesive bond line shear yielding to ensure patch and bondline durability

By varying the patch material and dimensions, the adhesive, and the curing temperature, the repair designer may be able to produce a patch meeting all of these

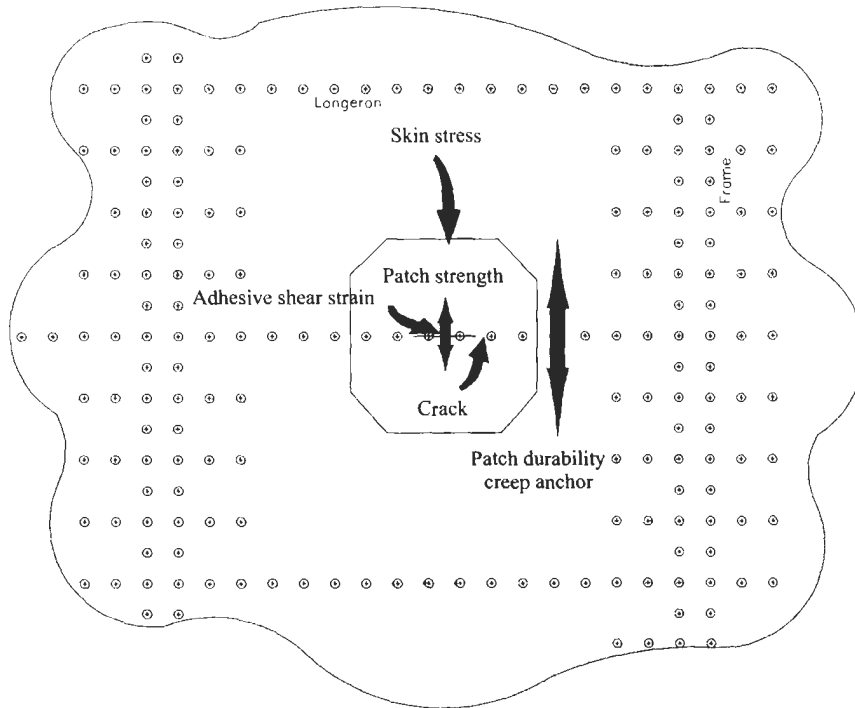


Fig. 14.2. Failure modes for bonded repairs.

goals for successful patching. However, in an operational maintenance environment, the design and analysis of bonded repairs must be able to be accomplished quickly, often without a detailed knowledge of the precise stress state in the cracked panel.

This section describes the results of detailed parametric studies performed on various repair designs based on the Rose model of crack patching [6–8]. It considers an infinite, center-cracked, isotropic plate loaded by a remote biaxial stress with a bonded orthotropic elliptical patch on one side of the plate. Several writers have published studies comparing various finite element-based crack patching models [9–11] with the Rose model.

Tarn and Shek [9] performed a detailed finite element analysis to compare the crack-bridging efficiency predicted by various elastic models of boron/epoxy patch repair of cracked aluminum sheets. Material responses were assumed to be linear elastic, and thermal effects were ignored.

With increased loading, inelastic material behavior is first observed in the adhesive layer. Therefore, to consider linearly elastic material behavior only, the adhesive in the Rose model was given an artificially high shear yield strength. In the elastic case shown in Figure 14.3, the reduction in K of Rose (shown as the “CalcuRep” result) matches well with the more complex finite element models from the literature. The maximum difference between Rose and [9] occurred when the repair patch was eight plies thick. Here Rose overestimated the K reduction by no more than 5%.

The assumption of various authors that the adhesive will behave elastically is questionable, especially when the patch extensional stiffness is roughly equal with

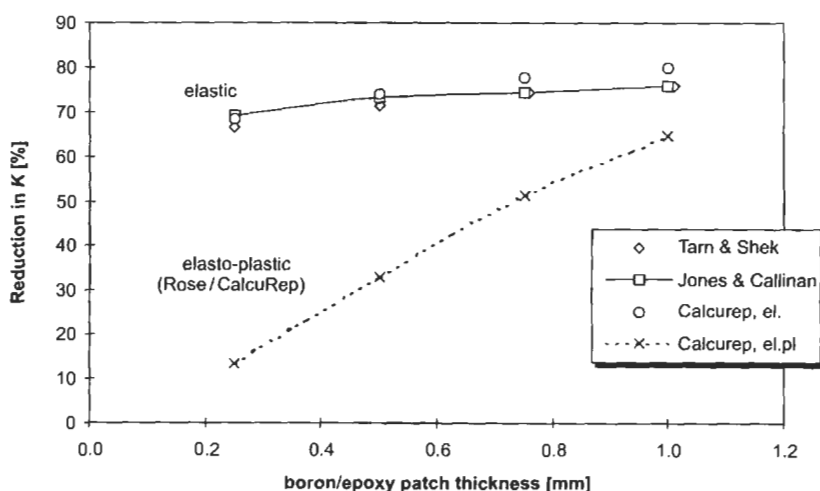


Fig. 14.3. Comparison of reduction in stress intensity factor for bonded boron/epoxy patches, elastic and elastic-plastic models of adhesive behavior.

the cracked plate stiffness. Thin patches experience large normal strains over the crack and induce large shear strains in the adhesive as well.

The lowest line in Figure 14.3 represents the Rose model's results when elastic-plastic adhesive behavior was allowed around the crack tip. The differences between the models are striking. With the elastic model, adhesive shear stresses are able to reach unrealistically high levels so thin patches appear to be quite effective at reducing K . However, including inelastic material effects in the model shows that when patch thicknesses are relatively low, the reduction in K is not nearly as significant. This is due to the patch strains being quite high, which can lead to early adhesive yielding and delamination, reducing crack-patching effectiveness. Therefore, it can be said that a realistic constitutive model of the adhesive is important, since the avoidance of large-scale adhesive yielding can be important for effective crack patching and good patch durability.

This result is consistent with the work of Marissen [12] and Roebroeks [13], who found that low fiber/metal ratios (i.e. low patch/plate stiffness ratios) resulted in poor crack-bridging efficiency for fiber metal laminates. The elastic results converge with the elastic-plastic model only when six boron plies are used. At this point, the extensional stiffness of the boron patch approaches that of the plate.

These results allowed sufficient confidence in Rose's basic approach to proceed with the parametric analysis, outlined in the following section. The study assesses the thermal considerations to be accounted for in the selection of patch materials.

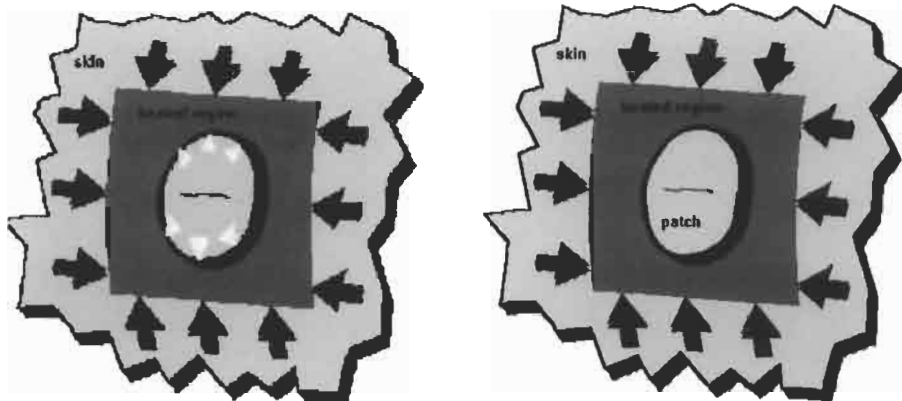
Crack patching of aircraft usually involves local heating of the repair area. During the curing process, the unheated structure surrounding the repair area constrains the thermal expansion of the heated area. But the patch, which is entirely inside the heated region, expands freely. In stiffened structures, the "effective" coefficient of thermal expansion (CTE) of the constrained structure is much less than the material CTE. Figure 14.4 illustrates this effect.

After cooling to room temperature, the bondline for patch materials with relatively low CTE, like boron- or carbon-fiber composites, is relatively stress free. This has been pointed out by various writers [7,11,14–16]. Moderate- to high-CTE patches actually place the crack in compression at room temperature. This reduces the stress intensity near the crack tip and decreases or even stops crack growth. Figure 14.5 shows the effect of cooling to room temperature for high- and low-CTE materials, respectively.

The blue arrows indicate the compressive stress in the skin acting on the crack. The additional tensile stress in the patch is less significant if composite patch materials are used with a higher fatigue threshold.

When a transport aircraft climbs to cruising altitude, its fuselage is cooled uniformly to the outside air temperature (-54°C at 10 km). The structure cools and contracts uniformly, but a low thermal expansion composite patch would not contract nearly as much.

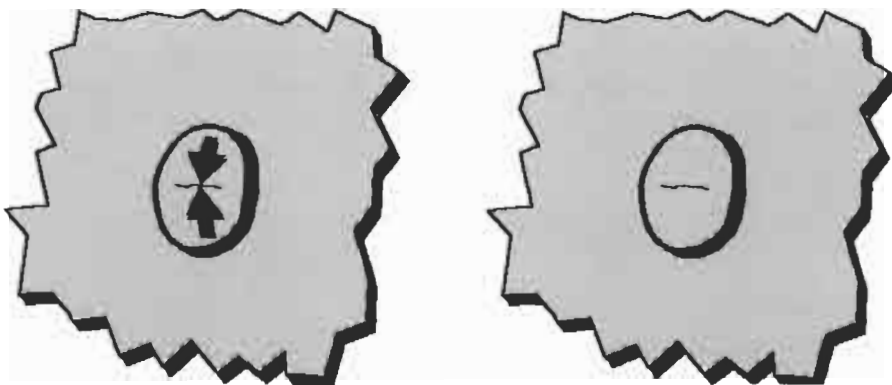
For example, a boron-epoxy patch shrinks only about 1/6 as much as the now-unconstrained aluminum fuselage. This induces an additional cyclic tensile (crack-opening) load on the crack tip at a time when the pressure-induced stress is highest. Further, the adhesive that was ductile and relatively flexible at room temperature is



High CTE patch (e.g., GLARE)

Low CTE patch (e.g., boron-epoxy)

Fig. 14.4. Thermal effects in skin and patch, due to the elevated temperature during bonding.



High CTE patch (e.g., GLARE)

Low CTE patch (e.g., boron-epoxy)

Fig. 14.5. Thermal effects in skin and patch at room temperature.

substantially stiffer and more brittle at -54°C . The additional tensile load due to these effects occurs every flight. On the other hand, a patch material with a moderate or high CTE, such as GLARE 2 will still cause some crack-closing compression in the skin. (GLARE 2 has a CTE of approximately two-thirds that of aluminum.)

Figure 14.6 compares the patching efficiency of two potential fuselage patch materials, boron-epoxy and GLARE[®] 2. The patching efficiency is defined as the reduction of the stress intensity factor, K , at the crack tip. A sufficient reduction of these stresses will slow down or even stop further crack growth. The stresses near

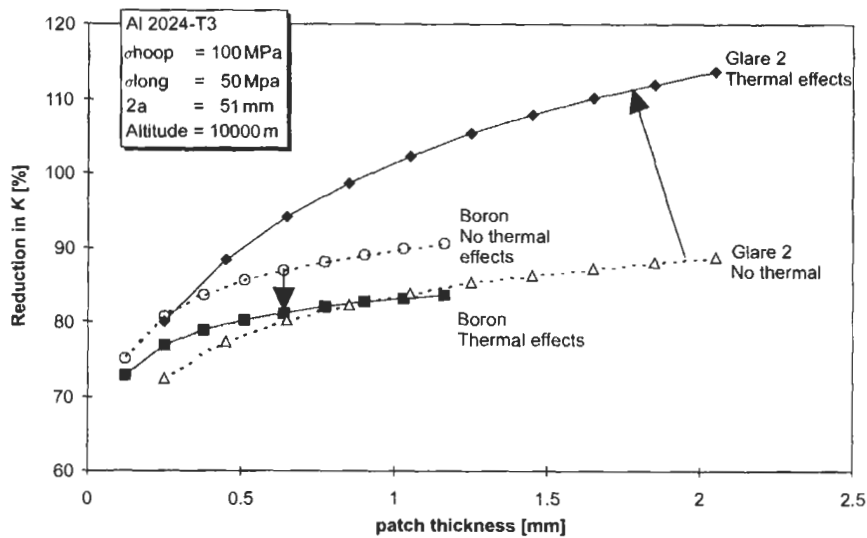


Fig. 14.6. Comparison of reduction in stress intensity factor for bonded GLARE 2 and boron patches, with and without considering thermal effects [5].

the crack tip are described with the stress intensity factor K . A 100% reduction in K means no crack opening. Higher than 100% means that the crack is still in compression at the given load due to the residual thermal stresses.

The comparison shown, using the Rose-model, was done for the case of a narrow-body fuselage at a cruising altitude of 10 km. In the 2024-T3 Aluminum skin of 1 mm thickness, a crack of 51 mm is modeled. The patch dimensions were the same for both materials. The patch length (perpendicular to the crack) was 140 mm, the patch width was 102 mm. To bond the patch over the crack, the adhesive AF-163-2K of 3M was used. The Shear Modulus, G , and the Yield Strength, τ_{yield} , of this material (modeled as elastic-perfectly plastic material) were corrected for the cruising temperature. The manufacturer-recommended cure temperature of 120 °C was used. A biaxial stress field of 100 MPa (hoop tension) and 50 MPa (longitudinal tension) was applied.

When thermal effects are ignored, the much stiffer boron/epoxy patch seems to do a better job closing the crack. However, when the complexities of constraint during bonding, and free thermal contraction during cruise flight are considered, GLARE 2 is predicted to be the more effective patch. At an often used stiffness ratio ($E_{\text{patch}} * t_{\text{patch}} / E_{\text{skin}} * t_{\text{skin}}$) of roughly one, the thickness of the Glare patch is 1.1 mm and the thickness for boron is 0.39 mm. The K -reduction is 100% for Glare and 78% for boron.

Thermal effects also change the situation with regard to skin stresses at the edge of the patch: Any thermal residual K reduction at the crack tip, gained by using a high-CTE patch, occurs at the expense of additional tension in the skin at the patch tip. The designer/analyst must strike the proper balance.

The choice of adhesive cure temperature can also affect the results. When repairs are performed on or near structures containing absorbed moisture (e.g. honeycomb core materials), cure temperatures under 100°C are desired to prevent damage from evolved steam. Furthermore, a lower cure temperature can reduce thermal buckling problems. Moreover, cure temperatures are limited by equipment capabilities, which in turn are driven by the size, material(s), structure, and substructure (which can act as an effective heat sink) of the repair area.

When materials of different coefficients of thermal expansion are bonded, cure temperature can affect residual stress states as well. Baker [17] recommends curing at "the lowest possible temperature" to minimize residual thermal stresses. If a patch has a higher effective coefficient of thermal expansion than the substrate, cooling from the cure temperature results in residual compression at the crack tip. As pointed out before, this should by itself be beneficial for fatigue crack retardation. If the patch's effective thermal expansion coefficient is lower than the substrate's, a residual tensile (crack-opening) load will exist at the crack tip. However, the change in cure cycle could (adversely) affect the adhesive properties.

Figure 14.7 shows the effect of various cure temperatures on the patching effectiveness of GLARE 2 and boron/epoxy patches in the Rose model at the cruise altitude situation described before. In the analyzed case, the effective expansion coefficient of the stiffened fuselage structure is approximately equal to that of boron/epoxy during the cure cycle of the adhesive (local heating). Thus, in fuselage skin repairs, boron/epoxy is not substantially affected by a change in the cure temperature. The large thermal effects with boron/epoxy occur in the cooling from room to cruise temperature of the complete structure, now the CTE of the structure

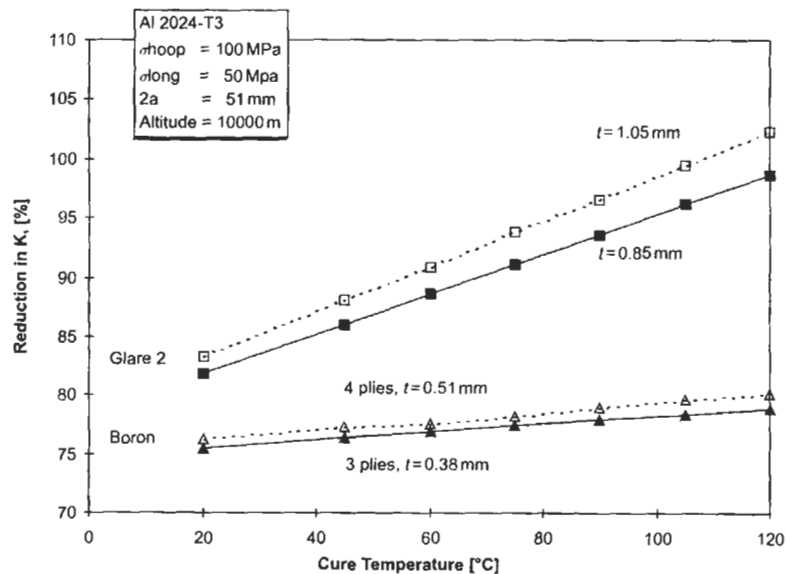


Fig. 14.7. Influence of adhesive cure temperature on patch effectiveness.

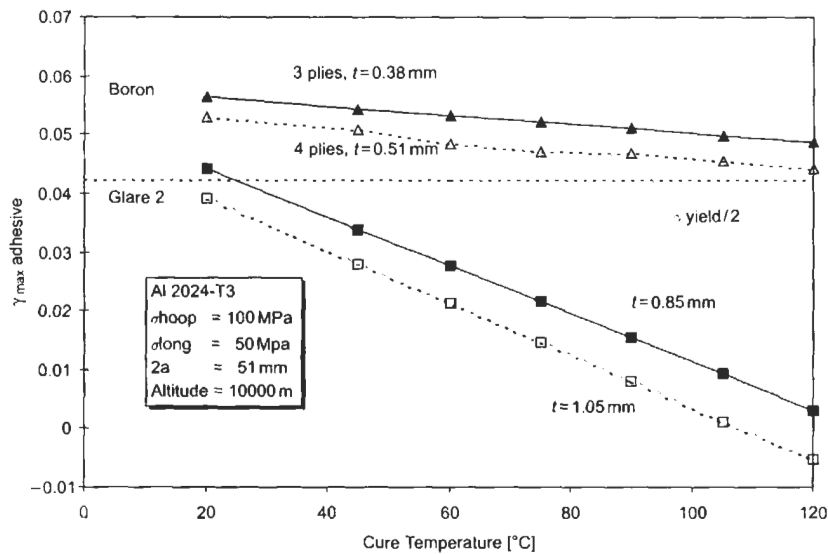


Fig. 14.8. Influence of adhesive cure temperature on maximum adhesive shear strain.

is higher since there is no local constraint and will be roughly equal to the CTE of aluminum.

Thermal effects have yet another significant impact on patch selection. The high adhesive shear strains experienced with some low CTE patches cannot be reduced significantly by curing at a lower temperature, as shown in Figure 14.8, generated using the Rose model under the same conditions as before.

With GLARE[®] 2, the effect is reversed due to the higher CTE of the patch during the cure cycle: A cure temperature of 100 to 120 °C actually benefits the bond by reducing adhesive shear strains at low operating temperatures. Furthermore, as can be seen in this figure, the global adhesive shear strains with the boron/epoxy patch remain above half the adhesive yield strain. Half the yield strain is a design limit for typical operating loads. Because of both effects mentioned, the bonded GLARE 2 patch repair will have a better durability. Also, a higher resistance against delamination might be expected.

A series of analyses were performed using the same narrow-body fuselage case at various cruise altitudes corresponding to different operating temperatures.

Figure 14.9 shows the influence of the operating (cruise) temperature on the four significant crack patching design parameters. Again, the shear modulus and yield strength of the adhesive were corrected for the various temperatures.

The boron/epoxy patch is strongly influenced by the warmer temperatures at lower altitudes, while the more thermally compatible GLARE 2 patch is less sensitive to temperature variations. The skin stresses adjacent to the boron/epoxy patches were consistently lower.

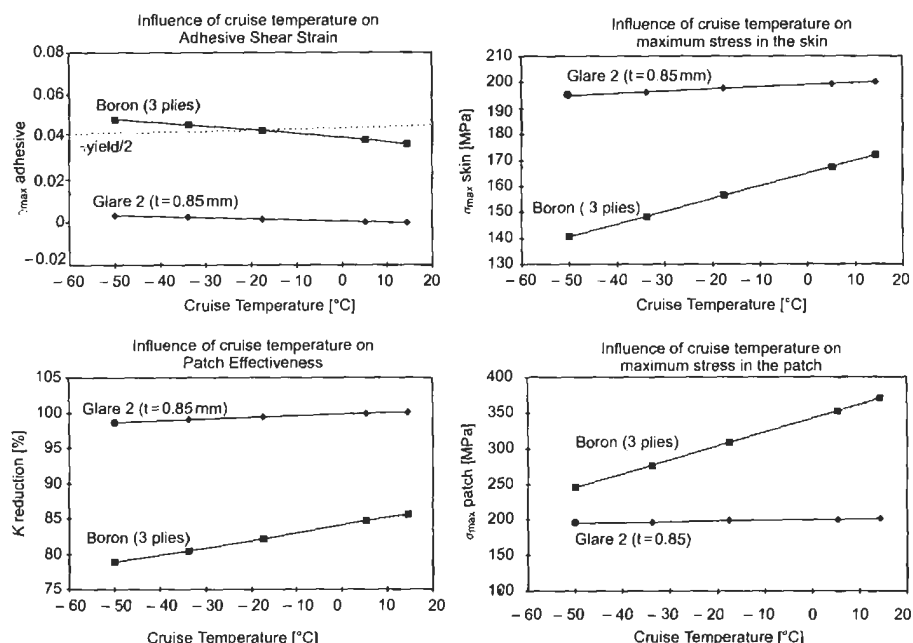


Fig. 14.9. Influence of cruise temperature on crack-patching design parameters.

14.3. Experimental results

Experimental results tended to bear out the analytical predictions: Both constant- and variable-amplitude fatigue testing was performed at room- and low-temperature conditions [18].

In experiments with single-sided bonded repairs to pre-cracked thin aluminum sheets, GLARE 2 patches always gave longer lives than equivalent (in terms of patch stiffness) boron/epoxy repairs. The largest difference was in the time to crack growth re-initiation after repair, see Figure 14.10. The aluminum panels were pre-cracked to 25 mm at different stress levels; 60, 80, and 120 MPa. After the patches were applied the fatigue tests were continued at 120 MPa, and $\sigma_{\min}/\sigma_{\max} = R = 0.05$. These experiments were performed to investigate the effect of the pre-crack level and the plastic zone on crack-growth rates after patching. The fact that the crack growth rates after patching are lower for the Glare patches indicates a lower K -repaired, just as predicted by the Rose-model. At a pre-crack level of 120 MPa, the plastic zone formed stops crack growth for roughly 250000 cycles after the Glare patch was applied, obviously ΔK is low enough to stop the crack from growing through the plastic zone immediately. The scatter in this period can be very large. Periods of 50000 up to 400000 cycles of no crack-growth are observed in similar specimens [19].

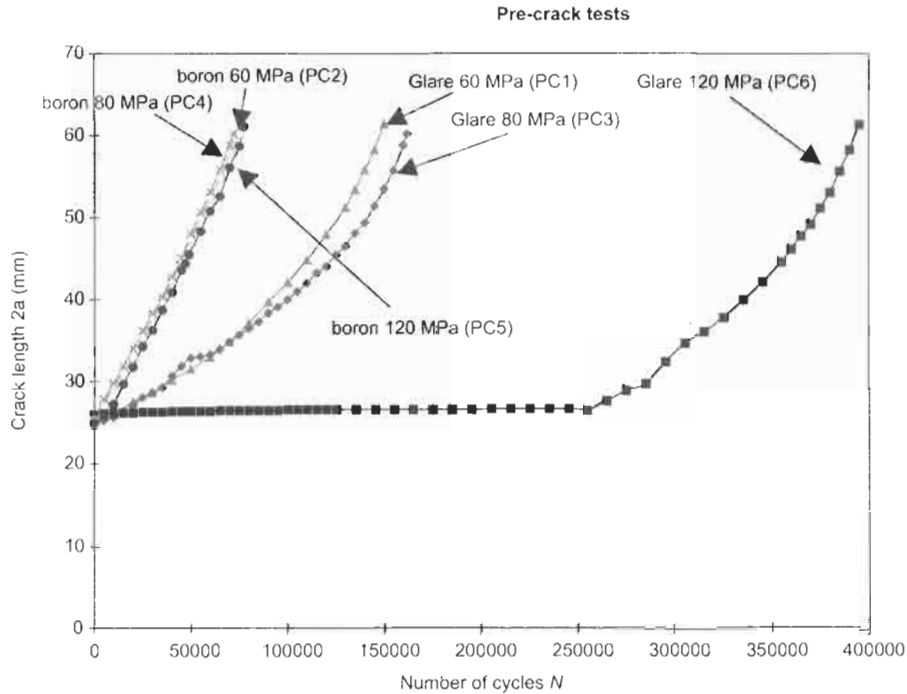


Fig. 14.10. Effect of pre-crack stress level and plastic zone on crack growth behavior after patching.

Previous research [1] has indicated that the 120°C cure cycle temperature is the dominant mechanism in determining the retardation period. Baker found that the cure cycle of the adhesive does affect the plastic zone created in the material before patching. These recent experiments appear to indicate that the CTE match between patch and substrate is another important feature in retardation of crack growth after patching.

In other experiments, the influence of overloads in variable amplitude fatigue testing of repairs was observed to be muted in comparison to unrepaired fatigue crack growth experience. An example of this behavior is given in Figure 14.11.

Overload experiments with patches specimens showed the classical fatigue behavior, an overload slows down the crack growth due to the plastic zone formed during the overload. The effect is smaller than with unpatched-cracked panels since the K is lower due to the patch. When testing different spectra, see Figure 14.11, this behavior was confirmed. The spectra used were derived from Lockheed stress data for the C-5A, see Chapter 31. The unfiltered spectrum contained all the loads, the filtered spectrum had less loads and allowed shorter testing times. The crack growth under the patch was the same for both spectra, however, the crack-growth rate of an unpatched crack was different for the filtered and the unfiltered spectra. This indicates again that some load cycles are less significant if a patched crack is

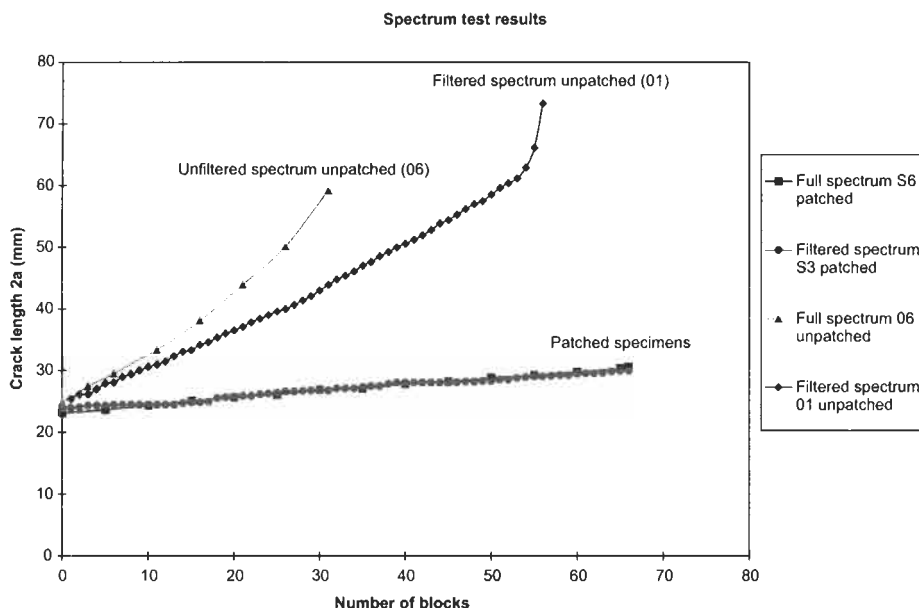


Fig. 14.11. Effect of spectrum loads.

tested. If all failure modes, for example a crack at the patch tip due to (high) skin stresses, are considered, the (filtered) spectrum must be used which results in the same unpatched crack growth rate.

At low temperatures, a mismatch in CTE between the patch and the skin can cause higher stresses in both the adhesive and at the crack tip. However, experiments show a surprising result. In Figure 14.12 the results of crack-growth experiments are shown for boron and Glare patches at -40°C . At the lower temperatures, the crack-growth rates for both patch materials are lower. There are two possible explanations for this behaviour:

1. Although the residual thermal stresses might be higher, the low temperature increases the shear modulus, G , of the adhesive. This can reduce crack opening and therefore reduce the crack-growth rate.
2. Aluminum has slower crack growth rates at low temperatures due to the lower humidity at the low temperatures. This explains the fact that both Glare and boron perform better at lower temperatures despite the increased thermal stresses.

14.4. Discussion

The analytical and experimental results clearly show the strong influence of the differential CTE effects on the stress intensity reduction and subsequent crack

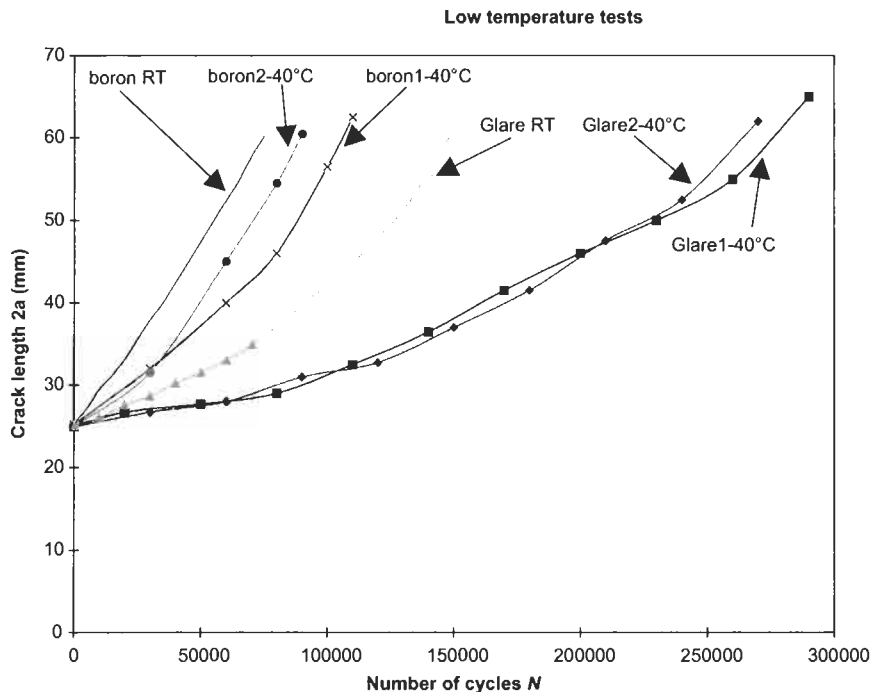


Fig. 14.12. Effect of low temperatures on crack-growth rates of patched panels.

growth. When the thermal effects are considered, boron/epoxy patches are less effective than the fiber metal laminate GLARE 2 at operating temperatures below the cure temperature of the adhesive.

Furthermore, the effect of the cure temperature can have a significant positive influence on the effectiveness of the GLARE 2 patch, while the boron/epoxy patch is only slightly influenced (Figure 14.7). In Figure 14.8, one can see the positive influence of an increasing cure temperature on the decreasing shear strain in the GLARE 2 patch, while the strains in the bond line of the boron/epoxy patch remain above the design limit for typical operating loads.

Figure 14.9 shows the influence of the operating temperature on the most significant crack patching design parameters. More thermally compatible composite patches are less sensitive to temperature variations. This results in better patching effectiveness at high- altitude/low-temperature cruise conditions, while keeping the adhesive shear strain in the bond line acceptably low. However, better crack closure comes at the expense of higher skin stresses at the edges of the repair. This increases risk of a new fatigue crack nucleating at the boundary of the patch, and must be considered in design.

The experiments show the same trends as predicted by the Rose-model: A closer CTE-match between the patch and the skin can result in more efficient patches for

a typical fuselage skin thickness (1 mm). Both the pre-crack stress level and the patch material used affect the re-initiation period of the crack after patching. If the same stress level is applied before and after patching, the Glare patches can result in significant retardation periods. This retardation period is not affected by the cure-cycle of the adhesive.

Overloads and spectrum loading does affect crack growth under patches in the same way as it does for unpatched cracks. However, the absolute effect is smaller due to the reduced K after patching. When testing bonded repairs under spectrum loading, the spectrum has to be verified on unpatched cracks.

The low temperature tests show that although the thermal stresses might increase, the crack-growth rate decreases. This is not what the models predict, therefore the change in crack-growth behavior of aluminium at low temperatures/humidities must be more dominant than the increase in thermal stresses under the repair. A higher G of the adhesive, might also contribute to the slower crack-growth rates.

This combination of analyses and experiments tends to indicate various niches where various candidate crack patching materials appear to be best suited. The high-modulus, low-CTE boron/epoxy composite excels in the repair of relatively thick cracked structures where peak flight loads are encountered at moderate to high service temperatures. In these cases, low patch volume could be critical for aerodynamic reasons, and CTE mismatch-related problems are minimal. Good examples of boron/epoxy applications include lower wing skins, wing/fuselage attachments, and fuselage keels beams.

In contrast, the moderate-modulus, high-CTE GLARE 2 patches appear to be best suited for repair of thin fuselage skins. The high stresses in these structures due to the maximum pressure level at low cruise temperature are increased by the additional temperature-related stresses. In repairs to thin-skinned fuselage structures, the slightly greater patch thickness associated with GLARE 2 is usually negligible. With the superior reductions in K and accompanying low adhesive shear strains, GLARE 2 patches promise superior durability, resistance against delamination, and excellent damage tolerance.

14.5. Summary and conclusions

The results of more than 20 years of experience with repairs of relatively thick cracked aircraft structures have shown boron/epoxy to be an excellent patch material. Peak flight loads at moderate to high service temperatures can be sustained by the high-modulus material, without demanding high patch volumes (thickness). Because of the thick structures, mismatch problems due to the curing temperature are minimal.

When the transition is made to the repair of cracked fuselage structures, thermal considerations become paramount. The fuselage will see its highest stress levels at low temperatures.

Detailed parametric studies were performed to calculate thermal effects. Variation of the patch thickness, cure temperature and cruising temperature for two competing patch materials, the fiber metal laminate GLARE[®] 2 and the traditional composite boron/epoxy, gave a good opportunity to compare those materials for a fuselage crack patching situation.

Experimental work was performed in constant- and variable-amplitude fatigue at room and low temperatures. The results showed several advantages of GLARE 2 over boron/epoxy patches in fuselage skin repairs due to improved thermal expansion compatibility between GLARE 2 and aluminum. The results predict GLARE 2 to be an effective, damage-tolerant fuselage repair material.

References

1. Baker, A.A. and Jones, R. (1988). Bonded Repair of Aircraft Structures (A.A. Baker and R. Jones, eds.). Boston: Martinus Nijhoff Publishers.
2. Fredell, R. and Gunnink, J. (1992). Fiber metal laminates for improved structural integrity. *Proc. of the Int. Workshop on Structural Integrity of Ageing Aircraft*, Atlanta, Georgia, April, pp. 362–375.
3. Fredell, R., Vlot, A. and Roebroeks, R. (1994). Fiber metal laminates: New frontiers in damage tolerance. *Proc. of the 15th Int. European Conference of the Society for the Advancement of Material and Process Engineering*, Toulouse, France, June, pp. 319–328.
4. Fredell, R. (1994). Damage Tolerant Repair Techniques for Pressurized Aircraft Fuselages. WL-TR-94-3134, Wright-Patterson Air Force Base Ohio, June.
5. Fredell, R., van Barneveld, W. and Vlot, A. (1994). Analysis of composite crack patching of fuselage structures: High patch elastic modulus isn't the whole story. *Proc. of the 39th Int. SAMPE Symposium and Exhibition*, Anaheim, California, April, pp. 610–623.
6. Rose, L.R.F. (1981). An application of the inclusion analogy. *Int. J. Solids and Structures*, **17**, pp. 827–838.
7. Rose, L.R.F. (1988). Theoretical Analysis of Crack Patching, in Bonded Repair of Aircraft Structures, (Baker, Jones, eds.). Dordrecht: Kluwer Academic Publishers, pp. 77–106.
8. Muki, R. and Sternberg, E. *Int. J. Solids and Structures*, **4**, pp. 75–94.
9. Tarn, J.Q. and Shek, K.L. (1991). Analysis of cracked plates with a bonded patch. *Engineering Fracture Mechanics*, **40**(6), pp. 1055–1065.
10. Chu, R.C. and Ko, T.C. (1989). Isoparametric shear spring element applied to crack patching and instability. *Theoretical and Applied Fracture Mechanics*, **11**, pp. 93–102.
11. Jones, R. and Callinan, R.J. (1980). *J. Structural Mechanics*, **8**(2), pp. 143–149.
12. Marissen, R. Fatigue Crack Growth in ARALL, Ph.D. thesis, Department of Aerospace Engineering, Delft University of Technology, Delft, the Netherlands.
13. Roebroeks, G.H.J.J. (1991). Towards GLARE: The Development of a Fatigue Insensitive and Damage Tolerant Material, Ph.D. thesis, Department of Aerospace Engineering, Delft University of Technology, Delft, the Netherlands, December.
14. Rose, L.R.F. (1988). Residual Thermal Stresses, in Bonded Repair of Aircraft Structures (Baker, Jones, eds.). Dordrecht: Kluwer Academic Publishers, pp. 90–91.
15. Baker, A.A., Davis, M.J. and Hawkes, G.A. (1979) *Proc. 10th Int. Symp. of the Int. Comm. on Aeronautical Fatigue*, paper 4.3.
16. Rose, L.R.F. (1982). *Int. J. Fracture*, **18**, pp. 135–144.
17. Baker, A.A. (1988). Crack Patching: Experimental Studies, Practical Applications, from Bonded Repair of Aircraft Structures (Baker, Jones, eds.). Dordrecht: Kluwer Academic Publishers, pp. 107–172.

18. Verhoeven, S. (1988). In Service Effects on Crack Growth Under Bonded Composite Repairs. Masters thesis, Department of Aerospace Engineering, Delft University of Technology, Delft, the Netherlands, July.
19. Guijt, C. and Fredell, R. (1996). Delamination Effects in Fuselage Crack Patching, SAMPE Anaheim.

Chapter 15

GRAPHITE/EPOXY PATCHING EFFICIENCY STUDIES

P. POOLE

*Structural Materials Centre, Defence Evaluation and Research Agency,
Farnborough, Hants, UK*

15.1. Introduction

Theoretical and experimental research on adhesively bonded graphite/epoxy patch repair of cracked metallic structures has been in progress at DERA for many years. The early experimental work [1–4] concerned the repair of central fatigue cracks in thin aluminium alloy panels and the influence of repair variables on the effectiveness of the patches in retarding crack growth, while the early theoretical work [5–7] involved the development of collocation [strip patch and isotropic disc patch] and 2D boundary element models, and their application to cracked sheet repairs. Graphite/epoxy patches were used for the initial investigations because various forms of woven cloth and prepreg were readily available, and because wet layup of graphite cloth had shown considerable promise for battle damage repair. Since that time, repairs to stiffened panels and thick sections containing fatigue cracks, and thin panels containing simulated battle damage, have been investigated, and a 3D boundary element/finite element computer program for the analysis of bonded patch repairs has been developed. In addition, the performance of graphite/epoxy [gr/ep] and boron/epoxy [b/ep] patch repairs have been compared and the effects of bondline defects and in-service variables on patch efficiency have been studied.

This chapter reviews DERA research on bonded composite patch repair of aluminium alloy structures; it contains nine main sections covering repair of thin skin components, repair of thick sections, gr/ep versus b/ep patches, effect of bondline defects, effect of impact damage, effect of service temperature, effect of exposure to hot-wet environments, repair of battle damage and future work.

15.2. Repair of thin skin components

Initial studies at DERA involved the use of adhesively bonded gr/ep patches to repair 1.6 mm thick aluminium alloy panels containing central fatigue cracks. Precured patches were manufactured from woven or unidirectional gr/ep prepreg [e.g. XAS/914] and adhesively bonded to cracked test panels in an autoclave, usually with a 120 °C curing epoxy film adhesive such as Redux 312/5. Constant amplitude fatigue tests were carried out to establish the effectiveness of the patches in retarding fatigue crack growth and patch efficiency was expressed in terms of the reduction in stress intensity factor range due to patching [$\Delta K^P/\Delta K^U$]. Figure 15.1 shows typical crack growth rate data obtained for $R=0.1$ fatigue testing of patched and unpatched panels, and illustrates the method that was used to determine ΔK^P and hence $\Delta K^P/\Delta K^U$. It can be seen that for a normalised crack length of $a/W=0.5$, the effective stress intensity factor range experienced by the crack in the patched specimen is just over 10 MPam^{1/2}, compared to about 22 MPam^{1/2} for the unpatched panel, i.e. $\Delta K^P/\Delta K^U \sim 0.45$.

Fatigue tests were carried out to study the effects of a wide range of repair and test variables on patch efficiency. The variables investigated included type of prepreg, layup, thickness, size and shape of patch, thickness, modulus and cure temperature of adhesive, surface treatment of aluminium alloy panels, pre-exposure to a warm, moist environment, type of fatigue loading and crack length. Most

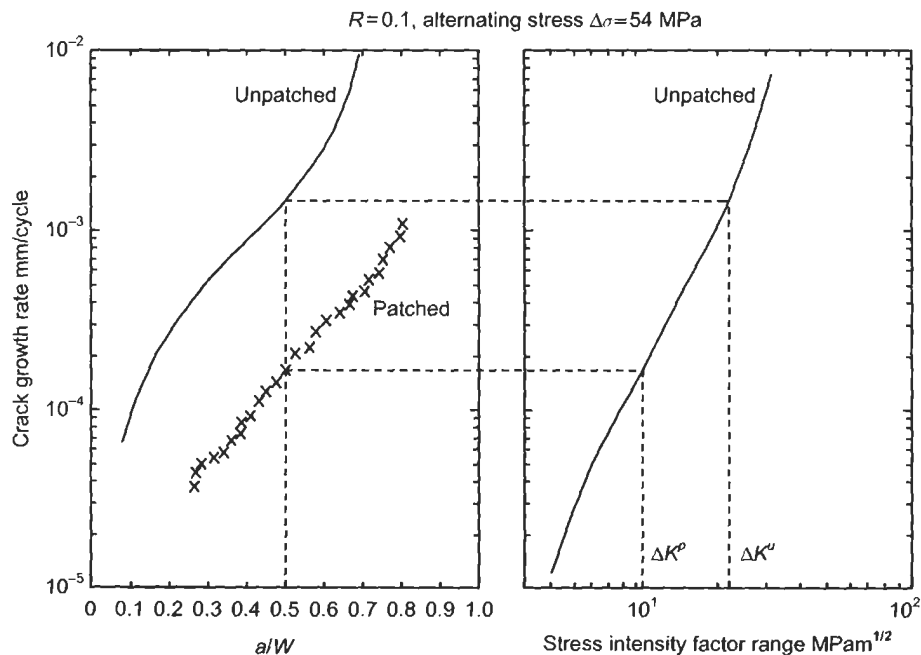


Fig. 15.1. Determination of effective stress intensity factor range ΔK^P for patched panels.

panels were patched on one side only, but a limited number were patched on both sides and in these cases crack arrest occurred. Some of the important conclusions from this work are summarised below:

- (a) The rate of crack growth after patching depended on the loading conditions used for precracking prior to patching. Thus, load shedding during precracking was recommended in order to ensure that the plastic zones associated with the final stages of precracking do not cause crack growth retardation when fatigue loading commences after patching.
- (b) In the case of asymmetric single-sided patch repairs, patch efficiency was improved by the use of anti-buckling plates which restricted out-of-plane-bending. For such repairs, the use of appropriate anti-buckling devices was recommended in order to avoid unrealistic pessimistic test results.
- (c) In general, patch efficiency improved with increasing crack length and patch stiffness, and with decreasing adhesive thickness. Varying the adhesive thickness had a relatively small effect. For example, in the case of repairs involving woven patches of stiffness approximately 55% that of the aluminium alloy panels, $\Delta K^P/\Delta K^U$ increased from 0.57 to 0.64 when the adhesive thickness was increased from 0.13 mm to 0.76 mm [3].
- (d) Tests on panels repaired with adhesives cured at room temperature, 120 °C and 175 °C indicated that patch efficiency was affected adversely by residual thermal stresses arising from differential thermal contraction of patch and aluminium alloy on cooling from the adhesive cure temperature.
- (e) Boeing wedge tests in 50 °C/96% RH indicated that the environmental durability of adhesively bonded aluminium alloy joints was improved markedly if a grit blast/silane swab pretreatment was used instead of grit blasting only. However, when panels were pretreated by various processes, including grit blasting only, no significant increase in $\Delta K^P/\Delta K^U$ was observed following exposure of patched panels to 70 °C/84% RH for 2150 h [3].
- (f) Although the results of early theoretical studies at DERA were consistent with experimental observations concerning the general effects of patch and adhesive variables on $\Delta K^P/\Delta K^U$, the models were unable to predict accurately the effects of repair variables on the rate of fatigue crack growth. This was not surprising since these preliminary models did not take into account the effects of debonding, residual stresses and out-of-plane bending.

The work on patch repair of fatigue cracked thin sheet was extended to stiffened panels through a contract with British Aerospace [8]. In this programme stiffened and unstiffened 1.6 mm thick aluminium alloy sheets containing centre cracks were repaired with precured woven and unidirectional gr/ep patches of equivalent stiffness. For the stiffened panel the initial design represented a two-bay fuselage panel with a central riveted U-section stiffener. However, owing to fatigue failures at the first fastener hole it was necessary to redesign the panel with the working section reduced to a width of 100 mm. Panels were precracked with load shedding, to give a 25 mm crack at the centre fastener hole, and 50 mm wide patches were applied using a 120 °C curing epoxy film adhesive. Constant amplitude [$R=0.1$, $\sigma_{\max}=80$ MPa] fatigue tests demonstrated that both unidirectional and woven gr/ep

patches reduced the rate of fatigue crack growth by a factor of 10, when cracks were grown from 25 mm to 70 mm. It was confirmed that crack growth under the gr/ep patches could be monitored effectively using an eddy current technique. Finite element analysis resulted in unconservative predictions, i.e. the predicted values of $\Delta K^P/\Delta K^U$ were lower than those indicated by the measured crack growth rate data.

15.3. Repair of thick sections

Initial work at DERA on repair of thick sections [9] was carried out in collaboration with AMRL, who supplied patched and unpatched specimens for testing. Figure 15.2 shows the main features of these symmetric specimens, which comprised two 11.2 mm thick 2024-T4 aluminium alloy plates containing centrally located surface flaws of surface length 40 mm and maximum depth 5.7 mm. Each plate was subjected to constant amplitude fatigue loading until cracking occurred at the base of the flaw. Ten-ply unidirectional b/ep patches were manufactured

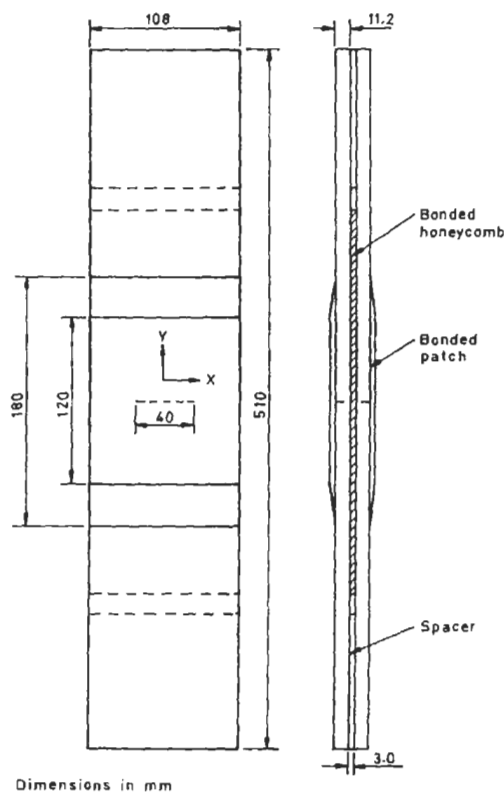


Fig. 15.2. Patched surface flaw specimen.

from 5521/4 prepreg, and FM73M adhesive was used to simultaneously bond the patches to cracked plates and the plates to aluminium honeycomb.

Table 15.1 summarises the fatigue life data obtained for patched and unpatched specimens tested under FALSTAFF [peak stress 137.8 MPa] and constant amplitude [$R=0.1$, $\sigma_{\max}=65.5$ MPa] loading. These results show that, for FALSTAFF loading, patching increased fatigue life by a factor of 5.8, which was much lower than the life improvement factor of 22 reported by AMRL for constant amplitude loading. When the remaining two specimens were tested under constant amplitude conditions similar to those used by AMRL, patching increased fatigue life by a factor of 28, which is in reasonable agreement with the AMRL results. The effect of patching on the growth of fatigue cracks was also studied at DERA [9], and examination of fracture surfaces showed that cracks grew through the plates before any surface crack growth was detected. The growth of surface cracks was monitored for patched and unpatched specimens, and Figure 15.3 shows crack growth rate data obtained for FALSTAFF loading. For some specimens, ultrasonic and SPATE techniques were used to monitor debonding of patches during fatigue testing. Extensive debonding was observed in the case of FALSTAFF loading, as illustrated in Figure 15.4, but no significant debonding was detected in the case of the patched specimen tested under constant amplitude loading. This observation is consistent with the fatigue life and crack growth data which indicated that patching was more efficient for constant amplitude loading than for FALSTAFF loading.

A second series of fatigue tests on similar thick section specimens was carried out at DERA using the same loading spectra and stress levels [10]. However, in this case, surface flaws in 12.4 mm thick aluminium alloy plates were repaired by bonding gr/ep [XAS/914] patches to the plates with a 120 °C curing epoxy film adhesive [Redux 312/5]. In agreement with the previous tests, the increases in

Table 15.1
Effect of patching on fatigue life.

Loading sequence	Patched/unpatched	Specimen	Cycles to failure
FALSTAFF	Unpatched	9/22U	344039
		5/6U	326056
		3/4U	411595
		7/8U	334778
		Mean	354117
	Patched	14/15P	1954783
		18/19P	2699357
		16/17P	1923680
		12/13P	1632406
		Mean	2052557
Constant amplitude	Unpatched	1/2U	37687
	Patched	20/21P	1041557

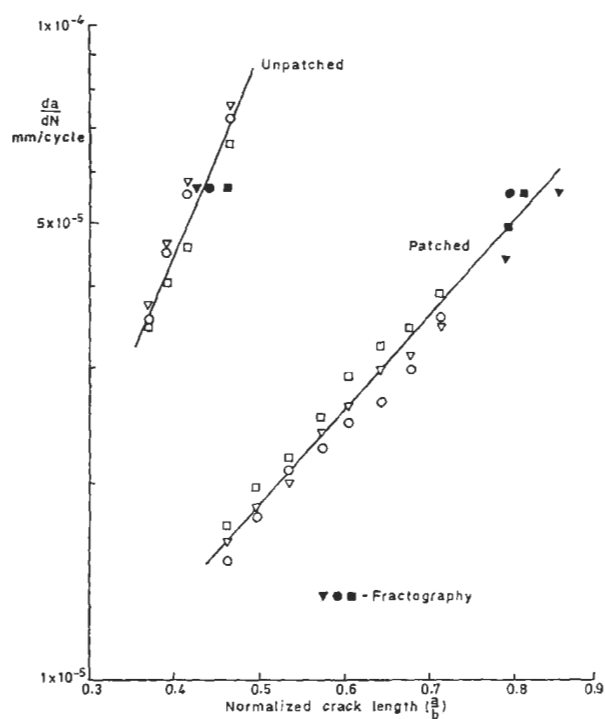


Fig. 15.3. Effect of patching on rate of growth of through-thickness cracks during FALSTAFF loading.

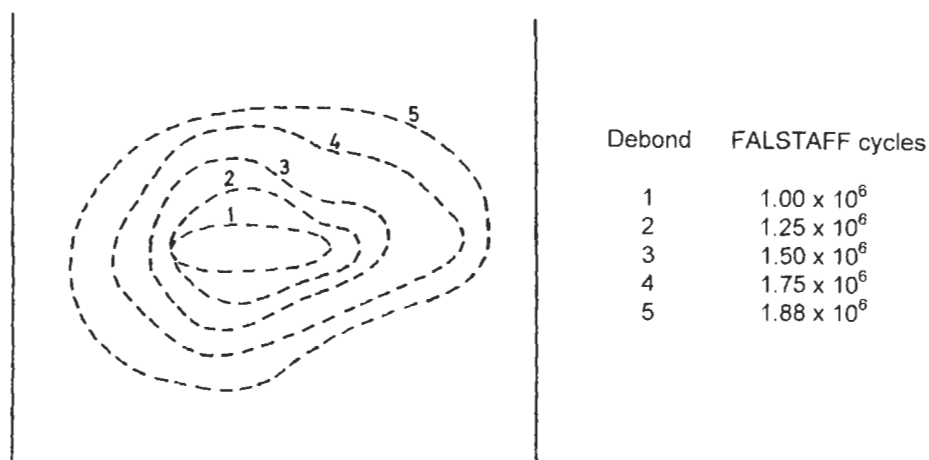


Fig. 15.4. Development of debond during FALSTAFF loading (specimen 16/17P).

fatigue lives and reductions in crack growth rates due to patching were much more pronounced for constant amplitude loading than for FALSTAFF loading, and debonding was observed for FALSTAFF loading only. The size and shape of the debonds indicated by ultrasonic inspection were in excellent agreement with the debonds observed following specimen failure. In general, the debonds were elliptical in shape, with the length of the major axis corresponding approximately to the crack length and the ratio of minor axis to major axis about 0.7, particularly at relatively long crack lengths. It is possible that fatigue damage of the adhesive and patch debonding were caused by the relatively high adhesive shear strains associated with high FALSTAFF loads. It should be noted that these high loads were selected for the thick section repairs in order to study patch repair efficiency when the adhesive is subjected to extremely demanding cyclic loading conditions. Additional fatigue tests showed that the extent of debonding was reduced by either doubling the adhesive thickness or increasing patch thickness by 50%, but a significant improvement in fatigue performance was only observed when patch thickness was increased.

A 2D boundary element model [6] was used to analyse the above thick section repairs after a through crack had developed from the surface flaw. The model was used to predict the effects of crack length, debonding, stress level, patch thickness and adhesive thickness on patch efficiency. In general, the predicted values of $\Delta K^P/\Delta K^U$ tended to be lower than the corresponding values determined from fatigue crack growth rate data, even when debonding was taken into account. However, reasonable agreement was obtained when a factor was applied to account for residual thermal stresses [10].

It was recognised that a 3D model was required to enable repairs to thick sections containing surface flaws to be analysed in detail and the effectiveness of patches in retarding crack growth to be predicted accurately. Thus, a 3D boundary element/finite element model was developed at DERA, where the cracked plate was modelled using the boundary element method and the composite patch was modelled using a partially mixed stress-displacement finite element method [11]. The mixed finite element formulation enabled direct coupling with the boundary element system in terms of displacement and traction compatibility conditions on the adhesion surfaces. The adhesive layer could have been included as one of the patch layers [i.e. a 3D elastic continuum] but for reasons of computational economy it was treated as a continuous spring mechanism, the properties of which were absorbed into the adhesion compatibility conditions. This simplified spring representation allows an efficient consideration of an elastoplastic adhesive layer. Residual stresses arising from differential thermal contraction of composite patch and metallic substrate are taken into account in the model.

Since 3D analysis is expensive and time consuming, it was decided to compare the values of $\Delta K^P/\Delta K^U$ predicted by the 3D model with corresponding values predicted by analytical formulae and a 2D boundary element model. The study was confined to double sided repairs of the type shown in Figure 15.5, where unidirectional gr/ep patches are bonded to both sides of an aluminium alloy sheet containing a central through crack. It was assumed that the patches were bonded

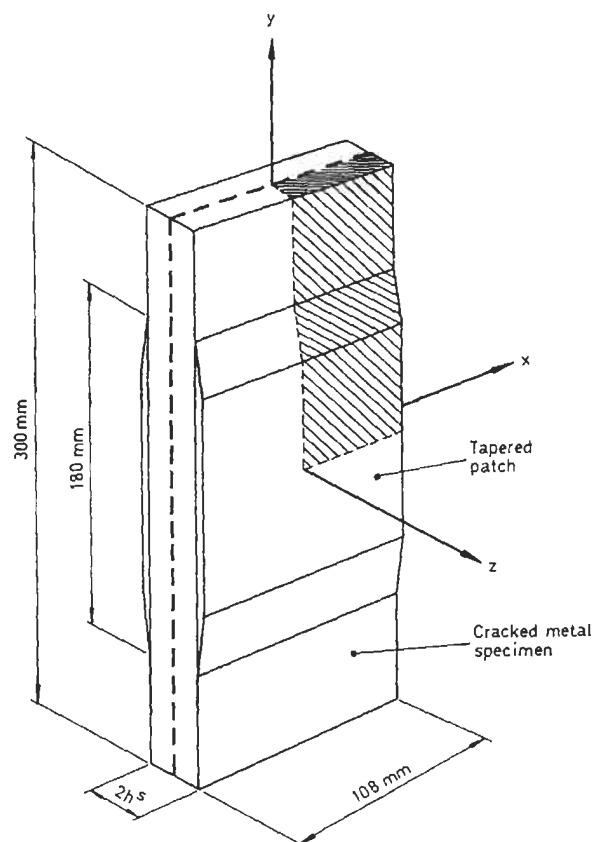


Fig. 15.5. Double-sided patched specimen.

with a 120 °C curing adhesive and that the patch fibres were aligned perpendicular to the crack. Five repairs were studied where the sheet thickness $[2h^s]$ was 1.55, 3.1, 6.2, 12.4 or 24.8 mm and the patch thickness $[h^p]$ varied with sheet thickness according to $h^p = 0.1645 h^s$, i.e. the ratio of patch stiffness to sheet stiffness was constant. The non-linear stress-strain behaviour of the adhesive was assumed to be consistent with the experimental behaviour reported in the literature for Redux 312 adhesive; it was found that this behaviour could be described accurately by the Ramberg-Osgood equation for pure shear $\gamma = \tau/G^a + A(\tau/\tau_c)^n$ with parameters $n = 14.26$, $\tau_c = 40$ MPa and $A = 0.04117$ for the range $0 < \gamma \leq 0.15$.

The 3D model was used to study the variation in stress intensity factor range ΔK through the thickness of patched and unpatched sheets subjected to constant amplitude loading [$R = 0.1$, $\sigma_{\max} = 65.5$ MPa]. These data were used to determine root mean square values of ΔK^P and ΔK^U , and hence $\Delta K^P/\Delta K^U$. The variation of

by using patches with a layer of glass/epoxy on the surface to be bonded, while ingress of moisture can be minimised by sealing edges of patches and cracks and by wet assembly of any fasteners passing through the patches. Theoretical work at DERA has established that patch efficiency is only slightly affected by the presence of one ply of woven glass/epoxy on the patch surface. For example, for the repair configuration described in Section 15.5 and a crack length of 15 mm, the 3D BE/FE model predicted that $\Delta K^P/\Delta K^U$ would be increased from 0.24 to 0.25 by the presence of a single ply of glass/epoxy.

The coefficient of thermal expansion for unidirectional b/ep is about $4.5 \times 10^{-6} (^\circ\text{C})^{-1}$ compared to $0.4 \times 10^{-6} (^\circ\text{C})^{-1}$ for gr/ep and $23 \times 10^{-6} (^\circ\text{C})^{-1}$ for aluminium alloy. This means that the residual stresses arising from differential thermal contraction of patch and aluminium alloy on cooling from the adhesive cure temperature will be greater for gr/ep than for b/ep. However, it is difficult to estimate the precise improvement in resistance to fatigue crack growth that will be achieved by using b/ep rather than g/ep patches of the same stiffness, and thus the work outlined below was undertaken at DERA [13].

Single and double-side patch repairs were carried out on 12.4 mm thick, 108 mm wide L97 aluminium alloy test pieces containing central through-thickness fatigue cracks [20 mm or 40 mm long]. 1.34 mm thick b/ep and 1.65 mm thick gr/ep patches were manufactured from Textron 5521 and Ciba-Geigy T800/924 prepregs, respectively. These thicknesses were selected in order to produce b/ep and gr/ep patches of similar stiffness, assuming Young's modulus was 208 GPa for 5521 and 168 GPa for T800/924. In addition, it was estimated that these thicknesses would result in measureable rates of crack growth and not cause crack arrest. The patches were 180 mm long, including 30 mm tapered portions at either end, and 108 mm wide; these patch sizes were selected to provide large residual stress effects. Following grit blast/silane treatment of the aluminium alloy surfaces, patches were applied using a 120 °C curing epoxy film adhesive [Redux 312/5]. Constant amplitude [$R=0.1$, $\sigma_{\max}=55$ MPa] fatigue tests were carried out on six patched and three unpatched specimens; Figure 15.8 summarises the crack growth rate data obtained. It can be seen that the rate of crack growth was reduced by a factor of about two in the case of single-side repairs, and by a factor greater than ten in the case of double-side repairs, and that b/ep patches were slightly more effective than gr/ep patches in retarding crack growth.

The DERA 3D BE/FE computer program was used to predict $\Delta K^P/\Delta K^U$ for both single and double-side repairs. Predicted values of $\Delta K^P/\Delta K^U$ are shown in Table 15.2 for crack lengths [$2a$] of 50 mm and 70 mm. The computer program was also used to predict the effect of residual thermal stresses on K_{\min}/K_{\max} [R -ratio] for patched specimens subjected to $R=0.1$, $\sigma_{\max}=55$ MPa remote loading. For $a=25$ mm, the predicted values of K_{\min}/K_{\max} were 0.64 and 0.68 for double-sided repairs with b/ep and gr/ep, respectively, and 0.33 and 0.36 for single-sided repairs with b/ep and gr/ep, respectively.

Values of $\Delta K^P/\Delta K^U$ were determined from the crack growth rate data summarised in Figure 15.8 and that determined for unpatched specimens loaded at $R=0.33$, 0.36, 0.64 and 0.68. For example, in the case of double-sided b/ep patch

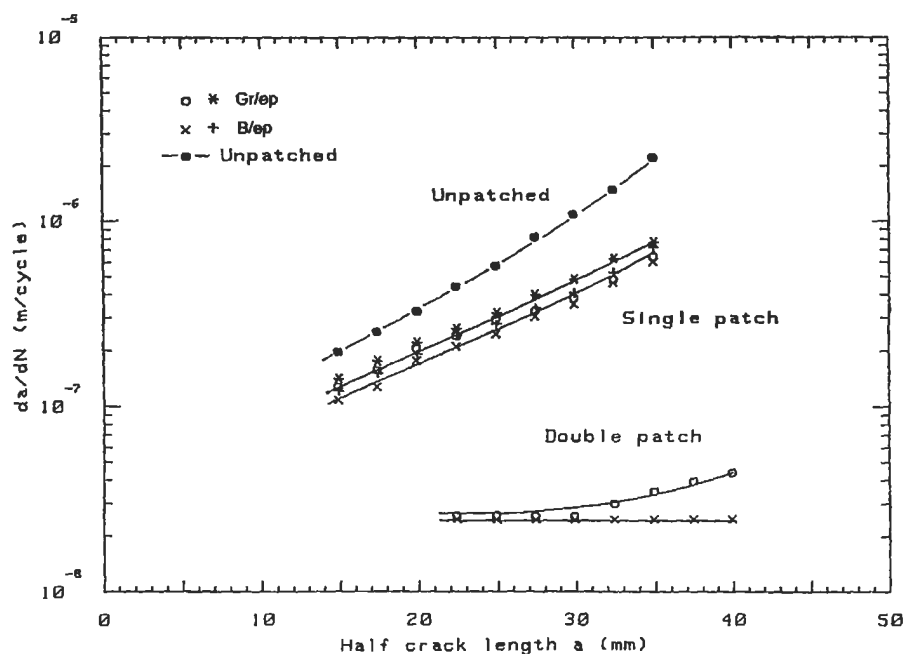


Fig. 15.8. Effect of patching on rate of crack growth ($R=0.1$, $\sigma_{\max}=55$ MPa).

repair and a half crack length of 25 mm, $da/dN = 2.35 \times 10^{-8}$ m/cycle was obtained directly from Figure 15.8 and the value of ΔK corresponding to this da/dN in da/dN - ΔK data for $R=0.64$ loading was assumed to be ΔK^P [4.6 MPa $m^{1/2}$]. Thus, for this particular repair it was estimated that $\Delta K^P = 4.6$ MPa $m^{1/2}$ and $\Delta K^P/\Delta K^U = 0.27$. Values of $\Delta K^P/\Delta K^U$ determined in this way from experimental

Table 15.2

Comparison of theoretical and experimental values of $\Delta K^P/\Delta K^U$.

Half crack length, a (mm)	Single/double	Patch type	$\Delta K^P/\Delta K^U$	
			Theory	Expt
25	S	B/ep	0.66	0.70
		Gr/ep	0.66	0.71
	D	B/ep	0.27	0.29
		Gr/ep	0.27	0.28
35	S	B/ep	0.61	0.66
		Gr/ep	0.61	0.67
	D	B/ep	0.20	0.20
		Gr/ep	0.20	0.21

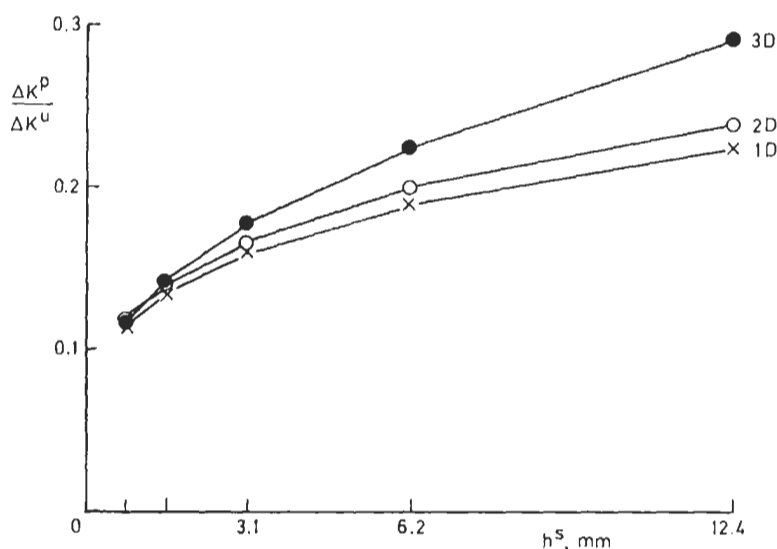


Fig. 15.6. Effect of analysis method and sheet thickness on $\Delta K^P/\Delta K^U$ ($a = 20$ mm).

$\Delta K^P/\Delta K^U$ with sheet thickness predicted by the 3D model for a half crack length $[a]$ of 20 mm is shown in Figure 15.6, together with corresponding $\Delta K^P/\Delta K^U$ data predicted by analytical formulae and a 2D boundary element model. It is evident that for $h^s \geq 3.1$ mm the values of $\Delta K^P/\Delta K^U$ predicted by the 3D model are significantly higher than those predicted by the other models. Thus, it is recommended that a 3D model should be used for the analysis of relatively thick sections, since it appears that the other methods will predict erroneous low rates of fatigue crack growth following patching. Relatively small differences in predicted values of $\Delta K^P/\Delta K^U$ were observed for the other two models; these have been discussed in detail elsewhere [11]. The 3D and 2D models were used to predict the effects of elliptical debonds, assuming that the major axis of the debond was equivalent to the crack length and the ratio of major axis to minor axis was 0.7. Typical data are shown in Figure 15.7 for repairs to thick plate [$h^s = 12.4$ mm]; it can be seen that both models predicted marked increases in $\Delta K^P/\Delta K^U$ with debonding and that the difference between the values of $\Delta K^P/\Delta K^U$ predicted by the two models was less pronounced when debonding was present.

The values of $\Delta K^P/\Delta K^U$ predicted by the 3D model were in excellent agreement with corresponding values determined from experimental crack growth data obtained for centre cracked 12.4 mm thick plate specimens [see Section 15.4] and edge cracked 4.0 mm thick sheet specimens [see Section 15.5]. In addition, patch surface stress distributions determined from SPATE [stress pattern analysis by thermal emission] and strain gauge measurements were in good agreement with distributions predicted by the 3D model, but in poor agreement with those predicted by the 2D model.

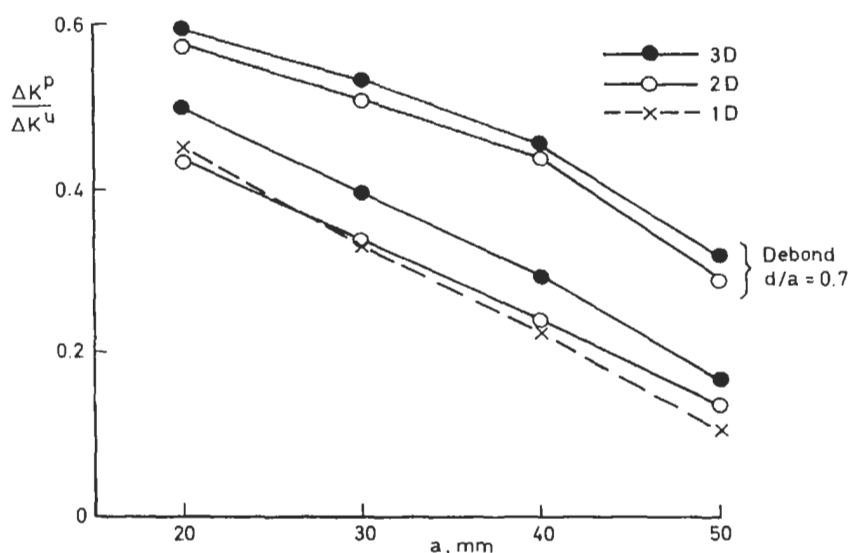


Fig. 15.7. Effect of analysis method, debonding and crack length on $\Delta K^P/\Delta K^U$ ($h^* = 12.4$ mm).

15.4. Graphite/epoxy versus boron/epoxy

Gr/ep materials were selected for bonded composite patch research at DERA because, compared to b/ep, a wide range of materials were readily available from various sources and because they were cheaper, easier to handle and more suitable for curved surfaces. Furthermore, 120 °C curing prepreps were available which would allow repairs to thin skins to be carried out efficiently by co-cure of adhesive and prepreg. Other researchers [12] have stated that they prefer b/ep, rather than gr/ep, for patch repairs because it offers (i) a superior combination of strength and stiffness, (ii) low electrical conductivity, and (iii) a higher coefficient of thermal expansion. These three advantages are considered separately below.

Although recent advances with gr/ep materials have resulted in tensile strength and stiffness properties which approach those of b/ep, it is recognised that b/ep still offers a stiffness advantage which will enable slightly thinner patches to be used for some repairs. This may be important for repairs to control surfaces if aerodynamic considerations dictate the use of minimum thickness patches.

It has been stated that the low electrical conductivity of boron is advantageous because it avoids the danger of galvanic corrosion associated with the use of gr/ep and allows the use of simple eddy current techniques to detect and monitor cracks under patches. However, work at British Aerospace, DERA and the RAF has shown that the growth of fatigue cracks under gr/ep patches can be monitored successfully using eddy current techniques. Furthermore, the author considers that potential corrosion problems associated with the use of gr/ep can be avoided or minimised by appropriate protection measures. Galvanic contact may be avoided

by using patches with a layer of glass/epoxy on the surface to be bonded, while ingress of moisture can be minimised by sealing edges of patches and cracks and by wet assembly of any fasteners passing through the patches. Theoretical work at DERA has established that patch efficiency is only slightly affected by the presence of one ply of woven glass/epoxy on the patch surface. For example, for the repair configuration described in Section 15.5 and a crack length of 15 mm, the 3D BE/FE model predicted that $\Delta K^P/\Delta K^U$ would be increased from 0.24 to 0.25 by the presence of a single ply of glass/epoxy.

The coefficient of thermal expansion for unidirectional b/ep is about $4.5 \times 10^{-6} (\text{°C})^{-1}$ compared to $0.4 \times 10^{-6} (\text{°C})^{-1}$ for gr/ep and $23 \times 10^{-6} (\text{°C})^{-1}$ for aluminium alloy. This means that the residual stresses arising from differential thermal contraction of patch and aluminium alloy on cooling from the adhesive cure temperature will be greater for gr/ep than for b/ep. However, it is difficult to estimate the precise improvement in resistance to fatigue crack growth that will be achieved by using b/ep rather than g/ep patches of the same stiffness, and thus the work outlined below was undertaken at DERA [13].

Single and double-side patch repairs were carried out on 12.4 mm thick, 108 mm wide L97 aluminium alloy test pieces containing central through-thickness fatigue cracks [20 mm or 40 mm long]. 1.34 mm thick b/ep and 1.65 mm thick gr/ep patches were manufactured from Textron 5521 and Ciba-Geigy T800/924 prepreps, respectively. These thicknesses were selected in order to produce b/ep and gr/ep patches of similar stiffness, assuming Young's modulus was 208 GPa for 5521 and 168 GPa for T800/924. In addition, it was estimated that these thicknesses would result in measureable rates of crack growth and not cause crack arrest. The patches were 180 mm long, including 30 mm tapered portions at either end, and 108 mm wide; these patch sizes were selected to provide large residual stress effects. Following grit blast/silane treatment of the aluminium alloy surfaces, patches were applied using a 120 °C curing epoxy film adhesive [Redux 312/5]. Constant amplitude [$R=0.1$, $\sigma_{\max}=55$ MPa] fatigue tests were carried out on six patched and three unpatched specimens; Figure 15.8 summarises the crack growth rate data obtained. It can be seen that the rate of crack growth was reduced by a factor of about two in the case of single-side repairs, and by a factor greater than ten in the case of double-side repairs, and that b/ep patches were slightly more effective than gr/ep patches in retarding crack growth.

The DERA 3D BE/FE computer program was used to predict $\Delta K^P/\Delta K^U$ for both single and double-side repairs. Predicted values of $\Delta K^P/\Delta K^U$ are shown in Table 15.2 for crack lengths [$2a$] of 50 mm and 70 mm. The computer program was also used to predict the effect of residual thermal stresses on K_{\min}/K_{\max} [R -ratio] for patched specimens subjected to $R=0.1$, $\sigma_{\max}=55$ MPa remote loading. For $a=25$ mm, the predicted values of K_{\min}/K_{\max} were 0.64 and 0.68 for double-sided repairs with b/ep and gr/ep, respectively, and 0.33 and 0.36 for single-sided repairs with b/ep and gr/ep, respectively.

Values of $\Delta K^P/\Delta K^U$ were determined from the crack growth rate data summarised in Figure 15.8 and that determined for unpatched specimens loaded at $R=0.33, 0.36, 0.64$ and 0.68 . For example, in the case of double-sided b/ep patch

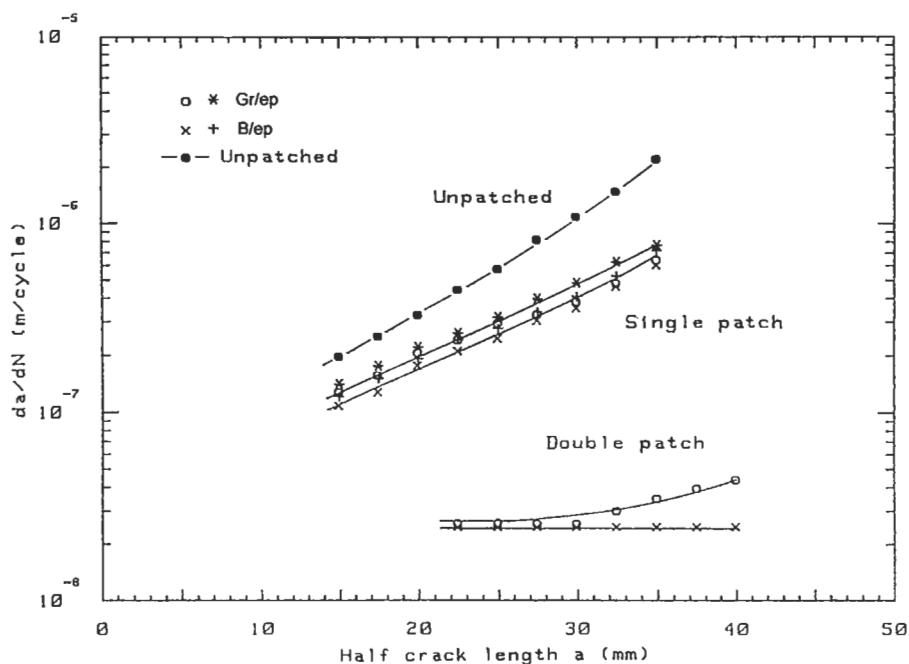


Fig. 15.8. Effect of patching on rate of crack growth ($R=0.1$, $\sigma_{\max}=55$ MPa).

repair and a half crack length of 25 mm, $da/dN = 2.35 \times 10^{-8}$ m/cycle was obtained directly from Figure 15.8 and the value of ΔK corresponding to this da/dN in $da/dN-\Delta K$ data for $R=0.64$ loading was assumed to be ΔK^P [4.6 MPa $m^{1/2}$]. Thus, for this particular repair it was estimated that $\Delta K^P=4.6$ MPa $m^{1/2}$ and $\Delta K^P/\Delta K^U = 0.27$. Values of $\Delta K^P/\Delta K^U$ determined in this way from experimental

Table 15.2

Comparison of theoretical and experimental values of $\Delta K^P/\Delta K^U$.

Half crack length, a (mm)	Single/double	Patch type	$\Delta K^P/\Delta K^U$	
			Theory	Expt
25	S	B/ep	0.66	0.70
		Gr/ep	0.66	0.71
	D	B/ep	0.27	0.29
		Gr/ep	0.27	0.28
35	S	B/ep	0.61	0.66
		Gr/ep	0.61	0.67
	D	B/ep	0.20	0.20
		Gr/ep	0.20	0.21

crack growth data are shown in Table 15.2 together with corresponding theoretical values predicted by the 3D BE/FE program. It is evident that excellent agreement between experimental and theoretical values of $\Delta K^P/\Delta K^U$ was obtained in the case of double-sided repairs, where large differences in crack growth rates were observed for patched and unpatched specimens. In the case of single-sided repairs, the predicted values of $\Delta K^P/\Delta K^U$ were lower than those determined experimentally. This observation may be associated with debonding, which would be more likely to occur in the case of the asymmetric single-sided repairs. This suggestion is consistent with the increase in crack growth rate with crack length observed for the single-sided repairs. Unfortunately, debonding was not monitored during this investigation because none had been detected in earlier work when symmetric patched thick section specimens were subjected to similar constant amplitude loading.

The investigation outlined above showed that the lower coefficient of thermal expansion of b/ep patches resulted in only slightly better performance than for gr/ep patches, even though the patch size had been selected to produce a large residual stress effect. In practise, the effect of residual thermal stresses will be less pronounced due to the restraint provided by surrounding structure, and therefore the use of b/ep rather than gr/ep patches will generally result in only very small improvements in fatigue performance due to reduced residual stresses.

For many applications it appears that efficient, durable repairs can be achieved using either b/ep or gr/ep patches. However, b/ep may be more suitable for some repairs [eg where maximum stiffness/minimum thickness patches are required] and gr/ep for others [e.g. where patches have to be applied to sharply curved surfaces]. Although this section has been confined to a comparison of b/ep and gr/ep patches, it should be noted that GLARE patches may be attractive for some applications, such as transport aircraft fuselage skins, because they offer improved fatigue performance due to reduced residual stress effects. The use of GLARE patches is considered in detail in Chapter 14.

15.5. Effect of bondline defects

Research at DERA on thick section repairs [see Section 15.3 above] showed that patch efficiency depended on the extent to which debonding developed during fatigue loading. However, it is possible that bondline defects may form during patching and it is essential that the effects of such defects on repair performance can be predicted accurately, since this will enable the acceptability of specific defects to be assessed and critical defect sizes to be defined. Thus, the research programme outlined below was undertaken to investigate the significance of a range of bondline defects on the performance of patch repairs to panels containing edge cracks [14].

145 mm wide panels, containing a 5 mm long single edge notch, were machined from 4.0 mm thick 2024-T3 aluminium alloy sheet. 2.5 mm long fatigue cracks were grown from the 5 mm slots under load shedding conditions, with the final 0.5 mm of

growth achieved by loading at $R = 0.05$, $\sigma_{\max} = 55$ MPa. Two cracked panels were bonded to aluminium alloy honeycomb and aluminium alloy end spacers to produce symmetric unpatched specimens.

Twelve ply unidirectional b/ep [5521] patches were supplied by AMRL, Melbourne for this programme. In addition, sixteen ply unidirectional gr/ep [T800/924] patches were manufactured. The average measured thicknesses of the patches were 1.645 mm for b/ep and 2.00 mm for gr/ep. These patch thicknesses were selected so that the b/ep and gr/ep patches would have similar stiffnesses, assuming Young's modulus was 208 GPa for 5521 and 168 MPa for T800/924. The patches were 132 mm long, including 30 mm or 33 mm tapered portions at either end, and 70 mm wide. The tapered portions of the b/ep patches consisted of eleven 3 mm steps, compared with fifteen 2 mm steps in the case of gr/ep patches. Prior to adhesive bonding, patch surfaces were lightly grit blasted while aluminium alloy surfaces were subjected to a grit blast/silane swab treatment. Redux 312/5 adhesive was used to bond gr/ep or b/ep patches to both sides of specimens at the same time as skin/honeycomb and skin/spacer bonding. For selected specimens, small [8 mm \times 10 mm] pieces of Teflon film were placed on the pretreated aluminium alloy surface prior to adhesive bonding, in order to produce bondline defects at the locations shown in Figure 15.9. These locations were selected because they were considered most likely to have a significant effect on the performance of patched specimens.

Unpatched and patched specimens were tested under $R = 0.05$, $\sigma_{\max} = 110$ MPa constant amplitude loading. For patched specimens, crack length was monitored using an eddy current technique [Elotest B1], while debonding was monitored using a pulse-echo ultrasonic technique, which involved a hand-held 10 MHz transducer. The fatigue lives of patched specimens were at least 70 times greater than for unpatched specimens, and were reduced by about 14% due to the presence of small [8 mm \times 10 mm] bondline defects at the onset of fatigue testing. Figure 15.10 shows that patching was very effective in reducing the rate of crack growth, and that the initial bondline defects resulted in relatively small effects. Although there is some overlap of data for patched specimens, it can be seen that b/ep patches without defects were most effective in reducing the rate of crack growth while gr/ep patches with defects were least effective. Ultrasonic inspection established that debonds developed from the initial defects located adjacent to the crack. Typical debond growth is illustrated in Figure 15.11, where the tip of the debond corresponds approximately to the crack tip position. In the absence of initial defects, debonds of similar shape developed although they tended to be narrower and the tip of the debond was located behind the crack tip. No debond growth was detected for defects located at the tapered edge of patches, [see defect X in Figure 15.11].

Repairs were analysed using the 3D BE/FE computer program, assuming rigid grips with displacement boundary conditions on the leading edges. Figure 15.12 shows the variation in K_{\min}/K_{\max} [R -ratio] with crack length predicted for patched specimens subjected to $R = 0.05$, $\sigma_{\max} = 110$ MPa loading, while Figure 15.13 indicates the effects of defects and debonding on predicted values of $\Delta K^P/\Delta K^U$ for both gr/ep and b/ep patch repairs. Table 15.3 compares predicted values of

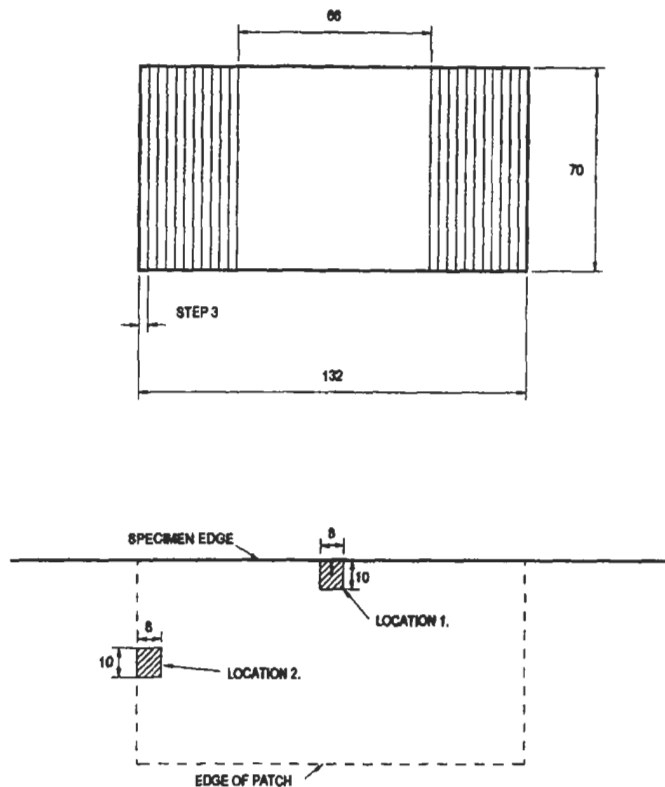


Fig. 15.9. Dimensions and locations of patches and bondline defects.

$\Delta K^P / \Delta K^U$ with corresponding values determined from crack growth rate data, where residual stress effects were taken into account by determining ΔK^P from da/dN - ΔK data for R -ratios predicted for patched specimens [as described in section 15.4 above]. It can be seen that there is excellent agreement between the predicted values of $\Delta K^P / \Delta K^U$ and those determined from experimental data, providing the effect of debonds and defects are taken into account in the analytical model. For ease of modelling, it was assumed that the shape of the debond relative to the initial defect and crack was as shown in Figure 15.14, i.e. the debond was as wide as the initial defect and extended to the crack tip. In general, the measured debonds were smaller than this, and therefore the values of $\Delta K^P / \Delta K^U$ predicted for defects and debonds were greater than those determined from experimental data. The only exception concerned gr/ep and a crack length of 60 mm, when the measured debond was slightly larger than that assumed for modelling purposes. The slightly better crack growth performance observed for b/ep patches, compared to gr/ep patches, [Figure 15.10] may be explained in terms of the lower R -ratio for b/ep [Figure 15.12], due to reduced residual stresses.

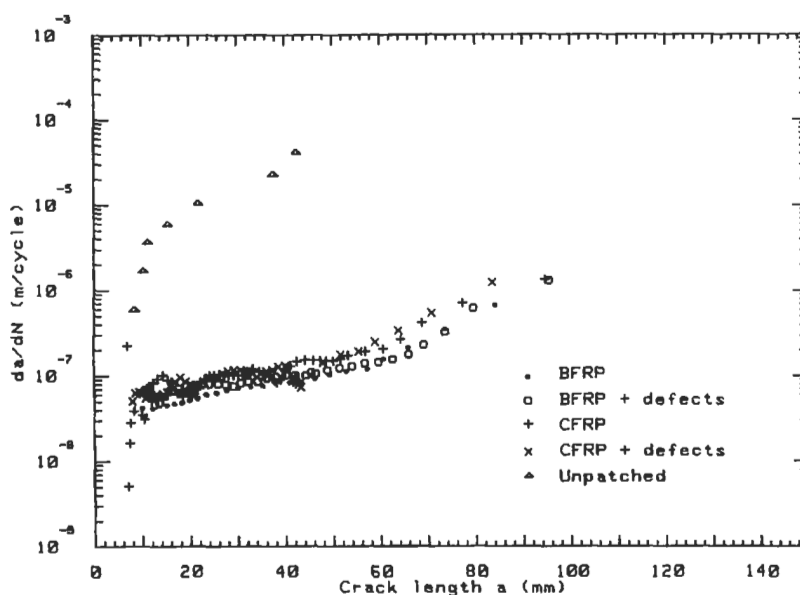


Fig. 15.10. Effect of patch type and defects on rate of fatigue crack growth ($R = 0.05$, $\sigma_{\max} = 110$ MPa).

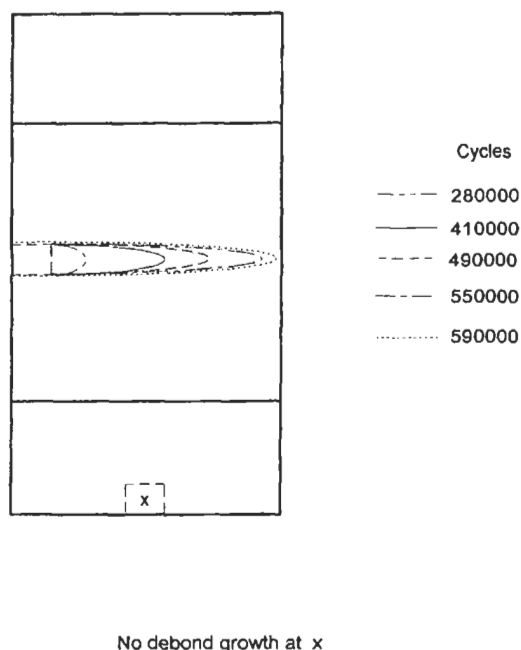


Fig. 15.11. Growth of debond from bondline defect in gr/ep patched specimen.

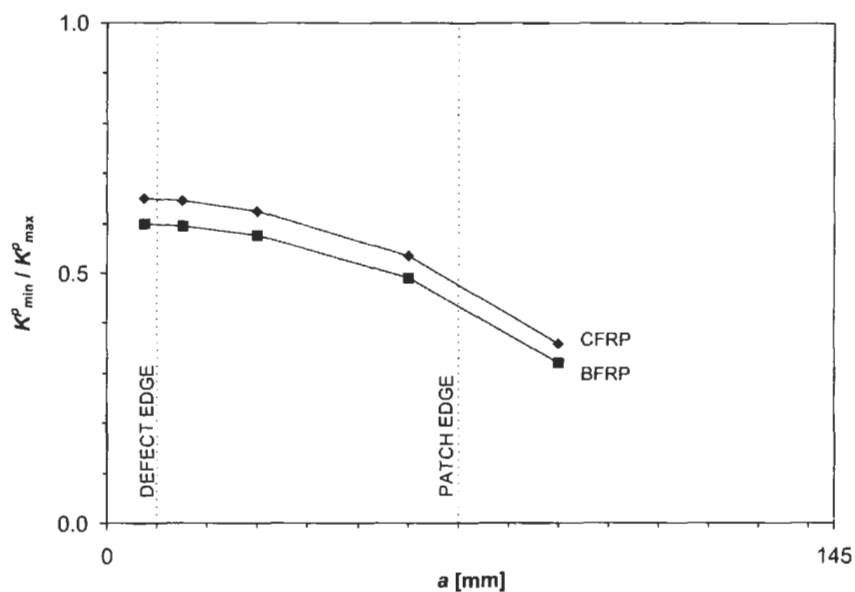


Fig. 15.12. Variation of K_{min}/K_{max} with crack length for b/ep and gr/ep patched specimens.

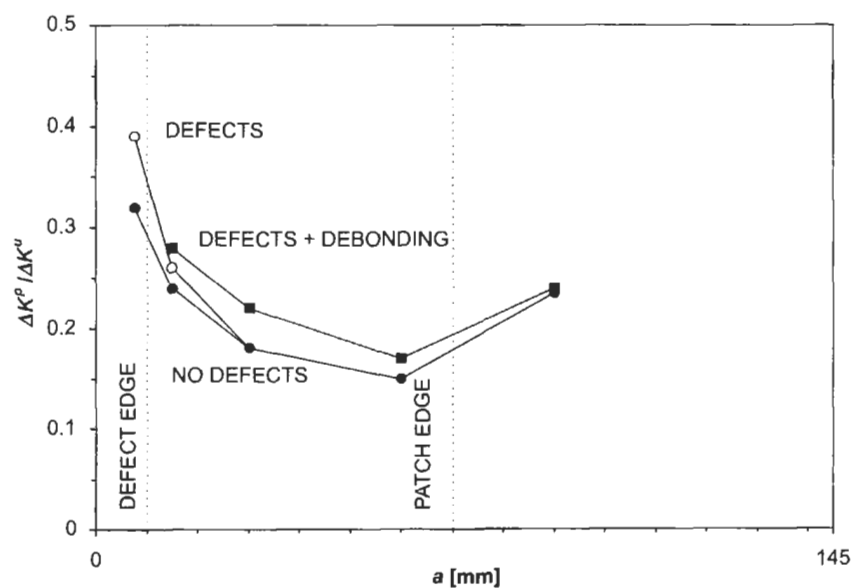


Fig. 15.13. Variation of $\Delta K^P/\Delta K^U$ with crack length, defects and debonding.

Table 15.3

Comparison of values of $\Delta K^P/\Delta K^U$ determined from experimental crack growth rate data with those predicted by analytical model.

Patch type	a, mm	$\Delta K^P/\Delta K^U$ (Expt)	$\Delta K^P/\Delta K^U$ (Theoretical)	
			No defect/debond	Defect and debond
B/ep	15	0.25	0.24	0.28
	30	0.20	0.18	0.22
	60	0.17	0.15	0.17
Gr/ep + defects	15	0.27	0.24	0.28
	30	0.21	0.18	0.22
	60	0.19	0.15	0.17

The analytical model was used to predict the effect of increasing the size of the initial bondline defect. Table 15.4 shows that, for a crack length of 15 mm, $\Delta K^P/\Delta K^U$ increased from 0.24 in the absence of bondline defects to 0.26 with a 10 mm \times 8 mm defect, and to 0.35 with a 20 mm \times 16 mm defect. It follows that the 20 mm \times 16 mm defect would have a significant effect on the rate of fatigue crack growth, while the 10 mm \times 8 mm defect would have little effect and would probably be acceptable. However, any assessment of bondline defects must take account of the load spectra which may be experienced in service.

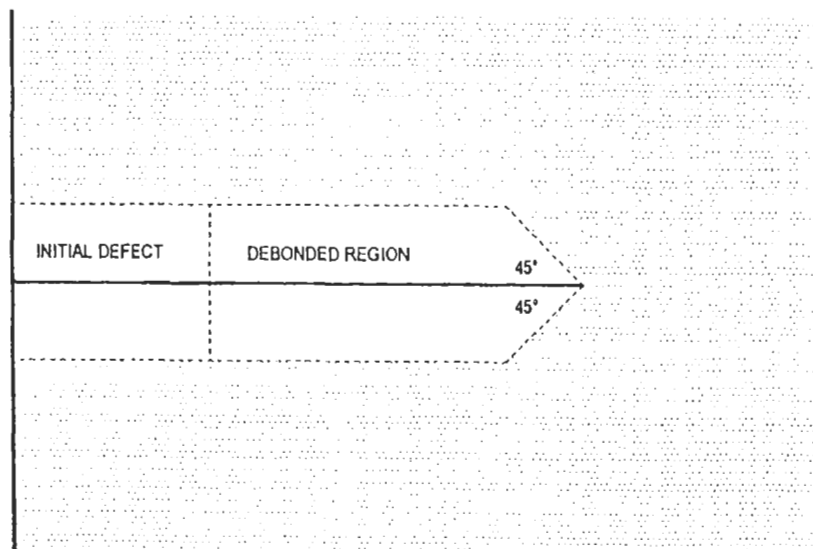


Fig. 15.14. Shape and size of debond region assumed in theoretical study.

Table 15.4
Effect of initial defect size on $\Delta K^P/\Delta K^U$ ($a = 15$ mm).

Patch	Defect size	$\Delta K^P/\Delta K^U$
B/ep	No defect	0.24
	10 mm \times 8 mm	0.26
	15 mm \times 12 mm	0.32
	20 mm \times 16 mm	0.35
Gr/ep	No defect	0.24
	10 mm \times 8 mm	0.26
	15 mm \times 12 mm	0.32
	20 mm \times 16 mm	0.35

15.6. Effect of impact damage

For many bonded composite patch repairs, particularly those on external surfaces, there is a risk that impact damage may occur in service. Thus, research was undertaken at DERA to investigate the influence of impact damage on the effectiveness of bonded patches in retarding the growth of fatigue cracks [15]. 12.4 mm thick aluminium alloy specimens containing 40 mm long central through-thickness cracks were repaired on both sides by bonding b/ep, gr/ep or gr/ep + gl/ep patches with Redux 312/5 adhesive. The gr/ep + gl/ep patches were manufactured using 13 plies of unidirectional gr/ep prepreg [T800/924] and 1 ply of woven gl/ep prepreg [924G/37%/7781]. Impact damage was introduced at sites 5 mm in front of the underlying fatigue cracks, using a Rosand impact machine with a 16 mm diameter hemispherical impactor. The impact energy was either 9 Joules [typical of impact involving a dropped tool] or 45 Joules [typical of impact with runway debris]. For patches subjected to low energy [9 Joules] impact, small areas of surface damage were visible and C-scans indicated that the damaged area was less than 5 mm diameter. This level of damage did not result in a significant increase in the rate of crack growth, i.e. patch efficiency was not reduced. In contrast, high energy [45 Joules] impact resulted in severe damage and subsequent acceleration of crack growth, as illustrated in Figure 15.15 for specimens repaired on both sides with gr/ep + gl/ep patches. Visual examination of the patches revealed extensive splitting, delamination and fibre breakage, with some damage present at the bonded surface of the patch. In most cases the damage appeared to be contained by an area approximately 12 mm wide and 50 mm long, located with its 50 mm length edges 18 mm and 30 mm from the centre of the patch.

The 3D BE/FE computer program was used to predict the effect of impact damage on patch efficiency. Since the precise nature of the damage was difficult to quantify, a worst case was assumed where two 12 mm wide, 50 mm long, full thickness portions of the patch were completely removed. This simulated damage was referred to as *full damage*. The effect of removing similar portions of patch, but of half thickness only, was also studied. This form of simulated damage, where the patch is of half thickness in the two 12 mm \times 50 mm areas, was referred to as *half*

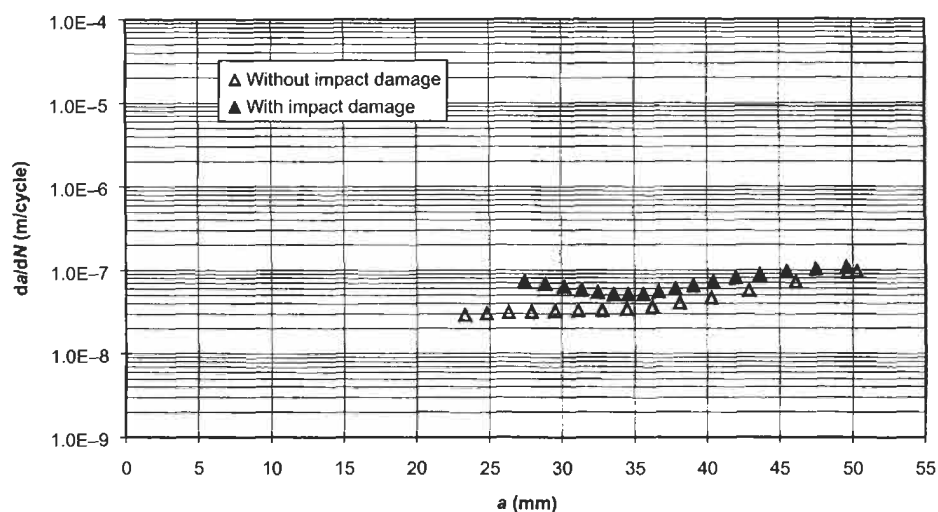


Fig. 15.15. Effect of high energy impact on rate of crack growth [double-sided repair with gr/ep + gl/ep patches].

damage. For comparison, the effect of two 12 mm \times 50 mm debonds at the patch/metal interface was investigated. The predicted effect of these different simulated damages on $\Delta K^P/\Delta K^U$ is shown in Figure 15.16. It can be seen that the values of

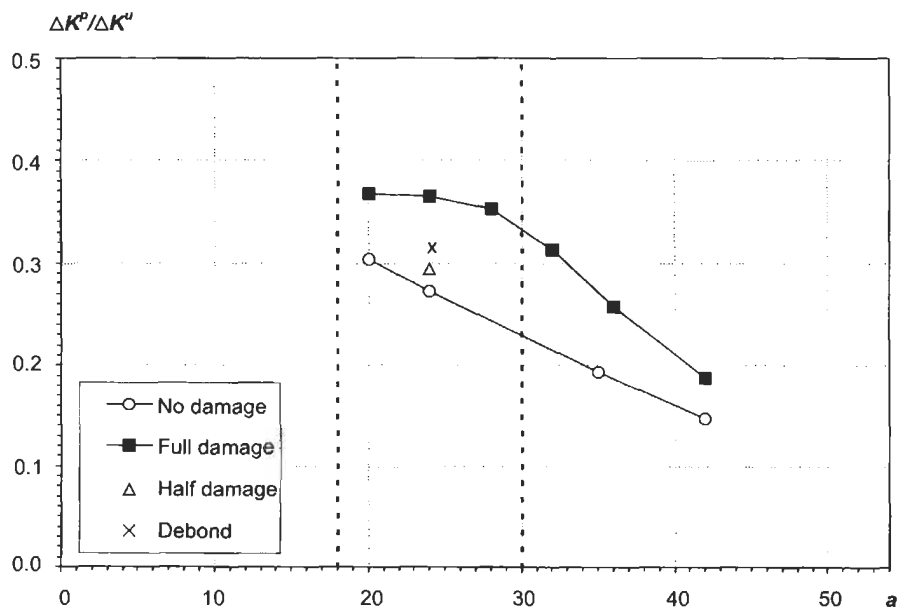


Fig. 15.16. Variation of $\Delta K^P/\Delta K^U$ with crack length for various damage scenarios.

$\Delta K^P/\Delta K^U$ for the *full damage* case exceed those for the *no damage* case by about 21% at $a = 20$ mm [i.e. when the crack tips are just inside the damage area], rising to a maximum of about 45% as the crack tips approach $a = 30$ mm, before tailing off to 27% at $a = 42$ mm. It is interesting to note that for the *half damage* case at $a = 24$ mm, $\Delta K^P/\Delta K^U$ is only 8% higher than for the *no damage* case, compared to 34% for *full damage* and 16% for the debonds.

Crack growth rates for patched specimens were predicted from the theoretical values of $\Delta K^P/\Delta K^U$ and R^P , and experimental da/dN - ΔK data for 2024-T3 alloy at various R -ratios, as described previously. In the absence of impact damage, the predicted and measured crack growth rates were in good agreement. However, the crack growth rates predicted for *full damage* were faster than those observed following high energy impact. This was expected because the *full damage* case was deliberately selected to represent more severe damage than that resulting from high energy impact.

The observed effects of impact damage on patch performance, and the C-scan evidence that growth of damage did not occur during fatigue testing, indicate that impact damage is unlikely to present serious in-service problems. Furthermore, it appears that visual examination of the patch surface will enable significant impact damage to be detected readily, and that an estimate of the maximum extent of such damage will allow a conservative estimate of its effect on patch efficiency.

15.7. Effect of service temperature

Accurate prediction of the influence of service temperature on the effectiveness of patch repairs in retarding fatigue crack growth is not straightforward because temperature may affect residual stresses, adhesive properties and resistance to fatigue crack growth. Recent research at DERA on the effect of test temperature on patch efficiency involved 12.4 mm thick specimens similar to those used for the impact damage investigation [15]. Theoretical and experimental work was carried out to investigate the effect of varying the test temperature in the range -55°C to 70°C . Fatigue testing demonstrated that increasing the test temperature from ambient to 70°C resulted in very small reductions in crack growth rate for specimens repaired on one side with b/ep or gr/ep patches. This observation was consistent with theoretical analysis which predicted that the opposing effects of reduced residual stresses and reduced adhesive modulus would result in a small reduction in crack growth rate. In contrast, for double-sided repairs, a small increase in crack growth rate was predicted.

Theoretical analysis predicted that reducing the test temperature to -55°C would result in an increase in crack growth rate for patched specimens, owing to increased residual stresses having a greater effect than any likely accompanying increase in adhesive shear modulus. Fatigue testing at -55°C to determine the magnitude of this effect has not yet been carried out. However, when a single sided gr/ep patched specimen was tested at -20°C , rather than at ambient laboratory conditions, a significant decrease in crack growth rate was observed. This

behaviour may be explained in terms of an increase in the crack growth resistance of 2024-T3 alloy, due to removal of moisture from the test environment at a temperature of -20°C . Fatigue tests on unpatched specimens confirmed that crack growth rates were significantly lower at -20°C than at room temperature. Thus, from the results of the DERA investigation [15] it appears that, for gr/ep patches bonded with a 120°C curing adhesive, patch efficiency under ambient conditions will not be reduced significantly by varying the service temperature in the range -55°C to 70°C . However, further work is required to establish the effect of increasing the temperature to 70°C following long term exposure to hot-wet conditions [see next section], and to confirm performance at -55°C .

15.8. Effect of exposure to hot-wet environments

The effectiveness of adhesively bonded composite patches in retarding fatigue crack growth in aluminium alloy structures may be affected adversely by long-term exposure to hot-wet environments, due to moisture causing reduced strength and stiffness of the adhesive, loss of adhesion at the aluminium alloy/adhesive interface and/or corrosion under the patch. Research has been carried out at DERA [16] to investigate the extent to which bonded gr/ep patch repairs are degraded when they are exposed to various hot-wet environments. In one programme, 1.6 mm thick, 150 mm wide aluminium alloy panels containing 38 mm long central fatigue cracks were repaired on one side with various patch/adhesive systems. Panel surfaces were subjected to a grit blast/silane swab treatment prior to bonding; an adhesive bonding primer was not used. Following patching, fatigue testing was carried out to grow cracks by approximately 4 mm and thereby enable the effect of patching on crack growth rate to be determined. These panels were then transported to Australia where they were exposed under load at Pin Gin Hill hot-wet cleared jungle site or Cowley Beach marine site for up to six years. After exposure for one or six years, panels were placed in sealed polyethylene bags and returned to DERA for fatigue testing. Thus, for each panel, fatigue crack growth rate data [for $R = 0.1$, $\sigma_{\max} = 60 \text{ MPa}$ loading] were obtained before patching, immediately after patching, and after exposure for one or six years. The main results of this investigation are summarised below:

- i For panels repaired by bonding precured patches with a 120°C curing film adhesive [Redux 312/5], exposure at the jungle or marine sites for one or six years had no significant effect on crack growth rate, i.e. patch efficiency was not affected. This is illustrated in Figure 15.17 by the crack growth rate data obtained for a patched panel exposed at the jungle site for six years.
- ii For panels repaired by bonding precured patches with a paste adhesive [Araldite 2005], crack growth rate data exhibited greater variability but again exposure appeared to have no significant effect on patch efficiency.
- iii In contrast, for panels repaired with wet laminated patches, exposure at the marine site for six years resulted in extensive debonding and almost no retardation of fatigue crack growth. This behaviour was attributed to

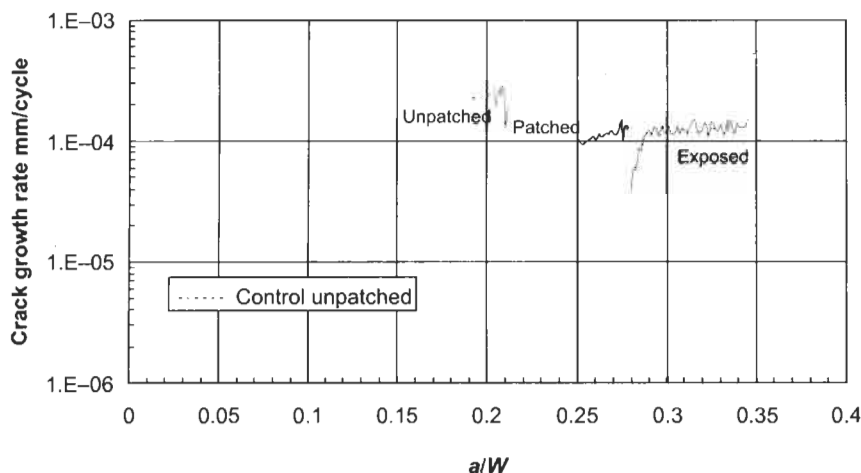


Fig. 15.17. Effect of exposure at jungle site for six years on fatigue crack growth rate for panel repaired with precured patch and Redux 312/5 adhesive.

corrosion under the patch, caused by high levels of salinity in the atmosphere and the galvanic action of the gr/ep patch. [No effort was made during patch application to avoid electrical contact between the graphite cloth and the aluminium panel, i.e. a layer of woven glass was not used to separate the graphite from the aluminium].

- iv In the case of panels repaired with wet laminated patches and exposed at the jungle site, patch efficiency improved as exposure time increased. This unexpected but consistent observation was attributed to additional curing of the wet laminated resin during exposure. Corrosion was not detected at/under the edges of the patches, which was not surprising since there was no salinity at the jungle site.

When similar panels were repaired with precured patches and a 120 °C curing film adhesive, exposed to 70 °C/84%RH for up to 408 days, and then fatigue tested, only very small increases in fatigue crack growth rate were observed. Other panels were exposed to a hot-wet-freeze cycle, comprising cooling from +50 °C to –55 °C over 70 min, dwell at –55 °C for 30 min, heating to +50 °C over 35 min, and dwell at 50 °C/96%RH for 585 min. Exposure to this cycle for up to 696 days, and then to 50 °C/96%RH for up to 720 days, resulted in small increases in crack growth rate, i.e. prolonged exposure to these relatively severe conditions had little effect on patch efficiency.

In another DERA study [16], 12.4mm thick specimens were repaired on both sides, using T800/924 patches and Redux 312/5 adhesive, and exposed to 70 °C/84%RH for about one year. Recent fatigue testing under ambient laboratory conditions indicated that this exposure had little effect on crack growth rate. However, higher crack growth rates were observed when exposed, patched

specimens were fatigue tested in an environmental cabinet at 70 °C/84%RH. Further work is in progress to confirm and explain this behaviour.

In general, the research outlined above indicates that the effectiveness of adhesively bonded composite patch repairs to aluminium alloy structures will not be affected significantly by long-term exposure to hot-wet environments, providing appropriate surface treatments, adhesives, patches and bonding processes are used. This general conclusion is supported by the excellent long-term service experience reported in this book for a wide range of repairs.

15.9. Repair of battle damage

Theoretical and experimental research has been carried out at DERA to assess the potential of adhesively bonded gr/ep patches for the “permanent” repair of battle damage. Work to date has concerned the repair of simulated battle damage in 3.175 mm thick, 160 mm wide 2024-T3 aluminium alloy test panels, where the damage consisted of holes with defects at various locations round the edges of the holes. Several damage configurations have been investigated, including those based on 5 mm or 40 mm diameter central holes with either [a] two slots at opposite sides of the holes and perpendicular to the loading axis, [b] one slot perpendicular to the loading axis, or [c] four slots at 45° to the loading axis. All test panels were fatigue loaded until a crack of specified length, e.g. 1 mm, developed at the end of each slot. Repairs were carried out using precured gr/ep [T800/924] patches and a 120 °C curing epoxy film adhesive [Redux 312/5].

A 3D boundary element/finite element model was used to study patch repair of various forms of damage, and to predict the influence of patch, adhesive and loading variables on repair efficiency. The through thickness variation of K was studied and root mean square values were determined for the entire crack front. Similar values of K were obtained if the crack front was assumed to be at 45° to, or perpendicular to, the patch plane, i.e. crack front shape had only a small effect on K , and therefore perpendicular cracks were assumed for the remainder of the study. In general, significant improvements in fatigue performance were predicted for single-sided patch repair of various forms of damage, with better performance predicted for thicker patches but only a small improvement predicted when adhesive thickness was reduced from 0.3 mm to 0.05 mm. Less efficient repairs were predicted for larger holes; for example, in the case of two cracks at opposite sides of the hole and a half crack length of 30 mm [measured from centre of hole], $\Delta K^P/\Delta K^U$ was about 0.48 for a 40 mm diameter hole compared to 0.42 for a 5 mm diameter hole. When panels containing four slots at 45° to the loading axis were fatigue loaded, cracks tended to grow perpendicular to the loading axis to produce kinked cracks of the type shown in Figure 15.18. When repair of this type of damage was compared with that of “equivalent” damage in the form of two cracks at opposite sides of a hole [see Figure 15.18], more efficient repairs were predicted in the case of the four kinked cracks, as illustrated in Table 15.5. In the case of the four kinked cracks, values of K_I , K_{II} and K_{III} were determined and it was shown

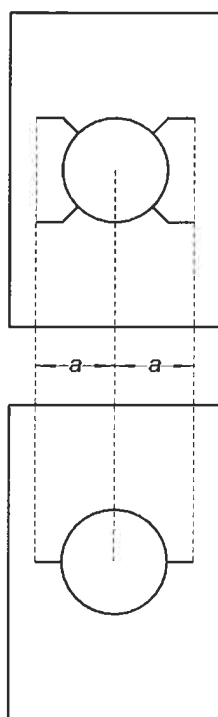


Fig. 15.18. Different damage configurations of "equivalent" width.

that the combined contribution of K_{II} and K_{III} to the effective stress intensity factor was less than 8% for the configurations studied.

Fatigue testing confirmed that various forms of damage could be repaired effectively with single patches. For example, the fatigue lives of panels containing 40 mm diameter holes and either single cracks or four 45° kinked cracks were improved by factors of 5.1 and > 15 , respectively, by single-sided repairs with a 1 mm thick patch [80 mm \times 80 mm]. The measured fatigue crack growth rates were

Table 15.5

Comparison of stress intensity factor ranges for four 45° kinked cracks and two diametrically opposite cracks, with tips at $x_1 = 40$ mm and hole radius = 20 mm ($R = 0.1$, $\sigma_{\max} = 65$ MPa).

Crack configuration	Patch thickness, mm	ΔK^P	ΔK^U	$\Delta K^P / \Delta K^U$
4 \times 45° kinked cracks	2.0	6.0	22.3	0.30
	1.0	8.8	22.3	0.39
2 \times diam. opposite cracks	2.0	11.3	27.7	0.41
	1.0	13.7	27.7	0.49

in good general agreement with theoretical predictions. For example, the mean crack growth rate of 9×10^{-9} m/cycle measured for four kinked cracks at a half crack length of 35 mm during $R=0.1$, $\sigma_{\max}=41.25$ MPa loading, was in good agreement with predicted values of $\Delta K^P=5.7$ MPa $m^{1/2}$ and $K_{\min}/K_{\max}=0.51$, and $da/dN-\Delta K$ data for 2024-T351 aluminium alloy sheet. Furthermore, the observed crack paths indicated little effect due to Mode II loading. In the case of a 40 mm hole and two cracks, double sided patching resulted in crack arrest, in agreement with theoretical predictions. Work is in progress to determine the effectiveness of patch repairs for other damage configurations.

15.10. Future work

Although adhesively bonded gr/ep patch repair of cracked metallic structures has been studied extensively and service experience with repairs has been good, it appears that further work is required to address some remaining problems and to assess the full potential of the repair technique. Specific research objectives include the following:

- (a) To investigate the effect of variable amplitude loading spectra on patch debonding and hence on patch efficiency. There is a clear requirement for a model to predict debonding, and for incorporation of this in a general model, which will enable the effect of patching on fatigue crack growth to be predicted for a wide range of loading spectra.
- (b) To assess the influence of hot-wet fatigue test environments on patch efficiency, and the effect of long-term pre-exposure to hot-wet environments on such behaviour.
- (c) To establish the advantages and limitations of repairs carried out by co-cure of prepreg and adhesive.
- (d) To develop and assess bonded patch repair schemes for applications involving elevated service temperatures.
- (e) To investigate the effectiveness of bonded patches for the repair of various forms of corrosion damage and battle damage in aluminium alloy structures.
- (f) To develop and assess patch repairs for applications involving bonding over fasteners.
- (g) To assess the potential of bonded patches for the repair of SPF/DB titanium alloy structures, and to develop optimum repair schemes.
- (h) To develop "Smart" patches for monitoring repair performance in service, and improved NDE techniques for (i) inspecting pretreated surfaces prior to bonding, and (ii) assessing the strength and durability bonded patch repairs.

15.11 Acknowledgements

© British Crown Copyright 2001. Published with the permission of the Defence Evaluation and Research Agency on behalf of the Controller of HMSO.

References

1. Kemp, R.M.J., Murphy, D.J., Butt, R.I., *et al.* (1983). RAE Technical Report TR 83005.
2. Sutton, G.R., Stone, M.H., Poole, P. *et al.* (1984). In: Repair and Reclamation, The Metals Society; pp. 17.1–17.6.
3. Poole, P., Stone, M.H., Sutton, G.R., *et al.* (1986). In: The Repair of Aircraft Structures Involving Composite Materials, AGARD-CP-402, pp. 9.1–9.21.
4. Sutton, G.R. and Stone, M.H. (1989). RAE Technical Report TR 89034.
5. Dowrick, G., Cartwright, D.J. and Rooke, D.P. (1980). RAE Technical Report TR 80098.
6. Young, A., Cartwright, D.J. and Rooke, D.P. (1988). *Aeronautical J.*, pp. 416–421.
7. Young, A., Rooke, D.P. and Cartwright, D.J. (1989). *Aeronautical J.*, pp. 327–332.
8. Ball, A.S. (1993). MOD Contract SLS 41B/2093, Final Report BAe-KDD-FCP-0104.
9. Poole, P., Brown, K. and Young, A. (1990). RAE Technical Report TR 90055.
10. Poole, P., Lock, D.S. and Young, A. (1991). In: Aircraft Damage Assessment and Repair. The Institution of Engineers, Australia, pp. 85–91.
11. Poole, P. and Young, A. (1992). In: Theoretical concepts and Numerical Analysis of Fatigue [A.F. Blom and C.J. Beevers, eds.], EMAS, pp. 421–438.
12. Baker, A.A. (1988). In: Bonded Repair of Aircraft Structures (A.A. Baker and R. Jones, eds.), Martinus Nijhoff, pp. 107–173.
13. Poole, P., Young, A. and Ball, A.S. (1994). In: Composite Repair of Military Aircraft, AGARD-CP-550, pp. 3.1–3.12.
14. Poole, P., Lock, D.S. and Young, A. (1997). In: *Proc. of 1997 USAF Aircraft Structural Integrity Conf.*, USAF.
15. Poole, P., Brown, K., Lock, D.S., *et al.* (1999). In: *Proc. of 1999 USAF Aircraft Structural Integrity Conf.*, USAF.
16. Poole, P., Stone, M.H., Sutton, G.R., *et al.* (2000). In: *Proc. of 2000 USAF Aircraft Structural Integrity Conf.*, USAF.

Chapter 16

REPAIR OF MULTI-SITE DAMAGE

R. JONES and L. MOLENT*

Defence Science and Technology Organisation, Air Vehicles Division, Monash University, Wellington Rd, Clayton, Victoria 3168, Australia

16.1. Introduction

The phenomenon of multi-site damage (MSD) in aircraft has been under examination in recent years by many in the aviation industry. This section investigates the feasibility of applying advanced bonding technology to commercial aviation structures containing MSD. The validity of this technology has already been proven in its application to fatigue and stress corrosion in military aircraft, as described in other chapters of this book.

The consequence of the undetected presence of MSD was dramatically illustrated through the in-flight failure of a fuselage lap joint on an Aloha Airlines B-737 aircraft on April 28, 1988. Essentially this failure occurred due to numerous small cracks along a fastener line linking together, causing the residual strength of the fuselage to be exceeded under pressurization. A test programme was conducted to reproduce this type of failure, and an adhesively bonded boron/epoxy doubler for use as a repair or preventative measure has been developed.

This chapter presents the results of a fatigue test programme, which also considers environmental and damage tolerance aspects, conducted using specimens representative of wide-bodied commercial aircraft fuselage lap joints. This work was reported in detail in [1–10].

Two separate generic specimens were considered, one representative of Boeing Commercial Aircraft Company (Boeing) and the other of Deutsche Airbus GmbH (Airbus) aircraft fuselage lap joints.

* *Air Frames and Engines Division, Aeronautical and Maritime Research Laboratory, Fishermans Bend, Victoria 3207, Australia.*

Following the development of a bonded-composite repair for MSD in the fuselage lap-joint of wide bodied transport aircraft a number of full scale demonstration repair/reinforcements were undertaken.

16.2. Specimen and loading

16.2.1. Boeing lap joints

Figure 16.1 details a typical configuration of a modern Boeing wide bodied aircraft pressurized fuselage construction. For the purpose of this work attention is focused on the lap joint area. Local details of this location vary depending on the age of the aircraft and specific manufacturers' details.

It should be noted that, in many cases, in addition to fasteners, the lap joints are bonded together, either using hot or cold setting adhesives. This is done for the purpose of increasing the fatigue life of the joint. In service, environmental degradation may cause this bond to become ineffective, and corrosion of the mating skins could accelerate the onset of MSD (as was the case in the Aloha incident). For these reasons bonded lap joints are not considered in this work.

In the present investigation a worst-case scenario was assumed, viz: a non-bonded, full depth, upper plate, counter-sunk configuration as shown in Figure 16.2(a). Here the counter-sunk rivet hole, if accompanied by improper rivet head seating, leads to a phenomenon known as "knife-edging" (i.e. the tip of the counter-sunk in the top plate "cutting" into the lower plate). This in turn leads to a reduction in the fatigue life of the joint, relative to the case where the counter-sunk does not fully penetrate the plate, due to the sharp corners accelerating the initiation of cracks.

The basic specimen used in this investigation (referred to as the "Boeing" type) consisted of two 2024-T3 clad aluminium alloy sheets 1.016 mm (0.04 inch) thick, fastened with three rows of BACR15CE-5, 100° shear head counter-sunk rivets, 3.968 mm (5/32 inch) diameter, as shown in Figure 16.3. The width of the specimen was chosen to coincide with the typical distance between tear straps of a B-737 aircraft.

The upper row of rivet holes contained crack initiation sites, induced by means of an electrical spark erosion technique, on either side, nominally 1.2 mm long. This length was chosen so that the defect was obscured by the fastener head, which is representative of possible undetectable flaws. These flaws were achieved by drilling the rivet holes undersize (3.85 mm diameter), spark eroding the initiation sites to 1.225 mm, and then machining the counter-sunk (4.039 mm) to achieve the required hole diameter. The accuracy to which the latter was performed determined the final configuration of the defects. In some cases the defects only remained on one side of the hole, the other being removed by the tool. Following this the fasteners were inserted.

The specimens were manufactured by the then Australian Airlines (now QANTAS), from material supplied by them, to aircraft standards. End tabs were

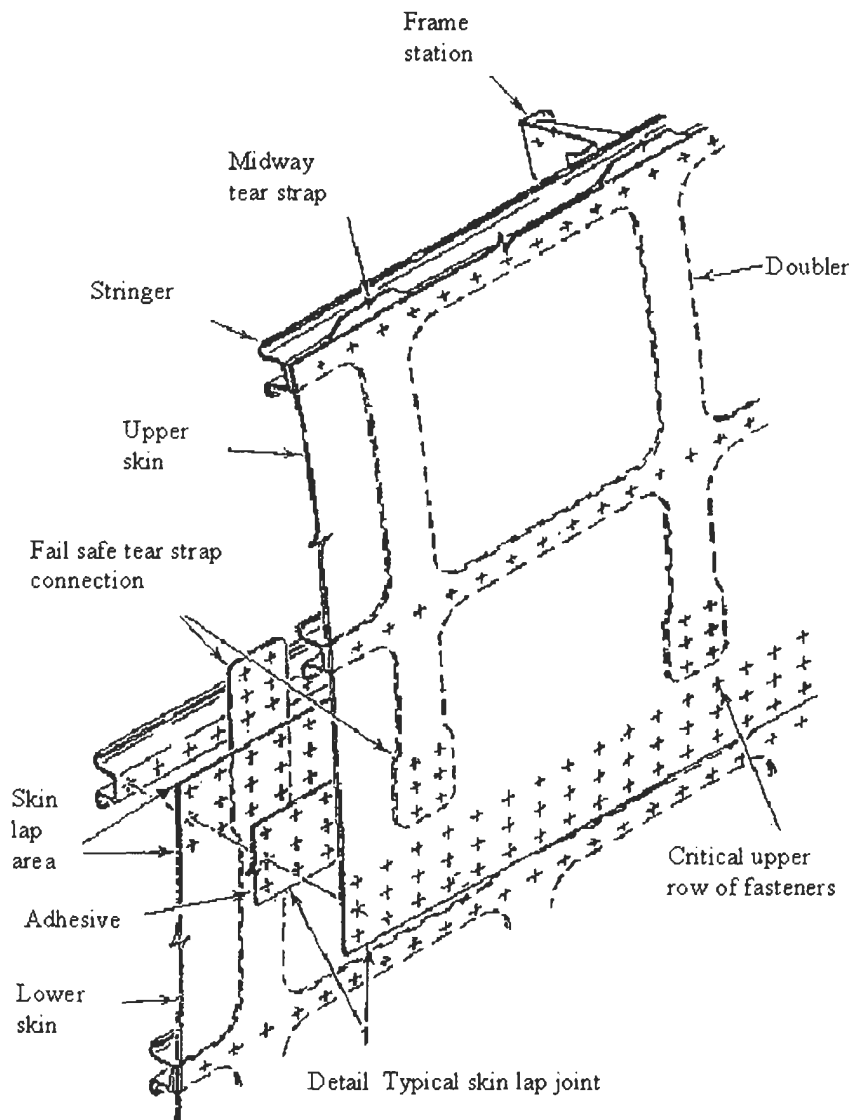


Fig. 16.1. Typical wide body fuselage construction (from Boeing).

bonded to the base specimen to ensure failure would not initiate from the specimen ends (see Figure 16.3).

Since the amount of out-of-plane bending due to fuselage curvature in a typical fuselage joint was unknown, the local bending was prevented by testing the specimens bonded back-to-back and separated by a 12.5 mm thick honeycomb

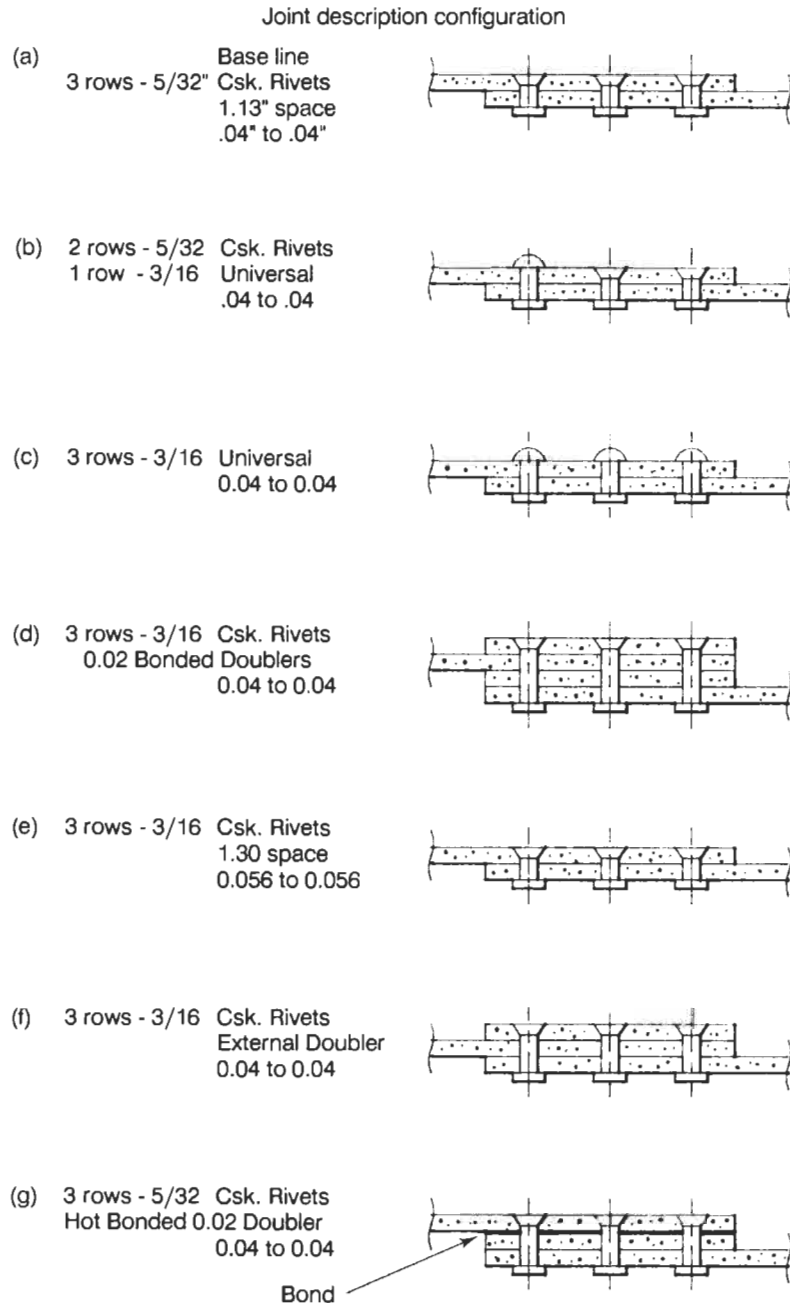


Fig. 16.2. Various fuselage lap joint configurations (from Boeing).

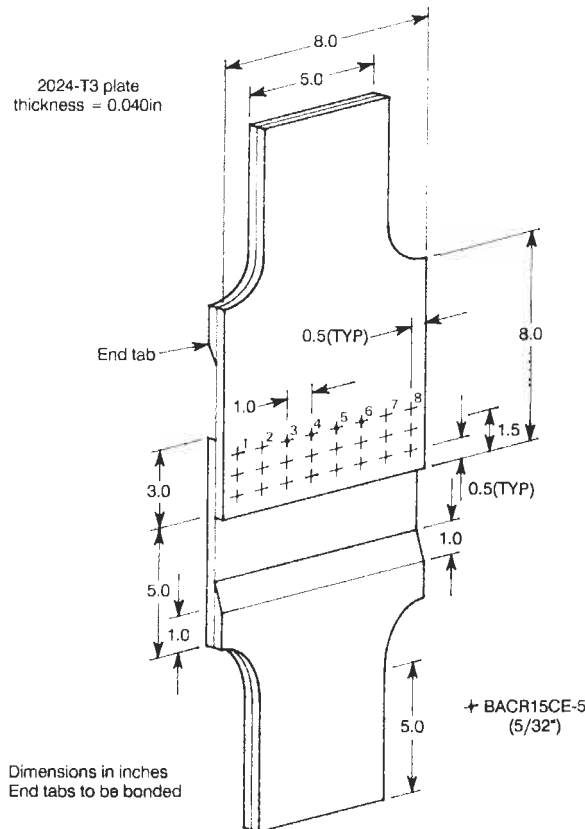


Fig. 16.3. Uniaxial "Boeing" type lap joint specimen. Note rivet numbering used in this chapter.

core. Details of the procedure used to construct the test specimens can be found in [2]. In this configuration strain gauge results indicated no global bending or parasitic stiffening due to the honeycomb.

One drawback of this method of testing is that the failure of one face (i.e. the base specimen) terminates further testing of the other. The over-riding advantage of this technique is that due to symmetry, a heat cured repair can be applied to the base specimens without inducing extensive bending due to the thermal expansion mismatch of the parent material and that of the repair. A view of the assembled test specimen is given in Figure 16.4.

The specimens were tested in various capacity servo-hydraulic test machines. The specimens were loaded in tension to give a remote plate stress of 92 MPa (13.4 ksi). This figure was determined from operational data obtained for the US DoT MSD Committee Review Board, see Table 16.1 (from [11]), for the B-737 aircraft.

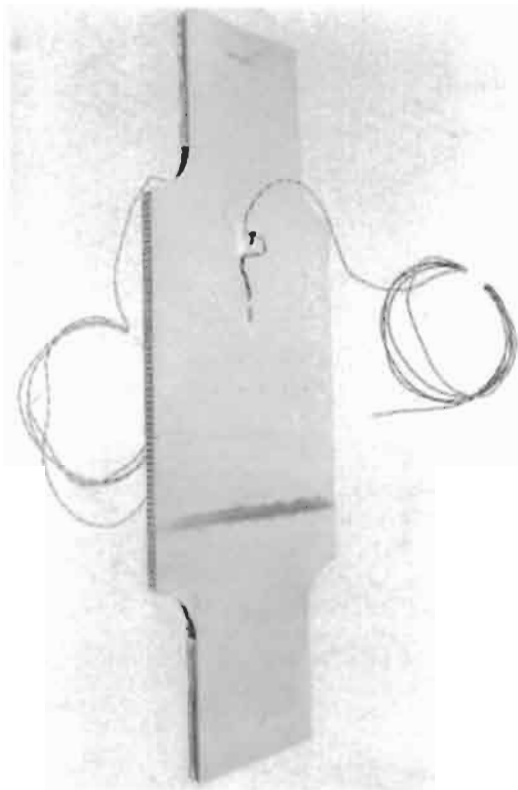


Fig. 16.4. Back to back bonded lap joint specimens.

Table 16.1
MSD committee review results [11].

Typical maximum normal operating stresses for Boeing 727 and 737 fuselage splices
Primary skin stress is pressure hoop stress

	P_R/T	At frames	Actual highest	Comment
Aircraft		psi		
B727	15900	10000	13200	Midway between frames
B737	16100	9800	13400	Middle of waffle strap area
			10400	Midway between frames
Maximum applied shear stresses are less than 25% of the 13000 psi hoop stresses				
Maximum principal stresses are:				
Tension – less than 110% of hoop stress				
Shear – less than 60% of hoop stress				

The applied constant amplitude loading used was:

$$P_{\max} = 40.0 \text{ kN}$$

$$P_{\text{mean}} = 21 \text{ kN}$$

$$P_{\min} = 2 \text{ kN} ,$$

at a frequency range between 2.5 and 3 Hz. This loading represents the hoop stress induced in the fuselage skin due to pressurization.

Pre-cracking of some specimens were conducted using the following loading:

$$P_{\max} = 50.0 \text{ kN}$$

$$P_{\text{mean}} = 26 \text{ kN}$$

$$P_{\min} = 1.2 \text{ kN} ,$$

at a frequency of 2.5 Hz. With this loading, cracks were initiated within 5000 cycles.

For the unreinforced specimen crack growth was monitored optically using a travelling microscope, with a magnification factor of 40.

For the unreinforced specimen the tests were terminated when the upper row of fasteners had completely failed (i.e. all cracks linked). For the reinforced specimens, eddy current techniques (see [2]) were used to check for crack growth beneath the doubler.

16.2.2. Airbus lap joints

Initial work had concentrated on the development of a bonded composite repair for MSD in joints similar to those encountered in Boeing aircraft. After discussions with Airbus, four “generic” specimens typical of current (7050-T73) fuselage construction were provided by Airbus for repair and testing. This work was reported in detail in reference [8]. The specimens had previously been fatigue tested to failure and each specimen had failed in the first row of rivets in the upper skin. On average the life to failure of the unrepaired specimens ranged from between 77200 to 2175600 cycles, depending on the test load which ranged from 80 MPa for the former to 43.7 MPa for the latter. The specimens were 115 mm wide and (nominally) 420 mm long. Two of the specimens had also failed at the ends of the specimen near the edge of the change of thickness at the joint. The skin thickness varied from 2.3 mm near the joint, to 1.6 mm elsewhere (see Figure 16.5).

In an attempt to reproduce the level of local constraint, as seen in service aircraft, the specimens were “paired” and mounted back to back on a 25.4 mm thick aluminium honeycomb core (this has negligible stiffness in the direction of the load, as demonstrated for the “Boeing” specimens).

Whilst these specimens had failed at the first row of rivets in the upper skin, the third row of rivets in the lower skin is also a potential failure location. To simulate cracking at this location a saw cut was inserted between the middle rivets in the lower skin of each of the four specimens (Figure 16.5). The specimens, along with the aluminium honeycomb and end tabs, were then assembled and bonded together

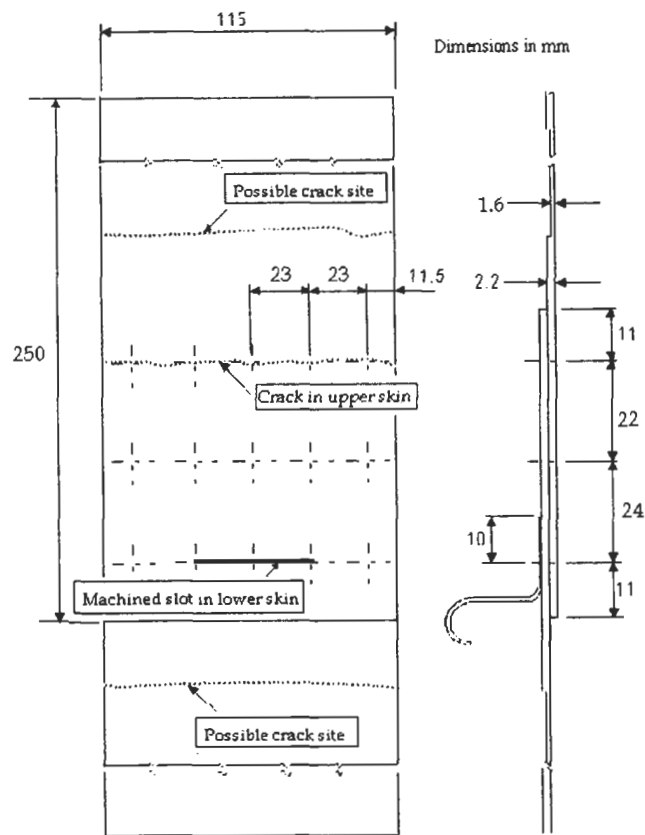


Fig. 16.5. "Airbus" lap joint specimen [8].

using an epoxy-nitrile structural thin-film adhesive which was cured at 120 °C in an autoclave.

The repaired specimens were fatigue tested under constant amplitude loading, with a maximum load of 47.49 kN and a minimum load of 4.83 kN. These loads correspond to a remote stress in the skin, suggested by Airbus, of 128.9 MPa and 13.1 MPa respectively.

16.3. Repairs

Conventional repair methods for detected cracking in fuselage lap joints involve removing the damaged material and the use of a riveted scab patch, see Figure 16.6.

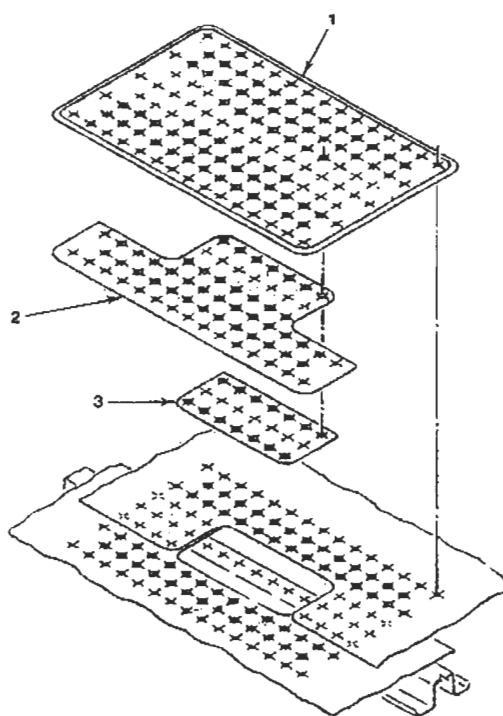


Fig. 16.6. Typical lap joint fastened repair.

The concern here is that this introduces further stress concentrations, due to the increase in fastener holes, and that the close proximity of these repairs may lead to a compromise in the damage tolerance of the structure. The objective of this investigation was to evaluate a possible bonded repair or life enhancement for mechanically fastened fuselage lap joints.

16.3.1. Repair philosophy

In 1990, with the support of the then Australian Civil Aviation Authority (CAA, now Civil Aviation Safety Authority), a world wide study into the commercial application of bonded repair technology was performed [12]. Thirty four organisations in eight countries, including ten manufacturers and seven Regulatory Authorities were consulted. The following proposed design rules and procedures were subsequently adopted by the CAA; viz:

1. Designs shall be substantiated against the Damage Tolerance provisions of the United States Federal Aviation Regulations (FAR) Part 25.571 at Amendment 45.

wing pivot fitting upper plate repair [13]. The doubler was applied after the specimens had been pre-cracked. In order to evaluate the fail-safe nature of the repair, two specimens were also repaired following complete failure of the upper row of fasteners.

In addition to the hot-curing adhesive (FM-73), a cold-setting adhesive (Flexon 241, Victoria, Australia) was also investigated.

The doublers were applied both as a reinforcement (specimens with short cracks emanating from rivet heads) and as a repair (specimens completely cracked through).

In one specimen pair (A9/A10) the stiffness of the doubler (upper section) was reduced by a third, in order to investigate the optimum thickness or stiffness required.

16.3.2.2. Airbus Specimens

To restore structural strength to the damaged Airbus lap joint specimens a 0.76 mm thick doubler was required. The dimensions of the doubler were 115 mm by 285 mm [8], similar to that described above for the Boeing lap joint specimen.

16.4. Stress analyses

Before implementing or considering a given repair it is best if the stress state and the failure mechanisms of the existing structure are understood. To that end, both thermo-elastic and finite element analyses of the specimen were undertaken to investigate the stress distribution of the lap joint.

16.4.1. Thermo-elastic analysis

An unreinforced “Boeing” specimen was placed in an Instron 500 kN electrohydraulic fatigue testing machine and cycled at 8 Hz with a load range of 13 kN to 2 kN, proportionally representative of the hoop stresses due to pressurisation, and thermal emission scans of various regions were then performed using a SPATE 8000 infrared camera located approximately 50 cm from the specimen. (Thermal emission techniques rely on the coupling between thermal and mechanical energies [14]. Under adiabatic conditions the observed signal is proportional to the sum of the three principal stresses, often referred to as the bulk stress. Since, in this case, the stress normal to the surface is zero, the bulk stress on the surface is equal to the sum of the principal in-plane stresses).

The three regions scanned were as follows, viz:

1. Region 1. A scan encompassing all three rows of rivets and regions of both the upper and lower skins. The area scanned was 113 mm by 98 mm. The scan generated an array of 114 by 105 data points.
2. Region 2. A scan encompassing three rivets in the first (i.e. critical) row of rivets. The area of the specimen scanned was 88 mm by 47 mm generating an array of 116 by 67 data points.

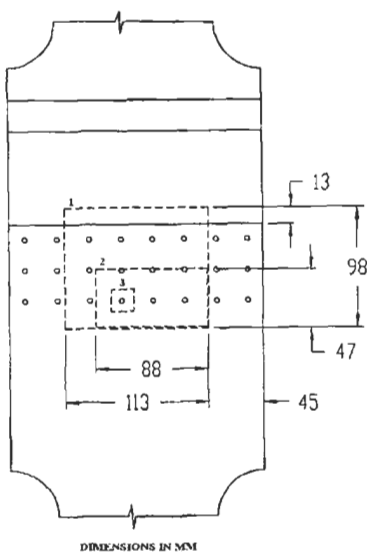


Fig. 16.8. Location of SPATE regions.

3. Region 3. A scan of a rivet in the first row. The area of the specimen scanned was 15 mm by 15 mm generating an array of 82 by 80 data points, each data point corresponding to a region approximately 0.2 mm square.

In each case the scan region was sprayed matt black to achieve a uniformly high infrared emissivity. The location of these regions are shown in Figure 16.8 and the resultant scans, in uncalibrated stress units, of regions 1–3 were shown in [6]. The SPATE scan for region 1 is shown in Figure 16.9.

16.4.1.1. Discussion of results

Figure 16.9 clearly shows the load path taken in the specimen. There are three distinct zones, in each of which the bulk stress is relatively uniform. The first zone is the region up to and including the first row of rivets. At the line of the rivets there is a rapid decrease in the bulk stress to a second relatively constant value. This decrease in the bulk stress reflects the load transferred at the first line of rivets. An analysis of this data reveals that approximately 45% of the load is transferred by this row of rivets.

The bulk stress undergoes another decrease at the second line of rivets. At this scale the stress concentration, in the bulk stress, at the first row of rivets, was not apparent.

A more detailed view of the bulk stress field around the first row of rivets was taken for region 2 [6]. This confirmed the rapid decay in the load at the first row of rivets, due to load transfer to the lower skin. Again at this scale, the stress concentration in the bulk stress was not apparent. This also illustrated the rapid decay of the stress concentration on the upper surface of the upper skin. However, we know that, in the fatigue test program outlined in Section 16.5.1, cracks always

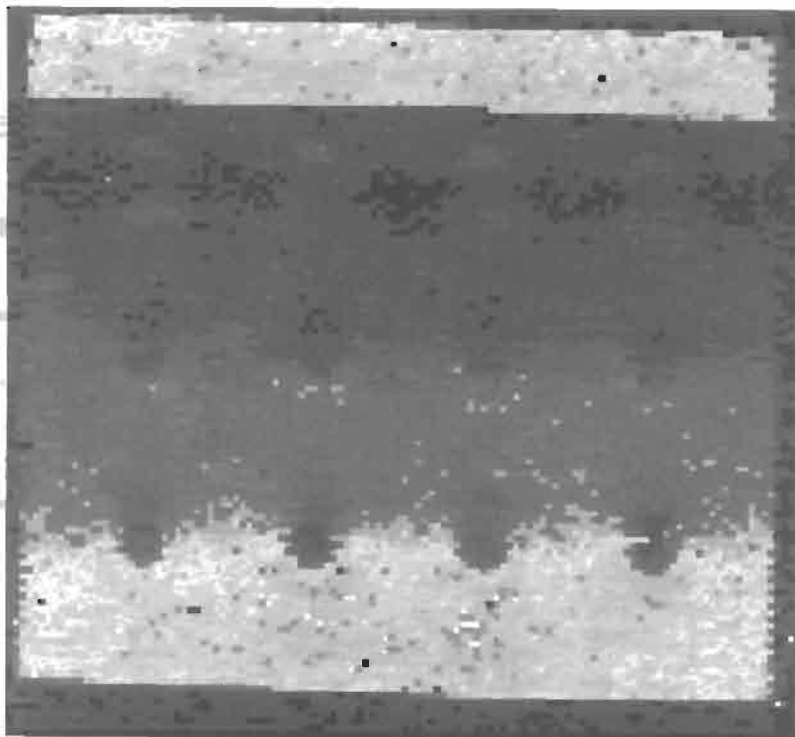


Fig. 16.9. SPATE scan of region 1.

initiated at the first row of fasteners. This highlights the role that the full depth counter-sunk plays in creating a fracture critical location at the lower surface. Unfortunately this surface is not observable via standard thermal emission techniques.

An even more detailed picture of the stress field around a fastener in the first row of rivets was taken for region 3 [6]. The concentration in the bulk stress at the upper surface of the upper skin was now visible. However, it was seen that this stress concentration, which is quite small, was very localised.

From these scans it was apparent that the lack of a bond between the upper and lower skins results in the major load transfer occurring at the first row of rivets. This will exacerbate the stress concentration effect of the full depth counter-sunk holes at the lower surface of the upper plate even though the stress concentration at the upper surface is particularly localised.

Had the upper and lower skins been bonded, a substantial proportion of the load would have been transferred prior to the first row of fasteners. The boron/epoxy doubler, described in Section 16.3.2.1, uses this concept to increase the damage tolerance of the joint. In this approach a boron/epoxy laminate is bonded to the

external surface of the joint so as to provide an alternate load path, from the upper to the lower skin, thus by-passing the critical row of fasteners.

16.4.2. Finite element analyses

A three dimensional finite element analysis of the specimen was undertaken to confirm the above results. The model contained 4296 nodes and had 10680 degrees of freedom with the counter-sunk rivets modelled separately as three dimensional isoparametric elements, see Figure 16.10. This analysis confirmed the rapid decay of the stress concentration in the bulk stress. The load transfer at the first row of rivets was also consistent with experimental measurements.

To confirm the low stress concentration at the rivet hole, the “Boeing” specimen was extensively strain gauged. A strip of ten micro-gauges was located on the surface of the upper skin adjacent to a rivet in the first row. The resultant strains for a remote stress of 92 MPa (13.4 ksi) are given in Table 16.2. These results confirm the results of the previous investigation, and yields a localised strain concentration, at the hole, of approximately 1.45.

16.4.2.1. Elastic-plastic analysis

As will be described in Section 16.5.1.1 it was noted in the fatigue tests performed on these “Boeing” specimens, that the linking of adjacent cracks appeared to occur when the remaining distance between the crack tips was approximately 2 mm. To examine this phenomenon a 3D elastic-plastic finite element analysis was performed. A main objective of this analysis was to determine if this “failure” was due to net section failure of the remaining 2 mm ligament, between the crack tips, or due to ductile fracture. The basic finite element model used is as described in Section 16.4.2.

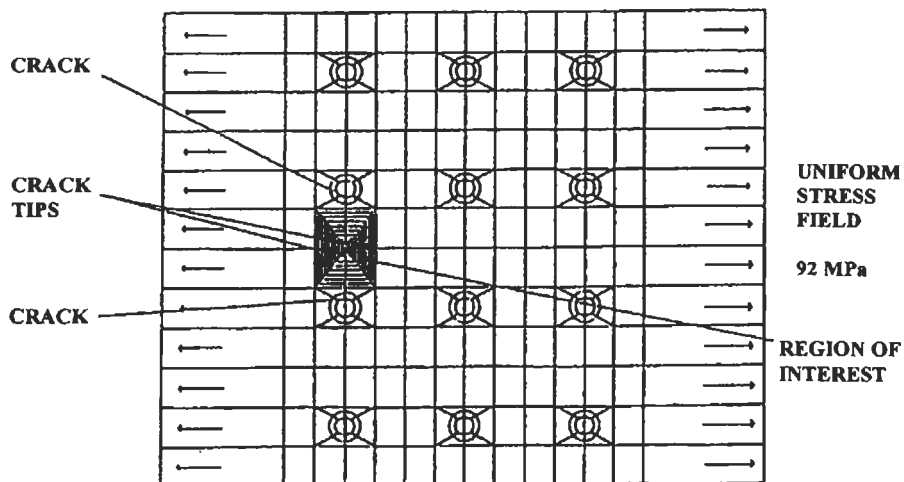


Fig. 16.10. Finite element model of cracked lap joint.

Table 16.2
Surface strains.

Distance from edge of rivet head (mm)	Hoop strain ($\mu\epsilon$)
0.5	1977
1.5	1612
2.5	1464
3.5	1388
4.5	1351
5.5	1335
6.5	1315
7.5	1312
8.5	1324
9.5	1368

This model was significantly refined about the rivets and includes two equal length cracks approaching each other from two adjacent fastener holes, see Figure 16.10. The elastic-plastic stress-strain curve for the material was taken from the MIL-Handbook-SE.

For mechanically fastened structures with multiple load paths, the commonly used J integral is path dependent, even for monotonic loading. To overcome this shortcoming the path independent T^* integral, see [15] for more details, was calculated along a number of separate paths for a remote stress of 92 MPa, which was the maximum stress applied to the specimens in the fatigue tests. At the peak load the equivalent stress intensity factor K , which was defined, as in linear elastic fracture, in terms of T^* and E (Young's modulus) as:

$$K = \sqrt{ET^*},$$

was found to be approximately $23.9 \text{ MPam}^{1/2}$ which is well below the fracture toughness of the material. However, the von Mises equivalent stress was found to exceed its ultimate permissible value for more than 0.5 mm of the 2.0 mm between the crack tips. This implies that failure of the ligament, which was a precursor to the total failure of the specimens, was due to net section failure. This result is consistent with experimental work (see [1,2] and Section 16.5.1) where it was found that, regardless of the length of the cracks emanating from two adjacent fastener holes, linking of these cracks was always observed when the remaining ligament was approximately 2 mm.

Whilst repairs to MSD in the first row of rivets has received considerable attention, and the fundamental mechanisms underpinning this technique determined, the ability of an external bonded doubler to repair cracks in the third row of rivets in the lower (hidden) skin has not previously been investigated analytically. To address this problem the lap joint described in Section 16.2.2 was also modelled, using two-dimensional eight-noded iso-parametric elements, with a 75 mm edge

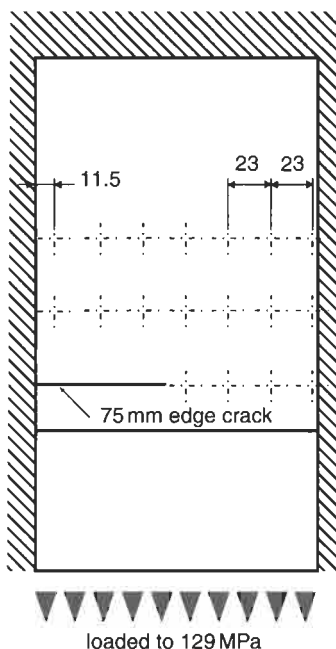


Fig. 16.11. Schematic of FEM lap joint with edge crack [8].

crack in the lower skin at the third row of rivets (Figure 16.11) [8]. In this analysis a remote stress of 129 MPa was applied to the aluminium skins and the mechanical properties used for the composite, adhesive and aluminium alloy are given in Table 16.3.

Table 16.3

Material properties used for the numerical analysis.

Composite boron/epoxy	Adhesive	Aluminium alloy 7050-T73
$E_{xx} = 208.116 \times 10^3 \text{ MPa}$	$G_{xy} = 750 \text{ MPa}$	$E_{xx} = 70.1 \times 10^3 \text{ MPa}$
$E_{yy} = E_{zz} = 25.440 \times 10^3 \text{ MPa}$	$\nu = 0.35$	$\nu = 0.33$
$G_{xy} = G_{yz} = G_{zx} = 7.240 \times 10^3 \text{ MPa}$	$\tau_{xy} = 30 \text{ MPa}$	
$\nu_{xy} = 0.17$		
$\nu_{yz} = 0.25$		
$\nu_{zx} = 0.02$		
$s_{xx} = 1520 \text{ MPa}$		
$s_{yy} = \sigma_{zz} = 150 \text{ MPa}$		
$\tau_{xy} = 97 \text{ MPa}$		

E = Tensile Modulus, G = Shear Modulus, ν = Poisson's Ratio, s = Tensile Strength and τ = Shear Strength

Table 16.4
Critical composite and adhesive stresses (see Fig. 16.7) [8].

Location	Composite				Adhesive			
	1	2	3	4	1	2	3	4
σ_{xx}	280.2	425.5	158.8	138.8	4.53	25.4	6.73	2.77
σ_{yy}	0.61	17.90	2.67	0.40	2.08	21.7	1.74	1.65
τ_{xy}	9.23	8.62	7.13	-7.75	7.75	21.5	1.98	-8.00

The stress intensity factor K was calculated, for both the unrepaired and repaired “Airbus” cases, using Eq. 16.1, see [16]:

$$K = \frac{E\nu}{4} \sqrt{\frac{2\pi}{l(1-\frac{2l}{a})}} \text{ for plane stress} \quad (16.1)$$

Here ν is the crack opening displacement at a distance l behind the crack tip and a is the half-crack length. For the unrepaired case K was calculated to be $47.1 \text{ MPam}^{1/2}$, and for the repaired case K reduced to $6.89 \text{ MPam}^{1/2}$ which is approximately the fatigue threshold value for this material.

The stresses at each of the critical points, see Figure 16.7, are given in Table 16.4 and were found to be beneath the design allowables. The adhesive shear stress was also found to be beneath the endurance limit of 25 MPa [17]. This implies that, during fatigue testing, crack growth should be very slow, the adhesive should exhibit adequate damage tolerance with minimal degradation in its performance and that delamination should not occur.

16.5. Specimen fatigue test results

16.5.1. Unreinforced baseline fuselage lap joint specimens

Only the “Boeing” type fuselage lap joint specimens were tested in this program.

Ten unreinforced specimens were tested (see Table 16.5). It should be noted that in the initial process used to bond specimens A1–A4 to the honeycomb, adhesive flowed between the two aluminium sheets and across the upper row of fasteners. This was detected subsequent to the failure of specimens A1/A2. This, in effect, enhanced the fatigue life of the upper row of fasteners, as can be seen from Table 16.5. This specimen failed within 140000 cycles of the last inspection, at which no damage had been detected. The failure of A2, although probably influenced by the final failure of A1, occurred through the inner plate at the lower fastener row, in contrast to all other specimens. This may indicate a possible danger in lap joint modifications which consider only the upper row. This is of concern, since damage occurring at the lower fastener is only detectable from the interior of the aircraft.

Table 16.5
 "Boeing" fuselage lap joint fatigue program.

Specimen	Status	Precracking cycles at 17.8 ksi	Cycles to failure at 13.4 ksi	Ligaments joined (top row)	Longest crack mm
A1*	Unreinforced	—	977600 ^a	Yes	—
A2*	Unreinforced	—	977600 ^a	No ^b	9.0
A3*	Reinforced	178400	> 2100000 ^φ	—	4.5
A4*	Reinforced	178400	> 2100000 ^φ	—	—
A3	Conditioned ^c	—	3217950 ^φ	No	—
A4	Conditioned	—	3217950 ^φ	No	—
A5	Unreinforced	5000	—	No	1.8
A6	Unreinforced	5000	25000	Yes	—
A5 ⁺	Unreinforced	n/a	41400	Yes	—
A6/2 ^(a)	Reinforced	n/a	see below	prior	—
A5/2 ^(a)	Reinforced	n/a	> 1300000 ^d	prior	—
A6/2 ^(a)	Reinforced	n/a	> 1316400	prior	—
A7	Reinforced	5000	> 4001000 ^φ	—	1.0
A8	Reinforced	5000	> 4001000 ^φ	—	1.0
A7	Conditioned	—	> 5500000 ^φ	No	—
A8	Conditioned	—	> 5500000 ^φ	No	—
A9	Unreinforced	—	—	No	7.1
A10	Unreinforced	—	105700	Yes	—
A9/2 ^(a)	Reinforced ^c	n/a	1000000	prior	—
A10/2 ^(a)	Reinforced ^c	n/a	1111000	prior	—
A11	Unreinforced	—	—	No	2.4
A12	Unreinforced	—	67000	Yes	—
A13	Unreinforced	—	57370	Yes	—
A14	Unreinforced	—	—	No	0.7

* Adhesive seepage occurred across top fastener row (enhanced fatigue life).

^a No crack detected at 837000 cycles.

^b Failed lower fastener row.

^c Patch stiffness decreased by a third.

^d Failed in grip area of A5.

^e Environmentally conditioned.

ⁱ Continuation of specimen test.

^(a) Repaired after complete failure, using room temperature curing adhesive (Flexon 241).

^φ Testing not completed.

To rectify the seepage of adhesive into the lap joint, a teflon strip was placed over the skin step.

During the cycling of the unreinforced specimens periodic crack measurements were made. A mean life to failure of approximately 59000 cycles was obtained. It was observed that, in each case, the initial linking of two adjacent cracks occurred when the remaining ligament was approximately 2 mm long.

Figure 16.12 presents typical crack growth data for specimen A6 which suffered total failure.

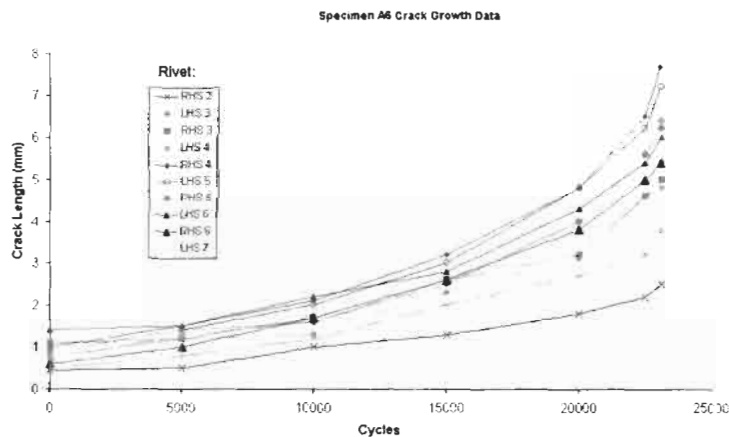


Fig. 16.12. Specimen A6 crack growth data.

Figure 16.13 presents a view of a failure surface. By referring to Figure 16.14 (from [18]) it is seen that these failures reflect the nature of in-service crack growth.

In Figure 16.15, a comparison of crack growth data for the two most prominent cracks for a number of specimen was plotted, from the same common initial crack length as used in data given by Boeing (see Figure 16.16). In these figures only data for the most significant cracks occurring on a specimen were plotted. In each figure the two curves corresponding to the least number of cycles, were the cracks which first linked.

Comparison of the experimentally obtained crack growth rates to the crack growth rates obtained from fleet data, shows good agreement. The experimental crack growth data are bounded, above and below, by the crack growth data obtained from service aircraft. This agreement implied that this specimen geometry could be used to study the repair of fuselage lap joints.

16.5.1.1. Discussion

It was observed that the variation in the fatigue lives of the unreinforced specimens was partly due to the nature of the cracking. In general, the shortest life occurred when the largest cracks in a specimen grew towards each other from adjacent fastener holes. A longer life occurred when cracks initiated and grew from widely separated holes.

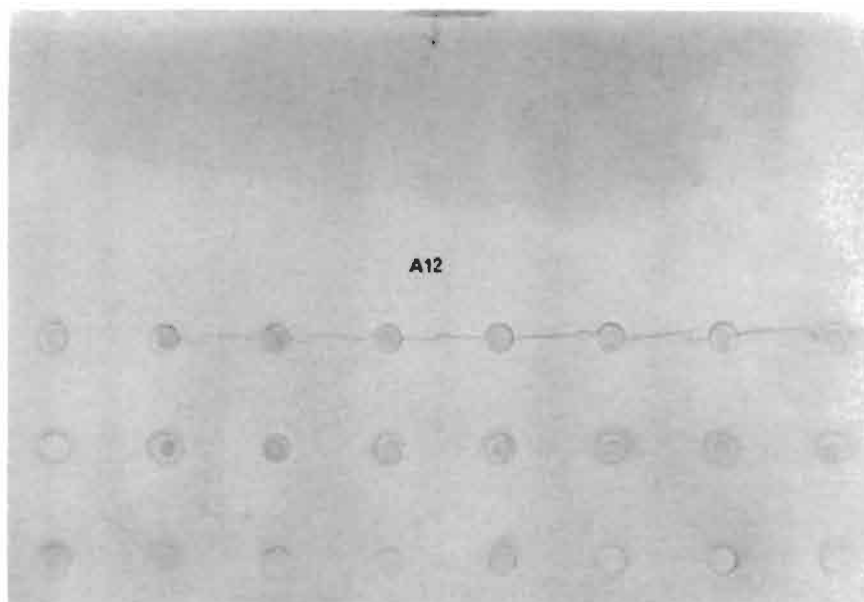


Fig. 16.13. Failure of specimen A12.

Even though, due to manufacturing tolerance, some notches were visible to one side of a fastener (i.e. notch larger than had been intended), this did not necessarily facilitate the initiation of the most prominent crack in a specimen. The “knife-edging” phenomenon was felt to be the dominant factor determining crack initiation.

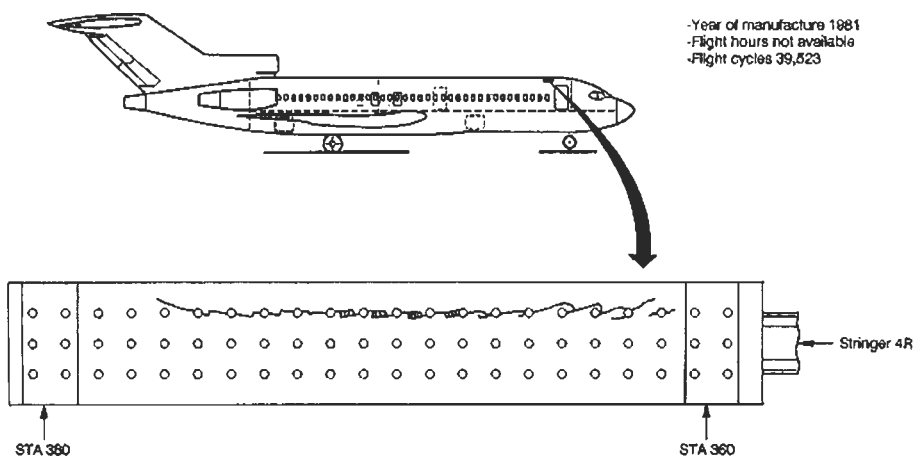


Fig. 16.14. Example of in-service cracking.

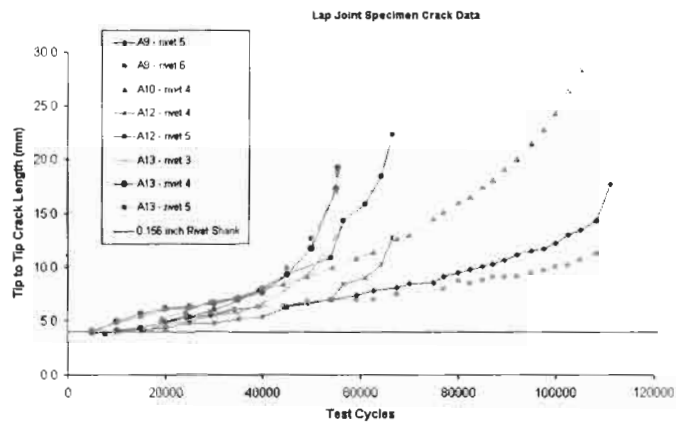


Fig. 16.15. Crack growth curve.

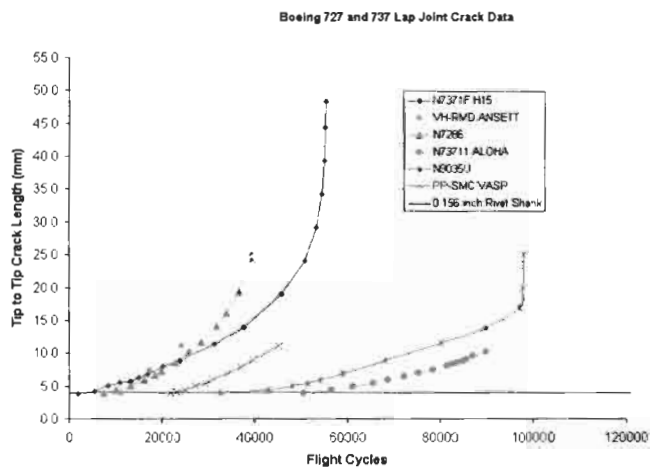


Fig. 16.16. Fleet crack growth data.

It was observed that before initial failure (i.e. two cracks linking) of a specimen, the remaining ligament length was consistently of the order of 2 mm.

In each case the number of cycles required to achieve initial failure did not differ significantly from that to final failure of the specimen.

16.5.2. Reinforced baseline fuselage lap joint specimens

16.5.2.1. Boeing specimens

From Table 16.5, it can be seen that the use of a bonded boron/epoxy doubler leads to an order of magnitude increase in the fatigue life of the basic specimens. Even the reduced stiffness specimens (A9/A10) experienced over 1000000 cycles without failure.

Once failure of A6 occurred, it was repaired using a boron/epoxy doubler, and testing continued until failure of specimen A5 occurred. Because of the increased stiffness due to the repair, the loading was increased in order to maintain a 92 MPa stress range for A5 [see 2]. Subsequent to the failure of A5, it was also repaired with a doubler and fatigue testing continued. As symmetrical conditions now applied, the loading reverted to that of Section 16.2.

Damage beneath the doublers was monitored using eddy current techniques. The results of periodic monitoring of the reinforced specimens was presented in [2]. None of the reinforced or repaired specimens experienced failure in the test section under fatigue loading. Given the large number of cycles experienced, this implies that the reinforcement also sufficiently suppresses the failure mode in the lower skin.

This investigation also showed that a bonded boron/epoxy doubler was capable of restoring the fatigue performance of a representative fuselage lap-joint containing MSD.

16.5.2.2. Airbus specimens

The repaired "Airbus" specimens were also fatigue tested, under constant amplitude loading, with a maximum load of 47.49 kN and a minimum load of 4.83 kN. These loads correspond to a remote stress in the skin, suggested by Airbus, of 128.9 MPa and 13.1 MPa respectively. After 365000 cycles the first pair of specimens failed in the aluminium outside the doubler. At this stage the doubler showed no sign of degradation. The second pair of specimens were subsequently tested to 100000 cycles without failure or degradation in the doublers.

This investigation again showed that a bonded boron/epoxy doubler was capable of restoring the fatigue performance of a representative fuselage lap joint containing MSD. The experimental program showed that after at least 100000 cycles the bonded-composite doubler was capable of withstanding the imposed fatigue loading. Also, the cracks (cut) in the lower (hidden) row had not grown.

16.5.3. Environmental evaluation of repairs

The initial testing of the reinforced and unreinforced specimens demonstrated that the bonded composite reinforcement significantly increased the fatigue life of

Table 16.6
Fuselage lap joint environmental fatigue programme.

Specimen	Pre-condition	Additional cycles at 92.4 MPa	Test Temperature (°C)
A3 ^a	No	> 2155550	20
A4 ^a	No	> 2155550	20
A3	Water for 7 days	> 522000 ^b	60
A4	at 60 °C	> 522000 ^b	60
A3	5% NaCl for	> 550000 ^c	60
A4	7 days at 60 °C	> 550000 ^c	60
A7	No	> 4001000	20
A8	No	> 4001000	20
A7	Water for 7 days	> 503000 ^b	60
A8	at 60 °C	> 503000 ^b	60
A7	5% NaCl for	> 1000000 ^c	60
A8	10 days at 60 °C	> 1000000 ^c	60

^a Adhesive seepage occurred across top fastener row (enhanced fatigue life).

^b Specimen failed in grip area. Testing continued with grips repaired.

^c Test stopped. All specimens are reinforced. Total cycles for each specimen on completion of environmental test programme are: specimens A3/A4, 3217950 cycle (intact); specimens A7/A8, 5504590 cycles (intact).

fuselage lap joints with MSD. As can be seen in Table 16.5, all “Boeing” reinforced specimens did in excess of one million cycles with no patch degradation, and one specimen (A7/A8) did in excess of four million cycles without failure of either the boron patch or the adhesive bond.

To further demonstrate the validity of the bonded repair scheme, environmental conditioning of the reinforced specimens was conducted. Table 16.6 details the processes applied to each specimen. Only the “Boeing” type fuselage lap joint specimens were tested in the AMRL environmental program.

16.5.4. Hot/wet

Specimens A3/A4 and A7/A8 were first soaked in a water bath for a minimum of seven days, with the temperature held constant at 60 °C. Although tap water was used, on removal the specimens showed signs of extensive corrosion of the aluminium. One week was considered sufficient time to thoroughly soak the boron doubler and the adhesive. Water temperature was continuously monitored throughout this time.



Fig. 16.17. Reinforced lap joint specimen sealed to retain moisture (note corrosion of aluminium ends).

On removal from the water bath the specimens were wrapped in plastic and sealed to retain their moisture content, see Figure 16.17. They were then immediately placed in the testing machine and wrapped in 250 mm \times 250 mm heater blankets, see Figure 16.18. The blankets were fixed directly to each side of the specimen, then covered with insulating material. Temperature was controlled by a single thermocouple, and monitored by another four thermocouples. The temperature controller was an ETHER “Digi”, which maintained a uniform temperature distribution of $60 \pm 4^\circ\text{C}$ over the specimen test area throughout the test.

Specimens were then cycled at the stated load levels, for a minimum of 500000 cycles, without failure and with no visible damage to the doubler system (see Table 16.5).

16.5.5. NaCl aqueous

Following testing under hot/wet conditions, the specimens were then exposed to a more corrosive environment. They were wrapped in aluminium tape to minimise corrosion in the grip area, and placed in a water bath containing a 5% NaCl aqueous solution. The temperature was maintained at 60°C , and specimens were immersed for a minimum of seven days. Figure 16.17 shows the typical condition of the specimen after removal from the salt bath.



Fig. 16.18. Environmental fatigue test set-up.

Testing was then continued, under the conditions described above, with the temperature maintained at 60 °C, and the moisture content retained, see Table 16.5 (Conditioned).

Specimens A3/A4 and A7/A8 were then examined, prior to environmental testing, using eddy current techniques, with the results detailed in [4]. Specimen A3 had small cracks emanating from some rivets, while A4 had no detectable cracking. It is interesting to note that A3 also had a crack emanating from a rivet in the second row. There was significant crack growth in specimens A7/A8. However, it must be noted that these specimens had experienced more than 4000000 cycles. Each specimen then experienced a very large number of additional cycles under adverse conditions without failure of either the specimen or the repair. In the case

of specimens A7 and A8 the crack lengths were such that, unrepaired, the specimens would have failed after a very few additional cycles.

Following the environmental conditioning and testing, the specimens were re-examined. No growth was detected for specimens A3/A4, however, crack growth had occurred in specimens A7/A8 [4]. In both specimens the left hand side (LHS) crack from rivet 2 (R2) had increased significantly in length. The cracks from R3 and R4 had joined, as had those from R7 and R8. All cracks had joined in specimen A8, except those from R1 and R2. If cycling had continued it could be expected that these specimens would have cracked completely through the aluminium section. However, as has been demonstrated previously, the doubler is more than capable of carrying the entire load. Testing was continued for both specimens (see below), with the cracks being periodically monitored. None of the reinforced or repaired specimens has experienced failure in the test section.

After more than 550000 cycles of testing in a hot/wet salt environment the doublers showed no sign of degradation or failure. This is in contrast to an average fatigue life of 59000 cycles for failure of the unreinforced specimens. Therefore environmental degradation is not considered a significant factor when using these repairs.

16.6. Damage tolerant evaluation of specimens

Six "Boeing" type specimens were used to investigate the damage tolerance of the proposed repair scheme. A summary of the specimen histories, prior to damage tolerance testing, is given in Table 16.5. Specimens A3, A4 and A5 had experienced a large number of fatigue cycles prior to the application of the impact damage.

Specimens A3, A4 and A5 only contained impact damage, whilst specimen A6 contained both impact damage and adhesive disbonds, and specimens A9 and A10 contained adhesive disbonds only, see Figure 16.19.

16.6.1. Adhesive disbonds

In specimen A6 the adhesive disbonds were simulated by inserting teflon release film between the aluminium sheet and adhesive during bonding of the doubler (repair). The size and the location of these inserts is shown in Figure 16.20.

For specimens A9 and A10 a deliberate attempt was made to produce a poor quality bond (see Figure 16.19). In this case the low temperature curing adhesive Flexon 241, which has an inferior durability performance to FM73 was used [17]. These specimens also contained areas in which the patch was not bonded. The extent of these disbonds was not known until the patches were removed after testing had been completed. The disbonded area in specimen A9 was approximately five percent of the total patch area, whilst for specimen A10 approximately twenty percent of the patch area was disbonded, see [9]. The adhesive thickness was also very uneven, varying from "zero" to approximately 1 mm.



Fig. 16.19. Specimen A10 with doubler removed.

16.6.2. Impact damage

Specimens A3, A4, A5 and A6 were subjected to low velocity impact damage using a 9.5 mm diameter impactor, of varying mass, dropped from a height of 1.3 m. A special impact test rig was used to record the absorbed impact energy. The rig consisted of a laser which was triggered by the impactor both before and after impact, producing initial and rebound pulses which were recorded on a digital oscilloscope (NICOLET 2090 MODEL 207) and analysed on a HP9816 computer. From these results the kinetic energy of the impactor before and after impact was determined. The impact site locations are shown in Figure 16.21, and the impact energies are summarised in Table 16.7.

Fatigue testing was conducted in a 1MN Instron servo-hydraulic test machine. The damaged specimens were subjected to a constant amplitude tensile fatigue loading with $R = 0.05$, a load amplitude of 38 kN, and a frequency of 2.5 Hz. This loading represents the hoop stress in the fuselage skin due to pressurization, as described previously. Testing was continued until failure of the specimen occurred, or a sufficient number of cycles had been accumulated to demonstrate the effectiveness of the repair.

The condition of the impacted specimens was monitored throughout the test using the shadow-Moire technique. A detailed description of this technique and its application to monitoring damage growth is given in [19]. The patches were coated

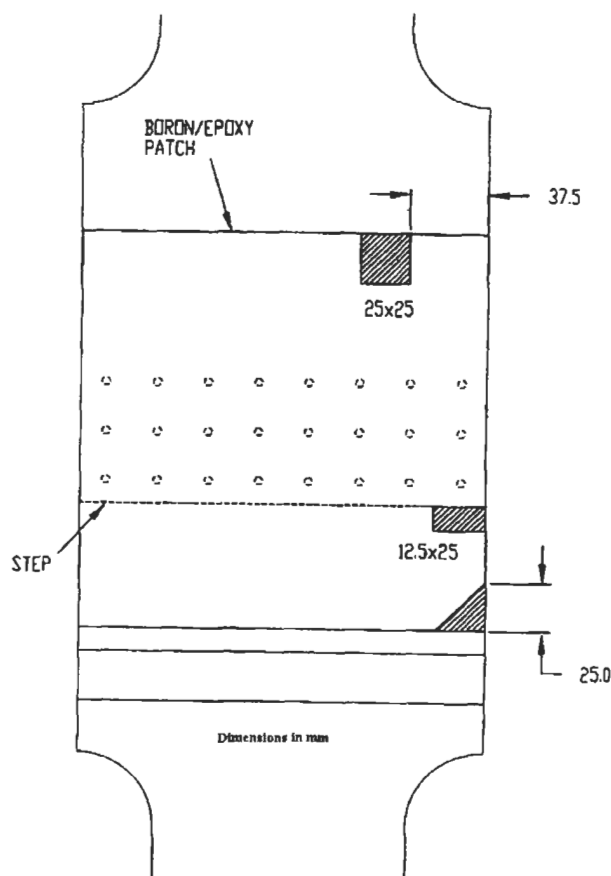


Fig. 16.20. Insert details for specimen A6.

with a white matte paint and two 100 mm by 125 mm glass plates with 1/1000 inch grid lines were placed directly over the area containing the damage. A collimated light source was then directed at the specimen at an angle of approximately 45° to the surface. The resulting Moire fringe pattern was monitored visually and also photographed at various stages during the test, thus enabling a qualitative assessment of patch disbonding to be made.

The number of fatigue cycles applied to each of the specimens (in addition to those demonstrated by Table 16.5) are shown in Table 16.8.

None of the repairs showed any significant sign of failure or degradation (no delamination growth) during the tests. This contrasts with an average life of 59000 cycles (discounting A1/A2 due to adhesive seepage) for the unrepaired specimens, refer Table 16.5.

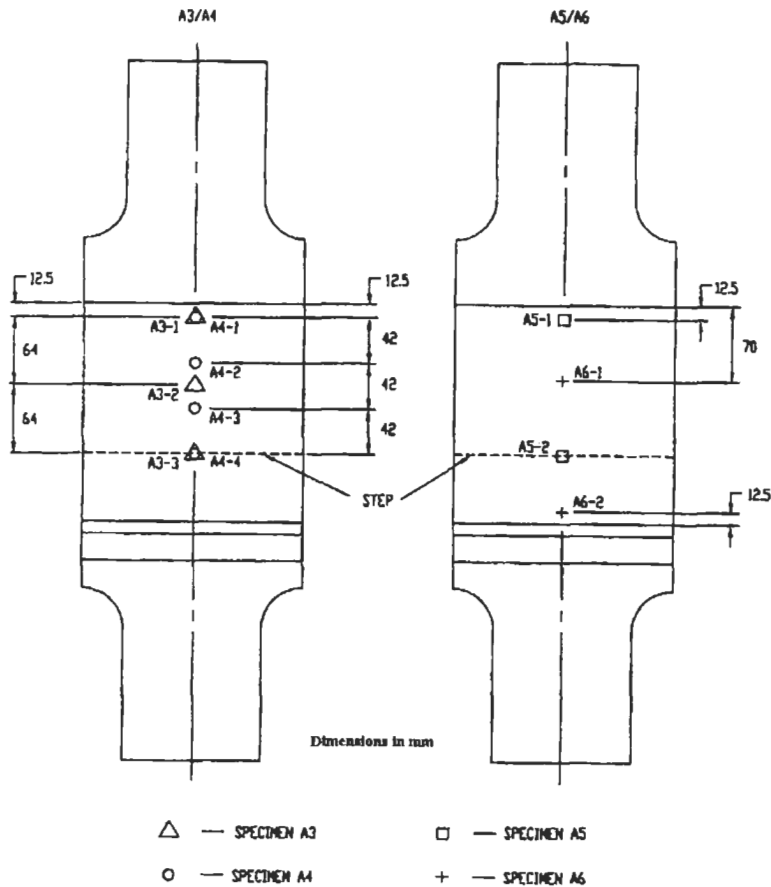


Fig. 16.21. Impact site locations.

More than 1000000 cycles were applied to specimens A9 and A10 without failure of the repairs (recall these specimens had reduced stiffness). It should be noted that for these specimens, prior to repair, the cracks at the first row of rivets had propagated across the entire width of the specimen (i.e. the specimen had failed). Despite the deliberate poor quality of these repairs and in particular the large disbond area in specimen A10, the composite doubler was able to carry the load without further degradation.

Specimen A6 withstood more than 1400000 cycles without failure or apparent disbond growth.

After impacting, specimens A3 and A4 were subjected to in excess of 450000 cycles. These failed by fatigue crack growth in the aluminium sheet outside the repair. It should be noted that these specimens had accumulated a total of more than 3000000 load cycles during previous testing. There was no sign of degradation

Table 16.7
Impact results.

Specimen no.	Impactor mass (g)	Impact site	Impact energy (J)
A3	200	1	1.6
		2	1.7
		3	1.2
A4	200	1	1.7
		2	2.0
		3 ^a	–
		4	1.4
A5	400	1	4.0
		2	3.7
A6	400	1	4.0
		2	4.2

^a impact energy not recorded.

Table 16.8
Damage tolerance testing results.

Specimen No.	Type of Damage	Fatigue Cycles (additional)
A3 ^a	impact	454670
A4 ^a	impact	454670
A5	impact	180000
A6	disbond	1316470
	impact	180000
A9	disbond	1000000
A10	disbond	1004330

^a specimen failed by fatigue in aluminium sheet outside repair area.

or failure of the repair. An eddy current inspection of the specimens was conducted to determine the extent of crack growth since impacting. It was found that no further crack growth had occurred during this test program.

Specimens A5 and A6 withstood 180000 cycles after impacting, again with no apparent degradation or failure. The Moire fringe pattern for these specimens, i.e. A3–A6, revealed that there had been no delamination growth, see [9] and Figure 16.22 (see Figure 16.21 location A6-1).

16.6.3. Tension testing

On completion of these fatigue tests four specimens, namely A3/A4 and A9/A10, were loaded to failure in tension in order to determine the strength of the “damaged” repair. For the purpose of comparison an undamaged and unrepaired, i.e. “as new”, lap joint specimen pair was also tested. Specimens A5/A6 were also

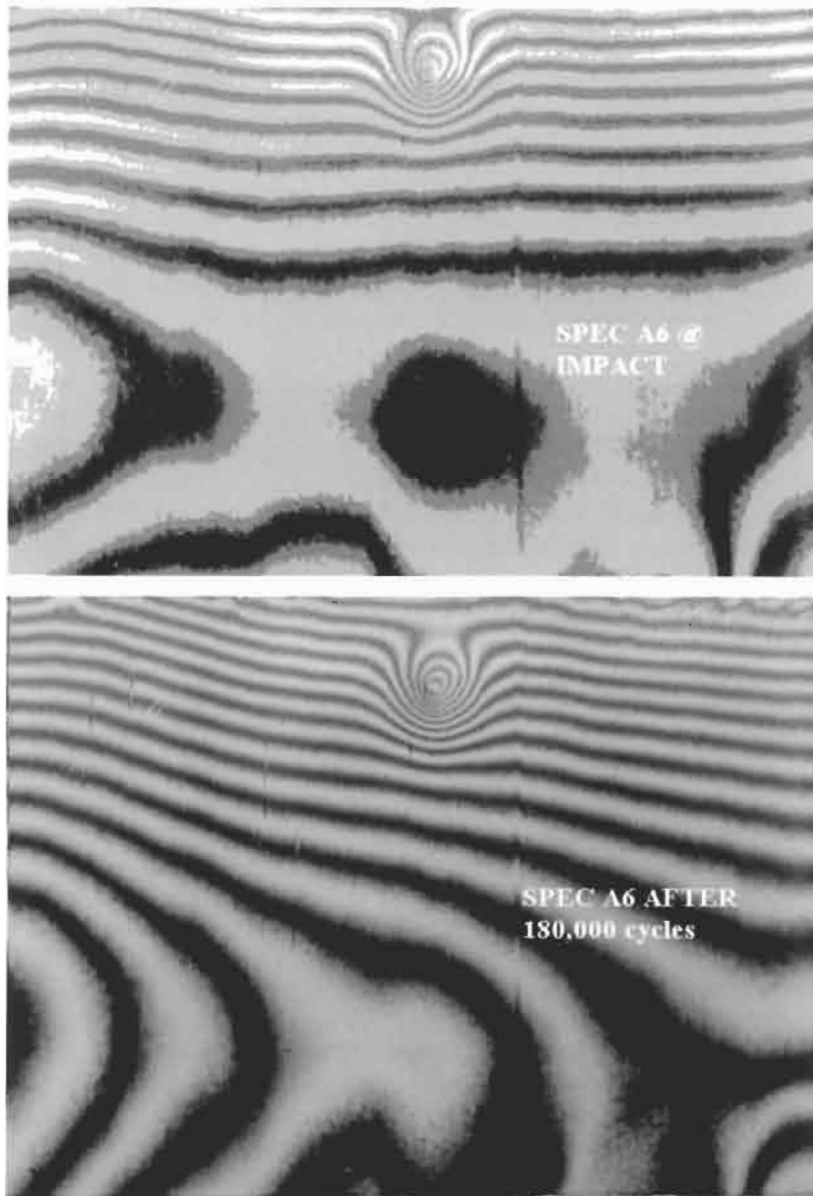


Fig. 16.22. Views of specimen A6 Moiré fringes.

loaded above normal limit load. In each case load was applied at a rate of 37.5 kN/min.

The specimen pair A3/A4, which had previously failed outside of the patched region, was repaired to enable the tensile test to be conducted, see [9]. The tension

Table 16.9
Tensile static test results.

Specimen	Total fatigue cycles	Static failure load (kN)
Undamaged Lap Joint	0	116
A3/A4	3672570	161
A5/	1480070	> 54*
A6	1496470	
A9/A10	1110030	121

* test terminated, no sign of failure.

test results are shown in Table 16.9. The repaired specimens exceeded the strength of the “as new” lap joint specimen. Specimens A3/A4 failed in the aluminium sheet outside the repair area, while specimens A9/A10 failed by debonding and tearing of the composite doublers. The significantly lower strength of specimens A9/A10 was expected due to the poor quality of the bond and the reduced stiffness. Despite this, the strength of these fatigued specimens still exceeded the strength of the standard, “as new” lap joint.

After the second pair of “Airbus” specimens were tested to 100000 cycles without failure or degradation in the doubler, they were then removed from the test machine and the doublers were subjected to low energy impact damage in the regions directly over the upper row of rivets and above the step between the upper and the lower skins. The impact damage was inflicted using a 1 kg mass from a height of 813 mm. This is equivalent to the “Mil Spec” standard 7.98 J impact test. In each case a rebound height of approximately 250 mm was recorded together with an absorbed energy of approximately 5.5 J. The specimens were then subjected to a further 100000 cycles, for a total of 200000 cycles, without failure and with the doubler showing no signs of degradation or damage growth.

This test program demonstrated that the presence of adhesive disbands and damage due to low velocity impacts does not degrade the boron/epoxy lap joint repairs, even after the repairs had experienced significant fatigue cycles. This was shown by demonstrating that the fatigue life of the repaired specimens, containing damage, far exceeds that of an unrepaired lap joint specimen. Inspection of the specimens during and after testing revealed no damage growth and that the MSD beneath the repair did not grow. It was also shown that the static strength of the damaged repairs exceeds that of an uncracked lap joint specimen.

16.7. Full scale repair demonstrators

16.7.1. Airbus A330/A340 fatigue test article

On demonstration of the repair schemes’ capability to restore strength and fatigue life to generic “Airbus” lap-joint specimens it was considered important to

examine the fatigue performance of the scheme under realistic loading conditions. To this end two doublers were applied to an Airbus A330/A340 full-scale fatigue-test article [8,20]. In-service loading conditions was used throughout the test program, including both representative short range and medium range mission profiles. A total of 80000 flight cycles was applied to the test article and the load spectrum included pressurisation, flight, gust, landing, take-off and ground loads.

Two simulated damage locations were considered:

- (a) a 220 mm crack in the top row of rivets in the outer skin of the lap-joint
 - (b) a 170 mm crack in the bottom row of rivets in the inner skin of the lap-joint.
- Airbus introduced this damage to the test article at stringer location P31 between stations C26.2, C26.3 and C26.4, C27 respectively by the use of a saw cut (see Figure 16.23).

During doubler application excessive heating of a region can cause local buckling of the parent structure that must be avoided as this can induce thermal stresses in the adhesive bondline. This is a common problem when heating thin skins with no stiffeners in the region to stop out-of-plane deformation. Prior to each hot-bond application a thermal survey was carried out to ensure that the cure temperature could be achieved and that the skin would not buckle excessively. The survey showed that the temperature varied from 120 °C at the centre of the repair to 80 °C at the edges and no buckling of the skin was observed. The application time was extended to eight hours to ensure complete cure of the adhesive and doubler.

The two cracks, representative of MSD, were repaired using two identical composite doublers bonded with an epoxy-nitrile structural film adhesive. The doublers were made from boron/epoxy pre-preg tape and measured 300 mm by 285 mm. As mentioned previously, the epoxy is an elevated temperature curing

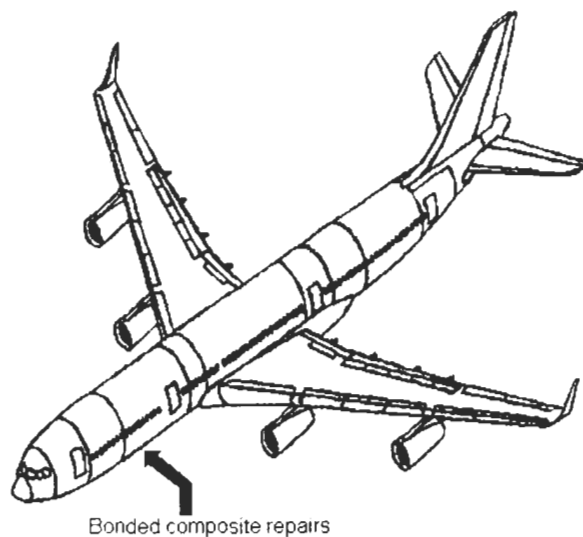


Fig. 16.23. Location of lap joint doublers on airbus fatigue test article [8].



Fig. 16.24. Doubler installed on A330 lap joint.

adhesive (120 °C for one hour) however the cure temperature can be modified to 80 °C for eight hours [17]. The doublers were designed as detailed previously and prefabricated at AMRL prior to arrival in Germany. The composite doublers were “B-staged” (laminate is partially cured and retains flexibility to accommodate curvature in the parent structure) with one layer of adhesive and then bonded with an additional layer of adhesive. Complete cure of the laminate was achieved during the hot-bond application of each doubler.

The durability of an adhesive bond is dependant on correct surface treatment of the adherends. The standard AMRL surface treatment and application technique was used to bond the two doublers to the aircraft skin.

Vacuum bags were used to apply pressure to the doublers and heating was accomplished using heater blankets which were controlled by analogue heater control units. Total application time, including surface treatment, for each doubler was between 12 and 14 h. Figure 16.24 shows one of the doublers bonded to the test article.

On completion of the application the doublers were non-destructively inspected using eddy-currents. The cracks were easily and accurately located and the crack lengths determined through the composite doublers. The doublers were inspected periodically throughout the fatigue test by eddy-currents to check for possible crack growth under the doubler. Strain gauges have also been bonded to the repair location to monitor the load path through and around the doublers as the test progressed. The doublers were applied to the test article at the first C-inspection at

12285 cycles in December 1992. At the completion of the test, 67715 flight cycles had been applied to the doublers with no deterioration of the doublers being observed. No crack growth in the saw cuts was detected, and the strain surveys revealed no strain redistribution during the testing.

16.7.2. Boeing 727, 747 and 767 in-flight demonstrators

As part of a demonstration program, nine bonded composite doublers were applied to a Boeing 747-300 aircraft in service with QANTAS Airways Limited [9,21,22 and Chapter 37]. The aim was to demonstrate the environmental durability of this type of repair, and thus the doublers were not applied to any damaged locations.

Important work in the area of bonded repair has also involved collaborative programs with commercial aircraft manufacturers and operators, including a series of demonstration programs to assess the durability of bonded-composite repairs. AMRL and Boeing have participated in such programs with the aim of allowing aircraft manufacturers, operators and the various regulatory authorities to gain confidence in the technology.

The first demonstration program was in March 1989, when the application of a boron/epoxy reinforcement to an aircraft in service with Ansett Airlines, B767-200 VH-RMF, restored stiffness in a (7150-T6511) keel beam damaged by multi-site corrosion [see 3,23 & Chapter 37]. This repair is shown in Figure 16.25. A similar,

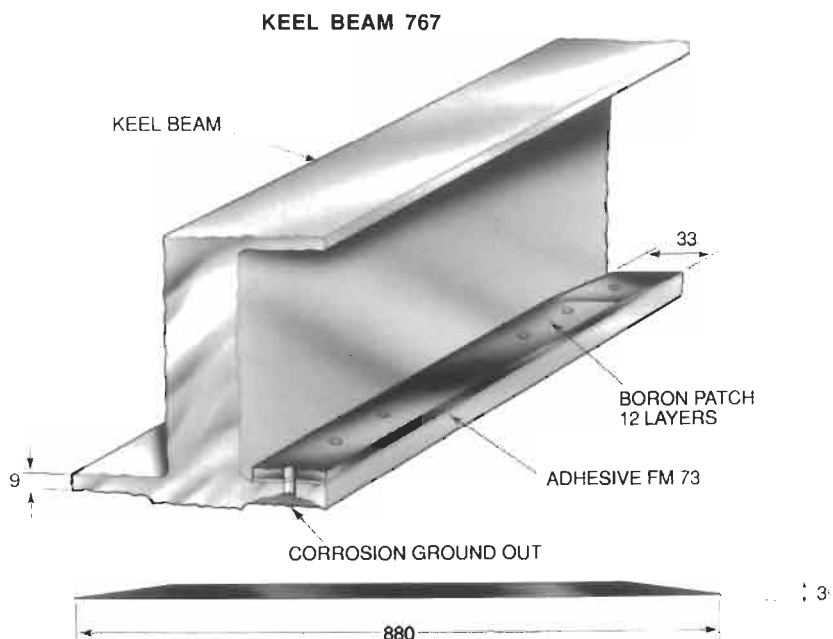


Fig. 16.25. Schematic of 767 keel beam repair to MSD corrosion.

but shorter, doubler was also applied to an non-damaged section of the keel beam using a cold setting acrylic adhesive. The second was in November 1989, when a boron/epoxy doubler was applied to a lap joint of an aircraft in service with Australian Airlines (now QANTAS), B727-200 VH-TBM [24]. In the second program there was no prior damage, the application was simply to demonstrate the feasibility of doubler application and its durability. This repair is shown in Figure 16.26. This aircraft is no longer in Australia, and as such the conditions of the repair is currently not known. AMRL has also applied bonded-composite repairs to fatigue cracks in the Boeing full-scale 747-400 fatigue-test fixture at Everett, in the USA [25]. The bonded boron/epoxy patches were applied to five fatigue cracks typical of in-service damage.

In October 1990, a repair team from AMRL and AMRL's licensee company Helitech Industries Pty Ltd (Helitech) applied nine demonstration doublers to a QANTAS Boeing 747-300 aircraft, VH-EBW [9,21]. These patches were applied under field conditions to typical problem areas (no prior damage present), which are exposed to severe environmental conditions. The patches were monitored to assess their durability (see Chapter 37).

The doubler locations were chosen on the following criteria:

- (a) If doubler failure occurs and the doubler becomes detached, it should not affect the function of the aircraft, i.e. it should not impinge on control surfaces, intakes, probes, *etc.*
- (b) The doublers should experience harsh environmental exposure, including high velocity air flow, vibration, exposure to aircraft oils and fluids, *etc.*

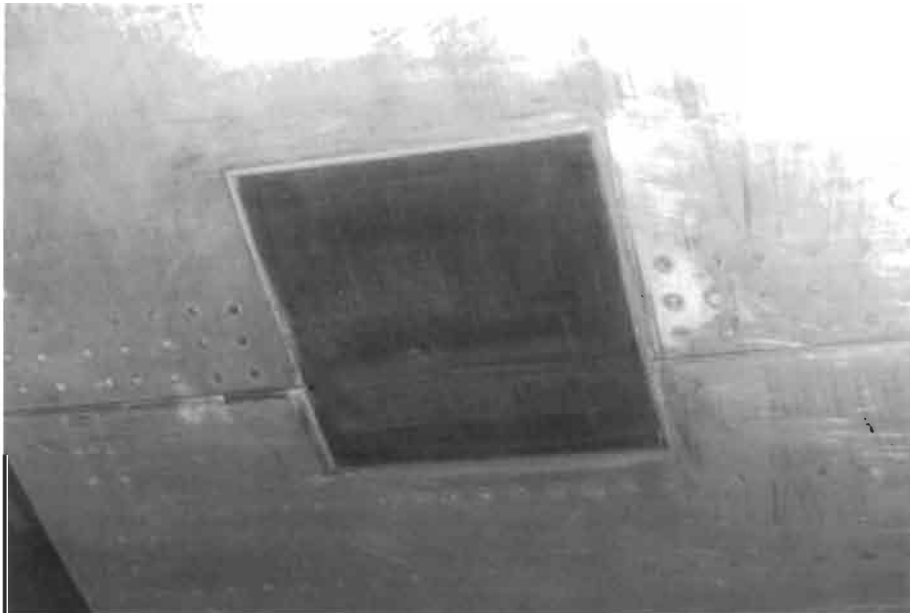


Fig. 16.26. Boeing 727 lap joint repair.

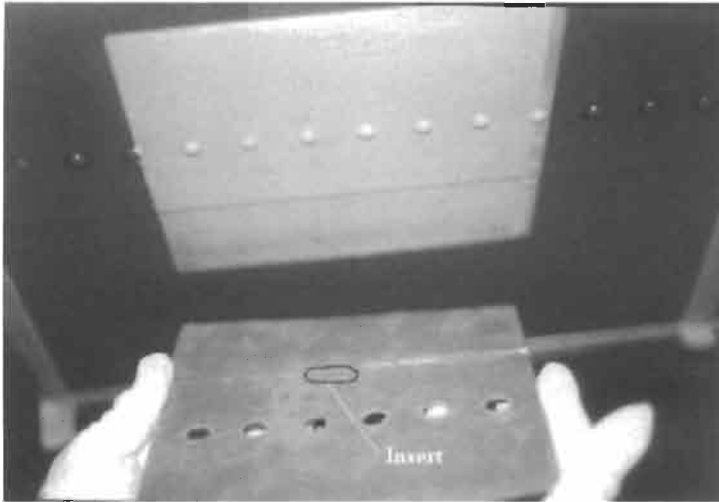


Fig. 16.27. B747-300 lap joint doubler.

- (c) The doublers should be positioned in areas that have a known high probability of inservice damage, i.e. from impact (e.g. ground-support equipment accidents, runway debris, bird strikes, *etc.*), fatigue cracking and corrosion.

The doubler applied to the fuselage lap joint was the AMRL standard MSD repair (see Section 16.3.2.1) with one modification. Boeing 747-300 aircraft have dome-head rivets in the upper row of the lap-joint. As a result of these protruding rivets, 12 mm diameter holes were shear-punched through the “B” staged doubler prior to application.

In order to demonstrate the damage-tolerant capability of the lap joint repair, a teflon film (25 mm by 12 mm, rounded at the corners), was inserted in the bondline to simulate an adhesive disbond. This film was placed in the centre of the lower section, close to the step (Figure 16.27).

Upon heating the lap joint doubler, it was found that the upper side was only achieving a temperature of 80 °C and therefore the standard cure time of one hour at 120 °C was extended to eight hours to ensure complete cure of the adhesive.

16.7.3. Doubler inspections

QANTAS regularly inspected the B747-300 doublers visually and with ultrasonics to locate damage, disbonds or delaminations (see Chapter 37). Some erosion damage of the doublers occurred due to high velocity airflow, ice and foreign object damage wearing the doubler edges during flight. Application of a protective coating has proved sufficient to prevent further erosion.

The teflon insert detailed above proved difficult to detect during regular ultrasonic inspections. However, if the inclusion was causing cracking or delamination it would be easy to detect and the difficulty strongly suggests that

the film was tightly sandwiched (effectively tightly bonded) within the adhesive and therefore did not causing a problem.

16.7.4. Demonstrator summary

The QANTAS doublers experienced a variety of environmental conditions, from the heat and humidity of the tropics to the cold of Europe in mid-winter. Also, they regularly experienced temperatures as low as -50°C whilst the aircraft was cruising at high altitude. As of August 1999 the aircraft had flown in excess of 37000 flying hours and experienced 7020 pressurisation cycles in a service environment with no evidence of any doubler failure (see Chapter 37).

The keel beam repair applied to a B767 aircraft, has received a “Structural Engineering Approval of Repair Station Process Specification” from the United States FAA, and the (then) Australian Civil Aviation Authority (CAA) has also certified the repair [23]. The application of the doublers to the QANTAS B747 aircraft is a further step towards demonstrating the in-service durability and performance of bonded repairs. It is envisaged that, as confidence is gained in the strength and durability of the technique by the regulatory authorities, aircraft manufacturers and operators, this will aid in complete certification of the technology.

16.8. Conclusions

This chapter investigated the potential of a bonded doubler to repair or reinforce MSD in typical commercial wide bodied aircraft lap joints. The findings are summarised below:

1. The specimen test program on unreinforced generic lap joints has shed some light on the phenomenon of MSD in typical wide-bodied aircraft pressurised fuselage lap joints. The test specimen used, although somewhat simplistic, gave crack growth rates consistent with fleet data. The crack growth data generated may assist in assessing the criticality of detected in-service cracks, and in setting of inspection intervals. Although this work was generic in nature, the results obtained should be directly applicable to current operational aircraft.

It was demonstrated that failure consistently occurred in the upper fastener row, as this location experiences the highest stress level and the effect of a full-depth counter-sunk in the upper plate. However, it was also shown that crack growth can occur in the inner skin at the lower fastener row, which is far more difficult to detect in-service. Consequently, any proposed repair should be applicable to both locations and preferably increase the required inspection interval for all fastener holes.

2. This work has shown thermal emission techniques can be used to reveal the load path in laboratory lap joint test specimens. This technique has a potential for optimising fastener patterns for mechanical repairs to MSD, evaluating the severity of various damage states and repair options, and for evaluating the effect of several repairs in close proximity. (This is important since it is now

recognised that multiple repairs may compromise the damage tolerant nature of the structure even though, in isolation, each repair may be acceptable).

This work has also revealed the extent of the load transfer at the fracture critical, first of row rivets in a typical fuselage lap joint. The stress concentration in the upper surface of the upper skin has been shown to be very localised and quite low (approximately 1.45). This highlights the role that the full depth counter-sunk plays in creating a fracture critical location at the lower surface.

3. A bonded composite repair was designed, tested and validated under fatigue loading conditions representative of typical wide-bodied aircraft pressurized fuselage lap joints.

The experimental investigation showed that a bonded-boron/epoxy doubler was capable of restoring the fatigue performance of a representative fuselage lap-joint containing MSD. The fatigue performance of the repaired specimens was an order of magnitude better than the undamaged baseline specimens. The numerical analysis showed that the stress intensity at the crack tip would be reduced in the lower hidden row such that no further crack growth should occur. Additionally the proposed doubler was shown to be safe under the applied static loading as the stress states predicted in the composite and adhesive are below the design materials allowables.

4. The experimental program demonstrated that the externally bonded composite reinforcement can significantly increase the fatigue life of fuselage lap joints containing MSD, even when exposed to an adverse hot/wet salt environment. Further more, no failure of any repaired specimens was observed, even after low velocity impact damage had been imparted. Thus the damage tolerance and environmental durability of these repairs was demonstrated.
5. Two bonded composite doublers were also applied to representative MSD in the fuselage of the Airbus A330/A340 full-scale fatigue-test article. These doublers experienced almost 70000 flight cycles, with no evidence of crack growth to underlining damage nor did the doubler shown any sign of deterioration or damage.
6. Nine boron/epoxy doublers, including a lap joint repair, were bonded to a Boeing 747-300 aircraft in service with QANTAS airways. The in-service demonstration doublers were placed at strategic locations to provide the greatest possibility for in-service damage and environmental conditioning.

The doublers have experienced a variety of environmental conditions, from the heat and humidity of the tropics to the cold of Europe in mid-winter. Also, they regularly experience temperatures as low as -50°C whilst the aircraft is cruising at high altitude. As of August 1999 the aircraft had flown in excess 37000 flying hours and experienced 7020 pressurisation cycles in a service environment with no evidence of any doubler failure.

The application of the doublers to the QANTAS B747 aircraft is a further step towards demonstrating the durability and performance of bonded repairs. It is envisaged that, as confidence is gained in the strength and durability of the technique by the regulatory authorities, aircraft manufacturers and operators, this will aid in the complete certification of the technology.

Thus the bonded composite repair meets the design requirements as mandated by the FAA.

References

1. Molent, L. and Jones, R. (1993). Crack growth and repair of multi-site damage of fuselage lap joints. *Eng. Frac. Mech.* **44**(4), pp. 627–637.
2. Molent, L., Wallace, G. and Currie, A. (1990). Crack growth and repair of multi-site damage of fuselage lap joints, DSTO, ARL-STRUC-TM-534, Melb. Australia, April.
3. Jones, R., Bridgford, N., Wallace, G., *et al.* (1991). Bonded repair of multi-site damage. *Structural Integrity of Aging Airplanes*, (S.N. Atluri, S.G. Sampath and P. Tong, eds.), Springer-Verlag, Berlin, pp. 199–212.
4. Molent, L., Bridgford, N., Rees, D., *et al.* (1992). Environmental evaluation of repairs to fuselage lap joints. *Composite Structures*, **21**(2) pp. 121–130.
5. Jones, R. (1991). Recent developments in advanced repair technology. *Proc. Int. Conf. on Aircraft Damage Assessment and Repair*, Melbourne, August, pp. 76–84, Published by Institution of Engineers Australia, ISBN (BOOK) 85825 5375, July.
6. Jones, R., Molent, L., Rees, D., *et al.* (1992). An experimental study of multi-site damage and repairs. *Proc. Ageing Commuter Aircraft Conf.*, Canberra, Australia, August.
7. Jones, R., Rees, D. and Kaye, R. (1992). Stress analysis of fuselage lap-joints. *Int. Workshop on Structural Integrity of Aging Airplanes*, Atlanta, 31st March to 2nd April (S.N. Atluri, C. Harris, A. Hoggard, W. Jones, N.J. Miller and S.G. Sampath, eds.).
8. Bartholomeusz, R., Kaye, R., Roberts, J., *et al.* (1992). Bonded-composite repair of a representative multi-site damage in a full-scale fatigue-test article. *Proc. 5th Int. Aeronautical Conf.*, Melbourne, Australia, September, pp. 207–212.
9. Bartholomeusz, R.A., Paul, J.J. and Roberts, J.D. (1993). Application of bonded composite repair technology to civil aircraft – 747 demonstrator program. *Aircraft Engineering and Aerospace Technology*, Bunhill Publications Ltd., April.
10. Rees, D., Molent, L. and Jones, R. (1992). Damage tolerance assessment of boron/epoxy repairs to fuselage lap joints, DSTO, ARL-STRUC-R-449, Melbourne, Australia, August.
11. Torkington, C. (1989). Note on overseas visit to USA and Egypt on ageing aircraft and ICAO matters: April 1989, Report SM-130, DOT, CAA, Canberra, Australia, May.
12. Torkington, C. (1991). The regulatory aspects of the repair of civil aircraft metal structures, *Proc. Int. Conf. on Aircraft Damage Assessment and Repair*, (R. Jones and N. J. Miller, eds.), Published by the Institution of Engineers, Australia, ISBN (BOOK) 85825 537 5, July.
13. Molent, L., Callinan, R.J. and Jones, R. (1989). Design of an all boron epoxy doubler for the F111C wing pivot fitting: Structural Aspects, *Composite Structures* **11**(1), pp. 57–83.
14. Thomson, W. (Lord Kelvin). (1878). On the thermo-elastic and thermo-magnetic properties of matter, *Q. J. Maths*, **1**, pp. 55–77, 1855, reprinted in *Phil. Mag.*, 5.
15. Brust, F.W., Nishioka, T., Atluri, S.N., *et al.* (1985). Further studies on elastic plastic stable fracture using the T* Integral, *Engng. Fract. Mech.*, **22**, pp. 1079–1093.
16. Williams, J.F., Jones, R. and Goldsmith, N. (1989). An introduction to fracture mechanics – theory and case studies. *Transactions of Mechanical Engineering*, **ME 14**(4) (1989), IEAust, Australia.
17. Baker, A.A. and Jones, R. (1998). Bonded Repair of Aircraft Structures, Martinus Nijhoff, The Netherlands.
18. 727 Fleet Data. (1989) Boeing Commercial Airplane Company, STRU-BY10B-P89, Seattle, USA.
19. Watters, K.C., Sparrow, J.G. and Jones, R. (1985). Shadow Moire Monitoring of Damaged Graphite/Epoxy Specimens, Aeronautical Research Laboratory, Aircraft Structures Technical Memorandum 398, February.
20. Neilson, T. (1991). A330/A340 Full Scale Fatigue Test EF2 Center Fuselage and Wing, Duetsche Airbus GmbH Technical Memorandum, TK. pp. 536–625/91.

21. Bartholomeusz, R., Paul, J. and Roberts, J. (1991). Report on a visit to QANTAS in October 1990 relating to the bonded composite repair demonstrator program, DSTO, ARL-APP-TM-033, Jan.
22. Bartholomeusz, R.A., Paul, J.J. and Roberts, J.D. (1991). Application of bonded composite repair technology to civil aircraft – 747 demonstrator program, *Proc. Int. Conf. on Aircraft Damage Assessment and Repair*, IEAust, ISBN (BOOK) 85825 537 5, Melbourne, Australia, 26–28 August.
23. Civil Aviation Authority – Australia. (1991). Supplemental Type Certificate – No. 157–1, Holder: Helitech Industries Pty. Ltd., dated 12 July.
24. Taylor, J.L. (1991). The practicalities of ensuring the continued structural integrity of aging aircraft in an airline environment, *Proc. Int. Conf. on Aircraft Damage Assessment and Repair*, IEAust, ISBN (BOOK) 85825 537 5, Melbourne, Australia, 26–28 August.
25. Molent, L. and Roberts, J.D. (1990). Bonded repair application to the Boeing 747–400 pressure test article – August 1990, ARL-STRUCT-TM-573, Aeronautical Research Laboratory, DSTO Melbourne, Australia.

Chapter 17

DAMAGE TOLERANCE ASSESSMENT OF BONDED COMPOSITE DOUBLER REPAIRS FOR COMMERCIAL AIRCRAFT APPLICATIONS

D. ROACH

FAA Airworthiness Assurance Center, Sandia National Laboratories

17.1. Introduction

This report describes a series of fatigue and strength tests which were conducted to study the damage tolerance and fatigue life enhancement capabilities of Boron-Epoxy composite doublers. Tension-tension fatigue and ultimate strength tests attempted to grow engineered flaws in coupons with composite doublers bonded to aluminum skin. An array of design parameters, including various flaw scenarios, the effects of surface impact, and other “off-design” conditions, were studied. The structural tests were used to: (1) assess the potential for interply delaminations and disbonds between the aluminum and the laminate, and (2) determine the load transfer and crack mitigation capabilities of composite doublers in the presence of severe defects. A series of specimens were subjected to ultimate tension tests in order to determine strength values and failure modes. It was demonstrated that even in the presence of extensive damage in the original structure (cracks, material loss) and in spite of non-optimum installations (adhesive disbonds), the composite doubler allowed the structure to survive more than 144000 cycles of fatigue loading. Installation flaws in the composite laminate did not propagate over 216000 fatigue cycles. Furthermore, the added impediments of impact – severe enough to deform the parent aluminum skin – and hot-wet exposure did not affect the doubler’s performance. Since the tests were conducted using extreme combinations of flaw scenarios (sizes and collocation) and excessive fatigue load spectrums, the performance parameters were arrived at in a conservative manner.

17.1.1. Damage tolerance and fracture control plan

Damage tolerance and analysis methodologies

Inspection requirements (sensitivity and inspection intervals) are driven by damage tolerance analyses (DTA). However, the stack of metal parent material (isotropic), composite lamina (anisotropic), and adhesive layers makes the analysis quite complex and hinders the calculation of an exact DTA. It is difficult to determine the effects of flaw size and the point at which a flaw size/location becomes critical. This is especially true of disbond, delamination, and porosity flaws. Thus, an increased emphasis is placed on quantifying the probability that a flaw of a particular size and location will be detected by a piece of NDT equipment. In any surveillance of aircraft structure there are three main aspects to the inspection requirements: (1) the damage tolerance analysis (DTA) which determines the flaw onset and growth data (especially critical flaw size information), (2) the sensitivity, accuracy, and repeatability of NDI techniques which, in concert with the DTA, establishes the minimum inspection intervals, and (3) the impediments that the NDI techniques must contend with while achieving the required level of sensitivity. Detailed discussions on damage tolerance assessments for composite doubler installations are presented in references [1–7].

The reference [6] observations mirror one of the primary results obtained in the damage tolerance assessment presented in this report: adhesively bonded doublers are extremely damage tolerant to large disbonds and other detrimental conditions such as impact and hot-wet conditioning. These results are quantified in this chapter. If, in fact, disbond and delamination flaws do not grow even under extreme environmental conditions, then an acceptable design should be predicated on the fact that the stresses in the adhesive are kept below a limiting or threshold value. As a result, reference [6] introduces an essential design methodology that considers damage tolerance. It uses a fatigue threshold load, P_f , and a fatigue threshold strain, ε_f , below which irreversible damage in the adhesive will not occur. For thin skin repairs, the equations used to determine the threshold load and strain values are as follows:

$$P_f = 2(tW_fET)^{1/2}, \quad (17.1)$$

$$\varepsilon_f = 2(tW_fE/T)^{1/2}, \quad (17.2)$$

where,

t = thickness of the adhesive,

T = thickness of the adherend (skin),

E = Young's modulus of the skin,

W_f = threshold value of the strain energy density of the adhesive.

W_f can be determined experimentally [7]. Reference [6] also describes the maximum load, P_{\max} , that can be carried by a bond in a symmetrical bonded joint as,

$$P_{\max} = 2(tW_cET)^{1/2} , \quad (17.3)$$

where W_c is the maximum strain energy density of the adhesive. Thus, composite doubler repair design guidelines are that P_{\max} is greater than the ultimate load for the repaired structure and that P_f is greater than the limit load. Reference [6] also points out that these critical design variables are affected by the loading rate. A conservative estimate for P_{\max} can be obtained by using the value of the maximum von Mises equivalent stress in the adhesive, σ_e , as measured in high strain rate tests. For FM73, the adhesive used in this study, $\sigma_e = P_{\max} = 5800$ psi and the threshold stress $\sigma_{th} = 3600$ psi. This analysis approach clearly shows the importance of the adhesive in determining the overall performance of the bonded repair. The approach outlined above can be used to certify that a composite doubler design will satisfy the damage tolerance provisions of the U.S. Federal Aviation Regulations (FAR) Part 25.

The fundamental result from the reference [8] NDI study is that a team of NDI techniques can identify flaws well before they reach critical size. The abilities of nondestructive inspection techniques to meet the DTA flaw detection requirements are presented in Chapter 23.

Analysis of composite repairs

Numerous efforts have developed, refined, and advanced the use of methodologies needed to analyze composite doubler installations. Obviously, this is a critical element in the repair process since a badly implemented repair is detrimental to fatigue life and may lead to the near-term loss of structural integrity. The difficulties associated with analyzing the stress fields and flaw tolerance of various composite doubler designs and installations are highlighted in references [3,5,9]. Doubler design and analysis studies [6,9–17] have led to computer codes and turn-key software [18,19] for streamlining the analyses. These developments have taken great strides to eliminate the approximations and limitations in composite doubler DTA. In references [3,13], Baker presents an extensive study of crack growth in repaired panels under constant amplitude and spectrum loading. The installation variables evaluated were: (1) doubler disbond size, (2) applied stress, (3) doubler thickness, (4) min-to-max stress ratios (R ratio), and (5) temperature.

In references [3,13], a predictive capability for the growth of cracks repaired with composite doublers was developed using Rose's analytical model [14] and experimental fatigue studies. The important stress variables include the stress range, $\Delta\sigma_{\infty}$, and stress ratio, R , where,

$$\Delta\sigma_{\infty} = \sigma_{\max} - \sigma_{\min} , \quad (17.4)$$

$$R = \sigma_{\min} / \sigma_{\max} \quad (17.5)$$

A Paris-type crack growth relationship is assumed between da/dN and ΔK for the repaired crack such that,

$$da/dN = f(\Delta K, R) = A_R \Delta K^{n(R)}, \quad (17.6)$$

where a is the crack length, N is the number of fatigue cycles, and A_R and $n(R)$ are constants for a given R value. Tests results in [3,13] produced crack growth constants and were used to validate the model for crack mitigation effects of composite doublers. It was determined that Rose's model for predicting the stress-intensity range, ΔK , provides a good correlation with measured crack growth data (da/dN), however, anomalies were observed in the cases of temperature and R -ratio effects. Estimates of crack growth in composite doublers containing various disbond sizes were also determined.

References [1,2,8,19], describe the validation program that accompanied the L-1011 door corner repair. In these four documents, the attempts to generalize the performance test results are discussed. Every effort was made to design the test specimens and extrapolate the results to as wide a range of composite doubler repairs as possible. The overall goal in this approach is to minimize and optimize the testing that must compliment each new composite doubler installation. In order for composite doubler technology to be useful to the commercial aircraft industry, the design-to-installation cycle must be streamlined. An ongoing study at the FAA Airtowthiness Assurance Center at Sandia National Labs is addressing composite doubler repairs on DC-10 fuselage skin [21] with the goal of streamlining the design, validation, and certification process. The end result will be the revision of the DC-10 Structural Repair Manual (alternate repairs for existing riveted metallic doublers) thus allowing more rapid and widespread use of specific doubler repairs. It should be noted that a closely monitored pilot program will be completed prior to any revision of the DC-10 Structural Repair Manual.

Need for damage tolerance assessments

One of the primary concerns surrounding composite doubler technology pertains to long-term survivability, especially in the presence of non-optimum installations. This test program demonstrated the damage tolerance capabilities of bonded composite doublers. The fatigue and strength tests quantified the structural response and crack abatement capabilities of Boron-Epoxy doublers in the presence of worst case flaw scenarios. The engineered flaws included cracks in the parent material, disbonds in the adhesive layer, and impact damage to the composite laminate. Environmental conditions representing temperature and humidity exposure were also included in the coupon tests.

17.1.2. Damage tolerance establishes fracture control plan

Establishing damage tolerance

Damage tolerance is the ability of an aircraft structure to sustain damage, without catastrophic failure, until such time that the component can be repaired or

replaced. The U.S. Federal Aviation Requirements (FAR 25) specify that the residual strength shall not fall below limit load, P_L , which is the maximum load anticipated to occur once in the life of an aircraft. This establishes the minimum permissible residual strength $\sigma_P = \sigma_L$. To varying degrees, the strength of composite doubler repairs are affected by crack, disbond, and delamination flaws. The residual strength as a function of flaw size can be calculated using fracture mechanics concepts. Figure 17.1 shows a sample residual strength diagram. The residual strength curve is used to relate this minimum permissible residual strength, σ_P , to a maximum permissible flaw size a_P .

A fracture control plan is needed to safely address any possible flaws which may develop in a structure. Nondestructive inspection is the tool used to implement the fraction control plan. Once the maximum permissible flaw size is determined, the additional information needed to properly apply NDI is the flaw growth versus time or number of cycles. Figure 17.2 contains a flaw growth curve. The first item of note is the total time, or cycles, required to reach a_P . A second parameter of note is a_d which is the minimum detectable flaw size. A flaw smaller than a_d would likely be undetected and thus, inspections performed in the time frame prior to n_d would be of little value. The time, or number of cycles, associated with the bounding parameters a_d and a_P is set forth by the flaw growth curve and establishes $H(\text{inspection})$. Safety is maintained by providing at least two inspections during $H(\text{inspection})$ to ensure flaw detection between a_d and a_P .

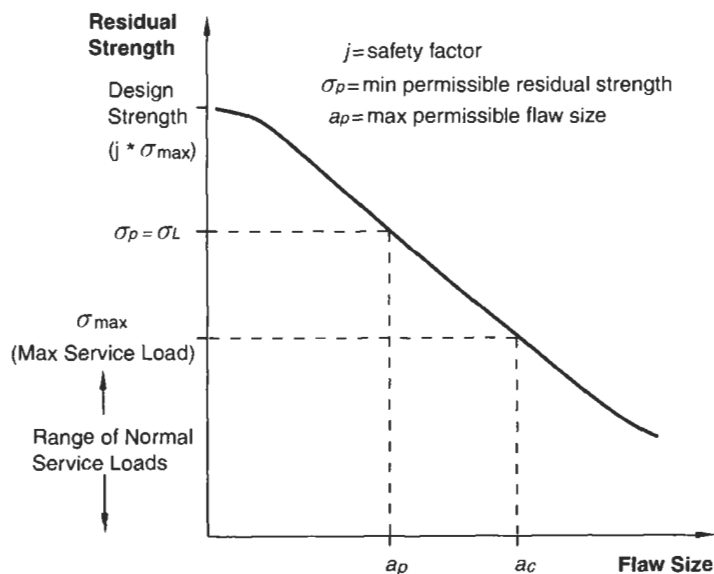


Fig. 17.1. Residual strength curve.

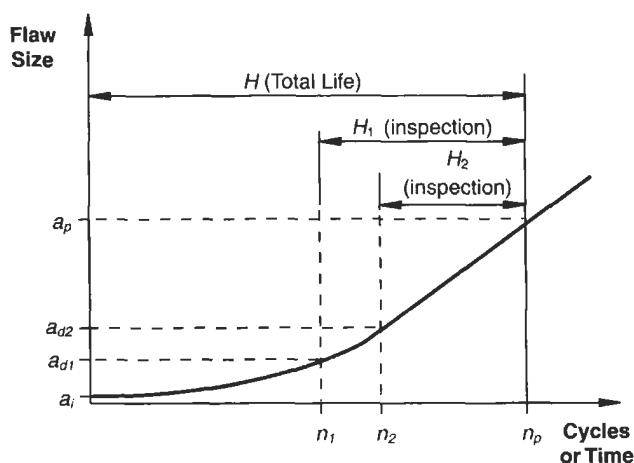


Fig. 17.2. Crack growth curve showing time available for fracture control.

Inspection intervals

An important NDI feature highlighted by Figure 17.2 is the large effect that NDI sensitivity has on the required inspection interval. Two sample flaw detection levels $a_d(1)$ and $a_d(2)$ are shown along with their corresponding intervals $n_d(1)$ and $n_d(2)$. Because of the gradual slope of the flaw growth curve in this region, it can be seen that the inspection interval $H_1(\text{inspection})$ can be much larger than $H_2(\text{inspection})$ if NDI can produce just a slightly better flaw detection capability. Since the detectable flaw size provides the basis for the inspection interval, it is essential that quantitative measures of flaw detection are performed for each NDI technique applied to the structure of interest. Chapter 23 discusses these quantitative, probability of flaw detection measures used to assess inspection performance.

As an example of the DTA discussed above, reference [22] describes the design and analysis process used in the L-1011 program. It presents the typical data – stress, strength, safety factors, and damage tolerance – needed to validate a composite doubler design. The design was analyzed using a finite element model of the fuselage structure in the door region along with a series of other composite laminate and fatigue/fracture computer codes. Model results predicted the doubler stresses and the reduction in stress in the aluminum skin at the door corner. Peak stresses in the door corner region were reduced by approximately 30% and out-of-plane bending moments were reduced by a factor of six. The analysis showed that the doubler provided the proper fatigue enhancement over the entire range of environmental conditions. The damage tolerance analysis indicated that the safety-limit of the structure is increased from 8400 flights to 23280 flights after the doubler installation (280% increase in safety-limit). It established an inspection interval for the aluminum and composite doubler of 4500 flights.

17.2. Composite doubler damage tolerance tests

Damage tolerance testing

A series of fatigue coupons were designed to evaluate the damage tolerance performance of bonded composite doublers. The general issues addressed were: (1) doubler design – strength, durability, (2) doubler installation, and (3) NDI techniques used to qualify and accept installation. Each specimen consisted of an aluminum “parent” plate, representing the original aircraft skin, with a bonded composite doubler. The doubler was bonded over a flaw in the parent aluminum. The flaws included fatigue cracks (unabated and stop-drilled), aluminum cut-out regions, and disbond combinations. The most severe flaw scenario was an unabated fatigue crack which had a co-located disbond (i.e. no adhesion between doubler and parent aluminum plate) as well as two, large, 1" diameter disbonds in the critical load transfer region of the doubler perimeter. Tension-tension fatigue and residual strength tests were conducted on the laboratory specimens. The structural tests were used to: (1) assess the potential for interply delaminations and disbonds between the aluminum and the laminate, and (2) determine the load transfer and crack mitigation capabilities of composite doublers in the presence of severe defects. Through-transmission ultrasonics, resonance UT, and eddy current inspection techniques were interjected throughout the fatigue test series in order to track the flaw growth. Photographs of the damage tolerance test set-up and a close-up view of a composite doubler test coupon are shown in Figure 17.3.

The two main potential causes of structural failure in composite doubler installations are cracks in the aluminum and adhesive disbonds/delaminations. When disbonds or delaminations occur, they may lead to joint failures. By their nature, they occur at an interface and are, therefore, always hidden. A combination of fatigue loads and other environmental weathering effects can combine to initiate these types of flaws. Periodic inspections of the composite doubler for disbonds and delaminations (from fabrication, installation, fatigue, or impact damage) is essential to assuring the successful operation of the doubler over time. The interactions at the bond interface are extremely complex, with the result that the strength of the bond is difficult to predict or measure. Even a partial disbond may compromise the integrity of the structural assembly. Therefore, it is necessary to detect all areas of disbonding or delamination, as directed by DTA, before joint failures can occur.

General use of results

The objective of this test effort was to obtain a generic assessment of the ability of Boron-Epoxy doublers to reinforce and repair cracked aluminum structure. By designing the specimens using the nondimensional stiffness ratio, it is possible to extrapolate these results to various parent structure and composite laminate combinations. The number of plies and fiber orientations used in these tests resulted in an extensional stiffness ratio of 1.2:1 $\{(Et)_{BE} = 1.2 (Et)_{AI}\}$. Independent Air Force [23] and Boeing studies [24] have determined that stiffness ratios of 1.2 to

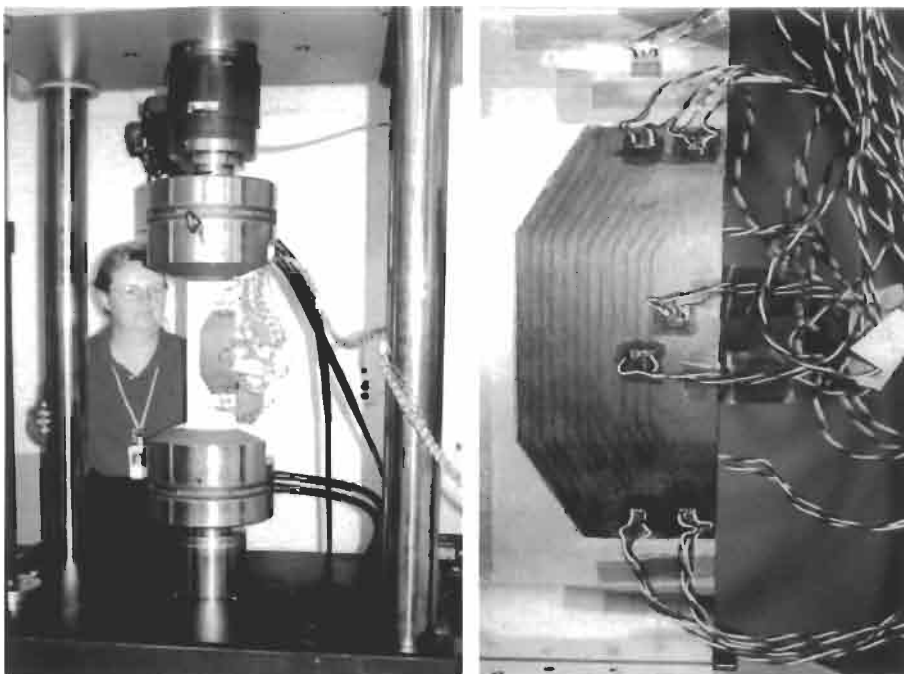


Fig. 17.3. Set-up for damage tolerance tests and close-up view of coupon specimen mounted in machine grips.

1.5 produce effective doubler designs. Lockheed-Martin has also used this range of stiffness ratios in military composite doubler designs.

17.3. Conformity inspection and FAA oversight

Appropriate conformity checks and FAA oversight was obtained on all aspects of specimen fabrication, testing, and data acquisition. The following items were witnessed by the FAA or an FAA designated representative. The test plan was reviewed and approved by a Designated Engineering Representative.

1. Fabrication of the test specimens – composite doubler fabrication and installation.
2. Impact and hot-wet conditioning of test specimens.
3. Conformity inspection of coupon test articles to assure adherence to specified structural configuration.
4. Verification that the calibration and operation of test equipment was current.
5. Verification of strain gage locations.

Coupon configuration

The nine specimen configurations that were tested are described below. Numerous specimens were tested for each configuration. Each specimen consisted of an aluminum “parent” plate, representing the original aircraft skin, with a bonded composite doubler. The doubler was bonded over a flaw in the parent aluminum. The specimens had the following basic design configurations:

1. BE-1: Unabated 0.5" fatigue crack at the edge of the aluminum plate; no engineered flaws in composite doubler.
2. BE-2: Stop-drilled, 0.5" sawcut edge crack in the aluminum plate with collocated 0.75" dia. disbond between composite doubler and aluminum; 0.75" dia. disbonds along doubler edge.
3. BE-3: Stop-drilled, 0.5" sawcut edge crack in the aluminum plate with collocated 1.0" dia. disbond between composite doubler and aluminum; 1.0" dia. disbonds along doubler edge (Figure 17.4).
4. BE-4: Unabated 0.5" fatigue crack at the edge of the aluminum plate with collocated 0.75" dia. disbond between composite doubler and aluminum; 0.75" dia. disbonds along doubler edge.
5. BE-5: 1" dia. hole in aluminum plate; no engineered flaws in composite doubler.
6. BE-6: Unabated 0.5" fatigue crack at the edge of the aluminum plate without a composite doubler. The fatigue crack growth observed in these “unrepaired baseline” specimens serves as the basis of comparison for the composite reinforced specimens.
7. BE-7: Composite doubler installed with no engineered flaws in the aluminum plate or the composite doubler. This represents the “repaired baseline specimen” with an optimum installation.
8. BE-8: Stop-drilled, 0.5" sawcut edge crack in the aluminum plate with collocated 300 in-lb impact damage from a 1" diameter hemispherical tip; collocated 1" diameter disbond; 160 °F hot-wet conditioning.
9. BE-9: Unabated 0.5" fatigue crack at the edge of the aluminum plate with collocated 300 in-lb impact damage from a 1" diameter hemispherical tip; similar impact damage along doubler edge; collocated 1" diameter disbonds at both impact locations; 160 °F hot-wet conditioning (Figure 17.5).

Specimen description

1. **Material** – The parent aluminum plate was 2024-T3. The Boron-Epoxy material was type 5521/4. The adhesive material was FM-73, or accepted substitute AF-163, (0.06 PSF) and the primer was Cytec BR-127. The Boron-Epoxy composite doubler was a multi-ply lay-up of 13 plies: $[0, +45, -45, 90]_3$ with a 0° cover ply on top. The plies were cut to different lengths in both in-plane directions in order to taper the thickness of the resulting doubler edges. This produced a more gradual load transfer between the aluminum and the doubler (i.e. reduces the stress concentration in the bondline around the perimeter). A ply taper ratio of approximately 30:1 was utilized; this results in a reduction in length of 30 times the ply thickness. The number of plies and fiber orientations produced an extensional stiffness ratio of Boron-Epoxy to aluminum of 1.2:1 $\{(Et)_{BE} = 1.2 (Et)_{Al}\}$.

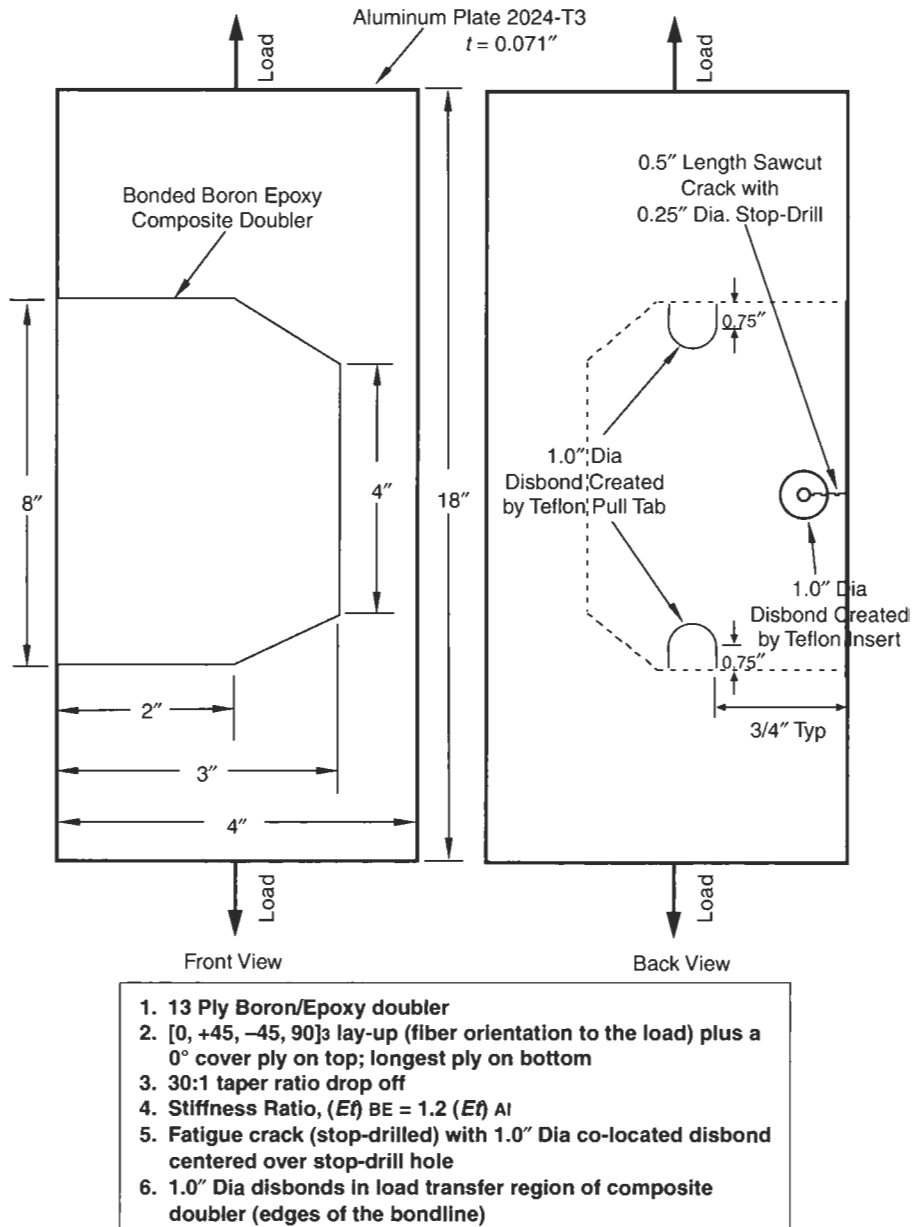
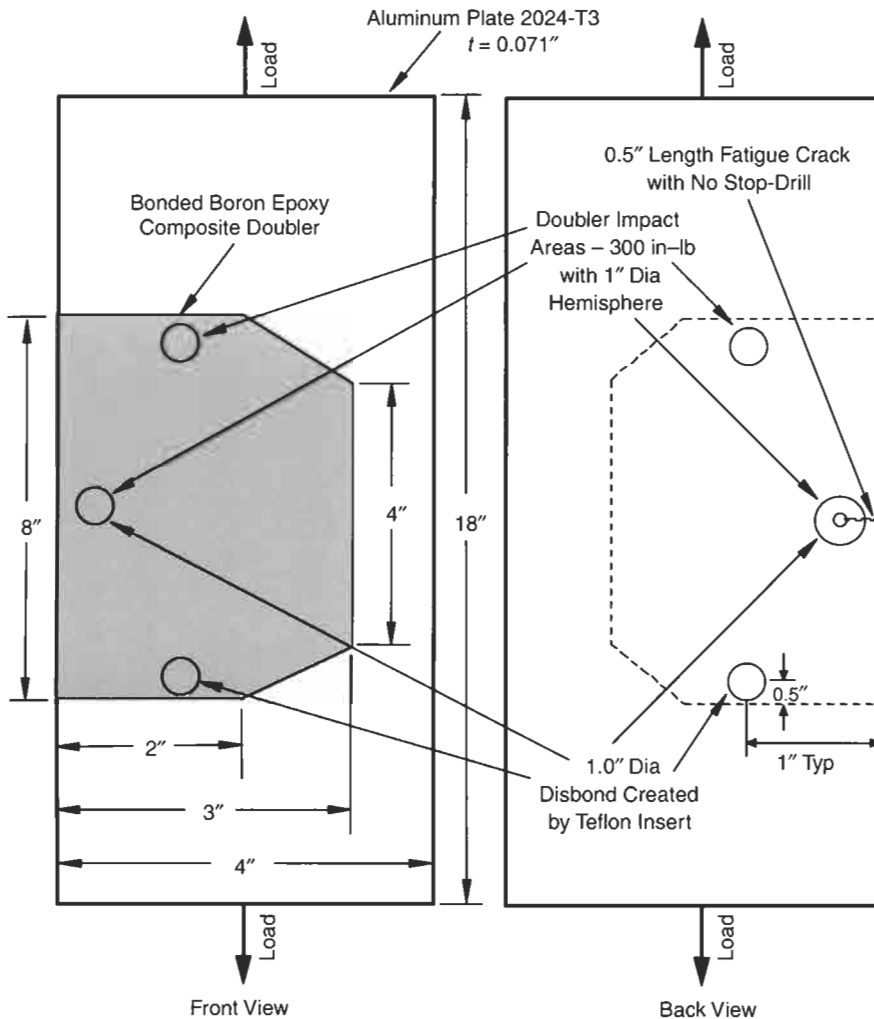


Fig. 17.4. Composite tension test coupon configuration BE-3.



1. 13 Ply Boron/Epoxy doubler
2. $[0, +45, -45, 90]_3$ lay-up (fiber orientation to the load) plus a 0° cover ply on top; longest ply on bottom
3. 30:1 taper ratio drop off
4. Stiffness Ratio, $(E\bar{\eta})_{BE} = 1.2 (E\bar{\eta})_{Al}$
5. Crack (stop-drilled) with 1.0" Dia co-located impact damage centered over stop-drill hole; 160°F hot, wet conditioned
6. 1.0" Dia disbond co-located over fatigue crack; disbond and impact damage in load transfer regions (edges of bondline)

Fig. 17.5. Composite tension test coupon – configuration BE-9.

2. Material thickness – The parent aluminum plate was 2024-T3, 0.071" thick. Each composite doubler had a nominal post-cure thickness of 0.080" (approximately 0.0057" per ply plus a nominal pre-cure adhesive layer of 0.010"; the post-cure adhesive thickness is approximately 0.006").
3. Tension specimen dimensions – The specimens were designed for a 4" W × 14" L test area. To accommodate two, 2" deep end grips, the final specimen lengths were 18".

Generation of cracks in aluminum substrate material

Prior to installing the composite doublers, seven of the coupon configurations (BE-1, BE-2, BE-3, BE-4, BE-6, BE-8, and BE-9) had cracks generated in the aluminum substrate plate. Specimen configurations BE-2, BE-3 and BE-8 had 0.5" sawcut cracks that were stop-drilled using a 0.25" diameter drill bit. Specimen configurations BE-1, BE-4, BE-6, and BE-9 had 0.5" fatigue cracks that were unabated (i.e. no stop-drill). The fatigue cracks were generated by tension-tension fatigue loads in a uniaxial, mechanical test machine.

Surface preparation and composite doubler installation

All test specimens were prepared using the phosphoric acid non tank anodize (PANTA) surface preparation procedure and the phosphoric acid containment system (PACS) equipment. The complete installation procedure is provided in reference [25]. The key installation steps are summarized below.

1. Aluminum surface preparation – Solvent clean per BAC 5750. Remove the oxide on the aluminum prior to Phosphoric Acid Anodize using Scotch Brite pads to achieve a 30 s water-break free condition. Phosphoric acid anodize (PAA) the aluminum surface using phosphoric acid containment system (PACS) equipment.
2. Primer and adhesive process – Prime the PAA aluminum surface using Cytec BR-127 primer (or equivalent: EC3960), type 1, grade A per BMS 5–89. Co-cure the Cytec FM-73 (or equivalent: AF163) structural film adhesive per BMS 5–101 simultaneously with the Boron-Epoxy doubler.
3. Boron-epoxy doubler installation and cure – Lay up the 5521/4 Boron-Epoxy doubler in accordance with the application design drawing. Cure for 90 to 120 minutes at 225 °F to 250 °F at 0.54 ATM vacuum bag pressure (equivalent atmospheric pressure is 7.35 psia) using standard composite "hot bonder" units. Use computer-controlled heater blankets to provide the proper temperature cure profile in the field. Use a series of thermocouples in an active feedback loop to maintain the proper temperature profile.

Following coupon fabrication, the specimens were visually inspected and ultrasonically scanned to determine if there were any disbond or delamination flaws other than the ones intentionally engineered into the specimens. The resulting flaw map (location, geometry, and depth) was recorded and the damage locations were marked directly on the specimens for future reference.

Application of impact damage to composite coupons

Following the composite doubler installation and prior to environmental conditioning, impact damage was imparted to Specimen Configurations BE-8 and BE-9. The locations for impact damage were selected to induce the most adverse effect on crack growth mitigation and/or the ability of the doubler to transfer load. The impact was performed with a 1 inch diameter steel hemisphere tip. The magnitude of the impact was 25 ± 0.5 ft-lb (300 ± 5 in-lb). Following impact, the specimens were ultrasonically scanned to determine the extent of the resulting damage. The resulting flaw map (location, geometry, and depth) was recorded and the damage locations were marked directly on the specimens.

Temperature and humidity conditioning

After applying the impact damage, Specimen Configurations BE-8 and BE-9 were subjected to temperature and humidity conditioning in order to simulate end-of-service moisture content. Conditioning of $160^\circ\text{F} + 5^\circ\text{F}$, $85\% \pm 5\%$ relative humidity was applied to the test article for a period of time sufficient to achieve saturation moisture content as determined by regular weighing of the test coupons.

Calculation of laminate-aluminum extensional stiffness ratio

This section describes the method that was used to arrive at the stiffness parameter, $E_x t$, for composite doublers. The calculations used classical laminated plate theory, along with Boron-Epoxy lamina properties, to arrive at the average cured laminate modulus E_x (where x is the direction of the fatigue load).

The Boron-Epoxy lamina properties at room temperature are:

$$\begin{aligned} E_{11} &= 28.0 \times 10^6 \text{ psi} & \nu_{12} &= 0.21 \\ E_{22} &= 2.7 \times 10^6 \text{ psi} & t_{\text{ply}} &= 0.0057 \text{ in} \\ G_{12} &= 0.8 \times 10^6 \text{ psi} \end{aligned}$$

The average laminate properties were calculated using the individual lamina properties listed above along with the following specific lay-up configuration: (1) 13 plies $\{[0, +45, -45, 90]_3, 0\}$, and (2) laminate thickness $t = 0.0741''$ (13 plies $\times 0.0057''/\text{ply}$). The resulting laminate properties were calculated:

$$\begin{aligned} E_x &= 11.873 \times 10^6 \text{ psi} & G_{xy} &= 3.77 \times 10^6 \text{ psi} \\ E_y &= 10.144 \times 10^6 \text{ psi} & \nu_{xy} &= 0.32 \end{aligned}$$

Compared to a 0.071'' thick, 2024-T3 aluminum plate, the stiffness ratio is,

$$\begin{aligned} R &= \frac{(E_x t_{\text{laminate}})_{\text{BE}}}{(E_x t)_{\text{Al}}} \\ &= \frac{(11.873 \times 10^6 \text{ psi})(0.0741'')}{(10.5 \times 10^6 \text{ psi})(0.071'')} \\ R &= 1.2 \end{aligned} \tag{17.7}$$

Test procedures and instrumentation

Tension-tension fatigue tests on the coupon specimens used baseline stress levels of 3.75 ksi to 20.75 ksi (1050–5810 lbs. load) to represent the 0–17 ksi hoop stress spectrum in fuselage skin during cabin pressurization. The lower stress limit, or test pre-load, was applied to eliminate the residual curvature in the test specimen. The post-installation residual curvature is caused by the different coefficients of thermal expansion between the aluminum and Boron-Epoxy materials. The upper stress limit was used to approximate hoop stresses created in an aircraft's skin by cabin pressurization. Load transfer through the composite doubler and stress risers around the defects were monitored using strain gage layouts such as the example shown in Figure 17.6. Biaxial gages were used to measure both the axial and transverse strains in the anisotropic composite material. Similar gage layouts were used for all of the damage tolerance test specimens. Crack growth was monitored using optical measurement devices (resolution 0.003") and eddy current inspection equipment that were applied to the non-composite doubler side of the specimens.

Fatigue tests with static strain measurements

1. A 1050 lb pre-load was applied to eliminate the residual curvature in the test specimens.
2. The 1050–5810 lb. cyclic fatigue loads (3.75–20.75 ksi stress) were applied at 4 Hz.
3. Each fatigue test was stopped and optical crack growth measurements were made at 36000, 54000, and 72000 fatigue cycles. 72000 cycles corresponds to two design lifetimes for the L-1011 aircraft. The fatigue tests continued until unstable flaw growth occurred or until at least 144000 cycles (4X the design objective) were reached. Some of the specimens were fatigue cycled until failure occurred and the crack propagated through the entire width of the specimen.
4. The specimens were inspected with ultrasonic and eddy current NDI techniques at 36000, 72000 and 144000 cycles. The NDI tests were performed in-situ to eliminate the removal of the specimens from the tension test machine following each fatigue interval.
5. Static strain measurements were acquired at the following four fatigue test stopping points: (1) Fatigue Cycles=0, (2) Fatigue Cycles=72000, and (3) Fatigue Cycles=144000. After pre-loading the specimen to the 1050 lb. pre-load, the strain gage bridges were balanced to produce a zero strain output signal. This data was used as the static tension test starting point (Test tension load=0 lbs.). The tension load was increased to at least the tabulated levels shown below. A load of 4760 lbs. produced the 17 ksi stress level in the specimen which corresponds to maximum fuselage pressurization. Most specimens were loaded in excess of 4760 lbs. but below yield stress levels. Strain values were acquired at each load level.

Static tension ultimate strength tests

Several specimens that were fatigued and other specimens that had implanted flaws but were not fatigued were subjected to static ultimate tension tests in order

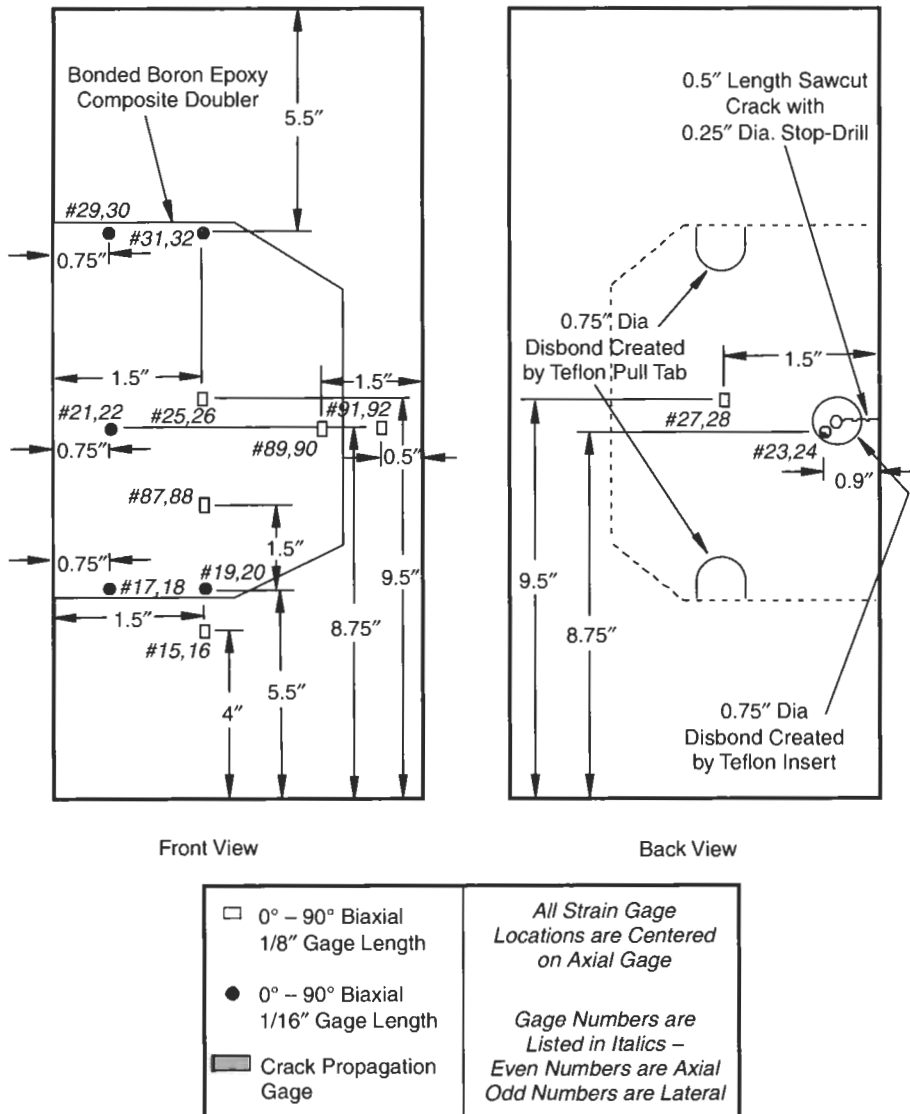


Fig. 17.6. Strain gage locations for composite tension test coupon – configuration BE-2.

to determine their ultimate strength and failure modes. The test procedures and data acquisition process was as follows.

1. A 1050lb. pre-load was applied to eliminate the residual curvature in the test specimens. After pre-loading the specimen, the strain gage bridges were balanced to produce a zero strain output signal. This data was used as the tension ultimate test starting point (Test tension load = 0 lbs.).

2. The load was increased, using displacement mode control, at a continuous rate of 0.05 inch/min. Failure was defined as the point where the specimen was unable to sustain an increasing load. The peak load recorded during each failure test was used to calculate the maximum stresses sustained by the flawed specimens (ultimate strength).
3. The machine's crosshead displacement transducer was used to obtain load vs. total displacement curves.

17.4. Test results

These damage tolerance tests provide a comprehensive evaluation of the effectiveness of composite doublers in reducing crack growth in aluminum substructure. Fatigue and strength tests were performed on specimens with various combinations of crack, disbonds, and impact flaws. The flaw sizes, locations, and combinations were engineered to produce extreme worst case conditions. Inspection requirements for on-aircraft doubler installations were established using a Damage Tolerance Analysis [22] and the results from this study. Disbond, delamination and crack sizes used in these damage tolerance tests were at least twice the size of those which will be detected by the NDI requirements. Thus, there is an inherent safety factor built into this damage tolerance assessment and the doubler performance cited here should be conservative.

17.4.1. Fatigue tests

The results from several of the fatigue tests are summarized in Table 17.1 and shown graphically in Figures 17.7 and 17.8. These results show that crack growth can be substantially reduced or completely eliminated for a number of fatigue lifetimes using composite doubler repairs. This is true in spite of the disbond and impact impediments – both at the critical load transfer region along the doubler's edge and directly over the crack – which were engineered into the specimens. In some specimens crack reinitiation did not occur until after several fatigue design lifetimes (e.g. one design lifetime of L-1011 aircraft = 36,000 cycles). Total crack growth of less than 0.6" was observed in some specimens after 144,000 fatigue cycles. Furthermore, testing up to 180,000 cycles show little or no additional crack growth. In many specimens, it can be seen that an allowable crack length of 1" would still not be present after 144,000 post-installation flight cycles.

The drop in total crack growth in the impact damaged specimens (config. BE-8) versus the BE-2 and BE-3 configurations may be due to the effects of the deformations produced by the impact. It is likely that the plastic deformation in the aluminum strain hardened the material and produced beneficial compressive strains that impeded crack growth in the area of impact. In addition, the complex geometry created by the indentation (i.e. lack of flat surface which is in plane with the tension loads) may have also slowed the crack growth in this area. Figure 17.8

Table 17.1
Composite doubler damage tolerance fatigue and ultimate strength test summary.

Config.	Description	Fatigue test results
BE-1	unabated 0.5" fatigue edge crack; no engineered flaws in composite doubler installation	<ul style="list-style-type: none"> ● crack propagated 1.78" in 144 K cycles ● no initiation of disbonds ● post-fatigue residual strength = 103 ksi
BE-2	stop-drilled 0.5" sawcut edge crack with collocated disbond; 0.75" dia. disbonds in edge of doubler	<ul style="list-style-type: none"> ● stop-drilled crack reinitiated after 126 K cycles ● crack propagated 0.875" in 144 K cycles ● no growth in disbonds; fracture of adhesive around crack ● post-fatigue residual strength = 88 ksi
BE-3	stop-drilled 0.5" sawcut edge crack with collocated disbond; 1.0" dia. disbonds in edge of doubler	<ul style="list-style-type: none"> ● stop-drilled crack reinitiated after 72 K cycles (small burr in stop-drilled hole acted as starter notch) ● crack propagated 1.71" in 144 K cycles ● no growth in disbonds; fracture of adhesive around crack
BE-4	unabated 0.5" fatigue edge crack with collocated disbond; 0.75" dia. disbonds in edge of doubler	<ul style="list-style-type: none"> ● crack propagated 2.21" in 144 K cycles ● fatigue test was extended until specimen failure occurred at 182 K cycles
BE-5	1" dia. hole in parent aluminum plate; no engineered flaws in composite doubler installation	<ul style="list-style-type: none"> ● 180 K fatigue cycles applied – no fatigue cracks generated ● no growth in disbonds
BE-6	unabated 0.5" fatigue edge crack; aluminum plate with no doubler	<ul style="list-style-type: none"> ● crack propagated until specimen failed at 9 K cycles ● duplicate specimen failed at 12 K cycles
BE-7	composite doubler installed without any engineered flaws; no flaws in aluminum plate	<ul style="list-style-type: none"> ● two specimens – no crack growth in 144 K and 216 K cycles ● no initiation of disbonds ● ultimate strength following fatigue = 70 ksi
BE-8	stop-drilled 0.5" sawcut edge crack with collocated impact/disbond damage on doubler; 160 °F hot, wet conditioned; tested at room temperature	<ul style="list-style-type: none"> ● three specimens – cracks reinitiated after 72 K, 90 K, and 90 K cycles ● cracks propagated 0.5" in 144 K cycles ● no growth in disbonds ● all three ultimate strength tests produced σ_u values in excess of 75 ksi
BE-9	unabated 0.5" fatigue edge crack with collocated impact/disbond damage on doubler; impact/disbond damage on edge of doubler; 160 °F hot, wet conditioned; tested at room temperature	<ul style="list-style-type: none"> ● three specimens – cracks propagated 0.7" in 144 K cycles ● no growth in disbonds ● average of three ultimate strength tests produced σ_u value of 72.4 ksi

* Crack growth rates in all composite doubler specimens were 10 to 20 times slower than the Control Specimens (BE-6) which had no reinforcing doublers.

shows that specimen Lock15 reached a plateau where the crack length did not change from 106000 to 180000 cycles.

Even in the cases of fatigue cracks with no abatement (BE-1, BE-4, & BE-9 configurations), the first noticeable change in crack length occurred after approximately 16000 cycles or 1/2 of an L-1011 lifetime. The BE-4 specimen shown in Figure 17.7 was tested beyond the test goals in order to demonstrate that the specimen could survive five L-1011 lifetimes (180000 cycles) without failure. The cycles-to-failure for this configuration was 182000 cycles. Once the crack

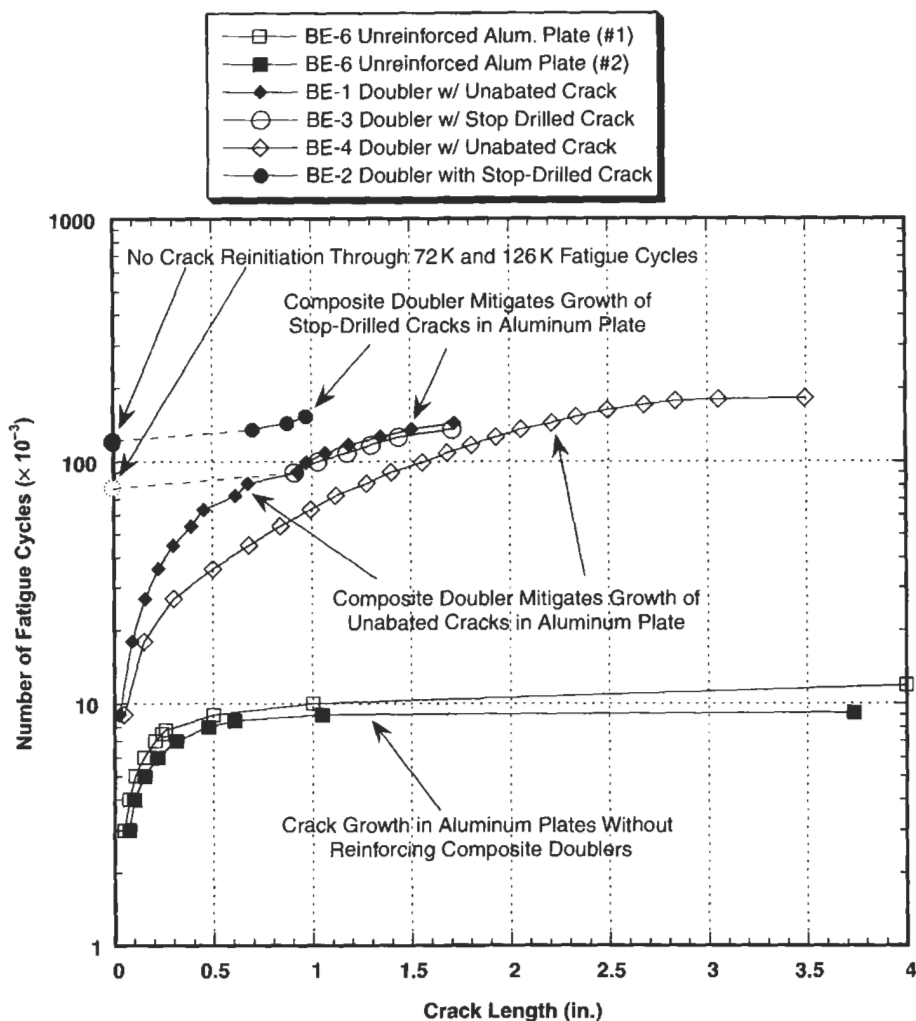


Fig. 17.7. Fatigue crack growth in 2024-T3 plates with and without reinforcing composite doublers (configurations BE-1 through BE-6).

propagated through the width of the aluminum, the adhesive was able to transmit stresses into the doubler which exceeded the material's ultimate strength. At this point, the Boron-Epoxy composite laminate fractured.

Specimens BE-1 and BE-4 produced very similar crack growth curves. The BE-1 configuration had a good doubler bond along the length of the fatigue crack while the BE-4 configuration had the added impairment of a disbond collocated with the fatigue crack. As a result, the initial rate of crack growth was slightly higher in this

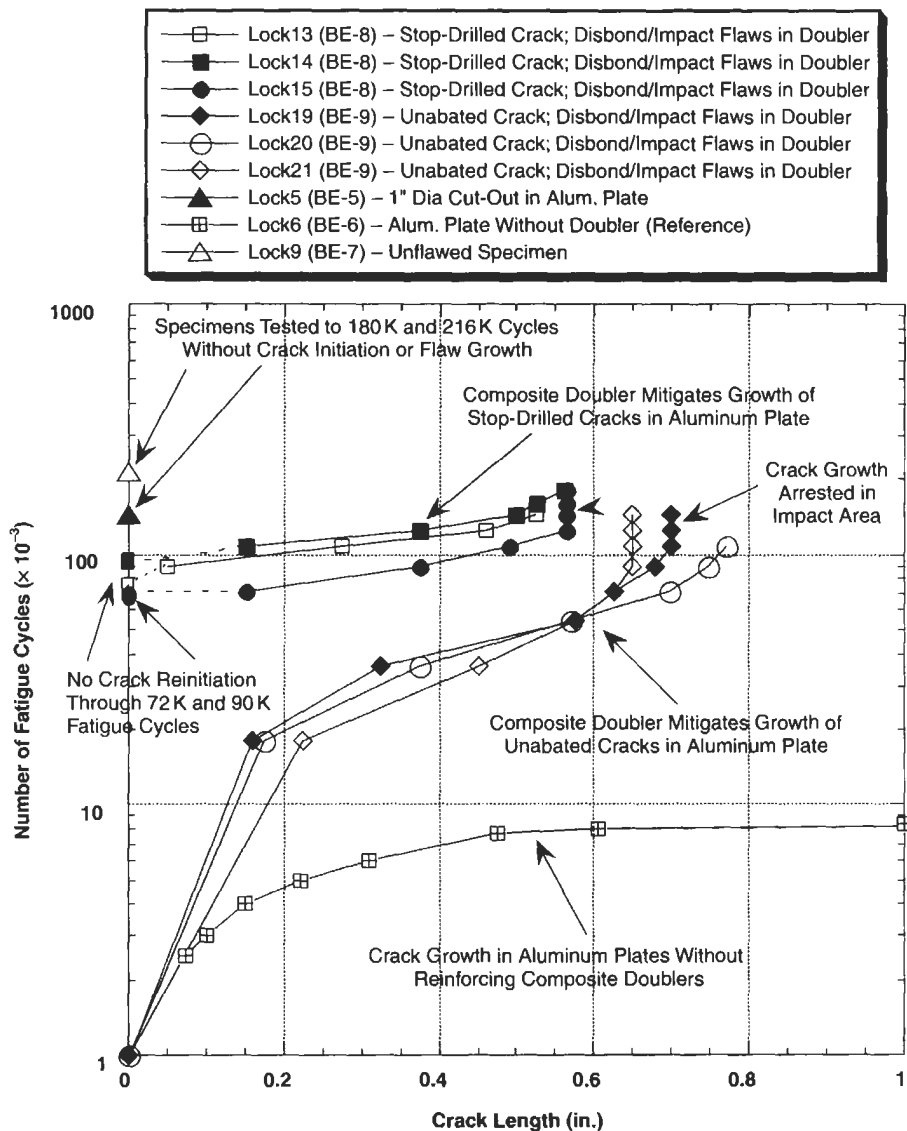


Fig. 17.8. Fatigue crack growth in 2024-T3 plates with and without reinforcing composite doublers (configurations BE-5 through BE-9).

BE-4. However, the two crack growth curves blended into a single propagation rate at a crack length (a) equal to 1.75". In fact, Figure 17.7 shows that regardless of the initial flaw scenario engineered into the test specimen, all of the flaw growth curves tend to blend into the same outcome as the crack propagates beyond 2" in length.

This is because all of the specimens degenerate into the same configuration at this point.

Material removed from parent plate and composite doubler reinforcement

The BE-5 specimen in Figure 17.8 had a 1" diameter hole simulating the removal of damage (e.g. crack or corrosion) in the parent structure. In this specimen, a fatigue crack did not initiate during 144000 fatigue cycles or four L-1011 lifetimes. The bonded composite doubler picked up load immediately adjacent to the cut-out so this type of material removal enhanced the overall performance of the installation. Although the large hole in the parent aluminum created a stress riser, the doubler was able to withstand the high local stresses and prevent any flaws (disbonds, cracks) from developing.

Control specimens and comparison of crack growth rates

Fatigue tests were also conducted on aluminum "control" specimens which were not reinforced by composite doublers (BE-6 configuration). Figures 17.7 and 17.8 show the crack growth exhibited by the unreinforced plates. In these tests, the fatigue cracks propagated through the width of the BE-6 specimens after approximately 10000 cycles. By comparing these results with specimens that had a composite doubler reinforcement, it can be determined that the overall fatigue lifetime was extended by a factor of 10–20 through the use of composite doublers. In Figures 17.7 and 17.8, the number of fatigue cycles are plotted using a log scale because it clearly shows the crack arresting affect of the composite doublers. The unreinforced panels asymptotically approach 10000 cycles-to-failure while the plates reinforced by composite doublers asymptotically approach 100000 to 200000 fatigue cycles. It should be noted that an optimum installation (see discussion below) would be able to sustain much higher fatigue cycles. Therefore, the life extension factor of 20, calculated using flawed doubler installations, is considered conservative.

Figures 17.7 and 17.8 also show that the crack growth rates for all of the specimens can be approximated by a bilinear fit to the data plotted on a semi-log scale. This simply demonstrates the well known power law relationship between fatigue cycles (N) and crack length (a). The first linear portion extends to (a) = 0.25" in length. The slopes, or crack growth rates, vary depending on the localized configuration of the flaw (e.g. stop-drilled, collocated disbond, presence of doubler). The second linear portion extends to the point of specimen failure. A comparison of these linear approximations shows that the crack growth rate is reduced 20 to 40 times (depending on the current length of the crack) through the addition of a composite doubler.

Baseline specimens: performance of an optimum installation

Through experimental demonstrations of acceptable doubler performance in the presence of worst case flaw scenarios, these tests showed that conservatism and appropriate safety factors are inherently built into a Boron-Epoxy doubler design. However, the most realistic basis of comparison for the performance of composite

doublers was provided by specimens with normal installation and no flaws. Two specimens with the BE-7 “optimum installation” configuration were subjected to fatigue tests. These unflawed specimens showed that crack growth and disbonds/delaminations could be eliminated for at least 216000 fatigue cycles.

Non-destructive inspection and propagation of adhesive flaws

These damage tolerance tests assessed the potential for loss-of-adhesion flaws to initiate and grow in the composite doubler installation. Disbonds can occur between the composite doubler and the aluminum skin while delaminations can develop between adjacent plies of Boron-Epoxy material. It has been shown in related studies that the primary load transfer region, which is critical to the doubler’s performance, is around its perimeter [3,9,10,14,16,24]. The purpose of the disbonds in configurations BE-2, BE-3, BE-4, BE-8, and BE-9 were to demonstrate the capabilities of composite doublers when large disbonds exist in the critical load transfer region as well as around the cracks which the doublers are intended to arrest. In this manner, severe worst case scenarios could be assessed and quantitative performance numbers could be established.

The fatigue specimens contained engineered disbonds of three to four times the size detectable by the doubler inspection technique. Despite the fact that the disbonds were placed above fatigue cracks and in critical load transfer areas, it was observed that there was no growth in the disbonds, delaminations, or impact flaws over 144000 to 216000 fatigue cycles (four to six L-1011 lifetimes). In addition, it was demonstrated that the large disbonds, representing almost 30% of the axial load transfer perimeter, did not decrease the overall composite doubler performance. Ultrasonic scanning was used to create 2D flaw maps of each test specimen before and after each fatigue test [26]. C-scan technology uses information from single point A-scan waveforms to produce an area mapping of the inspection surface (see Chapter 23). Signal variations corresponding to disbonds and delaminations are represented by dark black areas on the images. Figure 17.9 shows a sample of C-scan images created by the inspections. [Note: the NDI system produces color-coded maps, however, for the purposes of this document gray scale plots clearly show the flaws in the test specimens]. To provide a point of reference, a shape outline of the Boron-Epoxy doubler is superimposed on the C-scan image. Side-by-side comparisons of the before and after C-scans show that the original engineered flaws, which were detected prior to testing, remained unchanged even after multiple fatigue lifetimes.

Comments on fatigue loading spectrum and conservatism of results

The fatigue tests were conducted using a 3 ksi to 20 ksi sinusoidal load spectrum. The 3 ksi pre-load was intended to eliminate the residual curvature in the test specimens caused by the different coefficients of thermal expansion between the aluminum and boron-epoxy material. However, the pre-load was not able to completely eliminate all of the specimen curvature. As a result, there were bending loads introduced into the tension fatigue tests. The accompanying stress reversals produced a slight amount of “oilcanning” which is not commonly found in aircraft

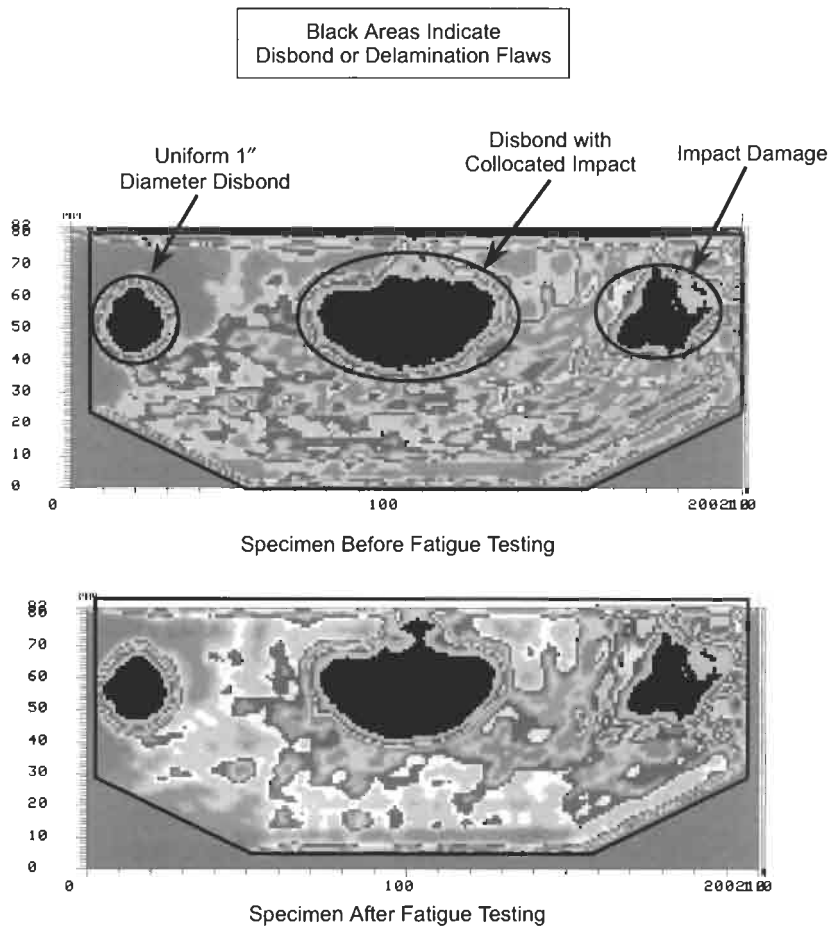


Fig. 17.9. Fatigue specimen lock19 (configuration BE-9) flaw profile before and after 144000 fatigue cycles; no change in flaw profile after four L-1011 fatigue lifetimes.

structures. Thus, the fatigue load spectrum exceeded the normal fuselage pressure stresses. In addition, high strain rates, that have been shown to be detrimental to a bonded doubler's performance [6], were incorporated into the fatigue tests. Because of these issues, the performance values cited here should be conservative.

17.4.2. Strain field measurements

Figure 17.6 shows a sample strain gage layout that was used to monitor: (1) the load transfer into the composite doublers and, (2) the strain field throughout the composite laminate and aluminum plate. The stress, strain, and load transfer values presented in this section provide additional insights into the doubler's ability to: (1)

resist crack initiation or mitigate crack growth, and (2) perform acceptably in spite of worst-case installations.

In general, it was observed that all strain responses from the simulated fuselage pressurization loads were linear. No residual strains were noted when the specimens were unloaded. Subsequent failure tests (see “Ultimate Strength” discussion below) showed that the strains induced by the fatigue load spectrum were well inside the linear elastic regime for the 2024-T3 aluminum and Boron-Epoxy composite materials.

The maximum doubler strains were found in the load transfer region around the perimeter (taper region) of the doubler. In all fatigue specimens, the strains monitored in this area were approximately 50% of the total strain in the aluminum plate. This value remained constant over four fatigue lifetimes indicating that there was no deterioration in the bond strength. The strain in the aluminum plate beneath the doubler is reduced in accordance with the strain picked up by the composite doubler. Despite large disbonds which affected approximately 1/3 of the critical load transfer region, the composite doublers were able to pick up the strains necessary to accomplishing their intended purpose of strain reduction and crack mitigation in the parent structure. This performance was achieved in spite of collocated flaw scenarios such as impact and disbond flaws which had been hot, wet conditioned (water absorption/ingress).

A sample of the strain fields in the fatigue test coupons – representing the hoop strains in an actual aircraft – can be seen in the series of curves shown in Figure 17.10. The maximum total axial strain in the aluminum plate (away from the doubler) was always around 3000 (for test load $P = 7300$ lbs.). Axial strains in the aluminum plate beneath the doubler were approximately 50% to 70% of this maximum value while axial strains in the composite doubler ranged from 30% to 50% of the total strain in the specimen. Figure 17.10 demonstrates that the load transfer is similar at the upper and lower tapered regions of the doubler (compare Ch. 18 and 30). The strain relief created by disbonds is evidenced by the low strains in Ch. 20 and 32. The large strains in gages immediately adjacent to the disbond (Ch. 18 and 30) demonstrate that the disbond effects are very localized. Strain reductions in the aluminum plate (compare Ch. 16 with Ch. 28) and the corresponding strain shedding into the doubler (Ch. 18 and 30) are evident. The doubler does not create excessive strain risers in the unreinforced aluminum immediately adjacent to the doubler (Ch. 92).

The complete set of strain field plots for all specimens in this study can be found in reference [2]. The similarity in strain fields among all damage tolerance fatigue specimens, including flawed and unflawed configurations, indicates that the relatively large disbond, delamination, and impact flaws produce only a localized effect on the doubler strains and have little effect on the overall performance of the doubler.

Effects of multiple fatigue lifetimes on strain fields

The NDI before-and-after results (see Figure 17.9 example) show that the initial “programmed” flaws did not change shape nor did any new flaws develop as a

result of the fatigue loads. Quantitatively, the strain gage values acquired before and after fatigue testing substantiate the NDI results. In each of the fatigue specimens, the vast majority of the strain field remained unchanged over the course of the fatigue tests. Several of the specimen configurations showed no change in strain levels from 0 fatigue cycles to 216,000 fatigue cycles. The only strain changes noted in any of the specimens occurred around the center crack growth area. In the specimens where crack growth grew beyond the perimeters of the implanted disbond flaw, strain changes were observed in the immediate area of the propagating crack. The results, however, highlight the ability of the composite doubler to pick up additional load in response to a loss of strength in the parent structure.

Stresses in aluminum plate and composite doubler

Strain data collected from the biaxial (axial and lateral) gages were used to calculate stresses in the composite doubler and parent aluminum skin. These

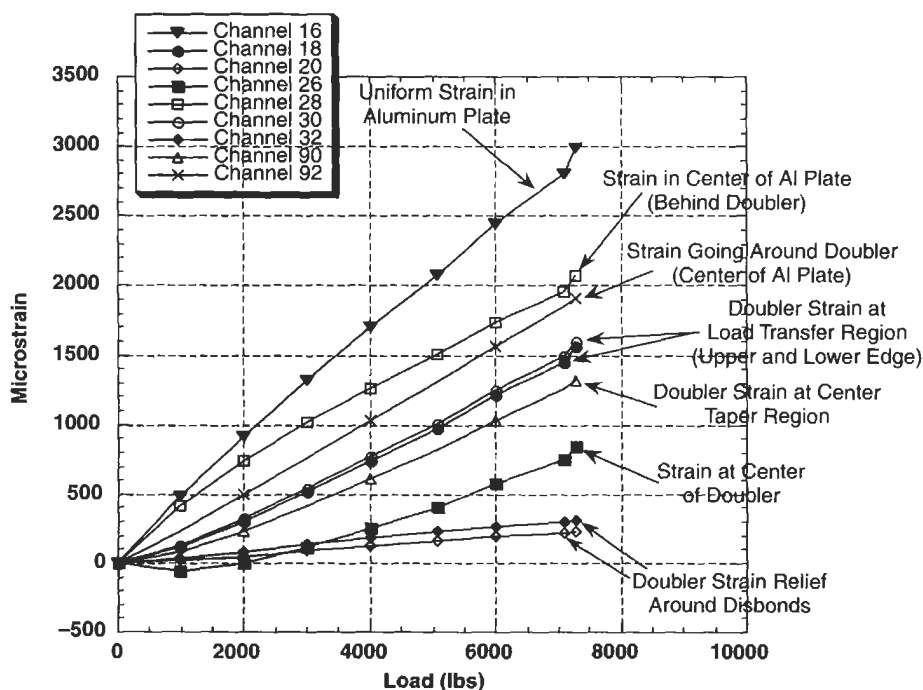


Fig. 17.10. Axial strain field in aluminum and composite for configuration BE-2 specimens (ref. strain gage locations shown in Fig. 17.6).

membrane stresses were determined using the following equations:

$$\sigma_a = \frac{E}{1 - \nu^2} (\varepsilon_a + \nu \varepsilon_l) , \quad (17.8)$$

$$\sigma_l = \frac{E}{1 - \nu^2} (\varepsilon_l + \nu \varepsilon_a) , \quad (17.9)$$

where E is the modulus of elasticity, ν is Poisson's ratio, σ_a is the axial stress in the skin, σ_l is the longitudinal stress in the skin, ε_a is the hoop strain, and ε_l is the longitudinal strain. From Mil-Handbook five, the modulus of elasticity and Poisson's ratio for 2024-T3 aluminum are: $E = 10.5 \times 10^6$ psi and $\nu = 0.33$, respectively. The properties of the Boron-Epoxy laminate are $E_x = 11.87 \times 10^6$ and $\nu = 0.32$.

Table 17.2 provides sample stress measurements from three of the specimen configurations. It shows that uniform stresses of 17 ksi, representing maximum hoop stresses during flight pressurization, or higher were achieved in the parent skin for each specimen configuration. Away from the fatigue crack, the maximum stresses in the aluminum beneath the doubler were roughly one-third the yield stress for 2024-T3. The maximum stresses in the composite doublers occurred at the edge of the doubler (load transfer region) and never exceeded 10 ksi. Stress risers near fatigue cracks, which normally amount to two or three times the uniform strain field away from the flaw, were essentially eliminated by the composite

Table 17.2

Stresses in aluminum and composite doubler at maximum fuselage pressure loads.

Spec. no. (config.)	Biaxial channels	Peak load (lbs)*	Stress at zero cycles (psi)	Stress after fatigue (psi)	No. of cycles	Location on test specimen
Lock1 (BE-1)	1, 2	5000	23010	22450	144000	Aluminum Away from Doubler
	5, 6	5000	3520	14350	144000	Doubler Near Flaw
	7, 8	5000	18410	No Data	144000	Aluminum Near Flaw
	9, 10	5000	4700	9510	144000	Doubler Center (full thickness)
	11, 12	5000	15359	1100	144000	Aluminum Center Beneath Doubler
	13, 14	5000	13340	10420	144000	Doubler Edge (upper taper region)
Lock2 (BE-2)	15, 16	6000	26200	26562	144000	Aluminum Away from Doubler
	17, 18	6000	14530	10900	144000	Doubler Edge (lower taper region)
	21, 22	6000	2270	5180	144000	Doubler Near Flaw
	23, 24	6000	25070	2510	144000	Aluminum Near Flaw
	25, 26	6000	6660	4180	144000	Doubler Center (full thickness)
	27, 28	6000	18840	19000	144000	Aluminum Center Beneath Doubler
	33, 34	4800	20780	20150	144000	Aluminum Away from Doubler
	35, 36	4800	10859	10875	144000	Doubler Edge (lower taper region)
Lock3 (BE-3)	39, 40	4800	-47	6030	144000	Doubler Near Flaw
	41, 42	4800	23280	22	144000	Aluminum Near Flaw
	43, 44	4800	3186	5310	144000	Doubler Center (full thickness)
	45, 46	4800	16760	1930	144000	Aluminum Center Beneath Doubler

* Load of 4800 lbs produces skin stress of 17 ksi – this corresponds to hoop stress at maximum L-1011 fuselage pressure levels.

doubler. The maximum aluminum stresses immediately adjacent to the fatigue cracks were less than, or in two cases approximately equal to, the uniform stress field outside the doubler. The columns in Table 17.2 comparing stresses before and after fatigue testing show that the doublers picked up additional stresses when the fatigue crack growth reduced the load carrying capacity of the parent aluminum (i.e. stress relief occurred in aluminum).

The Table 17.2 data for Specimen configuration BE-3 provides an excellent example of the increasing load picked up by the composite doubler as the aluminum crack propagates. At $N=0$ cycles, the stress at the center of the doubler (Ch. 43 and 44) amounted to 15% of the total stress in the aluminum plate. At $N=144000$ cycles, however, the stress the same region registered 30% of the total strain in the plate. The related reduction in plate stress can be seen by looking at the Ch. 45–46 before and after the fatigue tests (drop from 80% of total stress to less than 10% of total stress in plate). Note that stresses in the load transfer (tapered) region of the doubler remained unchanged at approximately 50% of the total stress in the aluminum skin. The stress results before and after fatigue testing indicate that: (1) the composite doublers were able to meet their design objectives and absorb additional load as required, and (2) the effects of crack growth was localized about the crack (i.e. the stress around the perimeter – especially in the critical load transfer region – remained unchanged).

Load transfer

Another way of studying the stress – strain data and inferring doubler performance is to calculate the load transfer (ratio between doubler strains and strains in corresponding portions of the aluminum parent skin: $\epsilon_{\text{doubler}}/\epsilon_{\text{alum(ref)}}$). A series of load transfer ratios were calculated for various doubler and aluminum reference channels. The results demonstrated that the load transfer into the doubler – and away from the aluminum – was similar in all fatigue specimens regardless of the type and degree of damage in the specimen. In the tapered portion of the doubler, the load transfer was consistently in the 50–60% range. In the center, where the doubler reaches its maximum thickness, the load transfer was in the 40–50% range. These values agree with general aircraft repair goals such that: (a) the doubler will possess the necessary crack mitigation capabilities, and (b) the doubler will not be so stiff as to draw added loads to the area and decrease the global fatigue life of the repair area. The spectrum of fatigue specimens ranged from unflawed (optimum installation) to large, collocated flaws (worst-case scenarios). However, the load transfer values were very consistent across the full spectrum of specimens despite the large variations in flaw scenarios. Furthermore, these load transfer values remained constant over four fatigue lifetimes. Once again, this indicates that there was no deterioration in the bond strength.

17.4.2.1. Static tension residual and ultimate strength tests

Residual tensile strength

Some of the specimens that were subjected to cyclic fatigue loads were subsequently tested to determine their static residual tensile strength. These were

not ultimate strength tests since the specimens were tested after flaws were engineered into the specimens and the implanted cracks were subsequently grown. By using the maximum load at failure and the original cross-section area at the start of the static residual strength test, the resulting residual tensile strength numbers are conservative. The measured residual strength numbers for the two configurations tested (BE-1 and BE-2) were 103 ksi and 88 ksi, respectively.

Figure 17.11 shows the strain field in specimen BE-2 up through failure. The aluminum plate away from the doubler (channel 16) began to yield at approximately 12000 lbs. while the doubler continued to increase its load in a linear fashion. This load/response process continued until failure occurred at 103 ksi and the specimen could no longer sustain an increasing load. Figure 17.11 illustrates that the composite doubler was able to transmit stresses in the plastic regime and that extensive yielding/loading beyond the initial yield level was required to fail the installation.

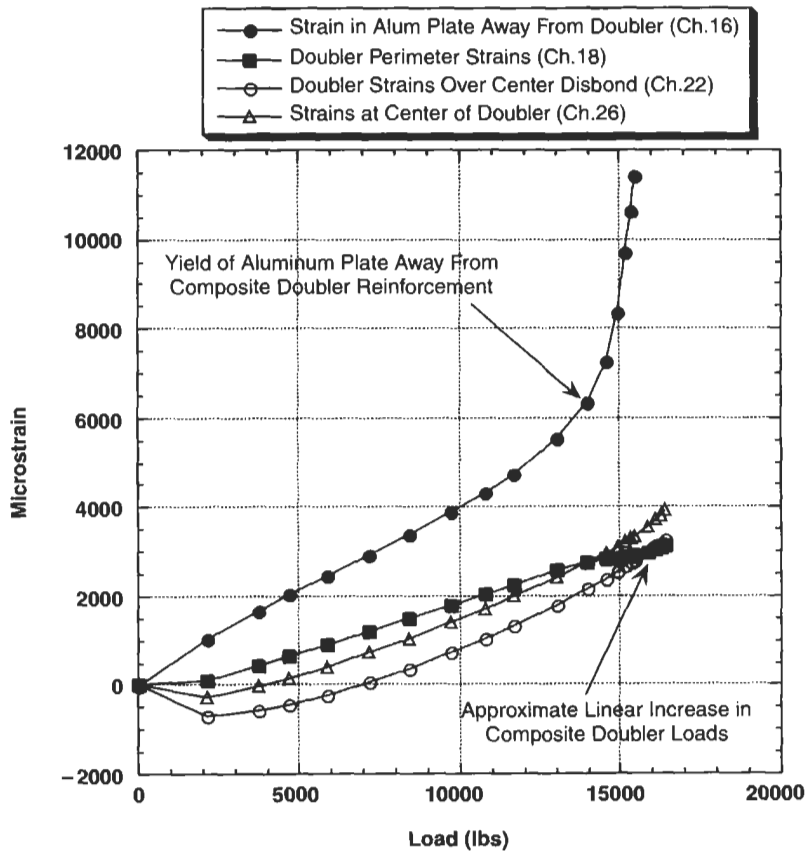


Fig. 17.11. Strain fields in composite doubler and aluminum plate during ultimate failure test (configuration BE-2).

Even in the presence of severe worst case installations (disbonds) and extensive damage growth (fatigue cracks extending through 50% of the specimen width), it was seen that the doubler-reinforced-plates were able to achieve residual tensile strengths (i.e. post-damage tensile strength) which exceeded the 70ksi Mil handbook listing for the ultimate tensile strength of 2024-T3 material. Thus, the Boron-Epoxy doubler was able to return the parent structure to its original strength (i.e. load carrying capability).

Ultimate tensile strength

Six specimens in the BE-8 and BE-9 configurations were subjected to ultimate tensile strength tests without prior fatigue loading. Although these specimens were not fatigued they did contain engineered flaws. Ultimate strength values are normally associated with test-to-failure on optimum, unflawed materials. Thus, these tests results are also conservative. To provide a basis of comparison, ultimate strength tests were also conducted on control specimens (unreinforced aluminum coupons) and baseline specimens (unflawed doubler installations). The ultimate strength values for each of the specimens tested was essentially the same regardless of the flaw scenario. Table 17.3 lists the ultimate tensile strength values obtained in this test series. Duplicate tests on similar specimens showed that the results were repeatable. The maximum scatter within a single specimen configuration was 1.9%. The maximum scatter across all of the ultimate strength results was 7.0%. These ultimate strength tests further demonstrated the ability of a Boron-Epoxy composite doubler to return a damaged aluminum structure to its original load carrying capacity.

Ultimate failure mode

Figure 17.12 shows a front view of a failed specimen from the BE-8 configuration. The implanted, 1" diameter disbond is clearly visible as is the stop

Table 17.3
Results from ultimate tensile strength failure tests.

Specimen configuration	Specimen number	Flaw summary	Ultimate tensile strength (psi) [†]
BE-6	6A*	No flaws	72570
BE-6	7A*	No flaws	72060
BE-7	9 ^Δ	Unflawed doubler installation	70530
BE-8	10	Impact/disbond doubler over a stop-drilled crack	75490
BE-8	11	Impact/disbond doubler over a stop-drilled crack	75480
BE-8	12	Impact/disbond doubler over a stop-drilled crack	75310
BE-9	16	Multiple impact/disbond flaws over an unabated crack	72450
BE-9	17	Multiple impact/disbond flaws over an unabated crack	73010
BE-9	18	Multiple impact/disbond flaws over an unabated crack	71680

[†]Mil-Hndbk-5 Value for 2024-T3 Aluminum = 70000 psi.

*Non-fatigued aluminum coupons without composite doubler.

^ΔPost-fatigue test but specimen was still unflawed.

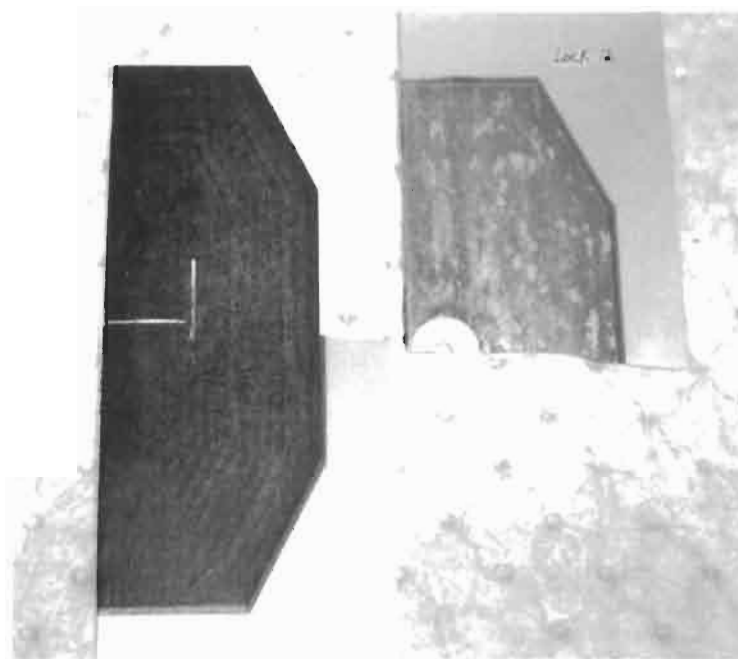


Fig. 17.12. Ultimate failure of BE-8 configuration (lock12) showing: (1) failure mode of the specimen, (2) fracture of the adhesive and (3) implanted disbond.

drilled crack. Each of the ultimate tensile strength tests produced the same failure mode which can be described as follows. Upon reaching the yield stress, the aluminum parent skin began to yield (ref. Figure 17.11). Initially, the yielding was primarily in the exposed, unreinforced area of the coupon. As the load was increased further, the aluminum beneath the doubler also began to yield and elongate. The yield zone traveled from the tapered edge of the doubler toward the center of the specimen. This caused the aluminum to sequentially pull away from the doubler which was not yielding or stretching at the same rate as the parent aluminum. The result was a rolling wave of cohesive failure in the adhesive layer. There was no disbond growth in the specimen as evidenced by the presence of adhesive on both the aluminum and mating composite doubler in Figure 17.12. Again, this indicates that the installation was successful and the full strength of the adhesive was achieved. During the course of the test it was possible to hear popping sounds corresponding to the fracture of the adhesive. When this cohesive failure (as opposed to adhesive, or disbond, failure) in the adhesive reached the center crack of the coupon, half of the aluminum plate was left without doubler reinforcement. At that point, the crack in the aluminum propagated rapidly across the entire width of the test specimen. Thus, the aluminum was severed in half, as shown in Figure 17.12, but the doubler remained in one piece.

17.5. Conclusions

One of the concerns surrounding composite doubler technology pertains to long-term survivability, especially in the presence of non-optimum installations. This test program demonstrated the damage tolerance capabilities of bonded composite doublers. The fatigue and strength tests quantified the structural response and crack abatement capabilities of Boron-Epoxy doublers in the presence of worst case flaw scenarios. The engineered flaws included cracks in the parent material, disbonds in the adhesive layer, and impact damage to the composite laminate. Environmental conditions representing temperature and humidity exposure were also included in the coupon tests.

General use of results

The objective of this damage tolerance analysis was to obtain a generic assessment of the ability of Boron-Epoxy doublers to reinforce and repair cracked aluminum structure. By designing the specimens using the nondimensional stiffness ratio, it is possible to extrapolate these results to various parent structure and composite laminate combinations. The number of plies and fiber orientations used in these tests resulted in an extensional stiffness ratio of 1.2:1 $\{(Et)_{BE} = 1.2 (Et)_{Al}\}$.

Summary of damage tolerance assessment in light of inspection requirements

Large strains immediately adjacent to the doubler flaws emphasize the fact that relatively large disbond or delamination flaws (up to 1" diameter) in the composite doubler have only localized effects on strain and minimal effect on the overall doubler performance (i.e. undesirable strain relief over disbond but favorable load transfer immediately next to disbond). This statement is made relative to the inspection requirement which will result in the detection of disbonds/delaminations of 0.5" diameter or greater. Obviously, disbonds will effect the capabilities of composite doublers once they exceed some percentage of the doubler's total footprint area. The point at which disbonds become detrimental depends upon the size and location of the disbond and the strain field around the doubler. This study did not attempt to determine a "flaw size vs. effect" relation. Rather, it used flaws which were twice as large as the detectable limit to demonstrate the ability of composite doublers to tolerate potential damage.

Similarly, the crack mitigation capabilities of Boron-Epoxy doublers were evaluated using crack sizes which exceeded the inspection threshold. The current inspection requirement calls for inspection intervals and sensitivity to detect cracks of 1" length. The damage tolerance tests presented in this document looked at crack growth beneath doublers of up to 3". The doublers were able to mitigate the crack growth by a factor of 20 versus the unrepaired aluminum. Test results showed that it would take two to three aircraft fatigue lifetimes (72000–108000 cycles) for a crack to propagate 1" beneath a reinforcing composite doubler. Finally, these tests showed that Boron-Epoxy composite doublers are able to achieve this performance level (i.e. reinforce and mitigate crack growth) even in the presence of extreme

worst-case flaw scenarios. This is the strongest evidence of the damage tolerance of bonded Boron-Epoxy doublers.

References

1. Roach, D.P. (1997). Results from FAA program to validate bonded composite doublers for commercial aviation use. *SAE Paper 972622, SAE Airframe Maintenance and Repair Conf.*, August.
2. Roach, D.P. (1998). Damage Tolerance Assessment of Bonded Composite Doubler Repairs for Commercial Aircraft Applications, Sandia National Laboratories/Dept. of Energy Report No. SAND98-1016, August.
3. Baker, A.A. (1997). Fatigue studies related to certification of composite crack patching for primary metallic aircraft structure. *FAA-NASA Symp. on Continued Airworthiness in Aircraft Structures*, Dept. of Transportation Report No. DOT/FAA/AR-97-2, I, July.
4. Fredell, R.S. (1994). Damage Tolerant Repair Techniques for Pressurized Aircraft Fuselages, Ph.D. Dissertation, Delft University.
5. Rice, R., Francini, R., Rahman, S., *et al.* (1993). Effects of Repair on Structural Integrity, Dept. of Transportation Report No. DOT/FAA/CT-93/79, December.
6. Jones, R., Chiu, C. and Paul, J. (1993). Designing for damage tolerant bonded joints. *Composite Structures*, **25**.
7. Chiu, W.K., Rees, D., Chalkley, P., *et al.* (1992). Designing for Damage Tolerant Repairs, ARL Aircraft Structures Report 450, August.
8. Roach, D.P. and Walkington, P. (1998). Development and Validation of Nondestructive Inspection Techniques for Composite Doubler Repairs on Commercial Aircraft Applications, Sandia National Laboratories/Dept. of Energy Report No. SAND98-1014, May.
9. Baker, A.A. and Jones, R. (1988). *Bonded Repair of Aircraft Structures*, Martinus Nijhoff Pub., The Netherlands.
10. Atluri, S.N., Park, J.H., Punch, E.F., *et al.* (1993). Composite Repairs of Cracked Metallic Aircraft Structures, Dept. of Transportation Report No. DOT/FAA/CT-92/32, May.
11. Fredell, R.S., van Barnveld, W. and Vlot, A. (1994). Analysis of composite crack patching of fuselage structures: high patch modulus isn't the whole story, *SAMPE Int'l. Symposium 39*, April.
12. Rose, L.R. (1987). Influence of disbonding on the efficiency of crack patching, *Theoretical Applied Fracture Mechanics*, **7**.
13. Baker, A.A. (1997). Growth characterization of fatigue cracks repaired with adhesively bonded boron/epoxy patches, *Proc. Of Int'l. Conf. Fracture, ICF-9*, April.
14. Rose, L.R. (1982). A cracked plate repaired by bonded reinforcements, *Int'l. J. of Fracture*, **18**.
15. Callinan, R.J., Rose, L.R. and Wang, C.H. (1997). Three dimensional stress analysis of crack patching, *Proc. of Int'l. Conf. Fracture, ICF-9*, April.
16. Rose, L.R. (1997). Design analysis and validation for a bonded composite repair to primary aircraft structure, *Proc. of Int'l. Conf. Fracture, ICF-9*, April.
17. Davis, M.J. (1995). A call for minimum standards in design and application technology for bonded structural repairs, *Int'l. Symp. on Composite Repair of Aircraft Structures in concert with ICCM-10*, August.
18. Fredell, R.S. and Marr, J. (1995). An engineering approach to the design and analysis of fuselage crack patching with the computer program calcurep for windows, *Int'l. Symp. on Composite Repair of Aircraft Structures in concert with ICCM-10*, August.
19. Xiong, X. and Raizenne, D. (1995). A design methodology and PC-based software for bonded composite repair in aircraft structure, *Int'l. Symp. on Composite Repair of Aircraft Structures in concert with ICCM-10*, August.
20. Roach, D.P. and Walkington, P. (1998). Full Scale Structural and NDI Validation Tests on Bonded Composite Doublers for Commercial Aircraft Applications, Sandia National Laboratories/Dept. of Energy Report No. SAND98-1015, November.

21. Roach, D.P. (2001). Commercial application of composite doublers for DC-10 fuselage repairs, *Int'l. SAMPE Symp. on Composites in Engineering*, May.
22. Jones, K.M. and Shah, S. (1996). Composite Repair – Upper Forward Corner of P-3 door – Model L-1011 Aircraft, Strength and Damage Tolerance Analysis, Report No. LG95ER0157, Part of Documentation Package for FAA Atlanta Aircraft Certification Office Project No. SP1798AT-Q, analysis plan December 1995, final report October.
23. Schweinberg, W., Jansen, R. and Fiebig, J. (1995). Advanced composite repairs of the C-141 wing structure, *Int'l. Symp. on Composite Repair of Aircraft Structures in concert with ICCM-10*, August.
24. Klemczyk, C. and Belason, E.B. (1994). Analysis of Maximum Stresses Associated with a Boron/Epoxy Doubler Bonded to Aluminum, Boeing Report under contract 6-1171-10A3397R4, January.
25. Berg, S.D. (1995). Process Specification for the Fabrication and Application of Boron-Epoxy Doublers onto Aluminum Structures, Textron Specialty Materials Specification No. 200008-001 (may also be referenced as the Boeing Specification D658-10183-1 which was written for Textron), dated 30 November, Textron Specialty Materials, Lowell, MA, 01851.
26. Walkington, P. and Roach, D. (1997). Ultrasonic Inspection Procedure for Bonded Boron-Epoxy Composite Doublers, Sandia Labs AANC Specification AANC-PEUT-Comp-5521/4-004, Sandia National Laboratories, Albuquerque, NM; also included in FAA Document SNL96ER0007 under Atlanta ACO Project SP1798AR-Q, FAA approval January.

Chapter 18

VALIDATION OF STRESS INTENSITY ESTIMATIONS IN PATCHED PANELS

B. AKTEPE and A.A. BAKER

Defence Science and Technology Organisation, Air Vehicles Division, Fishermans Bend, Victoria 3207, Australia

18.1. Introduction

The design models used to estimate the Mode I stress intensity K_I in patched panels are based on analytical or finite element approaches [1]. Initially to validate these models, studies were made to correlate the predicted K_I with observed fatigue crack-growth behaviour, based on an assumed Paris-type relationship for crack-growth rate. These studies were focused on Rose's analytical crack-patching model and fatigue results obtained from an edge-notched panel specimen [2] as described in Chapter 13.

Figure 18.1(a) depicts the edge-notched specimen fatigue tested under constant load amplitude and Figure 18.1(b) plots $\log da/dN$ versus $\log \Delta K$ predicted using Rose's model [3], where a is the crack length, N the number of cycles and K the stress intensity. These and other results [2] help to validate that this approach is a practical method for predicting ΔK in simple cracking geometries.

However, these fatigue experiments, whilst providing a useful validation of the models for practical application, are indirect, inaccurate, because of the use of log plots and subject to the influence of several variables. There is therefore a need to obtain a more direct validation of the design models. Thus, as described in this Chapter, an experimental approach is described in which K_I is directly measured using either conventional strain gauges or special K -gauges for a similar edge-notched specimen.

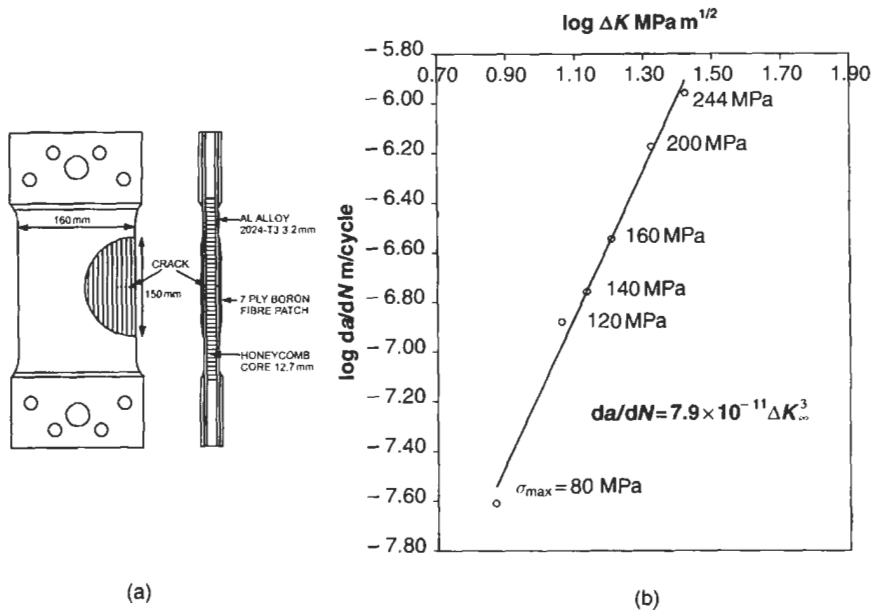


Fig. 18.1. (a) Generic structural detail test specimen for patched cracks in metallic structures used to validate the patching model and (b) plot of experimental log da/dN versus log ΔK , obtained from Rose's analytical patching model.

18.2. The K -gauge

Based on the fact that the stress intensity factor can be obtained by measuring the stress distribution around a crack tip, a specially patterned foil strain gauge called the K -gauge was developed by Kondo [4].

The K -gauge consists of four grids concentrically located about the crack tip. The outer grid on either side of the crack has elements that are perpendicular to the crack line as shown in Figure 18.2. These are used to measure the average strain in the vertical direction and hence K_I . The inner grid on either side of the crack has elements which are parallel to the crack line and these measure the average strain in the horizontal direction and hence K_{II} .

18.2.1. K -gauge equations

As described by Miyake et al. [5], the vertical elements of the K -gauge are used to measure the Mode I stress intensity factor K_I , where the average strain is the elongation divided by the gauge element length. From the outer elements on either side of the crack tip, numbered one and two, strains ϵ_1 and ϵ_2 are obtained which

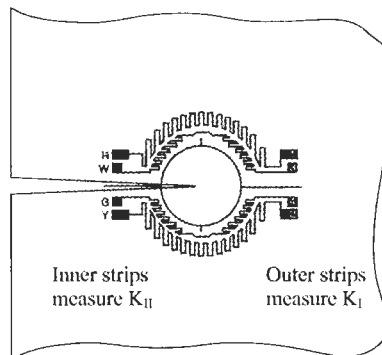
Fig. 18.2. Schematic diagram of the K -gauge.

Table 18.1

Values of c_1 for Eq. 18.1 (for an aluminium alloy with $E = 70.4$ GPa, and $\nu = 0.3$)

a [mm]	c_1 [kg.mm ^{-1.5}]
5	1.53
10	1.70
16	1.81
20	1.86
25	1.90
30	1.94

are related to K_I as follows:

$$K_I = c_1(\varepsilon_1 + \varepsilon_2) \quad (18.1)$$

The coefficient c_1 is derived empirically and is found to depend on the Young's modulus, E , the Poisson's ratio, ν , of the material being used, and the crack length. Miyake has obtained values for this constant (shown in Table 18.1) for an aluminium alloy with a Young's modulus of 70.4 GPa and a Poisson's ratio of 0.3, hence these values of c_1 are used here.

18.3. Theory of K_I measurement using strain gauges

18.3.1. Westergaard equations

To enable the use of individual strain gauges, a mathematical relationship is required which relates the strains to the stress intensity factor. The relationship

used here is obtained from the Westergaard equations [6] which are a suitable means of mathematically representing the strains in the vicinity of the crack tip.

It can be shown that for a rotated coordinate system with strain gauges aligned at an angle α from the crack centre line, as shown in Figure 18.3, K_I may be expressed in terms of the product of the shear modulus, G , and the radial strain, $\varepsilon_{x'x'}$:

$$K_I = \sqrt{8\pi r} G \varepsilon_{x'x'} \left\{ \begin{array}{l} (k - k^3) \sqrt{\frac{1}{1 - k^2}} \\ - \frac{1}{4} k \cos \left[5 \tan^{-1} \left(\frac{k}{\sqrt{1 - k^2}} \right) \right] \\ + \frac{1}{4} \sqrt{1 - k^2} \sin \left[5 \tan^{-1} \left(\frac{k}{\sqrt{1 - k^2}} \right) \right] \end{array} \right\}^{-1}, \quad (18.2)$$

where

$$k = \frac{1 - \nu}{1 + \nu} \quad (18.3)$$

For the 2024-T3 aluminium plate used in these experiments, the Young's modulus, E , equals 72 GPa, the shear modulus, G , equals 27 GPa, and the Poisson's ratio, ν , is 1/3. Hence:

$$k = \frac{1}{2} \Rightarrow K_I = \frac{16}{3} \sqrt{\frac{2\pi r}{3}} G \varepsilon_{x'x'}, \quad (18.4)$$

and using the ratio of moduli for 2024-T3 aluminium, $G/E = 3/8$, leads to the result:

$$K_I = \sqrt{\frac{8\pi r}{3}} E \varepsilon_{x'x'} \quad (18.5)$$

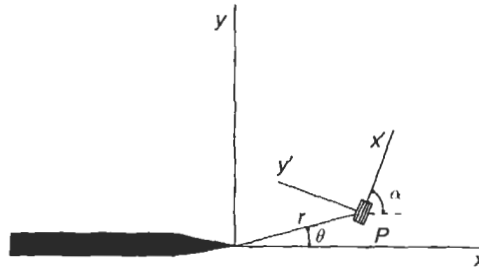


Fig. 18.3. Rotated axis system used for the strain-gauge approach.

18.3.2. Rose's inclusion model for stress intensity

Very briefly Rose's model [3] is based on a two-stage analysis. In the first stage the reduction of stress caused by the patch or reinforcement bonded to an uncracked plate is estimated. The reinforcement is modelled as a stiff inclusion. In the second stage a semi-infinite crack is assumed to exist, fully covered by the reinforcement. The energy release rate G is then estimated for an incremental growth of the crack.

The net result is that the stress intensity in the patched structure is given by the equation:

$$K_R = \sigma_0 \sqrt{\frac{\pi a \Lambda}{a + \Lambda}}, \quad (18.6)$$

$$\text{where } \pi \Lambda = \frac{1 + 1/S}{\beta} \left(= \beta E_p t_p \frac{t_A}{G_A} \right), \quad (18.7)$$

$$\text{and } \beta^2 = \frac{G_A}{t_A} \left(\frac{1}{E_p t_p} + \frac{1}{E_R t_R} \right), \quad (18.8)$$

σ_0 is the reduced stress in the plate at the prospective location of the crack, and is directly proportional to the applied stress. The constant of proportionality depends on the size, shape and elastic properties of the patch. S is the stiffness ratio of the patch to the plate, Λ is the characteristic crack length, and a is the crack length.

The upper bound for the stress intensity factor is given by the familiar equation:

$$K_{\infty} = \sigma_0 \sqrt{\pi \Lambda} \quad (18.9)$$

18.3.3. Wang's crack-bridging model

A somewhat different approach to the analysis of repaired cracks under in-plane mixed mode loading was developed by Wang and Rose [7]. The model termed the crack bridging model was developed based on a characteristic spring constant, κ , that is a function of the shear transfer length, stiffness ratio and the Poisson's ratio.

The stress intensity factor of a reinforced plate as predicted by the crack-bridging model is given by

$$K_R = \frac{\sigma_0}{\sqrt{\kappa}} \sqrt{\tanh \frac{\pi \kappa a}{1 + 0.345 \pi \kappa a}}, \quad (18.10)$$

where the characteristic spring constant is given by

$$\kappa = \frac{1}{\pi \Lambda} \quad (18.11)$$

18.4. Experimental procedure

To determine whether the method of using individual strain gauges was applicable to this study, a number of static tests were conducted on unpatched 2024-T3 specimens with a crack length of 10 mm. Since the stress intensity factor is jointly proportional to the square root of the distance and the radial strain, a number of strain gauges were radially placed at angles of 60° (as shown in Figure 18.4). A suitable uniform strain region to place these gauges was determined using a thermal imaging technique [8].

The degree of undesirable curvature in the specimen was also examined using the same thermal imaging technique. Thermal scans of both sides revealed only a small curvature that could easily be tolerated.

The patched specimen used in the test program was a 2024-T3 specimen with the same dimensions as the previous unpatched specimen. Boron/epoxy patches of 150 mm diameter were cocured with epoxy-nitrile film adhesive FM73 and then bonded by using the same adhesive onto the inside face of each aluminium plate.

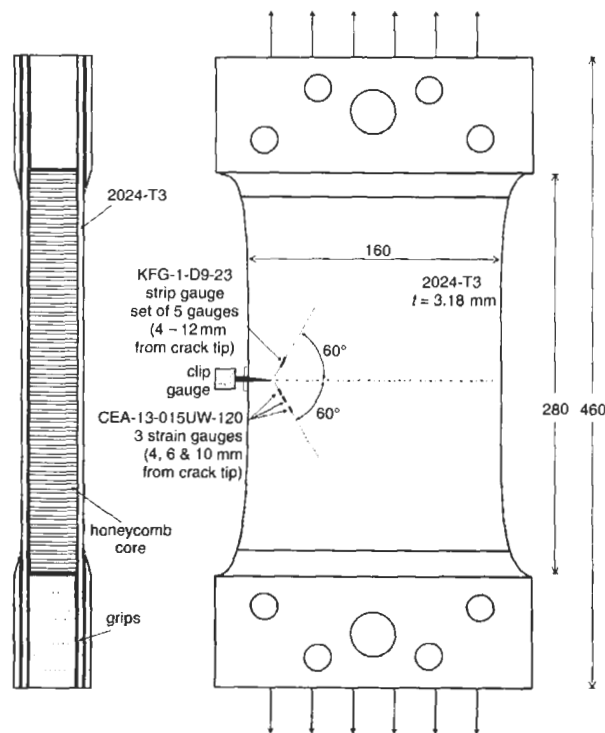


Fig. 18.4. Unpatched 2024-T3 specimen showing strain gauge locations for a crack with length $a = 10$ mm.

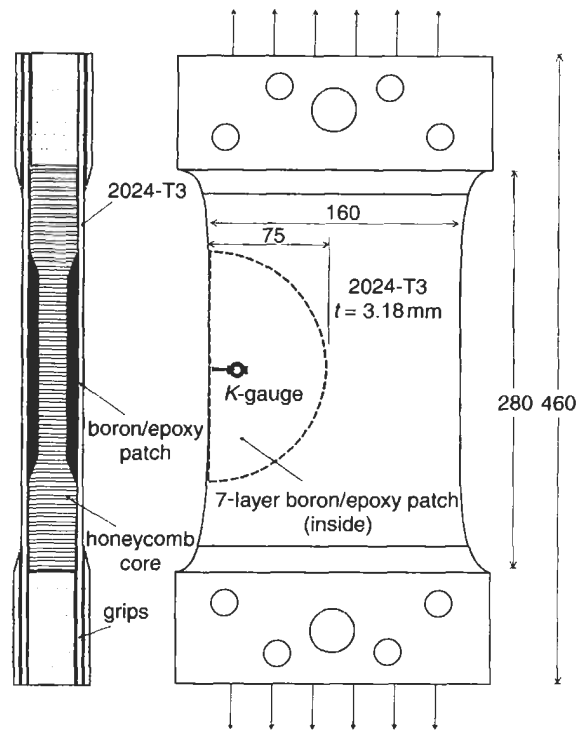


Fig. 18.5. Patched 2024-T3 specimen showing location of K-gauge for a crack with length $a = 10$ mm.

Bonding of the patches to the inside allows the cracks to be monitored during fatigue cycling, while also allowing the areas in the immediate vicinity of the crack tip to be instrumented. This patched specimen is shown in Figure 18.5.

The patches were bonded to the panels at the same time as the panels were bonded to the honeycomb core (i.e. cocured) (a) to minimise curvature due to thermal expansion mismatch with the patch and (b) to minimise the amount of secondary bending under load.

Testing was conducted on these specimens in the following combinations:

- (a) Unpatched specimen with crack length of 10 mm
- (b) Patched specimen with crack length of 10 mm
- (c) Unpatched specimen with crack length of 30 mm
- (d) Patched specimen with crack length of 30 mm.

Static tests on the specimens for positive loads were conducted up to 80 kN and for temperatures ranging from room temperature (20 °C) up to 100 °C.

The assumed properties of the materials and adhesive used in the experiments are shown in Tables 18.2 and 18.3.

Table 18.2
Assumed properties of the materials (from [2]).

	t [mm]	E [GPa]	G [GPa]	α [$^{\circ}\text{C}$]
2024-T3	3.14	72	27	23×10^{-6}
boron/epoxy	0.90	200	10	4×10^{-6}

Table 18.3
Assumed properties of the adhesive (from [2]).

	Temperature			
Adhesive properties	20 $^{\circ}\text{C}$	60 $^{\circ}\text{C}$	80 $^{\circ}\text{C}$	100 $^{\circ}\text{C}$
G [GPa]	0.57	0.25	0.17	0.11
τ [MPa]	36	16	12	8

18.5. Strain surveys

18.5.1. Unpatched specimen

For the unpatched specimen with a crack length of 10 mm, static tests were carried out at various temperatures, and radial strain was measured at 60° to the crack centre line at a distance of 6 mm from the crack tip. Stress intensity factors were calculated using Eq. (18.5). These results compared favourably with theoretical values calculated using the standard equation to determine K_I for an edge-crack [9] for an applied stress of 78.6 MPa. The results shown in Table 15.4 are in agreement with the theoretical value of $15.60 \text{ MPam}^{1/2}$, for a crack length of 10 mm, to within 5%, as shown by the numbers in brackets in the table.

These results demonstrate the validity of using a single strain gauge to determine the stress intensity factor for an unpatched specimen.

Table 18.4
Stress intensity factors determined using a single strain gauge aligned at 60° on an unpatched specimen with gauges located 6 mm from the crack tip.

Temp $^{\circ}\text{C}$	Experimental K_I
20	15.78 (1.2%)
40	15.65 (0.3%)
60	15.87 (1.7%)
80	16.27 (4.3%)

18.5.2. Patched specimen

A patched specimen was also instrumented with a single strain gauge at 6 mm from the crack tip with a radial sensing direction along the 60° line to the crack tip. In addition, a K -gauge was bonded to this specimen with the centre of the gauge being placed directly over the crack tip. As for the unpatched specimen, tests were conducted at temperatures up to 80°C .

To enable comparison to be made with theoretical results, plots of experimental and theoretical results are shown in Figure 18.6.

This figure shows firstly that the shapes of the experimental curves are different from the theoretically predicted curves. While both Wang and Rose predict a more-or-less linear increase in K_I with temperature, experiment indicates the existence of a fairly strong parabolic relationship.

It can be seen that the estimate of K_I based on the Rose equations at the lower temperatures agreed (to within 10%) with measurements taken from both the individual strain gauge at 6 mm from the crack tip and the K -gauge. However, at high temperature (80°C), the individual strain gauge overestimated the theoretical K_I by 15%. It can also be seen that the K -gauge underestimated theoretical values by up to 10% at the lower temperatures; however, it agreed well with the predictions at the high temperatures. Overall, considering the uncertainty in the adhesive properties used as input into the theoretical models, agreement with Rose's equations is reasonable.

The Rose–Wang crack-bridging model [7] yields K_I values 12% higher than those predicted by the Rose equations for this crack length at ambient temperature.

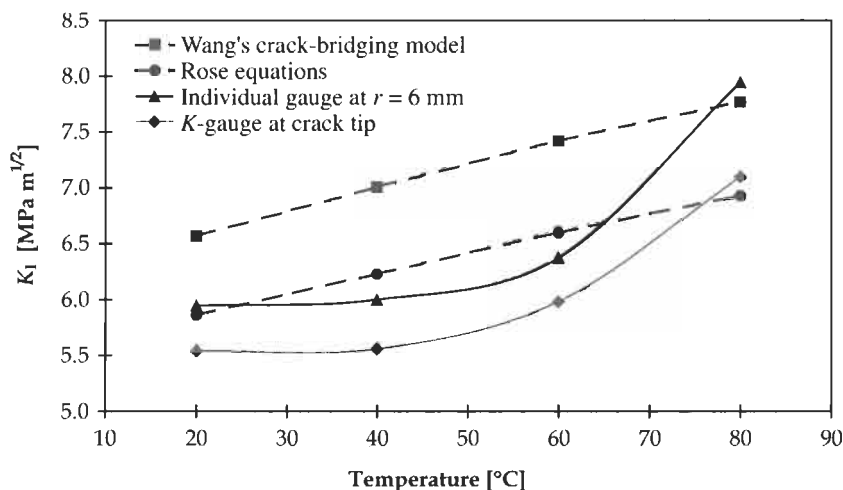


Fig. 18.6. Comparison of theoretical results for K_I from Rose's equations with measured values as a function of temperature (for $a = 10\text{ mm}$)

18.6. Crack length

Tests using only a K -gauge were conducted on a patched specimen at a crack length of 30 mm to check further the validity of the equations against the experimental results.

For a patched specimen, the Rose equations predict an increase in K_I from 5.86 to 6.77 $\text{MPa m}^{1/2}$ at 20 °C (for an applied stress of 78.6 MPa). Wang's model predicts an increase from 6.57 to 7.23 for an increase in the crack length from 10 mm to 30 mm for the same temperature, as shown in Figure 18.7. The standard value of K_I for a side edge-crack on an unpatched specimen with a nominal stress of 78.6 MPa is 27.03 $\text{MPa m}^{1/2}$. Note that the upper-bound estimate is quite good for crack lengths $a < 20$ mm, particularly for the Rose–Wang Model.

The results obtained using the K -gauge are shown in Table 18.5 and plotted in Figure 18.8. This figure shows that good agreement can be obtained with Rose's model at temperatures up to around 80 °C at $a = 30$ mm. However, poor agreement is obtained at temperatures over 80 °C where the patch is seen to become ineffective in reducing the stress intensity.

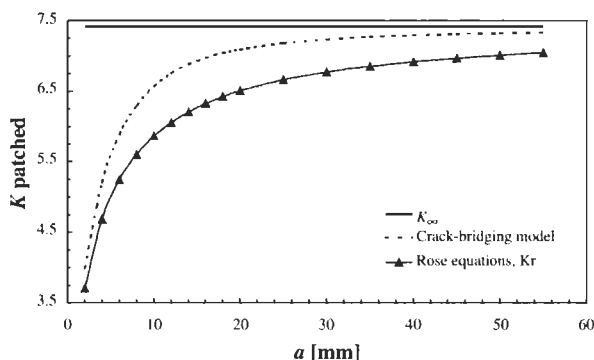


Fig. 18.7. Predicted variation of stress intensity K_I with crack length at 20 °C.

Table 18.5

K_I measurements using a K -gauge, on a patched specimen with $a = 30$ mm. (Note the Wang model predicts K_I to be 8% higher than the Rose model for $a = 30$ mm.)

Temp [°C]	Theory (Rose)	Experiment	Relative difference
RT	6.78	6.72	−1%
40	7.24	7.07	−2%
60	7.99	7.57	−5%
80	8.59	9.27	8%
90	8.93	14.00	57%
100	9.27	21.05	127%

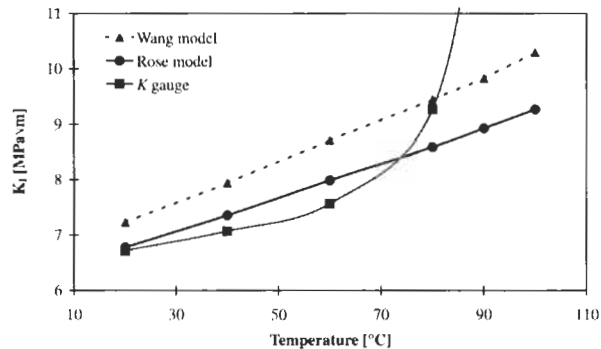


Fig. 18.8. Comparison of experimental and theoretical results for K_I for $a = 30$ mm, patched specimen.

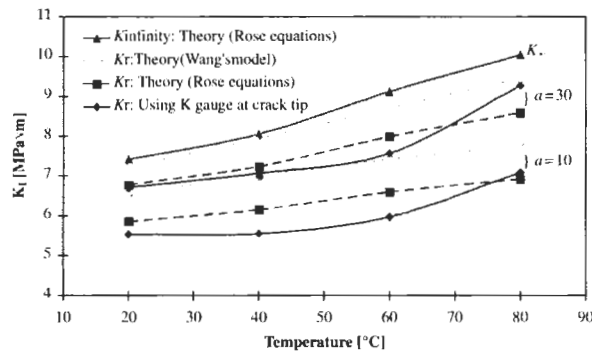


Fig. 18.9. Plots of results of K_I for a patched specimen for crack lengths of 10 and 30 mm, compared to predictions from Rose's equations.

Finally, for both crack lengths of 10 and 30 mm, Figure 18.9 shows that the Rose equations quite agree well with the K -gauge measured stress intensity factor, up to temperatures of about 75°C .

Since the rate of crack growth, da/dN , in patched panels is proportional to the stress intensity factor, the sharp rise in the K_I around approximately 80°C will be expected to lead to an acceleration in crack growth. This finding can be compared with fatigue results [2] that showed da/dN to increase only slightly at 80°C , Figure 18.10.

18.7. Time-dependent behaviour

Further tests were conducted at temperatures between 80 and 100°C to investigate time-dependent behaviour on patching efficiency. As before, the patched specimen with the 30 mm crack and the K -gauge were used. Each channel of the K -gauge and strain gauges was wired up to a data acquisition system and the

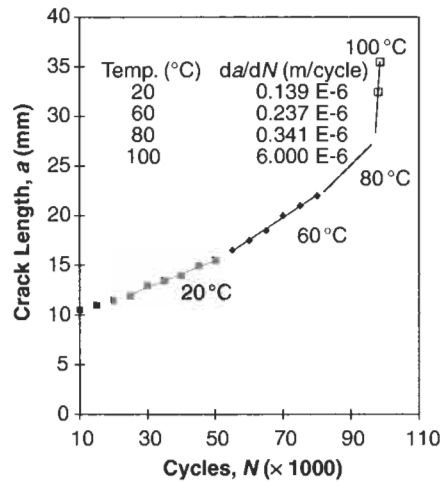


Fig. 18.10. Plot of crack length versus cycles at various temperatures, taken from reference [2], see also Chapter 13.

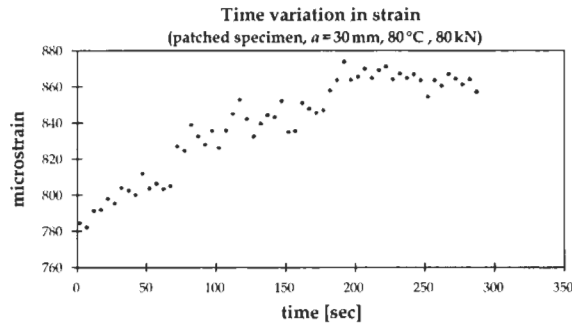


Fig. 18.11. Plot of strain versus time in a patched specimen with a 30-mm crack length (at 80°C and 80 kN).

sampling rate was set to 2 Hz. Strain data were recorded in applied stress increments of approximately 20 MPa up to 78.2 MPa.

The time dependency shown in at 80°C is for one channel of the K -gauge, whereby the strain over a period of approximately 3 minutes increases by over 10%. This behaviour was seen on both channels measuring ϵ_1 and ϵ_2 and it results in an increase in K_I of about 10%.

The time-dependent behaviour observed is almost certainly associated with stress relaxation or creep of the FM73 adhesive even though short-term properties are reasonable at this temperature, Table 18.3.

This observation of time dependency explains the fairly dramatic increase in K_I at 80°C, shown in Figure 18.11. However, as shown in Figure 18.10, the dramatic increase in K_I did not occur until 100°C for the fatigue test. The reason probably

being that in the fatigue tests the strain rate was quite high, since load cycles were applied at around 3 Hz so the adhesive would have much less time to creep or relax than in the static tests. Building these time-dependent effects into the patching models will be quite complex. A more desirable approach being to use more creep-resistant adhesives if a significant proportion loading of the repair occurs at elevated temperature.

18.8. Conclusions

The findings of the study described in this Chapter may be summarised as follows:

1. **Determination of K_I using individual strain gauges:** It was found that, with accurate placement and orientation of individual strain gauges of very small gauge length, K_I could be determined to within 5%. There were difficulties in deciding the precise distance from the crack tip to place the strain gauges. In these experiments thermal imaging techniques provided guidance.
2. **Determination of K_I using K -gauge:** The K -gauge was found to be sufficiently accurate for predicting the stress intensity factor in the patched specimen, when compared with the single gauge. At low temperatures, the K -gauge underestimated the single gauge values by about 10%.
3. **Comparisons with the models:** The functional relationship for the measured and theoretically predicted K_I as a function of temperature differed from that predicted by the models. At the lower temperature, measured and predicted values agreed reasonably well. However, at high temperatures the adhesive softened and models (using available data for the adhesive) could not predict the observed result. In all cases studied, it was found that the crack-bridge model predicted K_I values somewhat greater than the Rose model. The K -gauge measured values closer to those predicted by the Rose model.
4. **Time-dependent behaviour of FM73 adhesive at elevated temperature:** Significant time-dependent increases in K as a result of adhesive softening commenced at temperatures around 80°C. This is about 10°C lower than the fatigue test results had shown, suggesting that creep or relaxation of the adhesive was less at the higher rate of loading in the fatigue test.

18.9. Nomenclature

a	Crack length	S	Stiffness ratio of reinforcement to plate
N	Cycles	T	Temperature
c_1	K -gauge strain coefficient	t	Thickness
E_p	Young's modulus of plate	α	Coefficient of thermal expansion
E_R	Young's modulus of reinforcement	β	Reciprocal of the load transfer length

G	Shear modulus	ε	Strain
κ	Characteristic spring constant	Λ	Characteristic crack length
K_I	Mode I stress intensity factor	ν	Poisson's ratio
K_∞	Upper bound estimate of stress intensity factor	σ	Stress
r	Distance from crack tip to strain gauge		

References

1. Baker, A.A. and Jones, R. (eds). (1988). *Bonded Repair of Aircraft Structures*, Martinus Nijhoff Publishers, Dordrecht.
2. Baker, A.A. (1996). Fatigue studies related to certification of composite crack patching for primary metallic structure. *Proc. of the FAA/NASA Symp. on Continued Airworthiness of Aircraft Structures*, Atlanta, USA.
3. Rose, L.R.F. (1988). Theoretical analysis of crack patching, Chapter 6 in *Bonded Repair of Aircraft Structures*, (A.A. Baker and R. Jones, eds.) Martinus Nijhoff, pp. 107–173.
4. Kondo, Y. (1988). Stress intensity factor measurement in service condition using “K-gauge”. *VI Int. Congress on Experimental Mechanics*, Portland, Oregon, June 6–10.
5. Miyake, S., Nawa, Y., Kondo, Y., *et al.* (1989). Application of the “K-gauge” to Aircraft Structural Testing. *Proc. of ICAF*, Jerusalem.
6. Westergaard, H.M. (1939). Bearing pressures and cracks. *J. of Applied Mechanics*, pp. A-49–53.
7. Wang, C.H. and Rose, L.R.F. (1998). Bonded repair of cracks under mixed mode loading. *Int. J. of Solids*, **35**, pp. 2748–2773.
8. Ryall, T.G. and Wong, A.K. (1995). Design of a focal-plane array thermographic system for stress analysis. *Experimental Mechanics*, **35**, June, pp. 144–147.
9. Broek, D. (1986). *Elementary Engineering Fracture Mechanics*, Martinus Nijhoff Publishers, Dordrecht.

Advances in the Bonded Composite Repair of Metallic Aircraft Structure

The availability of efficient cost-effective technologies to repair or extend the life of aging military airframes is becoming a critical requirement in most countries around the world, as new aircraft become prohibitively expensive and defence budgets shrink. To a lesser extent a similar situation is arising with civil aircraft, with falling revenues and the high cost of replacement aircraft.

Fortunately a repair/reinforcement technology based on the use of adhesively bonded fibre composite patches or doublers can provide cost-effective life extension in many situations.

From the scientific/engineering viewpoint, this technology, although simple in concept, can be quite challenging, particularly when used to repair primary structure. This is because it is based on interrelated inputs from the fields of aircraft design, solid mechanics, fibre composites, structural adhesive bonding, fracture mechanics and metal fatigue. The technologies of non-destructive inspection (NDI) and, more recently smart materials, are also included. Operational issues are equally critical, including airworthiness certification, application technology (including health and safety issues) and training.

Most of these issues and the latest developments are discussed in this book, which contains contributions from leading experts in this technology from Canada, UK, USA and Australia. Most importantly, the book contains real case histories of application of the technology to both military and civil aircraft.

The cover picture is an Australian F-111 Aircraft, showing, schematically, a boron/epoxy repair patch applied to lower wing skin. Details of the region inside the wing where fatigue cracks develop are shown in the sketch. This repair is described in Chapter 27.

ISBN 0 08 042699 9



9 780080 426990